The University Of Sheffield.

Relationships between stability, structure, and energy density of nitrogen-rich Group 14 coordination compounds

By:

Rory Campbell

A thesis submitted in fulfilment of the requirements for the degree of Doctor of Philosophy

The University of Sheffield
Faculty of Science
Department of Chemistry

September 2016

Relationships between stability, structure, and energy density of nitrogen-rich Group 14 coordination compounds

Rory Campbell

Abstract

Two established methods for the stabilisation of polyazido complexes are incorporation into salts with bulky cations, or the use of neutral Lewis base ancillary ligands. Both methods reduce the sensitivity of the compound by 'diluting' the nitrogen content and inhibiting dissociation into the sensitive binary azide. The existing synthetic principles for the preparation of group 14 azides, $(PPN)_2[E(N_3)_6]$ and $E(N_3)_4(L_2)$, (E = Si, Ge), have been adapted, and applied to the synthesis of the first charge-neutral adducts of tin tetraazide, $Sn(N_3)_4(bpy)$ and $Sn(N_3)_4(phen)$. The adducts $Sn(N_3)_4(py)_2$ and $Sn(N_3)_4(pic)_2$ have been prepared by a new synthetic route involving reaction of SnF_4 with trimethylsilyl azide using the corresponding pyridine as solvent. A new method has been developed for the preparation of tin(II) azides from tin(II) fluoride and trimethylsilyl azide at ambient temperature. The adducts $Sn(N_3)_2(py)_2$ and $Sn(N_3)_2(pic)_2$ were obtained when the reaction was carried out in the corresponding pyridine solution, and guanidinium triazidostannate was obtained in the presence of guanidinium azide in acetonitrile. This triazidostannate salt has an extensively hydrogen bonded structure, and the simple pyridine adducts suggest the kinetic stabilisation afforded by bulky ligands employed previously is not mandatory for isolation of tin(II) azides. The nitrogen-rich salt guanidinium triazidostannate, and charge-neutral monodentate pyridine-based adducts of tin(II) azide have been fully characterised. A new method for synthesis of tin(II) azide from $Sn(N_3)_2(py)_2$ enables a tenfold reduction of reaction time, and avoids the use of silver azide or the need for anhydrous ammonia as solvent, which posed additional hazards in the recently published redox-based synthesis of tin(II) azide. The material afforded by the new method was crystalline, whereas only amorphous $Sn(N_3)_2$ was obtained previously. This enabled investigation of the solid state structure of the highly sensitive explosive, tin diazide, by a combination of Rietveld refinement of powder XRD data and complementary DFT calculations. The tin centre is pentacoordinate with a 3D framework given by 1,1-bridging azide ligands between adjacent $Sn(N_3)_2$ units in the *c*-axis direction, and a longer 1,3-bridging in the *b*-axis direction. The preparation of an array of nitrogen-rich tin polyazides, and their thermal characterisation has shown that tin(IV) azides are significantly more stable than their analogous tin(II) complexes, and confirmed the correlation of energy content with nitrogen content. To understand whether hydrogen bonds can confer a similar level of stability upon

polyazido complexes, the syntheses of some main group polyazido complexes with guanidinium counter ions were investigated. The lack of information available on the nitrogen-rich guanidinium azide and aminoguanidinium azide precursors prompted investigation of their syntheses, and the compounds were fully characterised by infrared (FTIR) and nuclear magnetic resonance (NMR) spectroscopies, and thermal analyses (DSC and TGA), and their structures were determined by single crystal X-ray diffraction (XRD). New salt-like compounds, $(G)_2[Sn(N_3)_6]$ and $(PPN)_2[Sn(N_3)_6]$, G = guanidinium, PPN = bis(triphenylphosphine)iminium, have been prepared and fully characterised, enabling the comparison of the structure and properties of the hexaazidostannate anion in the presence and absence of hydrogen bonds. Preparation of other nitrogen-rich salts $(AG)_2[E(N_3)_6]$, AG = aminoguanidinium, E = Si, Sn, and $(G)_2[Si(N_3)_6]$, and $(G)[P(N_3)_6]$ was attempted by extension of established procedures for the corresponding PPN salts. FTIR spectroscopic evidence for the formation of these nitrogen-rich polyazido complexes in solution are presented. The crystal structures of the side products guanidinium sodium azide, $Na_{0.33}(G)_{0.67}N_3$, and diazido(guanidinyl)(oxido)phosphorus(V), $[P(=O)(N_3)_2\{NC(NH_2)_2\}]$, were determined by single crystal X-ray diffraction. Guanidinium tetrazolate was synthesised for the first time from guanidinium carbonate and 1*H*-tetrazole, as it is a precursor to nitrogen-rich main group polytetrazolato complexes, and its crystal structure was determined by single crystal XRD. First and second level graph sets have been assigned to the complex 3D networks of hydrogen bonds in the structures of these nitrogen-rich salts. In an effort to go a step beyond intermolecular forces, the synthesis of 2,4,6-tris(tetrazol-1-yl)-1,3,5-triazine (TTT) was attempted, as it is a potential precursor to a novel ‘polymeric’ energetic compound by pressure-induced polymerisation.

Acknowledgements

This work was facilitated by a research studentship of the E-Futures Doctoral Training Centre based at the University of Sheffield, which was funded by the EPSRC and UKERC.

I would like to thank Dr. Peter Portius for helping the development of my laboratory and professional skills, maintaining a positive and inquisitive attitude throughout, and for being available and willing to provide advice and support from start to finish. This project would not have been possible without these efforts.

I gratefully acknowledge the work of Sumit Konar (University of Edinburgh) for carrying out Rietveld refinement of the powder diffraction data of tin diazide, and of Dr. Steven Hunter (University of Edinburgh) for performing DFT calculations on the structure of tin diazide. The collection of the powder X-ray diffraction for tin diazide would not have been possible without the help of Tom Roseveare and Elliot Carrington (University of Sheffield), and I thank them for their time and patience with setting up the experiments.

The MChem students John Seed and John Gallant assisted greatly during their level 4 research projects, which contributed directly to the work on guanidinium hexaazidosilicates, and TTT respectively.

Also essential for this work were the departmental staff and members of technical staff for providing the support necessary for data collection on specialised equipment. In particular, I would like to thank Harry Adams for an excellent training course in X-ray crystallography and his continued patience, expert advice and all-round friendly manner. Also thanks to Sue Bradshaw for recording ^{119}Sn and ^{14}N NMR data, Jenny Louth and Stephen Atkin for providing the elemental analysis service, and Rob Hanson for training on the use of the differential scanning calorimeter and the thermogravimetric analyser.

I would like to thank current and past members of the Portius group, especially fellow PhD students Ben Peerless, Ben Crozier, and Zoe Smallwood for their friendship throughout including the Alton Towers trips, being teammates for the summer football tournament, and many Friday pie-days.

Finally, I can’t express how important my fiancée, Louise, and my family have been throughout the whole process. Without their patience, love and support through the difficult periods, this journey would have been impossible.

List of abbreviations

AF	azidoformamidinium
AFZT	bis(azidoformamidinium) 5,5'-azotetrazolate
AG	aminoguanidinium
AGZT	bis(aminoguanidinium) 5,5'-azotetrazolate
AGZTH	bis(aminoguanidinium) 5,5'-azotetrazolate monohydrate
BAM	Bundesanstalt für Materialforschung und -prüfung (Federal Institute for Materials Research and Testing)
bpy	2,2'-bipyridine
BT	5,5'-bitetrazolate
Calcd.	calculated
CAN	ceric ammonium nitrate; ammonium cerium(IV) nitrate
CC	cyanuric chloride; 2,4,6-trichloro-1,3,5-triazine
CCD	charge-coupled device
CCDC	Cambridge Crystallographic Data Centre
cif	crystallographic information format
CL-20	hexanitrohexaazaisowurtzitane
CMOS	complementary metal–oxide–semiconductor
Cp	cyclopentadienyl
CSD	Cambridge Structural Database
DAG	1,2-diaminoguanidinium
DFT	density functional theory
DIPEA	diisopropylethylamine
DMF	*N*,*N*-dimethylformamide
DMSO	dimethylsulfoxide
DSC	differential scanning calorimetry
EIL	energetic ionic liquid
Elem. anal.	elemental analysis
EM	energetic material
eq.	molar equivalent(s)
ESD	electrostatic discharge
e.s.d.	estimated standard deviation
FEP	fluorinated ethylene propylene
FOX-7	1,1-diamino-2,2-dinitroethylene
FTIR	Fourier transform infrared
FWHM	full width of peak at half its maximum height
G	guanidinium

GATh	guanidinium 5-azidotetrazolate hemi-hydrate
GCT	guanidinium 5-cyanotetrazolate
GNT	guanidinium 5-nitrotetrazolate
GOF	goodness of fit
GS	graph set
GZT	bis(guanidinium) 5,5-azotetrazolate
HBT	5,5'-hydrazine-1,2-bis(1*H*-tetrazole)
HEDM	high energy density material
HMX	1,3,5,7-tetranitro-1,3,5,7-tetraazacyclooctane; octagen;
IL	ionic liquid
IR	infrared
IRFNA	inhibited red-fuming nitric acid
MeCN	acetonitrile
min	minutes
MMH	monomethylhydrazine
NC	nitrocellulose
NG	nitroglycerine; nitroglycerin; glyceryl trinitrate
NIT	5-amino-1-nitriminotetrazolate
NMR	nuclear magnetic resonance
NTO	dinitrogen tetroxide, N_2O_4
ONC	octanitrocubane
ORTEP	Oak Ridge thermal ellipsoid plot
PA	picric acid
phen	1,10-phenanthroline; *o*-phenanthroline
pic	4-picoline; 4-methylpyridine
PPN	bis(triphenylphosphine)iminium
PXRD	powder X-ray diffraction
py	pyridine
RDX	1,3,5-trinitro-1,3,5-triazacyclohexane; hexogen; *cyclo*-trimethylenetrinitramine
Ref.	reference
RT	room temperature
SADABS	Siemens Area Detector Absorption Correction
SAINT	Siemens Area Detector Integration
SI	supporting information
TAG	1,2,3-triaminoguanidinium; triaminoguanidinium
TAGHNT	1,2,3-triaminoguanidinium 5-nitrotetrazolate monohydrate
TAGN	1,2,3-triaminoguanidinium nitrate; triaminoguanidinium nitrate

TAGNT	1,2,3-triaminoguanidinium 5-nitrotetrazolate
TATB	2,4,6-triamino-1,3,5-trinitrobenzene
TAZ	1,2,3-triaminoguanidinium azide; triaminoguanidinium azide
TGA	thermogravimetric analysis
THF	tetrahydrofuran
TMS	trimethylsilyl
TNT	2,4,6-trinitrotoluene
TRIR	time-resolved infrared spectroscopy
TTT	2,4,6-tris(tetrazol-1-yl)-1,3,5-triazine
U_{eq}	The equivalent *isotropic* displacement parameter for an *anisotropically* refined atom in a crystal structure, which is calculated from the principal mean square atomic displacement parameters, and in this case used as a basis for calculating the isotropic displacement parameters of calculated hydrogens
vdW	van der Waals
XRD	X-ray diffraction
ZT	5,5'-azotetrazolate

Index of compounds

Structures of all compounds numbered in this list are shown overleaf.

1 – guanidinium azide
1a – guanidinium azide monohydrate
2 – aminoguanidinium azide
3 – bis(guanidinium) hexaazidostannate(IV)
4 – bis(aminoguanidinium) hexaazidostannate(IV)
5 – bis(guanidinium) hexaazidosilicate(IV)
6 – bis(aminoguanidinium hexaazidosilicate(IV)
7 – guanidinium hexaazidophosphate(V)
8 – diazido(guanidinyl)(oxido)phosphorus(V)
9 – bis{bis(triphenylphosphine)iminium} hexaazidostannate(IV)
10 – tetraazido(2,2-bipyridine)tin(IV)
11 – tetraazido(1,10-phenanthroline)tin(IV)
12 – tetraazidobis(pyridine)tin(IV)
13 – tetraazidobis(4-picoline)tin(IV)
14 – diazidobis(pyridine)tin(II)
15 – diazidobis(4-picoline)tin(II)
16 – tin diazide
17 – guanidinium triazidostannate(II)
18 – aminoguanidinium triazidostannate(II)
19 – guanidinium tetrazolate
20 – 2,4,6-tris(tetrazol-1-yl)-1,3,5-triazine
21 – 2,4-bis(tetrazol-1-yl)-1,3,5-triazinon-6-ate DMF solvate

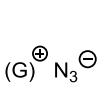

1

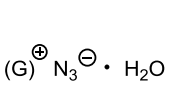

1a

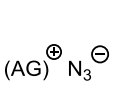

2

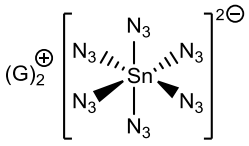

3

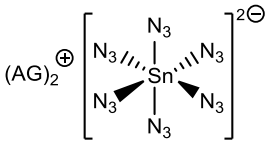

4

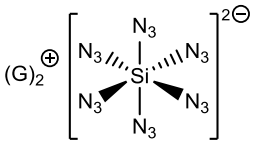

5

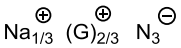

5b

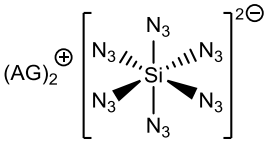

6

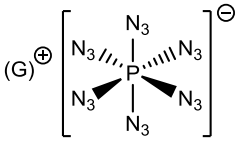

7

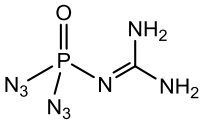

8

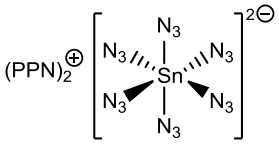

9

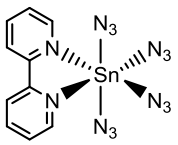

10

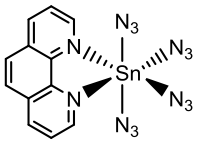

11

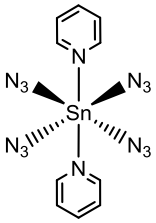

12

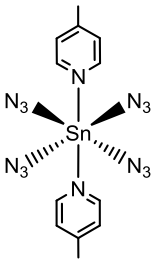

13

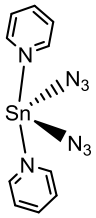

14

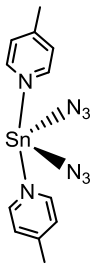

15

16

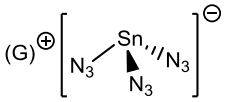

17

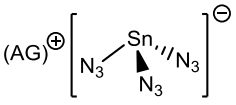

18

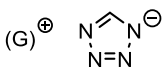

19

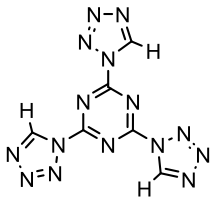

20

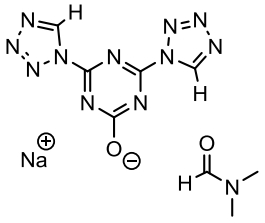

21

Contents

Theses

I. What are the properties of guanidinium azides and how can they be synthesised? What effects do hydrogen bonds have on the structure of nitrogen-rich guanidinium salts? Do particular hydrogen bond graph sets tend to involve characteristically stronger or weaker hydrogen bonds?

II. Are group 14 polyazido complexes stable in the presence of protic cations such as guanidinium? Are hydrogen bonding cations such as guanidinium a viable alternative to the traditional bulky cations? What effect do hydrogen bonding cations have on the properties of the hexaazidostannate anion?

III. What methods can be applied to the synthesis of tin(II) azide and its derivatives? Can simple pyridine based ligands stabilise tin(II) azides as effectively as large ancillary ligands? What is the structure of tin(II) azide?

IV. How do the structures and thermal properties of tin(II) and tin(IV) azides compare? What effect does the ligand sphere have on the bonding mode of azido ligands in these complexes?

V. Which ancillary ligands are suitable for stabilisation of tin(IV) polyazides? Can the already established syntheses for silicon and germanium azides be adapted to prepare new tin(IV) azides? What is the relationship between nitrogen content and energy content of nitrogen-rich polyazides?

VI. Can the 1,3,5-triazine unit be extended to form nitrogen-rich polyheterocyclic compounds? How reliable are the literature procedures for preparation of TTT? What other methods can be applied for synthesis of 2,4,6-tris(tetrazol-1-yl)-1,3,5-triazine (TTT)? Is hydrogen bonding involved in the crystal structure of TTT?

1. Introduction

Since the first reports on azides towards the end of the 19th century, and hydrazoic acid (HN_3) by Curtius,[1] a wide range of applications for azides have been developed, particularly in the fields of energetic materials and organic syntheses.[2] Azides are commonly associated with explosives, largely due to the reputation acquired by the highly shock sensitive hydrazoic acid, HN_3,[3] and binary azides of heavy metals.[4,5] The nature of an azide depends greatly on the element(s) it is combined with, where sensitivity of certain azides arises from a low activation barrier to N_2 release, particularly for heavy metal azides and highly covalent azides. This trend has been rationalised by the increasing covalence of the element-azide bond shortening the N_β–N_γ bond and 'pre-forming' N_2, thus lowering the activation barrier to thermally-induced decomposition (see Figure 1.8). The principal methods used to mediate the sensitivity of polyazido complexes rely on 'dilution' of nitrogen content by bulky hydrophobic 'spacer' cations (e.g. PPh_4, PPN) or coordination of Lewis bases to neutral complexes. The spacer cations help to inhibit shock propagation between energetic binary anions. Coordination of Lewis bases to main group and transition metal polyazido complexes has been demonstrated as a more moderate strategy, producing (relatively) insensitive compounds which generally retain a higher proportion the of specific energy content of the parent binary azide. Hydrogen bonding has been extensively cited as a reason for the apparent stability of energetic compounds, particularly for those which have high nitrogen content. Perhaps the most prominent example of this phenomenon is the extensively hydrogen bonded 1,3,5-triamino-2,4,6-trinitrobenzene (TATB), which is a powerful yet extremely insensitive secondary explosive. Although not particularly nitrogen-rich, its insensitivity may be considered surprising given the sensitivities of other trinitrobenzene derivatives such as picric acid (PA) and trinitrotoluene (TNT).

1.1 High Energy-Density Materials (HEDMs) and Energetic Materials

1.1.1 Classical and State-of-the Art Energetic Materials

High energy density materials (HEDMs) consist of compounds that have a large amount of chemical potential energy per unit mass. This energy is released upon decomposition, yielding thermodynamically more favoured products, which are primarily gases such as N_2, CO_2 and CO. This chemical potential energy can be stored in the form of endothermic groups ($–NO_2$, $–N_2O_2$, $–N_3$, etc.), as cage strain (see Figure 1.1), as large positive heats of formation or a combination thereof. These high-energy compounds must also have good thermal stability, long shelf life, and sensitivity characteristics appropriate to the application. Classical energetic

materials consisting of nitroglycerine (NG), nitrocellulose (NC), trinitrotoluene (TNT), *cyclo*-trimethylenetrinitramine (RDX), lead azide ($Pb(N_3)_2$) and black powder ($KNO_3/C/S_8$) are well-established for their respective applications, but the demand for improved performance and reduced environmental impact have driven the development of alternatives. CL-20 is produced on pilot scale (100 kg) plants, but ONC is only available in mg to g quantities owing to its difficult synthesis.[6] CL-20 has not found widespread use because it is more expensive than RDX, has sensitivity issues, and the desired higher density ε-polymorph is thermodynamically not favoured.

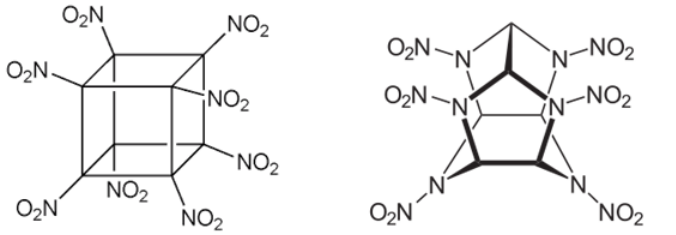

Figure 1.1. ONC[6] and CL-20 are two examples of energetic materials which have cage strain as well as 8 and 6 endothermic groups, respectively. Both compounds are extremely powerful explosives, but have not replaced the most common energetic organic CHNO compositions yet.

1.1.2 Quantifying the Sensitivity of Energetic Materials

When working with potentially hazardous energetic substances, it is important to know their sensitivity to various external stimuli so that the risks associated with handling and transportation are well-understood. Four of the main stimuli which can initiate the decomposition of energetic materials are mechanical impact, friction, electrostatic discharge (ESD) and thermal shock. Sensitivity testing (except for ESD) is generally carried out in accordance with the UN Recommendations for the Transport of Dangerous Goods,[7] which are not legally binding, but form the basis for some national laws on the subject. The following descriptions give a brief overview of some of the testing methodologies prescribed in the UN Recommendations.

Since the sensitivity of solid materials generally increases with larger grain (or crystal) size, the substance to be tested is usually sieved (0.5 mm mesh) to ensure consistency and repeatability of the tests. There are three possible outcomes from the tests: 1) no reaction, 2) decomposition (change of colour/odour), or 3) explosion (report, crackling, spark, or flame). Only "explosion" is regarded as a positive result in this context. The standard measure for impact sensitivity of energetic materials is the BAM Fallhammer (Figure 1.2), Fallhammer = drop weight, BAM = Bundesanstalt für Materialforschung und -prüfung (Federal Institute for Materials Research and Testing), where a steel weight (1 kg, 5 kg, or 10 kg) is dropped from a known height onto the sample of defined mass and diameter, resting on a solid steel base

which absorbs the shock. The impact energy (reported in J) is calculated from the height (m) and the mass of the drop weight (kg). The block is dropped from a series of increasing heights until there is a positive reaction in at least one of six trials. The impact sensitivity reported is the lowest energy for which there is at least one positive result in six trials. If there is no reaction at or below 40 J of impact energy, the substance is designated "insensitive" to impact. For friction testing of solids, a specially designed apparatus (for instance the BAM friction tester, Figure 1.2) is used, where the sample is placed between two porcelain surfaces, one fixed and the other on a cantilever. The cantilever is carefully placed on, and drawn over the substance to be tested. Incrementally decreasing weights attached to the arm impart less friction on the sample until there is no "explosion" in six trials. The series of tests begin with a single trial at a load of 360 N. If in the first trial at 360 N "decomposition" or "no reaction" is observed, up to five further trials are performed. If none of the six trials at the highest load result in an "explosion" the substance is deemed to be insensitive to friction. If however in the first trial at 360 N an "explosion" is observed, the series is continued with trials at stepwise lower loads until the result "decomposition" or "no reaction" is observed in at least six trials. The 'limiting load' is defined as the lowest friction load level where at least one explosion occurs in six trials. If the limiting load is below 80 N, the test result is (+) and the substance is too dangerous for transport in the form it was tested, otherwise the result is (–).[7] Another important consideration is the sensitivity of a material to electrostatic discharge (ESD), which is not covered in the Manual of Tests and Criteria of the aforementioned UN Recommendations on the Transport of Dangerous Goods.[7] Testing is generally carried out using a tuneable electric spark generator, which subjects a small sample of the material to different spark energies (typically 0.001–20 J) to determine the minimum energy which results in at least one positive test result (detonation) in a given number of trials. The test results seem to be strongly dependent on particle size, with finer powders having higher sensitivity than granular samples of a given material.[8] This is the opposite to friction sensitivity, which tends to be higher for larger crystals (or grains).

1.1.3 Traditional *vs.* Nitrogen-Rich EMs

Some of the most widely used compounds in energetic materials in use today, for example nitroglycerine (NG) and nitrocellulose (NC), have been around since the 19th century, but have persisted because their properties meet performance demands, and their syntheses and safe handling procedures are well developed. Formulations of NG / NC are still used in modern gun propellants, though replacement with nitrogen-rich EMs would be beneficial – reducing corrosion by promoting formation of iron nitride rather than iron carbide on the internal surface of the barrel – giving around a fourfold increase in barrel lifetime.[8] The benchmark compounds for performance of secondary explosives are trinitrotoluene (TNT) and hexogen (RDX), which are used for comparison to all newly developed compositions. Secondary

explosives like TNT, RDX and HMX rely on the oxidation of a hydrocarbon backbone to release the heat, whereas nitrogen-rich compounds derive their potential energy from their large heat of formation. Decomposition of nitrogen-rich compounds releases largely N_2, which is environmentally benign and gives the compounds inherently high heats of formation.[8]

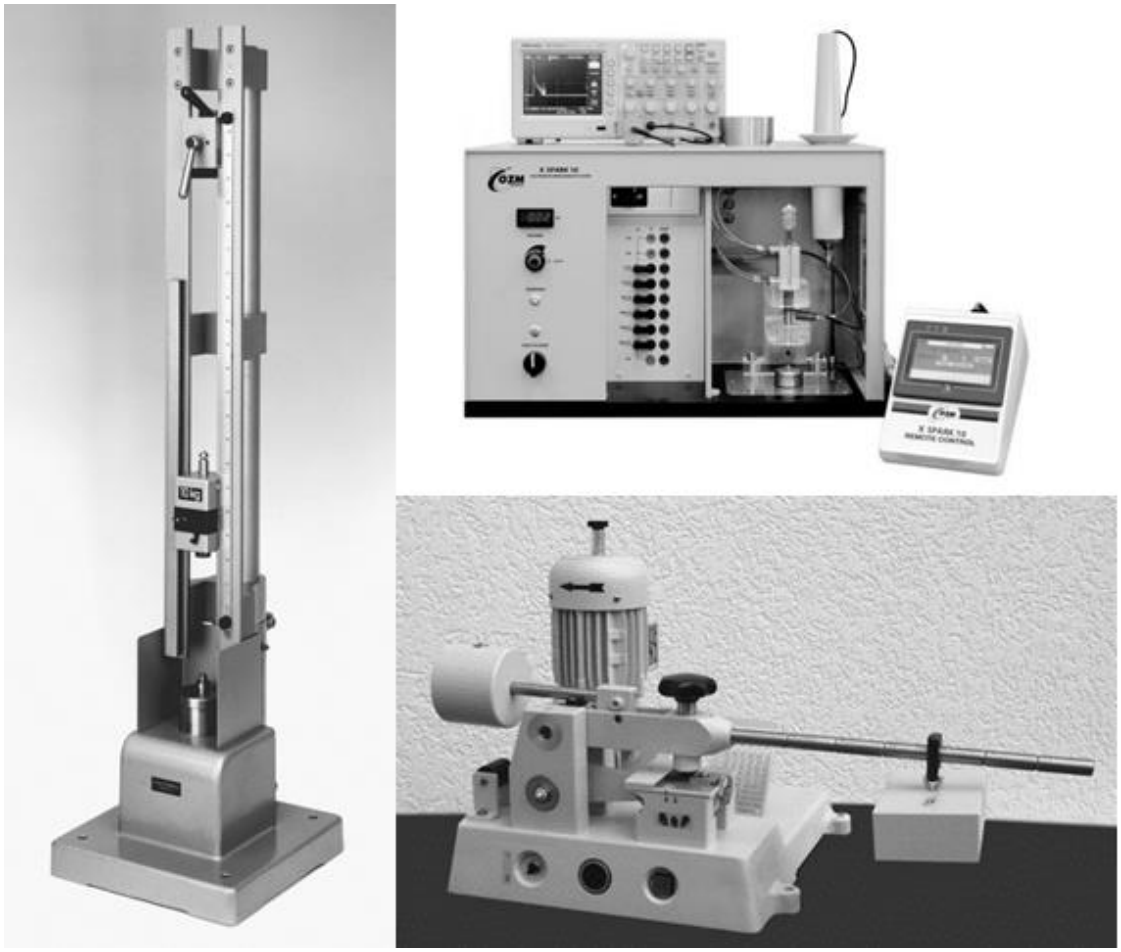

Figure 1.2. Specialised apparatus for standard, repeatable, quantitative testing of energetic materials. Left: BAM Fallhammer for impact sensitivity testing (Image copyright jbwebs.com 2010-2015, Reichel & Partner GmbH);[9] Top Right: Spark generator for electrostatic sensitivity testing (Image copyright OZM Research S.R.O. 1997-2016);[10] Bottom Right: BAM friction tester (Image copyright jbwebs.com 2010-2015, Reichel & Partner GmbH).[9]

Lead azide, $Pb(N_3)_2$, is one of the most commonly used primary explosives, and due to its sensitivity to friction it is used as an initiator. Having lead content in an energetic compound is not ideal, as the detonation of the material results in deposition of lead to the surroundings, which poses significant hazards to human health and the environment (Figure 2B in ref. [11] shows typical lead spatter from detonation of lead azide). Recently, some promising lead-free alternatives have been prepared (see Figure 1.3), including Potassium 1,1'-Dinitramino-5,5'-bistetrazolate ("K2DNABT") and Copper 5-nitrotetrazolate ("DBX-1").[12,13] Huynh and co-workers in the U.S. have developed a family of 'green' primaries based on 5-nitrotetrazolato complexes of iron and copper.[11,14] The desired sensitivity can be achieved by the choice of the appropriate counterions, coordination centre, and the number of nitrotetrazolato ligands.

The variation of properties within these coordination compounds demonstrates the ability to achieve a range of sensitivities, which can be designed systematically. For applications in pyrotechnics, a range of colours is achieved by the inclusion of alkali metal cations such as barium (green)[15,16] or strontium (red),[17,18] as their nitrate salts which have the dual function of colourant and oxidiser for the formulation, magnesium powder due to its highly exothermic oxidation, a chlorine source to produce the coloured metastable M(I) salts, and binders to prevent the composition from separating over time. Traditionally, perchlorates are used as the oxidiser for the composition because they are thermally stable, decompose exothermically, and enhance the reliability of ignition. The U.S. Environmental Protection Agency has set the maximum limit of 15 ppb perchlorate in drinking water, as it is teratogenic, and it is believed that it disrupts the normal function of the thyroid by competing with iodide for binding sites.[15] Energetic compounds which do not require an oxidiser component to act as an energetic material circumvent the need for perchlorates.

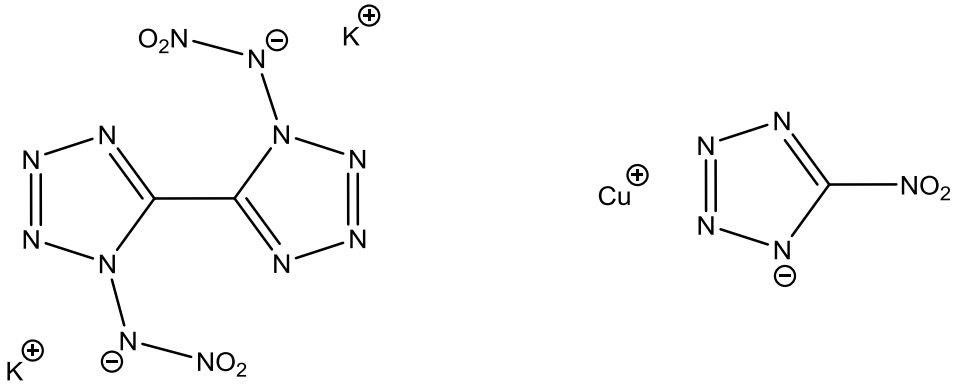

K_2DNABT **DBX-1**

Figure 1.3. Lead-free primary explosives potassium 1,1'-dinitramino-5,5'-bistetrazolate (K_2DNABT) and copper 5-nitrotetrazolate (DBX-1), which are promising candidates for replacement of lead azide and lead styphnate.[12,13]

1.2 Polynitrogen Chemistry

Nitrogen has the strongest preference of all elements for triple bonds (946 kJ mol^{-1}) over double or single bonds (409 kJ mol^{-1} and 163 kJ mol^{-1}, respectively).[19] This can be demonstrated clearly by comparing the 'effective' enthalpy per bond in Table 1.1 below:

Table 1.1. Molar enthalpies of single, double and triple N–N bonds.

Molar enthalpy [kJ mol^{-1}]	N–N	N=N	N≡N
Total molar enthalpy	163	409	946
Average contribution per bonding electron pair	163	204	315

The triple bond in N_2 (N≡N) is one of the strongest bonds known to chemists, which makes the formation of molecular dinitrogen highly thermodynamically favourable compared to single (N–N) or double (N=N) bonds. Combining these two pieces of information leads to the conclusion that solid *polymeric* nitrogen would be the ideal HEDM. Such a material would capitalise on the preference for the triple bond, releasing the maximum amount of N_2 per gram, giving an extremely high energy-density material free of by-products. The change in entropy accompanying the transformation of polymeric nitrogen to gaseous N_2 would be the highest achievable entropy change for a nitrogen-rich material. The hypothetical value for such a transformation has been calculated to give a tenfold increase in performance versus HMX.[20]

1.2.1 Polymeric Nitrogen

Polymeric nitrogen has been isolated as amorphous[21,22] and single-crystalline[23] solids under extremely high pressures (>140 GPa) in a diamond anvil cell equipped with *in-situ* XRD and Raman capabilities (Figure 1.4). Experiments such as this can help to aid development of theoretical models, and in demonstrating that such a transformation is possible. Decompression experiments on samples of polymeric nitrogen show that there is a large hysteresis of around 100 GPa at room temperature (and >170 GPa at 80 K), though attempts to recover polymeric nitrogen to ambient conditions always resulted in rupturing of the gasket at pressures of around 50 GPa. This is attributed to the 35 % volume increase accompanying the back-transition to the molecular phase.

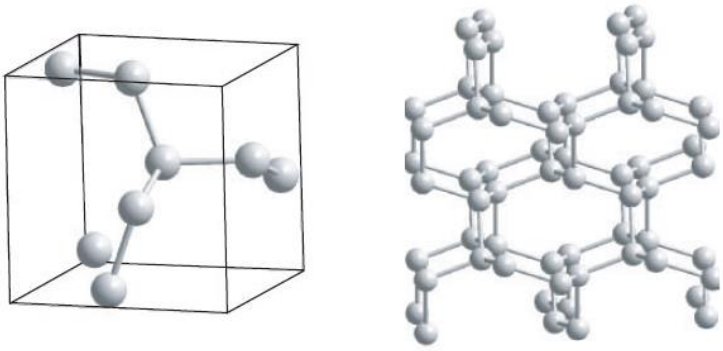

Figure 1.4. Cubic polymeric nitrogen, with N-atoms represented as spheres. *Left*: the unit cell, showing three covalent single bonds between N-atoms; *Right*: an extended view of the crystal packing.[22]

1.2.2 The structure and synthetic strategies of all-nitrogen species

Aside from dinitrogen and polymeric nitrogen, other all-nitrogen species include the azide anion $(N_3)^-$, the azidyl radical $(N_3)^{\cdot}$,[24] the pentazenium cation $(N_5)^+$,[25–27] and tetranitrogen (N_4).[28] So far, the only all-nitrogen species which have been produced in bulk are azide and pentazenium, and the existence of tetranitrogen and pentazolate species are based on mass spectrometry and NMR spectroscopic evidence, respectively.

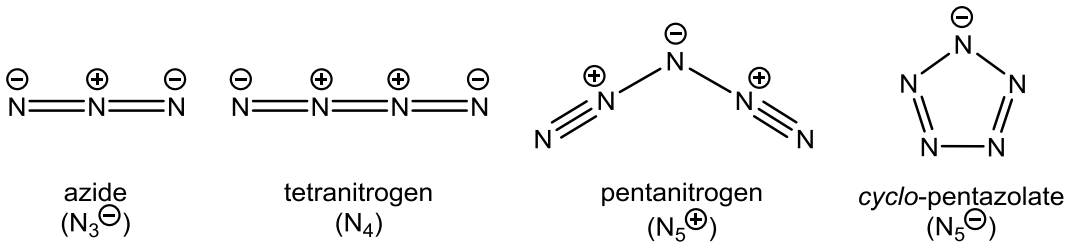

Figure 1.5. Lewis structures of the dominant resonance forms of some all-nitrogen ('polynitrogen') species. Electronic delocalisation within the structure increases the average N–N bond order significantly above 1, which seems to aid stability of polynitrogen species.

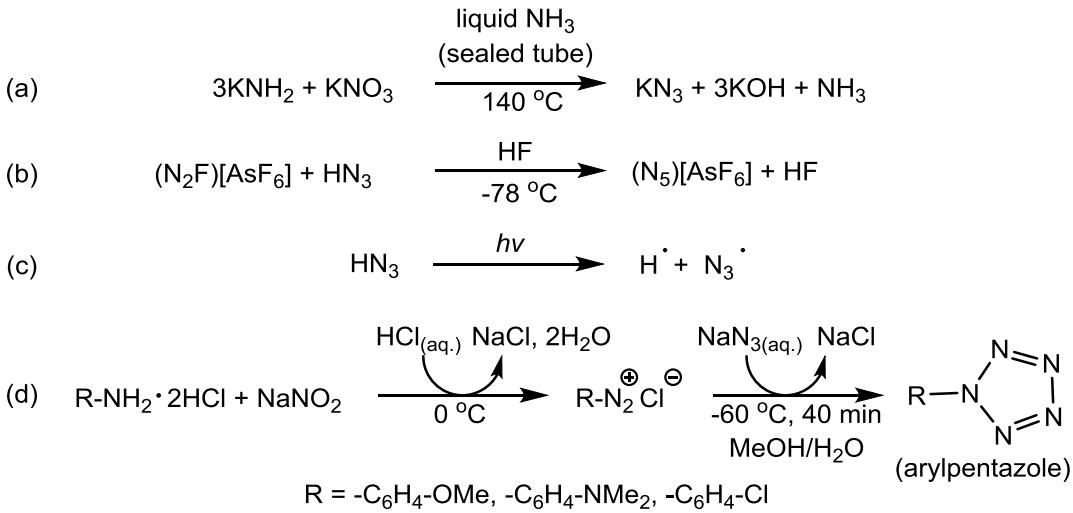

Scheme 1.1. Some reaction pathways to all-nitrogen species, including (a) the azide anion,[29] (b) pentazenium cation,[25,27,20,26] (c) azidyl radical,[24] and (d) arylpentazoles[30] – potential precursors to pentazole (HN_5).

1.2.3 The azide anion $(N_3)^-$, azidyl radical $(N_3)\cdot$ and tetranitrogen (N_4)

The azide anion is comparable in toxicity to the cyanide anion $(CN)^-$. Simple heavy metal azide salts such as lead azide are widely used as primary explosives (initiators). Organic azides are useful synthetic building blocks, for example in 'click' chemistry[31] where an azide participates in a [3+2]-cycloaddition with an alkene or nitrile leading to triazoles or tetrazoles, respectively. A comprehensive review was published on the preparation and a variety of synthetic uses of azides.[2] Sodium azide (NaN_3) is probably the most widely used azide reagent due to its relatively low cost, and insensitivity towards impact, friction, and electrostatic discharge. Azide salts are essential precursors in the synthesis of nitrogen-rich, highly endothermic compounds such as polyazido complexes.[19,32] In the synthesis of the latter, a common procedure is the reaction of an azide salt with the corresponding chloride. Other common azide transfer reagents are trimethylsilylazide (Me_3SiN_3) and silver azide (AgN_3). Trimethylsilylazide is a liquid at ambient temperature (b.p. 95–99 °C), meaning any excess is readily removed from reaction mixtures under vacuum along with the trimethylsilylchloride/fluoride by-product. Care must be taken to prevent exposure of Me_3SiN_3 to moisture, as it readily hydrolyses with the formation of explosive hydrazoic acid. Silver azide is sensitive to friction, impact and thermal shock, particularly when dry, but when

employed with care it is an effective means of preparing compounds that would otherwise be inaccessible, enforcing the production of highly endothermic species by precipitation of the insoluble silver halide from solution. IR spectroscopy is an excellent probe for azides, as the compounds tend to exhibit strong IR absorption due to the asymmetric N_3 stretch, $\nu_{as}(N_3)$, which appears in the spectral region 2000–2200 cm^{-1} in the solid state and in solution. This region is usually free from interference of solvent absorption bands, making IR spectroscopy ideally suited for *in-situ* reaction monitoring. The number of $\nu_{as}(N_3)$ absorption band(s), their relative intensity and position are indicators of the nature of an azide group, and the point symmetry of polyazido complexes. Purely ionic azides, such as $(PPN)N_3$, feature an absorption band at a spectral position of around 2005 cm^{-1},[33] whereas various covalent azido complexes exhibit a band around 2060–2115 cm^{-1}, and neutral covalent azides such as HN_3 and $Si(N_3)_4$ appear at 2139 cm^{-1} (MeCN) and 2173 cm^{-1}, respectively.[34] The correlation of ionic/covalent character with band position is not always observed, however, which is exemplified by sodium azide ($\nu_{as}(N_3) \approx 2130$ cm^{-1} (nujol suspension)), where instead electrostatic forces seem to have the greatest influence. The azidyl radical has been observed spectroscopically in high-intensity flash photolysis experiments on hydrazoic acid (HN_3) vapour.[24] The linear isomer of tetranitrogen (Figure 1.5) has sufficient lifetime (*ca.* 1 μs at 298 K) to be detected by specially designed mass spectrometry experiments with $^{14}N_2$ and $^{15}N_2$.[28] It is only metastable as the central bond between the two N_2 units is predicted to be very weak. Calculations carried out to determine the most stable nitrogen species have shown that the tetrahedral isomer – tetraazatetrahedrane – is a minimum on the potential energy surface, but it is higher in energy than the open chain configuration.[35] Though the azidyl radical and tetranitrogen have not been prepared 'in bulk', valuable information can be extracted from the experimental data to complement theoretical investigations, and aid future development in the field of polynitrogen chemistry.

1.2.4 The pentazenium cation, $(N_5)^+$

The pentazenium cation was first prepared as the 'marginally stable' highly energetic $(N_5)[AsF_6]$ salt, which reacts explosively with water and is a strong enough oxidiser to ignite foam rubber even at low temperature.[25] Subsequently this family of compounds has been expanded to include 'surprisingly stable' salts with other bulky perfluorinated anions such as $[B(CF_3)_4]^-$ and $[Sb_2F_{11}]^-$, and the friction sensitive $(N_5)_2[SnF_6]$ salt. Thermal stability of pentazenium salts seems to be limited by the cation ($T_{dec} \approx 50$–70 °C).[36]

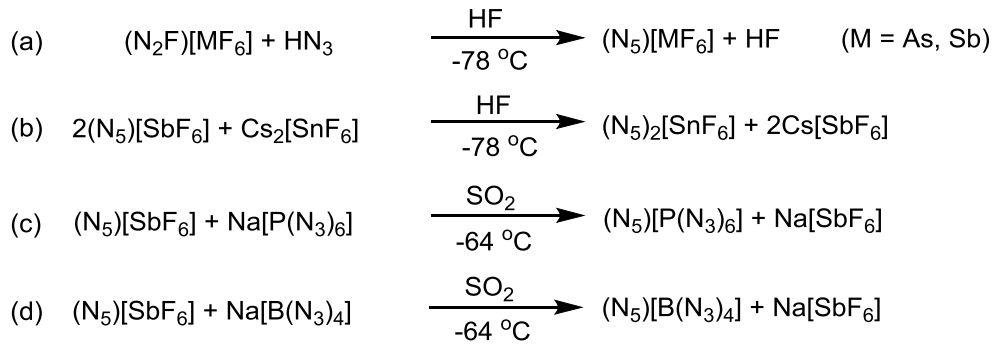

Scheme 1.2. Synthetic procedures for the preparation of pentazenium salts: (a) pentazenium formation;[25] (b) metathesis reactions to a 2 : 1 salt;[26] (c, d) metathesis reactions to extremely nitrogen-rich salts of polyazido complexes.[27]

Perhaps the most astounding examples of pentazenium salts are the nitrogen-rich 1:1 salts $(N_5)[P(N_3)_6]$ and $(N_5)[B(N_3)_4]$, the latter holding the record 95.7 % nitrogen for a salt.[27] These salts are accessed *via* the tetrafluoroammonium salts, of which relatively few are known. The components must also be compatible with the solvent (usually SO_2 or HF), and have sufficient solubility, as the metathesis reactions (b)–(d) rely on the precipitation of $Cs[SbF_6]$ or $Na[SbF_6]$. Both of the pentazenium polyazido salts are extremely shock sensitive, temperature sensitive, and explode violently with little or no provocation. This means that characterising the compounds was a challenge and resulted in 'significant' damage to equipment including a Raman instrument and numerous reaction vessels, limiting their characterisation to NMR and Raman spectroscopies.

1.2.5 Arylpentazoles and evidence for N_5^-

Another highly sought-after all-nitrogen species is the cyclopentazolate anion, N_5^- – the nitrogen analogue of cyclopentadienide, $C_5H_5^-$ – as the aromatic 6 π-electron system could offer the same type of stabilising effect. Arylpentazoles have been studied as potential precursors to N_5^-/HN_5 by cleaving the C–N_5 bond chemically or photolytically.[37,38] The current experimental evidence for the existence of N_5^- in the gas phase is limited to mass spectrometry,[30,39] and in solution to a ^{15}NMR study.[40] The action of a standard one-electron oxidant, ceric ammonium nitrate (CAN = $(NH_4)_2[Ce(ONO_2)_6]$), on *p*-methoxyphenylpentazole in MeOH/H_2O leads to the production of *p*-benzoquinone and pentazole (HN_5), which rapidly decomposes with loss of N_2. The initial report of N_5^- in solution was based on a signal observed in the ^{15}N NMR spectrum at –10 ppm, [41] which was assigned to the N_5^- anion as it was in agreement with theoretical predictions.[42] However, this interpretation of the data was disproven[43] as the same signal also appeared in a MeOH solution of CAN in the absence of the arylpentazole, and was in fact due to the presence of nitrate anion. A subsequent systematic study of ^{15}N labelled pentazoles seems to have upheld the claim, [40] by showing experimental evidence of the ^{15}N labelled azide anion. Several *p*-methoxyphenylpentazoles

(with 1, 2 or 3 labels) were prepared, and upon dearylation with CAN they yielded the corresponding ^{15}N labelled pentazole. Thermal decomposition of HN_5 is predicted to be rapid, with loss of N_2, leaving the respective labelled azide anions, which were investigated with NMR and presented as (indirect) proof of production of HN_5/N_5^-. Other potential methods of N_5 cleavage from arylpentazoles are electrochemical reduction or photolysis with an appropriate wavelength of UV-radiation. A time-resolved infrared spectroscopic (TRIR) study on the femtosecond excitation (λ_{exc} = 310 or 330 nm) of *p-N,N*-dimethylaminophenylpentazole (DMAP–N_5) was carried out to explore the possibility of photolytic C–N_5 bond cleavage.[37] The TRIR experiments were complemented by spectroelectrochemical measurements and DFT calculations, and the results showed that decomposition occurred *via* N_2 release from the N_5 ring rather than cleavage of the C–N_5 bond, yielding the corresponding azide/nitrene.

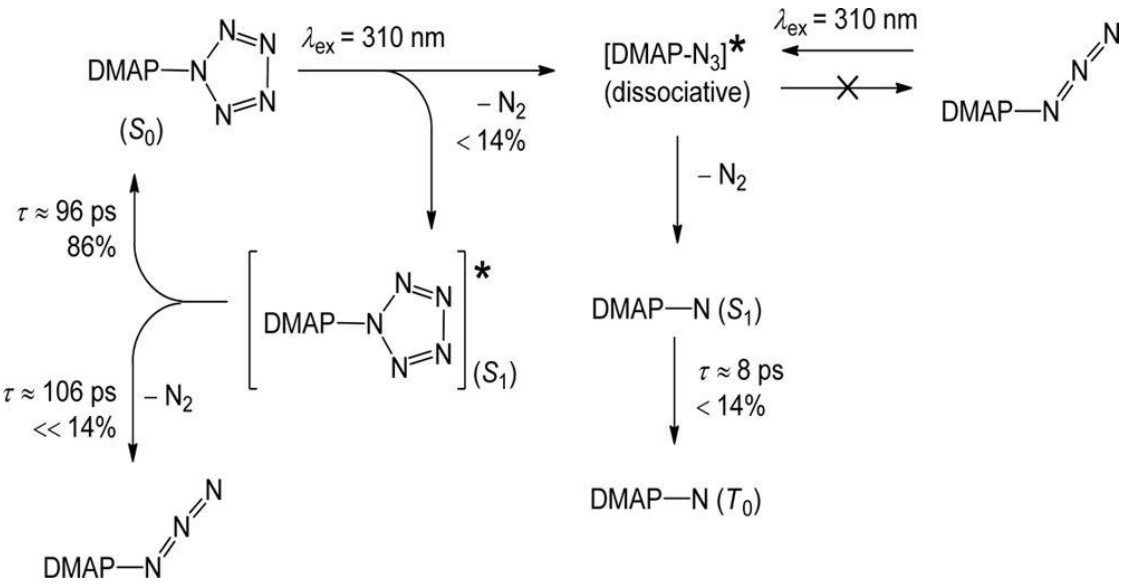

Scheme 1.3. Summary of the photoreactions of *p-N,N*-dimethylaminophenylpentazole and *p-N,N*-dimethylaminophenylazide in CH_2Cl_2 at 233 K. (Reproduction of Scheme 1 in ref. [37], copyright American Chemical Society, 2013).

The structure of the stable, isolable N_3^- and N_5^+ species implies that there may be a kinetic barrier to decomposition into N_2 present if the average N–N bond order is kept as far above 1 as possible. Whilst the challenging search for stable all-nitrogen species continues, a compromise can be made between nitrogen content and stability to prepare and characterise isolable nitrogen-rich compounds.

1.3 Neutral Nitrogen-Rich Compounds

As defined above in section 1.1, energetic materials react readily with the release of a large proportion of gaseous products, which have inherently much higher entropy than solids. The transformation from one mole of solid to gaseous species represents a massive increase in the entropy of the system. Dinitrogen is the major decomposition product of nitrogen-rich

compounds, and the energy released by the formation of this bond gives nitrogen-rich compounds their high heats of formation (and high energy density). Their high endothermicity means that the reaction of a nitrogen-rich energetic material to give gaseous dinitrogen is both exothermic and spontaneous (exergonic). Combination of nitrogen with other (light) elements results in compounds that can have the high intrinsic energy content, but are more readily accessible and isolable than all-nitrogen compounds under ambient conditions. Nitrogen-rich species' properties and sensitivities to external stimuli, to some extent, depend on whether the nitrogen is incorporated as ionic or neutral species.

1.3.1 Hydronitrogens: Ammonia and Hydrazine

Ammonia is the simplest hydronitrogen (82 % N), produced on a megaton scale by the Haber-Bosch process from N_2 and H_2. It is used in the manufacture of many synthetic nitrogen compounds, such as nitric acid, fertilisers and explosives. It is a useful polar solvent, which is well known for dissolving alkali metals to give 'solvated electrons'. Hydrazine (N_2H_4, 87 % N) is very nitrogen-rich, and has been used as a component in propellant formulations. The methyl derivative monomethylhydrazine (MMH) is used as rocket fuel as it exhibits hypergolic (spontaneous) ignition[44] with oxidisers such as inhibited red fuming nitric acid (IRFNA) and dinitrogen tetroxide (NTO). Both hydrazine and MMH are very toxic, highly flammable, and carcinogenic, which combined with their volatility under ambient conditions pose significant health hazards. The bipropellant system performs well, but large-scale use of these hazardous compounds leads to significant environmental contamination. Potential alternatives such as energetic ionic liquids (EILs)[45–47] are an attractive proposition, and could be suitable replacements, as some candidates exhibit hypergolic ignition with N_2O_4,[44,46] yet have negligible vapour pressure. As the chain length of nitrogen atoms in neutral hydronitrogens is increased, their stability is lessened as more weak N–N single bonds would be required *cf.* nitrogen's preference for multiple bonds over single bonds. Triazane and triazene, the N-analogues of propane and propene are not isolable as neutral species without terminal substituents.

1.3.2 Hydrazoic acid and Neutral binary azides

Hydrazoic acid (HN_3, Figure 1.6) could be regarded as the simplest nitrogen-rich (97.7 %) compound. It is a colourless, volatile liquid, which is highly toxic, and frequently explodes when subjected to friction or shock. It is a weak acid with p$K_a \approx 4.7$,[48] with a low boiling point of around 36 °C. It was first isolated by Curtius[1] in 1890 during an investigation of the action of nitrous acid on benzoylhydrazine (Scheme 1.4 below). Initially, benzoylazide was produced, which upon saponification gave sodium azide. After acidification (with sulphuric acid) of the obtained sodium azide, distillation from the reaction mixture afforded pure HN_3. Since pure HN_3 is a friction sensitive explosive liquid, this original method has

been modified to produce a dilute aqueous solution, [49] or preferably ethereal solution,[50] for safer and more convenient handling. Upon exposure to light, hydrazoic acid solutions photolyse slowly with liberation of dinitrogen to give ammonia, which immediately reacts to form ammonium azide.[50]

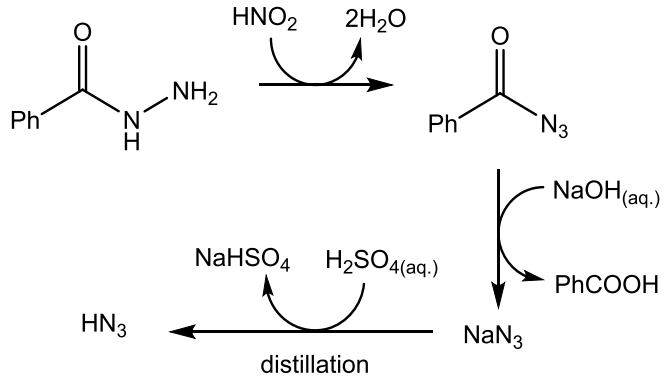

Scheme 1.4. The route by which Curtius discovered the azide anion, and subsequently hydrazoic acid.

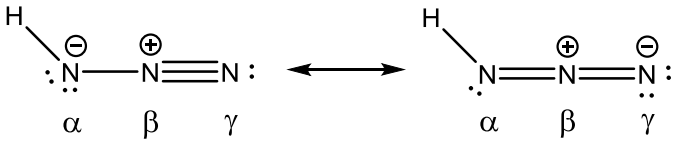

Figure 1.6. Resonance forms of hydrazoic acid. The N_β–N_γ bond is noticeably shorter than the N_α–N_β (1.121(5) Å *vs*. 1.241(5) Å), suggesting the dominant resonance form of the two pictured is on the left.

Hydrazoic acid has a chain structure, with a slightly bent N–N–N angle (*ca*. 173°). Its solid state structure was determined as late as 2011[51] by low temperature single-crystal X-ray diffraction, showing (almost) planar layers of hydrogen bonded tetramers (Figure 1.7 below).

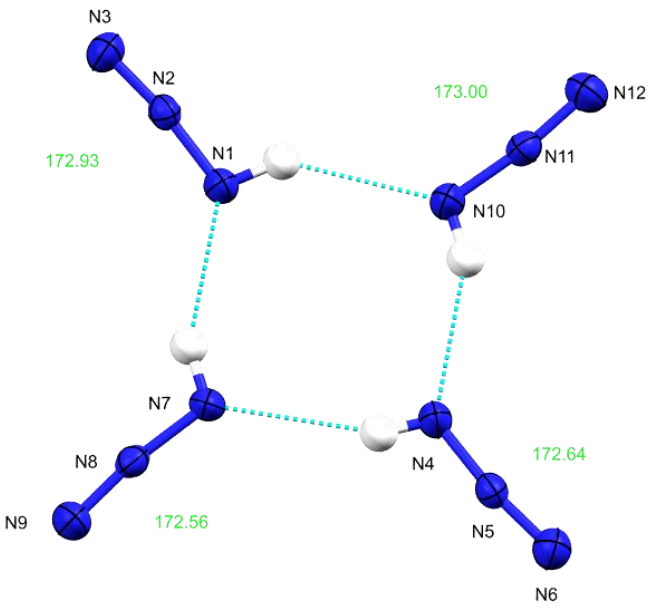

Figure 1.7. Thermal ellipsoid plot showing one of the hydrogen bonded tetramers in the crystal structure of HN_3 denoted R4,4(8).[51] Dashed blue lines represent hydrogen bonds, and the NNN angles are shown in green.

The ionic binary azides of alkali metals are not shock sensitive, and sodium and potassium azides in particular are useful precursors for many other azides, however some ionic azides of heavier elements such as barium- and silver azides are shock sensitive, and covalent binary azides are much more hazardous. Although neutral binary azides with many elements have been reported, often extremely high shock sensitivity limits their characterisation. The chemistry of covalent azides has been the subject of several extensive review articles.[52,32,19] Of the known *p*-block azides only lead azide, $Pb(N_3)_2$,[4] has found an application – as a primary explosive (initiator). Other binary azides are being investigated as potential precursors for thin film deposition of corresponding metal nitrides *via* controlled thermal decomposition.[53,54] Examples of neutral binary azides of metallic elements include titanium-[55] and vanadium tetraazides;[56] molybdenum- and tungsten hexaazides;[57] manganese-, europium- and zinc diazides;[54] mercury azides,[58] and silver azide.[59] Many neutral binary azides of *p*-block elements are known, particularly of groups 13-15, including tetraazidomethane,[60] silicon-[61,34] and germanium tetraazides,[62] tin-[54] and lead diazides,[4] also chalcogen-[63–65] and halogen azides, XN_3 (X = F, Cl, Br and I),[66] and hexaazido(cyclotriphosphazene) P_3N_{21},[67] though some have been studied more than others, and relatively few solid state structures have been determined. In the case of lead azide, its sensitivity to friction is advantageous for its use as an initiator, though for the rest of the above compounds, it merely presents challenges in their handling and characterisation. The higher sensitivity for neutral polyazide species over charged polyazido complexes can be rationalised by considering the nature of the coordinative bond (Figure 1.8 below). If the E–N_α bond is mostly covalent in character, the N_β–N_γ bond is close to a triple bond and therefore N_2 is 'pre-formed', resulting in an azide with more sensitive character because the barrier to N_2 release is

lower. If the E–N_α bond is more ionic in character, the N_α–N_β bond gains some resonance stabilisation.

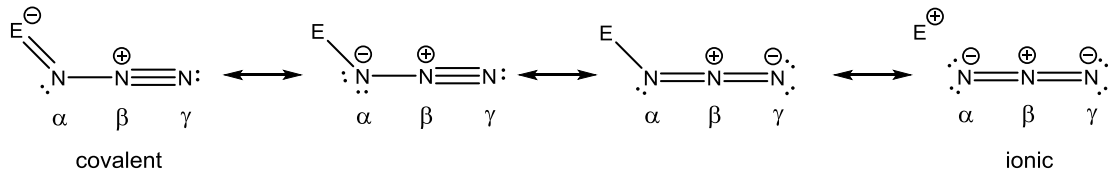

Figure 1.8. Canonical forms of a coordinated azide group, showing the bent (*ca.* 120°) E–N_α–N_β geometry, and the covalent and ionic extremes of the azide coordination.

In XRD studies, the difference in bond length between N_α–N_β and N_β–N_γ (denoted ΔNN),[19] can be used to gain insight into the extent of ionicity of the E–N_α bond. This was demonstrated in the study of cationic, neutral, and anionic Group 15 binary azide species,[68] as the ΔNN increased in the series anionic < neutral < cationic. There are many more Lewis base adducts of polyazides, and salts containing polyazido anions, and these compounds tend to be more stable than the parent binary azides in part because of the reasons discussed above.

1.3.3 Guanidines

Guanidines are a family of compounds containing a nitrogen-rich [CN_3] subunit, the simplest of which is guanidine itself (CH_5N_3, 71 % N, Figure 1.9 below), which was first obtained in 1861 by oxidation of guanine.[69] Despite its early discovery, its solid state structure was not solved until 148 years later.[70] The crystal structure is a complex 3D network of hydrogen bonds, which formed the basis for a theoretical study on cooperativity of hydrogen bonds within a network.[71] Its basicity (pK_a = 13.6)[72] is comparable to that of aqueous potassium hydroxide, which is due to the highly stable nature of its conjugate acid, the guanidinium cation (Figure 1.9). Given this high basicity of guanidine, it might be surprising that it can act as an acid, forming guanidinates with alkali metal cations.[73–75] Guanidines (and substituted guanidines) can form complexes with several different coordination modes depending on whether the substituents contain additional donor atoms. [76] In the absence of such donor atoms, guanidines exclusively bind to the coordination centre *via* the lone pair on the imine nitrogen (confirmed by a red-shift of the C=N stretch observed in the FTIR spectra). Cyanoguanidines can act as bridging ligands between two centres *via* the nitrile and imino nitrogens. Substitution of guanidines reduces the nitrogen content, therefore further discussion of their coordination chemistry is beyond the scope of this work.

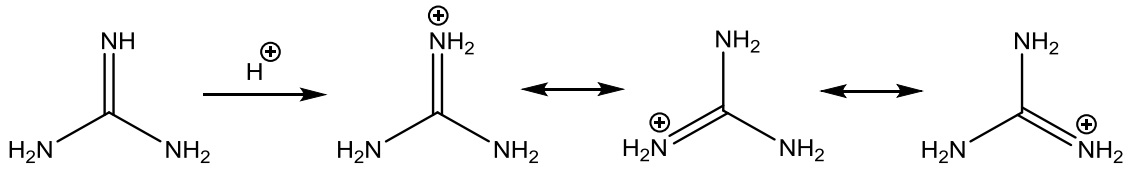

Figure 1.9. Protonation of guanidine (far left) to guanidinium, showing the three resonance forms that contribute equally, giving each of the C–N bonds in the cation a bond order of approximately 1.33.

In the crystal structure of guanidine the average C=N bond is 1.301 Å, which is appreciably shorter than the average C–N bonds (1.362–1.376 Å). Both amino nitrogen atoms are strongly pyramidal and the NH_2 groups are in the *anti*-conformation in agreement with gas phase calculations.[77] Although the above (Figure 1.9) representations of the guanidinium cation may suggest one double and two single bonds from the central carbon, the reality is that the C–N distances and N–C–N angles are indistinguishable within experimental error, forming a trigonal planar CN_3 skeleton. This delocalisation of π-electron density has been described as Y-aromaticity[78] or Y-conjugation,[79] though there is disagreement whether this phenomenon, or hydrogen bonding, is the reason for the stability of the guanidinium cation.[80]

1.4 Ionic Nitrogen-Rich Species

It is important to know the sensitivity of the nitrogen-rich compounds towards external stimuli, particularly thermal shock, impact, friction, and electrostatic discharge (ESD). These sensitivity properties of the compounds determine what applications (if any) are appropriate, and the scale on which it can be prepared safely in the laboratory. In the preparation of insensitive nitrogen-rich substances, ionic species (solid or liquid) have the added benefit of stronger interionic (*vs.* intermolecular) interactions, and tend to be thermally stable, and have lower vapour pressures than related neutral species. The aforementioned pentazenium salts, $(N_5)[B(N_3)_4]$ and $(N_5)[P(N_3)_6]$, are exceptions to this generalisation as both components of the salts confer friction and shock sensitivity on the compound because of close packing of the sensitive covalent polyazido anions.

1.4.1 Nitrogen-rich anions: Polyazido complexes

In the field of coordination chemistry, nitrogen-rich species can act as ligands to form new complex anions, such as polyazido[19,32] or polytetrazolato[81,82] complexes. Azido ligands coordinate almost exclusively as monodentate ligands, but can behave as a bidentate $\mu_{1,3}$ (end-to-end) or $\mu_{1,1}$ (shared) bridge between two coordination centres, particularly for coordinatively unsaturated complexes. These complex anions are typically studied with bulky non-coordinating cations such as PPN^+ (= $(Ph_3P)_2N^+$),[33,83–85] Ph_4P^+ [86,87,57,88] or Ph_4As^+ [89,90] to

dilute the nitrogen content and inhibit release of extremely sensitive neutral species such as $Si(N_3)_4$.[34]

$$Na[P(N_3)_6] \longrightarrow NaN_3 + P(N_3)_5 \qquad \Delta H_{latt} \approx -242\ (\pm 50)\ kJ\ mol^{-1}$$

$$(PPN)[P(N_3)_6] \longrightarrow (PPN)N_3 + P(N_3)_5 \qquad \Delta H_{latt} \approx -19\ (\pm 8)\ kJ\ mol^{-1}$$

Scheme 1.5. Rationalisation of the stabilising effect of the $(PPN)^+$ cation on its salts with polyazides.[84] The estimated gain in lattice enthalpy for dissociation of the hypercoordinate $[P(N_3)_6]^-$ anion with release of the neutral binary $P(N_3)_5$ species is estimated to be much less favourable for the case of $(PPN)N_3$ compared to NaN_3. (Full details of the calculations are available in the supporting information of ref. [84]).

For smaller cations such as sodium, the dissociation of the hypercoordinate complex with precipitation of its azide salt is favourable due to the high lattice enthalpy of sodium azide, whereas azide salts of bulky cations have lower lattice enthalpies, meaning the polyazido complex is preferred. Polyazido complexes of main group elements have been studied extensively, including those of boron,[91,27] silicon,[61,83,34] germanium,[33,92] tin,[86,85,92] phosphorus;[84,93,67] arsenic, antimony, and bismuth;[94,68] aluminium, gallium, indium, and thallium.[88,95] As mentioned earlier, synthetic strategies for homoleptic polyazido complexes tend to involve reaction of the corresponding element halide with an azide transfer reagent, most commonly NaN_3. Bulky, non-coordinating cations act as spacers and allow for the safe study and characterisation of these anions, however, the dilution of nitrogen content with carbonaceous counterions means the compounds are no longer nitrogen-rich overall. Combining polyazido complexes with nitrogenous cations could have a similar phlegmatic effect in forming insensitive salts by virtue of hydrogen bonding whilst retaining a higher proportion of the nitrogen content of the parent binary azide.

1.4.2 Nitrogen-rich cations

The smallest nitrogen-based cation is ammonium (NH_4^+, 78% N), salts of which are very well-characterised and (in general) chemically stable, but moving up to hydrazinium ($N_2H_5^+$, 85% N) there is a marked increase in the typical sensitivity of the salts. Incorporating a single carbon atom into the structure expands the range of available species without significantly compromising on nitrogen content. Triaminotetrazolium, and the various amino-substituted guanidinium cations are examples of such nitrogen-rich species that have been successfully incorporated into a variety of energetic nitrogen-rich salts.[96] More exotic examples of nitrogen-rich cations are the azidoformamidinium,[97] and triazidocarbenium.[98] Both are highly energetic, and have a tendency to form salts of high sensitivity towards impact, friction and ESD, owing to the introduction of one and three covalently bound azido groups respectively. The guanidinium cation has been the focus of several combined theoretical and experimental studies,[99,100] attracting interest for its denaturing influence on proteins, capacity to form supramolecular assemblies, and as a nitrogen-rich cation in energetic salts. Its

importance in these areas stems from its ability to form hydrogen bonds, and its trifunctionality means these hydrogen bonds can be propagated into 2D layers and/or 3D networks. Further substitution of hydrogens by up to three amino groups increases the nitrogen content of the cation by 10 % (Figure 1.10).

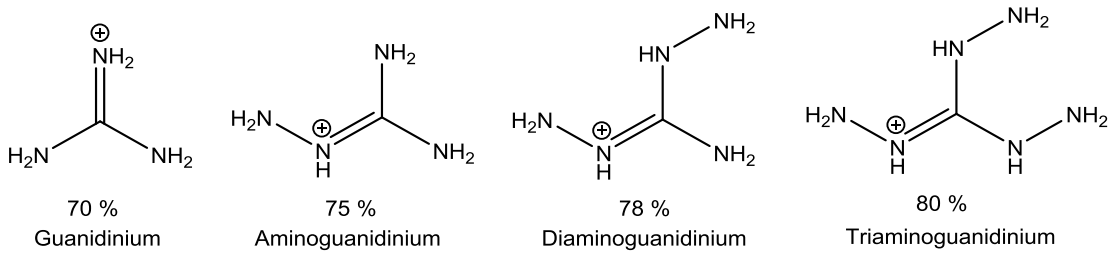

Figure 1.10. The percentage nitrogen content of guanidinium cations increases with subsequent substitution of protons with amino groups, though this is mitigated by an increase in cation volume, and reduction of packing efficiency due to lower symmetry.

There are many examples of salts of substituted guanidinium cations, which find applications as electrolytes,[101] and ionic liquids.[102,103] There are many known structures of these nitrogen-rich cations with energetic anions, including tetrazolates $(R–N_4C)^-$, triazolates $(R–N_3C_2)^-$,[104] perchlorate $(ClO_4)^-$,[105] trinitroformate $(C(NO_2)_3)^-$,[106] which have been developed as potential replacements for propellants and explosive compositions. The high nitrogen content of the cations increases the overall heat of formation of the salts compared to other cations.

1.5 Hydrogen Bonding

1.5.1 Defining the Hydrogen bond

The concept of the hydrogen bond is ubiquitous in chemistry, with more than one article every hour published on the subject, and in excess of 650,000 articles indexed in SciFinder, yet it is difficult to define it as a useful concept without being too broad and meaningless, or too restrictive and artificial. A review article concerning the hydrogen bond in the solid state was published by Steiner in 2002,[107] which begins with a definition (including its justification) of the hydrogen bond:

"An X–H···A interaction is called a hydrogen bond, if
1. it constitutes a local bond, and
2. X–H acts as a proton donor to A."

– Steiner, 2002

Needham[108] discussed the origin of the hydrogen bond and chemists' determination to develop a unifying definition, and showing how the concept has evolved and expanded during

the last century. An IUPAC task force made up of 14 crystallographers, spectroscopists, and theoreticians between 2005 and 2009, provided an updated definition[109] of the hydrogen bond supported by a technical report[110] in the same journal, discussing the history and perspectives from various fields within chemistry. The new definition consists of a preamble explaining and justifying the structure of the definition itself:

"The hydrogen bond is an attractive interaction between a hydrogen atom from a molecule or a molecular fragment X–H in which X is more electronegative than H, and an atom or a group of atoms in the same or a different molecule, in which there is evidence of bond formation."

– IUPAC Taskforce 2011

Next are a series of criteria (both experimental and theoretical) that strengthen the classification of an interaction as a hydrogen bond, followed by some characteristics of hydrogen bonded systems, and finally footnotes for the sake of clarity and completeness. Desiraju, a member of the taskforce, published an article[111] discussing the process and reasoning behind the newly formed definition, and offered a commentary on some of the items from the point of view of a crystallographer. With the definition of hydrogen bonds now extended from the 'classical' donors N–H and O–H to include weaker C–H,[112] P–H, and S–H, the breadth of interaction energies spans the gap of two orders of magnitude between van der Waals interactions (0.2 kcal mol^{-1}) and covalent bonds (40 kcal mol^{-1}). Within this range, hydrogen bonds are classified, broadly, as weak, moderate or strong. Strong and weak hydrogen bonds are those whose interaction energies are stronger or weaker than those found in the water-dimer, and moderate are about the same.[113] Geometric criteria are often applied to crystallographic data as a cut-off to determine whether a particular interaction should be considered a hydrogen bond or simply van der Waals forces. As the amassed crystallographic data archive expanded, thousands of datasets became available for comparative analyses, from which van der Waals (vdW) radii of the elements have been derived and tabulated, starting with Bondi in 1964, and Rowland and Taylor compiled an updated tabulation in 1996.[114] Intermolecular contact distances which were affected by hydrogen bonds were excluded from the study so as not to artificially shorten the apparent vdW radii. The updated values were generally within 0.05 Å of Bondi's values but hydrogen was estimated to be lower (around 1.1 Å rather than 1.2 Å), which has since been corroborated by neutron diffraction,[115] a technique which is inherently superior to X-ray diffraction for the accurate location of protons in crystal structures.

1.5.2 Graph set notation for description of hydrogen bonds in energetic compounds

Hydrogen bonding motifs can act cooperatively to make a 2- or 3-dimensional network in the solid state, which can be difficult to describe simply without loss of detail for meaningful comparisons. Graph set analysis was first formally applied to hydrogen bonds by Etter *et al.* in 1990,[116] and the principles expanded and clarified by a follow-up publication in 1995,[117] which included a series of case studies to aid understanding of the subject and prevent confusion. The notation is useful for describing compactly the hydrogen bond patterns in crystal structures, from simple intramolecular hydrogen bonds (S), dimeric or other finite interactions (D) to larger rings (R) and infinite chains (C) (Figure 1.11 below). The first level graph sets of a particular hydrogen bond network are those formed by a single crystallographically independent hydrogen bond, and second level graph sets are assigned in the form of a matrix by considering systematically the patterns formed by pairs of independent hydrogen bonds.

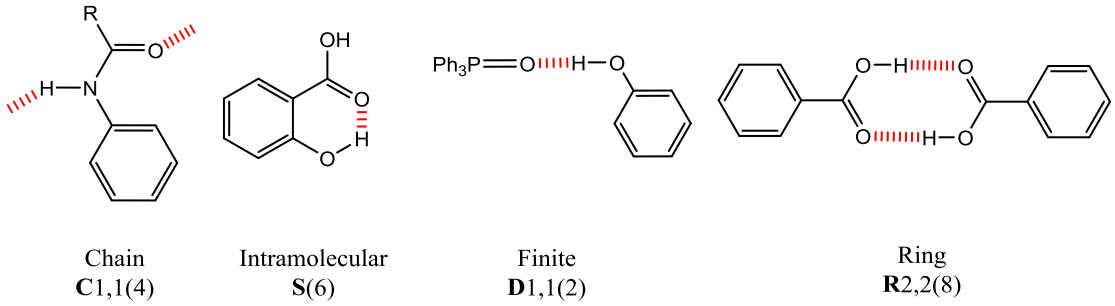

Figure 1.11. Examples of the different types of hydrogen bond patterns accompanied by their graph set descriptors. Adapted from ref. [117].

1.5.3 Hydrogen bonds in Energetic Compounds

Many nitrogen-rich salts have been realised in the past decade or so, particularly involving ammonium, hydrazinium, azidoformamidinium, aminotetrazolium, and guanidinium cations with various derivatives of tetrazole, including: 5,5'-bitetrazole,[118] 5,5'-azotetrazolate,[97] nitro- (NO_2),[119] azido- (N_3),[120] amino- (NH_2),[121,122] nitrimino- (N_2O_2),[123] and cyano- (CN)[124] tetrazolates (Figure 1.12 below). The thermochemical and sensitivity behaviour ranges from the thermally stable, insensitive salts of 5-aminotetrazole and 5-cyanotetrazole[124] to those of energetic, more sensitive 5-nitrotetrazole[119] and 5-azido-1*H*-tetrazole.[120] There are many more nitrogen-rich species than the few based on tetrazole discussed in this section, but the chosen examples cover a broad range of the sensitivity spectrum from the insensitive bis(guanidinium) 5,5'-bitetrazolate to the extremely sensitive guanidinium 5-azidotetrazolate hemihydrate.

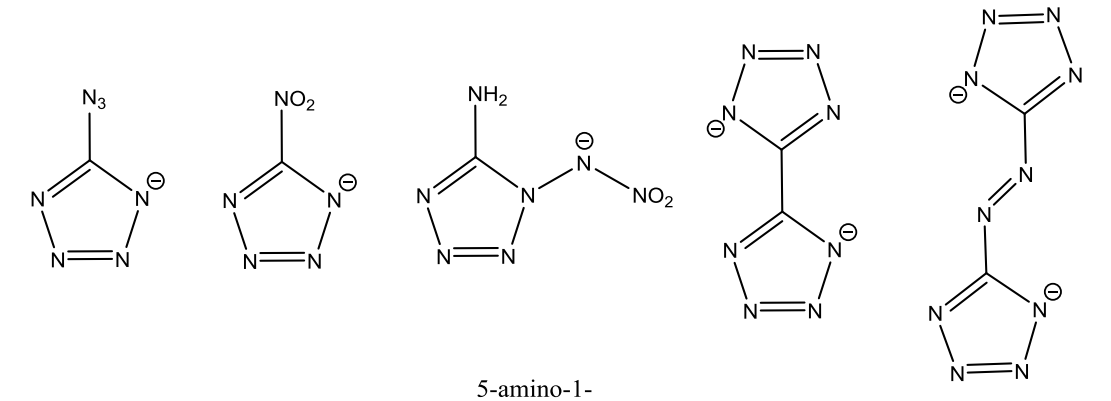

Figure 1.12. The structures of some energetic anions derived from tetrazoles, with their abbreviations in parentheses.

An example where hydrogen bonds with nitrogenous cations such as ammonium, hydrazinium, and guanidinium cations are insufficient to reduce the sensitivity are salts of 5-azidotetrazole, which have essentially the same sensitivity to friction (5–7 N) and impact (*ca.* 1 J) as the neutral compound 5-azidotetrazole (<5 N and <1 J). The introduction of a covalent azide increases the molar (kJ mol^{-1}) and specific (kJ g^{-1}) energy content but makes them some of the most sensitive derivatives of 1*H*-tetrazole. The inclusion of crystal water in the solid state structure provides extra opportunities for hydrogen bonds to form, and can result in an insensitive salt, but this is not the case for the guanidinium 5-azidotetrazolate hemihydrate (GATh). Another endothermic group that can be incorporated into energetic compounds is the nitro group ($–NO_2$), which can also participate in hydrogen bonds *via* the two oxygens. The reduced sensitivity of the 5-nitrotetrazolate versus 5-azidotetrazolate salts may be attributed to the availability of extra hydrogen bond acceptors, and the more symmetrical shape (C_{2h} *vs*. C_s) allows neater packing in the layer structure. The crystal structures of guanidinium 5-nitrotetrazolate (GNT) and guanidinium 5-azidotetrazolate hemihydrate (GATh) are shown in Figure 1.13. Graph set analysis enables concise descriptions of extended hydrogen bond networks, and can help to identify common features of hydrogen bonding patterns.[117]

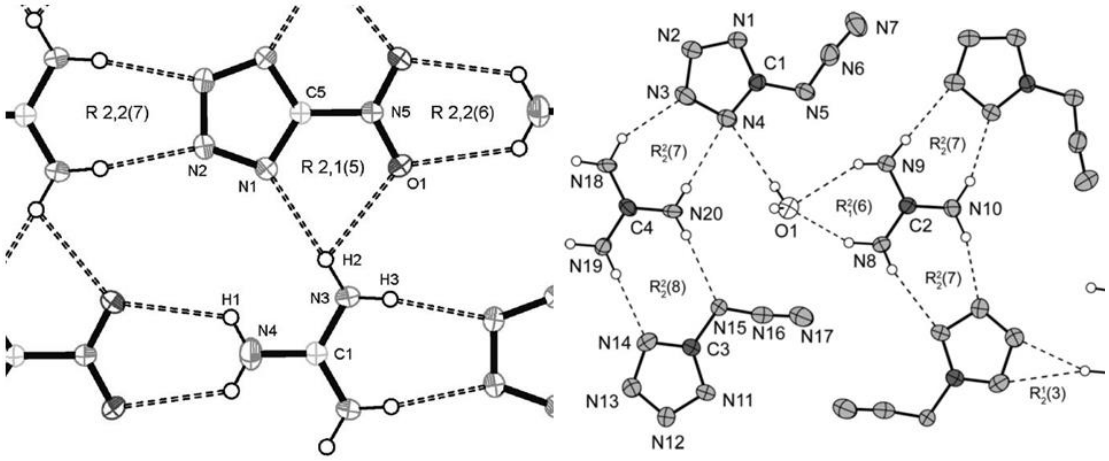

Figure 1.13. Thermal ellipsoid plots showing the hydrogen bonding patterns in the layered structures of guanidinium 5-nitrotetrazolate ("GNT", left)[119] and guanidinium 5-azidotetrazolate hemi-hydrate ("GATh", right).[120]

All six guanidinium protons are involved in hydrogen bonds in both structures with more or less bent D–H···A angles, which range from 126–177° and 150–172° for GNT and GATh respectively. The water molecule in GATh forms the sole interlayer hydrogen bond in the structure, whereas in GNT the coplanar guanidinium and 5-nitrotetrazolate ions form layers in a sort of 'chessboard' arrangement. There are cases where the crystal structure is not simply parallel hydrogen bonded sheets, for example guanidinium 5-cyanotetrazolate (GCT). Like the 5-azidotetrazolate ion, 5-cyanotetrazolate is a binary C/N moiety, but its salts with nitrogenous cations are at the opposite end of the sensitivity scale – most are insensitive to friction (>360 N), and impact (>40 J) and none of them detonate upon heating. The authors have identified 8 crystallographically independent hydrogen bonds in guanidinium 5-cyanotetrazolate between the planar ions, so it might be expected to form a structure similar to GNT and GATh (Figure 1.13 above). The R2,2(7), R4,4(10), and D graph sets combine to make intersecting 'ribbons' (Figure 1.14), with the R1,2(6) graph set connecting neighbouring ribbons. The ability of guanidinium to form extensively hydrogen bonded structures in layers or 'ribbons' with planar tetrazole derivatives such as 5,5'-azotetrazolate, 5-nitrotetrazolate, and 5-cyanotetrazolate may be significant in determining the relative sensitivity of the guanidinium salt compared to other non-planar nitrogen-rich cations. Figure 1.15 shows the sensitivity data reported for the 5-nitrotetrazolate salts investigated in ref. [119], showing guanidinium to be the least sensitive (anhydrous) salt. It is interesting to note that the anhydrous triaminoguanidinium salt (TAGNT) is the second most sensitive, but inclusion of crystal water into the structure (TAGHNT) renders the compound insensitive to friction (>360 N) and impact (>40 J).

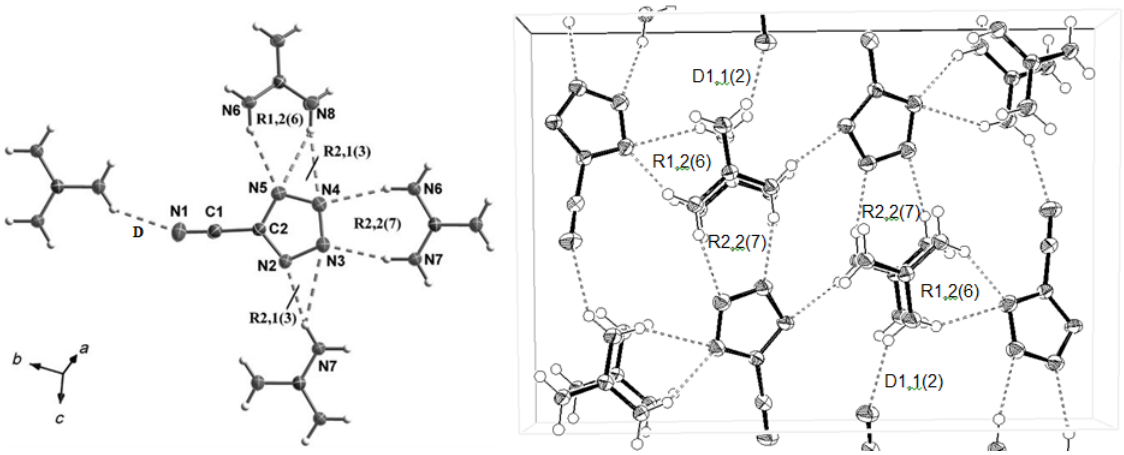

Figure 1.14. Representations of various hydrogen bond patterns in the structure of guanidinium 5-cyanotetrazolate (GCT), which are prevalent in a wide range of guanidinium salts. *Left*: Figure 8 from ref. [124] showing four guanidinium cations surrounding one 5-cyanotetrazolate anion, including the graph sets D1,1(2) and R2,1(3) – a bifurcated hydrogen bond donor; *Right*: A representation of four hydrogen bond patterns: D, the shortest hydrogen bond in GCT; R4,4(10), which connects alternately two anion/cation pairs; R2,2(7) between one cation/anion pair; R1,2(6) between one cation/anion pair.

In the case of an energetic non-planar tetrazole derivative, 5-amino-1-nitriminotetrazolate (NIT), guanidinium also forms the least sensitive salt compared with the neutral compound and nitrogenous salts in ref. [123]. This may be because guanidinium has the greatest number of potential hydrogen bond donors, and cannot hydrogen bond to itself, which has been observed in amino-substituted guanidinium cations (e.g. see Figure 1.18).

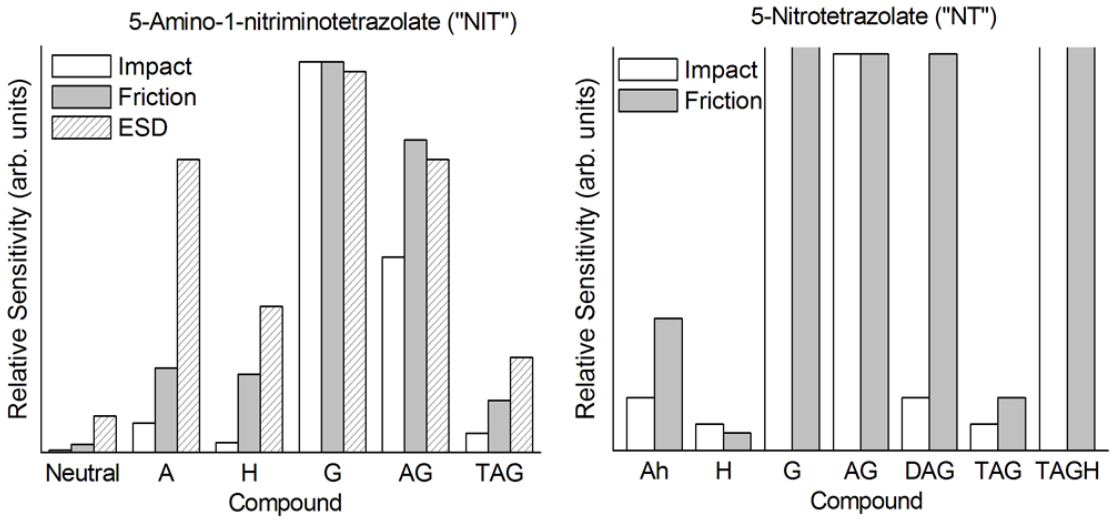

Figure 1.15. A compilation of sensitivity data reported for 5-amino-1-nitriminotetrazole[123] and its nitrogen-rich salts ("NIT", left), and 5-nitrotetrazole[119] salts ("NT", right). Qualitative testing of 5-nitrotetrazolate salts shows that only the hydrazinium salt is sensitive to electrostatic discharge (*ca.* 20 kV). Cations: A = ammonium, H = hydrazinium, G = guanidinium, AG = aminoguanidinium, DAG = diaminoguanidinium, TAG = triaminoguanidinium; h = hemi-hydrate, H = hydrate. Bars which exceed the height of the graph represent insensitive compounds (>360 N friction, and > 40 J impact sensitivity).

The 5,5'-azotetrazolate dianion ("ZT") enables preparation of higher nitrogen content compounds compared to tetrazolate without the extreme sensitivity accompanying 5-azidotetrazolate. However ZT salts are prone to decomposition in even mildly acidic conditions, but 5,5'-bitetrazolate ("BT") circumvent this issue by omission of the azo bridge. Both families of compounds are thermally stable, with the BT salts having lower impact sensitivities than the corresponding ZT salt (Figure 1.16), and generally comparable friction sensitivities.

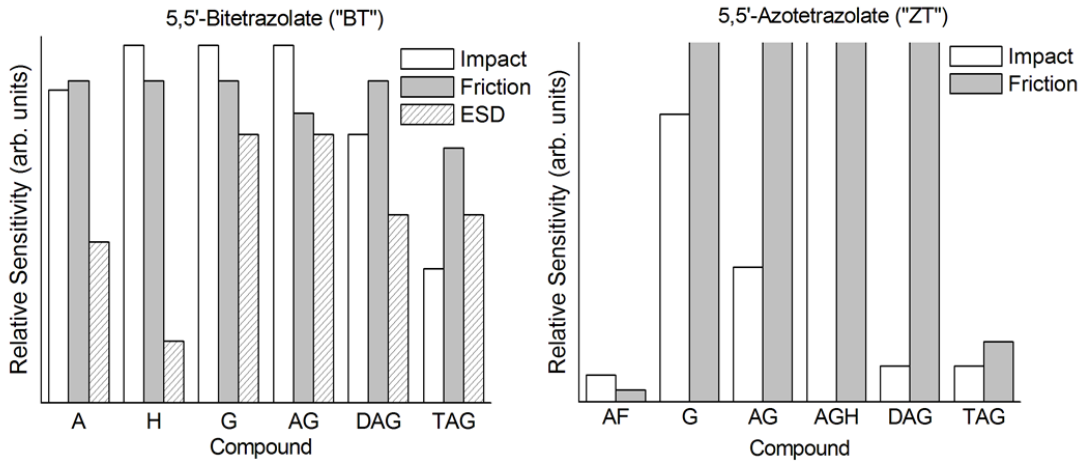

Figure 1.16. A comparison of the relative sensitivities of compounds based on 5,5'-bitetrazolate[125] (left) and 5,5'-azobis(tetrazolate)[97] (right) towards external stimuli. (ESD = electrostatic discharge). Cations: A = ammonium, H = hydrazinium, G = guanidinium, AF = azidoformamidinium, AG = aminoguanidinium, DAG = diaminoguanidinium, TAG = triaminoguanidinium; H = hydrate. Bars which exceed the height of the graph represent insensitive compounds (>360 N friction, and > 40 J impact sensitivity).

Of these nitrogen-rich cations, azidoformamidinium ("AF") forms the most sensitive compounds with ZT and BT, and lies between guanidinium and highly endothermic triazidocarbenium[98] ($C(N_3)_3^+$) in the series of azido substituted carbocations. It is perhaps not surprising that the introduction of a covalent azide yields a more sensitive salt. As in the case of 5-azidotetrazolate, the azide group does not participate in any hydrogen bonds, and the number of available hydrogen bond donors is reduced from six to four. The molecular structure of AFZT determined by single-crystal XRD is shown in Figure 1.17 below.

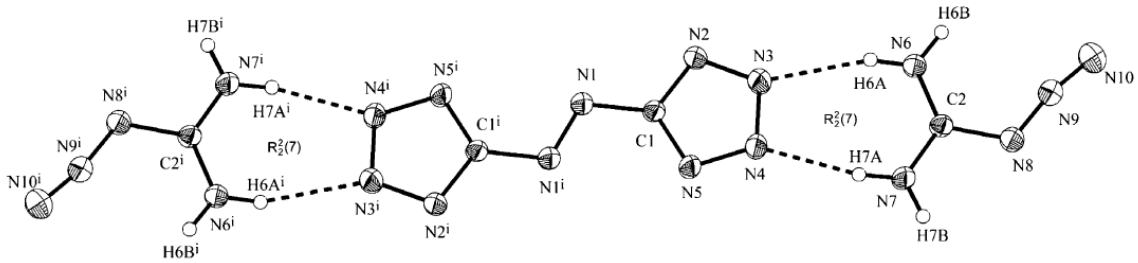

Figure 1.17. Thermal (displacement) ellipsoid plot showing the molecular structure of bis(azidoformamidinium) 5,5'-azotetrazolate ("AFZT"), Figure 2 from ref. [97]**.** There is an inversion centre at the middle of the anion, so only half of the above structure is crystallographically independent.

These four crystallographically independent N–H···N hydrogen bonds have non-bonded N···N distances in the range of 2.9037(5)–2.9976(5) Å, and N–H···N angles of 161–167°. The hydrogen bonds on the amino group *trans* to the azide group are slightly shorter, perhaps due to repulsive forces between (or steric hindrance of) the electron-rich tetrazolate ring and azido group. The azidoformamidinium cation participates in an R2,2(7) graph set at each end of the ZT anion, and to the first nitrogen of another tetrazolate ring. Bis(aminoguanidinium) 5,5'-azotetrazolate monohydrate (AGZTH) is the least sensitive salt of these 5,5'-azotetrazolate (ZT) salts, partially owing to the crystal water, which lessens the overall nitrogen content but provides additional hydrogen bond donors/acceptors. The geometry of the eight crystallographically independent hydrogen bonds is compiled in Table 1.2 below. The longest two hydrogen bonds in the structure are inter-guanidinium bonds, which are slightly longer as the donor/acceptor pair are both cations. The shortest is also an inter-guanidinium hydrogen bond, though it is likely not to be the strongest as it is furthest from linearity. The shortest, most linear hydrogen bonds are those from the amino group to the 1-position on the tetrazole ring, which incidentally is the site of deprotonation from the neutral species 5,5'-azotetrazole. The greater degree of hydrogen bonding in the structure, and the absence of a covalent azide group places AGZTH at the opposite end of the scale of sensitivity to AFZT. When the crystal water is removed (leaving AGZT), the compound is much more sensitive to impact (15 J *vs.* >40 J). The trend continues for further substitution of the guanidinium cation to the di- and triaminoguanidinium cations, which are even more sensitive to impact (*ca.* 4 J), which could be attributed to less effective hydrogen bonding capability due to loss of planarity of the ions, or the inclusion of more hydrazino- (N–N) moieties in the cation. GZT has a complex hydrogen bonding network, including R4,4(10), R2,2(9) and R1,2(7) graph sets (see Figure 1.19 below). There are more N–H protons available for hydrogen bonds than in the azidoformamidinium salt (AFZT, Figure 1.17), and no intercationic hydrogen bonds are possible unlike the structure of the aminoguanidinium salt (AGZTH, Figure 1.18). All ten ZT nitrogen atoms accept a total of 12 hydrogen bonds from a total of six guanidinium cations, and accordingly the guanidinium cations are surrounded by three ZT dianions. Unlike the AF cation, both the aminoguanidinium and guanidinium cations form hydrogen bonds to the azo nitrogen (Figures 1.18 and 1.19, respectively).

Table 1.2. Hydrogen bond geometries in bis(aminoguanidinium) 5,5'-azotetrazolate monohydrate (AGTZH), sorted firstly by net D, A charge difference and secondly by shortest to longest D···A distance.

D–H···A [Å]	D···A [Å]	D–H···A [°]	D, A Charges	Nature of D, A	1st Level Graph Set
N7–H7A···N5	2.933(3)	170(2)	+ / –	amino/tetrazolato	D2,2(8)
N7–H7B···N4^{v}	2.944(2)	179(3)	+ / –	amino/tetrazolato	D2,2(10)
N9–H9B···N2^{vii}	3.156(3)	162(2)	+ / –	hydrazino/tetrazolato	D2,2(8)
N6–H6A···N1	3.201(2)	165(3)	+ / –	amino/azo	D2,2(4)
O1–H1···N3	2.842(2)	172(3)	n / –	water/tetrazolato	D1,1(2)
N8–H8···O1^{iii}	2.884(2)	152(2)	+ / n	imino/water	D1,2(3)
N6–H6B···N9^{iv}	3.247(3)	151(3)	+ / +	amino/hydrazino	R2,2(10)[a]
N9–H9A···N8^{vi}	3.288(2)	148(2)	+ / +	hydrazino/imino	C1,1(3)

[a]Interguanidinium hydrogen bond. 'n' denotes neutral species. Symmetry codes: (iii) 0.5 – x, 1.5 + y, 0.5 – z; (iv) 1 – x, –y, 1 – z; (v) 0.5 – x, –0.5 + y, 0.5 – z; (vi) 1 – x, 1 – y, 1 – z; (vii) –0.5 + x, 0.5 + y, z.

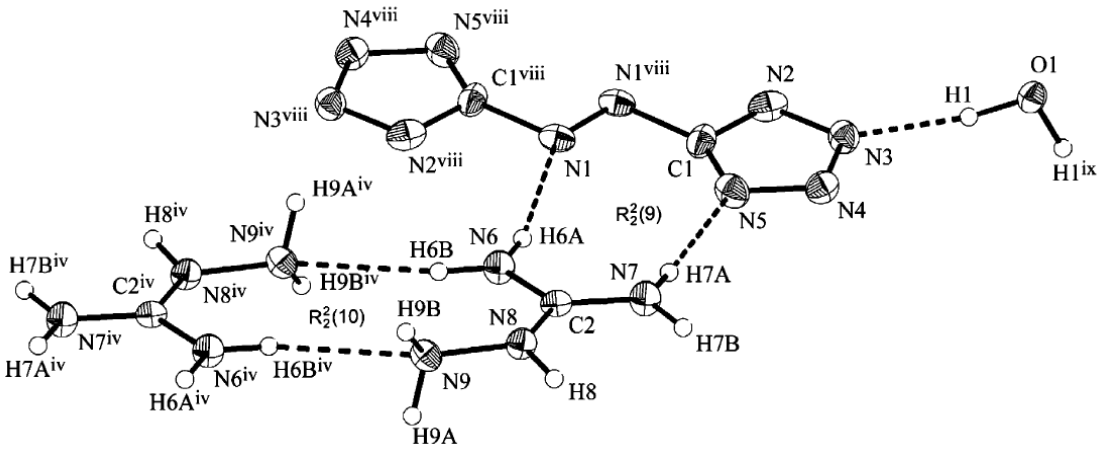

Figure 1.18. Thermal ellipsoid plot showing the hydrogen bonds in bis(aminoguanidinium) 5,5'-azotetrazolate monohydrate (AGZT), including the interguanidinium hydrogen bond (Figure 3 from ref. [97]).

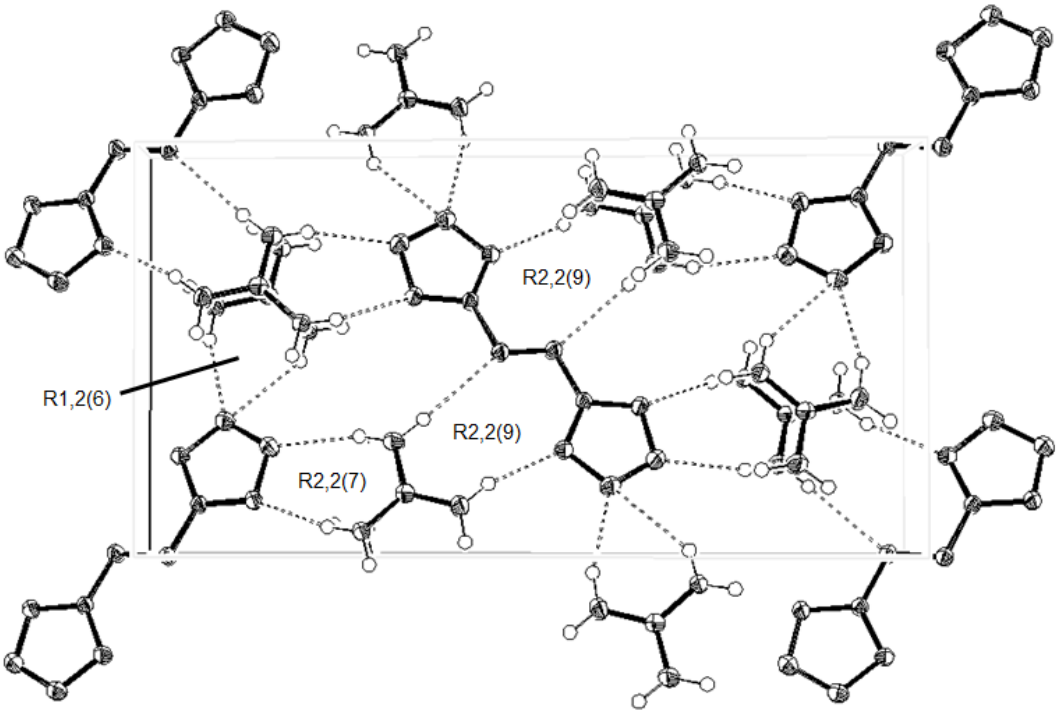

Figure 1.19. Thermal ellipsoid plot showing the hydrogen bonds in the unit cell of bis(guanidinium) 5,5'-azotetrazolate (GZT), including selected graph sets formed by the hydrogen bonds.[97]

1.6 Summary

Energetic materials have applications as explosives, propellants and pyrotechnics. There is a large volume of research toward nitrogen-rich replacements, motivated by environmental concerns, performance improvement, and smokeless compositions. The beneficial properties of contemporary nitrogen-rich compounds, such as low smoke (low residue), and environmentally inert gaseous by-products are suited particularly well to propellant systems. Rocket propellant systems are commonly bipropellants, where the high energy density material (monomethylhydrazine) is partitioned from the oxidiser (N_2O_4). The combination of high volatility, flammability, and toxicity of monomethylhydrazine poses serious health and environmental concerns. The development of suitable nitrogen-rich propellant formulations could circumvent the need for an oxidiser component as their high energy content is derived from high heats of formation. Some nitrogen-rich compounds are too sensitive for applications in their own right, but it is possible to achieve compromise between sensitivity and energetic nature through several existing methods. Their inclusion into a salt with bulky non-coordinating cations or into a neutral complex with ancillary ligands have both been demonstrated as practical strategies in this regard. This concept makes the study of these interesting species safer and more convenient, but their energy content is decreased proportionally as the nitrogen content is reduced.

The hydrogen bond covers a range of non-covalent interaction energies between 4 and 160 kJ mol^{-1} and it has proven difficult to determine a universal definition of the concept. Assigning hydrogen bonds solely on their geometry is convenient for structure searching, but a combination of experimental and theoretical evidence is preferred. The nature of the donor and acceptor groups should be considered, as both affect the strength of the hydrogen bond formed. Protic nitrogen-rich energetic compounds can generally be stabilised by incorporation into a salt in their deprotonated form, with a suitable cation capable of forming hydrogen bonds such that the energetic anions are well spaced. There are exceptions, including the 5-azidotetrazolate salts, which seem to be extremely sensitive even when paired with nitrogenous cations rich in hydrogen bond donors. The guanidinium salts of the energetic anionic species 5-nitrotetrazolate, 5-amino-1-nitriminotetrazolate, 5-cyanotetrazolate, 5,5'-bitetrazolate, and 5,5'-azotetrazolate seem to be the least sensitive compared to other similarly nitrogen-rich cations. There are many factors which govern the sensitivity of the energetic compounds, including the thermal stability of the individual components, the efficiency in the crystal packing arrangement, and the inclusion of crystal water. It seems that, in some cases, the formation of a hydrogen bonded network can overcome the sensitive nature of the constituents. If a network of hydrogen bonds is restricted owing to the geometry or the nature of either the donors or acceptors, then the sensitivity of the resulting compound may be higher.

2. Investigation into the stabilising effect of hydrogen bonds in nitrogen-rich guanidinium salts

Aims

I. Elucidate the effect of hydrogen bonds on the structures and properties of nitrogen-rich guanidinium salts with anionic polyazido complexes, azide and tetrazolate anions.
II. Characterise hydrogen bond networks in the crystal structures of compounds described in (I) by graph set analysis.
III. Determine the stabilising (or labilising) influence of replacing bulky, weakly coordinating cations in anionic polyazido complexes with guanidinium cations, with an emphasis on assessing the thermal stability and enthalpy of decomposition
IV. Establish qualitatively the effects of hydrogen bonding on the specific enthalpies of decomposition of nitrogen-rich salts

2.1 Introduction

2.1.1 Relationship between structure and sensitivity of nitrogen-rich compounds

Nitrogen-rich compounds have been the subject of research for new energetic materials as their decomposition primarily releases the environmentally benign dinitrogen (N_2) (for more details see section 1.1.3 above). Depending on the structure, high nitrogen content can be accompanied by higher sensitivity of a compound to impact or friction. This is exemplified by a plethora of azides and azole derivatives (particularly tetrazoles and bistetrazoles, and their salts) which have reported previously.[126,127] Nitrogen-rich salts have several advantages over their neutral molecular analogues. This includes a tendency for higher thermal stability and lower vapour pressures, and the greater flexibility to "tune" properties of the compound by varying both cation and anion of the salt. For example, ammonium azide and hydrazinium azide have nitrogen content exceeding 90 % (*w*/*w*) nitrogen, and these salts can be prepared by combination of some of the simplest nitrogen-rich building blocks.[50,128] The compounds are insensitive but are volatile by virtue of the volatility of their dissociation products, HN_3, and NH_3 or N_2H_4 respectively. This is contrasted by more exotic nitrogen-rich coordination compounds requiring sophisticated synthetic methods, such as the pentazenium salts $(N_5)[P(N_3)_6]$ and $(N_5)[B(N_3)_4]$ which have even greater nitrogen content, but are *highly* sensitive and this has hampered their characterisation.[27] From an organic chemistry

perspective, the synthesis of nitrogen-rich heterocyclic compounds have been subject to extensive investigations. These compounds have sensitivities ranging from the extremely sensitive salts of 5-azido-1*H*-tetrazole (82–88 % N)[120] or 5-nitrotetrazolates[119] to the insensitive 2-methyl-5-nitriminotetrazolates[129] or bis(hydrazinium) 5,5'-azotetrazolate (85.2 % N).[130] Likewise, some neutral compounds such as 5,5'-hydrazine-1,2-bis(1*H*-tetrazole) (HBT)[125] are insensitive, whilst others such as 5,5'-bitetrazole,[131] 5,5'-bistetrazolylamine[132] and 2,4,6-tris(tetrazol-1-yl)-1,3,5-triazine[133,134] ("TTT", **20**, see chapter 5) are sensitive. Whilst it is not possible to predict with confidence the sensitivity of a compound *ab initio*, comparison of its structure with related compounds available in the literature can hint at possible structure-sensitivity relationships. For this reason, previous investigations of nitrogen-rich species have often made use of weakly-coordinating counterions,[86,83,88] less-energetic ancillary ligands to form neutral complexes,[135,34,81,136] polyfunctional hydrogen bonding cations such as guanidinium.[127,126] The general consensus in the literature is that extensive hydrogen bonding within the structure of a compound tends to have a 'stabilising' effect (i.e. reduce propensity to detonate).[125,127] Two examples of such compounds are energetic compounds 2,4,6-triamino-1,3,5-trinitrobenzene (TATB)[137] and 1,1-diamino-2,2-dinitroethylene (FOX-7),[138,139] which are powerful yet insensitive explosives that have extensively hydrogen bonded structures between the complementary amino donors and nitro acceptors. For FOX-7 it is claimed that the hydrogen bonding interactions *increase* the barrier to cleavage of the reactive C–NO_2 bonds.[139] If such stabilisation of these reactive bonds within energetic compounds proves to be generally applicable, it may allow the preparation of new nitrogen-rich compounds containing weak N–N bonds. Whilst this notion has been considered for organic CHNO explosives, its extension to coordination compounds may allow the preparation of insensitive polyazides or polytetrazolato complexes without relying on bulky cations or ancillary ligands. This chapter explores the (potential) stabilising effect of hydrogen bonds on complex nitrogen-rich anions such as polyazides.

2.1.2 Review of the literature on guanidinium azides

Guanidinium azides have been the subject of patents from the 1960s,[140] as mixed salts with various nitrogenous bases[141] in the context of propellants research. Tetra- and hexamethylguanidinium azides have been employed in the preparation of organic azides and 5-substituted tetrazoles, where solubility of the azide transfer reagent in organic solvents is advantageous.[142,143] The synthesis of guanidinium azide (**1**) was first described under the name 'guanidine trinitride' in 1934,[144] before the term 'azide' became the accepted systematic name. Guanidinium azide (**1**) was first prepared from an aqueous solution of guanidinium chloride, -sulphate, or -carbonate with silver azide, barium azide, or hydrazoic acid, respectively. The authors preferred the latter method in order to achieve high yield and allow convenient purification by evaporation of the volatile acid, and to avoid the handling of

sensitive silver- or barium azides. Crystallisation from water yielded guanidinium azide monohydrate (**1a**), which was dried by storing over P_4O_{10}. Its identity was confirmed by elemental analysis, and by reactions with $FeCl_3$, and CS_2 (forming guanidinium azidodithiocarbonate), and a melting point of 93.5 °C was reported.[144] Diaminoguanidinium azide has been prepared by exploiting the reaction of potassium azide with guanidinium tetrafluoroborate in isopropanol, during the course of an investigation into new energetic ionic liquids.[47] Triaminoguanidinium azide was the subject of a patent from 1967,[145] and a technical report in 1988, which compiled the existing literature and provided detailed insight into the surprisingly challenging synthesis.[146] The difficulties described in the report may account for the (relatively) recent determination of its crystal structure, which was only reported in 1990.[147] A study which compared the burning characteristics of high-nitrogen compounds including guanidinium- (**1**), aminoguanidinium- (**2**), and 1,2,3-triamino-guanidinium azide (TAZ) concluded that salts of more basic amines tend to have reduced combustion stability.[148] Aside from the literature summarised above, there is little information available on the characterisation of guanidinium azide, and aminoguanidinium azide (**2**) is absent from the literature, to the best of our knowledge. In the following results, the research relevant to the aims stated above will be reported, including the optimisation of syntheses of azides **1** and **2**, and the characterisation of the compounds by FTIR and NMR spectroscopies, thermal analyses (DSC and TGA), elemental analysis, and the solid state structures determined by single crystal X-ray diffraction.

2.2 Results and Discussion

2.2.1 Syntheses and physical properties of nitrogen-rich guanidinium salts

The preparation of the guanidinium azides precursors was essential in order to investigate the guanidinium salts of hexaazido complexes. Due to the lack of information available on guanidinium azides at the outset of this project, it was not clear whether these salts would themselves be sensitive as their nitrogen content exceeds 82 %. It seems that neither guanidinium azide or aminoguanidinium azide are sensitive, though this is based on primitive qualitative tests and anecdotal evidence as no quantitative sensitivity testing was possible. The syntheses of the new compounds described in this chapter are outlined in Scheme 2.1 below.

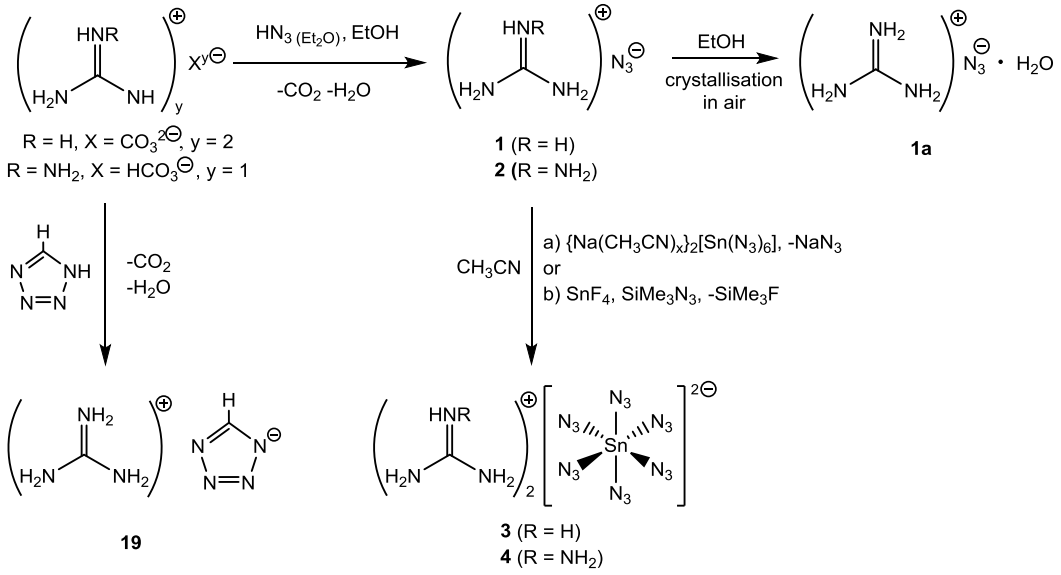

Scheme 2.1. Synthesis of guanidinium azides, guanidinium tetrazolate, and bis(guanidinium) hexaazidostannate salts.

Syntheses and properties of guanidinium azides

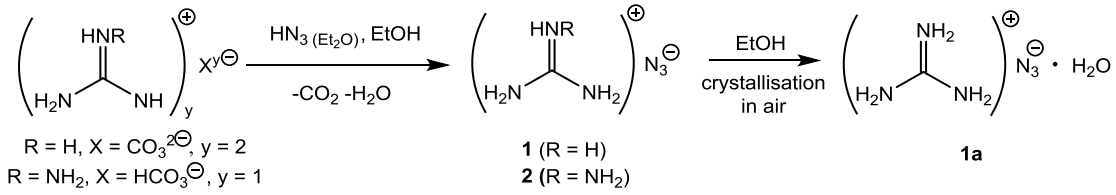

Scheme 2.2. Syntheses for guanidinium azide (**1**), guanidinium azide monohydrate (**1a**) and aminoguanidinium azide (**2**).

Guanidinium azide (**1**) is a hygroscopic crystalline colourless solid which is highly soluble in water, pyridine, dimethylsulfoxide, and alcohols; it is insoluble in hydrocarbons, benzene, ethyl acetate, Et_2O, CH_2Cl_2, and THF, and sparingly soluble in MeCN. Upon exposure to moist air crystalline **1** deliquesces to form guanidinium azide monohydrate (**1a**). Initially during this work **1** was prepared *via* reaction of the free base guanidine with ethereal hydrazoic acid (HN_3), though sodium ethoxide impurity in the guanidine led to contamination of **1** with NaN_3 from which separation was achieved using a Soxhlet extraction apparatus with acetonitrile. This could be prevented by purification of guanidine by sublimation, as described since the original publication detailing its synthesis.[74] The most convenient procedure for preparation of anhydrous **1** is reaction of excess ethereal HN_3 with a suspension of guanidinium carbonate in dry ethanol (see Scheme 2.2 above). The choice of ethanol instead of water, as in the published procedure, allows the direct synthesis of anhydrous **1**, bypassing the monohydrate (**1a**). Aminoguanidinium azide (**2**), whilst not hygroscopic gradually turns pink-orange in colour upon long-term storage in air, which is similar to the behaviour of triaminoguanidinium azide (TAZ),[146] which turns a darker pink colour, and triaminoguanidinium nitrate (TAGN)[149] which turns brown/pink. The proposed origin of the

discolouration is oxidation of the free base 1,2,3-triaminoguanidine (Scheme 2.3 below) in the presence of air, which is catalysed by the presence of transition metal impurities.[149]

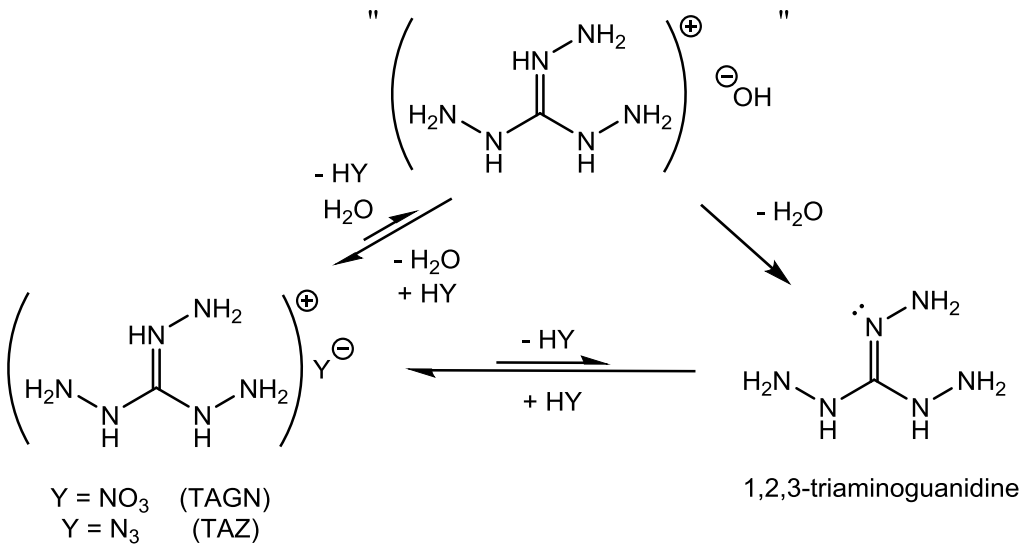

Scheme 2.3. Possible mechanisms for the formation of free base 1,2,3-triaminoguanidine from triaminoguanidinium pseudohalide salts 1,2,3-triaminoguanidinium nitrate (TAGN) and 1,2,3-triaminoguanidinium azide (TAZ). Subsequent oxidation of this reactive species is the proposed source of the discolouration of samples of TAGN and TAZ upon storage in air, which is also observed for aminoguanidinium azide (**2**).

During the synthesis of **2** in this work, a possible source of metal ions could have been the action of dilute HN_3 in the solution on the stainless steel filter canula. Compound **2** was prepared similarly to **1** starting from aminoguanidinium bicarbonate, which proved less reactive towards ethereal HN_3 than guanidinium carbonate, with a yield of only 12 % after 24 hours. Heating the mixture to 40 °C greatly improved the conversion efficacy, though concomitantly increased the evaporation rate of the volatile ethereal HN_3 (b.p. 36 °C). Sealing the system would hinder removal of CO_2 from the equilibrium and could have led to excessive pressure build up in the vessel. Therefore, addition of a second excess of ethereal HN_3 was necessary to replenish the evaporative losses. The solubility of aminoguanidinium azide (**2**) in ethanol is considerably lower than guanidinium azide (**1**). Compound **2** is highly soluble in water and dimethylsulfoxide, moderately soluble in alcohols, insoluble in hydrocarbons, Et_2O, CH_2Cl_2, and THF, and sparingly soluble in MeCN. The third homologue belonging to the class of (amino)guanidinium azides is triaminoguanidinium azide, for which the unexpectedly challenging syntheses were reviewed in a technical report.[146] Initial methods for preparation of the azide included reaction of the free base triaminoguanidine with methanolic HN_3 solution or metathesis between sodium azide and triaminoguanidinium sulphate. However, preparation of triaminoguanidine is not trivial, and the materials obtained *via* these two routes had nitrogen contents that deviated considerably and unacceptably from the theory (found 83 % *vs.* required 85.7 %). The metathetical product always contained sodium sulphate impurity. In the case of TAGN, exclusion of atmospheric oxygen and the use of deionised water minimised the

discolouration, and acceptable TAZ purity was achieved by using a non-aqueous ion-exchange resin.[146] Inspection of the FTIR spectrum of a sample of TAZ exposed to air (in a closed vial) for 4 months reveals an additional sharp but weak band at 2158 cm^{-1}, which could be trapped HN_3, as assigned in the infrared spectrum of (solid) ammonium azide.[150] A new synthetic procedure has been developed for TAZ, starting from newly available **2**, by a similar procedure to triaminoguanidinium chloride[151] by heating to reflux a mixture of compound **2** with two equivalents of hydrazine hydrate in ethanol, and recrystallisation from anhydrous ethanol.

Synthesis and properties of bis(guanidinium) hexaazidostannate (3)

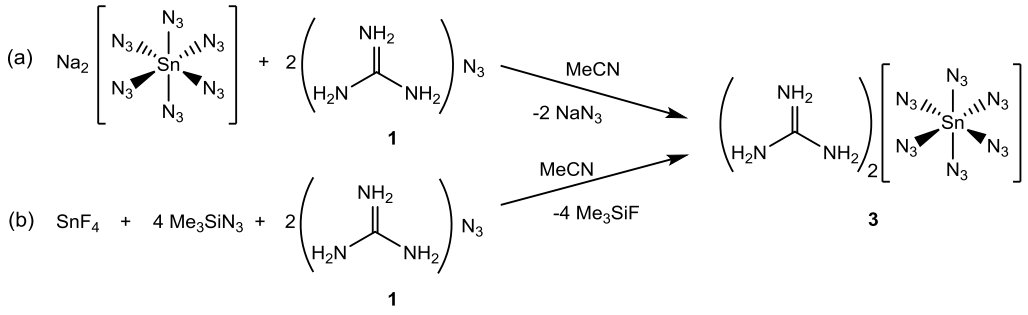

Scheme 2.4. Syntheses of bis(guanidinium) hexaazidostannate (**3**).

Bis(guanidinium) hexaazidostannate, $\{C(NH_2)_3\}_2[Sn(N_3)_6]$ (**3**), is a moisture sensitive crystalline solid with a relatively low melting point of 116 °C, which is highly soluble in MeCN and THF, and completely insoluble in CH_2Cl_2 and Et_2O. Hydrolysis occurs more quickly than $(PPN)_2[Sn(N_3)_6]$ (**9**) in solution and in the solid state upon air exposure, which can be attributed to the more hydrophilic nature of the guanidinium cation compared to $(PPN)^+$. Compound **3** can be prepared *via*: (a) metathesis of guanidinium azide (**1**) with disodium hexaazidostannate as for the $(PPN)^+$ salt,[85] or (b) tin tetrafluoride and trimethylsilyl azide in the presence of **1** in acetonitrile (see Scheme 2.4 above). Both $Na_2[Sn(N_3)_6]$ and $\{C(NH_2)_3\}_2[Sn(N_3)_6]$ are very soluble in CH_3CN, and the presence of either seems to increase the solubility of **1** in CH_3CN, so fractional crystallisation to remove the slight excess of unreacted guanidinium azide is necessary before crystallisation of **3**. Also **3** is accessible by reaction of $SnCl_4$ with two successive batches of **1** in a large excess, but separation from the guanidinium azide/chloride mixture is less convenient than either method (a) or (b). Preparation *via* $SnCl_4/NaN_3$ has the advantage of the cheapest most readily available starting materials, whereas the ligand exchange reaction is faster for $SnF_4/TMS–N_3$ due to the strong enthalpic preference for Si–F versus Si–N bonds. Addition of a slight excess of trimethylsilyl azide ($TMS–N_3$) to an acetonitrile suspension of guanidinium azide and SnF_4 (2.2 : 1 mixture), and stirring for 16 h at 45 °C with overpressure relief leads to formation of **3** in solution under loss of TMS–F (b.p. 15 °C). Needle crystals of **3** are obtained by slow cooling of a saturated acetonitrile solution. The elemental analysis values for material tended to have slightly high

nitrogen content (0.6 %), which could be a trace amount of guanidinium azide which is solubilised by the high concentration of **3** in the supernatant solution.

Synthesis and properties of guanidinium tetrazolate, {C(NH$_2$)$_3$}N$_4$CH (19)

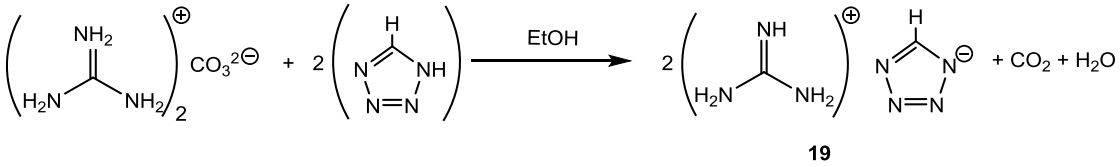

Scheme 2.5. Synthesis of guanidinium tetrazolate (**19**).

A range of alkali metal salts of 1*H*-tetrazole, as well as ammonium- and hydrazinium tetrazolate have been prepared previously,[152] but there are no reports on the nitrogen-rich guanidinium salts. In order to investigate the viability of nitrogen-rich coordination compounds such as guanidinium salts of hexakis(tetrazolato) complexes, it was necessary to develop a synthesis for guanidinium tetrazolate. Addition of an ethanolic solution of 1*H*-tetrazole to a slight excess of guanidinium carbonate suspended in ethanol resulted in rapid evolution of gas through the attached paraffin bubbler and the solution became virtually clear after around 10 minutes (see Scheme 2.5 above). The majority of the excess guanidinium carbonate precipitated after concentration of the reaction solution, and was removed by filtration. Further concentration of this filtrate solution yielded crystalline guanidinium tetrazolate after slow cooling of this warm solution to –19 °C overnight. Elemental analyses suggested the presence of residual guanidinium carbonate despite several recrystallisations, suggesting further refinement of the synthesis is necessary. Use of a strictly stoichiometric ratio of 1*H*-tetrazole and guanidinium carbonate, or a slight excess of 1*H*-tetrazole may prove a slightly more convenient separation.

2.2.2 Attempted syntheses of guanidinium salts of other main group hexaazido complexes

Attempted syntheses of bis(aminoguanidinium) hexaazidostannate(IV) (4)

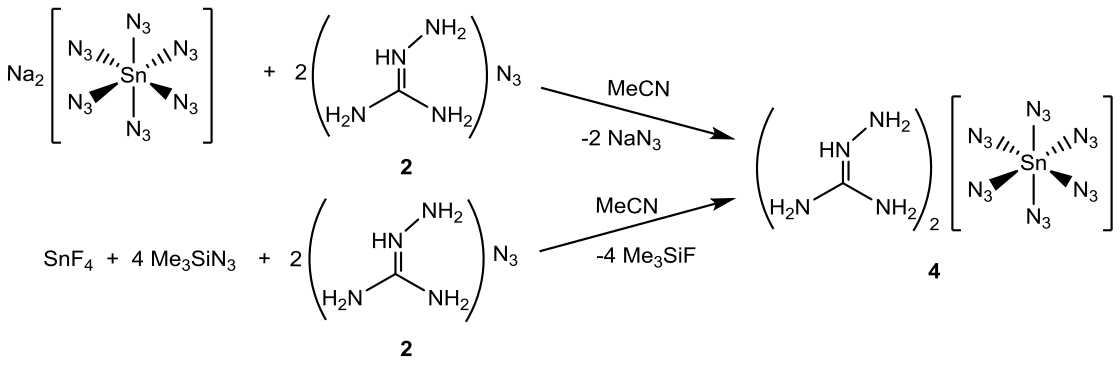

Scheme 2.6. Proposed reaction schemes for synthesis of bis(aminoguanidinium) hexaazidostannate (**4**).

Two different synthetic protocols described for bis(guanidinium) hexaazidostannate (**3**) were applied in attempts to prepare bis(aminoguanidinium) hexaazidostannate (**4**) (Scheme 2.6 above). It seems as though compound **4** is accessible using either SnF_4 or $Na_2[Sn(N_3)_6]$ as starting material, though attempts at crystallisation were unsuccessful. When an acetonitrile solution of disodium hexaazidostannate was stirred at RT for 24 h over a slight (*ca.* 10 %) excess of aminoguanidinium azide (**2**), the FTIR spectrum of the reaction solution (see Figure 2.1 below, black line) showed the emergence of four moderately strong, broad absorption bands for the N–H stretches, and an intense C–N stretch of the aminoguanidinium cation in addition to asymmetric (2079 cm^{-1} and 2112 cm^{-1}) and symmetric (1339 and 1287 cm^{-1}) azide stretching vibrations of $[Sn(N_3)_6]^{2-}$. Figure 2.1 shows a comparison of the obtained reaction solution with a genuine sample of bis(guanidinium) hexaazidostannate (**3**) in acetonitrile, and in both spectra the intensity of the N–H (3453–3285 cm^{-1}) and C–N absorption bands (1683 and 1669 cm^{-1}) of the respective guanidinium cations are similarly high, and much greater than a saturated solution of **2** in acetonitrile, supporting the formation of **4** in solution as it has higher solubility in acetonitrile than azide **2**. Upon filtration to remove insoluble material the presence of NaN_3 in the precipitate was confirmed by the intense asymmetric azide stretch in the FTIR spectrum of the residue (not shown) at 2130 cm^{-1} and distinctive sharp but weak bands at 3389 cm^{-1} and 3300 cm^{-1}. Weaker bands at 2056 cm^{-1} and 2024 cm^{-1} suggested the presence of a small amount of residual **2**. These observations seem to suggest that aminoguanidinium has displaced sodium from solution to form bis(aminoguanidinium) hexaazidostannate (**4**)**,** but cannot determine whether the exchange is complete. Repeated attempts at crystallisation by cooling the concentrated MeCN filtrate solution to –19 °C overnight were unsuccessful, resulting only in translucent oily residue, which upon addition of Et_2O turned into a slightly sticky solid. A FTIR spectrum of the solid (Figure 2.2, black line) seemed to suggest the presence of **4** with a trace of NaN_3 impurity, which may have hindered crystallisation.

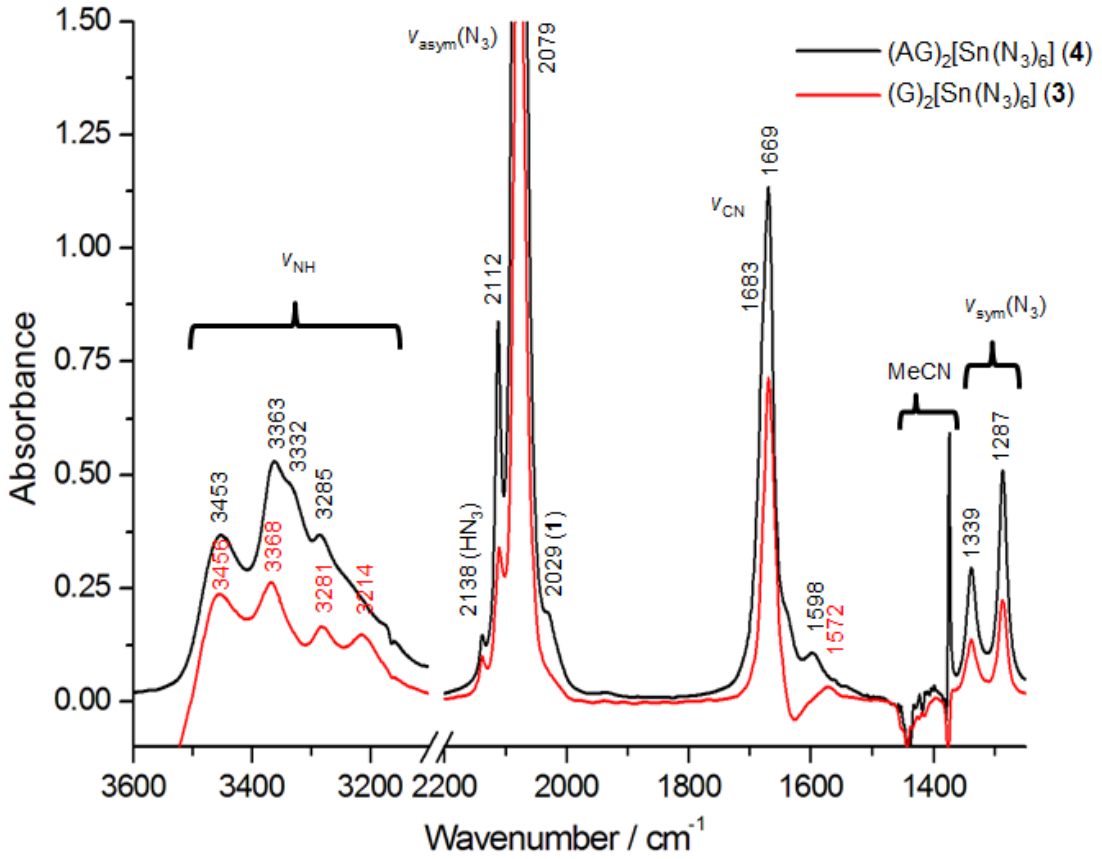

Figure 2.1. FTIR spectrum of the solution obtained after reaction of $Na_2[Sn(N_3)_6]$ with a slight excess of aminoguanidinium azide in MeCN (black), alongside a genuine sample of bis(guanidinium) hexaazidostannate (**3**) in the same solvent (red). The $\nu_{asym}(N_3)$ bands at 2112 and 2079 cm^{-1}, $\nu_{sym}(N_3)$ bands at 1339 and 1289 cm^{-1}, and N–H stretches between 3453–3285 cm^{-1} suggests the presence of bis(aminoguanidinium) hexaazidostannate (**4**) in solution. However, these observations alone cannot confirm whether the reaction is complete, as all IR active bands of $Na_2[Sn(N_3)_6]$ coincide with those of **4**, and the limited solubility of **2** in MeCN obscures the true remaining proportion.

Alternatively the reaction of a slight excess of TMS–N_3 with an acetonitrile suspension of **2** and SnF_4 at 40 °C for 16 h resulted in the formation of **4** in solution. The slight excess of **2** was crystallised out by cooling of the concentrated filtrate solution to –19 °C overnight. Subsequent attempts to crystallise **4** were unsuccessful, and resulted in translucent oily residues which partially solidified again upon addition of Et_2O. An FTIR spectrum of the crude **4** (sticky solid) thus obtained is shown in Figure 2.2 below.

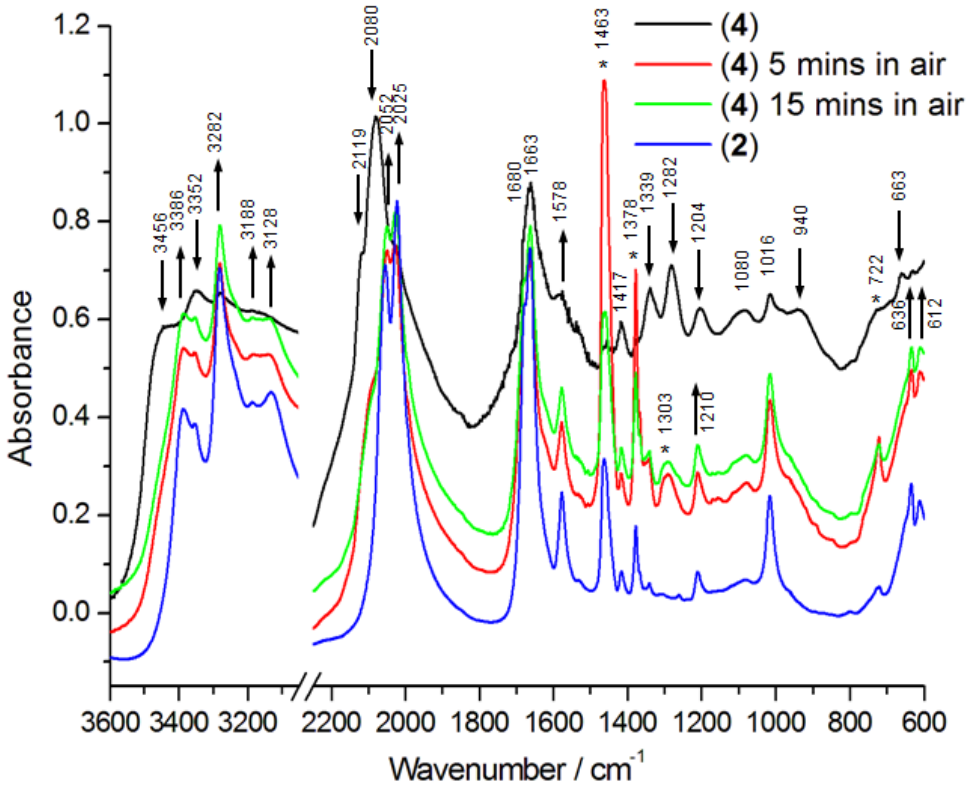

Figure 2.2. Series of FTIR spectra showing the effect of air exposure on a nujol suspension of crude bis(aminoguanidinium) hexaazidostannate (**4**, black) prepared *via* SnF_4 after 5 minutes (red) and 15 minutes (green) alongside a reference spectrum of aminoguanidinium azide (**2**, blue). Bands marked with an asterisk belong to the mulling agent (nujol); spectral window 3050–2250 cm^{-1} omitted to allow expanded view of the key spectral features; no baseline correction applied.

According to the spectral series in Figure 2.2 (above), exposure of the sticky solid residue to air resulted in relatively fast hydrolysis, as observed upon exposure of guanidinium salt **3** under the same conditions. In the N–H stretch region, the broad feature at 3456 cm^{-1} disappeared rapidly along with the bands assigned to asymmetric azide stretches at 2119 and 2080 cm^{-1}, symmetric stretches at 1339 and 1282 cm^{-1} and deformation at 663 cm^{-1}. The decay of the absorption bands of $[Sn(N_3)_6]^{2-}$ was accompanied by the rise of those corresponding to aminoguanidinium azide – an air stable hydrolysis product – at $\tilde{\nu}$ [cm^{-1}] = 3386, 3352, 3282, 3128, 2052, 2025, 1016, 636, and 612. This is similar to the hydrolysis of bis(guanidinium) hexaazidostannate, where guanidinium azide remains upon decomposition. The absence of other azide bands in the asymmetric stretch region suggests any potential tin azide hydroxide intermediates formed during hydrolysis are even more reactive than aminoguanidinium hexaazidostannate.

Attempted syntheses of bis(guanidinium) hexaazidosilicate(IV) (5) and bis(aminoguanidinium) hexaazidosilicate(IV) (6)

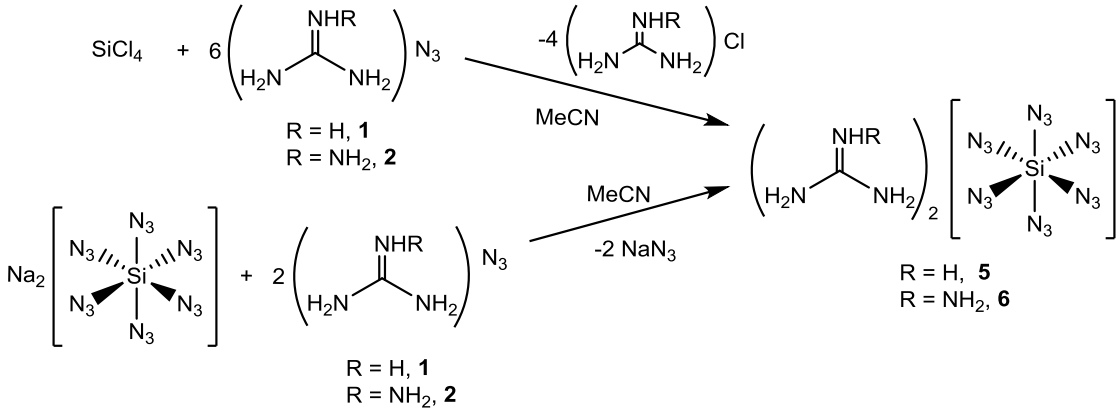

Scheme 2.7. Proposed syntheses for bis(guanidinium) hexaazidosilicate (**5**) and bis(aminoguanidinium) hexaazidosilicate (**6**).

Various synthetic routes towards nitrogen-rich bis(guanidinium) hexaazidosilicates were explored (see Scheme 2.7 above), using the original procedure for the preparation of $(PPN)_2[Si(N_3)_6]$ as a starting point.[83] The reaction of $SiCl_4$ with 14 equivalents of guanidinium azide (**1**) in acetonitrile results in the formation of $[Si(N_3)_6]^{2-}$ in solution according to the intense absorption at 2110 cm^{-1} in the solution FTIR spectrum with only guanidinium available as counter ion. The moisture sensitivity of the silicon azides combined with the increased hydrophilicity of guanidinium compared to hydrophobic bulky cations such as $(PPN)^+$ has the consequence that hydrazoic acid is produced readily. Hydrazoic acid is detectable by an absorption band at 2138 cm^{-1} in the *in-situ* infrared spectra and is present to a greater or lesser degree throughout any spectroscopic work with covalent azides (also observed for disodium hexaazidosilicate solutions). In the synthetic experiments that involved $SiCl_4$ as starting material, the guanidinium chloride by-product seemed to have greater solubility in MeCN than the insoluble NaN_3 by-product when disodium hexaazidosilicate was used. After the initial filtration which removed the majority of the guanidinium azide / chloride mixture, and concentration of the filtrate solution, a white crystalline precipitate was obtained. A comparison of the FTIR spectrum of the precipitate with reference spectra of genuine samples revealed that the obtained product consisted of a poorly defined mixture of guanidinium azide and guanidinium chloride. Repeated attempts to crystallise **5** from acetonitrile were futile.

Due to the aforementioned details it can be concluded that the preparation from guanidinium azide (**1**) and $Na_2[Si(N_3)_6]$ makes more efficient use of guanidinium azide, because complete azide / chloride exchange requires a large excess of an azide transfer reagent. The synthetic route is preferred in which cheap and readily available transfer reagent can be employed, which is the case for the $SiCl_4$ / NaN_3 route as opposed to $SiCl_4$ / $\{C(NH_2)_3\}N_3$. The reaction

of an excess of **1** with an acetonitrile stock solution of disodium hexaazidosilicate results in the precipitation of sodium azide after stirring for 24 h at ambient temperature. An FTIR spectrum of the solution after filtration showed the presence of both guanidinium and hexaazidosilicate ions in solution, as well as (**1**) due to its residual solubility. Concentration of this solution and cooling to –19 °C yielded rod shaped crystals of the mixed salt sodium guanidinium azide. The sodium content in the crystals may indicate that the cation exchange is incomplete, or that the sodium azide / guanidinium azide mixture has greater solubility in acetonitrile in the presence of **5**. Attempts to crystallise bis(guanidinium) hexaazidosilicate were unsuccessful.

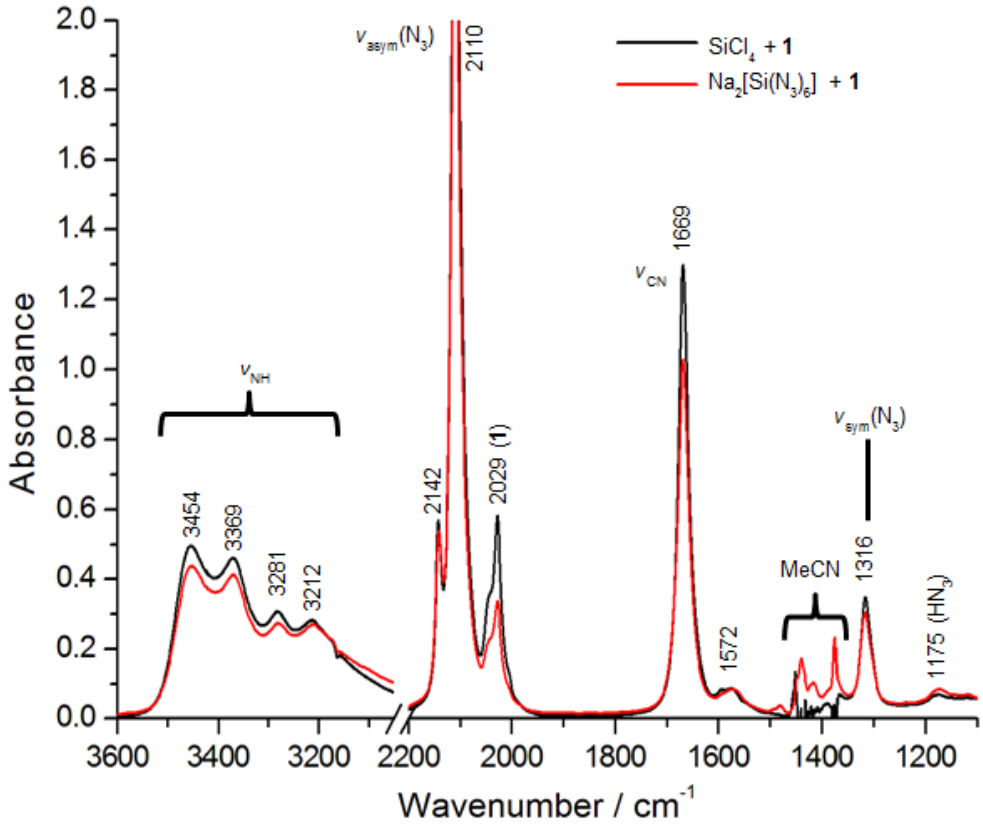

Figure 2.3. FTIR spectrum in MeCN of the solutions obtained after reaction of azide **1** with $SiCl_4$ (black), and $Na_2[Si(N_3)_6]$ (red). The characteristic $\nu_{asym}(N_3)$ at 2110 cm^{-1} and $\nu_{sym}(N_3)$ at 1316 cm^{-1} are in excellent agreement with published data for $[Si(N_3)_6]^{2-}$,[83] and in conjunction with the N–H stretching vibrations at 3454, 3369, 3281, and 3212 cm^{-1}, and C–N stretch at 1669 cm^{-1} suggest the presence of bis(guanidinium) hexaazidosilicate (**5**) in solution. A weaker absorption band is visible at 2142 cm^{-1}, which is higher than HN_3 in MeCN (2139 cm^{-1}) and may belong to the $[Si(N_3)_6]^{2-}$ anion. Guanidinium azide (**1**) is also visible at 2029 cm^{-1}.

When $SiCl_4$ was treated with 15 equivalents of aminoguanidinium azide (**2**) in acetonitrile for 24 h, the FTIR spectrum of the solution (Figure 2.4 below) seemed to be consistent with the formation of $[Si(N_3)_6]^{2-}$, and therefore bis(aminoguanidinium) hexaazidosilicate (**6**), by the presence of peaks at 2113 and 1316 cm^{-1} for the asymmetric and symmetric azide stretches respectively. In the solution IR spectra of guanidinium hexaazidosilicate salts **5** and **6** (Figures 2.3 and 2.4), the principal absorption band for the asymmetric azide stretching vibration of

$[Si(N_3)_6]^{2-}$ appears around 2110–2113 cm^{-1}, and an additional weak band is present at 2143 cm^{-1} which is also tentatively assigned to $[Si(N_3)_6]^{2-}$ by the following comparison with the equivalent IR absorption bands of the heavier Ge and Sn homologues. The difference in spectral positions of the principal and secondary absorption bands is $\Delta\tilde{\nu}$ = 33 cm^{-1}, which is similar to the equivalent secondary bands of hexaazidogermanate and hexaazidostannate complexes. In the FTIR spectrum of $(PPN)_2[Sn(N_3)_6]$ in MeCN solution the weaker band appears at 2112 cm^{-1} *vs*. 2079 cm^{-1}, $\Delta\tilde{\nu}$ = 33 cm^{-1},[85] and in the FTIR spectrum of $\{Na(THF)_x\}_2[Ge(N_3)_6]$ in THF solution the weaker band appears at 2123 cm^{-1} *vs*. 2089 cm^{-1}, $\Delta\tilde{\nu}$ = 34 cm^{-1}.[33] In the case of hexaazidosilicate the presence of this secondary band may be masked or hidden completely depending on the concentration of HN_3 (2139 cm^{-1}) present in solution due to hydrolysis. In the case of the hexaazidogermanate and hexaazidostannate anions these secondary absorption bands are more readily distinguishable from the bands of HN_3 at 2130 cm^{-1} in THF and 2139 cm^{-1} in MeCN, respectively. After filtering the suspension to remove the insoluble solid consisting of aminoguanidinium chloride and unreacted **2**, concentration of the filtrate solution gave a white precipitate that did not re-dissolve upon warming or addition of more solvent. This precipitate had a markedly different FTIR spectrum from **2**. Subsequent filtrations gave initially clear solutions which gradually became turbid upon standing. After removal of all solvent under vacuum, the FTIR spectrum of the solid residue (Figure 2.5 below) showed evidence of an unknown silicon azide with intense asymmetric azide stretches at 2134, 2118 cm^{-1}, a slightly weaker broad band at 2037 cm^{-1} (*cf.* **2** at 2024, 2057 cm^{-1}), a broad symmetric azide stretch at 1313 cm^{-1}, and an azide deformation at 694 cm^{-1}. As observed in the reactions of other group 14 chlorides with azides, a large excess of the latter is required, sometimes in sequential batches, to ensure complete ligand exchange. During these attempts at preparation of guanidinium hexaazidosilicates **5** and **6** *via* $SiCl_4$, the enthalpic driving force of the guanidinium chloride by-product is less favourable compared to AgCl or NaCl. As a consequence the aminoguanidinium chloride may not be removed from the solution as effectively, and a mixture of aminoguanidinium chloride and **2** could be responsible for the lower energy absorption band at 2031 cm^{-1}. The spectrum also shows features of aminoguanidinium N–H stretches at 3424 (shoulder), 3348, and 3157 cm^{-1}, C–N stretches at 1669 and 1572 cm^{-1}, and a band at 1261 cm^{-1}. The simplest interpretation of the spectrum is that the residue is a mixture of **2** and **6**, with the presumably extensive hydrogen bonding in the solid state leading to reduced $[Si(N_3)_6]^{2-}$ symmetry and broadening the absorption bands. An alternative explanation could be the coordination of aminoguanidinium (or its free base aminoguanidine) to the silicon centre *via* either the 'imino' nitrogen or the terminal sp^3-hybridised amino nitrogen, by displacement of azide anions as hydrazoic acid. FTIR spectroscopy alone cannot unambiguously determine whether the outcome of the reaction was formation of bis(aminoguanidinium) hexaazidosilicate (**6**) or the

neutral aminoguanidine adduct of $Si(N_3)_4$. Further investigation of this mixture was hampered by the insolubility of the material in suitably inert solvents.

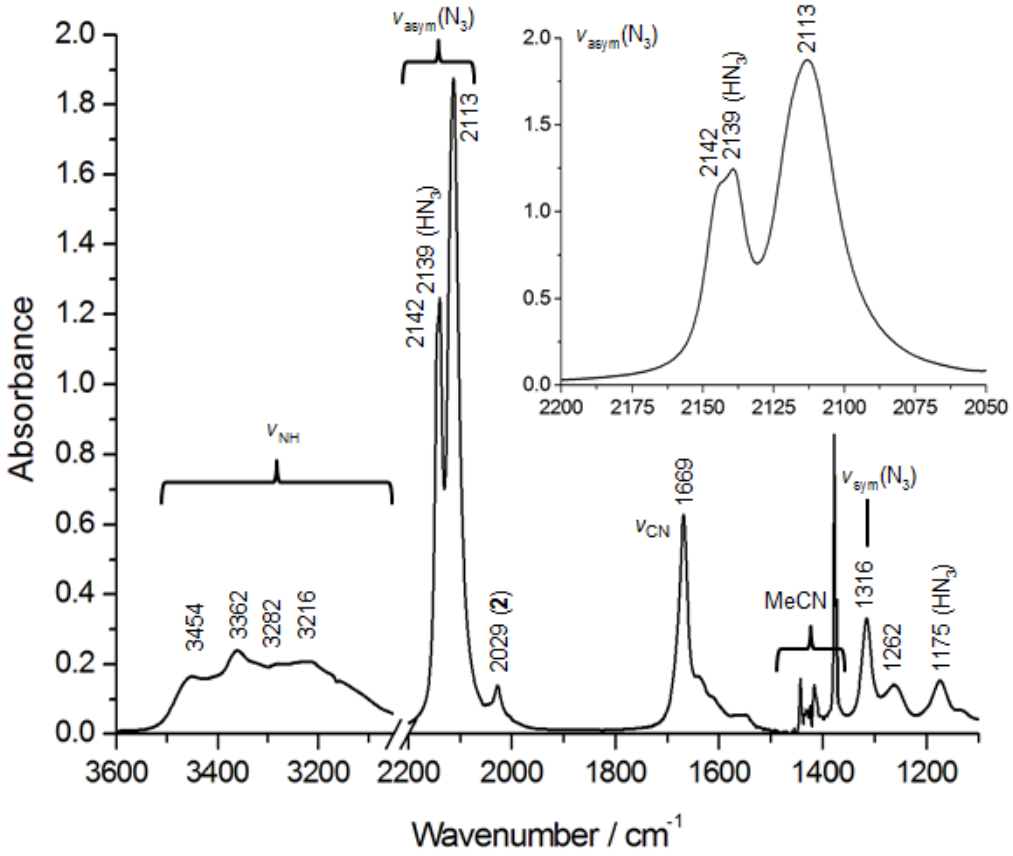

Figure 2.4. FTIR spectrum of the solution after reaction of $SiCl_4$ with a large excess of azide **2** in MeCN. The characteristic $\nu_{asym}(N_3)$ at 2113 cm^{-1} and $\nu_{sym}(N_3)$ at 1316 cm^{-1} are in very good agreement with literature values for $[Si(N_3)_6]^{2-}$,[83] and in combination with the N–H stretching vibrations at 3454, 3362, 3282, and 3216 cm^{-1}, and C–N stretch at 1669 cm^{-1} suggests the presence of bis(aminoguanidinium) hexaazidosilicate (**6**) in solution. Inset: Expanded view of the asymmetric stretch vibrations, where a weaker absorption band is visible at 2143 cm^{-1}, which may belong to the $[Si(N_3)_6]^{2-}$ anion though overlaps slightly with the HN_3 signal at 2139 cm^{-1}. Aminoguanidinium azide (**2**) is also visible at 2028 cm^{-1}.

The accessibility of bis(aminoguanidinium) hexaazidosilicate (**6**) *via* reaction of $Na_2[Si(N_3)_6]$ with **2** was investigated, and the resultant FTIR spectrum of the acetonitrile reaction solution (not shown) after 24 hours stirring was indistinguishable from the above spectrum (Figure 2.3) when starting from $SiCl_4$ and **2**. After filtration of the suspension, an FTIR spectrum of the filter residue (not shown) contained some NaN_3 but mostly excess **2**. The filtrate solution gradually became turbid upon standing, and after several concentration and filtration cycles, evaporation of the solution to dryness left behind a white residue, the FTIR spectrum of which was similar to that of the insoluble residue obtained from reaction of $SiCl_4$ with **2**. Figure 2.5 shows a comparison of the FTIR spectra (nujol mulls) of the insoluble residues obtained by each method. The $\nu_{as}(N_3)$ absorption bands appear at 2135, 2118, 2051 and 2039 cm^{-1} in the FTIR spectrum of the residue obtained from $Na_2[Si(N_3)_6]$ (Figure 2.5, red line), which are slightly different from the $\nu_{as}(N_3)$ bands at 2136, 2117, and 2031 cm^{-1} observed in the FTIR

spectrum of the material obtained directly from $SiCl_4$ (Figure 2.5, black line). This could be due to the absence of mixed Cl/N_3 species in the residue obtained from $Na_2[Si(N_3)_6]$, as no Cl/N_3 ligand exchange would be necessary. The absorption bands at 1313 cm^{-1} and 694 cm^{-1}, are common to the FTIR spectrum of the materials obtained from both methods, and are tentatively assigned to the symmetric azide stretch (ν_s) and azide deformation (δ) vibrations of $[Si(N_3)_6]^{2-}$ respectively. The insolubility of the obtained residues in suitably inert solvents hampered further investigation.

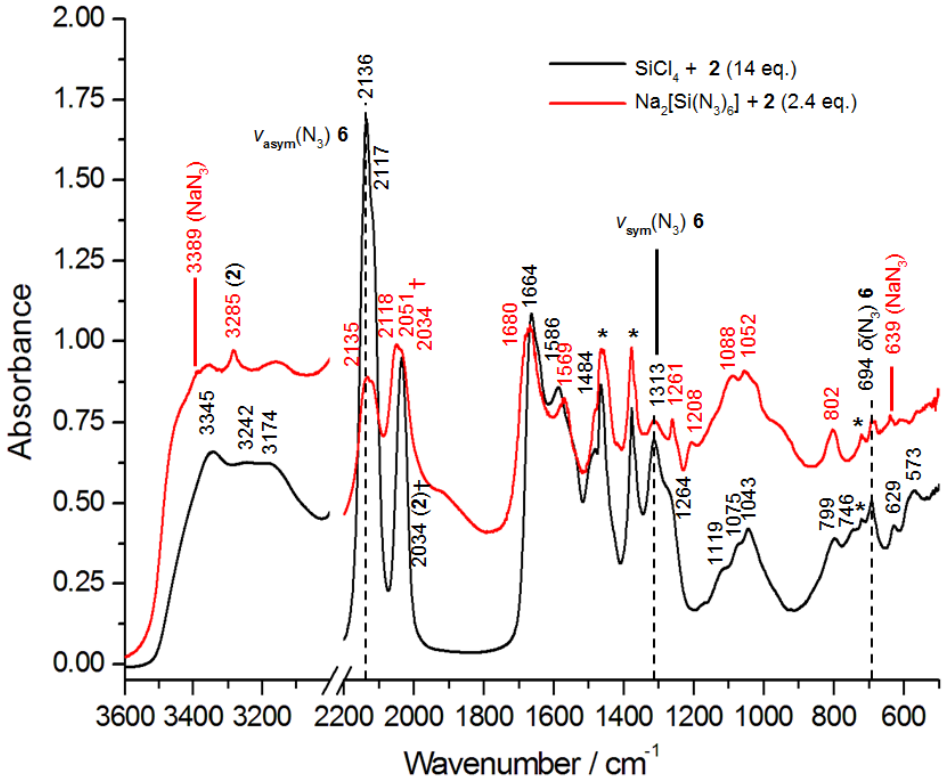

Figure 2.5. FTIR spectra of the insoluble white solids obtained after reaction of $SiCl_4$ with excess **2** (black), and $Na_2[Si(N_3)_6]$ with a slight excess of **2** (red). The features common to both spectra are presumed to originate from **6** including the $\nu_{asym}(N_3)$ around 2117 and 2135 cm^{-1}, $\nu_{sym}(N_3)$ at 1313 cm^{-1} and $\delta(N_3)$ at 694 cm^{-1}. † Both spectra seem to show the presence of **6** and a mixture of **2**/(AG)Cl or **2**/NaN_3 depending on the starting material; *Asterisks denote mulling agent absorption bands at 1465, 1378 and 721 cm^{-1}.

The reactivity of the neutral complex $Si(N_3)_4(bpy)$ with guanidinium azide (**1**) was investigated as a possible route towards bis(guanidinium) hexaazidosilicate (**5**) to avoid the presence of sodium (and chloride) ions which may have hindered crystallisation of **5** (and **6**) as described above. Addition of an acetonitrile solution of $Si(N_3)_4(bpy)$ to two equivalents of azide **1** eventually resulted in a clear solution after stirring for 4 hours, and a series of FTIR spectra were recorded to monitor the progress of the reaction, which are presented in Figure 2.6 below. The FTIR spectrum of the solution after 4 hours showed a dramatic reduction in the intensity of absorption bands for $Si(N_3)_4(bpy)$ at 2151, 2125, 2117, and 1624 cm^{-1} and the emergence of bands corresponding to **5**, and the characteristic weak absorption band for the 'ring-breathing' mode of free 2,2'-bipyridine at 1584 cm^{-1}. Addition of one further equivalent

of **1** resulted in almost complete disappearance of the absorption bands for $Si(N_3)_4(bpy)$ and a proportional increase in the concentration of **5**. The absorption bands at 3452, 3369, 3282 and 3216 cm^{-1} are assigned to the N–H stretching vibrations, and the asymmetric CN stretch, ν(CN), of the guanidinium cation appears at 1669 cm^{-1}. The intense band at 2110 cm^{-1}, and medium intensity band at 1317 cm^{-1} are attributed to the $\nu_{as}(N_3)$ and $\nu_s(N_3)$ of $[Si(N_3)_6]^{2-}$, respectively. After concentration of the reaction solution under vacuum, and storing for around two weeks at –19 °C, colourless crystals of **1** had formed, and the FTIR spectrum of the filtrate solution showed partial reformation of the original $Si(N_3)_4(bpy)$ complex, as well as **1** and hydrazoic acid. These observations suggest that the reaction is reversible, and that bis(guanidinium) hexaazidosilicate is not accessible without first removing 2,2'-bipyridine from the equilibrium.

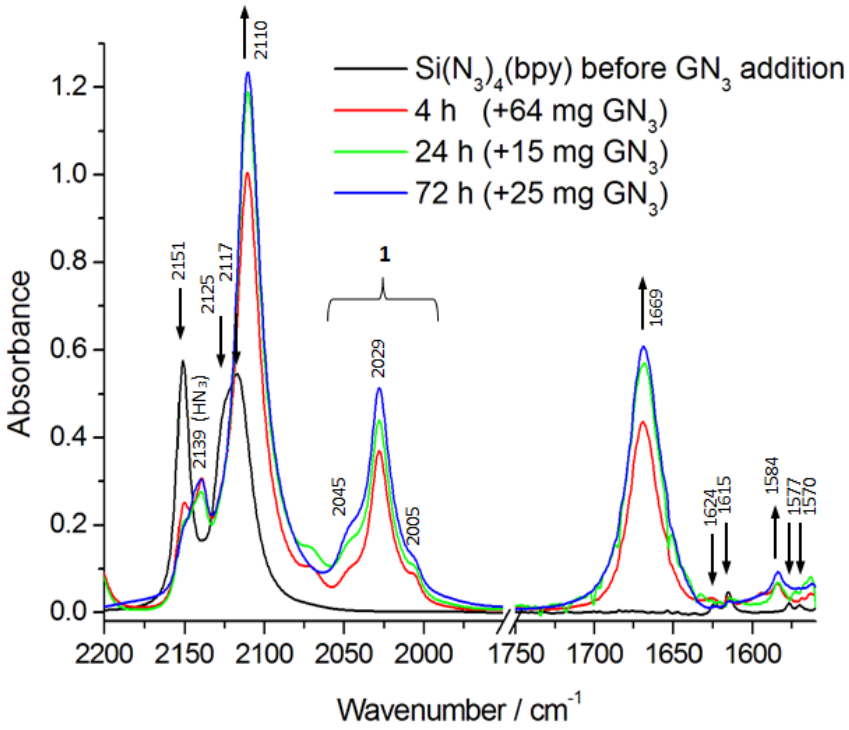

Figure 2.6. *In-situ* FTIR spectra showing the reaction of $Si(N_3)_4(bpy)$ with guanidinium azide (**1**). Black: $Si(N_3)_4(bpy)$ in MeCN; red: 64 mg of **1** added and stirred for 4 h; green: further 15 mg of **1** added and stirred for 24 h (total); blue: further 25 mg of **1** added and stirred for 72 h (total).

Attempted synthesis of guanidinium hexaazidophosphate(V) (7), and subsequent crystallisation of an unexpected novel phosphorus azide $[P(=O)(N_3)_2\{NC(NH_2)_2\}]$ (8)

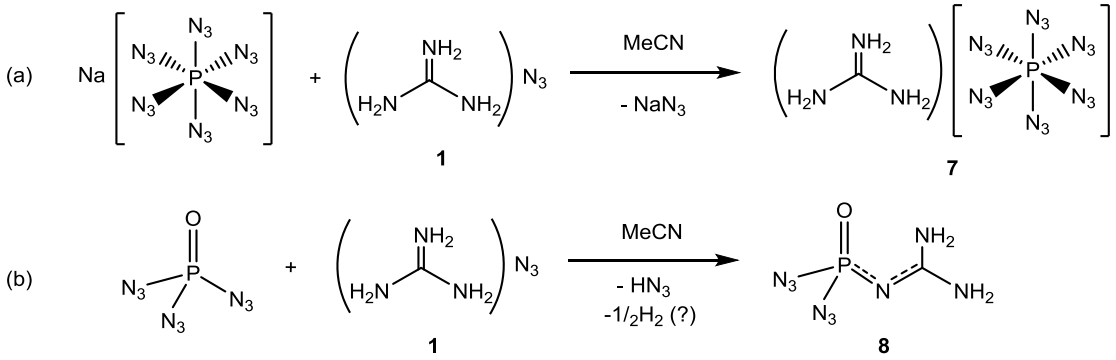

Scheme 2.8. (a) Proposed synthesis of guanidinium hexaazidophosphate (**7**); (b) A possible explanation for the formation of side product diazido(guanidinyl)(oxido)phosphorus (**8**).

The preparation of guanidinium hexaazidophosphate was attempted by reaction of an acetonitrile stock solution of sodium hexaazidophosphate with a slight excess of guanidinium azide (**1**) (see Scheme 2.8 above). After stirring the mixture overnight at low temperature (initially –35 °C, increased to –16 °C overnight) an FTIR spectrum of the solution exhibited an intense absorption band for $\nu_{as}(N_3)$ and $\nu_s(N_3)$ of the $[P(N_3)_6]^-$ anion at 2116 cm^{-1} and 1287 cm^{-1}, respectively. Several broad absorption bands for N–H stretching vibrations are present at 3460, 3369 and 3281 cm^{-1} and the asymmetric CN stretch, ν(CN), of the guanidinium cation appears at 1669 cm^{-1}. The $\nu_{as}(N_3)$ and $\nu_s(N_3)$ absorption bands for HN_3 were present at 2138 cm^{-1} and 1175 cm^{-1}, as $Na[P(N_3)_6]$ solutions hydrolyse readily upon exposure to atmospheric moisture, as shown in Figure 2.7 below. The relative absorbance of these bands suggested the HN_3 concentration was comparable to that of $[P(N_3)_6]^-$. After filtration of the obtained suspension, an FTIR spectrum of the filter residue showed almost exclusively the features of sodium azide, suggesting at least partial cation exchange of sodium for guanidinium in solution. After concentration of the clear orange filtrate solution, and cooling to –19 °C overnight, a few slightly yellow shard crystals were obtained (< 20 mg). Single crystal XRD confirmed the identity of the crystals to be diazido(guanidinyl)(oxido)phosphorus (**8**), $[P(=O)(N_3)_2\{NC(NH_2)_2\}]$. Evaporation of the supernatant solution to dryness left a viscous orange oil, from which no crystals upon storage at –19 °C for several days. Close inspection of the solution FTIR spectrum of the initial $Na[P(N_3)_6]$ stock solution reveals a low, but noticeable, concentration of $P(=O)(N_3)_3$, which seems to have reacted with guanidinium azide to give the side product **8**. The absorption bands at 2173 cm^{-1} and 2193 cm^{-1} are in good agreement with the published IR data for $P(=O)(N_3)_3$ (vapour, 298 K).[153] This unusual side product is a covalent phosphorus azide with almost 67 % nitrogen. The fact that only a few crystals were isolated suggested the majority of the material remained in the viscous oil, from which it was not possible to crystallise guanidinium hexaazidophosphate.

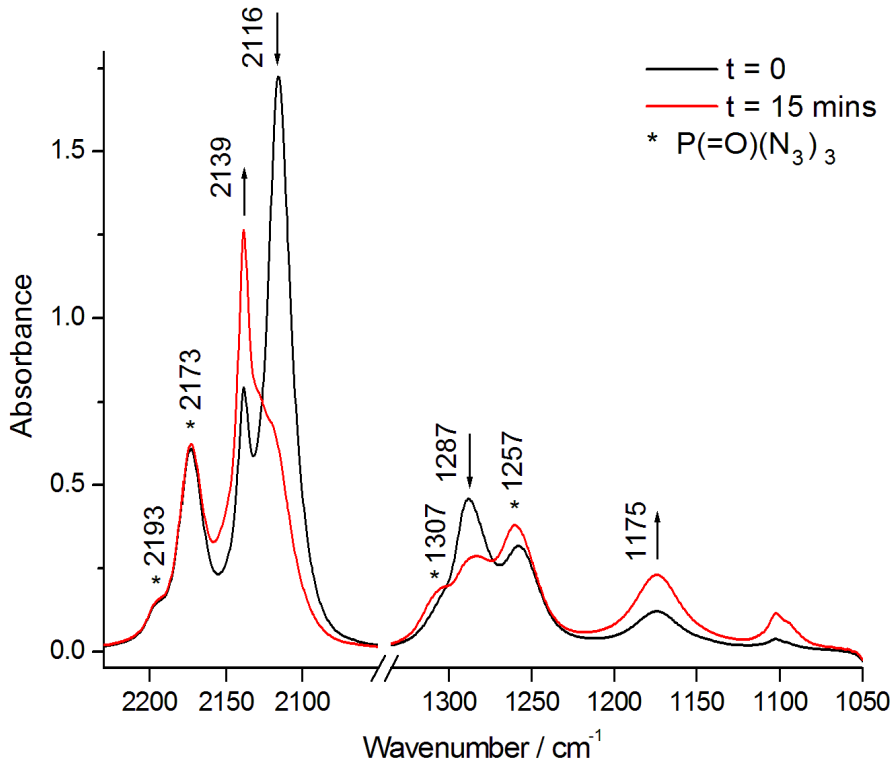

Figure 2.7. FTIR spectra showing the effect of 15 minutes air exposure on the $Na[P(N_3)_6]$ stock solution in acetonitrile. FTIR spectrum of the asymmetric, and symmetric azide stretch regions of $Na[P(N_3)_6]$ in CH_3CN, showing significant hydrolysis (formation of HN_3) after just 15 minutes in air. The dominant feature at 2116 cm^{-1} is the asymmetric stretch vibration of the $[P(N_3)_6]^-$ anion, the features (marked *) at 2193 (weak) 2173, and 1254 cm^{-1} are in good agreement with the IR absorption frequencies of $[P(=O)(N_3)_3]$ reported in the literature.[153]

2.2.3 X-Ray crystallographic investigations into the structures of nitrogen-rich guanidinium salts

X-ray diffraction *vs*. neutron diffraction for hydrogen atom location

The hydrogen bonds in nitrogen-rich compounds described in this chapter have been investigated by single crystal XRD, and whilst it remains a convenient technique for determining solid state structures, the inherent problems must be considered when conclusions are drawn from hydrogen bond geometries. The location of hydrogen atoms using X-ray diffraction is subject to systematic error, as the determination of atomic coordinates are based on electron density maxima. The X-ray scattering factor of the elements increases proportionally with the number of electrons (atomic number), meaning the atoms of the element hydrogen are the weakest. As a result the electron density of E–H bonds is polarised towards the heavier atom, and the electron density maximum no longer coincides with the nuclear position, giving an artificially shortened E–H bond. Neutron diffraction is the favoured technique for *high-resolution* studies of hydrogen-containing solids, but application of neutron diffraction methods is sometimes less practical than X-ray diffraction. For example the large crystals (*ca*. 1 mm^3) required for single crystal neutron diffraction can be chemically impractical, or have a greater degree of twinning.

Crystal structures of guanidinium azides, guanidinium hexaazidostannate, and guanidinium tetrazolate

Single crystal X-ray diffraction measurements on guanidinium azide (**1**), guanidinium azide monohydrate (**1a**), aminoguanidinium azide (**2**), bis(guanidinium) hexaazidostannate (**3**), and guanidinium tetrazolate (**19**) were carried out to determine their solid state structures and study the hydrogen bond interactions. The double salt sodium guanidinium azide (**5b**) and diazido(guanidinyl)(oxido)phosphorus, $[P(=O)(N_3)_2\{NC(NH_2)_2\}]$ (**8**), were obtained as side products during attempted preparation of bis(guanidinium) hexaazidosilicate (**5**), and guanidinium hexaazidophosphate (**7**) respectively, which unfortunately could not be crystallised. Thin hexagonal plate-like crystals of **1**, small colourless prisms of **2**, and shards of **19** were obtained by slow cooling of their respective concentrated dry ethanol solutions. Colourless needle crystals of the monohydrate **1a** were obtained by slow evaporation of the ethanol/ether solution of **1** in air. Needle crystals of **3** were grown by slow cooling of a saturated acetonitrile solution from RT to –19 °C overnight. The supernatant solution was decanted from the crystals of **3** whilst maintaining the temperature at –20 °C to prevent rapid dissolution of the crystalline **3** when allowed to warm beyond 0 °C. Rod-shaped crystals of **5** were obtained by concentration of a reaction mixture containing sodium hexaazidosilicate and **1** (see experimental section 6.2.9b). Shard-like crystals of **8** were obtained from a reaction mixture containing **1**, $Na[P(N_3)_6]$, and hydrolysis product $P(=O)(N_3)_3$. Crystals of compounds **1a**, **1**–**3**, **8** and **19** have monoclinic symmetry, crystallising in the statistically most common space group $P2_1/c$, except for **1** and **8** which crystallise in $C2/c$ and $I2/a$ respectively. Crystals of **5b** have higher symmetry, crystallising in the orthorhombic space group *Ibam*. All of the aforementioned structures are dominated by 3D hydrogen bond networks of varying complexity, ranging from four to thirty independent hydrogen bonds. A systematic description of the networks formed by the hydrogen bonds identified in the structures of the guanidinium azides has enabled comparison of the networks' construction. The complexity of the graph sets formed increases with the number of crystallographically independent hydrogen bonds and crystal symmetry. The labels applied to the hydrogen bonds are based on the label of the hydrogen atom (e.g. 1A), and if a hydrogen is considered part of two hydrogen bonds, then the hydrogen bond closest to the ideal (linear D–H···A angle) geometry takes the label, and the other is distinguished by a dash (e.g. 4A and 4A').

Crystal structure of guanidinium azide (1)

Guanidinium azide (**1**) crystallises in the monoclinic space group $C2/c$ with 24 formula units in the unit cell and a relatively low density of 1.399 g cm^{-3} at 100 K. The thin hexagonal plate crystals of **1** were prone to twinning (see Figure 2.8), and many crystals were screened before a suitable specimen crystal was found, as the smaller crystals lacked diffraction intensity whereas the larger crystals showed more pronounced twinning. Incidentally, the structural CH_6N_6 isomer hydrazinium tetrazolate also has a relatively low density (1.385 g cm^{-3})

compared to similar structures,[152] and crystallises in very thin plates causing similar challenges with crystal structure determination. As a result of the limited structure quality, hydrogen atoms could only be located geometrically, and implement SADI restraints on some interatomic distances during refinement with the *Shelxtl* software suite. Furthermore, distance restraints were applied to keep the C–N bond lengths similar within each cation, and the pairs of N–N bond lengths similar within each azide anion. However, even after this refinement, the R_1 value for the structure remains at 0.0756, which must be considered for any discussion of interatomic distances (particularly those involving H atoms). As a result some of the fine detail of the structure is obscured, and an in-depth discussion of the effect(s) of hydrogen bonding on the asymmetry of the azide anion environments is not possible.

Anhydrous **1** exhibits an interesting staggered 3-layer structure (see Figure 2.9) where two sheets of guanidinium cations parallel to the *ab* plane are bridged by azide anions *via* multiple hydrogen bonds. The high symmetry of both cation and anion allow for the propagation of a complex 3D network of 30 crystallographically independent hydrogen bonds through the structure. This network of hydrogen bonds is extensive within layers (see Figure 2.10) but non-existent in the *c*-axis direction due to adjacent cation layers between which only dipolar attractive forces can act. The anisotropy of the interionic forces presumably accounts for the thin plate-like morphology of the crystals. The 'tilt' angles between pairs of mean planes through heavy atoms of the three independent cations are 1.9°, 3.3° and 4.3°, meaning the layers of cations are almost flat. There are four independent azide anions in the asymmetric unit, two of which have N_β on special positions and are generated by symmetry (see Figure 2.8). The arrangement of the azide groups between the cation layers form hollow rectangular 'channels' (not shown) in three directions approximately 3.80–3.96 Å × 3.47–3.59 Å ≈ 13 Å^2 cross-sectional area. Adjacent layers of guanidinium cations are stacked directly above one another with a separation of approximately 2.5–2.6 Å, with the cations in a perfectly staggered alternating arrangement to minimise intercationic repulsion. All guanidinium cations are linked to six adjacent azide anions *via* hydrogen bonds (DHA angles in parentheses), where cation 1 forms six relatively straight hydrogen bonds (142–157°), and cations 2 and 3 form six conventional hydrogen bonds (cation 2: 144–149°; cation 3: 145–147°) and six 'bent' (cation 2: 99–107°; cation 3: 102–105°) hydrogen bonds which are bifurcated at the azide anion, giving a total of thirty crystallographically independent hydrogen bonds. Accordingly each azide anion is surrounded by six guanidinium cations, with three at each end. The interionic donor-acceptor distances, d(D···A), lie in the range 2.962(7)–3.225(8) Å with angles between 99–157° (see Table 2.1), which indicates a range of hydrogen bonds strengths between the ideal *linear* geometry and more *bent* hydrogen bonds that are mostly electrostatic in nature.

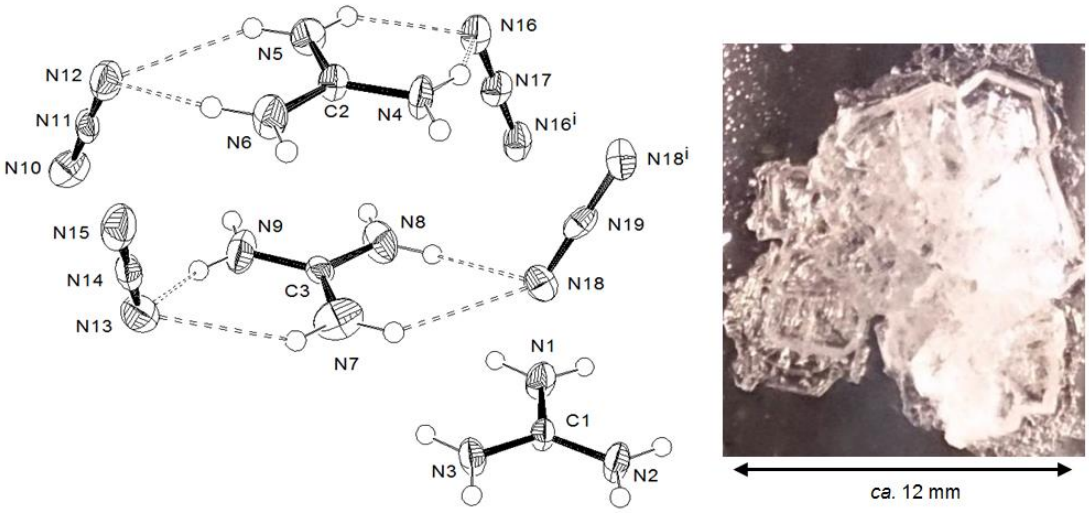

Figure 2.8. Left: ORTEP diagram of the asymmetric unit of **1** showing selected hydrogen bonds in the crystal structure at 100 K. Thermal ellipsoids at the 50 % probability level, hydrogen atoms represented by spheres of radius 0.15 Å. H-atom labels omitted for clarity, and superscripts denote fragments completed by symmetry equivalent atoms. Right: Photograph of hexagonal plate-like crystals of (**1**) [*Photo: Rory Campbell, June 2013*]. Monoclinic (*C*2/*c*, *Z* = 24), *a* = 20.410(3) Å, *b* = 11.6649(15) Å, *c* = 12.2223(16) Å, *β* = 90.101(6)°, *V* = 2909.9(6) Å^3, R_1 = 0.0756. Selected bond lengths [Å] and angles [°]: C1–N1 1.326(4), C1–N2 1.332(4), C1–N3 1.321(4), C2–N4 1.320(3), C2–N5 1.326(3), C2–N6 1.326(3), C3–N7 1.317(3), C3–N8 1.320(3), C3–N9 1.315(4), N10–N11 1.173(5), N11–N12 1.174(5), N13–N14 1.173(5), N14–N15 1.178(5), N16–N17 1.194(5), N18–N19 1.189(5); N10–N11–N12 179.6(6), N13–N14–N15 178.9(6), N16–N17–N16^i 178.4(8), N18–N19–N18^i 179.4(9).

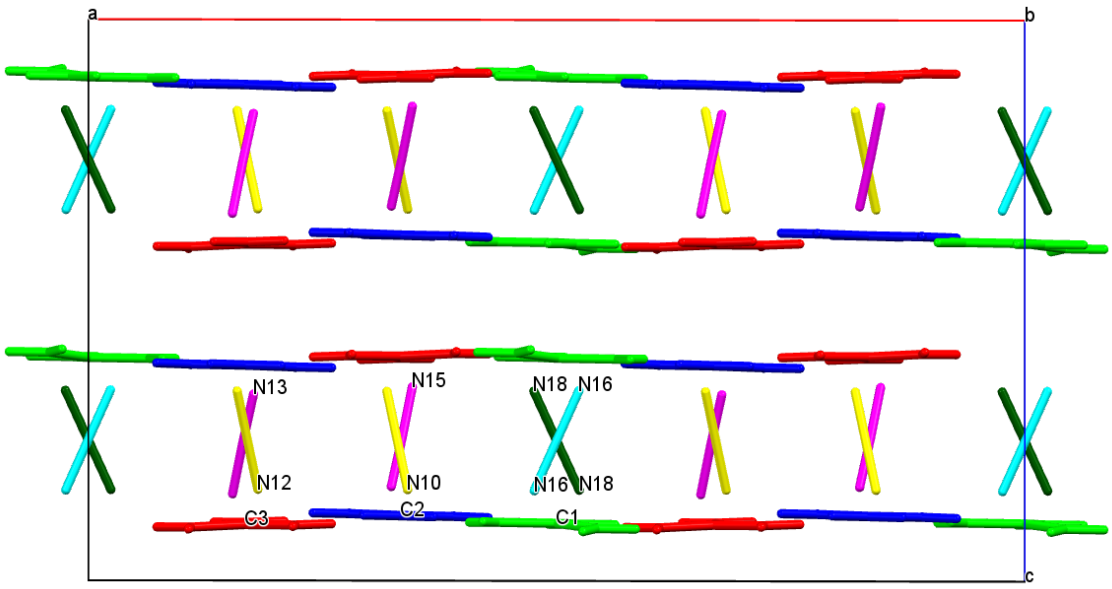

Figure 2.9. A simplified representation of the unit cell in the crystal structure of **1**, with molecular fragments drawn as capped sticks to allow a clear view along the *b*-axis showing the layer structure. The ions are coloured by symmetry equivalence. Guanidinium cations: red, green, blue; azide anions: cyan, yellow, magenta, dark green.

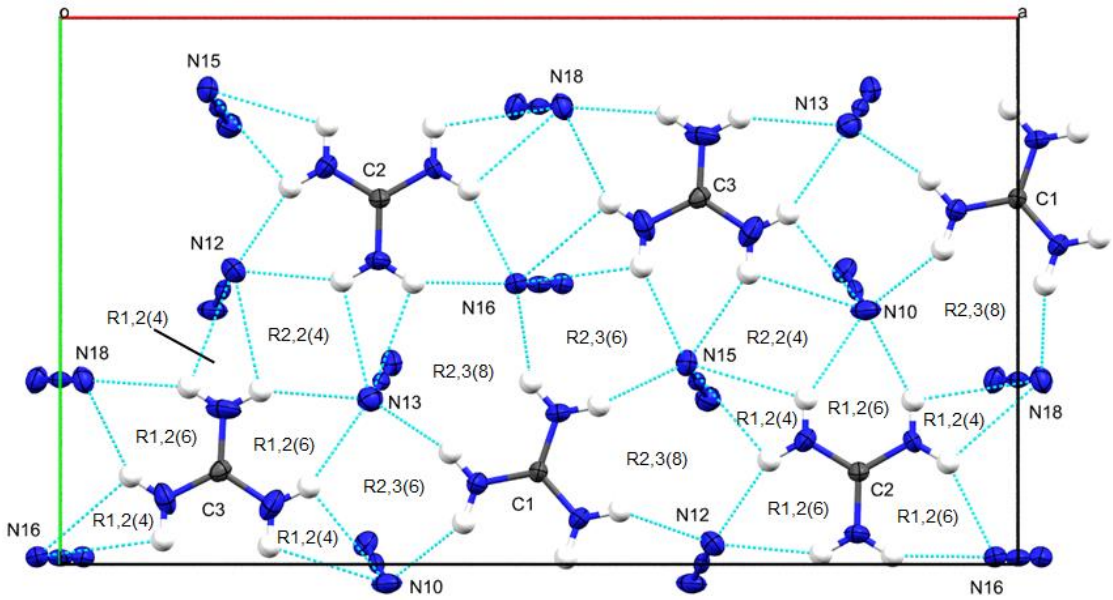

Figure 2.10. Hydrogen bonding network formed by a layer of guanidinium cations and intervening azide anions viewed along the *c*-axis. Carbon labels show symmetry equivalence of cations, for which selected ring graph sets are labelled. Numerous chain graph sets formed from two or more hydrogen bonds exist throughout the structure but are omitted for clarity.

The extent of hydrogen bonding means the interionic N···N distances are a compromise between all hydrogen bonds in the structure in order to minimise the overall energy of the structure. Hydrogen bonding patterns include the common 'chelating' geometry in which two protons on different donor atoms of the same cation form R1,2(6) graph sets with an azide terminus. Also observed are patterns formed by geminal protons to an azide group denoted R1,2(4), and conventional linear 1 : 1 hydrogen bonds.

Table 2.1. Hydrogen bond geometries in the crystal structure of **1**, including the graph sets formed by each motif. The full second level graph set matrix is included in the appendix.

#	D–H	A	*d*(D···A) [Å]	DHA [°]	1° GS [a]
1A	N1–H1A	N16	2.995(6)	143	D2,2(5)
1B	N1–H1B	N15	3.008(7)	157	D
2A	N2–H2A	N18	3.014(7)	148	D2,2(5)
2B	N2–H2B	N12	3.006(7)	142	D
3A	N3–H3A	N13	3.013(7)	154	D
3B	N3–H3B	N10	2.962(7)	144	D
4A	N4–H4A	N10	3.030(6)	149	D
4A'	N4–H4A	N18	3.096(6)	99	D2,2(5)
4B	N4–H4B	N16	3.080(6)	144	D2,2(5)

#	D–H	A	*d*(D···A) [Å]	DHA [°]	1° GS [a]
4B'	N4–H4B	N18	3.096(6)	107	D2,2(5)
5A	N5–H5A	N16	3.032(7)	146	D2,2(5)
5A'	N5–H5A	N13	3.025(7)	100	D
5B	N5–H5B	N12	3.142(7)	144	D
5B'	N5–H5B	N13	3.025(7)	105	D
6A	N6–H6A	N10	3.100(7)	145	D
6A'	N6–H6A	N15	3.046(7)	106	D
6B	N6–H6B	N12	3.011(7)	151	D
6B'	N6–H6B	N15	3.046(7)	101	D
7A	N7–H7A	N13	3.225(8)	145	D
7A'	N7–H7A	N12	3.064(8)	105	D
7B	N7–H7B	N18	3.134(8)	147	D2,2(5)
7B'	N7–H7B	N12	3.064(8)	102	D
8A	N8–H8A	N15	3.157(7)	145	D
8A'	N8–H8A	N16	3.100(7)	100	D2,2(5)
8B	N8–H8B	N18	3.179(7)	145	D2,2(5)
8B'	N8–H8B	N16	3.100(7)	105	D2,2(5)
9A	N9–H9A	N13	3.193(8)	147	D
9A'	N9–H9A	N10	3.064(8)	102	D
9B	N9–H9B	N15	3.190(8)	144	D
9B'	N9–H9B	N10	3.064(8)	103	D

[a] 1st level graph set. The hydrogen atoms were located geometrically with D–H distances of 0.88 Å, therefore H···A distances are omitted.

Crystal structure of guanidinium azide monohydrate (1a)

The hygroscopic nature of **1** leads to the crystallisation of monohydrate **1a** upon slow evaporation of the ethanol/ether solution in air. Hydrate **1a** crystallises in the space group $P2_1/c$ with 4 formula units per unit cell with the same density (ρ = 1.399 g cm^{-3}) as the anhydrous compound at 100 K (see Figure 2.11). As in the structure of **1**, the guanidinium cations are stacked in the *c*-axis direction with a larger separation of d_{cation} = 3.23–3.25 Å (*cf.* **1** d_{cation} = 2.5–2.6 Å) and perfectly staggered to maximise favourable alignment of the cation C–N dipoles. Each guanidinium cation is surrounded by five azide anions and two water molecules, and each azide anion is surrounded by five guanidinium cations and two water molecules. A total of 12 independent hydrogen bonds have been identified in the structure of

1a with D···A distances in the range 2.858(1)–3.151(1) Å (see Table 2.2). The azide anion has slightly skewed N–N bond lengths which could be from the subtle differences in hydrogen bond environment at each end or electrostatic bias due to more adjacent cations at N6. Atom N4 accepts hydrogen bonds (3 interionic) whereas N6 accepts 6 hydrogen bonds (4 interionic) which could explain the slight asymmetry of the azide anion 1.1897(9) Å *vs*. 1.1709(9) Å.

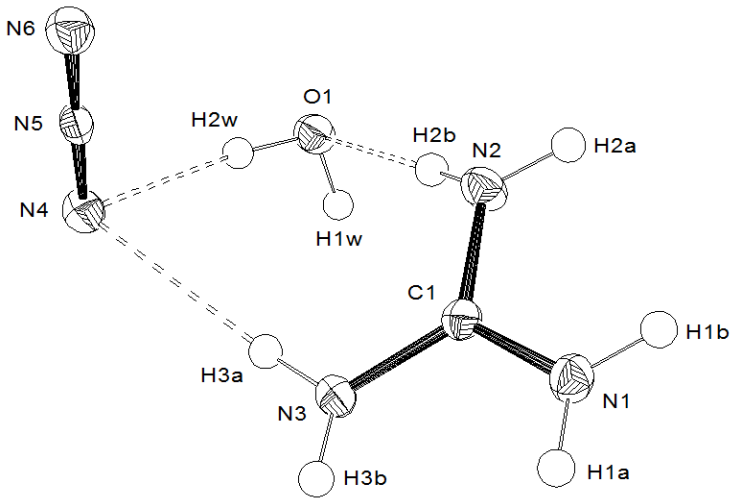

Figure 2.11. Thermal ellipsoid plot showing the asymmetric unit in the crystal structure of **1a** at 100 K. Thermal ellipsoids at the 50 % probability level, and hydrogen atoms represented by spheres of radius 0.15 Å. Monoclinic ($P2_1/c$, Z = 4), a = 8.3174(6), b = 10.9115(8), c = 6.4713(4), β = 103.776(3), V = 570.41(7) Å^3, R_1 = 0.0265. Selected bond lengths [Å] and angles [°]: C1–N1 1.3256(11), C1–N2 1.3322(9), C1–N3 1.3311(9), N4–N5 1.1897(9), N5–N6 1.1709(9); N1–C1–N2 119.66(7), N1–C1–N3 119.71(7), N2–C1–N3 120.63(8), N4–N5–N6 179.40(8), H1w–O1–H2w 105.3(11). N–H distances range: 0.840(12)–0.854(12) Å, and O–H distances range: 0.855(15)–0.875(15) Å.

The R2,3(8) graph set observed in **1a** (see Figure 2.12) is also present in the structure of anhydrous **1** where the place of the water molecule in the graph set is instead taken by an azide anion and guanidinium cation, and the C2,2(6) graph set which links alternately water molecules and azide anions is found in the structure of **2**, where the sp^3-hybridised amino terminus mimics the hydrogen bond donor functions of the water molecule in the structure of **1a**.

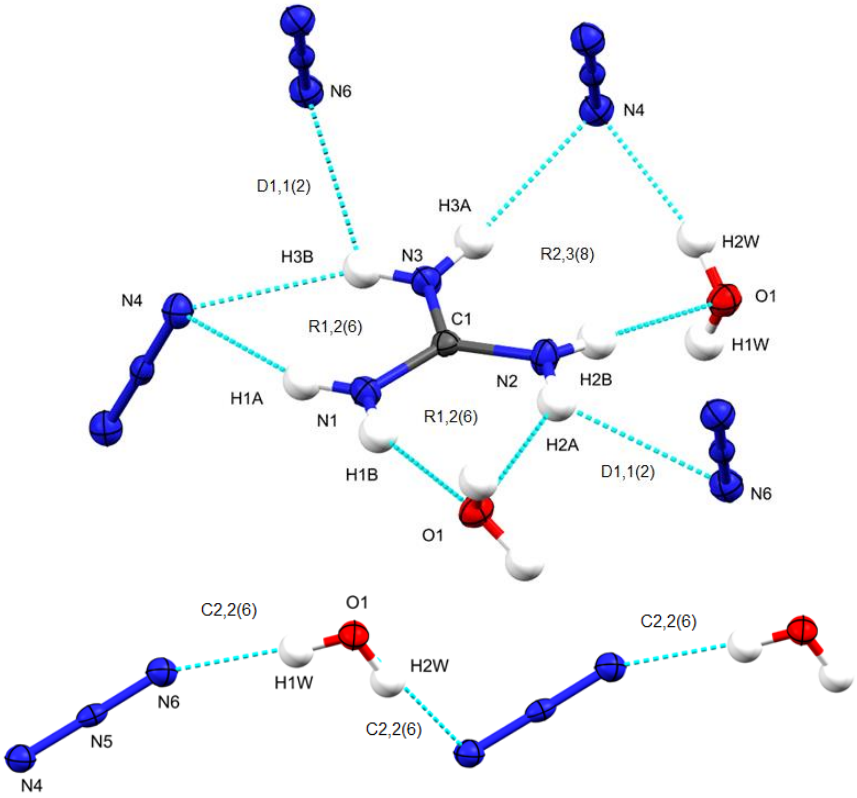

Figure 2.12. Projections of the most prominent graph sets formed by hydrogen bonds in the crystal structure of **1a**. Note: Two different orientations have been used for the above projections to optimise clarity of the graph set assignment.

Table 2.2. Hydrogen bond geometries in the structure of **1a** at 100 K.

#	D–H	A	D–H [Å]	*d*(D···A) [Å]	*d*(H···A) [Å]	DHA [°]	1° GS [a]	D, A charges
1A	N1–H1A	N4	0.841(12)	3.062(1)	2.285(12)	154	D	+/–
1A’	N1–H1A	N6	0.841(12)	3.005(1)	2.636(12)	108	D	+/–
1B	N1–H1B	O1	0.840(12)	2.979(1)	2.191(12)	156	D	+/0
1B’	N1–H1B	N6	0.840(12)	3.005(1)	2.753(12)	99	D	+/–
2Aw	N2–H2A	O1	0.854(12)	3.151(1)	2.413(12)	145	D	+/0
2A	N2–H2A	N6	0.854(12)	3.085(1)	2.470(12)	130	D	+/–
2B	N2–H2B	O1	0.851(13)	2.993(1)	2.142(13)	178	D	+/0
3A	N3–H3A	N4	0.844(13)	3.087(1)	2.257(13)	168	D	+/–
3B	N3–H3B	N4	0.844(12)	3.140(1)	2.386(12)	149	D	+/–
3B’	N3–H3B	N6	0.844(12)	3.110(1)	2.578(12)	122	D	+/–
1w	O1–H1W	N6	0.855(15)	2.858(1)	2.007(15)	173	D	0/–
2w	O1–H2W	N4	0.875(15)	2.887(1)	2.040(15)	163	D	0/–

[a] 1st level graph set.

Crystal structure of aminoguanidinium azide (2)

The substitution of a proton by an amino group facilitates intercationic hydrogen bonding as the terminal sp^3 amino group acts as both donor and acceptor, and this deviation from planarity prevents the formation of a layer structure found in **1**. A total of 9 independent hydrogen bonds have been identified in the structure of **2** (see Figure 2.14 and Table 2.3). The two protons are projected symmetrically out of the plane of the cation (Figure 2.13), forming an infinite helical chain parallel to the *b*-axis of interconnecting azide anions *via* hydrogen bonds in a C2,2(6) pattern. This is similar to the pattern formed between water molecules along the *c*-axis in **1a**.

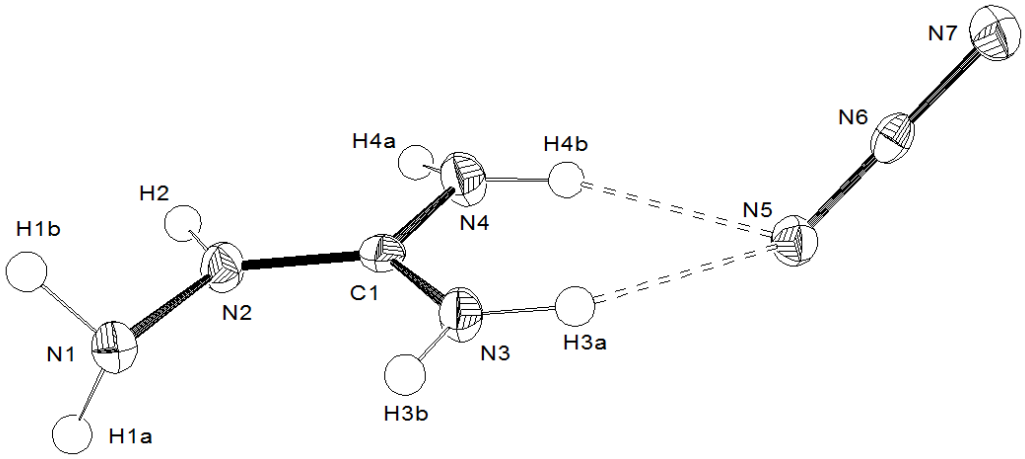

Figure 2.13. ORTEP drawing showing the asymmetric unit in the crystal structure of **2** at 100 K. Thermal ellipsoids at the 50 % probability level, and hydrogen atoms represented by spheres of radius 0.15 Å. Dashed lines represent hydrogen bonds. Monoclinic ($P2_1/c$, Z = 4), a = 7.3030(4) Å, b = 12.3379(7) Å, c = 6.1442(3), β = 107.583(2), V = 527.75(5) Å^3, R_1 = 0.0280. Selected bond lengths [Å] and angles [°]: N1–N2 1.4109(11), C1–N2 1.3287(12), C1–N3 1.3245(11), C1–N4 1.3327(12), N5–N6 1.1802(10), N6–N7 1.1787(10); N1–N2–C1 120.17, N2–C1–N3 121.12(8), N3–C1–N4 120.08(9), N4–C1–N2 118.78(8), N5–N6–N7 179.57(9).

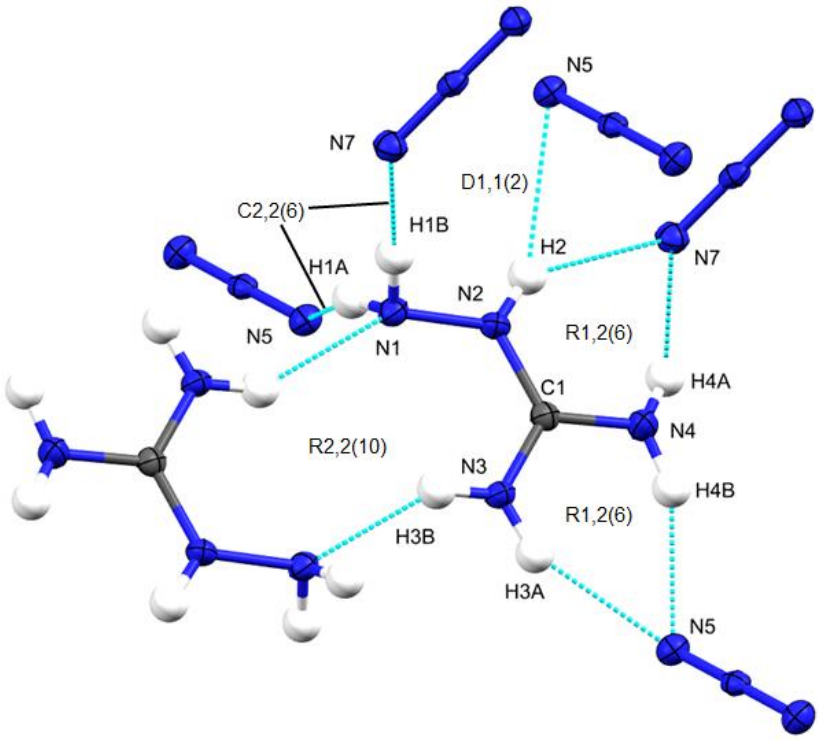

Figure 2.14. Projection of graph sets formed by hydrogen bonds in the structure of **2**.

The distinctive R2,2(10) graph set between adjacent aminoguanidinium cations has been observed in other salts with amino- substituted guanidinium cations such as aminoguanidinium chloride[154] and bis(aminoguanidinium) 5,5'-azotetrazolate[97] as they can both accept and donate hydrogen bonds, unlike guanidinium which functions solely as a hydrogen bond donor.

Table 2.3. Hydrogen bond geometries in the crystal structure of **2** at 100 K.

#	D–H	A	D–H [Å]	*d*(D···A) [Å]	*d*(H···A) [Å]	DHA [°]	1° GS [a]	D, A charges
1A	N1–H1A	N5	0.880(12)	3.105(1)	2.303(13)	152.7	D	+/–
1A'	N1–H1A	N7	0.880(12)	3.285(1)	2.681(13)	125.8	D	+/–
1B	N1–H1B	N7	0.909(13)	3.148(1)	2.271(15)	163.8	D	+/–
2	N2–H2	N7	0.870(13)	3.217(1)	2.493(14)	141.2	D	+/–
2'	N2–H2	N5	0.870(13)	3.082(1)	2.436(13)	133.4	D	+/–
3A	N3–H3A	N5	0.893(14)	3.007(1)	2.224(15)	147.4	D	+/–
3B	N3–H3B	N1	0.882(12)	3.024(1)	2.255(14)	148.5	R2,2(10)	+/+
4A	N4–H4A	N7	0.845(14)	2.967(1)	2.147(15)	162.6	D	+/–
4B	N4–H4B	N5	0.886(13)	2.947(1)	2.123(15)	153.5	D	+/–

[a] 1st level graph set.

Crystal structure of bis(guanidinium) hexaazidostannate (3)

Only two examples of hexaazidostannate salts have been investigated by single crystal X-ray diffraction, which are with $(PPh_4)^+$ and $(PPN)^+$ (**9**) cations.[86,85] The symmetry of almost all other known group 13–16 hexaazido complexes including In and Tl,[88] Si,[83] Ge,[33] Sn,[86,85] Pb,[90] As and Sb,[68] Se,[63] and transition metal hexaazido complexes of Ti, V, Nb, and Ta, and W, are approximately S_6 symmetry. Notable exceptions are hexaazidotellurate[87] where the N_3 ligands have variable covalent/ionic character within the same complex, and hexaazidobismuthate[155] where the stereochemically active lone pair gives the complex a monocapped octahedral geometry. In the structure of **3** the $Sn[N]_6$ skeleton is octahedral (Figure 2.15 below), though overall the complex anion has symmetry closer to C_2, which seems to be imposed by pairs of hydrogen bonds to pairs of N_α atoms. The most distinctive graph sets making up the hydrogen bond network are the R2,2(8) ring graph sets with three cations per anion (Figure 2.17 below), which are similar to the pattern formed in guanidinium carbonate, where the carbonate dianion forms six R2,2(8) patterns with the surrounding cations.[156] There are 7 crystallographically independent hydrogen bonds to each cation, giving a total of 14 independent hydrogen bonds in the crystal structure of **3** (see Table 2.4 and Figure 2.16). Cation 1 forms two R2,2(8) patterns with the N_α atoms of adjacent azide groups, one R1,2(6) graph set with a terminal nitrogen N_γ atom, and an isolated D1,1(2) graph set with another N_γ atom. Cation 2 forms one R2,2(8) pattern with the remaining pair of *cis* N_α atoms and two R1,2(6) graph sets with the remaining N_γ. A comparison of the average D···A distances for the R2,2(8) and R1,2(6) graph sets reveals no difference within experimental uncertainty, though on average the hydrogen bonds involved in the R2,2(8) graph set are closer to the ideal 180° DHA angle. The ionicity of the azido ligands does not seem to be affected by hydrogen bonding by comparison of the bonding geometries in **3** versus $(PPN)_2[Sn(N_3)_6]$ (**9**).

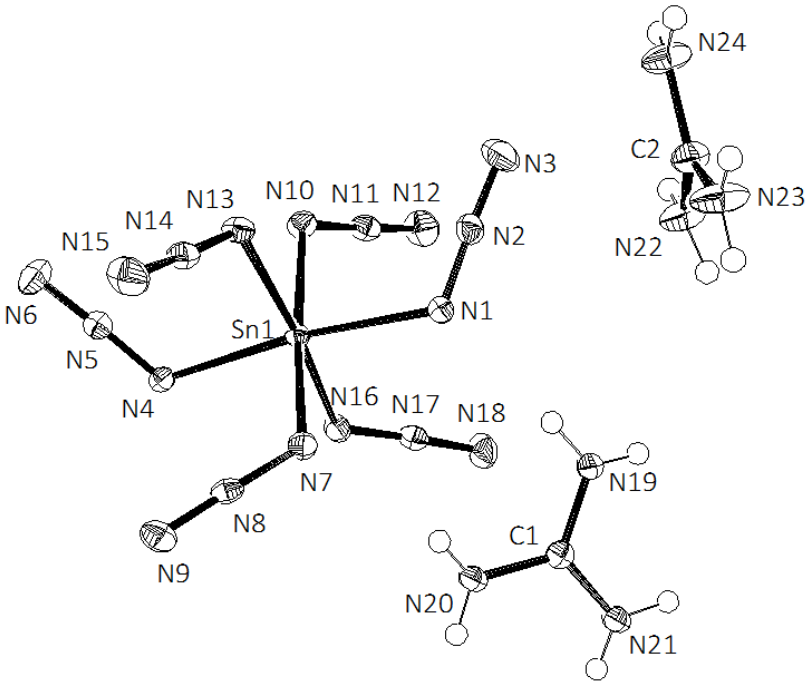

Figure 2.15. ORTEP drawing showing the asymmetric unit in the crystal structure of **3** at 100 K. Thermal ellipsoids at the 50 % probability level, and hydrogen atoms represented by spheres of radius 0.15 Å. H-atom labels omitted for clarity. Monoclinic ($P2_1/c$, Z = 4), a = 8.2382(5) Å, b = 28.1101(16) Å, c = 8.7003(5) Å, β = 117.525°, V = 1786.73(18) Å^3, R_1 = 0.0180. Selected bond lengths [Å] and angles [°]: Sn1–N1 2.1399(14), N1–N2 1.2201(19), N2–N3 1.139(2), Sn1–N4 2.1365(13), N4–N5 1.2104(19), N5–N6 1.1419(19), Sn1–N7 2.1365(14), N7–N8 1.2221(19), N8–N9 1.1405(19), Sn1–N10 2.1369(14), N10–N11 1.2270(19), N11–N12 1.140(2), Sn1–N13 2.1052(13), N13–N14 1.2188(19), N14–N15 1.140(2), Sn1–N16 2.1341(13), N16–N17 1.2098(19), N17–N18 1.1442(19); Sn1–N1–N2 117.24(11), Sn1–N4–N5 119.64(11), Sn1–N7–N8 119.07(11), Sn1–N10–N11 114.55(11), Sn1–N13–N14 118.56, Sn1–N16–N17 123.21(11), N1–Sn1–N4 172.48(5), N7–Sn1–N10 173.81(5), N13–Sn1–N16 172.07(6).

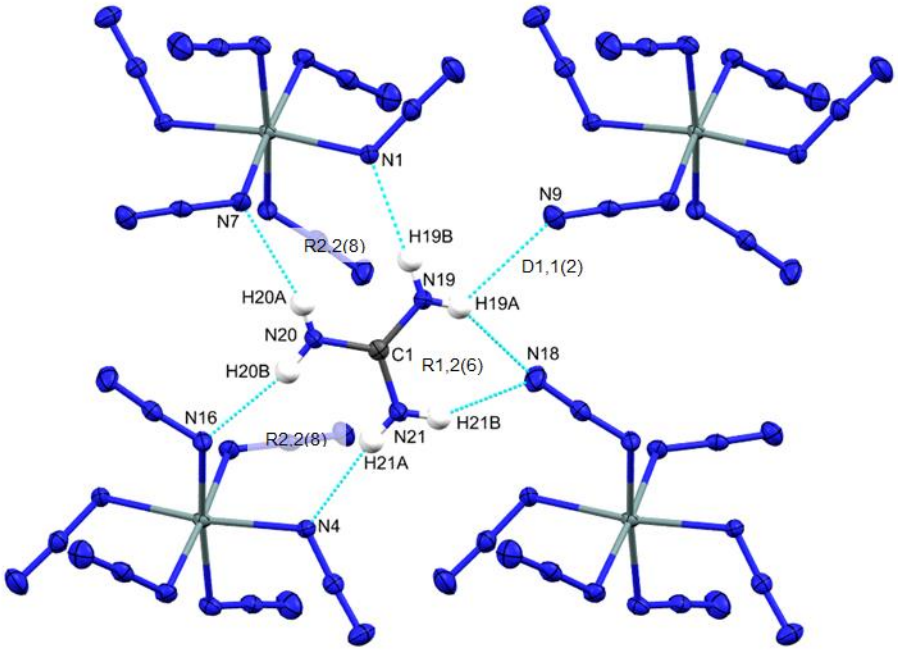

Figure 2.16. Three of the graph sets formed by the hydrogen bonds to one of the two independent guanidinium cations in the structure of **3**.

As a result of the extensive hydrogen bonding, combinations of adjacent R2,2(8) graph sets describe infinite chains of rings linking the hexaazidostannate anions in three dimensions (see Figures 2.16 and 2.17). For amino-substituted guanidinium cations of lower symmetry the situation may be more complicated, or the formation of this kind of extended network may no longer be possible.

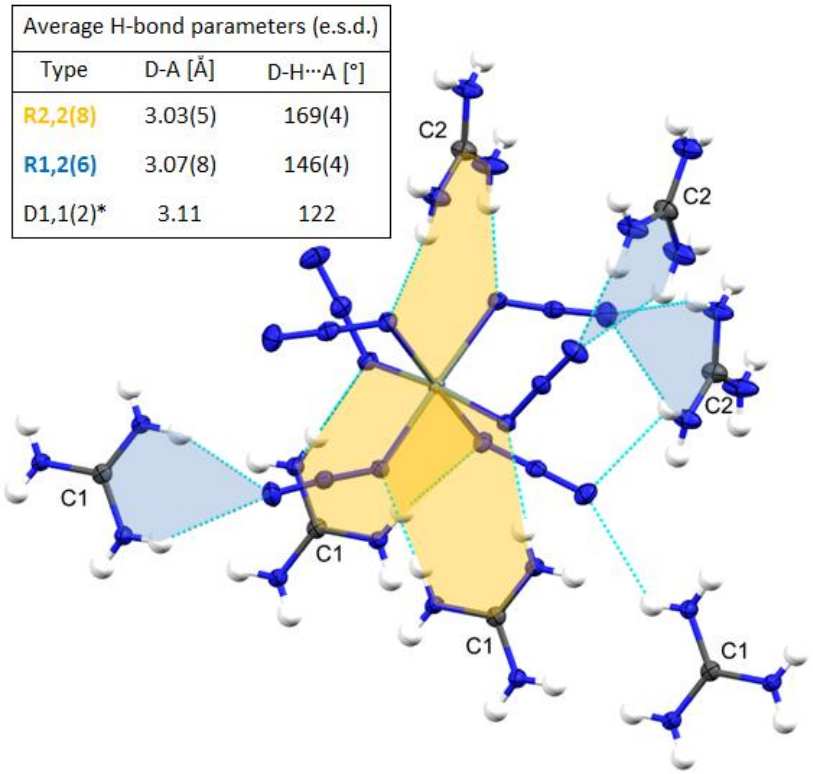

Figure 2.17. The coordination sphere of the hexaazidostannate anion in the crystal structure of **3** at 100 K showing all 14 crystallographically independent hydrogen bonds. Inset: tabulated summary of average hydrogen bond parameters by graph set; *average of only two values.

Table 2.4. Hydrogen bond geometries in the crystal structure of **3** at 100 K.

#	D–H	A	D–H [Å]	*d*(D···A) [Å]	*d*(H···A) [Å]	DHA [°]	1° GS [a]
19A	N19–H19A	N18	0.77(2)	3.125(2)	2.45(2)	147	D
19A'	N19–H19A	N9	0.77(2)	3.133(2)	2.60(2)	128	D
19B	N19–H19B	N1	0.84(2)	3.053(2)	2.23(2)	169	D
20A	N20–H20A	N7	0.78(2)	3.118(2)	2.37(2)	163	D
20B	N20–H20B	N16	0.82(2)	3.014(2)	2.21(2)	167	D
21A	N21–H21A	N4	0.79(2)	3.011(2)	2.23(2)	172	D
21B	N21–H21B	N18	0.83(2)	3.003(2)	2.24(2)	152	D
22A	N22–H22A	N15	0.80(2)	3.203(2)	2.53(2)	143	D
22A'	N22–H22A	N9	0.80(2)	3.095(2)	2.66(2)	116	D

#	D–H	A	D–H [Å]	*d*(D···A) [Å]	*d*(H···A) [Å]	DHA [°]	1° GS [a]
22B	N22–H22B	N10	0.82(2)	3.008(2)	2.20(2)	171	D
23A	N23–H23A	N13	0.79(2)	2.968(2)	2.18(2)	173	D
23B	N23–H23B	N6	0.84(2)	3.001(2)	2.29(2)	143	D
24A	N24–H24A	N6	0.82(2)	3.026(2)	2.33(2)	143	D
24B	N24–H24B	N15	0.83(2)	3.056(2)	2.31(2)	150	D

[a] First level graph set assigned to each hydrogen bond motif.

Crystal structure of guanidinium sodium azide (5b)

This crystal of composition $Na_{1/3}\{C(NH_2)_3\}_{2/3}N_3$ was crystallised as a side product during the attempted preparation of bis(guanidinium) hexaazidosilicate. The sodium ions have typical octahedral coordination of azide anions with guanidinium cations in the interstices formed by the extended NaN_3 3D framework (Figure 2.19). The R1,2(6) and R2,2(8) graph sets formed by pairs of hydrogen bonds are prevalent in this structure (Table 2.5). The high symmetry of the crystal means that all hydrogen bonds form chain (C) or ring (R) graph sets even at the first level.

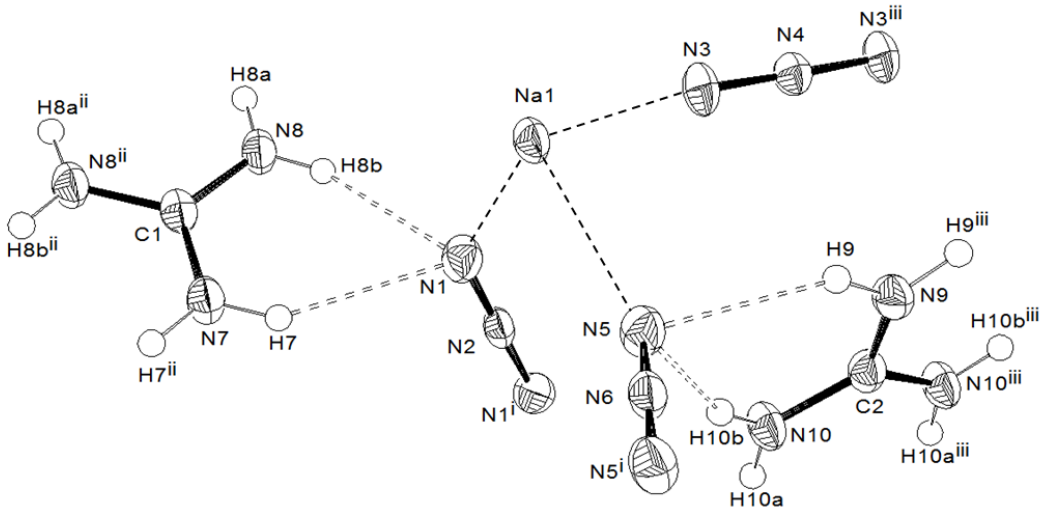

Figure 2.18. Asymmetric unit of **5b** with symmetry equivalent molecular fragments completed for clarity (superscripts denote symmetry equivalent atoms). Thermal ellipsoids at the 50 % probability level, and hydrogen atoms represented by spheres of radius 0.15 Å. Dashed bonds represent hydrogen bonds. Orthorhombic (*Ibam*, Z = 8), a = 12.7824(5) Å, b = 13.3056(9) Å, c = 13.9637(5) Å, V = 2374.9(2) Å^3, R_1 = 0.0377. Selected bond lengths [Å] and angles [°]: C1–N7 1.324(3), C1–N8 1.331(2), C2–N9 1.325(3), C2–N10 1.3289(19), N1–N2 1.1731(15), N3–N4 1.1768(13), N5–N6 1.1834(15), Na1–N1 2.4825(15), Na1–N3 2.3835(13), Na1–N5 2.5916(15); N1–Na1–N3 92.18(5), N1–Na1–N5 91.89, N3–Na1–N5 92.09(5), Na1–N1–N2 135.71(12), N1–N2–N1' 179.9(2), Na1–N3–N4 165.52(17), N3–N4–N3' 178.4(3), Na1–N5–N6 138.06(12), N5–N6–N5' 179.7(2). N1–Na1–N1' = N3–Na1–N3' = N5–Na1–N5' = 180.0.

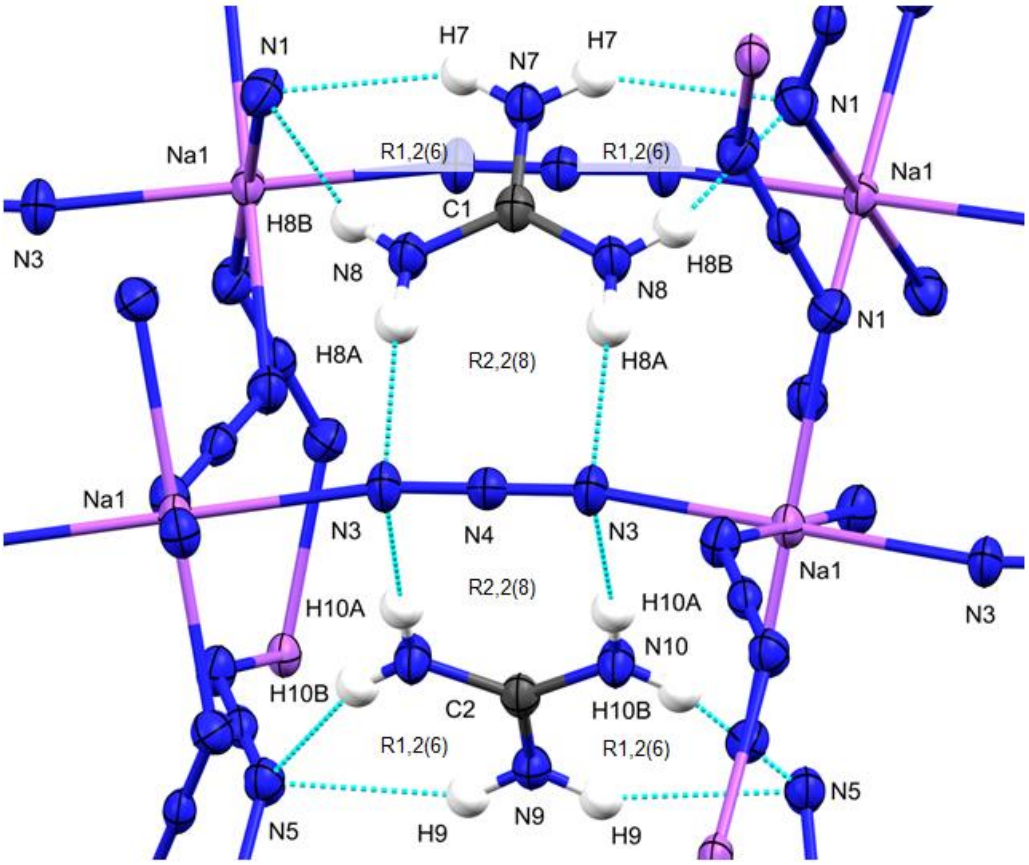

Figure 2.19. Selected graph sets formed by hydrogen bonds in the crystal structure of **5b**.

Table 2.5. Hydrogen bond geometries in the crystal structure of sodium guanidinium azide, $Na_{1/3}\{C(NH_2)_3\}_{2/3}N_3$ (**5b**) at 100 K.

#	D–H	A	D–H [Å]	*d*(D···A) [Å]	*d*(H···A) [Å]	DHA [°]	1° GS [a]
7	N7–H7	N1	0.879(19)	3.0649(15)	2.31(2)	144.2	C2,2(6)
8A	N8–H8A	N3	0.89(2)	3.011(2)	2.12(2)	173.5	R2,2(8)
8B	N8–H8B	N1	0.83(2)	2.952(2)	2.16(2)	159.6	C2,2(8)
9	N9–H9	N5	0.88(2)	3.0940(14)	2.32(2)	148.0	C2,2(6)
10A	N10–H10A	N3	0.87(2)	3.118(2)	2.26(2)	173.0	R2,2(8)
10B	N10–H10B	N5	0.831(19)	3.005(2)	2.212(19)	159.7	C2,2(6)

[a] First level graph set assigned to each hydrogen bond motif.

Crystal structure of diazido(guanidinyl)(oxido)phosphorus [P(=O)(N_3)$_2${NC(NH_2)$_2$}] (8)

No hydrogen atoms could be located on either the oxygen (O1) or nitrogen (N7) bound to the phosphorus centre and upon inspection of the packing in the crystal structure, protonation of N7 would cause a clash with H8B (see Figure 2.21). A comparison of this unusual species (Figure 2.20) with structurally related compounds is given in Table 2.6. The P=O bond is slightly elongated (1.4747(10) Å at T = 100 K) compared to the P=O bond in the crystal structure of [P(=O)(N_3)$_3$] (1.4591(19) Å at T = 140 K),[153] but very close to the P=O bond length in diethylphosphorylguanidine hemi(guanidinium chloride) (1.481(4) Å at RT (283–303 K).[157] The P1–N7 bond (1.5936(11) Å) is significantly shorter than the P–N single bonds to the azido ligands (average 1.6957(12) Å), suggesting significant double bond character. The three C–N distances of the guanidinyl moiety range from 1.319(7) to 1.346(7) Å with C1–N8 the longest (and furthest from the phosphorus) and C1–N7 the shortest (and closest to phosphorus). All four protons in this structure are involved in hydrogen bonds (Table 2.7), including an intramolecular S(6) hydrogen bond accepted by the oxygen. A complementary R2,2(8) graph set is formed by neighbouring complexes *via* N8–H8B and N7.

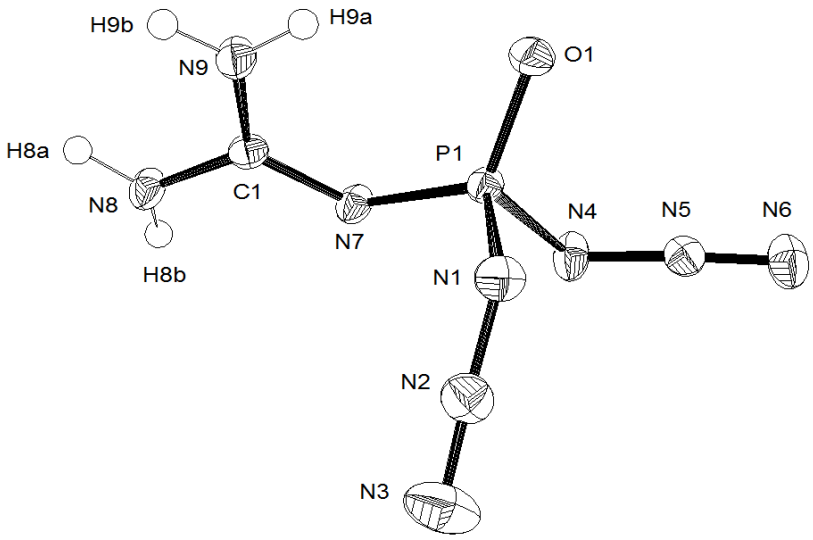

Figure 2.20. Asymmetric unit in the crystal structure of **8** at 100 K. Thermal ellipsoids at the 50 % probability level, hydrogen atoms represented by spheres of radius 0.15 Å. Monoclinic ($I2/a$, Z = 8), a = 10.5081(13) Å, b = 11.7968(8) Å, c = 12.2631(8) Å, β = 92.677(2)°, V = 1518.5(2) Å^3, R_1 = 0.0271. Selected bond lengths [Å] and angles [°]: P1–O1 1.4747(10), P1–N1 1.7025(12), N1–N2 1.2440(18), N2–N3 1.1190(19), P1–N4 1.6890(12), N4–N5 1.2512(15), N5–N6 1.1191(16), P1–N7 1.5936(11), C1–N7 1.3391(16), C1–N8 1.3311(17), C1–N9 1.3422(16); P1–N1–N2 117.14(9), N1–N2–N3 174.05(15), P1–N4–N5 115.82(9), N4–N5–N6 174.11(14), O1–P1–N1 104.35(6), O1–P1–N4 114.56(6), O1–P1–N7 121.57(6), N1–P1–N4 105.26(6), N1–P1–N7 110.86(6), N4–P1–N7 99.36(5), P1–N7–C1 122.74(9), N7–C1–N8 118.15(11), N7–C1–N9 124.35(12), N8–C1–N9 117.49(12).

Table 2.6. Selected bond lengths in the crystal structure of $[P(=O)(N_3)_2\{NC(NH_2)_2\}]$ **8**, compared to the equivalent bond lengths in $(PPN)[P(N_3)_6]$[84] at 150 K, $P(=O)(N_3)_3$[134] at 140 K, and $[P(=O)(OEt)_2\{NC(NH_2)_2\}]\cdot 0.5\{C(NH_2)_3Cl\}$ at room temperature.[157]

	8	$(PPN)[P(N_3)_6]$	$P(=O)(N_3)_3$	$[P(=O)(OEt)_2\{NC(NH_2)_2\}]$[a]
Ref.	this work	[84]	[153]	[157]
T [K]	100	150	140	283–303 [b]
P=O [Å]	1.4747(10)	-	1.4591(19)	1.481(4)
$P–N_\alpha$ [Å]	1.6957(12)[c]	1.8077(12)[c]	1.6709(11)[c]	-
$N_\alpha–N_\beta$ [Å]	1.2476(18)[c]	1.2275(18)[c]	1.2462(16)[c]	-
$N_\beta–N_\gamma$ [Å]	1.1191(19)[c]	1.1311(18)[c]	1.1176(16)[c]	-
P–N7 [Å]	1.5936(11)	-	-	1.595(5)
C1–N7 [Å]	1.3389(16)	-	-	1.319(7)
C1–N8 [Å]	1.3418(16)	-	-	1.346(7)
C1–N9 [Å]	1.3311(17)	-	-	1.333(7)

[a] Compound is 2:1 co crystal with guanidinium chloride; [b] Default value reported for room temperature on the CCDC's *Conquest* database (v1.18); [c] Average of all equivalent bonds in the compound.

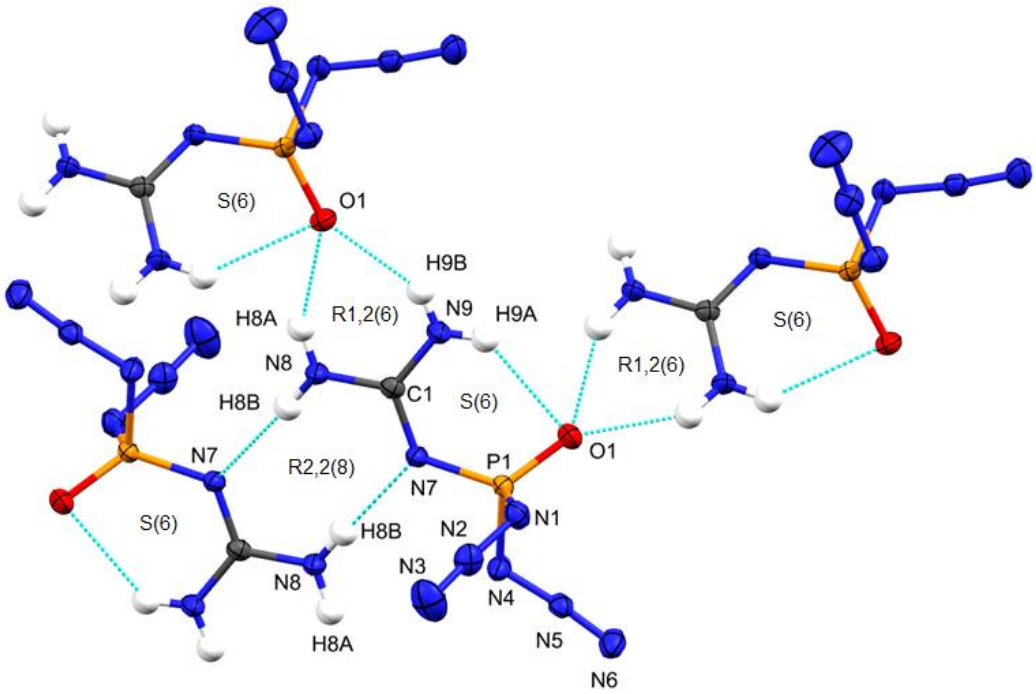

Figure 2.21. Projection of selected graph sets formed by hydrogen bonds in the crystal structure of **8**.

Table 2.7. Hydrogen bond geometries in the crystal structure of **8** at 100 K.

#	D–H	A	D–H [Å]	*d*(D···A) [Å]	*d*(H···A) [Å]	DHA [°]	1° GS [a]
9A	N9–H9A	O1	0.812(19)	3.0704(16)	2.437(18)	135.6(16)	S(6)
9B	N9–H9B	O1	0.830(18)	2.8770(16)	2.129(18)	149.8(16)	D1,1(2)
8A	N8–H8A	O1	0.873(18)	2.9159(15)	2.136(19)	148.6(15)	D1,1(2)
8B	N8–H8B	N7	0.875(19)	2.9700(16)	2.095(19)	177.9(17)	R2,2(8)

[a] First level graph set assigned to each hydrogen bond motif.

Guanidinium tetrazolate (19)

Several guanidinium salts with planar tetrazolate derivatives have layered crystal structures, which may be due to the presence of the additional hydrogen bond acceptors, such as for example the $–NO_2$ group in nitrotetrazolate. In the case of guanidinium tetrazolate (**19**), the absence of an electronegative substituent (and hydrogen bond acceptor) may be a factor preventing such a structure. The coordination environment of one guanidinium cation is shown in Figure 2.23 below, where one of the tetrazolates is reasonably close to being coplanar with guanidinium, with a 13° torsion angle between the least-squares derived mean planes of the respective ions. The remaining tetrazolate anions are virtually perpendicular with torsion angles of 87°. Accordingly, the tetrazolate anion is hydrogen bonded to one guanidinium cation in the plane *via* the graph set R2,2(7), and to four other guanidinium cations which are perpendicular *via* R1,2(6), D, or extended R4,4(16) graph sets *via* a total of seven crystallographically independent hydrogen bonds (Table 2.8).

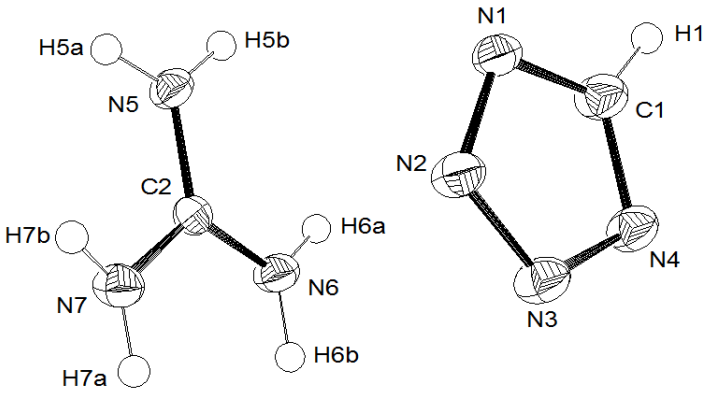

Figure 2.22. Asymmetric unit in the crystal structure of **19** at 100 K. Thermal ellipsoids at the 50 % probability level, and hydrogen atoms represented by spheres of radius 0.15 Å. Monoclinic ($P2_1/c$, Z = 4), a = 4.7296(16) Å, b = 13.894(5) Å, c = 8.754(3) Å, β = 92.96(2)°, V = 574.5(3) Å^3, R_1 = 0.0523. Selected bond lengths [Å] and angles [°]: C1–N1 1.328(2), N1–N2 1.350(2), N2–N3 1.318(2), N3–N4 1.356(2), N4–C1 1.330(2), C2–N5 1.327(2), C2–N6 1.317(2), C2–N7 1.337(2); C1–N1–N2 103.74(15), N1–N2–N3 109.88(15), N2–N3–N4 109.17(14), N3–N4–C1 103.79(15), N4–C1–N1 113.42(17).

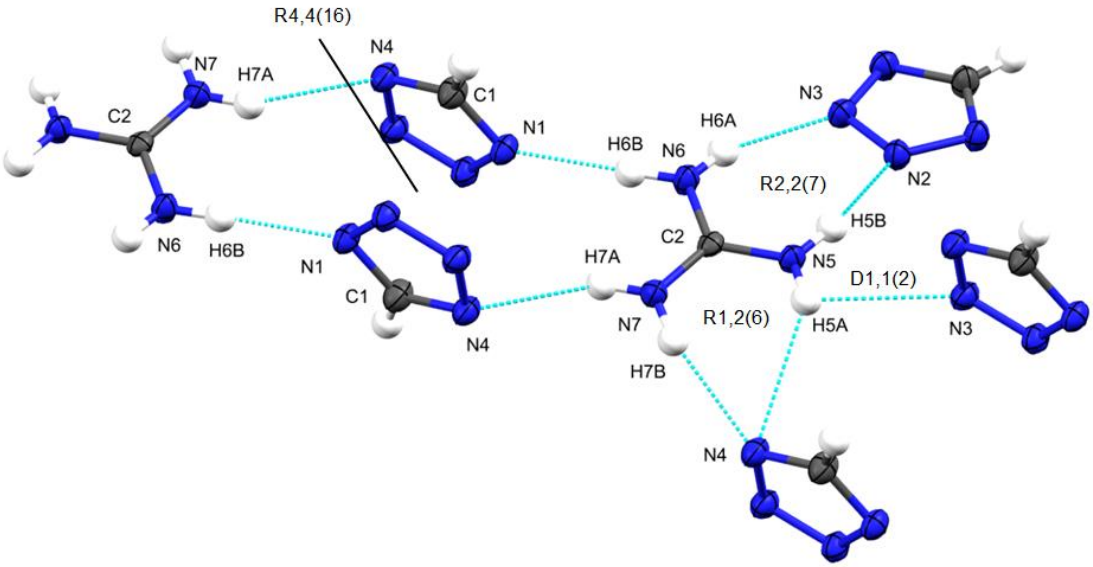

Figure 2.23. Selected graph sets formed by hydrogen bonds in the crystal structure of **19** at 100 K.

Table 2.8. Hydrogen bond geometries in the crystal structure of guanidinium tetrazolate (**19**) at 100 K.

#	D–H	A	D–H [Å]	*d*(D···A) [Å]	*d*(H···A) [Å]	DHA [°]	1° GS [a]
5A	N5–H5A	N4	0.88(2)	3.310(2)	2.61(2)	137	D
5A’	N5–H5A	N3	0.88(2)	3.053(2)	2.60(2)	113	D
5B	N5–H5B	N2	0.92(2)	2.925(2)	2.02(2)	166	D
6A	N6–H6A	N3	0.84(2)	3.105(3)	2.30(2)	162	D
6B	N6–H6B	N1	0.90(3)	2.949(2)	2.05(3)	178	D
7A	N7–H7A	N4	0.85(2)	3.179(2)	2.51(2)	137	D
7B	N7–H7B	N4	0.86(2)	3.063(3)	2.23(2)	162	D

[a] First level graph set assigned to each hydrogen bond motif.

Comparing hydrogen bond geometries of common graph sets within guanidinium salts

Some of the most common graph sets encountered in the structures of guanidinium salts are the R1,2(6) and R2,2(*x*), where ‘*x*’ varies between 7 and 9 depending on the nature of the acceptor. In the R1,2(6) graph set, protons on two neighbouring nitrogen atoms form a hydrogen bond with the same acceptor atom forming a ring pattern. Also common are patterns where two nitrogen atoms of guanidinium are hydrogen bonded to separate acceptor atoms which are part of one moiety that is denoted R2,2(*x*), and where *x* is the total number of atoms in the resulting pattern. There is little or no difference between the average D···A distances

between different hydrogen bond graph sets, and there is significant variation of hydrogen bond lengths – approximately 2.93–3.32 Å – within most of the structures discussed here.

Table 2.9. Average D···A distances [Å] for N–H···N of common hydrogen bond patterns (graph sets) in the crystal structures of nitrogen-rich guanidinium salts, phosphorus azide **8** and tin polyazides **3** and **17**.

	Average D···A distances [Å]			
Graph Set	R1,2(6)	R2,2(x)[a]	D	Overall
$(G)N_3$ (**1**)	3.12	3.00	3.07	3.075(67)
$(G)N_3{\cdot}H_2O$ (**1a**)	3.101	N/A	3.067	3.059(51)
$(AG)N_3$ (**2**)	3.03	3.02[b]	3.08	3.08(11)
$(G)_2[Sn(N_3)_6]$ (**3**)	3.07	3.03	3.11	3.058(67)
$Na_{0.33}(G)_{0.67}N_3$ (**5b**)	3.03	3.06	N/A	3.041(62)
$[P(=O)(N_3)_2\{NC(NH_2)_2\}]$ (**8**)	N/A	2.97[b]	N/A	2.97[b]
$(G)[Sn(N_3)_3]$ (**17**)	3.138	3.001	N/A	3.12(15)
$(G)N_4CH$ (**19**)	3.19	3.02	3.12	3.08(13)

[a] x = 7–9 depending on the structure of the acceptor; [b] The only example of N–H···N hydrogen bond of its type in the crystal structure.

The key parameters for the crystal structures of the compounds described in this chapter are outlined in Table 2.10 below, along with parameters for the original crystallographic data sets. In all cases the data-to-parameter ratio exceeds 11:1 and the completeness of the data are close to 100 % and with the exception of guanidinium azide (**1**) the data were of sufficient quality to locate protons on heteroatoms from electron density maxima on the Fourier difference map. In the case of guanidinium azide the pronounced twinning of the crystals required application of restraints (see above section 2.2.3). The nitrogen content of the compounds ranges from 67 % for the phosphorus azide (**8**) to more than 83 % for aminoguanidinium azide (**2**). Guanidinium azide (**1**) has the largest unit cell as it contains 24 formula units compared to 4 or 8 for the remaining compounds. The CHNO compounds have the lowest X-ray attenuation coefficients, μ [mm^{-1}], whereas tin polyazide **3** has by far the greatest, and compounds **8** and **5b** have larger coefficients than the CHNO compounds. Unsurprisingly a similar trend is observed for the density of the compounds, hexaazidostannate **3** having the highest density at 1.825 g cm^{-3} as it contains tin, followed by phosphorus azide **8**, sodium guanidinium azide (**5b**) and guanidinium tetrazolate (**19**) with densities of 1.654, 1.506 and 1.493 g cm^{-3} respectively. Aminoguanidinium azide (**2**) has a density of 1.474 g cm^{-3}, slightly higher than guanidinium azide (**1**) or its monohydrate **1a** (both 1.399 g cm^{-3}).

Table 2.10. Summary of crystallographic data for guanidinium azide (**1**), guanidinium azide monohydrate (**1a**), aminoguanidinium azide (**2**), bis(guanidinium) hexaazidostannate (**3**), sodium guanidinium azide (**5b**), $[P(=O)(N_3)_2\{NC(NH_2)_2\}]$ (**8**), and guanidinium tetrazolate (**19**).

	1	**1a**	**2**	**3**	**5b**	**8**	**19**
Empirical formula	CH_6N_6	CH_8N_6O	CH_7N_7	$C_2H_{12}N_{24}Sn$	$C_2H_{12}N_{15}Na$	CH_4N_9OP	$C_2H_7N_7$
M_r [g mol^{-1}]	102.1	120.13	117.14	491.05	269.26	189.10	129.15
N [%]	82.3	70.0	83.7	68.5	78.0	66.7	75.9
Crystal system	monoclinic	monoclinic	monoclinic	monoclinic	orthorhombic	monoclinic	monoclinic
Space group	*C*2/*c*	*P*2$_1$/*c*	*P*2$_1$/*c*	*P*2$_1$/*c*	*Ibam*	*I* 2/*a*	*P*2$_1$/*c*
a [Å]	20.410(3)	8.3174(6)	7.3030(4)	8.2382(5)	12.7824(5)	10.5081(13)	4.7296(16)
b [Å]	11.6649(15)	10.9115(8)	12.3379(7)	28.1101(16)	13.3056(9)	11.7968(8)	13.894(5)
c [Å]	12.2223(16)	6.4713(4)	6.1442(3)	8.7003(5)	13.9637(5)	12.2631(8)	8.754(3)
α [°]	90	90	90	90	90	90	90
β [°]	90.101(6)	103.776(3)	107.583(2)	117.525(2)	90	92.677(2)	92.96
γ [°]	90	90	90	90	90	90	90
V [Å^3]	2909.9(6)	570.41(7)	527.75(5)	1786.73(18)	2374.9(2)	1518.5(2)	574.5(3)
Z	24	4	4	4	8	8	4
D_{calc} [g cm^{-3}]	1.399	1.399	1.474	1.825	1.506	1.654	1.493
μ [mm^{-1}]	0.110	0.117	0.116	1.480	0.148	0.333	0.115
F (000)	1296	256	248	968	1120	768	272
Crystal size [mm × mm × mm]	0.50 × 0.48 × 0.15	0.46 × 0.32 × 0.18	0.45 × 0.40 × 0.40	0.50 × 0.35 × 0.30	0.45 × 0.25 × 0.25	0.48 × 0.45 × 0.40	0.6 × 0.20 × 0.20
Crystal habit	hexagonal plate	needle	prism	shard	rod	shard	shard
θ range for data collection [°]	3.3337, 24.7334	3.1376, 27.4615	3.3024, 27.5664	2.7376, 27.4943	2.9175, 25.2513	2.3969, 27.4715	2.9321, 23.7057
Limiting indices *h*; *k*; *l*	–24, 26; –15, 15; –15, 15	–10, 10; –14, 14; –8, 8	–9, 9; –16, 13; –8, 7	–10, 10; –36, 36; –11, 11	–16, 16; –17, 16; –18, 18	–13, 13; –11, 15; –15, 15	–4, 6; –17, 15; –11, 9
Reflections collected	17272	5293	4955	36901	13521	10716	6101
Independent reflections	10914	1235	1221	4097	1428	1746	1304
R_{int}	N/A	0.0243	0.0156	0.0304	0.0522	0.0273	0.0839
Completeness to *θ* [%]	100.0 (*θ* = 25.00°)	99.9 (*θ* = 25.24°)	99.8 (*θ* = 25.00°)	100.0 (*θ* = 25.00°)	99.9 (*θ* = 25.24°)	99.4 (*θ* = 25.24°)	100.0 (*θ* = 25.00°)
Solution	[a]	[a]	[a]	[a]	[a]	[a]	[a]
Refinement	[b,c]	[b]	[b]	[b]	[b]	[b]	[b]

	1	1a	2	3	5b	8	19
Data / restraints / parameters	10914 / 12 / 192	1235 / 0 / 105	1221 / 0 / 101	4097 / 0 / 292	1428 / 0 / 116	1746 / 0 / 125	1304 / 0 / 110
GoF F^2	1.083	1.084	1.026	1.080	1.030	1.014	1.065
Final R indices [$I > 2\sigma(I)$]	0.0756	0.0265	0.0270	0.0180	0.0377	0.0272	0.0523
R_1 (all data)	0.1333	0.0277	0.0311	0.0218	0.0621	0.0309	0.0816
Largest diff. peak / hole [e Å^3]	0.353 / –0.472	0.256 / –0.234	0.209 / –0.210	0.338 / –0.298	0.255 / –0.179	0.429 / –0.283	0.270 / –0.314

[a] direct methods, *SHELXS-97*;[b] Full-matrix least squares on F^2, *SHELXL-2014*; [c] Twin refinement using *ROTAX* within *WinGX*, and due to this HKLF5 refinement no R_{int} is available.

2.2.4 Thermal Analyses

Differential scanning calorimetry (DSC) consists of two independently heated temperature-controlled compartments containing the sample and inert reference, respectively, and measures the difference in heat flow required to maintain the same temperature at a controlled heating rate. The peak shapes of observable thermal effects such as melting, phase changes, crystallisation (upon cooling), or decomposition vary depending on the chosen heating rate. Slow heating rates (< 5 °C min^{-1}) lead to less easily discernible peaks, whereas fast heating rates (> 10 °C min^{-1}) might be affected by thermal lag. A heating rate of 10 °C min^{-1} was chosen for the measurements as a compromise.

Differential scanning calorimetric measurements of guanidinium azides and bis(guanidinium) hexaazidostannate

DSC measurements were carried out on guanidinium azide (**1**), its monohydrate (**1a**), aminoguanidinium azide (**2**), and bis(guanidinium) hexaazidostannate (**3**) to investigate their thermal stability and energy content (enthalpies of decomposition). The results are summarised in Table 2.11 below, where $(PPN)_2[Sn(N_3)_6]$ (**9**) is included for comparison (see chapter 3 for details). DSC measurements are frequently carried out in crimped aluminium pans, whereas these experiments were carried out using stainless steel high-pressure capsules under nitrogen flow with a heating rate of 10 °C min^{-1}. With the exception of hydrate **1a**, the samples (typically 2.5–7 mg) were loaded into the DSC pans and sealed under a protective atmosphere of argon in the glovebox. Melting and decomposition temperatures quoted are extrapolated onset temperatures, as the peak temperature varies with sample mass. The extrapolation of onset temperatures is based on the intersection of the baseline with the tangent to the maximum gradient of the endotherm (or exotherm). Enthalpies of fusion (ΔH_{fus}) and decomposition (ΔH_{dec}) have been calculated from the DSC traces by dividing the integrated

peak areas by the heating rate, with positive values denoting endothermic processes. Full details are included in the experimental section. Guanidinium azides **1**, **1a**, and **2** were also subjected to thermogravimetric analysis (TGA). Additionally **1** and **2** were subjected to flame tests on 100 mg scale (see Figure 2.24). Both compounds melted to colourless liquids after 7 and 10 seconds respectively, before deflagration (loud crackling) with a bright orange flame after 12 and 4 seconds respectively. There seemed to be slightly more residue upon deflagration of **1** than for compound **2**.

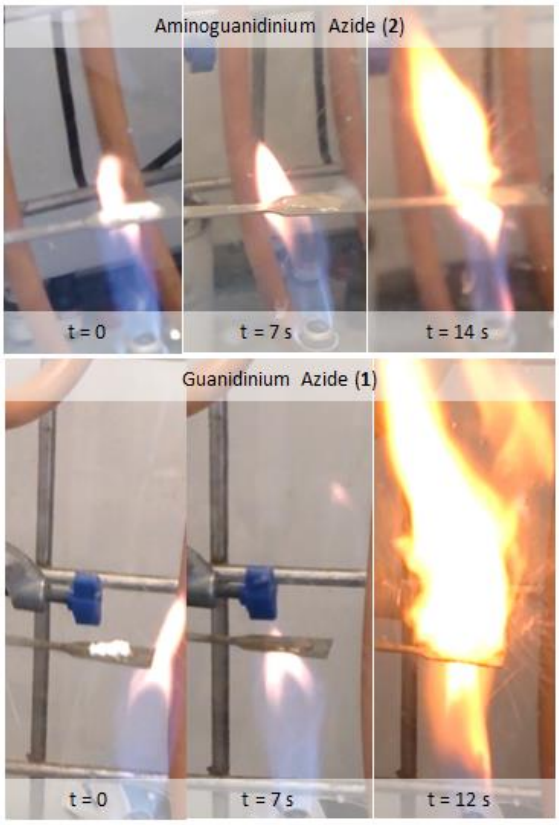

Figure 2.24. Still images taken from video footage captured during flame tests of guanidinium azide (**1**, bottom, 100 mg), and aminoguanidinium azide (**2**, top, 100 mg). Left: before melting, centre: after melting, and right: during deflagration. A butane/propane gas mixture was used for the experiments. *[Photos: Rory Campbell, September 2013]*

Bis(guanidinium) hexaazidostannate (**3**) and bis{bis(triphenylphosphine)iminium} hexaazidostannate (**9**) have the highest molar enthalpies of decomposition of –1270(30) kJ mol^{-1} and –1100 kJ mol^{-1} respectively, though compound **3** has more than treble the specific enthalpy of decomposition than **9** (–2.60(5) *vs*. –0.76 MJ kg^{-1}). This confirms that employment of a nitrogen-rich cation instead of a bulky weakly coordinating cation dramatically increases the specific energy content. The molar enthalpies suggest a contribution of around 200 kJ mol^{-1} for each coordinated azide group, which is in keeping with previous investigations into the related Si, Ge, and P compounds.[84] Aminoguanidinium azide (**2**) has the highest specific enthalpy of decomposition (–2.80 MJ kg^{-1}) out of the available data for

compounds considered in Table 2.11, which is probably because it has the highest nitrogen content (83.7 %) and a relatively weak N–N bond in the cation which is absent in guanidinium salts **1** and **3**.

Table 2.11. A summary of the key parameters associated with the melting and decomposition determined by DSC analyses for guanidinium azide (**1**), guanidinium azide monohydrate (**1a**), aminoguanidinium azide (**2**), and hexaazidostannate salts of guanidinium (**3**) and (PPN) (**9**). Literature values for di- and triaminoguanidinium azides $(DAG)N_3$ and $(TAG)N_3$ are included for comparison. The numbers in parentheses represent a crude estimation of the error based on an average of at least two samples, where available.

	1	**1a**	**2**	$(DAG)N_3$ [a]	$(TAG)N_3$ [b]	**3**	**9**
T_{on}^{m} [°C] [c]	99.9(3)	41.6(3)	125(2)	109	100	116(1)	218
ΔH_{fus} [kJ mol^{-1}]	13.7(10)	23.0(2)	28.6(2)	-	[d]	34(3)	-
ΔH_{fus} [J g^{-1}]	134(10)	191(2)	244(2)	-	[d]	70(5)	-
T_{on}^{dec} [°C] [c]	253(6)	258(5)	200(4)	189	172	250(3)	300, 365
ΔH_{dec} [kJ mol^{-1}]	–243(8)	–226(6)	–328(7)	-	–13.5 [e]	–1270(30)	–1100
ΔH_{dec} [MJ kg^{-1}]	–2.38(8)	–1.88(5)	–2.80(6)	-	–0.0921 [e]	–2.60(5)	–0.76

[a] ref. [47]; [b] ref. [158]; [c] extrapolated onset temperature; [d] endothermic loss of HN_3 precedes melting of the remaining solid; [e] decomposition is multi-stage process discussed in ref. [158].

Guanidinium azide (**1**), its monohydrate (**1a**), and hexaazidostannate salt **3** have indistinguishable decomposition onset temperatures, though the hydrate has a much lower melting point (T_{on}^{m} = 41 °C) than anhydrous **1** (T_{on}^{m} = 99 °C) or **3** (T_{on}^{m} = 116 °C). The comparison of the decomposition temperatures to triaminoguanidinium azide ($(TAG)N_3$) may not be appropriate, as the sample containment may not have been the same. According to ref. [158] triaminoguanidinium azide loses HN_3 in an endothermic step at 115 °C leaving triaminoguanidine which melts at 172 °C and releases far less energy upon decomposition than a typical azide compound. Hexaazidostannate **3** has the highest enthalpy of fusion, which may be a result of the stronger interionic forces in a 2 : 1 salt. Despite having a similarly extensive hydrogen bond network guanidinium azide has the lowest ΔH_{fus}, which may be due to the weakness of the interionic forces between the adjacent layers in the crystal lattice. The lower thermal stability of the amino-substituted guanidinium azides could be due to the relatively weak N–N bonds in the cation, which are absent in **1** and **3**. The onset temperatures for decomposition of hexaazidostannate salts **3** and **9** occur close to those of their respective azide salts **1** ($T_{on}^{dec} \approx$ 250 °C) and $(PPN)N_3$ (T_{on}^{dec} = 300 °C)[84] suggesting that their thermal stability is limited by that of the cation rather than by hexaazidostannate itself.

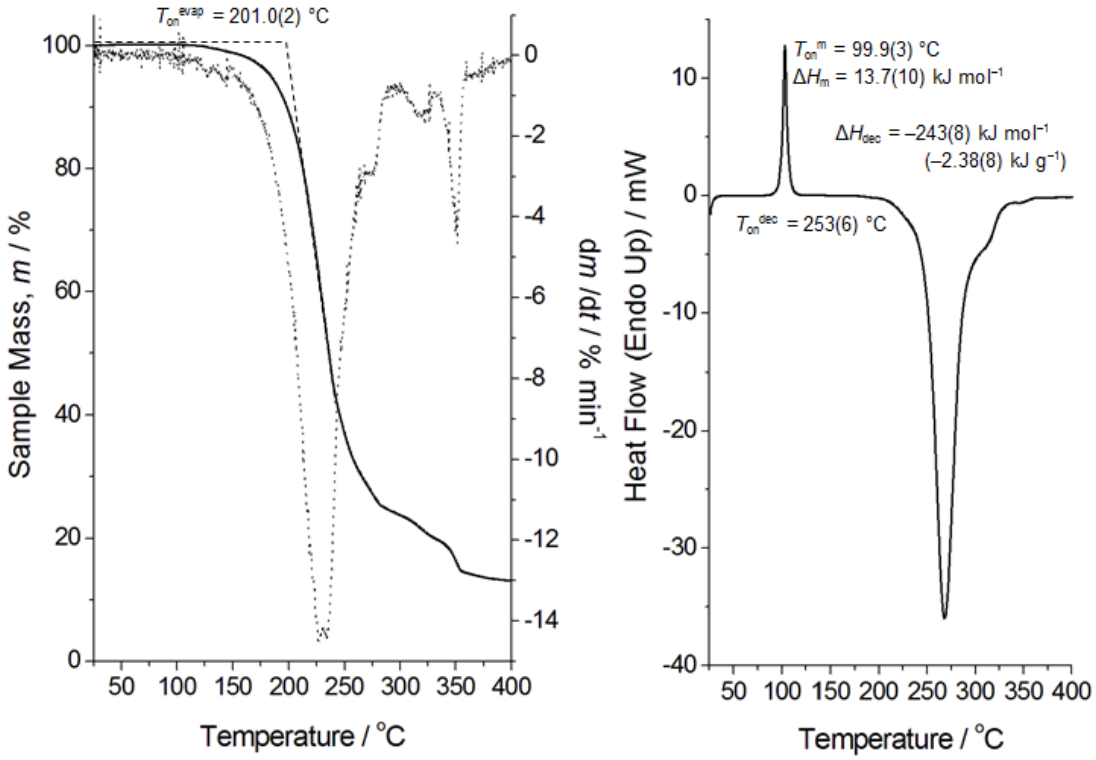

Figure 2.25. Thermograms of guanidinium azide (**1**). Left: Thermogravimetry (open crucible, 20 ml min^{-1} nitrogen flow) showing the sample mass (——) and rate of mass loss (----); Right: DSC (closed stainless steel capsule). The heating rate for both measurements was 10 °C min^{-1}.

Under the conditions of the DSC measurements guanidinium azide (**1**) melts at 100 °C, followed by exothermic decomposition with extrapolated onset temperature around 253 °C, which is complete around 350 °C. In the thermogravimetry experiments, which were carried out under a protective stream of N_2, the mass of **1** remained virtually constant until just after melting, after which evaporation started with an extrapolated onset temperature of 201 °C, reaching a maximum rate at around 225 °C. Above 275 °C the gradient of the mass loss curve became irregular (dotted line, left of Figure 2.25), and varied slightly between samples. This is perhaps not surprising as it is above the onset of decomposition observed in DSC measurements.

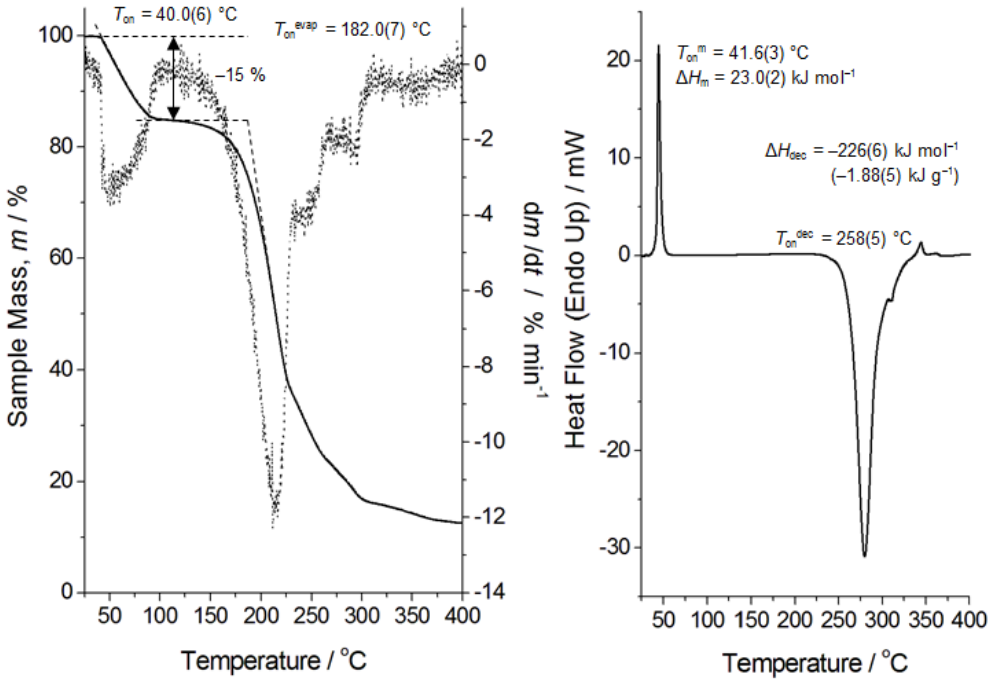

Figure 2.26. Thermograms of guanidinium azide monohydrate (**1a**). Left: Thermogravimetry (open crucible, 20 ml min^{-1} nitrogen flow) showing the sample mass (——) and rate of mass loss (----); Right: DSC (closed stainless steel capsule). The heating rate for both measurements was 10 °C min^{-1}.

The first step between 42–100 °C corresponds to a weight loss of 15% due to the loss of crystal water after melting. The onset of the second weight loss step occurs at 182 °C, which is around 20 °C lower than anhydrous guanidinium azide under the same conditions. Other than the loss of water, the rate of mass loss follows a very similar pattern to the anhydrous material, which slows slightly during the exothermic decomposition processes between around 225–300 °C, and slows further above 300 °C leaving 13–14 % residue by 400 °C.

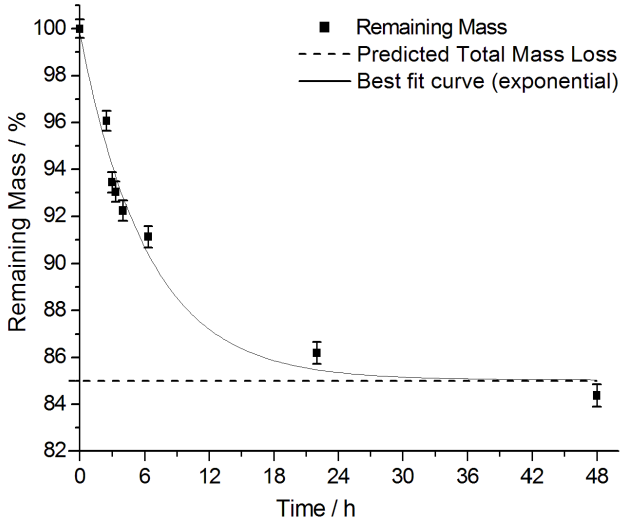

Figure 2.27. The percentage mass remaining upon drying a sample of guanidinium azide hydrate (**1a**) at 35 °C under dynamic vacuum over a period of 48 h. Curve fit: $y = y_0 + Ae^{-x/t}$, parameter values: y_0 = 0.8504, A = 0.1481, t = 6.2332; R^2 = 0.97668. Error bars are based solely on uncertainty of weighing operations.

In a separate experiment a sample of guanidinium azide monohydrate (*ca.* 1 g) was heated to 35 (±1) °C in a thermostat-controlled oil bath under dynamic vacuum (4×10^{-2} mbar) and the mass loss was recorded over 48 hours (Figure 2.27). The removal of water was confirmed by the melting point and FTIR spectrum of the residue. This experiment was carried out slightly below the melting point (41 °C) of **1a** to prevent sintering of the solid, though given the thermal stability of guanidinium azide it may be possible to accelerate the drying process by increasing the temperature. Based on extrapolation by the fitted exponential curve, the time taken to remove the crystal water (to below detectable limit of 1 mg) would be around 45 h. Extrapolating the fitted curve to 'infinite' time a total mass loss of 14.96 % would be expected, assuming no additional water was present, and neglecting loss of hydrazoic acid or guanidine *via* evaporation or sublimation, respectively.

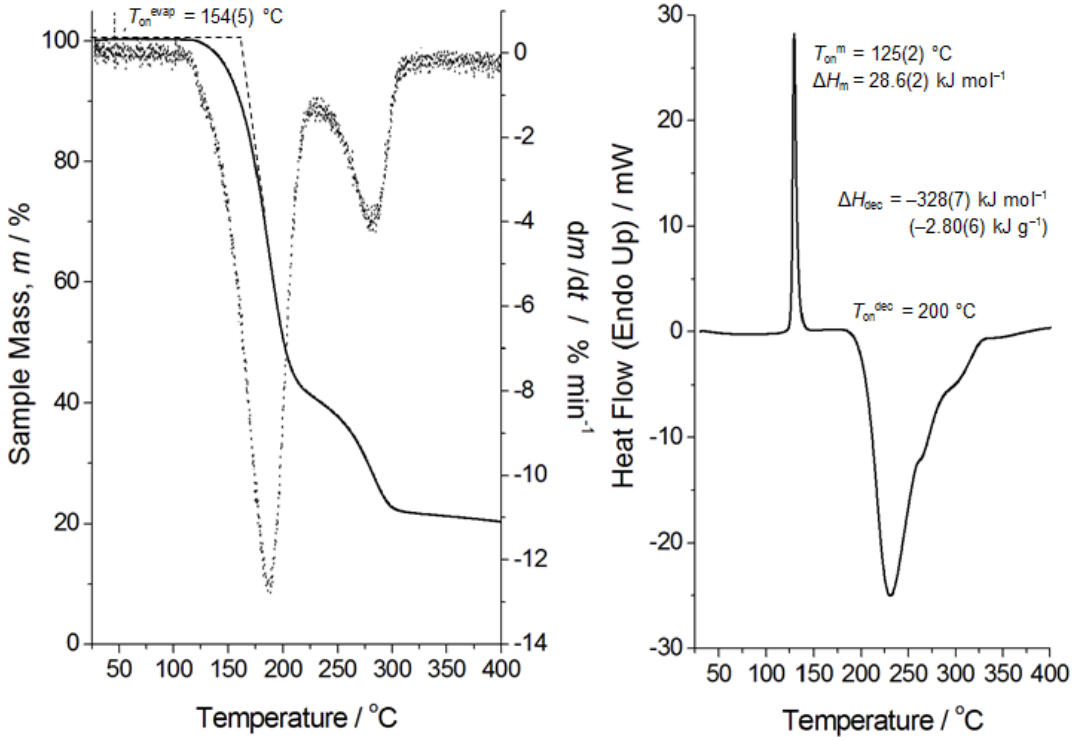

Figure 2.28. Thermograms of aminoguanidinium azide (**2**). Left: Thermogravimetry plot showing the sample mass (——) and rate of mass loss (----) (open crucible, 20 ml min^{-1} nitrogen flow); Right: DSC (closed stainless steel capsule). The heating rate for both measurements was 10 °C min^{-1}.

The melting point of aminoguanidinium azide determined by DSC to be 125 °C, slightly higher than guanidinium azide, followed by highly exothermic decomposition (ΔH_{dec} = –328 ± 7 kJ mol^{-1}) begins with an onset of around 200 °C. The increased molar enthalpy of decomposition suggests a significant contribution from the aminoguanidinium cation. The lower onset temperature of decomposition compared to guanidinium azide may be explained by analogy with the study of $(TAG)N_3$, [158] which suggests this is due to cleavage of the N–N bond with loss of NH_4N_3 (as HN_3/NH_3). The highly exothermic nature of the decomposition suggests that hydrazoic acid does not dissociate before decomposition as in the mechanism

proposed for (TAG)N_3. Thermogravimetry experiments showed the sample mass to be constant below 125 °C, after which evaporation occurs with an extrapolated onset temperature of around 154 °C, reaching maximum evaporation rate at around 190 °C. The mass loss rate slowed above 225 °C, presumably during the exothermic decomposition step observed using DSC.

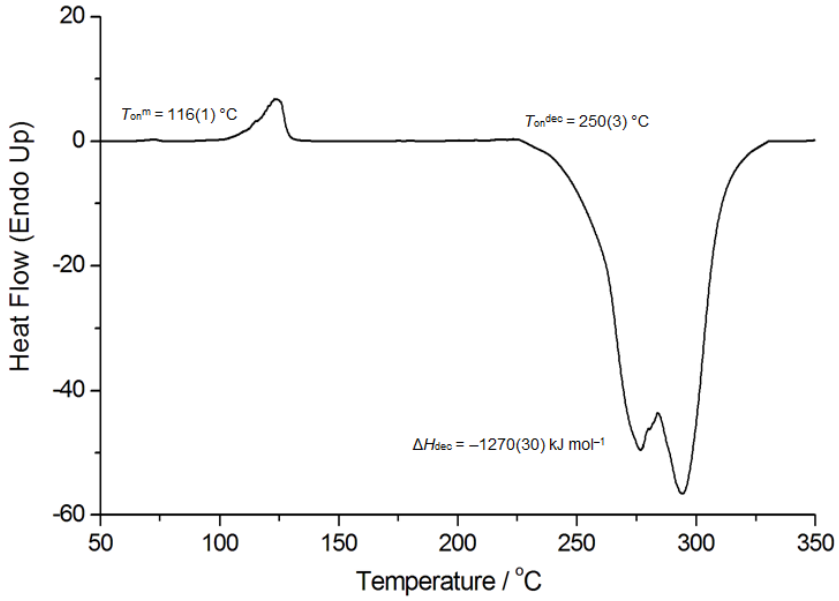

Figure 2.29. DSC trace of bis(guanidinium) hexaazidostannate (**3**), heating rate 10 °C min^{-1}.

Bis(guanidinium) hexaazidostannate (**3**) has significantly higher nitrogen content than $(PPN)_2[Sn(N_3)_6]$ (**9**) (68 % *vs.* 19 %), and according to DSC measurements, the compound has proportionately greater specific enthalpy of decomposition (–2.5 MJ kg^{-1} *vs.* –0.76 MJ kg^{-1}), and similar molar enthalpy of decomposition (–1270(30) kJ mol^{-1} *vs.* –1100 kJ mol^{-1}). Hexaazidostannate **3** was deemed too hygroscopic to obtain reliable thermogravimetric data. The guanidinium salt has a much lower melting point (T_{on}^{m} = 116 °C) than PPN counterpart **9** (T_{on}^{m} = 218 °C), which is also observed for their corresponding azide salts, guanidinium azide (T_{on}^{m} = 99 °C) and (PPN)N_3 (214–216 °C),[159] respectively.

2.2.5 FTIR and NMR spectroscopic investigations into nitrogen-rich guanidinium salts

Fundamental IR-active vibrations of the azide anion and azido complexes

Infrared spectroscopy is a particularly important tool for investigations into azide chemistry, as the most prominent azide absorption bands fall in a region 2200–2000 cm^{-1}, which is usually clear and without interference from solvent absorptions. In both 'free' and coordinated environments the azide ligand has several types of vibration which may be observed (Figure 2.30 below).

	asymmetric stretch ν_{as}	symmetric stretch ν_s	deformation (bending) δ
ionic azide	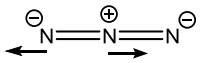	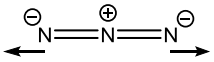 (IR inactive)*	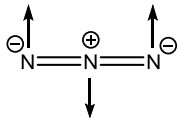
covalent azide	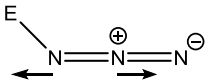	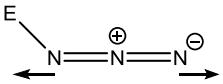	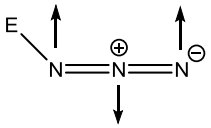

Figure 2.30. Illustration of three fundamental vibrations for ionic and covalent azides. Except for the symmetric stretching vibration of ionic azides,* all others are infrared active vibrations. *Strong perturbations on the azide anion observed in the solid state, for example by neighbouring sodium cations in sodium azide, mean a weak band for this vibration is observed in solid state spectra. Vectors denote the oscillation of atoms which describe the vibration.

The uneven charge distribution between nitrogen atoms of the azide group means the vibrations are accompanied by a significant electric dipole moment change, which enables effective absorption of the incoming infrared radiation. This high IR absorption cross section for azides means the IR spectra are sensitive to changes in concentration, and is often useful for *in-situ* monitoring of reactions. In azide exchange reactions the presence (or absence) of azide vibrations in the solution can confirm whether or not a reaction has occurred. A further example is monitoring the consumption of an azide-containing starting material in 'click' reactions with nitriles, where progress may be assessed by the intensity of the asymmetric azide band(s). Where two or more azides are coordinated to the same centre, multiple in-phase and out-of-phase combinations are possible, and the number and relative intensity of absorption bands can give indirect information on the symmetry of the species. The position of the asymmetric azide stretching vibrations of polyazido complexes gives an indication of the degree of covalence in the bonding. In general, predominantly ionic azides appear closer to 2000 cm^{-1}, and more covalent azides appear towards 2200 cm^{-1}, for example triazidocarbenium tetrafluoroborate – which contains highly covalent azide groups – appears at 2222 cm^{-1}.

Infrared spectral properties of guanidinium azides, bis(guanidinium) hexaazidostannate, and bis(guanidinium) hexaazidosilicates

FTIR spectra of compounds **1**–**3** were recorded in the solid state as nujol suspensions and in suitable solvents where appropriate. The effects of the extensive hydrogen bonding in the solid state structures of **1**–**3** are evident from the broad absorption bands for those vibrations which are most affected. In particular the prominent asymmetric azide stretching vibrations, $\nu_{as}(N_3)$, are sensitive to the surrounding hydrogen bond environment. The crystal structure of **1** has four crystallographically independent azide anions, which is reflected in the solid state FTIR spectrum showing multiple asymmetric azide stretches at $\nu_{as}(N_3)$ = 2019, 2027, 2061 and

2079 cm^{-1} (Figure 2.31 below). By comparison, the azide anion exhibits a sharp intense band around 1998–2005 cm^{-1} in salts with non-coordinating cations such as $(PPh_4)^+$ (see Figure 2.31, black line) and $(PPN)^+$, and broad intense bands around 2029–2033 cm^{-1} in nitrogen-rich ammonium[150] and hydrazinium azides.[128] The conversion of guanidinium azide (**1**) to its monohydrate (**1a**) can be observed by the coalescence of these bands into a single, broader absorption band at 2046 cm^{-1} (see Figure 2.31). In parallel, grinding the mull between the NaCl windows appears to lead to formation of sodium azide which can be seen by the emergence of several sharp bands at 3389, 3300, and 639 cm^{-1}, and a broader absorption around 2140 cm^{-1}.

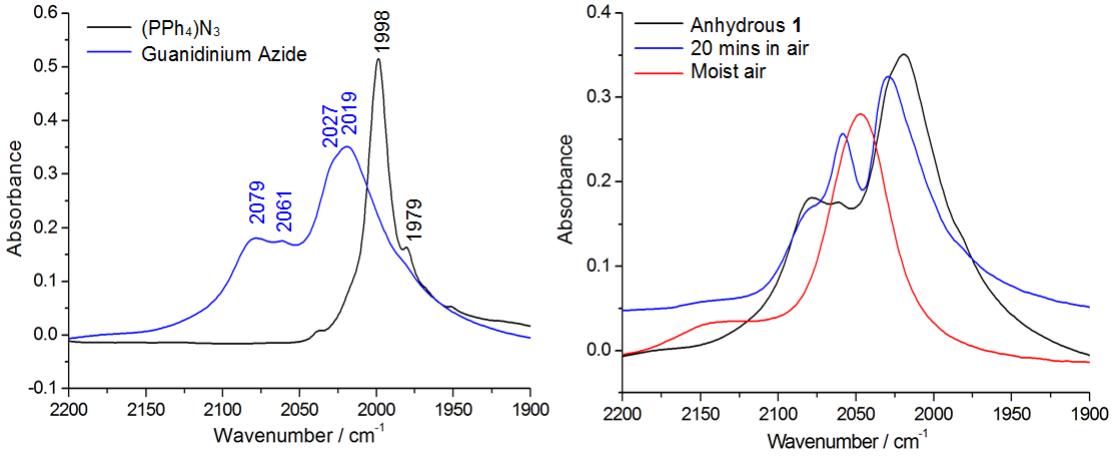

Figure 2.31. Left: Comparison of the asymmetric azide stretch region of the solid state (nujol suspension) FTIR spectra of guanidinium azide (blue) and $(PPh_4)N_3$ (black), showing the broadening of absorption bands due to extensive hydrogen bonding. Right: FTIR spectra showing the coalescence of absorption bands upon conversion of guanidinium azide to its monohydrate.

In the solution FTIR spectrum of bis(guanidinium) hexaazidostannate (**3**) in MeCN the asymmetric (2112 and 2079 cm^{-1}) and symmetric azide stretches (1339, 1288 cm^{-1}) are virtually identical to the sodium and (PPN) salts, suggesting that there is negligible influence of the guanidinium cation on $[Sn(N_3)_6]^{2-}$ in solution. In the solid state, however, the asymmetric azide stretching vibrations are strongly influenced by the crystal packing interactions, including hydrogen bonding. The absence of strong interionic interactions in $(PPN)_2[Sn(N_3)_6]$ leaves the hexaazidostannate ion relatively unperturbed from the S_6-symmetric structure present in solution, giving rise to a relatively sharp and intense peak at 2074 cm^{-1} (see Figure 2.32, red line) as all of the crystallographically independent azide groups are very close in energy. In the solid state FTIR spectrum of **3**, however, there are at least four broad and overlapping $\nu_{as}(N_3)$ absorption bands (2116, 2100, 2078, and 2065 cm^{-1}) arising from the reduced symmetry of $[Sn(N_3)_6]^{2-}$ and the subtle differences in hydrogen bonding environments of the six crystallographically independent azido ligands (Figure 2.32, black line).

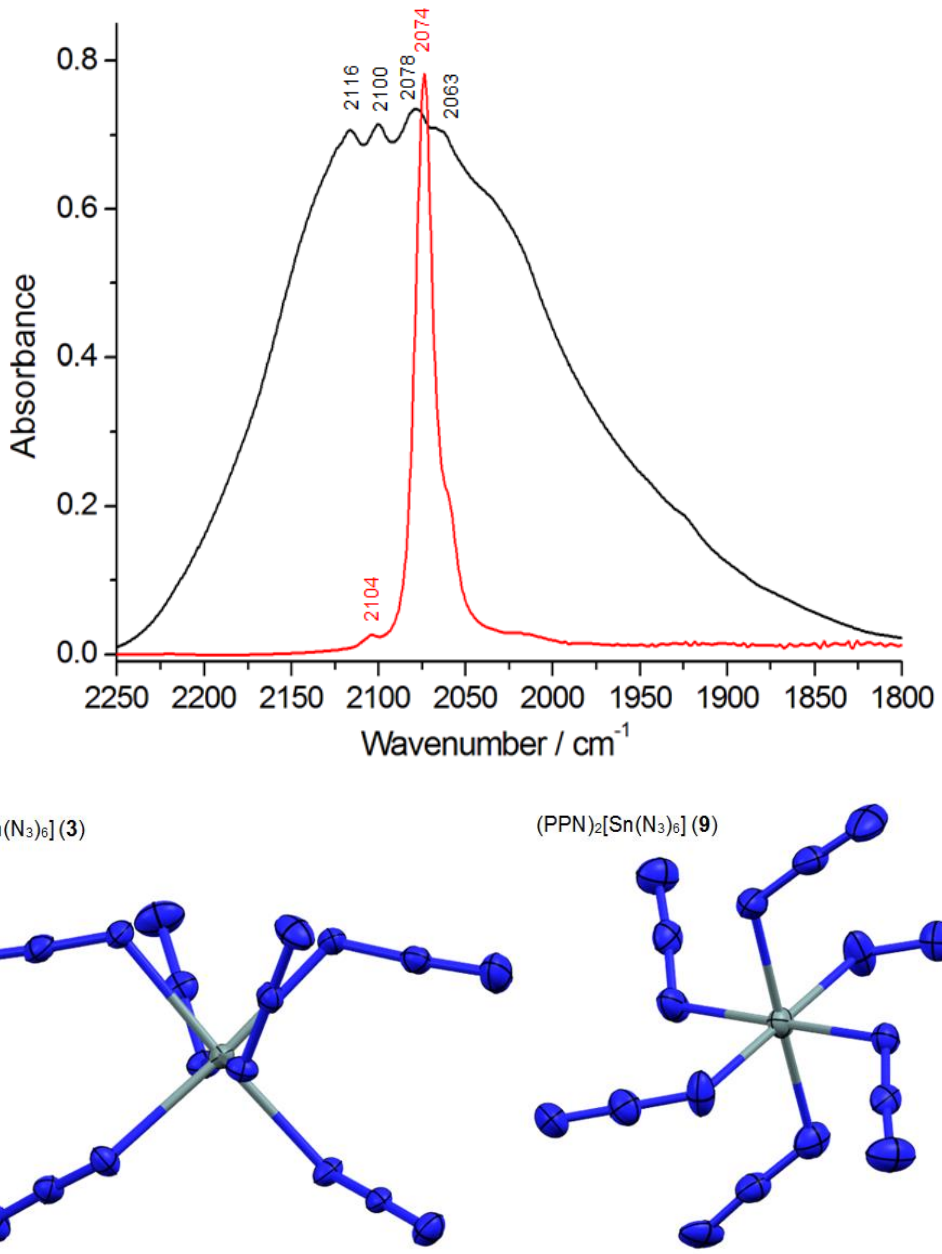

Figure 2.32. Top: Comparison of the asymmetric azide stretch region in the FTIR spectra of the $[Sn(N_3)_6]^{2-}$ in bis(guanidinium) hexaazidostannate (**3**, black), and bis{bis(triphenylphosphiniminium)} hexaazidostannate (**9**, red) showing stark contrast in the presence (**3**) and absence (**9**) of an extensively hydrogen bonded structure. Bottom: Thermal ellipsoid plots of the $[Sn(N_3)_6]^{2-}$ anion in the crystal structures of **3** (left) and **9** (right), with approximate C_2 and S_6 symmetry respectively. Element colours: N = blue; Sn = grey.

The C–N stretching band of the guanidinium cation is shifted to slightly higher energy on average (1662 *vs.* 1657 cm^{-1}). There are around six discernible absorption bands for N–H stretching vibrations at 3454, 3432, 3378, 3335, 3250 and 3181 cm^{-1}. Exposure of a nujol suspension of **3** results in hydrolysis of the $[Sn(N_3)_6]^{2-}$, as observed by the decay of the asymmetric azide stretches of **3** and the concurrent rise of those for guanidinium azide, a process which seems to be almost complete after 25 minutes (Figure 2.33 below).

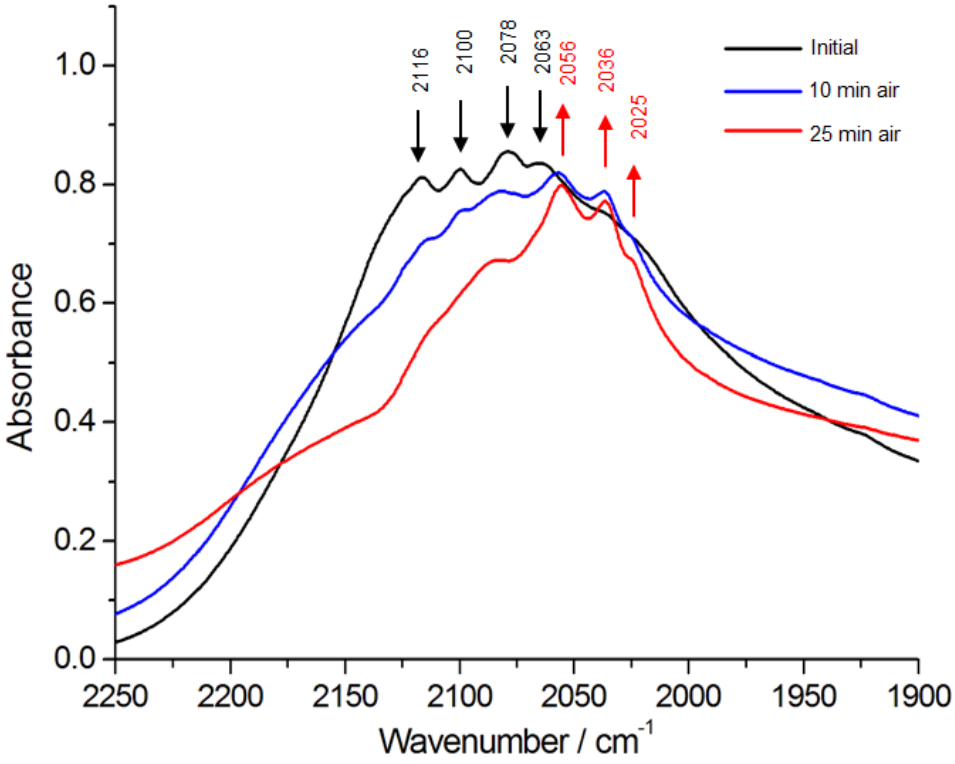

Figure 2.33. The effect of air exposure of a nujol suspension of bis(guanidinium) hexaazidostannate (**3**) showing the asymmetric azide stretch region, where the absorption bands for **3** decay rapidly (black arrows) with the concurrent rise of bands of guanidinium azide (**1**, red arrows).

^{14}N NMR spectroscopy of azides and polyazides[160,161]

Both nitrogen-14 and nitrogen-15 are NMR active, where the former has spin 1 and abundance >99.6 % and the latter has spin ½ but natural abundance of around 0.4 %. Since ^{14}N has nuclear spin of 1, the ^{14}N relaxation times are dominated by the more efficient quadrupole relaxation mechanism, leading to short lifetimes and often resulting in broad signals. Highly symmetrical environments like the ammonium ion give sharp resonances because the quadrupolar coupling constant is very small, so this particular ^{14}N behaves like a spin ½ nucleus. For less symmetrical environments the tendency is towards an unevenly distributed electric field around the nucleus, and a higher nuclear quadrupole coupling constant, leading to fast relaxation times and broadening the observed signals. This effect is observable in the ^{14}N NMR spectra of azido complexes in which the coordinated nitrogen atom (N_α) is in the least symmetrical environment and gives the broadest signal, whilst the opposite is true for the central nitrogen (N_β). The appearance of three distinct signals for the metal azide complexes, and similarity of this pattern to hydrazoic acid and organic azides such as MeN_3 and EtN_3, was some of the earliest experimental evidence used to support the covalent nature of the bonding.[162]

NMR spectroscopy of guanidinium azides and guanidinium hexaazidostannate

Compounds **1**–**3** and **19** were investigated by multinuclear NMR spectroscopy (^{1}H, ^{13}C, ^{14}N), and additionally **3** was investigated by ^{119}Sn NMR. In D_2O the exchange with guanidinium protons of **1**, **1a**, and **19** is fast, meaning only a broad peak at 4.70 ppm is observed, and without an external calibrant this gives little further information. The tetrazolate proton of **19** appears at 8.4 ppm in D_2O. The solubility of **1** in acetonitrile was sufficient to observe the proton signal at 6.42 ppm, but the ^{13}C resonances could not be observed. The greater solubility of **1**, **1a**, and **2** in dmso-d_6 enabled the determination of ^{1}H, ^{13}C and ^{14}N spectra, whereas spectra for **3** were recorded in CD_3CN. The presence of exactly one equivalent of crystal water (δ = 3.40 ppm) in **1a** is corroborated by the peak integrals, and does not affect the chemical shift of **1** at 6.95 ppm, which is 0.53 ppm higher than in the less polar CD_3CN. The seven aminoguanidinium protons in **2** are split into four environments with peaks at 4.68, 7.21, 6.83, and 8.61 ppm, in a ratio of 2 : 2 : 2 : 1. The sp^3 hybridised amino group has a sharp resonance at 4.68 ppm, suggesting it does not participate in proton exchange. The broad peak at 8.61 represents the sole 'imino' proton, and the remaining two partially overlapped broad peaks at 6.83 and 7.21 ppm are the sp^2 hybridised amino groups most similar in nature to the unsubstituted guanidinium protons. In **3** the guanidinium signal appears at 6.14 ppm, 0.28 ppm lower than **1** in the same solvent. The ^{13}C signal for the tetrazolate anion in **19** appears at 149.2 ppm, which is almost identical to the chemical shift observed in other tetrazolate salts.[152] The ^{13}C resonances in dmso-d_6 for the guanidinium cations in **1**–**3** and **19**, all appear around 158–159 ppm, with **2** having the marginally higher chemical shift of the two azide salts at 159.0 *vs*. 158.0 ppm, 158.3 in **19**, and **3** appears at 159.0 in CD_3CN. The sole ^{13}C resonance for aminoguanidinium-, triaminoguanidinium-, and azidoformamidinium perchlorates are reported at 159.2–159.5 ppm (D_2O).[105] This suggests the carbon is not very sensitive to substitution of the guanidinium protons, counter ions, or choice of solvent. The ionic azides **1** and **2** show two signals corresponding to the azide anion in their ^{14}N NMR spectra for N_β at –131.7 (–131.9, **2**) and N_α and N_γ at –276.2 (–276.7, **2**). No signals are visible for the guanidinium or $(PPN)^+$ cations presumably because the symmetrical environments lead to fast relaxation times. In the ^{15}N NMR spectrum of aminoguanidinium perchlorate the nitrogen resonances (in D_2O) are reported at –285 (imino NH), –312 (sp^2 amino), and –327 ppm (sp^3 amino).[105] Two relatively weak, broad signals for the two tetrazolate anion environments are observed in the ^{14}N NMR spectrum of **19** in D_2O, at –4.6 ppm (N2, N3) and –73.3 ppm (N1, N4), which are very close to values observed for other tetrazolate salts.[152] No ^{14}N signals were observable for **19** in dmso-d_6 due to lower solubility. Covalent azides such as **3** usually exhibit distinct peaks for each of the three azide nitrogen environments, though the CD_3CN solvent peak obscures the N_β signal, and only two peaks are visible at –215.9 (N_γ) and –301.6 ppm (N_α) at similar positions to $(PPN)_2[Sn(N_3)_6]$ (**9**) –219.6 (N_γ) and –301.0 ppm (N_α).

The subtle difference of the positions of the N_γ peaks may be due to influence from the smaller, more polarising guanidinium cation. A single ^{119}Sn resonance is observed for hexaazidostannate anion in **3** at –600.9 ppm in CD_3CN, which is close to a previously reported value for $(NEt_4)_2[Sn(N_3)_6]$ at –605.0 ppm in CH_2Cl_2.[163]

2.3 Conclusions

Simple nitrogen-rich salts guanidinium azide (**1**) and aminoguanidinium azide (**2**) have been fully characterised and appear to be insensitive to friction, impact, and electrostatic discharge despite their high nitrogen content (82–84 %). Neither compound is volatile unlike the similarly nitrogen-rich ammonium[50] and hydrazinium azides.[128] This property may be expected as their respective guanidine bases are less volatile than hydrazine or ammonia. Compound **1** is hygroscopic, and forms a monohydrate (**1a**) upon exposure to atmosphere. Compound **2**, however, decomposes very gradually upon long-term storage in air. The two compounds exhibit extensive hydrogen bonding in their solid state structures, featuring R1,2(6), R2,2(8), and C2,2(6) graph sets commonly observed for guanidinium salts. Guanidinium azide has a multi-layered structure which seems to be dictated by the preference for hydrogen bonds *within* rather than *between* layers, whereas the reduced symmetry of the aminoguanidinium cation prevents the formation of isolated layers in the structure of **2**. Preparation of **2** has provided an alternative (not necessarily better) route to the preparation of triaminoguanidinium azide in a similar way to triaminoguanidinium chloride.[151] Bis(guanidinium) hexaazidostannate (**3**) is the first example of a polyazido complex incorporated into a fully characterised nitrogen-rich salt and it seems to be insensitive to impact, friction and static discharge despite its 68 % nitrogen content. On the one hand, these observations place it in between the low-nitrogen content, bulky cation polyazido salts, and the extremely sensitive nitrogen-rich pentazenium salts of polyazido complexes. On the other hand, having guanidinium as counter ion rather than traditional bulky hydrophobic cations, for example $(PPN)_2[Sn(N_3)_6]$ (**9**), seems to increase greatly the rate of hydrolysis of $[Sn(N_3)_6]^{2-}$ in the solid state and in solution. Spectroscopic evidence has been presented for the formation of other nitrogen-rich polyazido complexes including bis(aminoguanidinium) hexaazidostannate (**4**) and the lighter silicon homologues bis(guanidinium) hexaazidosilicate (**5**) and bis(aminoguanidinium) hexaazidosilicate (**6**). During the attempted preparation of guanidinium hexaazidophosphate (**7**) a side reaction of guanidinium with phosphoryl triazide impurity, $[P(=O)(N_3)_3]$, in the sodium hexaazidophosphate stock solution produced crystals of an interesting neutral phosphorus azide $[P(=O)(N_3)_2\{NC(NH_2)_2\}]$ (**8**) containing 67 % nitrogen, though insufficient material was available to investigate further. The synthesis of guanidinium hexachlorophosphate was attempted as part of an alternative route towards guanidinium hexaazidophosphate (**7**), but only starting materials PCl_5 and guanidinium

chloride were recovered. Guanidinium tetrazolate (**19**) was prepared for the first time towards a parallel research effort into nitrogen-rich salts of polytetrazolato complexes. The crystal structure was determined by single crystal X-ray diffraction, but purity of the bulk material needs improvement as satisfactory elemental analyses could not be obtained. A new procedure for the preparation of triaminoguanidinium azide from **2** has been demonstrated based on the synthesis of triaminoguanidinium chloride, which provides the basis for extension of this investigation to salts of higher substituted (di- and triaminoguanidinium) cations with hexaazido complexes, or nitrogen-rich polytetrazolato analogues of **3**–**7**.

3. Syntheses of tin(IV) polyazides, and a combined crystallographic, spectroscopic and calorimetric investigation of their structures and properties

Aims

I. Adapt syntheses for silicon(IV) and germanium(IV) azides to prepare new tin(IV) azides
II. Investigate alternative synthetic routes to tin(IV) azides
III. Determine which ligands are suitable for stabilisation of tin(IV) polyazides and their effects on the bonding of the azido ligands
IV. Determine the stability, thermal behaviour and energy density of tin(IV) azides
V. Determine the nature of the bonding of hexaazidostannate(IV) in relation to neutral tin(IV) azides and its group 14 homologs hexaazidosilicate and hexaazidogermanate

3.1 Introduction

p-Block elements form neutral binary azides of the type $E(N_3)_n$, n = 1–4. The known Group 14 compounds of this type are the tetraazides of carbon[60] and silicon[34] as well as lead diazide[164] and the recently reported tin diazide.[54] Wiberg and Michaud's report on the synthesis of disodium hexaazidostannate was published concurrently with their investigations into boron and aluminium triazides, and silicon tetraazide,[61] whereas tin tetraazide, $Sn(N_3)_4$, remains elusive. Stability and sensitivity of binary azides are primarily determined by the degree of covalence of the E–N bonds and the nitrogen content. In Group 14, $C(N_3)_4$ leads in these criteria containing the highest nitrogen content (93 %) and the most covalent E–N bonds, rendering it extremely sensitive to thermal shock, friction, and impact, or even apparently explosive decomposition without provocation. As a consequence these Group 14 tetraazides themselves cannot be isolated without extreme caution, though their investigation has added valuable insight into the diversity of reactivity of covalent polyazides, and they can be used as precursors to other nitrogen-rich species. In contrast, previous work has demonstrated that the complex ions $[E(N_3)_6]^{2-}$,[33,83] and neutral adducts $E(N_3)_4(L_2)$, E = Si,[34] Ge,[33] L_2 = bpy, phen, have significantly increased stability (T_{dec} up to *ca.* 250 °C) and reduced sensitivity compared to the corresponding binary azide, which has enabled their isolation and full characterisation. The origin of the increased stability in these coordination compounds is due to the combined effects of reduced nitrogen content, and influence of hypercoordination on the E–N bonds

giving a more ionic contribution to the azide ligands' bonding. The 'dilution' of the nitrogen content in turn reduces the specific endothermicity of the compound, and this increase in ionicity of the E–N bonds raises the activation barriers for N_2 elimination. It has been proven previously[19,32] that these stable, negatively charged complex hexa(azido) ions as well as the charge-neutral adducts of binary azides with nitrogen heterocycles[34,33,135,136] can be synthesised by reactions of NaN_3 with appropriate chlorides, followed by either salt metathesis or ligand exchange. In such reactions the net gain in lattice energy between NaN_3 (732 kJ mol^{-1})[165] and NaCl (787 kJ mol^{-1})[166] plays an important role. This methodology opens up an exciting route to the thus far elusive $E(N_3)_4(L_2)$ polyazido complexes of the heavier homologue tin. Ionic azido-group transfer reagents, in particular NaN_3, have been employed in the syntheses of many covalent main group element azides including the first known organotin azides, $R_3Sn–N_3$, R = Ph,[167] Me.[168] Silver azide, AgN_3, can perform similar metathesis reactions with suitable halides where the net lattice enthalpy gain using NaN_3 is insufficient, though this comes with increased risk in using the highly sensitive AgN_3. Other versatile approaches use covalent transfer reagents hydrazoic acid,[61] which reacts with suitable hydrides, or azidotrimethylsilane, $TMS–N_3$,[135,155,136,88,56,63,57] with a wide variety of fluorides including Group 5,[56] Group 6,[57] Group 13,[88] Group 15,[135,136,155] (or chlorides as demonstrated for $AsCl_4^-/AsCl_4^+$ and $SbCl_4^-$)[68] and Group 16[63] elements. $TMS–N_3$ can, with extreme caution and where necessary, be used as reaction solvent with ease of separation from the sensitive binary azides due to its volatility (b.p. 95–99 °C) and that of the by-product TMS–F (b.p. 15 °C), which is especially advantageous when working at low temperature. The driving force for the azido-group transfer reaction involving $TMS–N_3$ and fluorides arises from the unusually high dissociation energy of covalent Si–F bonds.[19] Whilst this route provides an efficient means for complete azide-fluoride exchange, the reactive nature of many fluorides necessitates the use of specialist stainless steel/FEP Schlenk lines and vessels. Similar to organic azides, tin azides undergo N_2 elimination reactions with phosphines to yield phosphinimines, and cycloaddition reactions with alkynes and nitriles to afford triazoles and tetrazoles.[31] Whilst tin polyazides of the types $[Sn(N_3)_6]^{2-}$,[169,89,170–172,163,86,173,85] $[\{Fe(CO)_2(Cp)\}_2Sn(N_3)_2]$,[174], $[Ar_2Sn(N_3)_2]$; Ar = 2,6-$(NMe_2)_2C_6H_3$–,[175] $[SnMe_2(N_3)_4]^{2-}$,[176] $[SnF_m(N_3)_n]^{2-}$, m+n = 6,[177] $SnCl_2(N_3)_2$[178] and $[SnCl_4(N_3)_2]^{2-}$ [179] have been known for some time, charge-neutral nitrogen-rich tin complexes including $Sn(N_3)_4$ have not been reported, probably owing to its expected high sensitivity. Early insight into the structure and bonding in poly(azido)stannate(IV) complexes was based on vibrational,[170,89,171] Mössbauer,[180,181] ^{14}N NMR[162] and ^{119}Sn NMR[163] spectroscopies. Within this work the first successful synthesis, isolation and characterization of neutral tetra(azido)tin(IV) complexes bearing mono- or bidentate pyridine-based ancillary ligands are presented. Analytical, spectroscopic and crystallographic data provide valuable insight into the structure and bonding in this class

of compounds, and differential scanning calorimetry gives a measure of the endothermicities *via* their enthalpies of decomposition.

3.2 Results and Discussion

3.2.1 Syntheses

The reactivities of tin tetrafluoride and tin tetrachloride with azide transfer reagents NaN_3 and trimethylsilyl azide (TMS–N_3) were investigated in various solvents.

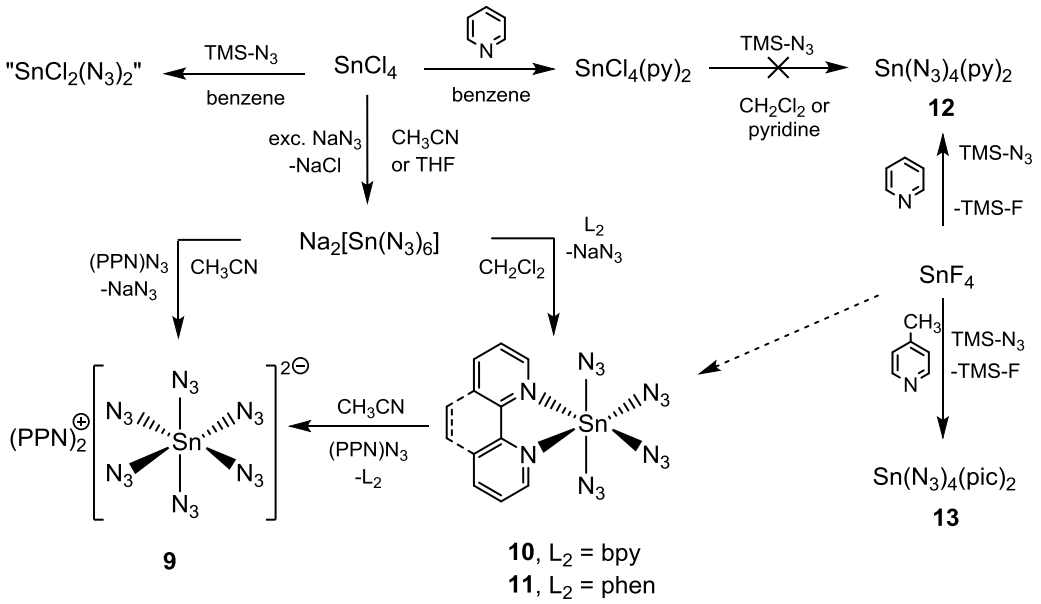

Scheme 3.1. Summary of the reactivity of tin(IV) halides with azide transfer reagents. The dotted line indicates an untested synthetic route towards, which is *likely* to be feasible for synthesis of the 2,2'-bipyridine and 1,10-phenanthroline complexes **10** and **11**.

Reaction of $SnCl_4$ with TMS–N_3 in benzene seems to lead to formation of the insoluble $SnCl_2(N_3)_2$ as observed in CH_2Cl_2 previously.[178] The syntheses of the tin(IV) azides bis{bis(triphenyl-phosphine)iminium} hexaazidostannate (**9**), tetraazido(2,2-bipyridine)tin (**10**), tetraazido(1,10-phenanthroline)tin (**11**), tetraazidobis(pyridine)tin (**12**), and tetraazidobis(4-picoline)tin (**13**) presented in this work rely on the application of two of the methods outlined above, starting from tin(IV) chloride and tin(IV) fluoride respectively. The versatile disodium hexaazidostannate intermediate was prepared by slight modification of the literature procedure,[169] involving reaction of tin tetrachloride with two successive batches of sodium azide in large excess to ensure complete Cl/N_3 exchange, using acetonitrile instead of THF as reaction solvent. Disodium hexaazidostannate is used *in-situ* as a stock solution, as evaporation of the solution could result in coprecipitation of the sensitive binary $Sn(N_3)_4$ with NaN_3. The risk comes from the potential gain in overall lattice enthalpy due to the formation of sodium azide, whereas an azide salt with significantly smaller lattice enthalpy, such as

(PPN)N_3, reduces the benefit of the complex dissociation as explained in the supporting information of ref. [84].

Bis{bis(triphenylphosphine)iminium} hexa(azido)stannate(IV), (PPN)$_2$[Sn(N$_3$)$_6$] (9)

Bis(triphenylphosphine)iminium (PPN^+) is a bulky, hydrophobic, weakly coordinating cation which can be incorporated into salts with energetic anions to enable their characterisation with reduced risk and without perturbation from strong interionic interactions, as demonstrated by preparation of bis{bis(triphenylphosphine)iminium} hexaazidostannate (**9**). Dissolution of a stoichiometric amount of (PPN)N_3 in an aliquot of a stock solution of $Na_2[Sn(N_3)_6]$ in MeCN led to rapid precipitation of NaN_3 from solution within 30 minutes, which was separated by filtration. Crystalline **9** was obtained in 70 % yield upon cooling of the filtrate solution to –19 °C.

Neutral Adducts of Tin Tetraazide

Alternatively nitrogen-rich tin azides can be stabilised by the use of ancillary ligands such as mono- or bidentate pyridines without dramatic reduction in nitrogen content or specific energy content. Compounds **10**–**13** are the first neutral Lewis base adducts of the elusive binary $Sn(N_3)_4$ with nitrogen content of 41–44 %. Chelate complexes $Sn(N_3)_4$(bpy) (**10**) and $Sn(N_3)_4$(phen) (**11**) were prepared by reaction of 2,2'-bipyridine or 1,10-phenanthroline with $Na_2[Sn(N_3)_6]$, whereas $Sn(N_3)_4(py)_2$ (**12**) and $Sn(N_3)_4(pic)_2$ (**13**) were obtained by the action of trimethylsilyl azide on SnF_4 in pyridine and 4-picoline respectively. The reactivity of the tin azides seems to be subtly different to complexes of the lighter homologs silicon and germanium, which are readily accessible by reaction of the ligand with a $Na_2[E(N_3)_6]$ stock solution (E = Si, Ge), with displacement of sodium azide. Interestingly the analogous reactions of 2,2-bipyridine and 1,10-phenanthroline with $Na_2[Sn(N_3)_6]$ in polar co-ordinating solvents MeCN and THF show no changes in the *in-situ* FTIR spectra. However, after evaporation of the reaction mixture and addition of CH_2Cl_2 to the white powder residue (in which $Na_2[Sn(N_3)_6]$ is insoluble), new absorption bands are visible in the solution FTIR spectra indicating the formation of complexes **10** and **11** respectively. The reaction of pyridine with $Na_2[Sn(N_3)_6]$ was investigated, but isolation of the pure compound **12** *via* this route was impractical due to difficulties in its separation from traces of similarly insoluble NaN_3 by-product. Tin(IV) fluoride is relatively inert due to its polymeric structure, but nevertheless represents a convenient route to tin(IV) azides. Dropwise addition of trimethylsilyl azide to a stirred suspension of SnF_4 in pyridine or 4-picoline leads to the formation of tetraazides **12** and **13**, but the low solubility of SnF_4 and the tetraazide products results in a relatively slow reaction rate at ambient temperature, despite the formation of volatile trimethylsilyl fluoride (b.p. 15 °C). This is supported by the elemental analysis of the bulk material of **13** which was prepared at ambient temperature – found: 38.89 % N *vs.* calcd: 41.45 % N – suggests residual

fluorine even after stirring overnight. Allowing for overpressure relief and heating to 45 °C increases the reaction rate and the rate at which TMS–F is removed from the equilibrium, enabling the azide-fluoride exchange to approach completion, as shown by the microanalysis results for **12** which was heated to 45 °C overnight – found: 43.70 % N *vs.* calcd: 44.05 % N. (N = nitrogen content)

Reactivity of SnX_4 (X = F, Cl) with TMS–N_3

In the polar solvents THF and MeCN, reaction of $SnCl_4$ with a large excess of NaN_3 results in the formation of disodium hexaazidostannate.[169,85] The reactivity of $SnCl_4$ with TMS–N_3 was investigated in a non-coordinating solvent (benzene) to determine whether $Sn(N_3)_4$ would be accessible *via* a parallel route for $Si(N_3)_4$, but only resulted in the isolation of the previously characterised $Sn(N_3)_2Cl_2$.[178]. The reaction of SnF_4 with TMS-N_3 in benzene (<1 mmol scale) yielded an insoluble residue resembling the original suspension of SnF_4 after stirring for 8 days (30–40 °C). On one occasion the contact of a metal spatula with this residue resulted in a violent detonation which shattered the glass ampoule. An FTIR spectrum of the residue left on the filter head showed a broad asymmetric azide stretch at 2100 cm^{-1} with a sharp shoulder at 2131 cm^{-1} which could be a trace of the excess TMS–N_3. A subsequent ^1H and ^{19}F NMR scale investigation into the reactivity of SnF_4 with TMS-N_3 in benzene-d_6 showed the presence of TMS-F after an extended reaction time, implying at least partial fluoride-azide exchange (see section 3.2.3). The NMR-scale reaction provided insight into the reaction, but little quantitative information due to the relatively large uncertainties of weighing measurements. Due to the absence of protons on the species of interest, and the apparent insolubility of SnF_4 and tin azides $SnF_x(N_3)_{(4–x)}$ in benzene, only TMS–N_3 (–0.08 ppm) and TMS–F (0.03 ppm) were observable in the ^1H NMR and spectra. After 7 days the ratio of TMS-F/TMS–N_3 showed the conversion had reached 95 %. In the ^{19}F NMR spectra, a multiplet belonging to TMS–F was visible at –157.1 ppm (*vs.* $CFCl_3$), identifiable by its ^{29}Si satellites (J = 275 Hz).[182] After decanting the C_6D_6 solution from the insoluble residue and addition of CD_3CN and excess of 2,2'-bipyridine the ^1H NMR appeared to show only one type of 2,2'-bipyridine complex, although the ^{19}F NMR showed several weak signals at –143.7, –151.8, –157.5, and –167.9 ppm in the ratio 1 : 0.15 : 0.63 : 0.68. These very weak signals are in a similar region to the tin(IV) fluoride adducts, for example the chemical shifts for SnF_4(bpy) are –149.8 and –179.8 ppm (triplets) for the axial and equatorial environments.[183,184] The predominant formation of **10** in solution and absence of detectable intermediate $SnF_x(N_3)_{(4–x)}$(bpy) complexes implies the formation of $Sn(N_3)_4$ at some stage in the reaction mixture, though there is no direct evidence as it would be insoluble throughout.

trans-$SnCl_4(py)_2$ was prepared by dropwise addition of pyridine to a solution of $SnCl_4$ in benzene, and its reactivity was tested with TMS–N_3 in coordinating (pyridine) and

non-coordinating (CH_2Cl_2) polar solvents. In CH_2Cl_2 there was no observable reaction according to the solution FTIR spectra recorded over approximately 1 week, even when the mixture was heated to 50 °C. In pyridine a new azide band was observed at 2076 cm^{-1} after heating $SnCl_4(py)_2$ with 5 equivalents of TMS–N_3 to 80 °C, but was almost negligible in comparison to that of the remaining TMS–N_3. No increase (or decrease) in the absorbance of the new species was observed after heating to 85 °C for a further 24 hours, suggesting the reaction had reached equilibrium. This avenue of investigation was not pursued further since the reactivity of SnF_4 with TMS–N_3 was found to be a more suitable for the purpose of preparing tin tetraazides such as **12** and **13** as described above.

3.2.2 X-Ray crystallographic investigation into the structures of neutral tin(IV) tetraazide adducts and the hexaazidostannate(IV) anion

Crystals suitable for examination by single crystal X-ray diffraction were obtained by cooling their respective saturated solutions slowly to –20 °C overnight, except for $Sn(N_3)_4(py)_2$ (**12**) and $Sn(N_3)_4(pic)_2$ (**13**), which were obtained by slow cooling of a hot (*ca.* 65 °C) MeCN-pyridine (MeCN-4-picoline) solution to ambient temperature. The data sets were of high quality, yielding accurate molecular structures for all five tin(IV) azides (Table 3.3). The crystallographic data for **9**–**12** were deposited in the Cambridge Structural Database (CSD), and can be obtained free of charge from the Cambridge Crystallographic Data Centre *via* www.ccdc.cam.ac.uk/data_request/cif *via* the following CCDC deposition numbers: $(PPN)_2[Sn(N_3)_6]$ (**9**), 1039721; $(Sn(N_3)_4(bpy)$ (**10**), 1039722; $Sn(N_3)_4(phen)$ (**11**), 1039723; $Sn(N_3)_4(py)_2$ (**12**), 1062323.[85]

Determination of accurate structural detail of the hexaazidostannate anion[85]

The first crystallographic report on the hexaazidostannate anion concerned bis(tetramethylammonium) hexaazidostannate, where the authors sought to confirm the now familiar bent coordination geometry of the azide group proposed by a preceding infrared spectroscopic study.[170] Their elemental analysis results confirmed the composition of the material, but despite repeated attempts no suitable single crystals were obtained, and a powder X-ray diffraction study was employed to determine the unit cell. The first and only single crystal X-ray diffraction study of the hexaazidostannate anion was presented 14 years later, by crystallisation of bis(tetraphenylphosphonium) hexaazidostannate.[86] As it was one of the first crystal structures of a homoleptic polyazido complex, no "library of data" on *p*-block- and transition metal polyazido complexes was available for comparison at the time. The bent coordination of the azido ligands, postulated from the hexaazidostannate IR spectrum[170] was confirmed, although the bond lengths for one of the azido ligands in $(PPh_4)_2[Sn(N_3)_6]$ are unusual as the N_β–N_γ distance is longer than the adjacent N_α–N_β (see table 3.1 below). This difference may be due to incomplete Cl/N_3 exchange or unresolved orientational disorder of

the ligands from thermal motion, as the diffraction data were collected at 293 K. To investigate closely the structure of the hexaazidostannate anion, and determine whether it is affected by hydrogen bonding, the crystal structures of bis(guanidinium)- (**3**) and bis{bis(triphenylphosphine)iminium} hexaazidostannate (**9**) salts were determined during this work. Their preparation also enabled direct comparability between the structure of $[Sn(N_3)_6]^{2-}$ and related group 14 hexaazido complexes, $[E(N_3)_6]^{2-}$, E = Si, Ge, Pb. In these structures the N_α–N_β bonds are longer than the corresponding N_β–N_γ bonds, in line with the convention observed for many other main group azido complexes.

Table 3.1. The geometries of the three independent azido ligands (N1–N3) in the crystal structure of $(PPh_4)_2[Sn(N_3)_6]$ determined by Fenske *et al*.[86] compared to those in the crystal structures of the guanidinium (**3**) and (PPN) (**9**) salts.

	label	N_α–N_β [Å]	N_β–N_γ [Å]	ΔNN [Å]	*T* [K]
	N1	1.162(5)	1.084(6)	0.078(8)	
$(PPh_4)_2[Sn(N_3)_6]$ [a]	N2	1.195(6)	1.090(8)	0.105(10)	293
	N3	1.071(5)	1.189(8)	–0.118(9)	
$\{C(NH_2)_3\}_2[Sn(N_3)_6]$ (**3**)		1.218(5)	1.141(6)	0.077(8)	100
$(PPN)_2[Sn(N_3)_6]$ (**9**) [b]		1.212(13)	1.141(14)	0.07(2)	100

[a] ref. [86]; [b] This work, published in ref. [85].

As mentioned in section 3.1, the molecular structure of the hexaazidostannate anion was reported 32 years previously[86] in the $(PPh_4)_2[Sn(N_3)_6]$ salt, which was amongst the first crystallographic investigations into homoleptic azido complexes. $(PPh_4)_2[Sn(N_3)_6]$ crystallises in triclinic space group $P\bar{1}$, and the $[Sn(N_3)_6]^{2-}$ Sn atom occupies a special position with inversion symmetry that renders only three N_3 groups crystallographically independent (see Table 3.1). The data collection for the original structure was carried out at room temperature,[86] whereas crystals of **9**–**13** were studied at low temperature. Hexaazidostannate salt $(PPN)_2[Sn(N_3)_6]$ (**9**), built up with even larger cations, also crystallises in $P\bar{1}$; however, tin occupies a general position resulting in six crystallographically unique N_3 groups of which four are disordered. Figure 3.1 shows a thermal (displacement) ellipsoid plot of $[Sn(N_3)_6]^{2-}$ in the crystal structure of **9**, with the disordered components omitted for clarity. Any Cl / N_3 ligand substitutional disorder in the crystal of **9** was confirmed absent by elemental analysis. Therefore, the comparably large displacement ellipsoids for several ligating N atoms found in the early stages of the structure solution of $(PPN)_2[Sn(N_3)_6]$ are attributed to a concerted

wagging vibration about the N_β−Sn−N_β' axes. The weak interionic interactions between the non-coordinating PPN^+ cation and $[Sn(N_3)_6]^{2-}$ presumably allow for this conformational flexibility with approximate S_6 symmetry. The disorder model adopted to account for this motion involved splitting both N_α and N_γ or all atoms of the azido group into two half-occupied positions. Suitable restraints were applied during refinement such that the geometry of disordered components within each azido group was similar (SADI, SIMU, DELU commands). Further refinement details and crystallographic data are included in the supporting information of ref. [85].

Bis(bis(triphenylphosphine)iminium) hexaazidostannate, $(PPN)_2[Sn(N_3)_6]$ (9)

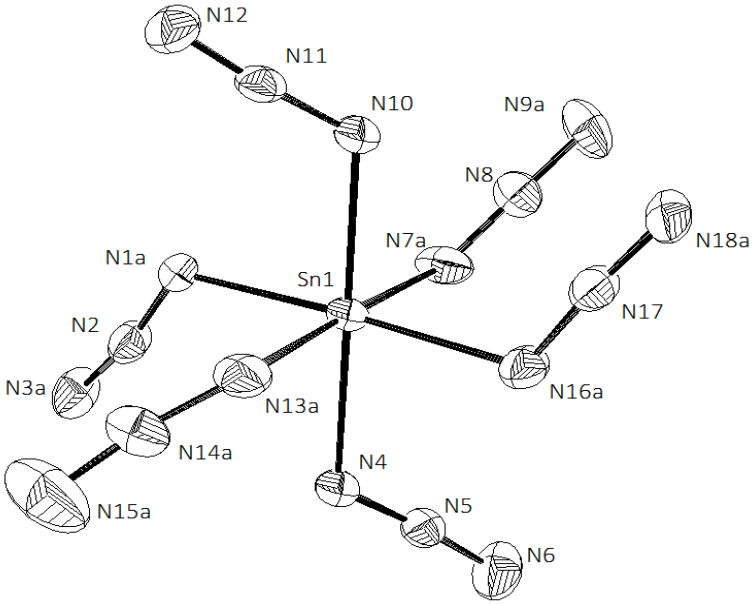

Figure 3.1. ORTEP drawing showing one part of the disordered $[Sn(N_3)_6]^{2-}$ anion in the crystal of **9** at 100 K with displacement ellipsoids at the 50% probability level. Triclinic ($P\bar{1}$, Z = 2), a = 11.7012(8) Å, b = 12.5721(9) Å, c = 24.4651(17) Å, α = 94.143(4)°, β = 101.080(4)°, γ = 103.058(4)°, V = 3415.3(4) Å^3, R_1 = 0.0283. Selected bond lengths [Å] and angles [°]: Sn1–N1a 2.131(3), Sn1–N4 2.1222(17), Sn1–N7a 2.146(3), Sn1–N10 2.1220(18), Sn1–N13a 2.147(3), Sn1–N16a 2.133(3), N1a–N2 1.207(4), N2–N3a 1.142(4), N4–N5 1.210(3), N5–N6 1.148(3), N7a–N8 1.206(4), N8–N9a 1.146(4), N10–N11 1.212(3), N11–N12 1.143(3), N13a–N14a 1.222(10), N14a–N15a 1.128(6), N16a–N17 1.213(4), N17–N18a 1.146(4). N1a–Sn1–N16a 178.7(3), N4–Sn1–N10 177.84(7), N7a–Sn1–N13a 177.9(3), Sn1–N1a–N2 120.2(3), N1a–N2–N3a 176.4(9), Sn1–N7a–N8 122.3(3), N9a–N8–N7a 174.0(13), Sn1–N13a–N14a 118.6(17), N13a–N14a–N15a 170(3), Sn1–N16a–N17 119.3(3), N18a–N17–N16a 175.5(16).

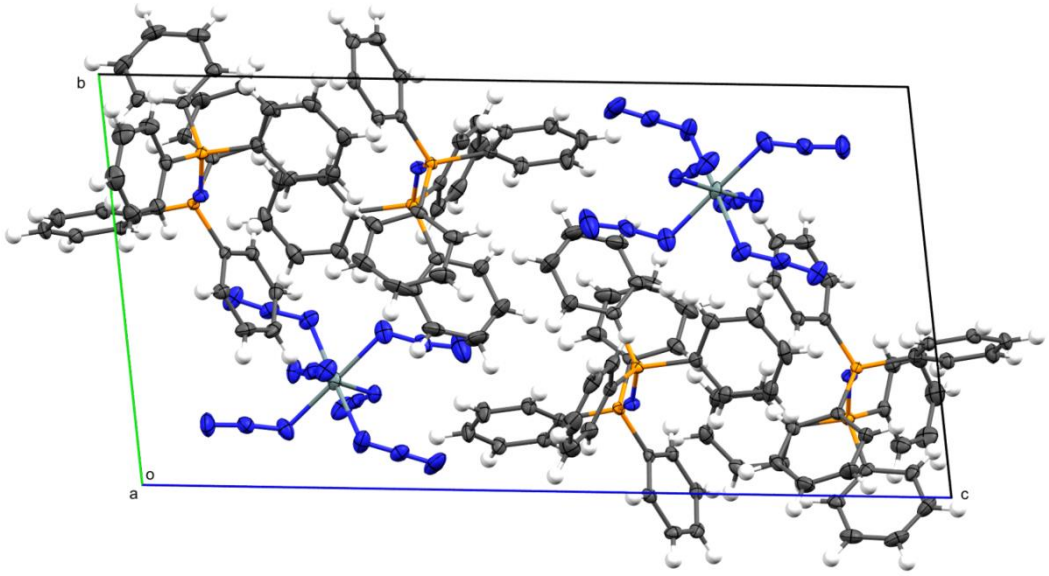

Figure 3.2. View along the *a*-axis showing the packing in the crystal structure of **9** at 100 K. One disordered component of the $[Sn(N_3)_6]^{2-}$ anion is omitted for clarity.

Tetraaazido(2,2'-bipyridyl)tin, $Sn(N_3)_4$(bpy) (10)

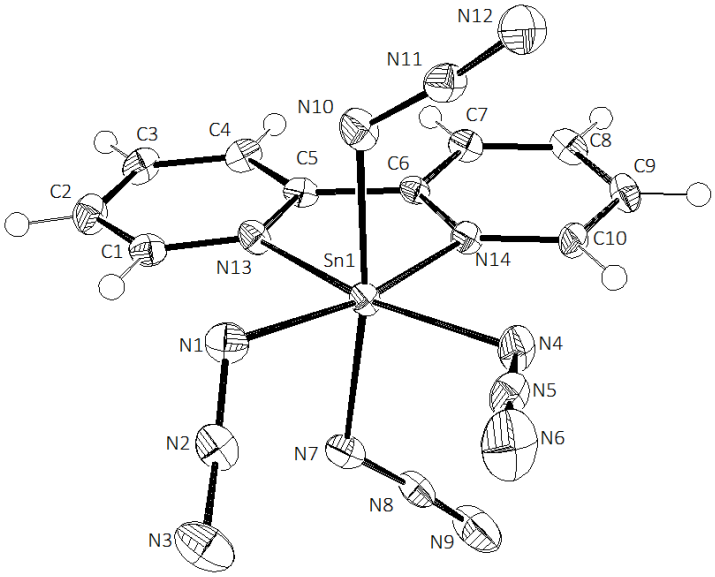

Figure 3.3. ORTEP drawing showing the molecular structure of **10** at 120 K with displacement ellipsoids at the 50 % probability level, and hydrogen atoms represented by spheres of radius 0.15 Å. Monoclinic (*Cc*, Z = 4), a = 11.6427(19) Å, b = 8.3153(13) Å, c = 15.866(2) Å, β = 96.783°, V = 1525.2(4) Å^3, R_1 = 0.0325. Selected bond lengths [Å] and angles [°]: Sn1–N1 2.097(6), Sn1–N4 2.110(5), Sn1–N7 2.101(6), Sn1–N10 2.101(6), Sn1–N13 2.204(6), Sn1–N14 2.211(5), N1–N2 1.214(8), N2–N3 1.144(8), N4–N5 1.204(9), N5–N6 1.150(10), N7–N8 1.203(8), N8–N9 1.136(9), N10–N11 1.228(8), N11–N12 1.126(8), N13–Sn1–N14 74.3(2), N1–Sn1–N4 102.6(2).

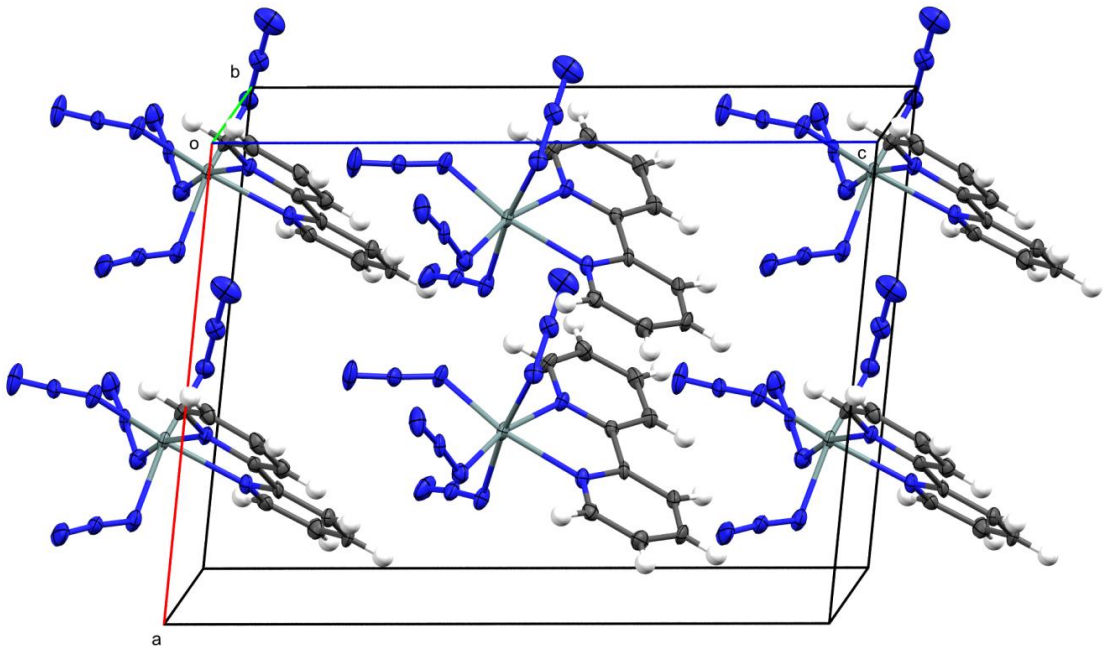

Figure 3.4. Diagram showing the packing in the unit cell of **10** at 120 K.

Tetraazido(1,10-phenanthroline)tin, $Sn(N_3)_4(phen)$ (11)

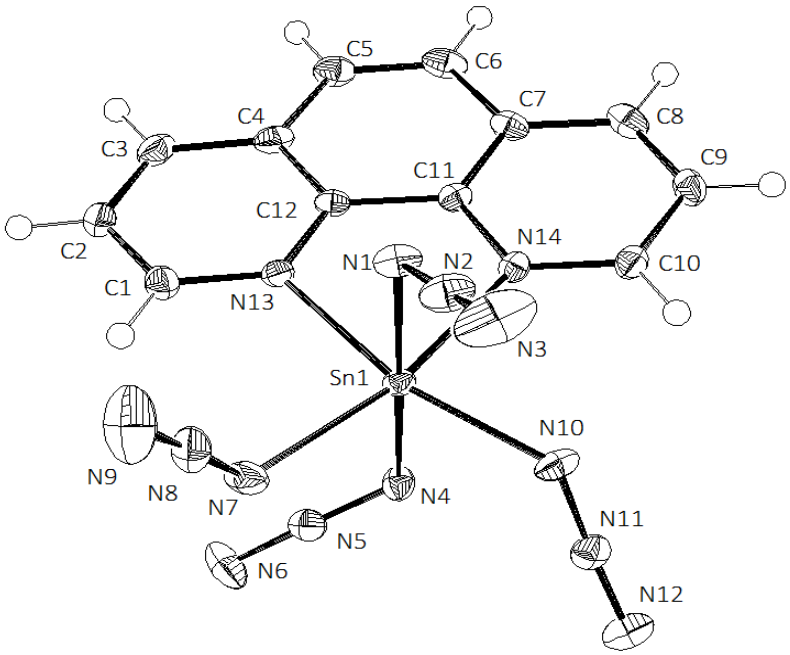

Figure 3.5. ORTEP drawing showing the molecular structure of compound **11** at 100 K with displacement ellipsoids at the 50% probability level, and hydrogen atoms represented by spheres of radius 0.15 Å. Trigonal ($P3_1$, Z = 3), a = 9.985(5) Å, b = 9.985(5) Å, c = 14.325(5) Å, α = 90.000(5), β = 90.000(5), γ = 120.000(5), V = 1236.9(13) Å^3, R_1 = 0.0123. Selected bond lengths [Å] and angles [°]: Sn1–N1 2.109(2), Sn1–N4 2.113(2), Sn1–N7 2.118(2), Sn1–N10 2.090(2), Sn1–N13 2.225(2), Sn1–N14 2.228(2), N1–N2 1.218(3), N2–N3 1.141(3), N4–N5 1.216(3), N5–N6 1.144(3), N7–N8 1.213(3), N8–N9 1.144(3), N10–N11 1.222(3), N11–N12 1.142(3), N13–Sn1–N14 74.56(7), N7–Sn1–N10 104.11(9).

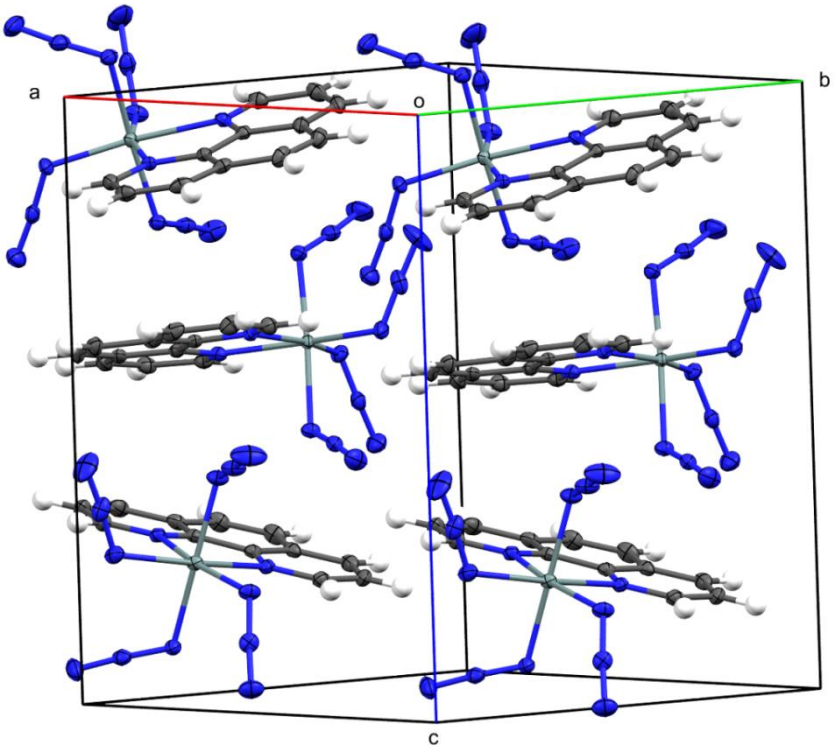

Figure 3.6. Diagram showing the unit cell packing in the crystal structure of **11** at 100 K.

Tetraazidobis(pyridine)tin, $Sn(N_3)_4(py)_2$ (12)

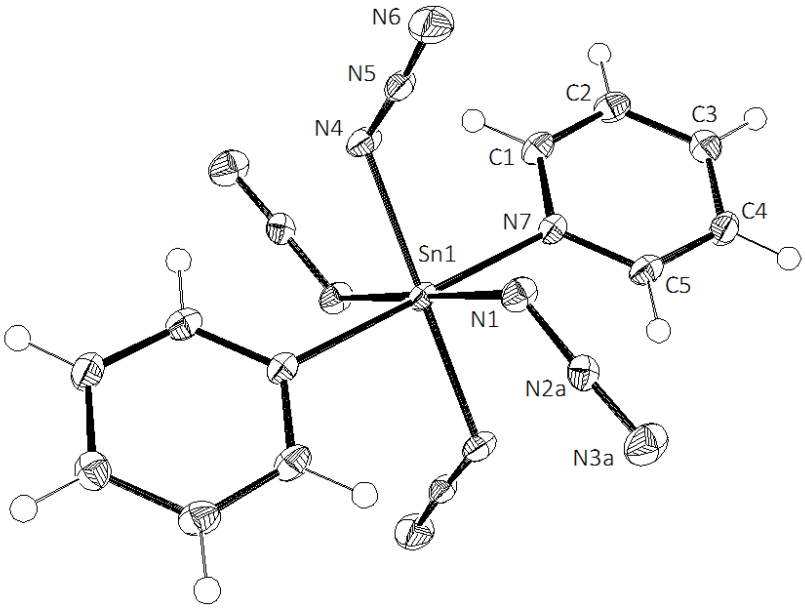

Figure 3.7. ORTEP drawing showing the complex *trans*-$Sn(N_3)_4(py)_2$ (**12**) in the crystal at 100 K with displacement ellipsoids at the 50 % probability level, and hydrogen atoms represented by spheres of radius 0.15 Å. One component of the disordered azido group is omitted for clarity. Triclinic ($P\bar{1}$, Z = 1), a = 7.2058(7) Å, b = 8.1954(8) Å, c = 8.4689(7) Å, α = 116.634(6)°, β = 94.618(7)°, γ = 109.252(6)°, V = 406.31(7) Å^3, R_1 = 0.0190. Selected bond lengths [Å] and angles [°]: Sn1–N1 2.1051(15), Sn1–N4 2.1195(16), Sn1–N7 2.2262(16), N1–N2a 1.221(3), N2a–N3a 1.142(3), N1–N2b 1.222(3), N2b–N3b, 1.142(3), N4–N5 1.218(2), N5–N6 1.140(2), N1–Sn1–N7 90.95(6), N4–Sn1–N7 89.80(6).

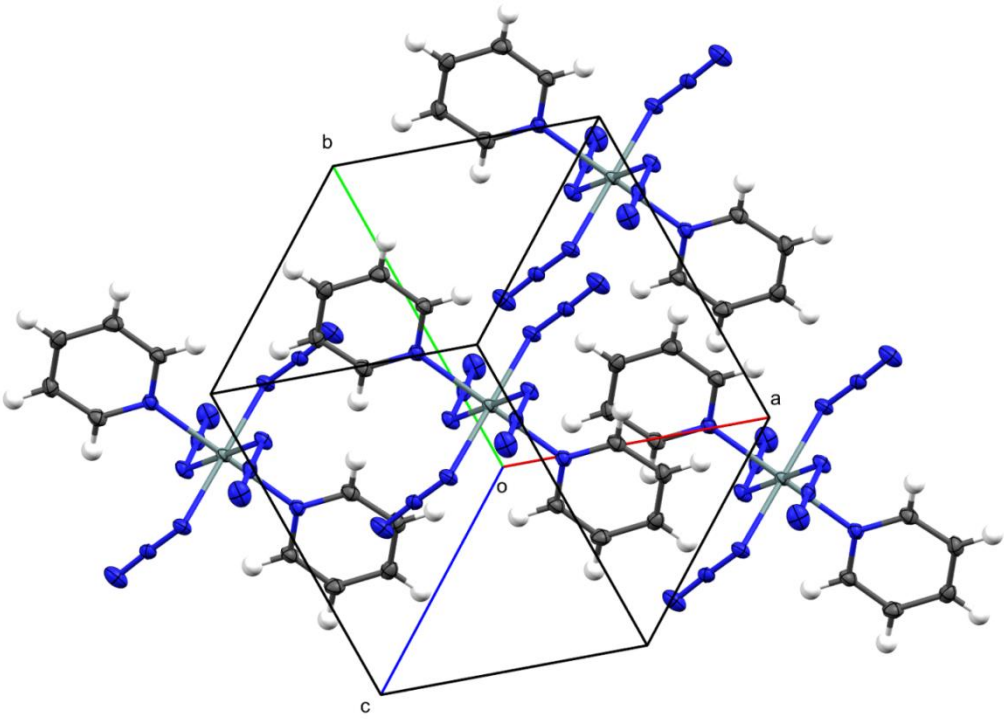

Figure 3.8. Diagram showing the unit cell packing in the crystal structure of **12** at 100 K.

Tetraazidobis(4-picoline)tin, $Sn(N_3)_4(pic)_2$ (13)

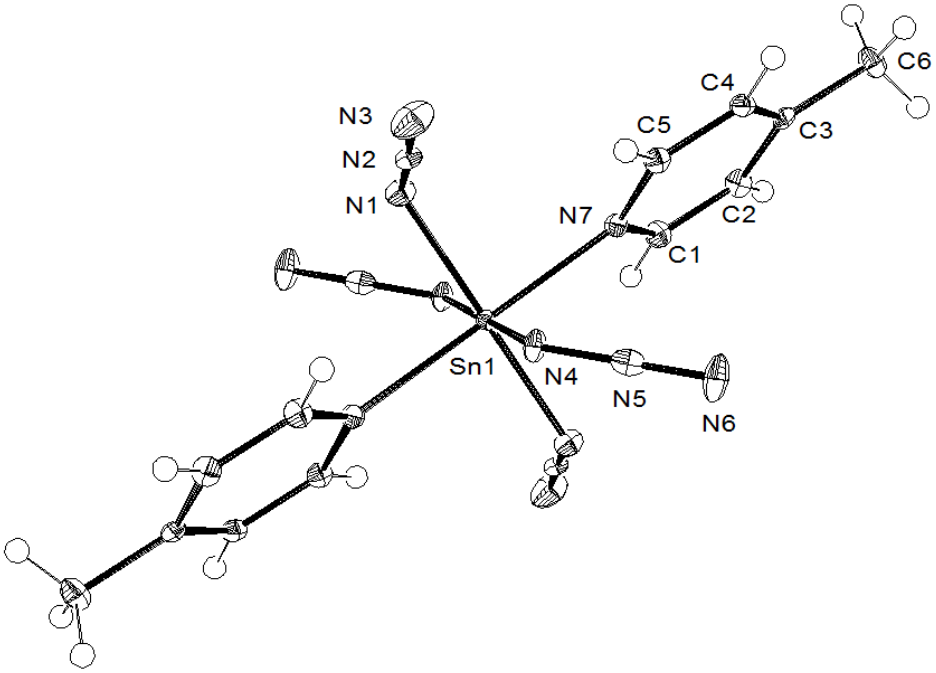

Figure 3.9. ORTEP drawing showing the complex *trans*-$Sn(N_3)_4(pic)_2$ (**13**) in the crystal at 100 K with displacement ellipsoids at the 50% probability level, and hydrogen atoms represented by spheres of radius 0.15 Å. Monoclinic ($P2_1/c$, $Z = 2$), $a = 8.3796(3)$ Å, $b = 14.5515(6)$ Å, $c = 7.9765(3)$ Å, $\beta = 113.9102(14)°$, $V = 889.15(6)$ Å^3, $R_1 = 0.0254$. Selected bond lengths [Å] and angles [°]: Sn1–N1 2.119(2), Sn1–N4 2.098(2), Sn1–N7 2.215(2), N1–N2 1.223(3), N2–N3 1.136(3), N4–N5 1.217(3), N5–N6 1.149(3), N1–Sn1–N4 89.38(9), N1–Sn1–N7 88.66(9), N4–Sn1–N7 88.23(8).

In the structure of **12** the two components of the disordered azido ligand are out of the $Sn[N_\alpha]_4$ plane by 4.6° and 9.0° respectively, and the other non-disordered ligand by 6.7°, which is approximately half way in between. In the silicon complex, two of the azido ligands are out of the $Si[N_\alpha]_4$ plane by 16.4°, and the others virtually in the plane (1.6°). The silicon and germanium analogues (**13–Si** and **13–Ge**) are isostructural with one another, crystallising in the orthorhombic space group *Pbca* with only a modest unit cell volume expansion given by replacement of Si with Ge (**13–Si**: 15.7331(4) Å, 11.0884(3) Å, 20.2648(5) Å; **13–Ge**: 15.8908(6) Å, 11.1459(4) Å, 20.2078(8) Å; T = 100 K) corresponding to a 1 % expansion in the *a*- and *b*-axis and 1 % contraction in the *c*-axis direction. Unlike **13–Si** and **13–Ge**, crystals of compound **13** have lower symmetry, crystallising in the monoclinic space group $P2_1/c$, and the 4-picoline rings in **13** are strictly coplanar (as the tin atom occupies a crystallographic inversion centre) rather than almost perpendicular (both 85.6°). Opposite pairs of azide ligands are bent out of the plane by 47.7° and 8.7° respectively in **13**, whereas in **13–Si** and **13–Ge** the four independent ligands deviate further from the plane by an average of 42° and 43°, respectively. The short contacts between 4-picoline and azido ligands (N_γ) are in the range 2.69–2.74 Å, with C–H···N angles of 124–164°, whereas in **13–Si** and **13–Ge** the d(H···N) between adjacent complexes range from 2.42–2.73 Å, with C–H···N angles of 130–162°.

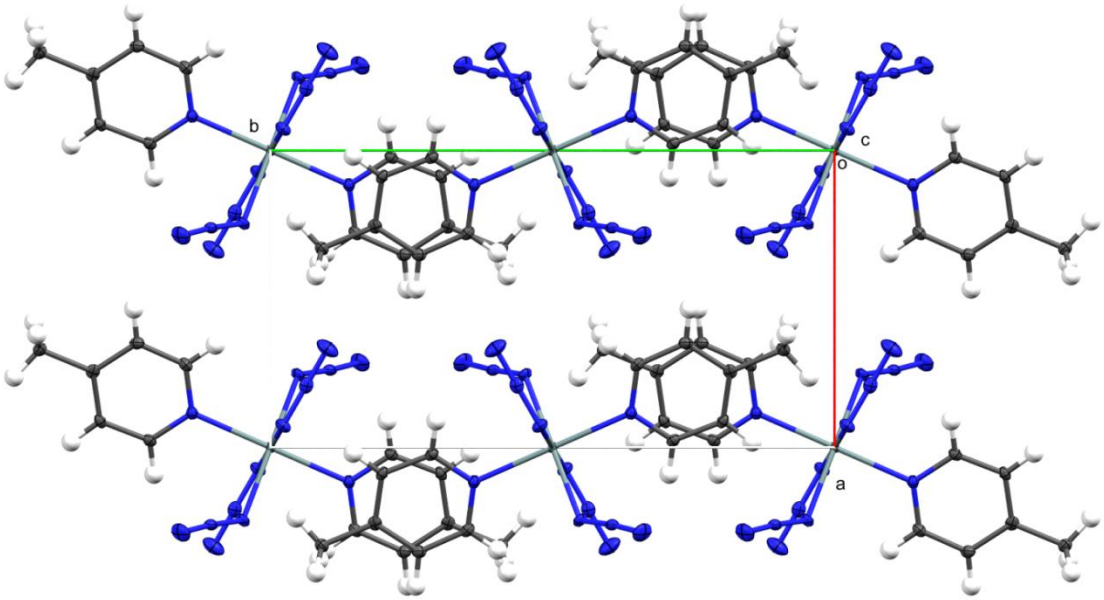

Figure 3.10. View along the *c*-axis showing the unit cell packing in the crystal structure of **13** at 100 K.

Tin(IV) azides crystallographic data overview

A comparison of the minimum and maximum Sn–N_α bond lengths of azido ligands, ΔNN parameters, as well as other valence angles and bond lengths are compiled for hexaazidostannate salts **3** and **9**, and tetraazides **10-13** in Table 3.2. Equivalent data for the Si and Ge analogues from the literature are included, where available. The tin tetraazides, as well

as the hexa(azido)stannate anion, have an octahedral $Sn[N]_6$ coordination skeleton, though the bis(pyridine) complex is less distorted than the chelated bipyridine and phenanthroline complexes. In PPN salt **9** the $[Sn(N_3)_6]^{2-}$ anion is closer to ideal octahedral geometry with *trans* N_α–Sn–N_α angles in the range 176–179°, whereas those in guanidinium salt **3** in the range 172–174° indicate a slightly more distorted $Sn[N]_6$ skeleton. As described in chapter 2 (Figure 2.32) the approximate symmetry of the $[Sn(N_3)_6]^{2-}$ is reduced to approximately C_2, with the torsion angles between mutually *trans* azide groups of 30, 130 and 138°, whereas those in compound **9** at 165–178° are closer to the 'ideal' 180° for S_6 symmetry. The molecular structures of hexaazidostannate **9**, and bidentate pyridine adducts **10** and **11** resemble those of the lighter $[E(N_3)_6]^{2-}$ and $E(N_3)_4(L_2)$ homologs, whereas monodentate pyridine complexes **12** and **13** adopt an all-*trans* OC-6-11 geometry. In the latter complexes all four azido ligands are in the equatorial plane and both axial pyridine (or 4-picoline) ligands are strictly coplanar as the tin atom occupies a crystallographic inversion centre. All Sn–N_α bonds in tin azides **10**–**13** lie within the range 2.090(2)–2.120(2), and *cis* and *trans* positions are indistinguishable, falling in the ranges, 2.097(6)–2.110(5) Å and 2.090(2)–2.118(2) Å, respectively. Furthermore, this suggests the *trans* influence of azide and pyridine-based ligands on N_3 ligands in the tin complexes are indistinguishable crystallographically (Sn–N_α(*cis*) in **10** and **11**, 2.09–2.12 Å; Sn–N_α(*trans*) in **12** and **13**, 2.10–2.12 Å). Being a poorer σ-electron donor, Sn–N bonds to phenanthroline are somewhat longer, by 1.5(6) pm than those to bipyridine. The same observation can be made for Si and Ge complexes: 1.3(2) pm (Si), 1.4(2) pm (Ge). The substitution of all four chloro ligands for N_3 ligands in the tetrachloro analogues $SnCl_4$(bpy) 2.236(6) Å,[185] and $SnCl_4$(phen) 2.237(3) Å,[186] leads to a shortening of the Sn–$N(L_2)$ bonds by about 2 pm and this reveals the weaker σ-electron donor capabilities of N_3 ligands which is in line with conclusions drawn from the NMR data (see Table 3.3). The Sn–N_L bonds in *trans*-$Sn(N_3)_4(L)_2$ complexes **12** and **13** are longer than those of chelating ligands in compounds **10** and **11**. The *trans* complexes $SnCl_4(py)_2$ and $SnBr_4(py)_2$ have been investigated previously,[187] but their low solubility hampered crystallisation attempts and hence precluded accurate structure determination. The Sn–N_α bonds of the homoleptic negatively charged hexaazidostannate anion are significantly longer (2 to 3 pm) than the neutral polyazides **10–13**, 2.122(2)–2.147(3) Å *vs.* 2.090(2)–2.120(2) Å, suggesting the complex charge is the factor with the greatest influence on the Sn–N_α distances. This charge effect is of the same extent in the analogous Si and Ge systems. The relative orientation of the azido ligands appears to be governed by numerous, weak intermolecular C–H···(N_3-ligand) interactions (d [Å]: $(PPN)_2[Sn(N_3)_6]$ (**9**) = 2.5; $Sn(N_3)_4$(bpy) (**10**) = 2.3; ($Sn(N_3)_4$(phen) (**11**) = 2.4; $Sn(N_3)_4(py)_2$ (**12**) = 2.7; $Sn(N_3)_4(pic)_2$ (**13**) = 2.7) at the level of van der Waals contacts (d_{vdW}(NH) = 2.7 Å) as well as intramolecular N_α, N_β dipole-dipole interactions as short as 3.0 Å (**9**,**10**), and 2.9 Å (**11**–**13**) (N.B. d_{vdW}(NN) = 3.32 Å).[188] The larger covalent radius of tin causes increased E–$N(L_2)$ distances compared to the silicon and germanium

complexes, necessitating narrower bite angles and permitting the angle between the opposing (equatorial) N_3 ligands to open slightly to 103° and 105° respectively. Their geometries are slightly further from ideal octahedral symmetry (90°) than for silicon and germanium, but the axial N_3 ligands are close to the required positions and share angles of 170° ($Sn(N_3)_4$(bpy)) and 176° ($Sn(N_3)_4$(phen)), respectively.

Table 3.2. Crystallographically determined bonding parameters of Group 14 poly(azido) complexes **9**–**13** and their silicon and germanium homologs (where available), including minimal and maximal coordinative bond lengths (E–N_α), and ΔNN (see footnotes), and chelate ligand bite angles (where applicable).

Compound	d(E–N_α) [Å]	ΔNN [pm] [a]	N–E–N [°] [b]	Ref.
$[Sn(N_3)_6]^{2-}$ (**3**)	2.1341(13), 2.1502(13)	6.2(3), 8.7(3)	-	[c]
$[Sn(N_3)_6]^{2-}$ (**9**)	2.122(2), 2.147(2)	5.9(6), 9.5(11)	-	[85]
$[Ge(N_3)_6]^{2-}$	1.969(2), 1.980(2)	6.1(7), 7.1(6)	-	[33]
$[Si(N_3)_6]^{2-}$	1.866(1), 1.881(1)	5.4(4), 6.0(4)	-	[83]
$Sn(N_3)_4$(bpy) (**10**)	2.100(6), 2.116(6)	5.8(19), 9.9(16)	74, 103	[85]
$Ge(N_3)_4$(bpy)	1.925(2), 1.972(2)	6.6(5), 8.6(6)	79, 99	[33]
$Si(N_3)_4$(bpy)	1.818(2), 1.864(2)	6.5(4), 8.6(4)	81, 97	[34]
$Sn(N_3)_4$(phen) (**11**)	2.090(2), 2.118(2)	6.4(5), 8.0(4)	75, 105	[85]
$Ge(N_3)_4$(phen)	1.939(2), 1.963(2)	7.9(4), 9.0(4)	80, 100	[d]
$Si(N_3)_4$(phen)	1.828(1), 1.860(1)	7.2(4), 8.4(3)	82, 98	[34]
$Sn(N_3)_4(py)_2$ (**12**)	2.105(2), 2.120(2)	6.8(6), 8.7(6)	-	[85]
$Si(N_3)_4(py)_2$	1.8422(8), 1.8412(8)	7.2(2), 7.6(2)	-	[81]
$Sn(N_3)_4(pic)_2$ (**13**)	2.098(2), 2.119(2)	6.8(4), 8.7(4)	-	[c]
$Ge(N_3)_4(pic)_2$	1.9476(19), 1.9563(19)	6.3(4), 7.3(4)	-	[81]
$Si(N_3)_4(pic)_2$	1.8392(16), 1.8499(16)	6.7(3), 7.3(3)	-	[81]

[a] Minimum and maximum values of ΔNN = $d(N_\alpha–N_\beta)$–$d(N_\beta–N_\gamma)$ with e.s.d.'s in parentheses; [b] N_L–E–N_L bite angle; N_α–E–N_α (*cis*) inter azido ligand angle in the plane of the bidentate ligand (where applicable); [c] this work [d] CCDC 1415857, see SI of ref. [85].

Table 3.3 below summarises key parameters for the crystal structures of tin(IV) azides **9-13**. All data sets have a data-to-parameter ratio of 10.3–12.2 (including restraints), and in combination with R_1 values of 0.0123–0.0325 suggest the data are of high quality. $(PPN)_2[Sn(N_3)_6]$ has the largest unit cell volume – V = 3415.3(4) Å^3 – of the $(PPN)_2[E(N_3)_6]$ salts, E = Si–Sn, compared to V = 1693.9(7) Å^3 for Si or V = 1694.6(11) Å^3 for Ge.[83,33] Whilst all three salt-like compounds have triclinic symmetry, the coordination centres of Si and Ge lie on special crystallographic positions, meaning their asymmetric units contain only one (PPN) cation and half of the $[E(N_3)_6]^{2-}$ anion. Of the neutral tin tetraazide adducts, $Sn(N_3)_4$(bpy) (**10**) has the lowest volume per molecule (V / Z) of 381 Å^3, and the other tetraazides have volumes of 412, 406, and 444 Å^3, respectively.

Table 3.3. Summary of crystal structure refinement parameters for $(PPN)_2[Sn(N_3)_6]$ (**9**), and neutral tin tetraazide adducts **10**–**13**.[85]

	$(PPN)_2[Sn(N_3)_6]$ (**9**)	$Sn(N_3)_4$(bpy) (**10**)	$Sn(N_3)_4$(phen) (**11**)	$Sn(N_3)_4(py)_2$ (**12**)	$Sn(N_3)_4(pic)_2$ (**13**)
Empirical formula	$C_{72}H_{60}N_{20}P_4Sn$	$C_{10}H_8N_{14}Sn$	$C_{12}H_8N_{14}Sn$	$C_{10}H_{10}N_{14}Sn$	$C_{12}H_{14}N_{14}Sn$
M_r	1447.93	442.93	466.95	444.94	472.99
Nitrogen [%]	19.3	44.3	42.0	44.1	41.5
Crystal system	triclinic	monoclinic	trigonal	triclinic	monoclinic
Space group	$P\bar{1}$	Cc	$P3_1$	$P\bar{1}$	$P2_1/c$
a [Å]	11.7012(8)	11.6427(19)	9.985(5)	7.2058(7)	8.3796(3)
b [Å]	12.5721(9)	8.3153(13)	9.985(5)	8.1954(8)	14.5515(6)
c [Å]	24.4651(17)	15.866(2)	14.325(5)	8.4689(7)	7.9765(3)
α [°]	94.143(4)	90	90	116.634(6)	90
β [°]	101.080(4)	96.783(6)	90	94.618(7)	113.9102(14)
γ [°]	103.058(4)	90	120	109.252(6)	90
V [Å^3]	3415.3(4)	1525.2(4)	1236.9(10)	406.31(7)	889.15(6)
Z	2	4	3	1	2
T [K]	100	120	100	100	100
D_{calc} [g cm^{-3}]	1.408	1.929	1.881	1.819	1.767
μ [mm^{-1}]	0.527	1.706	1.583	1.601	11.721
F (000)	1484	864	684	218	468
Crystal size [mm × mm × mm]	0.50 × 0.38 × 0.30	0.27 × 0.18 × 0.10	0.37 × 0.27 × 0.20	0.17 × 0.06 × 0.06	0.22 × 0.15 × 0.15
Crystal habit	block	prism	block	needle	block
Θ range for data collection [°]	1.68, 25.00	2.59, 25.00	2.36, 24.97	2.79, 27.96	5.7758, 66.5446

	$(PPN)_2[Sn(N_3)_6]$ (**9**)	$Sn(N_3)_4(bpy)$ (**10**)	$Sn(N_3)_4(phen)$ (**11**)	$Sn(N_3)_4(py)_2$ (**12**)	$Sn(N_3)_4(pic)_2$ (**13**)
Limiting indices *h*; *k*; *l*	–13, 13; –14, 14; –29, 29	–13, 13; 9, –9; –18, 18;	–11, 11; –11, 11; –17, 17	–9, 9; –10, 10; –10, 10	–9, 9; –14, 17; –9, 8
Reflections collected	58063	6895	12903	5861	4031
Independent reflections	11980	2683	2761	1767	1528
R_{int}	0.0513	0.0404	0.0204	0.0283	0.0242
Completeness to Θ [%]	99.8 (Θ = 25.00°)	99.8 (Θ = 25.00°)	100.0 (Θ = 24.97°)	99.0 (Θ = 25.24°)	97.1 (Θ = 33.27°)
Refinement method	[a]	[a]	[a]	[a]	[a]
Data / restraints / parameters	11980 / 66 / 959	2683 / 2 / 226	2761 / 1 / 244	1767 / 38 / 133	1528 / 0 / 125
GoF F^2	1.077	1.170	1.120	1.065	1.119
R_1 [$I > 2I(\sigma)$]	0.0283	0.0325	0.0123	0.0190	0.0254
R_1 (all data)	0.0361	0.0362	0.0124	0.0195	0.0273
Largest diff. peak / hole [e Å^{-3}]	0.510 / –0.724	0.840 / –0.983	0.256 / –0.234	0.499 / –0.501	0.462 / –1.255
CCDC Deposition No	1039721	1039722	1039723	1062323	-

[a] Full matrix least squares on F^2.

3.2.3 Results of FTIR and NMR spectroscopic investigations into tin(IV) polyazides

Infrared Spectroscopic data

Vibrational spectroscopy techniques including FTIR and Raman spectroscopies gave some of the earliest insight into the structure and bonding of polyazido complexes, and remain convenient tools for *in-situ* monitoring and structural characterisation, since the wavenumbers of the asymmetric azide stretches typically fall in the relatively clear spectral window 2000–2200 cm^{-1}. Depending on the counter ion, or ancillary ligands, the spectral window of the symmetric azide stretch ($\nu_s(N_3)$) around 1200–1350 cm^{-1} can be more congested, making unambiguous assignment of the symmetric stretches more difficult (see Figure 3.12). In acetonitrile solution, the asymmetric azide stretches ($\nu_{as}(N_3)$) of the homoleptic azido complexes $[E(N_3)_6]^{2-}$ (E = Si, Ge) give rise to a single intense absorption band at 2109 and 2083 cm^{-1}, respectively, whereas $[Sn(N_3)_6]^{2-}$ has an intense principal absorption band at 2079 cm^{-1} and a second weak absorption at 2112 cm^{-1}.[170] The absorption spectra of polyazido complexes can vary depending on the solvent, which is shown by the spectra of $Na_2[Sn(N_3)_6]$ in acetonitrile and THF solutions (Figure 3.11). In the solid state FTIR spectra (nujol

mulls), the intermolecular (or interionic) interactions packing arrangement often enforces reduced symmetry on the complexes, giving rise to multiple $\nu_{as}(N_3)$ absorption bands. This is demonstrated in Figure 3.2.3b (below), which shows a comparison of the solid state FTIR spectra of $Na_2[Sn(N_3)_6]$ and $(PPN)_2[Sn(N_3)_6]$. For the latter non-coordinating (PPN) cation, the crystallographic data (see Figure 3.1 above) suggest the symmetry of the $[Sn(N_3)_6]^{2-}$ anion is close to the S_6-symmetric species present in solution, and exhibits a single intense $\nu_{as}(N_3)$ absorption band. Whereas for smaller cations like sodium and guanidinium (see Figure 2.32), the interionic interactions have a profound effect of the number and shape of absorption bands for the $[Sn(N_3)_6]^{2-}$ anion. In solution the *trans*-$Sn(N_3)_4(L)_2$ complexes **12** and **13** have similar absorption profiles for the $\nu_{as}(N_3)$ region, with a principal intense absorption band at around 2080 cm^{-1} and a weak secondary band at higher energy around 2108 cm^{-1}. The complex geometries in their crystal structures are different as the additional methyl group of the 4-picoline ligands enforces a change in the packing (Figures 3.7 and 3.9 respectively). The two crystallographically independent azido ligands of the pyridine complex lie almost in the $Sn[N_\alpha]_4$ plane, with angles of 4.6–9.0°, whereas those of the 4-picoline complex are at 8.7° and 47.7°. This reduced local symmetry gives rise to two intense $\nu_{as}(N_3)$ absorption bands at 2073 and 2088 cm^{-1} and a weaker band at 2108 cm^{-1}, whereas a single slightly broader band is observed at 2086 cm^{-1} for $\nu_{as}(N_3)$ of $Sn(N_3)_4(py)_2$. The FTIR spectra of $Si(N_3)_4(L)_2$ and $Ge(N_3)_4(L)_2$ show that the complexes are in equilibrium with the binary azide and free ligand. Incremental addition of the corresponding pyridine to the acetonitrile solution increases the concentration of the complex. No such observations have been made from the FTIR or NMR data for the neutral tin adducts, although they have reduced solubility than their silicon and germanium counterparts.

Table 3.4. Comparison of selected characteristic IR absorption bands of hexaazidostannate salts **3** and **9**, and charge-neutral pyridine adducts **10–13** in MeCN solution (and other solvents where stated), and as nujol suspensions. The corresponding data for the silicon and germanium homologs, and for $Na_2[Sn(N_3)_6]$ are shown for comparison where available.

Compound	$\nu_{as}(N_3)$ [cm^{-1}] [a]		$\nu_s(N_3)$ [cm^{-1}] [b]	
	MeCN	nujol	MeCN	nujol
$Na_2[Sn(N_3)_6]$	2079 [c] THF: 2118sh, 2083	2077, 2108, 2119	1338, 1288	1348, 1296
$(G)_2[Sn(N_3)_6]$ (**3**)	2079 [c]	2116, 2100, 2078, 2063	1338, 1288	1342, 1289, 1271
$(PPN)_2[Sn(N_3)_6]$ (**9**) [85]	2079 [c]	2074 [d]	1338, 1289	1337, 1288
$(PPN)_2[Ge(N_3)_6]$ [33]	2083	-	1297	-
$(PPN)_2[Si(N_3)_6]$ [83]	2109 CH_2Cl_2: 2108	2104	1316	1320, 1315
$Sn(N_3)_4(bpy)$ (**10**) [85]	2112, 2085	2110, 2092, 2075, 2067	1337, 1282	1332, 1318, 1277, 1273
$Ge(N_3)_4(bpy)$ [33]	2120, 2097, 2091	-	1288	-
$Si(N_3)_4(bpy)$ [34]	2151, 2126, 2116	2151, 2142, 2114, 2103	1316	1311
$Sn(N_3)_4(phen)$ (**11**) [85]	2112, 2086	2114, 2096, 2082, 2068	1331, 1279	1332, 1275
$Ge(N_3)_4(phen)$ [33]	2120, 2093	-	1286	-
$Si(N_3)_4(phen)$ [34]	2150, 2126, 2118	2147, 2121, 2113, 2102	1315	1315
$Sn(N_3)_4(py)_2$ (**12**) [85]	2111, 2083	2103sh, 2085	1335, 1285	1332, 1280
$Ge(N_3)_4(py)_2$ [81]	2117, 2091 THF: 2110, 2094 CH_2Cl_2: 2113, 2097	2094	-	-
$Si(N_3)_4(py)_2$ [81]	2145, 2119	2121	-	1321
$Sn(N_3)_4(pic)_2$ (**13**)	2108, 2079 [e]	2108, 2089, 2073	1333, 1282	1331, 1275
$Ge(N_3)_4(pic)_2$ [81]	2116, 2092 THF: 2117, 2093 CH_2Cl_2: 2114, 2096	2089	-	-
$Si(N_3)_4(pic)_2$ [81]	2144, 2126 THF: 2150, 2122	2115	-	-

[a] Asymmetric N_3 stretch; [b] Symmetric N_3 stretch; [c] a second weak band is observed at 2112 cm^{-1}; [d] a second weak band is observed at 2104 cm^{-1}; [e] in 4-picoline.

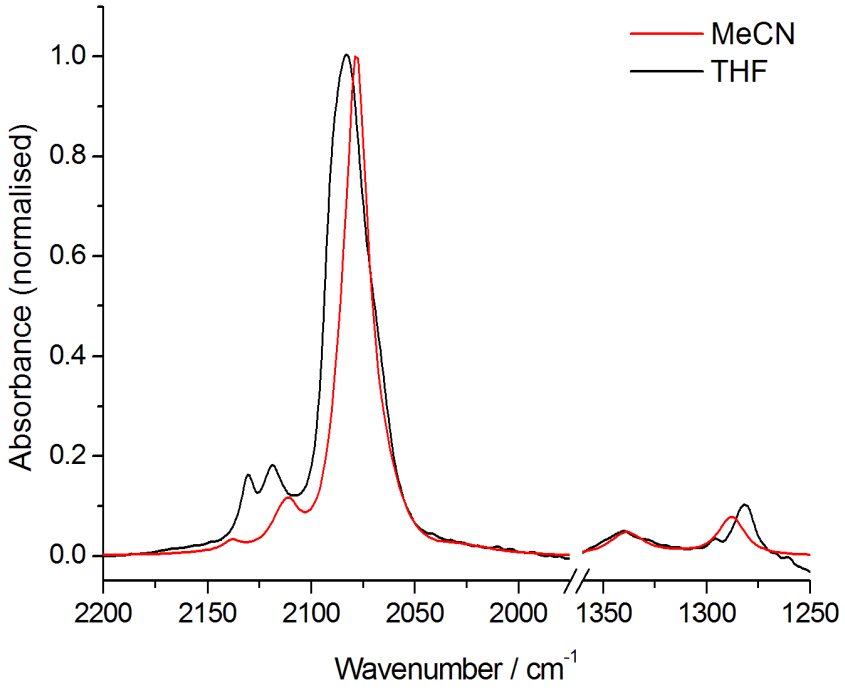

Figure 3.11. FTIR spectra of $Na_2[Sn(N_3)_6]$ in MeCN (red) and THF (black) solutions. A trace of HN_3 is visible at 2138 cm^{-1} and 2130 cm^{-1} in MeCN and THF respectively. Slight interference of a THF (solvent) absorption band at 1290 cm^{-1} means the true position of the $\nu_{sym}(N_3)$ stretch at 1282 cm^{-1} may be closer to 1284 cm^{-1}.

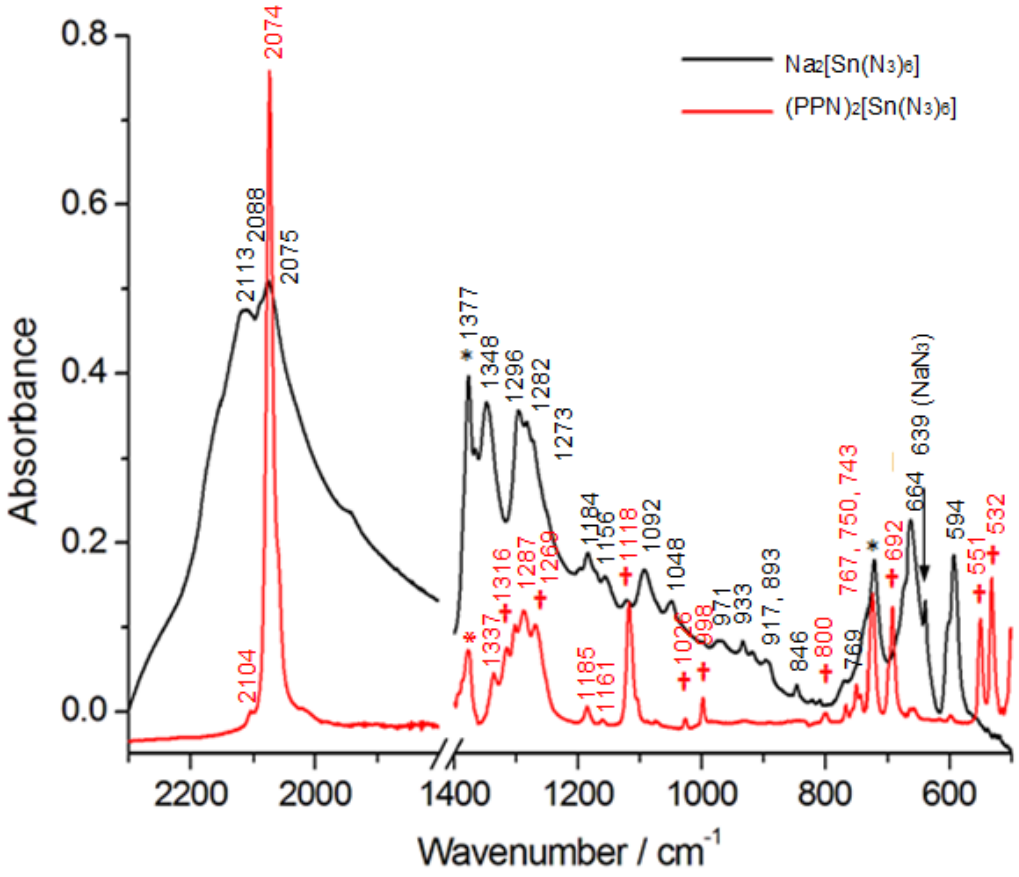

Figure 3.12. Comparison of solid state FTIR spectra of $Na_2[Sn(N_3)_6]$ (black) and $(PPN)_2[Sn(N_3)_6]$ (red) in the region 2200–500 cm^{-1}. Bands marked with an asterisk belong to the mulling agent (nujol), and those marked (†) are attributed to the $(PPN)^+$ cation. Spectral window 1800–1400 cm^{-1} omitted to allow expanded view.

The absence of strong interionic interactions in the latter leads to a relatively sharp absorption band at 2074 cm^{-1} in contrast to $Na_2[Sn(N_3)_6]$ which has at least two broad bands between 2114 and 2077 cm^{-1} due to presumably stronger interactions with the sodium cations. The symmetric azide stretching vibrations of $[Sn(N_3)_6]^{2-}$ fall in the same region as several bands for the $(PPN)^+$ cation, so those bands which are closest to the published values[170] at 1288 and 1337 cm^{-1} have been assigned to the $[Sn(N_3)_6]^{2-}$ anion in **9**.[85] The absence of cation-based vibrations in $Na_2[Sn(N_3)_6]$ allows the assignment of the symmetric stretches (ν_s) at 1347 cm^{-1} and 1296 cm^{-1}, deformation vibrations ($\delta(N_3)$) at 662 and 593 cm^{-1} their corresponding overtones ($2\nu_s$) at 2642, 2540–2575 cm^{-1}, and the combination bands ($\nu_s + \nu_{as}$) between 3242–3447 cm^{-1}. A trace of NaN_3 impurity is visible in $Na_2[Sn(N_3)_6]$ with a slight shoulder at 2130 cm^{-1} and a sharp band at 639 cm^{-1}.

NMR Spectroscopy

Depending on the central element and ancillary ligands on polyazido complexes a range of NMR-active nuclei are available. In the case of tin azides **9**–**12** $^{117}Sn/^{119}Sn$ and $^{14}N/^{15}N$ nuclei are available to probe the complex directly, and for chelate complexes **10** and **11** ^{1}H and ^{13}C NMR can be used indirectly by observation of subtle shifts in the ligand protons. The relative peak positions of the 2,2'-bipyridine (or 1,10-phenanthroline) protons seem to stay the same for the halide and azide complexes of Si–Sn, but with lesser or greater chemical shift differences.

Table 3.5. ^{1}H NMR chemical shifts δ [ppm] [a] for **10** and **11**, showing silicon, germanium, fluoro-, chloro-, and bromo- analogues for comparison where available.

Complex	$\delta(H_A)$	$\delta(H_B)$	$\delta(H_C)$	$\delta(H_D)$	$\Delta\delta_{DA}$	solvent	Ref.
$Sn(N_3)_4$(bpy) (**10**)	8.08	8.55	8.72	9.12	1.04	CD_3CN	[85]
$Ge(N_3)_4$(bpy)	8.06	8.52	8.81	9.35	1.29	THF-d_8	[33]
$Si(N_3)_4$(bpy)	8.00	8.48	8.63	9.40	1.40	CD_3CN	[34]
SnF_4(bpy)	8.49	8.99	9.15	9.41	0.92	CD_3NO_2	[183]
$SnCl_4$(bpy)	8.38	8.84	9.35	9.66	1.28	[b]	[189]
$SnBr_4$(bpy)	8.46	8.87	9.39	9.81	1.35	[b]	[189]
$Sn(N_3)_4$(phen) (**11**)	8.34	8.39	9.09	9.42	1.08	CD_3CN	[85]
$Ge(N_3)_4$(phen)	8.34	8.41	9.08	9.59	1.25	THF-d_8	[33]
$Si(N_3)_4$(phen)	8.28	8.38	9.03	9.60	1.32	CD_3CN	[34]
SnF_4(phen)	8.45	8.45	9.16	9.35	0.90	$CDCl_3$	[183]

[a] H_A, H_B, H_C and H_D refer to $H_{5,5'}$, $H_{4,4'}$, $H_{3,3'}$, $H_{6,6'}$ of 2,2'-bipyridine, and $H_{3,8}$, $H_{4,7}$, $H_{5,6}$, $H_{2,9}$ of 1,10-phenanthroline, respectively; $\Delta\delta_{DA} = \delta(H_D)–\delta(H_A)$; [b] *N*,*N*-dimethylacetamide.

The difference between the most and least sensitive protons, 6,6'- and 3,3'- positions in bipyridine, and 3,8- and 2,9- positions in phenanthroline, seems to follow the trend of the electronegativity of the halogens in the order Br > Cl > F. The strength of the electron-withdrawing effect of azide ligands on the heterocyclic ligand protons seems to be between that of Cl and F, though the deshielding effect decreases from Si–Sn.

^{1}H and ^{19}F NMR investigation into the reactivity of SnF_4 with TMS–N_3 in C_6D_6

TMS–N_3 (27 mg, 0.23 mmol) was dissolved 1 ml C_6D_6 in an NMR tube equipped with a Young's greaseless stopcock. A ^{1}H NMR was recorded as a reference spectrum. SnF_4 (9 mg, 0.05 mmol) was added to the tube in the glovebox and a ^{1}H NMR recorded after 10 minutes showed no change. After 2½ h at RT without stirring, the ratio of TMS–N_3/TMS–F was 318:1, and when heated to 45 °C for 2 h the ratio was 60:1 corresponding to < 2 % conversion assuming no loss of the volatile TMS–F (b.p. 15 °C). The tube was immersed in an oil bath to just above the level of solvent and held at 40 °C for 7 days, after which the conversion of TMS–N_3 to TMS–F was around 95 % according to the ^{1}H NMR spectrum. The C_6D_6 solution was carefully decanted from the tube, leaving an off white solid in a minimal amount of approximately 0.05–0.1 ml C_6D_6, to which 1ml CD_3CN and 5–10mg of 2,2'-bipyridine were added, dissolving some of the solid. After warming to 40 °C briefly, ^{1}H and ^{19}F spectra were recorded, and the coordinated 2,2'-bipyridine protons acted as a sensitive probe to determine the nature of the (soluble) material.

The insolubility of SnF_4 combined with the absence of agitation severely hindered the initial reaction rate, which was increased significantly by heating to 45 °C. The decrease in the TMS–N_3 peak at –0.08 ppm (benzene-d_6) accompanied by the increase in the TMS–F doublet centred at 0.03 ppm (J = 7.4 Hz) confirms the azide-fluoride ligand has taken place, but the small scale and relatively large errors in weighing operations mean quantitative information is limited. To determine the identity of the covalent tin azides without the risks associated with their manipulation, a CD_3CN solution of 2,2'-bipyridine was added after careful decantation of the C_6D_6 reaction solvent. The ligand protons acted a sensitive probe by comparison with the reference spectrum of $Sn(N_3)_4$(bpy) (**10**) (see Table 3.6 below).[85] There were traces of the hydrolysis product (hexamethyldisiloxane) at 0.12 ppm,[190] and diglyme throughout the experiment originating from the TMS–N_3. Apart from the excess 2,2'-bipyridine, there is only one set of additional peaks which are very close to the values for $Sn(N_3)_4$(bpy) (**10**, see Table 3.6), suggesting that **10** is the only 2,2'-bipyridine complex present in solution. The slight differences in chemical shift could be due to the residual amount of C_6D_6 which remained after decantation, which would slightly reduce the polarity of the solvent. The ^{1}H NMR spectrum of **10** in CD_2Cl_2, a less polar solvent than CD_3CN, shows shifts of the peaks in the same direction.

Table 3.6. Comparison of the chemical shifts of the 2,2'-bipyridine protons of **10** in CD_3CN obtained by reaction of SnF_4 and TMS–N_3 in C_6D_6, compared to literature values in CD_3CN and CD_2Cl_2.[85]

	$\delta(H_{5,5'})$	$\delta(H_{4,4'})$	$\delta(H_{3,3'})$	$\delta(H_{6,6'})$
10 (CD_3CN)	8.08	8.55	8.72	9.12
10 (CD_2Cl_2)	8.04 (–0.04)	8.47 (–0.08)	8.52 (–0.20)	9.21 (+0.09)
this sample	8.06 (–0.02)	8.51 (–0.04)	8.66 (–0.06)	9.15 (+0.03)

The observation of TMS–N_3 conversion to TMS–F (see Figure 3.13), and the similarity between the obtained spectrum of **10** and the literature values seems to imply the presence of tin tetraazide in the reaction mixture; however this cannot be proven because the benzene solution was not completely decanted to avoid risks associated with its isolation. The nature of the acetonitrile-insoluble material could not be determined, which casts further doubt upon whether the azide-fluoride exchange proceeds to $Sn(N_3)_4$ under these conditions or stops at an intermediate stage such as $SnF_2(N_3)_2$ as in the analogous reaction with $SnCl_4$.[178] To determine the extent of azide-fluoride exchange, the solid $SnF_x(N_3)_{(4-x)}$ would need to be freed of TMS–N_3 by drying under vacuum or by repeated washing with a suitable solvent, and dissolved by an excess of 2,2-bipyridine solution in acetonitrile.

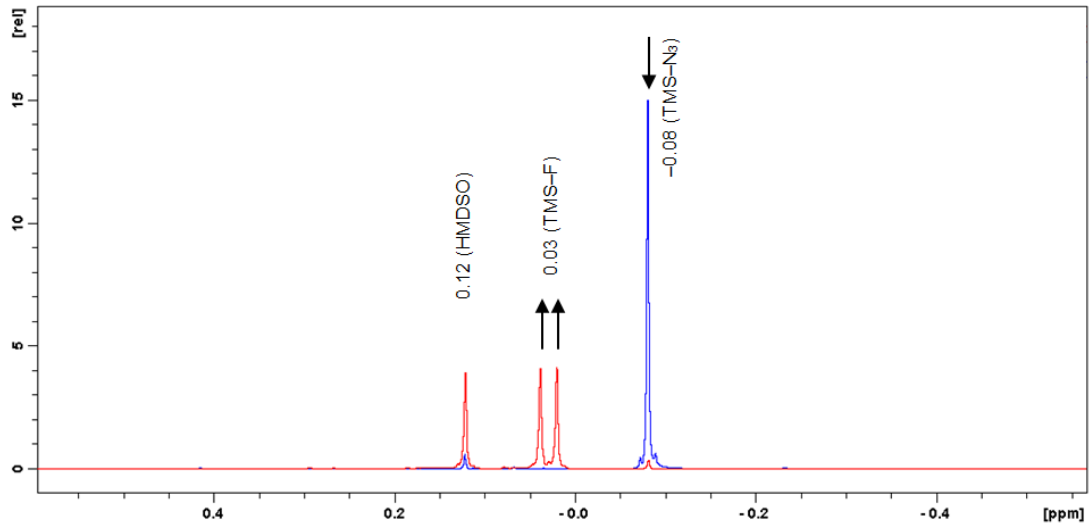

Figure 3.13. Overlay of ^{1}H NMR spectra of TMS–N_3 in C_6D_6 before (blue) and after (red) reaction with SnF_4 for 8 days. TMS–N_3: δ = –0.08 ppm; TMS–F: δ = 0.03 ppm. Hexamethyldisiloxane (HMDSO) is visible at 0.12 ppm, which was a persistent impurity due to hydrolysis and seemed to increase in concentration during the reaction period. The disappearance of the TMS–N_3 peak at –0.08 ppm and the rise of the TMS–F doublet at 0.03 ppm shows that SnF_4 has reacted with TMS–N_3 which is indirect proof of the formation of a new tin(IV) azide species.

3.2.4 Thermal Analyses

The thermal behavior of the tin polyazides was investigated by differential scanning calorimetry (DSC) measurements according to which the onset of exothermic decomposition occurred at temperatures in the range 265–305 °C, which are higher than those of the silicon and germanium homologs (Table 3.7). To the best of our knowledge, complex $Sn(N_3)_4(py)_2$ (**12**) has the highest onset temperature, T_{on}^{dec} = 305 °C, of any group 14 polyazide (including $Pb(N_3)_2$). Incidentally the decomposition temperature for **12** is significantly higher than the tetrafluoro analogue, $SnF_4(py)_2$, which decomposes around 220 °C.[191] All thermograms exhibit large decomposition exotherms (for example see Figures 3.14 and 3.15) from which the molar heats of decomposition, ΔH_{dec} (MJ mol^{-1}), of –1.10, –0.89, –0.93, and –0.77 were derived for the compounds **9**, **10**, **11**, and **12** respectively.

Table 3.7. Thermal properties of tin(IV) azides **9**–**12** determined from DSC measurements in comparison to the lighter group 14 homologs.[a]

Compound	T_{on}^{m} [°C]	T_{on}^{dec} [°C]	ΔH_{dec} [kJ g^{-1}]	Ref.
$(PPN)_2[Sn(N_3)_6]$ (**9**)	218	300, 365	–0.76	[85]
$(PPN)_2[Ge(N_3)_6]$	194	256, 312	–0.85	[33]
$(PPN)_2[Si(N_3)_6]$	214	256, 321	–0.92	[83]
$Sn(N_3)_4(bpy)$ (**10**)	180	265	–2.00	[85]
$Ge(N_3)_4(bpy)$	190	252	–2.13	[33] [b]
$Si(N_3)_4(bpy)$	212	265	–2.42	[34]
$Sn(N_3)_4(phen)$ (**11**)	200	301	–2.00	[85]
$Ge(N_3)_4(phen)$	192	251, 303	–1.39 [d]	[33] [b,c]
$Si(N_3)_4(phen)$,	216	239	–2.29	[34] [c]
$Sn(N_3)_4(py)_2$, (**12**)	265	305	–1.74	[85]

[a] T_{on}^{m}, onset temperature of melting; T_{on}^{dec}, onset temperature(s) of decomposition; ΔH_{dec} enthalpy of decomposition as determined from the integrated area under the exotherm, calibration detailed in experimental section; [b] see corresponding SI: [c] MeCN hemisolvate; [d] upper limit.

While the specific enthalpies for these compounds are less negative in comparison to their lighter homologs, the accuracy of measurements (< ±10%) does not allow for an evaluation of subtle molar enthalpic differences between homologs from variations in bond energies. The specific enthalpies of decomposition of the Sn compounds can be predicted to be ΔH_{dec} [kJ g^{-1}] = –0.83(±3) (**9**), –1.91(±6) (**10**), –1.81(±6) (**11**), –1.90(±6) (**12**). However, the available data on the Si, Ge and Sn compounds reveals a strong correlation (R^2 = 0.98) between the nitrogen content n(N) × 14.01 / M_r and the specific enthalpy of decomposition. By analysis of a series of covalent polyazides, each N_3 ligand is estimated to contribute –208(±7) kJ mol^{-1} (on average) to the molar enthalpy of decomposition.

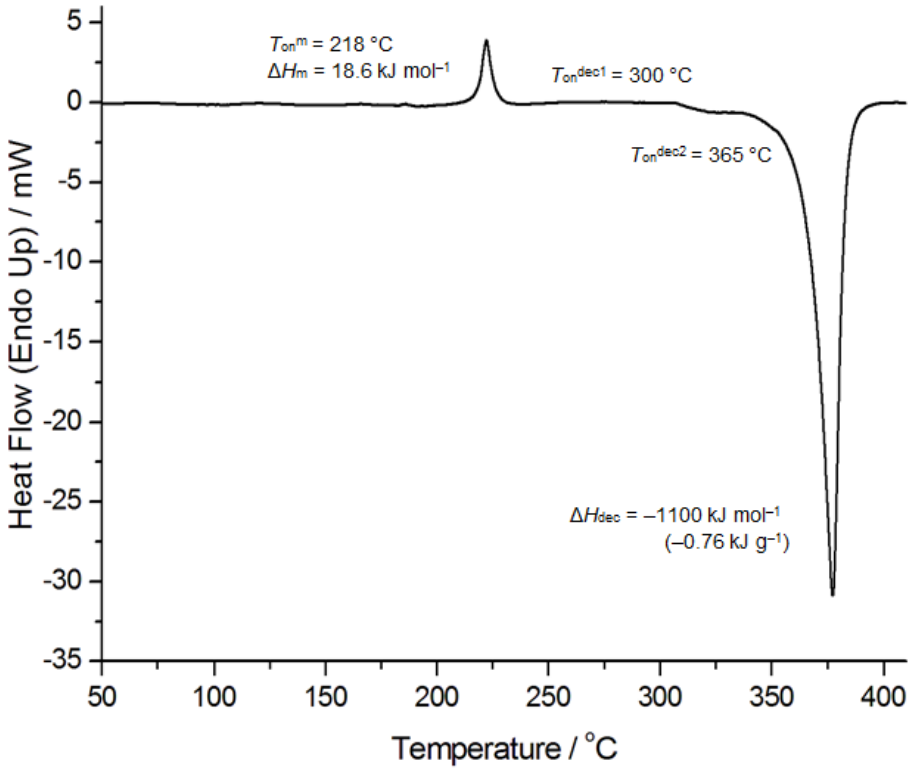

Figure 3.14. Differential scanning calorimetry trace of $(PPN)_2[Sn(N_3)_6]$ (**9**) showing melting at T_{on}^{m} = 218 °C and a 2 step exothermic decomposition which begins at T_{on}^{dec1} = 300 °C, and T_{on}^{dec2} = 365 °C with an overall enthalpy of decomposition of –1100 kJ mol^{-1} (–0.76 kJ g^{-1}).

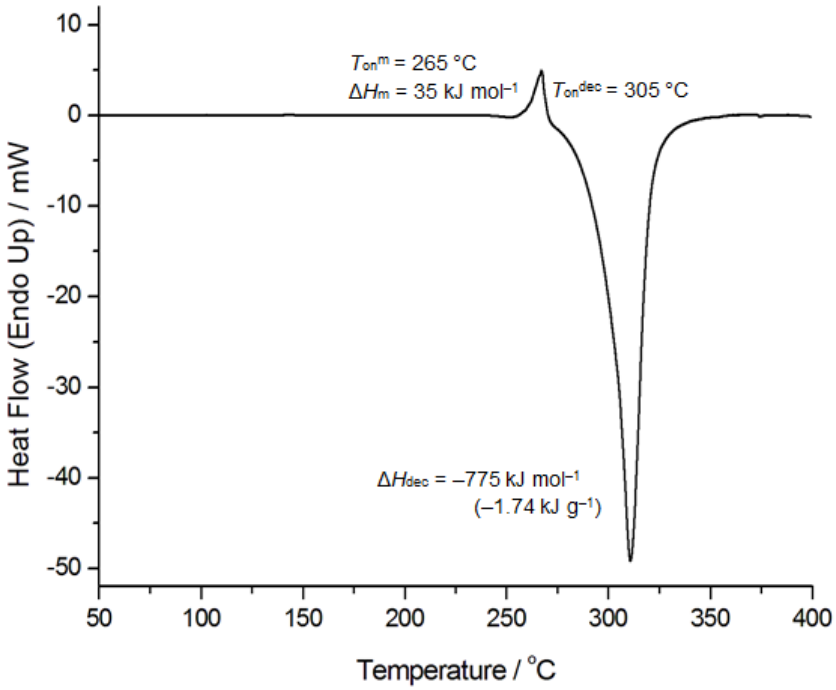

Figure 3.15. Differential scanning calorimetry trace of tetraazidobis(pyridine)tin (**12**). Heating rate 10 °C min^{-1}, nitrogen flow rate 20 ml min^{-1}.

3.3 Conclusions

The first neutral tin(IV) tetraazides with mono and bidentate pyridine based ligands have been prepared *via* ligand exchange from SnX_4 (X = F, Cl) and TMS–N_3/NaN_3. The seemingly insensitive tin azides constitute some of the most nitrogen-rich (41–44 wt%) compounds of tin, comparable with $Sn(N_3)_2$ itself,[54] and have been characterised by FTIR and multinuclear NMR spectroscopies, differential scanning calorimetry (DSC) and X-ray crystallography. The reaction of tin(IV) fluoride with trimethylsilyl azide has been shown to be an effective route to covalent tin azides using an appropriate polar coordinating solvent.[85] In the absence of a coordinating solvent or suitable ancillary ligands the N_3/F ligand exchange reaction produces a highly sensitive explosive covalent tin(IV) azide which is most likely $Sn(N_3)_{4-x}F_x$ where $0 < x < 2$. Dissolving this residue in an acetonitrile solution of 2,2'-bipyridine gives $Sn(N_3)_4$(bpy) (**10**) as the only detectable soluble species, though there is no direct evidence for the formation of thus far unknown tin tetraazide, $Sn(N_3)_4$. A new hexaazidostannate salt, $(PPN)_2[Sn(N_3)_6]$ (**9**), has been prepared and fully characterised including a detailed examination of its structure by single crystal XRD at low temperature. In initial structure solutions the thermal displacement ellipsoids of N_α and N_γ atoms were systematically larger than the N_β, but the adoption of a disorder model allowing for flexibility of N_3 ligand orientation significantly improved the structure quality. The absence of N_3/Cl substitutional disorder has been confirmed by elemental analysis. The tin azides investigated showed lower moisture sensitivity than their silicon and germanium counterparts, and remarkable thermal

stability (T_{on}^{dec} > 250 °C), particularly **12** with T_{on}^{dec} = 305 °C, which is comparable with lead azide itself. The preparation of $(PPN)_2[Sn(N_3)_6]$ enables the comparison of the effect of hydrogen bonding on polyazido complexes such as bis(guanidinium) hexaazidostannate (**3**), which represents a further step towards even more nitrogen-rich (68 wt%) tin compounds.

4. New syntheses for tin(II) azides, and investigation of their structural characteristics and thermal behaviour

Aims

I. Determine methods that are suitable for the synthesis of tin(II) azide and its derivatives

II. Determine whether simple pyridine-based ligands stabilise tin(II) azides as effectively as the typically large ancillary ligands employed previously

III. Investigate stability, reactivity, thermal behaviour and energy density of tin(II) azide derivatives

IV. Compare the structure and properties of tin(II) azides with related tin(IV) azides

V. Determine the structure of tin(II) azide

4.1 Introduction

The recent report detailing the first synthesis of tin diazide[54] has shown it to be a sensitive, explosive solid like the well-known heavier lead homologue, $Pb(N_3)_2$.[164] Lead diazide is a primary explosive, finding application as an initiator due to its sensitivity towards external stimuli, low solubility in water, hydrolytic and thermal stability. The search is ongoing for a lead azide replacement that would eliminate lead metal deposition at the point of use, avoid the need for inconvenient and hazardous disposal methods but deliver at least equivalent performance.[11,14] The sensitivity of covalent binary azides presents obstacles to their characterisation, meaning relatively few compounds have been studied crystallographically. The binary azides $As(N_3)_3$ and $Sb(N_3)_3$ are sufficiently volatile to be crystallised by careful sublimation, and their structures were determined by single crystal XRD,[192] and the solid-state structure of three polymorphs of $Zn(N_3)_2$ have been determined recently.[193] In order to study them relatively safely, new azido species are first prepared with ancillary ligands or incorporated into salt-like compounds. The common feature of the first reported tin(II) azides is the use of sterically demanding chelate ligands for stabilisation. The known compounds in this class (denoted **A**–**H**) are summarised below (Scheme 4.1 below).

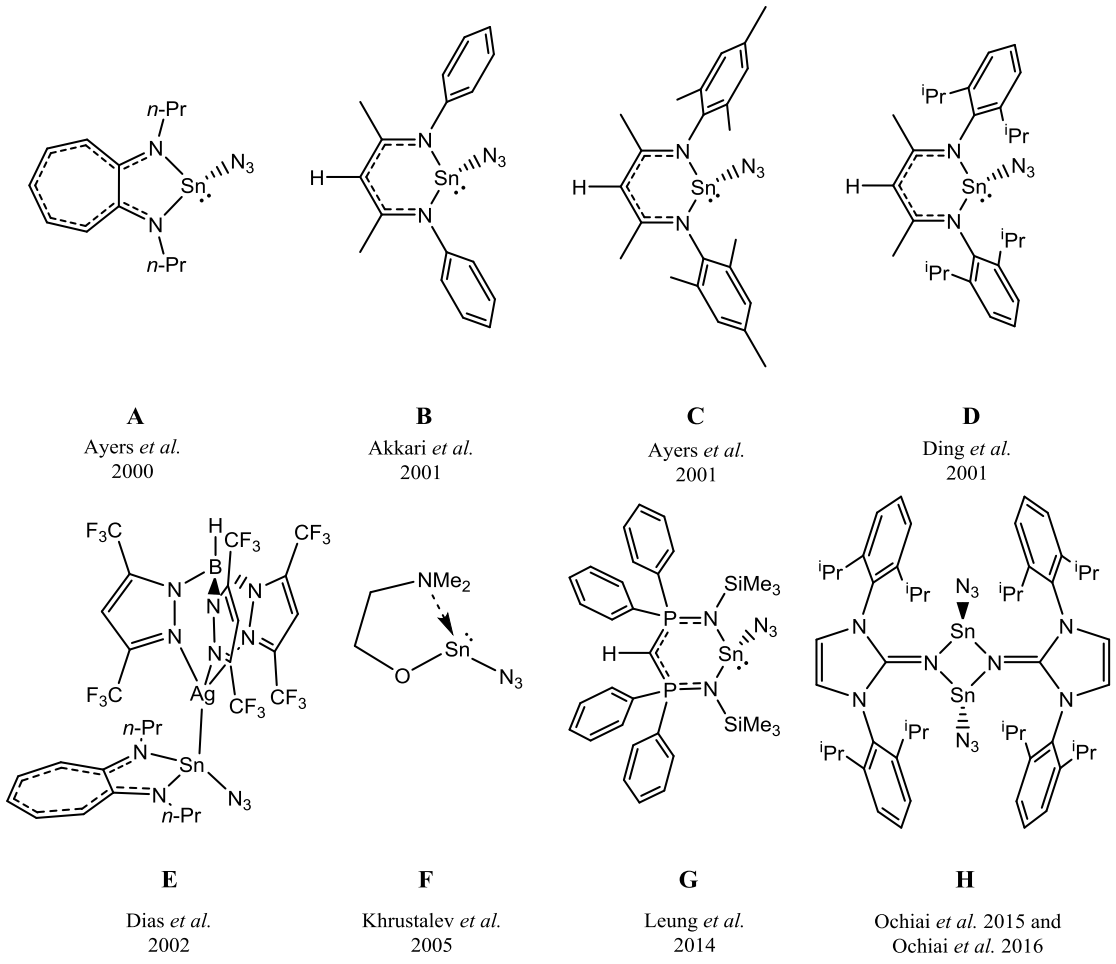

Scheme 4.1. The structures of all known neutral tin(II) azide complexes (**A**–**H**) in approximate order of publication.

The first such example of a tin(II) azide was {(*n*-Pr)$_2$ATI}SnN$_3$ (**A**)[194] using the rigid but not especially bulky troponiminate ligand, [(*n*-Pr)$_2$ATI]$^-$ = *N*-(*n*-propyl)-2-(*n*-propylamino)-troponiminate). Two years later, its 1 : 1 adduct with {HB(3,5-(CF$_3$)$_2$Pz)$_3$}Ag (denoted **E**),[195], where [HB(3,5-(CF$_3$)$_2$Pz)$_3$] = hydrotris(3,5-bis(trifluoromethyl)pyrazolyl)borate. Several more related tin(II) azides (**B**–**D**) were reported in the intervening period, which instead employed the bulkier 2,4-dimethyl-*N*,*N*′-diaryl-1,5-diazapentadienyl ligands, [(Ar)$_2$DAP]$^-$, including {(Ar)$_2$DAP}SnN$_3$ (**B**: Ar = Ph ;[196] **C**: Ar = 2,4,6-trimethylphenyl;[197] **D**: Ar = 2,6-diisopropyl-phenyl).[198] An exception to the trend of sterically demanding ligands is the dimeric azido(*N*,*N*-dimethylaminoethoxy)tin(II) (**F**),[199] which is instead stabilised by intermolecular Sn–O bridges. The bis(iminophosphoranyl)methanide complex {HC(PPh$_2$=NSiMe$_3$)$_2$SnN$_3$} (**G**) was synthesised as part of a reactivity study on the corresponding stannylene chloride.[200] The homoleptic complex triazidostannate [Sn(N$_3$)$_3$]$^-$ anion was recently synthesised for the first time, utilising the large weakly-coordinating tetraphenylphosphonium cation,[92] which has a similar effect to the bulky ligands, reducing the nitrogen content of the compound (21.6 %) and spacing out the energetic anions, preventing shock propagation and hence reducing sensitivity. Low valent main group elements often have a stereochemically active lone pair which influences the behaviour and coordination geometry. An elegant example is

the adduct {HB(3,5-$(CF_3)_2Pz)_3$}$AgSnN_3${(n-Pr)$_2$ATI}, which has an unsupported Ag–Sn bond *via* the lone pair on the tin atom rather than *via* the terminal nitrogen of the azide group as for azidoadamantane.[195] The coordination geometry of the tin(II) centre allows for weaker secondary interactions between adjacent units in a dimeric or polymeric fashion with suitable halide or pseudohalide ligands, the most recent of which is the dimeric $\{N_3Sn(NIPr)\}_2$ (**H**), where NIPr = bis(2,6-diisopropylphenyl)imidazolin-2-imido).[201,202] On the other hand there is the monomeric bis(iminophosphoranyl)methanide complex (**G**) in which the $SiMe_3$ groups provide sufficient steric hindrance to prevent any dimeric interaction.[200] During this work nitrogen-rich tin(II)- and tin(IV) polyazides have been prepared and characterised to better understand where the borderline is with respect to sensitivity and nitrogen content, and to study their salts with hydrogen bonding cations, and adduct formation with mono- and bidentate nitrogen bases.

4.2 Results and Discussion

4.2.1 Syntheses of tin(II) azides

It has been shown previously that tin(II) azides are accessible *via* azide-chloride exchange with sodium azide,[92,194,197] displacement of a dimethylaminoethoxy ligand by azidotrimethylsilane (TMS–N_3),[199] or even oxidation of Sn metal using silver azide.[54] The neutral binary azide $Sn(N_3)_2$ has been prepared previously through oxidation of Sn metal by AgN_3 in absolutely water-free ammonia at –40 °C for a period of 10 days.[54] The need for daily manipulation to restore the crust of AgN_3 on the walls of the reaction vessel to the solution could cause detonation of either highly sensitive AgN_3 or $Sn(N_3)_2$. The difficulties arising from the shock sensitivity are compounded by the requirement of low temperature, resulting in a slow reaction rate, and therefore requiring more manipulations. Evaporation of the ammonia solution yielded an amorphous tin azide with undefined ammonia content. During the course of this work a new, more convenient method has been developed for preparing tin(II) azide and derivatives thereof, *via* the reaction of trimethylsilyl azide (TMS–N_3) with tin(II) fluoride, with facile elimination of the volatile TMS–F (b.p. 15 °C). The strong enthalpic preference for Si–F bonds over relatively weak Sn–F bonds coupled with mild conditions allow for effective conversion on a shorter timescale. A multitude of transition metal and main group hetero- and homoleptic polyazides have been prepared from the reaction of their fluorides with trimethylsilyl azide, TMS–N_3 with elimination of trimethylsilyl fluoride, TMS–F. The volatility of both TMS–N_3 (b.p. 95–99 °C) and the TMS–F by-product (b.p. 15 °C) aids the separation of the target azido complex.

$Sn(N_3)_2$ adducts with pyridine (14) and 4-picoline (15), and a safer, more convenient method for preparation of $Sn(N_3)_2$ (16)

During the course of this work the most convenient route to tin azides was found to be the reaction of a slight excess of trimethylsilyl azide ($TMS–N_3$) with the corresponding tin fluoride, with facile elimination of the volatile TMS–F (b.p. 15 °C) under mild conditions. When the reactions were carried out in pyridine or 4-picoline the corresponding adduct of the per(azido) complexes were obtained. SnF_2 reacted much more readily than SnF_4 with $TMS–N_3$, which is perhaps unsurprising as the polymeric structure of SnF_4 renders it insoluble and relatively inert. The initial suspension of SnF_2 in pyridine/4-picoline became almost clear within half an hour, and *in-situ* FTIR spectroscopy showed the $TMS–N_3$ was almost fully depleted after 2 h, suggesting the azide/fluoride exchange was close to completion. After stirring at ambient temperature overnight, and filtration to remove any traces of insoluble material, the complexes $Sn(N_3)_2(L)_2$ (L = pyridine, **14**; L = 4-picoline, **15**) were readily crystallised by slow cooling of their respective saturated filtrate solutions to –19 °C. The melting point of 4-picoline is around 2 °C so occasionally the solution froze, but once thawed the solution was readily decanted from the crystalline $Sn(N_3)_2(pic)_2$.

Whilst investigating the solubility and reactivity of $Sn(N_3)_2(py)_2$ (**14**) it was found that addition of acetonitrile (or THF, Et_2O, CH_2Cl_2) to the crystals causes precipitation of the solvent-free $Sn(N_3)_2$ (**16**), evidenced by the absence of coordinated pyridine absorption bands in the FTIR spectrum of the solid (Figure 4.25). The new synthetic route has several advantages over the published procedure described above. Carrying out the reaction at 65 °C higher temperature, and using the pyridine-miscible azide transfer reagent, $TMS–N_3$, leads to a greatly improved reaction rate since silver azide only dissolves in ammonia after stirring for 24 h. The solid obtained by precipitation of $Sn(N_3)_2$ from solution is well-defined and crystalline, making it suitable for powder XRD, whereas amorphous material was obtained previously.

Guanidinium triazidostannate (17)

Guanidinium triazidostannate (**17**), $(G)[Sn(N_3)_3]$, can be prepared from a stoichiometric mixture of $Sn(N_3)_2$ and anhydrous guanidinium azide (**1**) in acetonitrile, or directly from SnF_2, $TMS–N_3$ and **1**. Upon stirring the solution became clearer during the first 15–20 minutes as **17** dissolves readily in acetonitrile. After stirring for a total of 2 h, and filtration to remove residual **1**, the highly moisture sensitive compound **17** was obtained as colourless needle crystals by slow cooling of a saturated solution to –19 °C overnight. During the crystal screening stage, use of anhydrous nujol (stored over Na) was essential to protect the crystals sufficiently until mounted in the nitrogen stream on the diffractometer. When ‘wet’ nujol was used the hydrolysis could be observed directly as bubbles in the nujol emanating from the

crystals (Figure 4.11). Further indication of the moisture sensitivity of **17** was given by exposure of a specimen solution (FTIR sample) to air over the course of an hour. The hydrazoic acid produced as a result of the hydrolysis oxidises the complex to the tin(IV) azide $(G)_2[Sn(N_3)_6]$ (**3**), which itself hydrolyses, albeit more slowly than the tin(II) azide **17**.

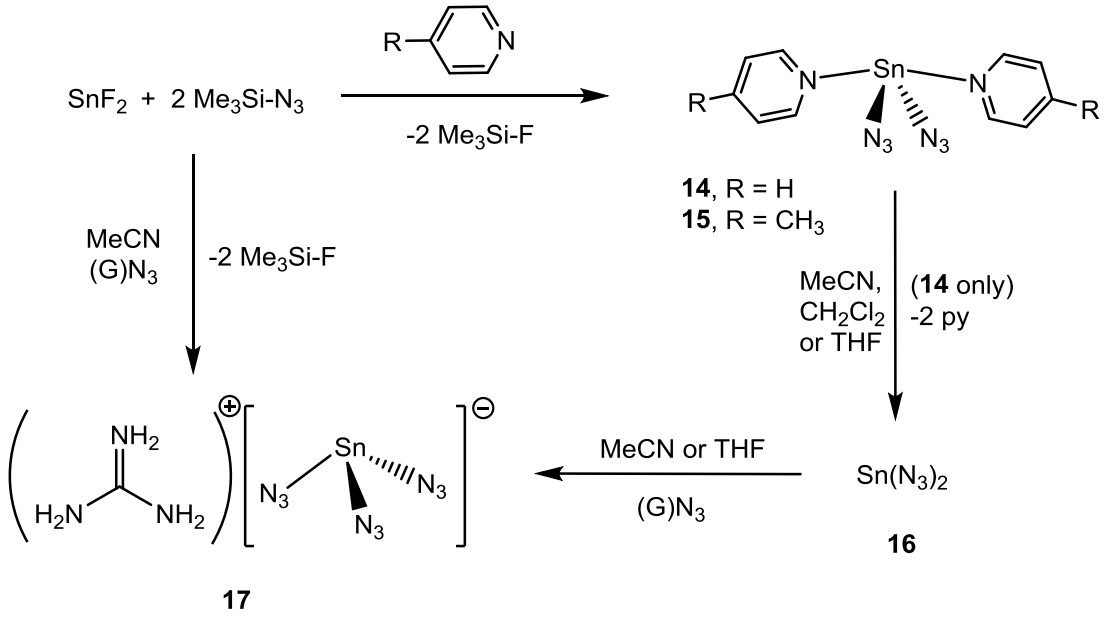

Scheme 4.2. Reaction scheme for the preparation of tin(II) azides **14–17**. G = guanidinium, $C(NH_2)_3^+$.

Attempted synthesis of aminoguanidinium triazidostannate (18)

The above procedure for the preparation of guanidinium salt **17** was applied in an attempt to prepare aminoguanidinium triazidostannate (**18**). After addition of TMS–N_3 to a suspension of SnF_2 and aminoguanidinium azide (**2**) in a molar ratio of 2.4 : 1 : 1.2 in acetonitrile the mixture became almost clear after 3 hours. The intense asymmetric stretching vibrations spanned the range 2090–2042 cm^{-1} in the solution FTIR spectrum, confirming the presence of coordinated azide(s) which appears in the correct range for triazidostannate, but the absorbance was too high (A_{max} > 2.5) to give further insight. The symmetric azide stretches at 1324 appeared at the same position as in **17** with absorbance values of 0.3–0.55. In combination with the broad N–H stretches at 3453, 3362, 3325, and 3281 cm^{-1}, and the C–N stretch at 1670 cm^{-1} strongly suggested the presence of **18** in solution. The high concentration of **18** meant a small but appreciable amount of the tin(IV) oxidation product was detectable as shoulders at 2112 and 1287 cm^{-1}. After filtration to remove the slight excess **2** the clear solution was concentrated and cooled to –19 °C overnight, giving a colourless microcrystalline solid but no suitable single crystals for XRD study. Comparison of the FTIR spectrum of the solid with a genuine sample of **17** combined with its air sensitivity suggested the presence of **18** and a trace of **2** either from hydrolysis or co-precipitated excess starting material.

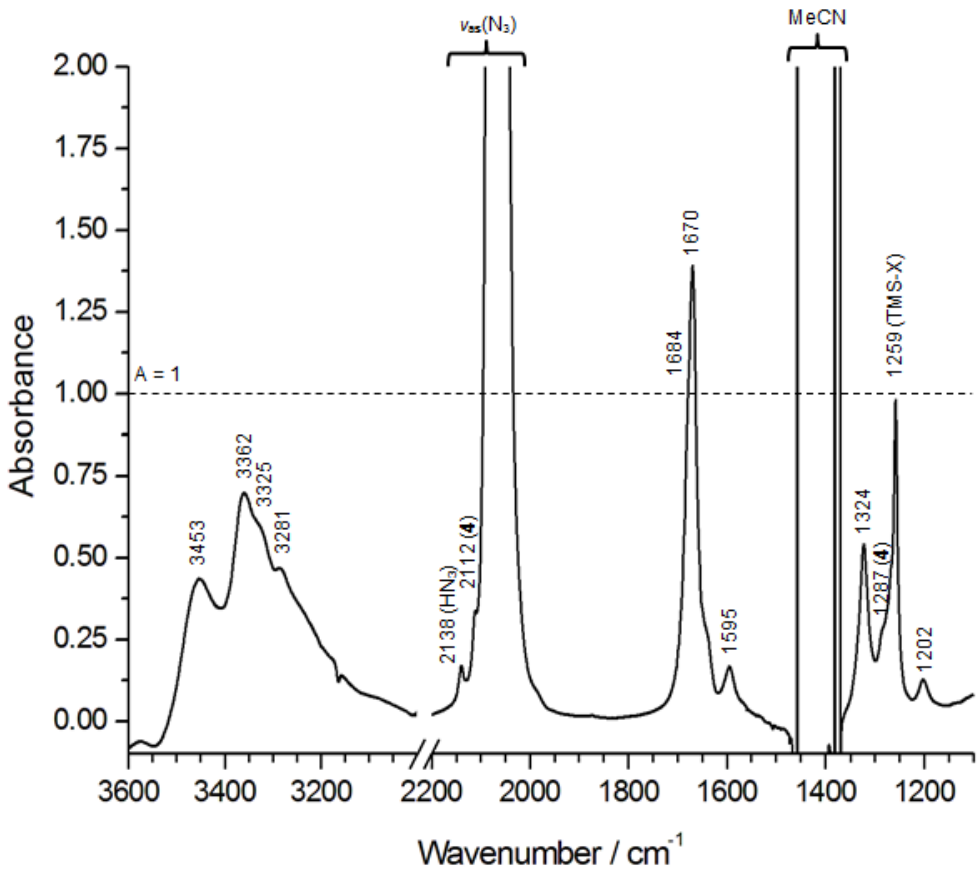

Figure 4.1. FTIR spectrum showing aminoguanidinium triazidostannate (**18**) in the acetonitrile reaction solution after reaction of SnF_2 with TMS–N_3 and aminoguanidinium azide (**2**). Spectral window 3000–2200 cm^{-1} omitted to allow expanded view. The absorbance of the asymmetric azide band is too high to determine the identity of the species present in solution, but the symmetric azide stretch at 1324 cm^{-1} appears to be consistent with that of $[Sn(N_3)_3]^-$ in **17**. Also visible are TMS–X (X = N_3, F) at 1258/1268 cm^{-1}, and traces of HN_3 (2139 cm^{-1}), and tin(IV) oxidation product bis(aminoguanidinium) hexaazidostannate (**4**) at 2112 cm^{-1} and 1287 cm^{-1}.

Reactivity of $SnCl_2$ towards NaN_3 and TMS–N_3

Tin dichloride, $SnCl_2$, has been used to prepare triazidostannate salts by reaction with a large excess of NaN_3 in the presence of $(PPh_4)N_3$ or $(PPN)N_3$ in THF.[92] In the absence of weakly coordinating cations, it was not clear whether sodium triazidostannate was stable with respect to dissociation into NaN_3 and $Sn(N_3)_2$. Addition of 20 equivalents of NaN_3 to a stirred THF solution of $SnCl_2$ resulted in a FTIR spectrum with absorption maxima at 2053 (shoulder), 2061 and 2083 cm^{-1}, and HN_3 was visible at 2131 cm^{-1}. The dominant feature of the spectrum is the asymmetric azide stretch at 2061 cm^{-1} which is very similar to the previously observed intermediate $(PPh_4)[Sn(N_3)Cl_2]$ at 2064 cm^{-1}. This suggests that the initial addition of NaN_3 to form $Na[Sn(N_3)Cl_2]$ is fast, but the rate of subsequent Cl/N_3 ligand exchange seems to be slower than the equivalent reaction of $(PPh_4)[Sn(N_3)Cl_2]$. This could mean a larger excess of NaN_3 is required or that preparation of sodium triazidostannate *via* $SnCl_2$ is not practical.

Sodium triazidostannate may be more readily accessible *via* $Sn(N_3)_2$ (**16**) where no ligand exchange is necessary.

When pyridine was used as solvent for the reaction of $SnCl_2$ with two successive batches of NaN_3 the complex $Sn(N_3)_2(py)_2$ (**14**) was obtained. After the first batch of NaN_3 the predominant species in solution seemed to be $SnCl(N_3)(py)_2$, which was subsequently converted into **14** by reaction with a second batch of NaN_3.

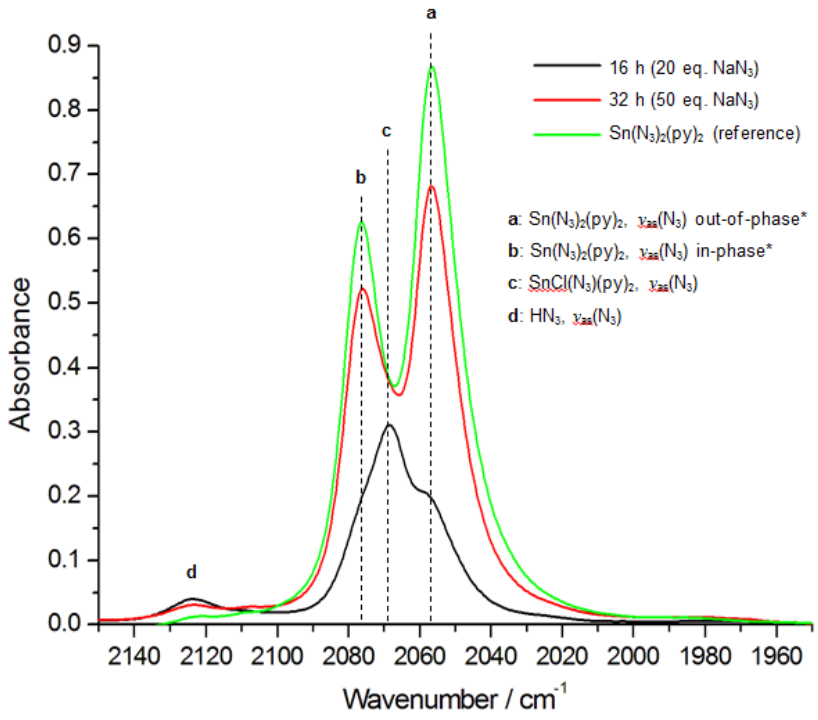

Figure 4.2. *In-situ* FTIR spectra from the reaction of $SnCl_2$ with NaN_3 in pyridine, compared to a reference spectrum of $Sn(N_3)_2(py)_2$. Black: Reaction solution after reaction of $SnCl_2$ with NaN_3 (20 eq.); red: after reaction with second batch of NaN_3 (30 eq.); green: reference spectrum of a genuine sample of $Sn(N_3)_2(py)_2$ (**14**) in pyridine prepared by *via* SnF_2. *Assignment of these bands to the in-phase and out-of-phase asymmetric stretches is only tentative in the absence of a computational investigation.

Addition of TMS–N_3 to a suspension of $SnCl_2$ in pyridine gave rise to a new absorption band at 2069 cm^{-1} in the solution FTIR spectrum, indicating some azide-chloride exchange. The single absorption band, and its positioning between the two $\nu_{as}(N_3)$ bands of **14** suggests it is the mono-azide $Sn(N_3)Cl(py)_2$. The relatively high concentration TMS–N_3 remaining in solution also suggests the ligand exchange has not gone to completion. The analogous reaction of $SnCl_2$ with trimethylsilyltetrazole in pyridine led to crystallisation of the mono-tetrazolato intermediate $Sn(N_4CH)Cl(py)_2$.[82]

4.2.2 Sensitivity and Physical Properties of Tin Diazide, $Sn(N_3)_2$ (16)

During loading of $Sn(N_3)_2$ into a capillary, contact of the Teflon-coated spatula on *ca.* 10 mg of the material in a sapphire mortar caused a violent detonation accompanied by a bright orange flash and loud sharp report, leaving a dull dark grey residue (Sn metal). This suggests the cause was electrostatic build-up rather than friction, so $Sn(N_3)_2$ should be considered very sensitive to ESD. On one occasion a 5 mg sample of $Sn(N_3)_2$ was carefully loaded into a flame-sealed Pasteur pipette and the sample sonicated to collect the material at the bottom. In the process of flame-sealing the top end, the residual material on the walls was sufficient to act as a fuse, propagating with a bright orange flash down the capillary causing detonation with a loud, sharp crack.

Figure 4.3. Deposited grey metallic residue on the mortar (top) and Teflon-coated spatula (bottom) after detonation of *ca.* 10 mg of $Sn(N_3)_2$ in the glovebox.

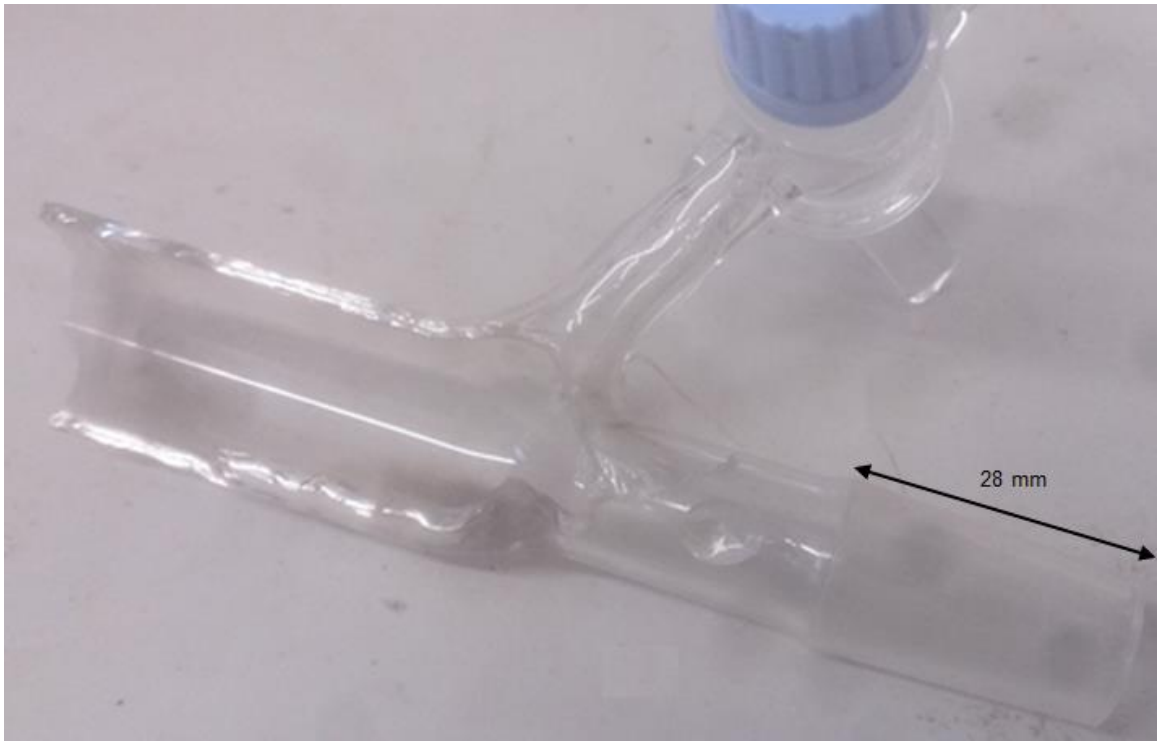

Figure 4.4. Metallic grey residue after the detonation of $Sn(N_3)_2$ (*ca*. 15–20 mg) in a Schlenk tube, caused by scratching the material with a metal spatula.

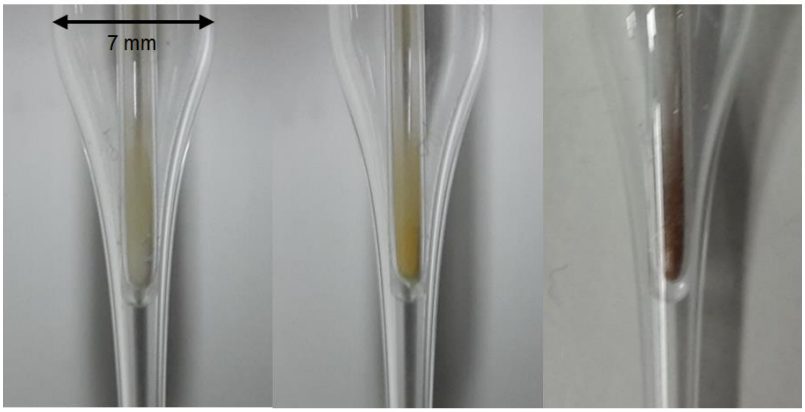

Figure 4.5. A series of photographs showing the effect of sunlight on $Sn(N_3)_2$ (**16**). *Left*: The inward-facing side of the capillary, showing the original white colour after 4 hours; *Centre*: The outward-facing side of the capillary turned yellow within 4 hours showing the selective discolouration of the side facing sunlight, and after 4 days the sample was pale pink-brown; *Right*: After 6 weeks the sample was red-brown in colour. A control sample stored under argon and protected from sunlight showed no discolouration.

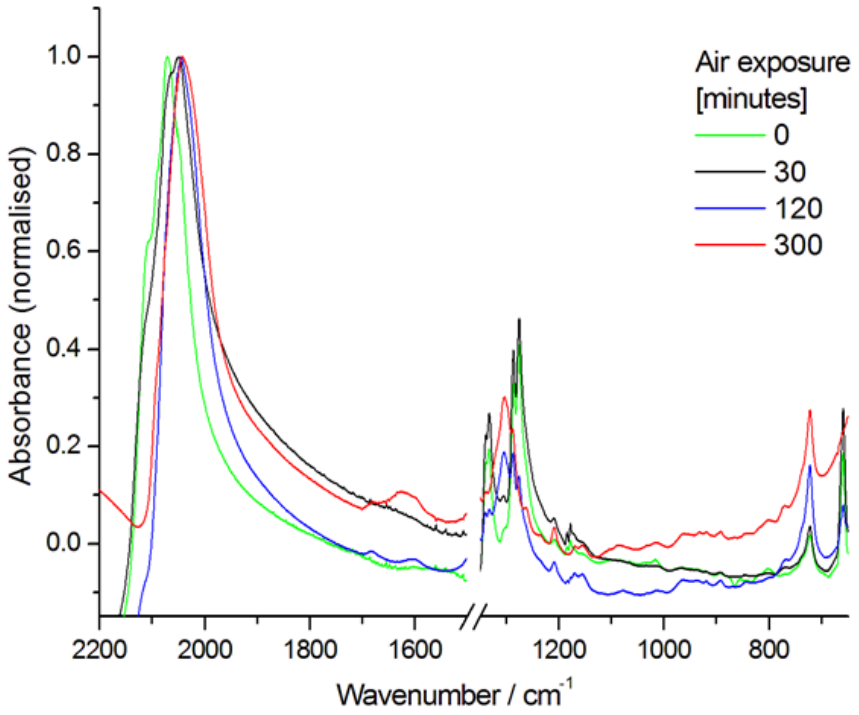

Figure 4.6. Series of normalised FTIR spectra showing the effect of exposing $Sn(N_3)_2$ to air over a period of 5 hours. The gradual shift to lower energy of the $\nu_{asym}(N_3)$ from 2070 to 2043 cm^{-1} is accompanied by a relative intensity decrease of around 1/3. The relatively weak, broad features around 3492 (not shown) and 1626 cm^{-1} could indicate the uptake of moisture by the material, and the emergence of weak, broad bands at 963 and 770 cm^{-1} is likely to be due to Sn–O species formed from oxidation, for example $(N_3)_2Sn(\mu\text{–}O)_2Sn(N_3)_2$, by comparison with the assigned spectrum of SnO_2.[203] The absorbance of the $\nu_{sym}(N_3)$ of $Sn(N_3)_2$ at 1339, 1332, 1286, and 1276 cm^{-1} have almost completely disappeared, and the emergence of a broad feature at 1303 cm^{-1} (and shoulder at 1297 cm^{-1}) seems to correspond to the new azide-containing species.

4.2.3 Single crystal XRD of Sn(II) azides

Crystal structure of $Sn(N_3)_2(py)_2$ (14)

In this case, twin refinement resulted in a modest improvement of the overall structure solution quality and decreased R_1 from 6 % to 4.5 %. The complex has a see-saw structure with the two azide groups occupying *cis* 'equatorial' sites and the pyridine ligands occupying the 'axial' positions. The angle between the opposite pyridine ligands is 153.14(16)°, and all *cis*-N–Sn–N angles are between 79.2(2)–82.5(2)°, showing the influence of the Sn(II) lone pair. One unusual feature is the absence of a dimeric (Sn–N_α···Sn') interaction between adjacent Sn centres, which has observed in other tin(II) azides whether sterically hindered or not. These secondary interactions are also observed in other coordinatively unsaturated polyazides such as $[Te(N_3)_5]^-$.[64] The shortest non-bonded Sn···N_α distance is 3.80 Å, which is considerably longer than other tin(II) azides (Table 4.1 below).

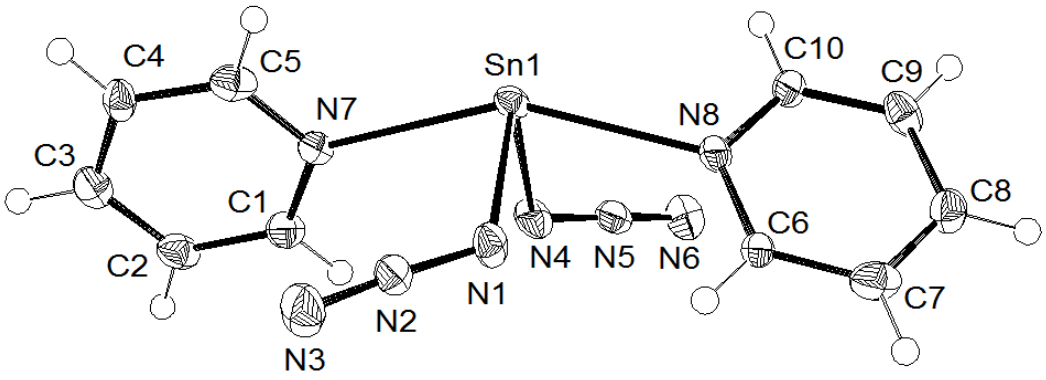

Figure 4.7. ORTEP drawing of the asymmetric unit in the molecular structure of $Sn(N_3)_2(py)_2$ at 100 K. Thermal ellipsoids at the 50 % probability level, and hydrogen atoms represented by spheres of radius 0.15 Å. Monoclinic ($P2_1/c$, Z = 4), a = 9.9291(4) Å, b = 7.8096(3) Å, c = 17.4056(7) Å, β = 97.7471(19)°, V = 1337.35(9) Å^3, R_1 = 0.0454. Selected bond lengths [Å] and angles [°]: Sn1–N1 2.178(5), Sn1–N4 2.195(6), Sn1–N7 2.468(5), Sn1–N8 2.472(5), N1–N2 1.216(8), N2–N3 1.139(8), N4–N5 1.209(8), N5–N6 1.143(9); N1–Sn1–N4 92.0(2), N7–Sn1–N8 153.14(16). Torsion angle between calculated (LS) planes of pyridine rings is 71.75°.

The absence of a strong interaction such as this could explain the lability of pyridine under vacuum or by addition of virtually any other solvent (e.g. MeCN, THF, Et_2O, CH_2Cl_2) in contrast to the analogous 4-picoline complex, which is stable under dynamic vacuum at RT. The shortest Sn···Sn distance is 3.750 Å, which is relatively short compared to the structures of **15**, **17**, and $(PPh_4)[Sn(N_3)_3]$.[92] The face of one of the pyridine ligands is oriented directly at the Sn atom at a centroid–Sn distance 3.618 Å (weak lone-pair-π interaction) which is shorter than the sum of vdW radii for tin (2.42 Å) and carbon (1.77 Å). There are various weak C–H···N interactions between pyridine protons and azide ligands with distances in the range 3.36–3.50 Å and angles between 128–159°. There are a few similar structures of similar azide complexes of other elements in the literature including $Cu(N_3)_2(py)_2$[204] and $Zn(N_3)_2(py)_2$,[205] though their geometries are different owing to the stereochemically active lone pair on Sn(II). The copper complex has higher symmetry, octahedral geometry with a 1,1-bridging azido group and a weak 1,3-bridging interaction (total 3 Cu with distances approximately 2.0, 2.5, and 2.75 Å; r_{vdW}(Cu) = 2.38 Å, r_{vdW}(N) = 1.66 Å).[188] The bridging azide group seems to have smaller ΔNN than the azide group which is only coordinated to one copper, which shows the influence of the bonding environment on the ionicity of the azido ligand. The azide groups are mutually *trans* and roughly in the plane perpendicular to the pyridine–Cu–pyridine axis. The $Zn(N_3)_2(py)_2$ complex is tetrahedrally coordinated with less asymmetry in the azide NN distances. $SnBr_2(py)_2$ forms an infinite network of bonded and non-bonded Sn···Br contacts in 3 dimensions.[206] The coordinative Sn–N bond to pyridine in **14** is slightly shorter at 2.468(5)–2.472(5) Å than the equivalent Sn–N bond in $SnBr_2(py)_2$ at 2.557(4) Å (200 K).

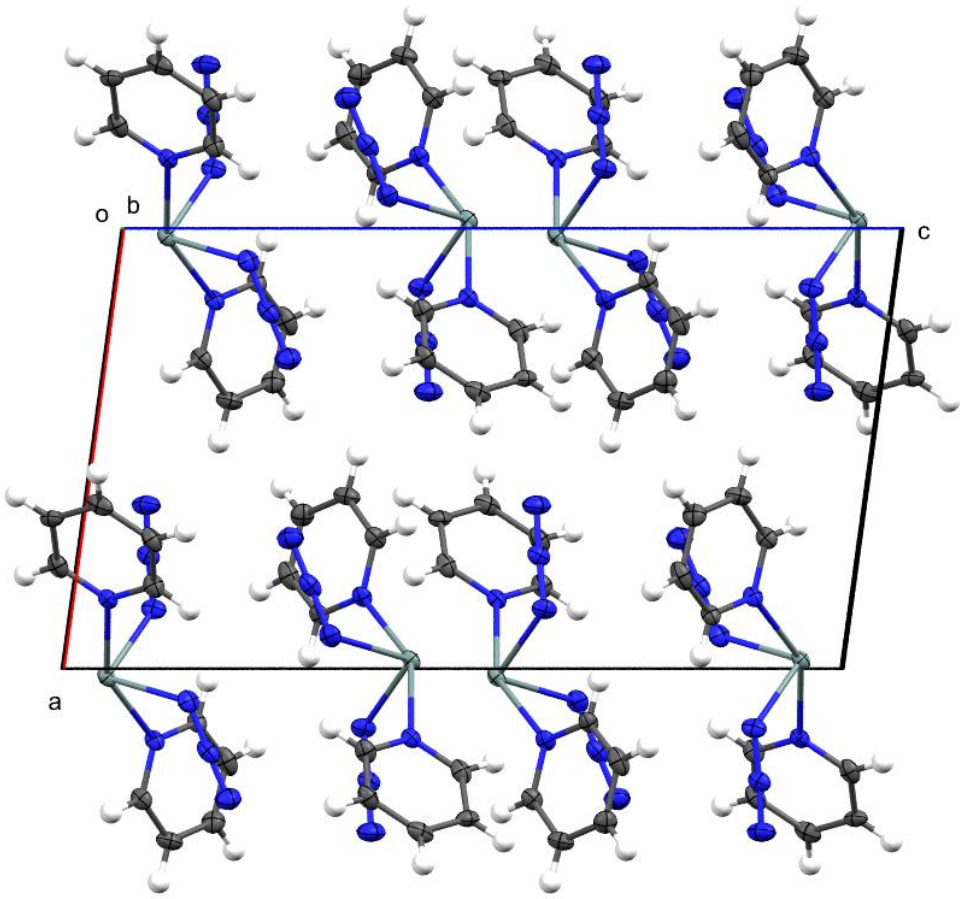

Figure 4.8. Unit cell of $Sn(N_3)_2(py)_2$ (**14**) viewed along the *b*-axis, with ellipsoids at the 50 % probability level.

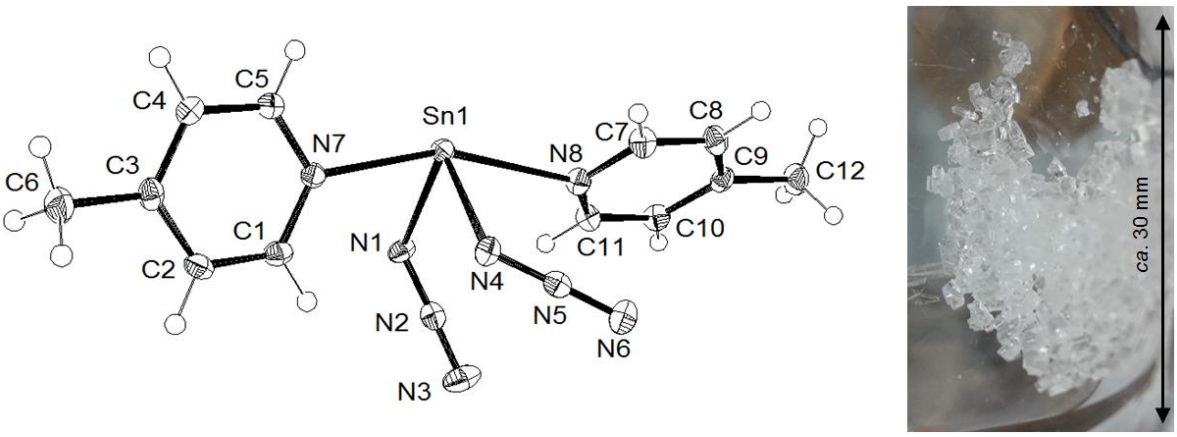

Figure 4.9. ORTEP diagram showing the asymmetric unit of $Sn(N_3)_2(pic)_2$ at 100 K, ellipsoids at 50 % probability, and hydrogen atoms represented by spheres of radius 0.15 Å. Inset: photograph of crystalline **15**. Triclinic ($P\bar{1}$, Z = 2), a = 9.1912(2) Å, b = 9.3972(2) Å, c = 10.0132(2) Å, α = 115.8848(13)°, β = 99.0170(13)°, γ = 90.6836(13)°, V = 765.32(3) Å^3, R_1 = 0.0202. Selected bond lengths [Å] and angles [°]: Sn1–N1 2.1992(17), N1–N2 1.213(2), N2–N3 1.145(2), Sn1–N4 2.2396(17), N4–N5 1.210(2), N5–N6 1.154(2), Sn1–N7 2.4203(16), Sn1–N8 2.5858(17); Sn1–N1–N2 119.45(13), N1–N2–N3 178.1(2), Sn1–N4–N5 122.36(13), N4–N5–N6 176.7(2), N1–Sn1–N4 86.53(6), N7–Sn1–N8 158.90(5).

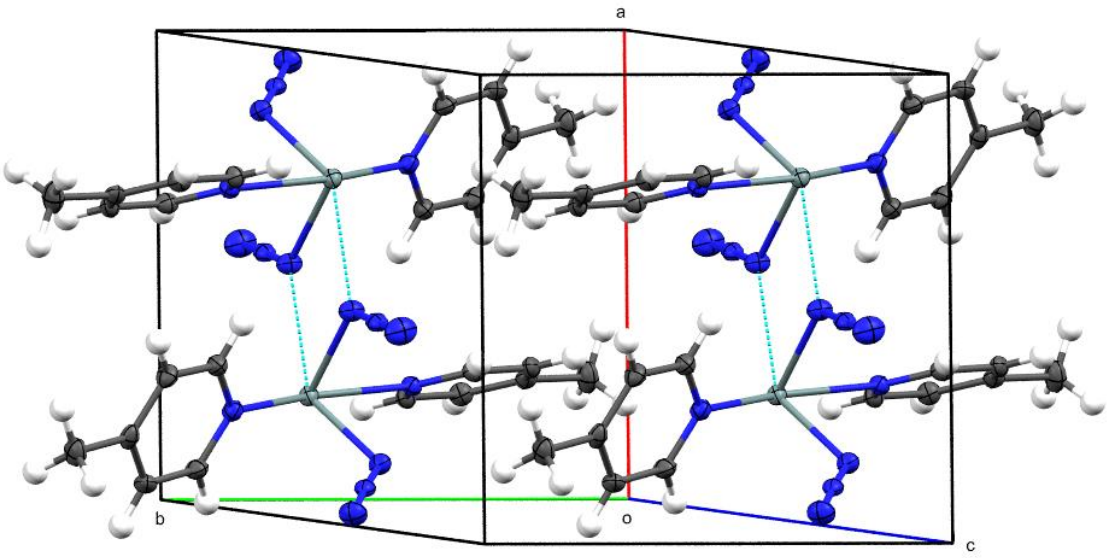

Figure 4.10. Unit cell packing of $Sn(N_3)_2(pic)_2$ (**15**) showing the 'dimeric' interaction (dashed blue lines) between two neighbouring Sn–N_α units.

Guanidinium triazidostannate (17)

Compound **17** is soluble in CH_3CN and THF, and completely insoluble in CH_2Cl_2, which is qualitatively similar to $(G)_2[Sn(N_3)_6]$ (**3**) solubility, except the latter is *highly* soluble in CH_3CN and THF. A few crystals suitable for XRD were transferred to a microscope slide and placed under nujol, and inspected under a microscope equipped with camera. Gas evolution (presumably HN_3, see Figure 4.11 below) from the crystals was observed in the form of bubbles emanating throughout the nujol. Several crystals were mounted on the goniometer but short exposure still images showed the crystals had decomposed. A second batch of crystals was examined under anhydrous nujol in the glovebox, from which no HN_3 bubbles were observed during crystal selection.

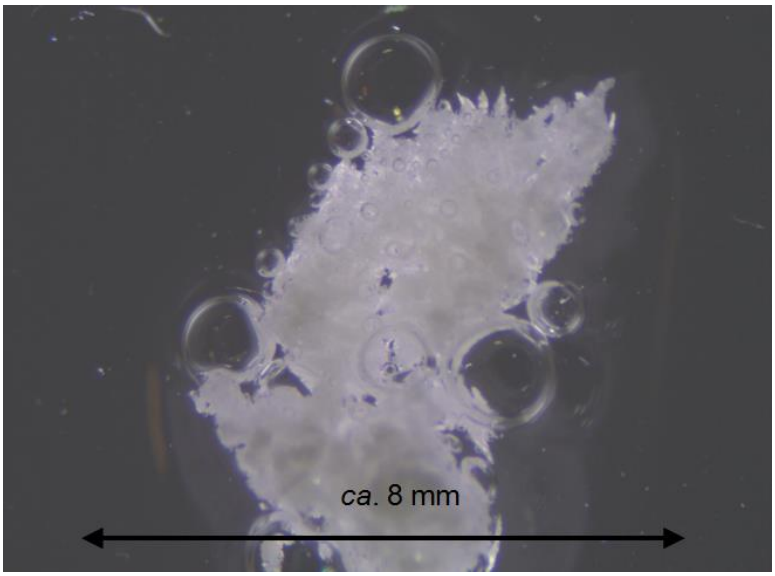

Figure 4.11. Still image captured of guanidinium triazidostannate (**17**) crystals under a microscope showing evolution of HN_3 due to hydrolysis, which was caused by 'wet' nujol. Scale of the image is an estimate only.

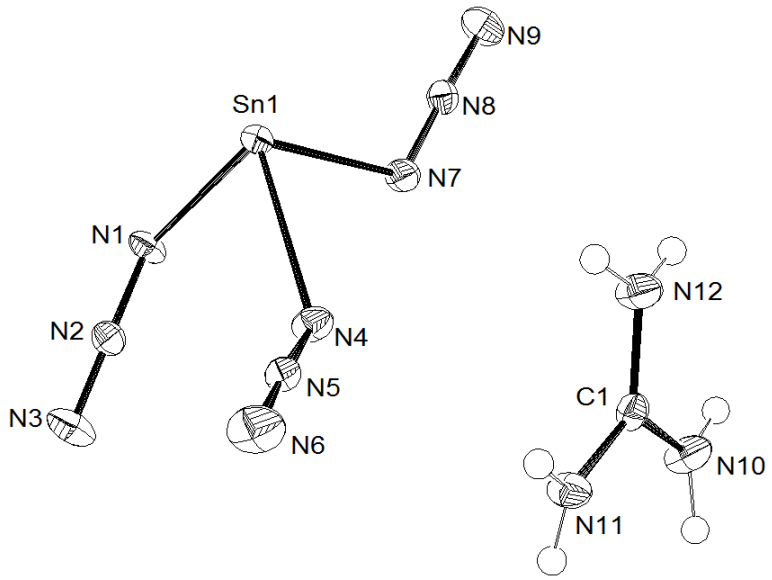

Figure 4.12. ORTEP drawing of the asymmetric unit in the molecular structure of **17** at 100 K with displacement ellipsoids at the 50 % probability level, and hydrogen atoms represented by spheres of radius 0.15 Å. Monoclinic (*C*2/*c*, *Z* = 8), *a* = 18.8171(6) Å, *b* = 7.1260(2) Å, *c* = 13.9984(4) Å, *β* = 95.1374(18)°, *V* = 1869.51(10) Å^3, R_1 = 0.0180. Selected bond lengths [Å] and angles [°]: Sn1–N1 2.2380(19), N1–N2 1.206(3), N2–N3 1.143(3), Sn1–N4 2.2736(19), N4–N5 1.198(3), N5–N6 1.156(3), Sn1–N7 2.2142(19), N7–N8 1.208(3), N8–N9 1.150(3); Sn1–N1–N2 118.28(15), N1–N2–N3 179.1(3), Sn1–N4–N5 126.61(16), N4–N5–N6 177.5, Sn1–N7–N8 118.27(15), N7–N8–N9 178.0(2), N1–Sn1–N4 83.00(7), N4–Sn1–N7 81.98(7), N1–Sn1–N7 88.77(7).

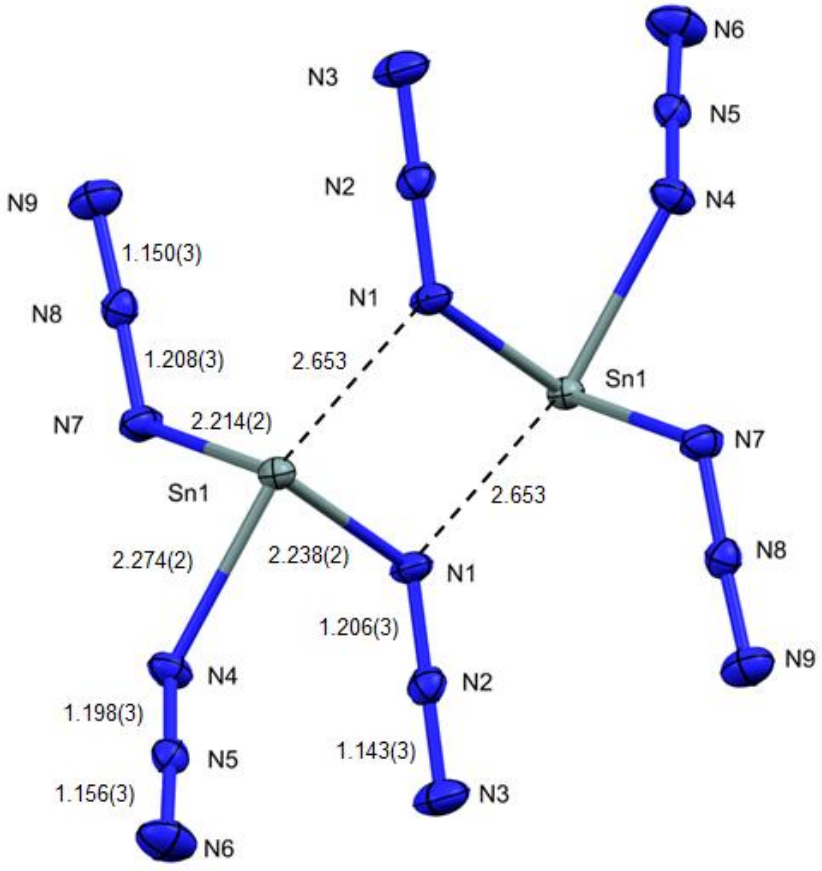

Figure 4.13. ORTEP diagram showing the dimeric interaction between pairs of $[Sn(N_3)_3]^-$ units the in the molecular structure of guanidinium triazidostannate (**17**).

In the crystal structures of both triazidostannate salts, and **15** the Sn–N_α bond opposite the bridging $\mu_{1,1}(N_3)$ is the longest by 3.6(4) pm (guanidinium), 5.5(4) pm (PPh_4), and 3.5(4) pm (**15**). In both **15** and **17** the same azido ligand has the shortest ΔNN parameter which would be consistent with a more ionic bonding mode. In $(PPh_4)[Sn(N_3)_3]$ however the disorder affecting the bridging azido ligand limits the precision and the usefulness of any comparison. The two azido ligands in $(PPh_4)[Sn(N_3)_3]$ not affected by disorder seem to have indistinguishable ΔNN distances despite one having a longer Sn–N bond.

Table 4.1. Comparison of $[Sn(N_3)_3]^-$ geometry in the structures of (**17**) and $(PPh_4)[Sn(N_3)_3]$[92] to assess whether there are any discernible effects due to hydrogen bonding. The geometries of azido ligands in **15** are shown to compare the effect of the complex charge, and bridging azido ligand ($\mu_{1,1}(N_3)$) interactions.

	$(PPh_4)[Sn(N_3)_3]$ [92]			$(G)[Sn(N_3)_3]$ (**17**)			$Sn(N_3)_2(pic)_2$ (**15**)	
	$\mu_{1,1}(N_3)$	opp.[a]	adj.[b]	$\mu_{1,1}(N_3)$	opp.[a]	adj.[b]	$\mu_{1,1}(N_3)$	opp.[a]
Sn–N_α [Å]	2.207(3)	2.262(3)	2.193(3)	2.238(2)	2.274(2)	2.214(2)	2.199(2)	2.234(2)
N_α–N_β [Å]	1.189(7)[c]	1.203(4)	1.200(5)	1.206(3)	1.198(3)	1.208(3)	1.213(2)	1.210(2)
N_β–N_γ [Å]	1.163(8)[c]	1.148(5)	1.143(5)	1.143(3)	1.156(3)	1.150(3)	1.145(2)	1.154(2)
ΔNN [Å]	0.026(11)[c]	0.055(6)	0.057(7)	0.063(4)	0.042(4)	0.058(4)	0.068(3)	0.056(3)
Sn–N–N [°]	124(1)[c]	123.6(3)	119.4(2)	118.3(2)	126.6(2)	118.3(2)	119.5(1)	122.4(1)
N–N–N [°]	177(2)[c]	177.5(4)	177.5(4)	179.1(3)	177.5(2)	178.0(2)	178.1(2)	176.7(2)

[a] N_3 ligand which is directly opposite the short Sn–N_α bridging interaction; [b] N_3 ligand adjacent to the bridging interaction; [c] Based on average of two disordered components.

In the crystal structure of **17**, Guanidinium cations are stacked directly above one another with staggered alternating orientation, and a C···C separation of only 3.288 Å. This non-bonded contact is within the sum of the van der Waals radii ($2 \times r_{vdW}(C) = 3.54$ Å) despite having like charges. There are two shorter Sn···N_γ contacts (3.269 Å opposite N7 with angle 157.31°, 3.368 opposite N1 with angle 158.53°) than in the (PPh_4) salt. The next closest Sn···N_γ contact is 3.648 Å (N6···Sn1 roughly where the lone pair sits). With the bulkier PPh_4 cation there is only one Sn···N_γ contact, and the coordination site equivalent to the second Sn···N_γ contact in **17** is occupied by a phenyl ring whose centroid is 4.122 Å from Sn1 (i.e. around the sum of the vdW radii for Sn–C = 2.42 + 1.77 = 4.19 Å). The graph sets formed by hydrogen bonds between the guanidinium cation and triazidostannate anion are qualitatively similar to those in

the crystal structure of bis(guanidinium) hexaazidostannate. All protons are involved in a total of seven hydrogen bonds in either R1,2(6) or R2,2(7) graph sets, and a single D motif.

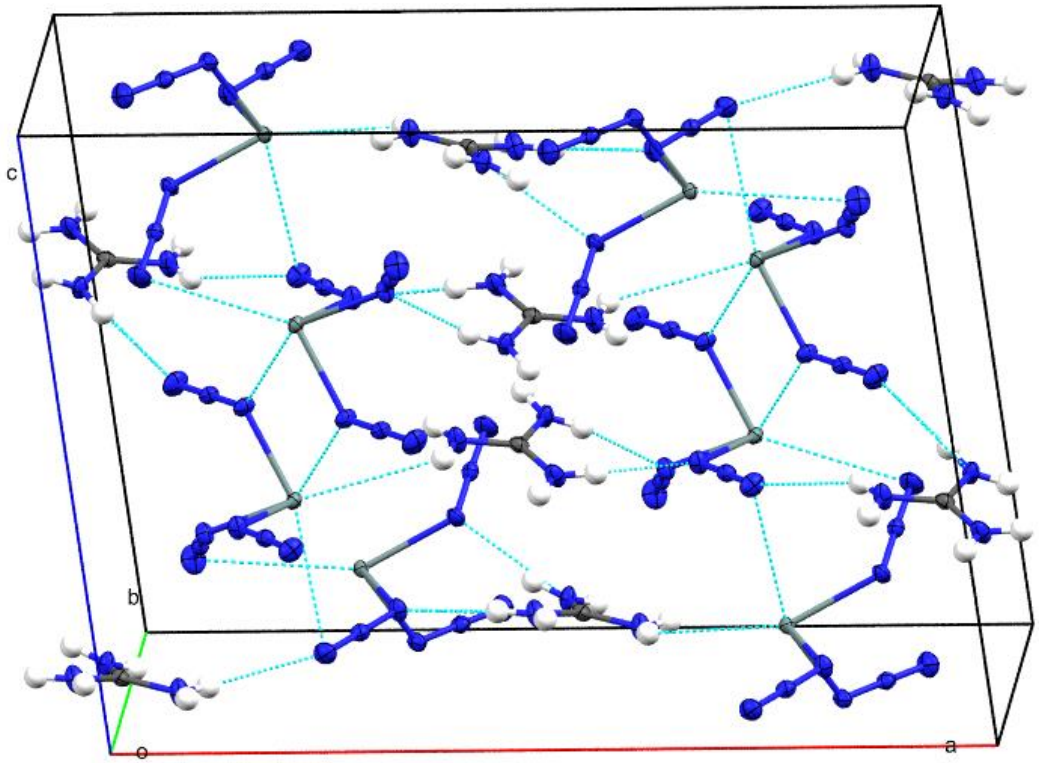

Figure 4.14. ORTEP drawing showing the unit cell packing and intermolecular contacts shorter than the vdW radii sum (including hydrogen bonds and the 'dimeric' interaction) in the molecular structure of guanidinium triazidostannate (**17**) at 100 K. Thermal ellipsoids are at the 50 % probability level.

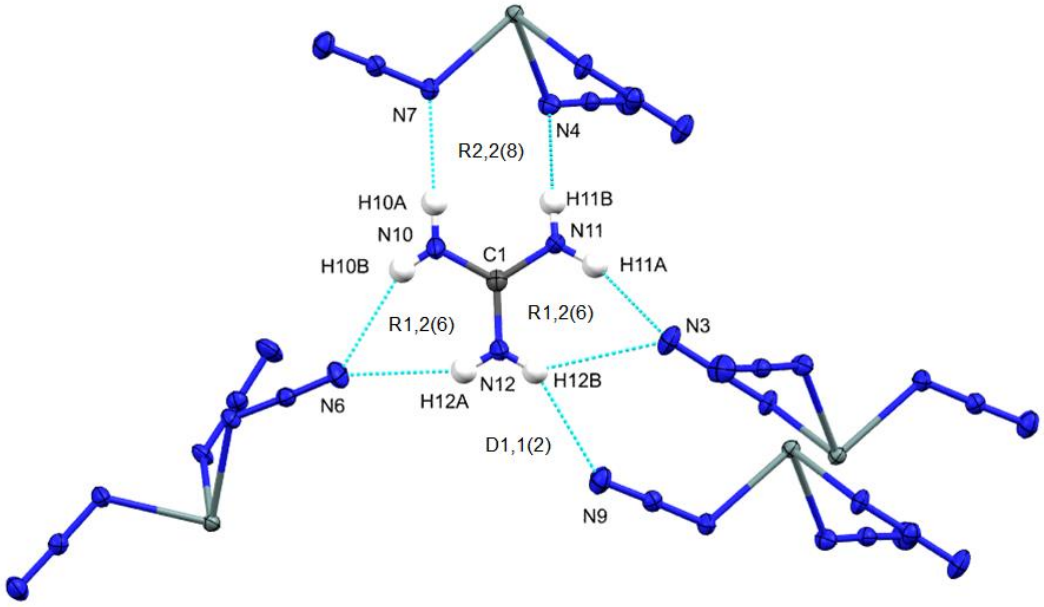

Figure 4.15. ORTEP diagram showing the graph sets assigned to hydrogen bonds in the structure of guanidinium triazidostannate (**17**).

Table 4.2. Hydrogen bond geometries in the crystal structure of guanidinium triazidostannate (**17**) at 100 K.

#	D–H	A	D–H [Å]	*d*(D···A) [Å]	*d*(H···A) [Å]	DHA [°]
1	N10–H10A	$N7^{ii}$	0.86(3)	3.040(3)	2.18(3)	178(3)
2	N10–H10B	$N6^{iv}$	0.76(3)	3.089(3)	2.39(3)	152(3)
3	N11–H11A	$N3^{i}$	0.86(3)	2.991(3)	2.18(3)	157(2)
4	N11–H11B	$N4^{ii}$	0.84(3)	2.961(3)	2.14(3)	168(3)
5	N12–H12A	$N6^{iv}$	0.78(3)	3.152(3)	2.47(3)	148(3)
6	N12–H12B	$N3^{i}$	0.88(3)	3.321(3)	2.75(3)	129(3)
7	N12–H12B	$N9^{iii}$	0.81(3)	3.315(3)	2.60(3)	149(2)

Symmetry codes: i) [x, –y, z+1/2], ii) [–x+1, y, –z+3/2], iii) [–x+1/2, y–1/2, –z+3/2], iv) [x, y+1, z]; First level graph sets are D1,1(2) for all hydrogen bonds in this structure.

The hydrogen bonds in the structure of **17** form a similar pattern to those of cation 2 in the structure of bis(guanidinium) hexaazidostannate (**3**), except that the close proximity of the fourth $[Sn(N_3)_3]^-$ ion to the guanidinium cation that forms the D1,1(2) motif causes one of the R1,2(6) hydrogen bonds to be longer (see Figure 4.15 above).

Table 4.3. Comparison of the closest non-bonded Sn···N contacts and Sn···Sn distances in the crystal structures **14**, **15**, and **17** compared to tin(II) azides in the literature.

Compound	Sn···N_α [Å] [a]	Sn···N_γ [Å] [b]	Sn···Sn [Å] [c]	T [K]
$(PPh_4)[Sn(N_3)_3]$ [d]	2.673	3.568	4.049	100
$(G)[Sn(N_3)_3]$ (**17**)	2.653	3.269, 3.368	4.068	100
$Sn(N_3)_2(py)_2$ (**14**)	3.799	-	3.750	100
$Sn(N_3)_2(pic)_2$ (**15**)	2.826, 3.694 [e]	3.551	4.271	100
$\{(Mes)_2DAP\}SnN_3$ [f]	2.91	N/A	N/A	228(3)
$\{(n\text{-}Pr)_2ATI\}SnN_3$ [g]	2.87	N/A	N/A	198
$\{N_3Sn(NIPr)\}_2$ [h]	2.178(3)/ 2.194(3)	3.724 [e]	3.411	150(2)

[a] 'dimeric' interaction; [b] closest terminal azide contact(s); [c] Sn–Sn distance; [d] ref. [92]; [e] Next closest contact probably dictated by packing rather than any specific 'dimeric' interaction; [f] ref. [197]; [g] ref. [194]; [h] ref. [201,202], bridges are formed *via* the ancillary ligand rather than the azide.

The azide group involved in the dimeric interaction in **15** has a slightly shorter Sn–N_α (2.1992(17) Å) and N_β–N_γ bond (1.145(2) Å) than the other {Sn–N_α = 2.2396(17), N_β–N_γ = 1.154(2)}, yet the N_α–N_β bonds are indistinguishable at 1.213(2) and 1.210(2) Å respectively. In the structures of both triazidostannates (**17**) and $(PPh_4)[Sn(N_3)_3]$, the longest Sn–N_α bond is directly opposite the shortest Sn···N_α interanionic contact. This bridging 'dimer' interaction also occurs in $\{(Mes)_2DAP\}SnN_3$[197] at a longer distance of 2.91 Å (T = 228(3) K for data collection). The complex $\{N_3Sn(NIPr)\}_2$ has by far the shortest interactions of 2.178–2.194(3) Å (T = 150(2) K for data collection) between adjacent Sn–N units as the interaction is a 'partially dative' bond between the ancillary ligand and the tin centres.[201,202]

Table 4.4. Comparison of the azido ligand geometries in the crystal structures **14**, **15**, and **17** compared to tin(II) azides in the literature.

Compound	Sn–N_α [Å] [a]	N_α–N_β [Å] [a]	N_β–N_γ [Å] [a]	ΔNN [Å]	T [K]
$(PPh_4)[Sn(N_3)_3]$ [b]	2.221(5)	1.197(8)	1.151(9)	0.046(12)	100
$(G)[Sn(N_3)_3]$ (**17**)	2.242(3)	1.204(5)	1.150(5)	0.054(7)	100
$Sn(N_3)_2(py)_2$ (**14**)	2.187(8)	1.213(11)	1.141(12)	0.071(17)	100
$Sn(N_3)_2(pic)_2$ (**15**)	2.219(2)	1.212(3)	1.150(3)	0.062(4)	100
$\{(Mes)_2DAP\}SnN_3$ [c]	2.198(5)	1.208(8)	1.109(8)	0.099(11)	228(3)
$\{(n\text{-}Pr)_2ATI\}SnN_3$ [d]	2.253(4)	1.188(5)/ 1.105(6)	1.156(6)/ 1.177(6)	0.032(8)/ –0.072(8)	198
$\{L_3Ag\}SnN_3\{(n\text{-}Pr)_2ATI\}$ [d]	2.157(4)	1.116(5)	1.186(6)	–0.070(8)	208(2)
$\{N_3\text{–}Sn\text{–}OCH_2CH_2NMe_2\}_2$ [e]	2.220(5)	1.214(7)	1.149(8)	0.065(11)	158(2)
$\{N_3Sn(NIPr)\}_2$ [f]	2.110(9)/ 2.136(7)	1.210(13)/ 1.224(17)	1.136(19)/ 1.163(13)	0.07(2)/ 0.06(2)	150(2)

L_3Ag = $HB(3,5\text{-}(CF_3)_2Pz)_3$; [a] average of independent distances; [b] ref. [92]; [c] ref. [194]; [d] ref. [197]; [e] ref. [199]; [f] ref. [201,202]; G = guanidinium.

Table 4.5. Summary of crystal structure refinement parameters for tin(II) azides **14**–**17**.[85] The unit cell parameters and a reasonable quality structure solution of **16** were obtained from powder X-ray diffraction (PXRD) data. All other structures were determined by single crystal XRD.

	$Sn(N_3)_2(py)_2$ (**14**)	$Sn(N_3)_2(pic)_2$ (**15**)	$(G)[Sn(N_3)_3]$ (**17**)	$Sn(N_3)_2$ (**16**) [e]
Empirical formula	$C_{10}H_{10}N_8Sn$	$C_{12}H_{14}N_8Sn$	$CH_6N_{12}Sn$	N_6Sn
M_r	360.92	388.98	304.80	202.73
Nitrogen [%]	31.0	28.8	55.1	41.4
Crystal system	monoclinic	triclinic	monoclinic	monoclinic
Space group	$P2_1/c$	$P\bar{1}$	$C2/c$	$P2_1/c$
a [Å]	9.9291(4)	9.1912(2)	18.8171(6)	6.4536 [d]
b [Å]	7.8096(3)	9.3972(2)	7.1260(2)	11.71480 [d]
c [Å]	17.4056(7)	10.0132(2)	13.9984(4)	6.0648 [d]
α [°]	90	115.8848(13)	90	90
β [°]	97.7471(19)	99.0170(13)	95.1374(18)	94.249 [d]
γ [°]	90	90.6836(13)	90	90
V [Å^3]	1337.35(9)	765.32(3)	1869.51(10)	457.255 [d]
Z	4	2	8	4
T [K]	100	100	100	298
D_{calc} [g cm^{-3}]	1.793	1.688	2.166	2.945 [c]
μ [mm^{-1}]	1.911	1.676	2.722	5.448 [c]
F (000)	704	384	1168	N/A
Crystal size [mm × mm × mm]	0.27 × 0.13 × 0.10	0.17 × 0.16 × 0.10	0.14 × 0.05 × 0.05	N/A
Crystal habit	block	shard	needle	N/A
Θ range for data collection [°]	2.070–26.394	3.154–27.554	2.173–27.508	N/A
Limiting indices h; k; l	–12, 12; –9, 9; –21, 21	–11,11; –12,12; –12,13	–24, 24; –8, 9; –18, 17	N/A
Reflections collected	13446	16634	15303	N/A
Independent reflections	3004	3503	2154	N/A
R_{int}	0.0363 [f]	0.0349	0.0343	N/A
Completeness to Θ [%]	98.6 (Θ = 25.00°)	99.8 (Θ = 25.242°)	100.0 (Θ = 25.242°)	N/A
Refinement method	[a,b]	[a]	[a]	[e]
Data / restraints / parameters	3004 / 0 / 173	3503 / 0 / 192	2154 / 0 /151	N/A

	$Sn(N_3)_2(py)_2$ (**14**)	$Sn(N_3)_2(pic)_2$ (**15**)	$(G)[Sn(N_3)_3]$ (**17**)	$Sn(N_3)_2$ (**16**) [e]
GoF F^2	1.005	1.030	0.985	N/A
Final R indices $[I > 2I(\sigma)]$	0.0454	0.0402	0.0180	N/A
R_1 (all data)	0.0498	0.0418	0.0235	N/A
Largest diff. peak / hole [e Å^{-3}]	1.66 / –2.05	0.61 / –0.34	0.40 / –0.31	N/A

[a] Full matrix least squares on F^2; [b] Refined as a two component twin using twinning tools within WinGX, which reduced the residual electron density and improved R_1 from 0.0577 to 0.0454; [c] Values calculated by the IUCr checkCIF tool (http://journals.iucr.org/services/cif/checkcif.html); [d] No e.s.d's available at present; [e] Unit cell parameters determined by Pawley refinement, and structure determined using the Rietveld method by Sumit Konar and Rowan Clark (University of Edinburgh); [f] Before twin refinement

4.2.4 FTIR and NMR Spectroscopy

FTIR Spectroscopy

Comparison of solution versus solid state FTIR spectra shows the influence of the 'dimeric' type interaction between neighbouring pairs of the tin(II) azide units. In solution all three complexes exhibit two absorption bands in the $\nu_{as}(N_3)$ region, whereas in the solid state the differences in packing are apparent. For $Sn(N_3)_2(py)_2$ there is a single principle absorption band at 2066 cm^{-1} in the asymmetric stretch region, but in $Sn(N_3)_2(pic)_2$ and $(G)[Sn(N_3)_3]$ the influence of the dimeric interaction gives rise to a secondary band at 2042 and 2033 cm^{-1} respectively. The crystallographic data for $Sn(N_3)_2(pic)_2$ and $(G)[Sn(N_3)_3]$ suggest that one azido ligand has a slightly longer Sn–N bond, and in conjunction with the solid state FTIR spectra could explain this secondary absorption band at lower energy for the slightly more ionic azido group. Alternatively bridging N_3 groups in similar transition metal complexes have attributed to the lower energy band to and the higher energy to the end-to-end or non-bridging ligand(s).[207]

Table 4.6. Comparison of solution and solid state FTIR spectra of azides **14**–**18** with the available literature data for Sn(II) azides.

Compound	$\nu_{asym}(N_3)$ [cm^{-1}]	$\nu_{sym}(N_3)$ [cm^{-1}]	Medium	Ref.
$Sn(N_3)_2(py)_2$ (**14**)	2077, 2057	1325	pyridine	-
	2065	1326	nujol	
$Sn(N_3)_2(pic)_2$ (**15**)	2076, 2057	1324	4-picoline	-
	2063, 2041	1321	nujol	
	2082, 2060	1324	MeCN	
$Sn(N_3)_2$ (**16**)	2107, 2090, 2070	1339, 1333, 1286, 1276	nujol	-
{(*n*-Pr)$_2$ATI}SnN_3	2039	1308	KBr	[194]
	2051	-	toluene	
{L_3Ag }SnN_3{(*n*-Pr)$_2$ATI}	2070	-	KBr	[195]
{(Mes)$_2$DAP}SnN_3	2060	1310**	KBr	[197]
{$HC(PPh_2{=}NSiMe_3)_2$}SnN_3	2048	-	KBr	[200]
(G)[$Sn(N_3)_3$] (**17**)	2086, 2056	1323	MeCN	-
	2060, 2034	1332	nujol	
	2081, 2055	1320	THF	
(AG)[$Sn(N_3)_3$] (**18**)	{2086*, 2049*}	1323	MeCN	-
(PPh_4)[$Sn(N_3)_3$]	2081, 2050	-	THF	[92]
	2069, 2060, 2034	1320	nujol	

G = guanidinium; AG = aminoguanidinium, {$C(NH_2)_2(NHNH_2)$}; L_3Ag = {HB(3,5-$(CF_3)_2Pz)_3$Ag}; **$\nu_{sym}(N_3)$ cannot be unambiguously assigned due to presence of multiple peaks in region; *A_{max} too high for determination of exact peak position.

FTIR spectra of $Sn(N_3)_2(py)_2$ (14) and $Sn(N_3)_2(pic)_2$ – Solution vs. solid state

In solution both adducts have two asymmetric azide stretch bands for the synchronous and asynchronous vibrations of the complexes. However, in the solid state the symmetry of 4-picoline adduct **15** is reduced to C_1 from approximate C_2 symmetry of the pyridine complex **14**. Additionally a dimeric interaction between adjacent Sn–N_α units in **15** further distinguishes the azide ligands from one another.

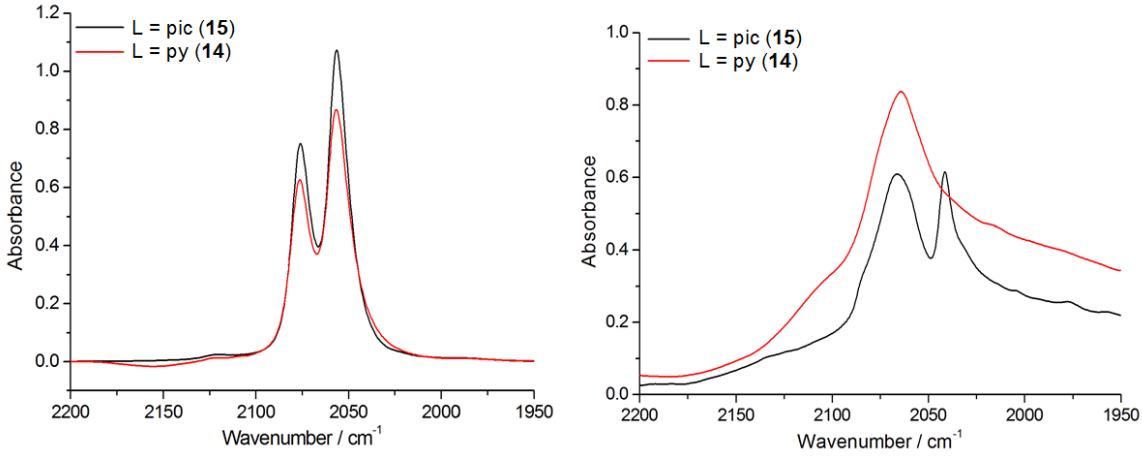

Figure 4.16. FTIR spectra of neutral tin(II) azide adducts $Sn(N_3)_2(L)_2$ in their respective solvents, L, and as nujol suspensions: L = pyridine (**14**), red; L = 4-picoline (**15**), black). The asymmetric azide stretching vibrations are very similar in solution suggesting the presence of comparable monomeric species in solution. However, in the solid state the appearance of a second band at lower energy ($\tilde{\nu}$ = 2041 cm^{-1}) for **15** seems to be related to the dimeric interaction between adjacent $Sn(N_3)_2(pic)_2$ units, but absent in the crystal structure of pyridine complex **14**.

Oxidation of $Sn(N_3)_2(L)_2$ to $Sn(N_3)_4(L)_2$ with ethereal HN_3 (L = py (14); L = pic (15))

The reactivity of tin azides **14** and **15** with ethereal hydrazoic acid was investigated to determine whether they could be oxidised to their tin(IV) analogues. Ethereal hydrazoic acid was prepared by a published procedure,[50] and trap-to-trap condensed after stirring over Sicapent™ (P_4O_{10} with moisture indicator). An FTIR spectrum of the solution (Figure 4.17) confirmed the removal of water and showed the concentration had approximately doubled from *ca.* 1.5 to 3 mol dm^{-3}. In the initial experiment of the oxidation of $Sn(N_3)_2(py)_2$ (**14**) on 0.17 mmol scale, an excess of anhydrous ethereal HN_3 (0.5 ml, *ca.* 1.5 mmol) was added to a pyridine solution of **14**. After stirring for 15 minutes a FTIR spectrum was recorded (see Figure 4.18), showing a decrease in the intensity of absorption bands of **14**, and the rise of those for oxidation of a significant proportion of the tin(II) azide to tin(IV)of $Sn(N_3)_4(py)_2$ (**12**). A repeat of the above experiment over 16 h (see Figure 4.19) showed the complete conversion of $Sn(N_3)_2(py)_2$ ($\tilde{\nu}$ = 2076, 2057, 1324, 1274 cm^{-1}, to the oxidised species $Sn(N_3)_4(py)_2$ ($\tilde{\nu}$ = 2109, 2081, 1334, 1283 cm^{-1}), by comparison with a reference spectrum of **12** in pyridine.

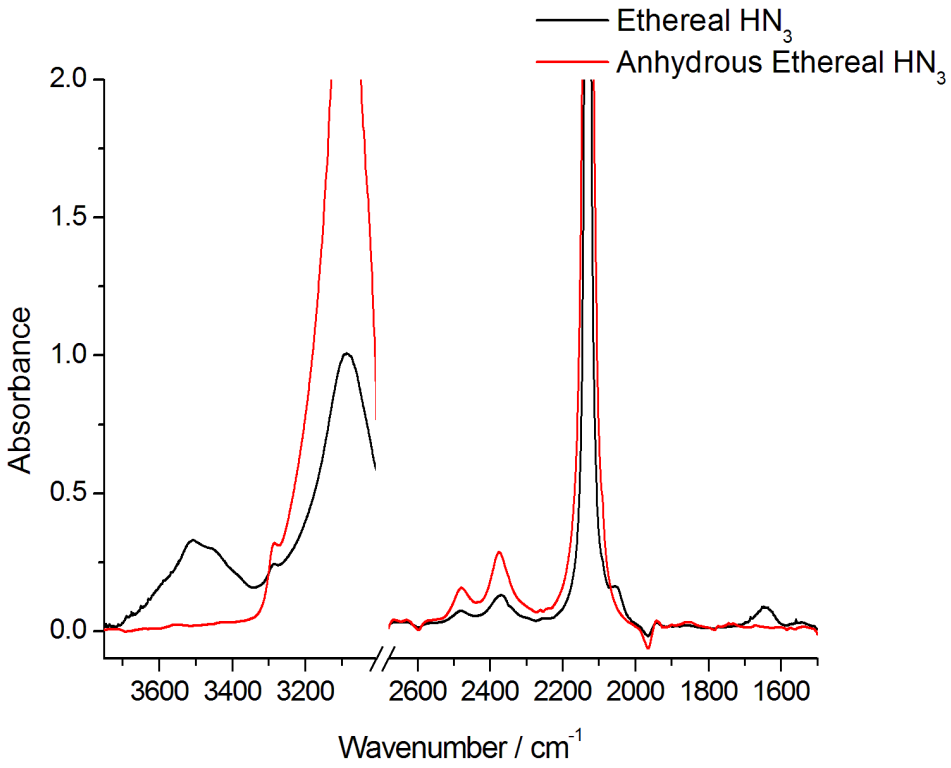

Figure 4.17. FTIR spectra of ethereal HN_3 before (black) and after (red) drying with Sicapent. Spectral window 3005–2860 cm^{-1} omitted due to intense absorptions by Et_2O. The FTIR samples were prepared without dilution of their respective stock solutions. The disappearance of the broad bands centred at 3510 and 1644 cm^{-1} confirms the removal of water.

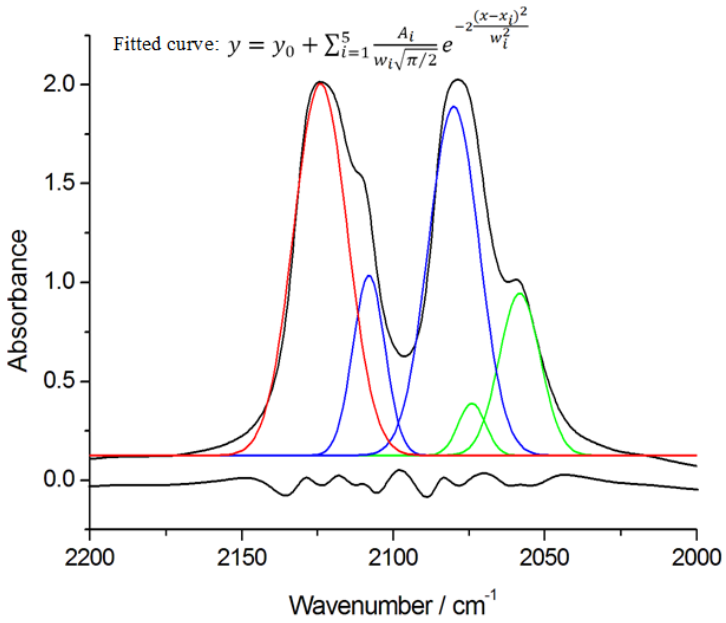

Figure 4.18. FTIR spectrum of $Sn(N_3)_2(py)_2$ in pyridine shortly after addition of excess ethereal HN_3, which results in oxidation to $Sn(N_3)_4(py)_2$ (black). Overlay of curve fitting results showing the peak positions corresponding to $Sn(N_3)_2(py)_2$ (green), $Sn(N_3)_4(py)_2$ (blue), and HN_3 (red) respectively. Deconvolution of overlapping peaks in the infrared spectrum was achieved by fitting multiple Gaussian functions within *Origin 6.0* (equation overlaid on the above spectrum). The difference plot of the observed spectrum minus the fitted peaks is shown in black at the bottom. The largest discrepancies are the 'tails' of the peaks, and the significant overlap of the bands at 2080 and 2075 cm^{-1} means many possible combinations would give an acceptable fit.

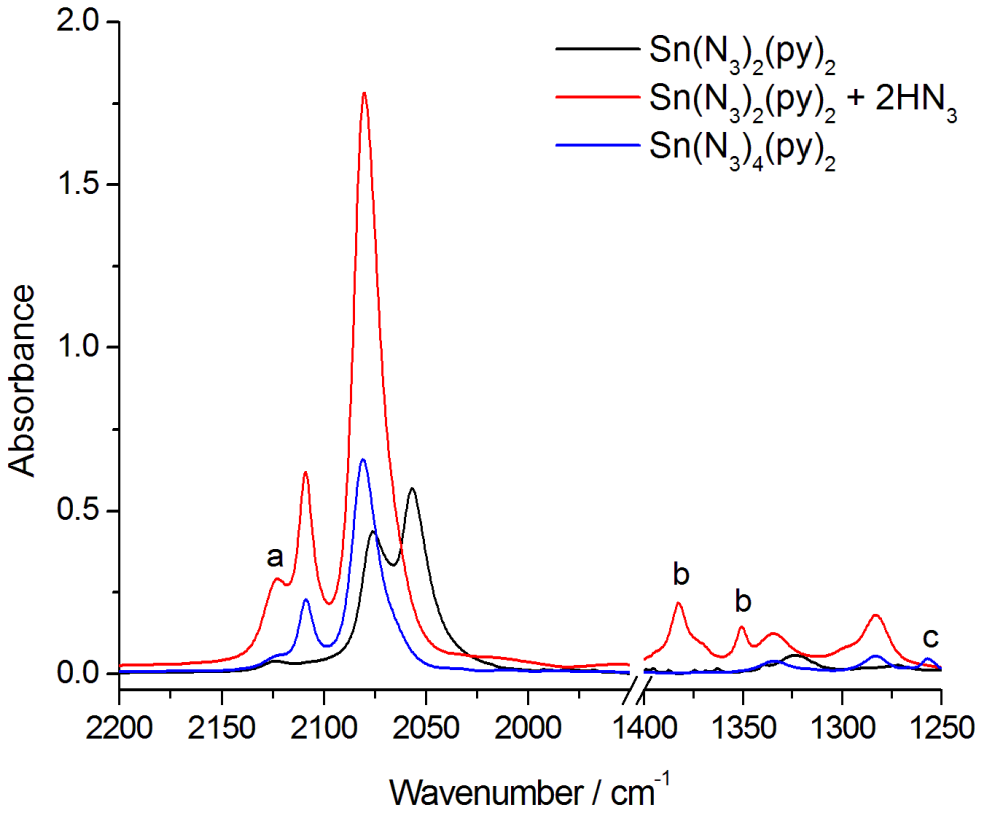

Figure 4.19. FTIR spectrum of the pyridine solution of $Sn(N_3)_2(py)_2$ (**14**) after oxidation with excess ethereal HN_3 for 16 h to give $Sn(N_3)_4(py)_2$ (**10**, red), alongside a reference spectrum of **14** (black), for comparison. [a] HN_3, $\tilde{\nu}$ = 2123 cm^{-1}); [b] Et_2O, $\tilde{\nu}$ = 1382, 1351 cm^{-1}; [c] Residual TMS–F/TMS–N_3 dissolved in reaction solution, $\tilde{\nu}$ = 1257 cm^{-1}.

$Sn(N_3)_2(pic)_2$ (25 mg, 0.064 mmol) was dissolved in 1 ml anhydrous 4-picoline, and ethereal HN_3 (0.05 ml, 0.075 mmol) was added and the solution agitated by hand intermittently over 10 minutes. An FTIR spectrum (black) showed little evidence of a reaction, so further ethereal HN_3 (0.1 ml, 0.15 mmol) was added and the solution warmed to around 50 °C, after which the FTIR spectrum (red) showed a significant proportion $Sn(N_3)_2(pic)_2$ had been oxidised to $Sn(N_3)_4(pic)_2$, though significant overlap of the absorption bands of the two complexes, as well as the excess HN_3 means the exact proportion is unclear.

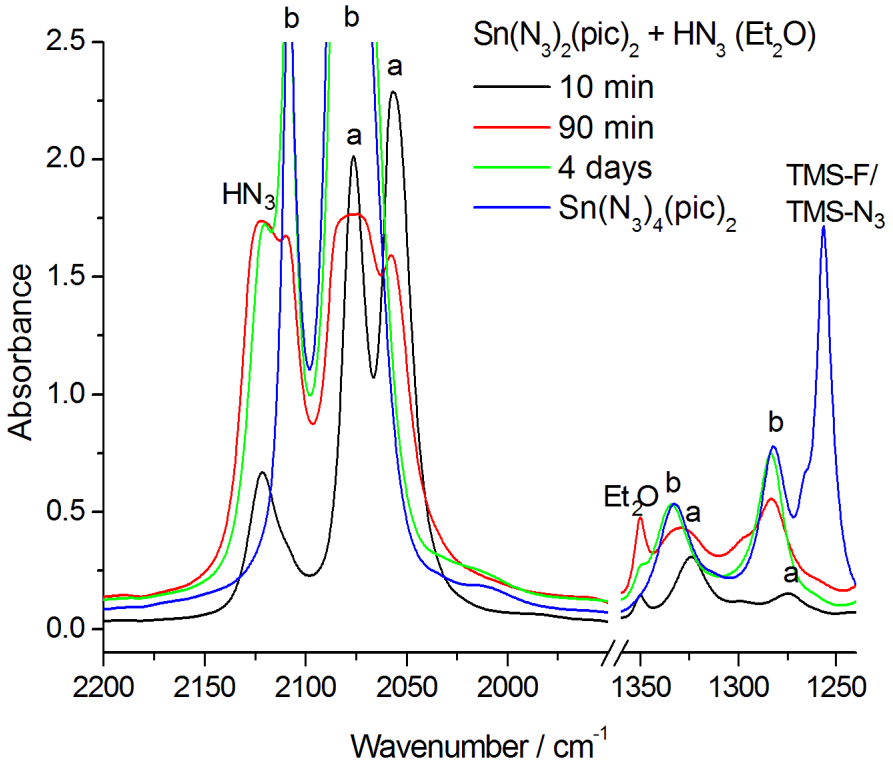

Figure 4.20. FTIR spectra showing the oxidation of $Sn(N_3)_2(pic)_2$ (a; black) to $Sn(N_3)_4(pic)_2$ (b; red & green) by ethereal HN_3, with a spectrum of $Sn(N_3)_4(pic)_2$ (blue) for comparison. After 4 days the conversion is complete, as shown by the absence of the absorption band at 2057 cm^{-1}. N.B. The reference spectrum is from a reaction solution of SnF_4 with TMS–N_3, so contains TMS–N_3/ TMS–F at 1257 cm^{-1}.

Contrasting stabilities of $Sn(N_3)_2(L)_2$ upon air exposure (L = py (14); L = pic (15))

Pyridine complex **14** has a single relatively sharp asymmetric azide stretching vibration at 2067 cm^{-1} in the solid state (nujol suspension). Absorption bands for coordinated pyridine are visible at 1639, 1602, and 1573 cm^{-1}, though exposure of a crystalline sample of **14** to air in a sample vial for a prolonged period led to the disappearance of bands attributed to coordinated pyridine and a shift of the primary $\nu_{as}(N_3)$ to lower energy. The thermogravimetry measurements of **14** and **15** (see section 4.2.5 below) show that for the former, the rate of mass loss (of solvent) is significant even at 25 °C in a stream of nitrogen, whereas the onset is higher for the 4-picoline complex **15**, which seems to be air stable (Figure 4.22 below). Complex **15** shows remarkable air stability considering the lack of sterically demanding ligands to shield the Sn(II) centre from oxidation. Also in contrast with **14** is the appearance of a second $\nu_{as}(N_3)$ band at lower frequency $\nu(N_3)$ at 2044 cm^{-1}, which shows the effect of the dimeric interaction, which seems to slightly increase the ionicity of the azido ligand '*trans*' to the short Sn···N_α interaction. The other tin(II) azides including guanidinium- (**17**) and tetraphenylphosphonium triazidostannate which have this interaction exhibit a similarly split azide region of the spectrum in the solid state (Figure 4.23), whereas **14** does not have this type of interaction.

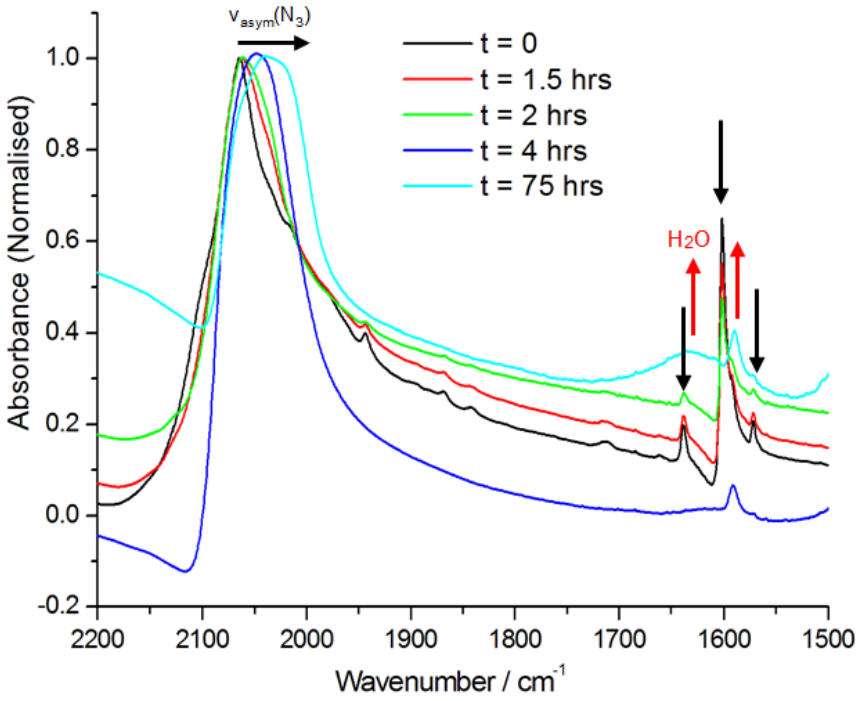

Figure 4.21. Series of normalised solid state FTIR spectra showing the loss of pyridine, and broadening and shift of $v_{asym}(N_3)$ absorption band upon air exposure of $Sn(N_3)_2(py)_2$ (**14**). The spectra are normalised* with respect to the $v_{asym}(N_3)$ band to show the relative decrease in the intensity of coordinated pyridine at 1602 cm^{-1}. As well as shifting to lower energy, the absolute intensity of the asymmetric azide stretch decreases over time due to hydrolysis. *A new sample was used each time, resulting in variable concentration, which has been normalised for clarity.

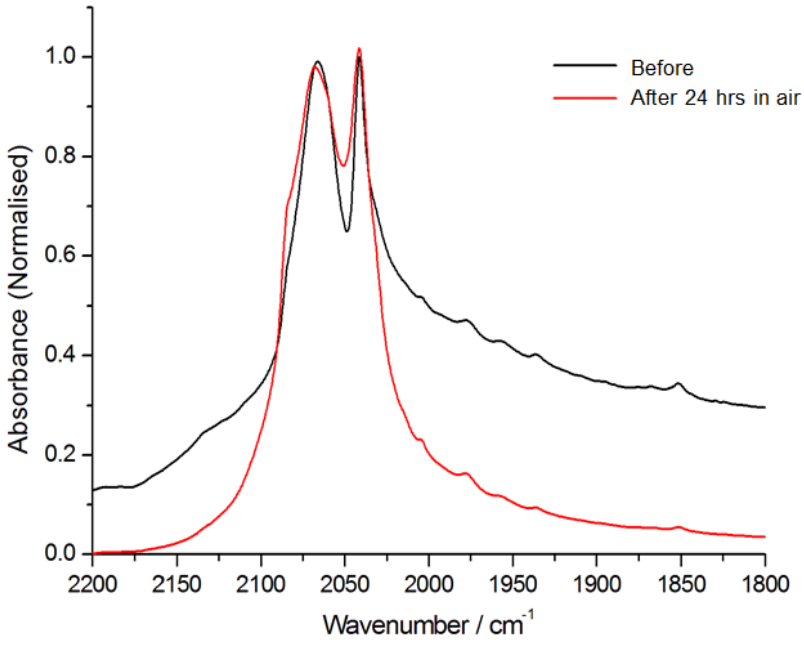

Figure 4.22. FTIR spectra showing the effect of air exposure of a nujol suspension of $Sn(N_3)_2(pic)_2$ (**15**). Unlike the pyridine complex, **15** shows no appreciable loss of 4-picoline upon exposure to air, and only a slight trace of oxidation product as a shoulder at 2080 cm^{-1} on the main absorption band.

FTIR spectroscopic study of guanidinium triazidostannate (17)

In the case of hydrogen bonded bis(guanidinium) hexaazidostannate (**3**) the asymmetric azide stretch region of the FTIR spectrum is significantly more complex than in the absence of hydrogen bonds in the $(PPN)_2[Sn(N_3)_6]$ salt (**9**). However, the hydrogen bonds in guanidinium triazidostannate seem to have less influence as the symmetry of the anion in both crystal structures is C_1, as shown in Figure 4.23.

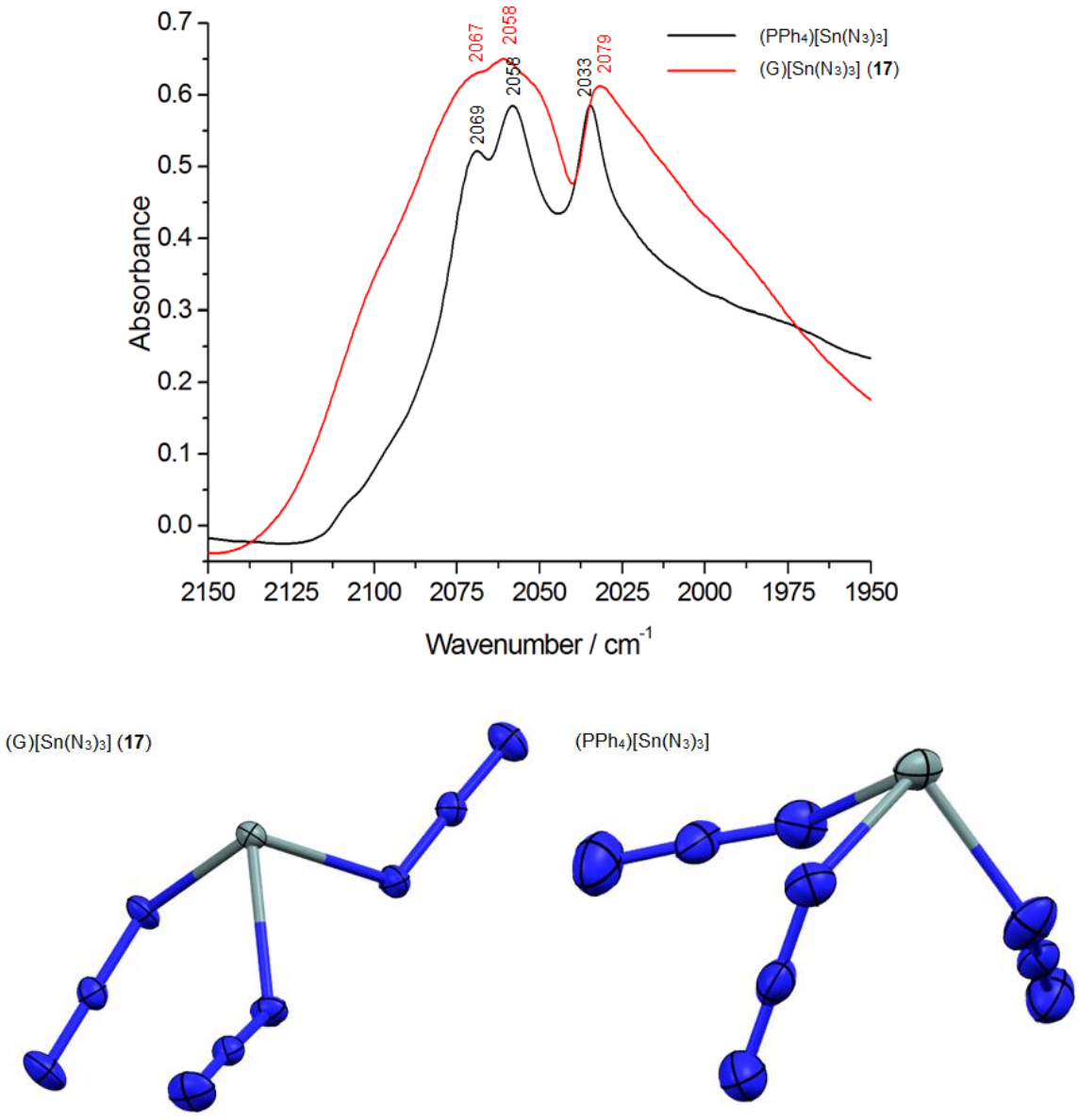

Figure 4.23. Top: Comparison of the FTIR spectra of $(G)[Sn(N_3)_3]$ with $(PPh_4)[Sn(N_3)_3]$.[208] Bottom: Thermal ellipsoid plots from the crystal structures of guanidinium triazidostannate (left) and tetraphenylphosphonium triazidostannate (right).[92] In both structures the $[Sn(N_3)_3]^-$ anion has C_1 symmetry and accordingly three distinct asymmetric azide stretching vibrations are observed.

Exposure of an acetonitrile solution of guanidinium triazidostannate (**17**) to air leads to its gradual oxidation to bis(guanidinium) hexaazidostannate (**3**). The hydrazoic acid produced upon hydrolysis of $[Sn(N_3)_3]^-$ oxidises Sn(II) to Sn(IV). This process is demonstrated in the

following spectral series (Figure 4.24), with the decay of absorption bands of $[Sn(N_3)_3]^-$ and the rise of absorption bands of $[Sn(N_3)_6]^{2-}$. Eventually hexaazidostannate **3** decomposes via hydrolysis, though more slowly than low-valent triazidostannate **17**. The increase in water concentration of the solution can be followed by the absorption around 1630 cm^{-1}, and a gradual increase in the concentration of HN_3 by the bands at 2139 cm^{-1} and 1179 cm^{-1}.

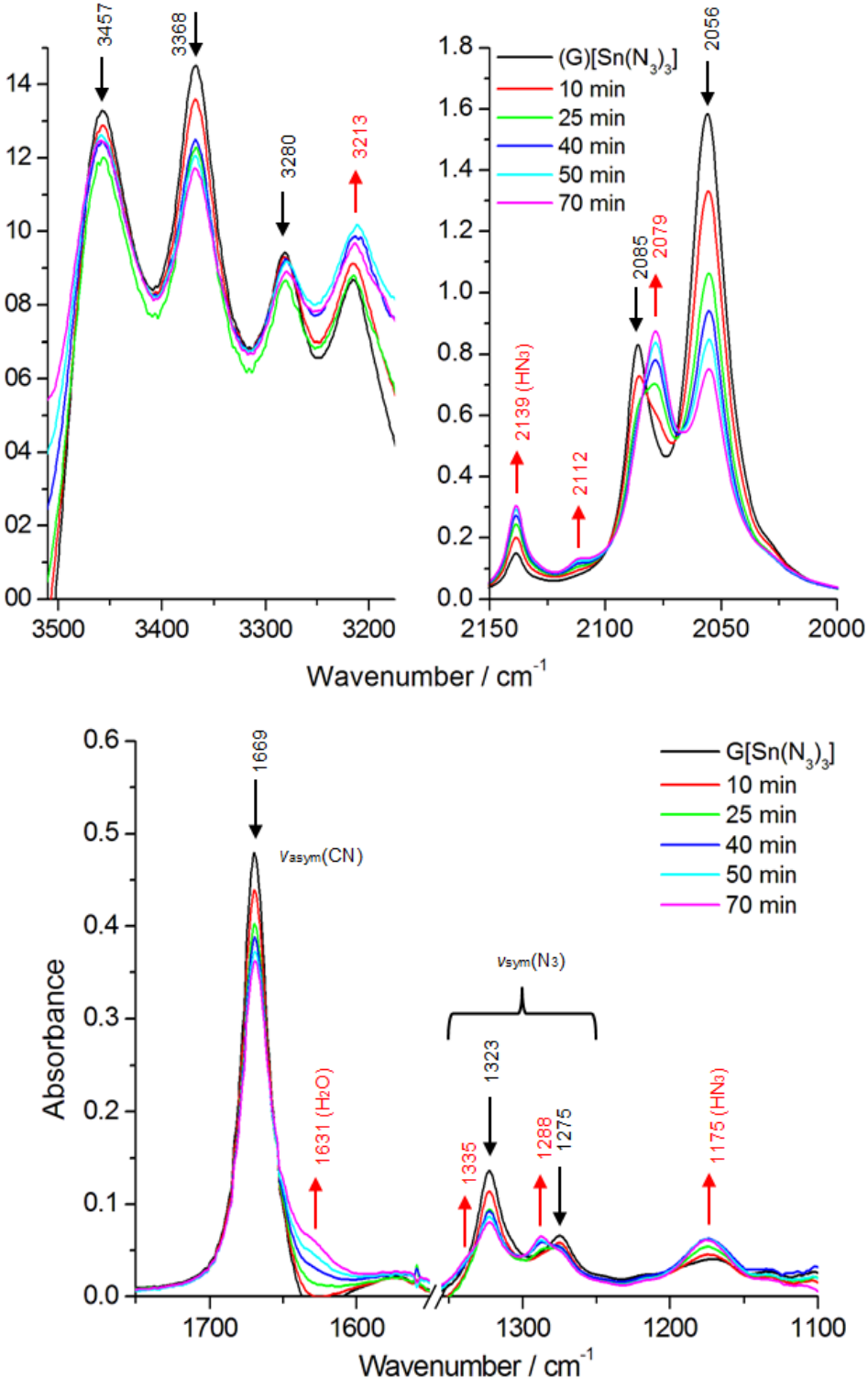

Figure 4.24. FTIR spectra showing the gradual oxidation of $(G)[Sn(N_3)_3]$ (**17**) to $(G)_2[Sn(N_3)_6]$ (**3**) upon exposure to air over a period of 70 minutes in acetonitrile solution.

FTIR spectrum of tin diazide (16)

The FTIR spectrum contains several overlapping asymmetric azide stretches in the range 2107–2070 cm^{-1}, slightly higher than either the neutral adducts **14** and **15**, or the triazidostannate salt **17** which suggests tin diazide has the most covalent coordinative bonds of all the tin(II) azides described here.

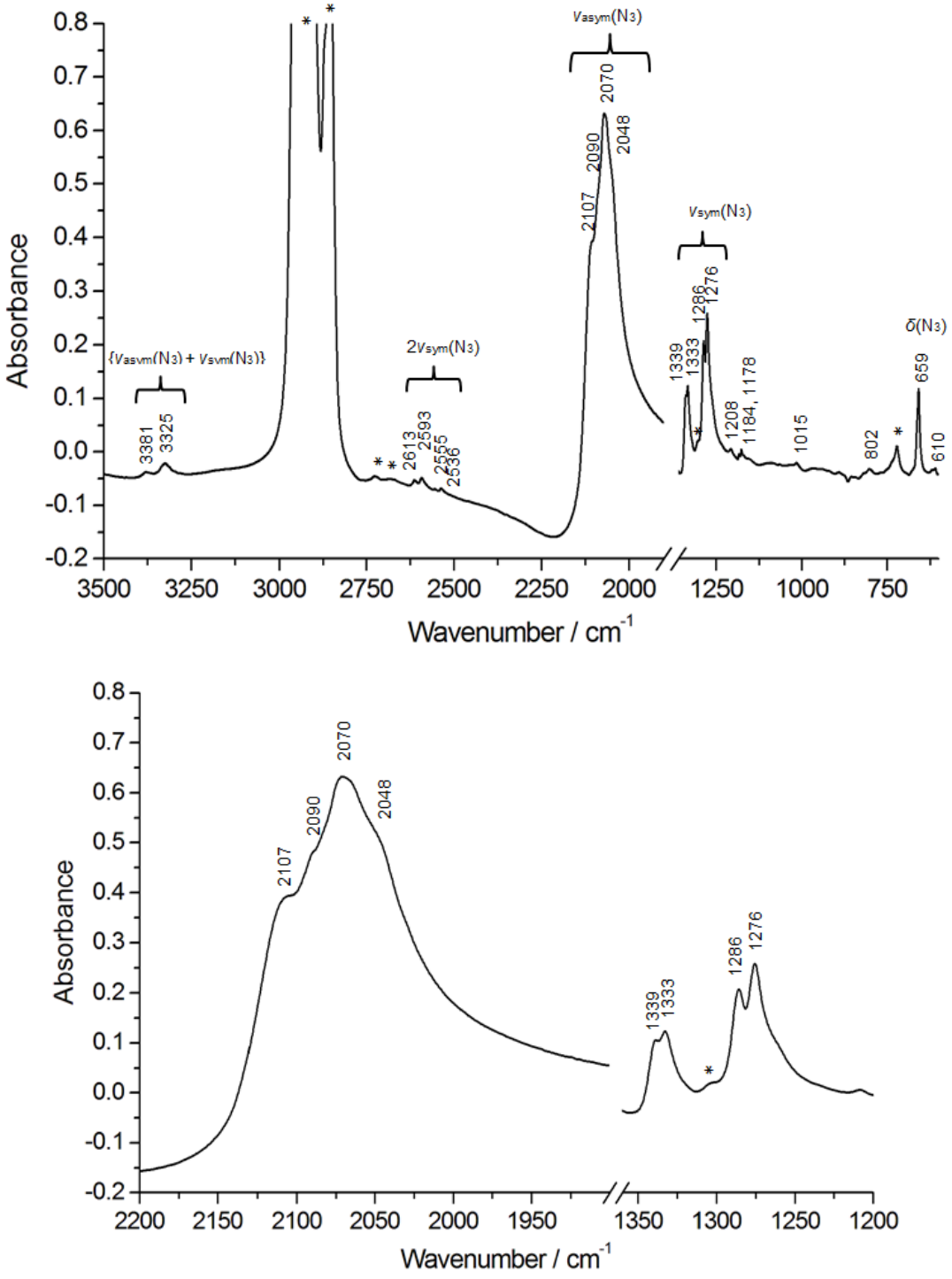

Figure 4.25. Solid state FTIR spectrum of $Sn(N_3)_2$ (**16**) as a nujol suspension. Top: Full spectrum. Bottom: An expanded view showing the asymmetric and symmetric azide stretch regions. (N.B. For both spectra the region 1900–1360 cm^{-1} is omitted to allow expanded view).

Four absorption bands are present in the symmetric azide stretch region at 1339–1276 cm^{-1}, of which overtones are visible around 2613–2536 cm^{-1}, as well as the sum-frequency bands from mixing of symmetric and asymmetric stretching vibrations at 3381–3325 cm^{-1}. The azide deformation (bending) mode is visible at 659 cm^{-1}.

Multinuclear NMR spectroscopic investigations into polyazido complexes

^{14}N NMR Spectroscopy is a useful tool to analyse polyazides as the three azide nitrogens N_α, N_β and N_γ give rise to distinct signals in the case of covalent azides, and two signals for ionic azides where the terminal nitrogen environments are equivalent. Spectroscopic data was particularly valuable before the first crystallographic studies on azides. The spectral linewidths of the terminal nitrogen atoms, particularly N_α, are broad and can be difficult to distinguish from the baseline or not observable at all. The N_β signals tend to be sharper due to their more symmetrical environment. The ^{14}N NMR spectra of pyridine-based adducts **14** and **15** in pyridine-d_5 appear virtually identical, with a sharp peak due to N_β at –135 ppm, and subtle differences in the chemical shift of N_α are noticeable (–258.7 ppm *vs*. –260.4 ppm) whereas N_γ is not observed in either case. Based on the data in Table 4.7 below, the ^{14}N chemical shift for N_α of the azide ligands tends to be around –260 ppm for tin(II) azides, and around –290 to –300 ppm for tin(IV) azides. However, the ^{14}N signals for N_α of the neutral tin(II) azides {(Mes)$_2$DAP}SnN_3 and {(*n*-Pr)$_2$ATI}SnN_3 appear at –292 and –256 ppm respectively, which suggests the nature of the coordination centre may not be the dominant influence on the adjacent ^{14}N nuclei. Based on the available data in Table 4.7, there is no obvious correlation between the chemical shifts of ^{119}Sn and those of coordinated ^{14}N nuclei (N_α). On the other hand guanidinium and tetraphenylphosphonium triazidostannates have very similar ^{14}N NMR spectra typical for covalent azides with weak, broad signals for N_α and N_γ around –260 ppm and –217 ppm respectively. The ^{119}Sn chemical shifts of guanidinium- (**17**) and tetraphenylphosphonium triazidostannate are separated by 64 ppm, with guanidinium triazidostannate appearing at lower frequency in the same solvent (CD_3CN). It seems that exchanging the bulky PPh_4^+ cation for guanidinium has a profound effect on the ^{119}Sn chemical shift, which could be due to stronger association of ions in solution. Alternatively, the difference might arise from more effective disruption of the 'dimeric' interaction of $[Sn(N_3)_3]^-$ by the smaller guanidinium cation. The tin(IV) analogue of **17**, bis(guanidinium) hexaazidostannate (**3**), appears at a much lower frequency of –601 ppm compared to –285 ppm for triazidostannate **17**. The peak position of –601 ppm is very similar to previously reported ^{119}Sn data for hexaazidostannate salts, and suggests there is little difference between the ^{119}Sn environments of the tetrabutylphosphonium-, tetraethylammonium-, and guanidinium hexaazidostannates.

Table 4.7. Comparison of ^{14}N and ^{119}Sn NMR chemical shifts of compounds **14**, **15**, and **17** with hexaazidostannate(IV) salts **3** and **9**, and available literature data for other tin(II) and tin(IV) azides.

NMR [ppm]	δ (^{14}N) [ppm]				δ (^{119}Sn) [ppm]	Solvent	Ref.
	N_α	N_β	N_γ	N_L			
$\{(Mes)_2DAP\}SnN_3$	–292	–136	–223	-	–276	CD_2Cl_2	[197]
$\{(Ph)_2DAP\}SnN_3$	-	-	-	-	–156	$CDCl_3$	[196]
$\{(Dipp)_2DAP\}SnN_3$ [a]	-	-	-	-	–237	C_6D_6	[198]
$\{(n\text{-}Pr)_2ATI\}SnN_3$	–256	–136	–217	–202	–122	CD_2Cl_2	[197]
$\{L_3Ag\}SnN_3\{(n\text{-}Pr)_2ATI\}$ [b]	-	-	-	-	90	-	[195]
$\{HC(PPh_2{=}NSiMe_3)_2\}SnN_3$	-	-	-	-	–200	THF-d_8	[200]
$\{N_3Sn(NIPr)\}_2$	-	-	-	-	–285	THF-d_8	[201]
$Sn(N_3)_2(py)_2$ (**14**)	–259	–135	[c]	[d]	–459	C_5D_5N	-
$Sn(N_3)_2(pic)_2$ (**15**)	–260	–135	[c]	[d]	–459	C_5D_5N	-
$(PPh_4)[Sn(N_3)_3]$	–260	[d]	–219	N/A	–220	CD_3CN	[92]
$(G)[Sn(N_3)_3]$ (**17**)	–260	[d]	–217	N/A	–285	CD_3CN	-
$(G)_2[Sn(N_3)_6]$ (**3**)	–302	[d]	–216	N/A	–601	CD_3CN	-
$(PPN)_2[Sn(N_3)_6]$ (**9**)	–302	[d]	–220	N/A	-	CD_3CN	[85]
$(AsPh_4)_2[Sn(N_3)_6]$	–293	–143	–225	N/A	-	CH_2Cl_2	[162]
$(PBu_4)_2[Sn(N_3)_6]$	-	-	-	N/A	–604	CH_2Cl_2	[163]
$(NEt_4)_2[Sn(N_3)_6]$	-	-	-	N/A	–605	CH_2Cl_2	[163]

[a] Dipp = 2,6-diisopropylphenyl; [b] L_3 = hydrotris(3,5-bis(trifluoromethyl)pyrazolyl)borate; [c] too weak; [d] Obscured by solvent peak at –63 ppm (C_5D_5N) or –136 ppm (CD_3CN). All ^{14}N NMR and ^{119}Sn NMR chemical shifts are referenced to CH_3NO_2 and $SnMe_4$ respectively.

4.2.5 Thermal Properties: DSC and TGA

Thermogravimetry of $Sn(N_3)_2(py)_2$ (14) and $Sn(N_3)_2(pic)_2$ (15)

Compounds **14** and **15** were subjected to thermogravimetry measurements to determine the lability of the respective pyridine-based ligands. Compound **14** crystallises as the bis(pyridine) complex, which seems to be in equilibrium with pyridine in the vapour phase. When stored in a tightly sealed container in inert atmosphere the compound saturates the available volume of the vessel with an equilibrium pressure of pyridine, which inhibits the loss of further pyridine from the material. The thermal characterisation data obtained are consistent with the formula $Sn(N_3)_2(py)_2$, though several elemental analyses of the compound have returned values close

to the mono-pyridine complex, $Sn(N_3)_2(py)$, due to partial loss of pyridine during the course of the analysis. The TG data support this interpretation, as **14** clearly starts to lose mass at ambient temperature, with an extrapolated onset temperature of 48 °C for the first step, and around 83 °C for the second. 4-Picoline complex **15** appears more thermally stable, with the mass loss steps having extrapolated onset temperatures of 75 °C and 111 °C. The difference in the onset temperatures for mass loss of **14** and **15** is *ca.* 30 °C, which is close to the difference in boiling point between pyridine (115 °C) and 4-picoline (145 °C) suggesting the onset temperature may be related to the volatility of the free base. The measurements were curtailed well below the decomposition temperature of **14** and **15** (T_{on}^{dec} = 170 °C), but showed the desolvation of both to $Sn(N_3)_2$ upon controlled heating under nitrogen flow.

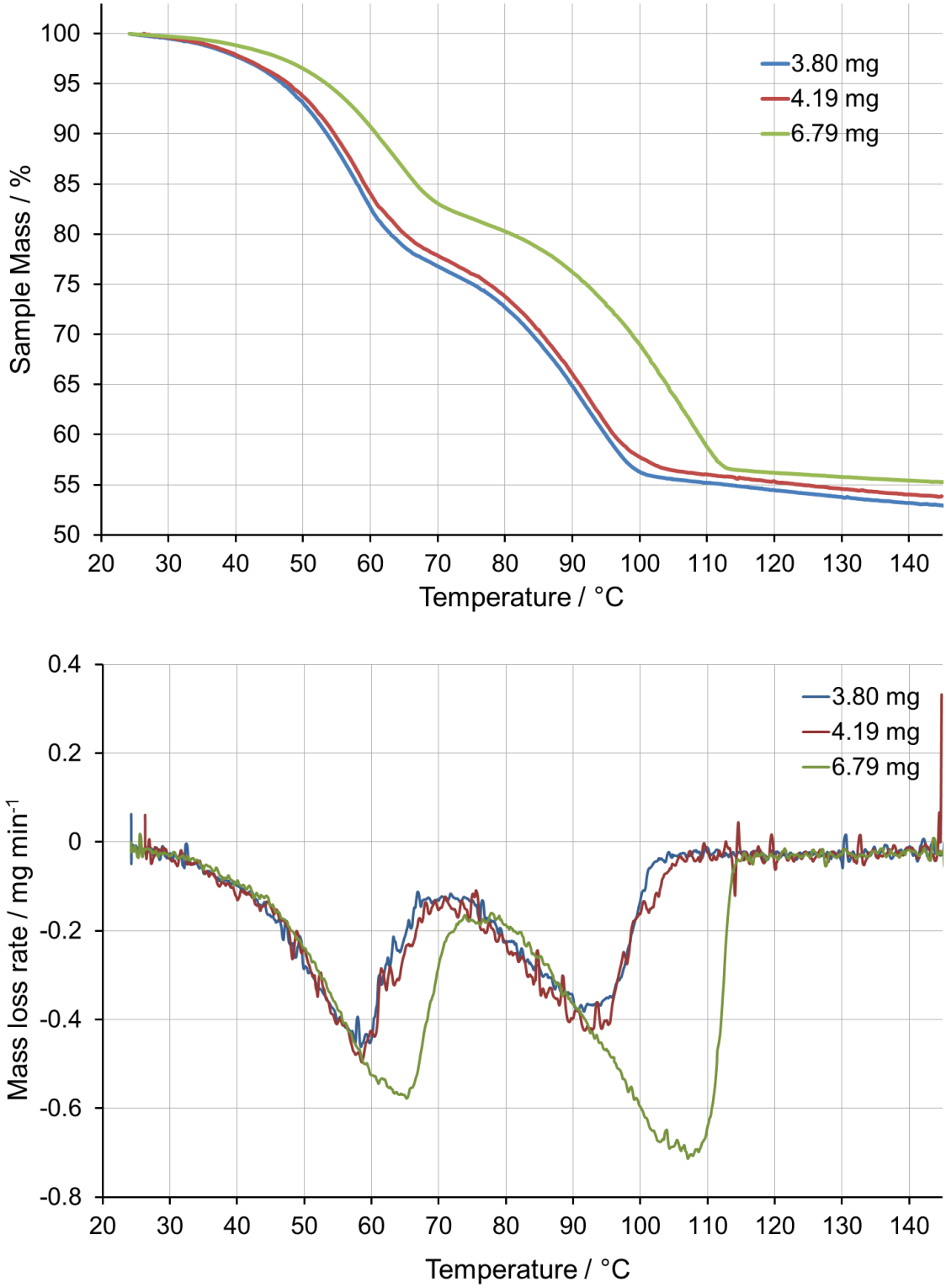

Figure 4.26. Top: Thermogravimetry of $Sn(N_3)_2(py)_2$ (**14**) showing two mass loss steps, 1 for each equivalent of pyridine, leaving behind $Sn(N_3)_2$ (**16**). Bottom: Derivative of the TG curves showing the mass loss rate with increasing temperature. The sample of highest mass (6.79 mg, green curves) shows the effect of thermal lag compared to the other two samples with lower mass.

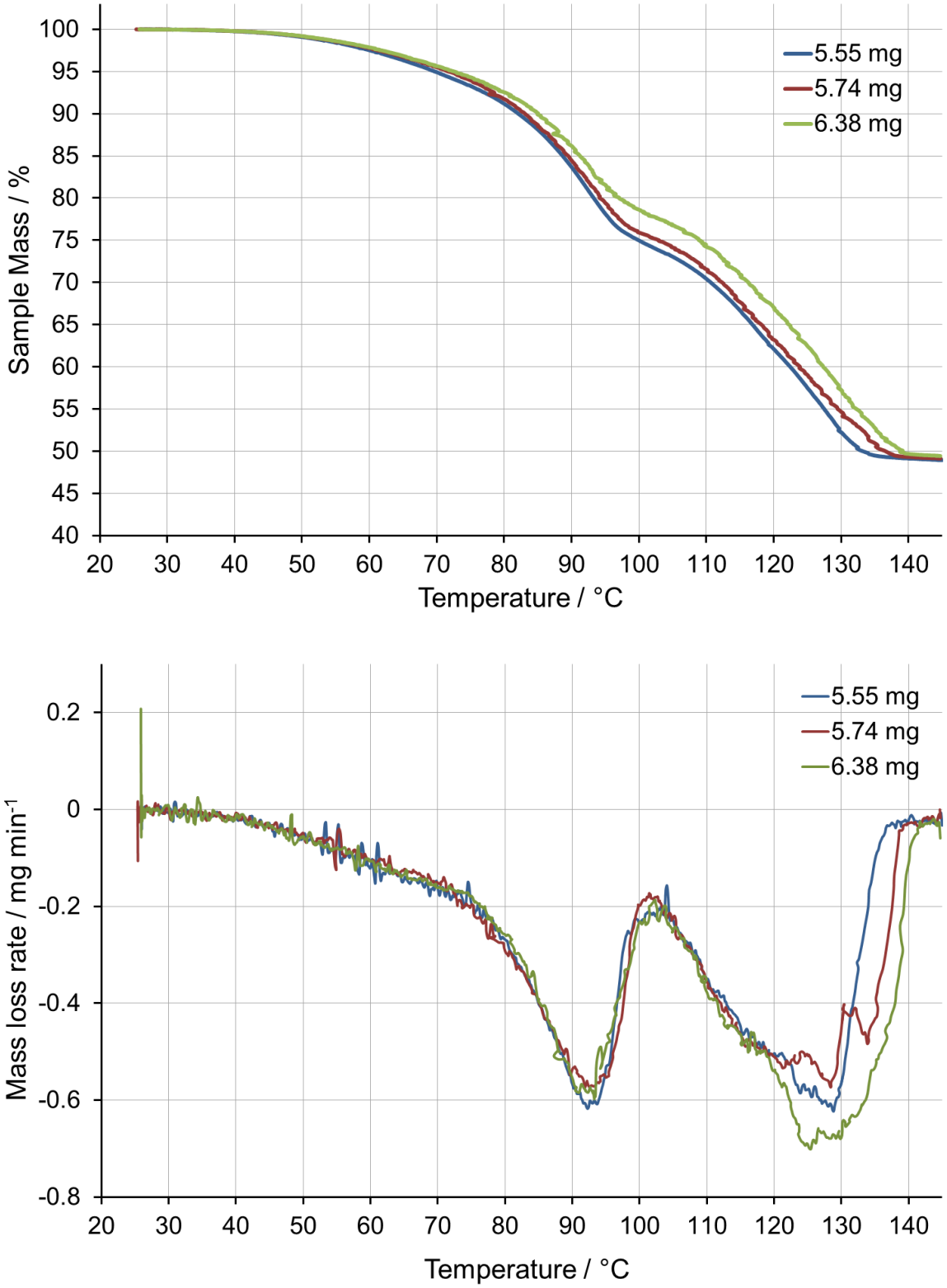

Figure 4.27. Top: Thermogravimetry of $Sn(N_3)_2(pic)_2$ (**15**) showing two mass loss steps, 1 for each equivalent of 4-picoline, leaving behind $Sn(N_3)_2$ (**16**). Bottom: Derivative of the TG curves showing the mass loss rate with increasing temperature. The sample of highest mass (6.38 mg, green curves) shows the effect of thermal lag.

Differential scanning calorimetry of tin(II) azides

Compounds **14**–**17** were investigated by DSC to determine their thermal properties including stability and enthalpies of decomposition. The thermal behaviour of diazides **14** and **15** is different depending on whether the system is open or closed, as the complementary TGA results show that the complex loses pyridine in the nitrogen stream (Figures 4.26 and 4.27 above). In a closed stainless steel high-pressure DSC capsule, **14** has a relatively sharp melting point (T_{on}^{m} = 62 °C), followed by a more gradual endotherm at T_{on} = 101 °C close to the boiling point of pyridine (see Figure 4.28). The strongly exothermic decomposition has an onset temperature of T_{on}^{dec} = 172(3) °C with ΔH_{dec} = –1.0(1) kJ g^{-1} (–369(26) kJ mol^{-1}). The 4-picoline complex **15** has a higher melting point of 99.9(5) °C and similar thermal stability (Figure 4.29), decomposing with an onset temperature of 180(3) °C with ΔH_{dec} = –1.07(4) kJ g^{-1} (–416(17) kJ mol^{-1}). Pyridine adduct **14** has a sharp decomposition exotherm, whereas a much broader exotherm is exhibited during decomposition of **15**, suggesting the decomposition occurs more gradually. Upon controlled heating, tin diazide showed no indication of melting or phase changes before detonation, which occurred during the recording of both thermograms. The detonation of only 1.4 mg of $Sn(N_3)_2$, which occurred during the recording of the second thermogram, was powerful enough to rupture the base of the stainless steel DSC sample capsule (Figure 4.30, inset (right)) and deform the platinum cover in the sample compartment of the DSC apparatus. After this experiment no further DSC measurements were carried out. The value quoted for the specific enthalpy of decomposition of **16** is based on the first thermogram, and represents a lower limit for the true value as upon close inspection, the peak is truncated by the instrument (see Figure 4.30, inset (left)). Additionally, the enthalpy change was so fast that the exotherm maximum was not captured, and the breached capsule altered the required heat flow to the sample, in turn skewing the baseline (Figure 4.30). These physical properties of **16** are perhaps not surprising considering it is closely related to lead diazide, which is an established powerful primary explosive.

Table 4.8. A summary of key parameters associated with the melting and decomposition of $Sn(N_3)_2(py)_2$ (**14**), $Sn(N_3)_2(pic)_2$ (**15**), $Sn(N_3)_2$ (**16**), and $(G)[Sn(N_3)_3]$ (**17**) determined by DSC measurements. Published values for triazidostannate salt $(PPh_4)[Sn(N_3)_3]$ are shown for comparison.[92]

	(**14**)	(**15**)	(**16**)	(**17**)	$(PPh_4)[Sn(N_3)_3]$ [92]
T_{on}^{m} [°C] [a]	62.4(2)	99.9(5)	-	77.3(1)	115
ΔH_m [kJ mol^{-1}]	20.0(3)	28.8(9)	-	7.81(9)	-
T_{on}^{dec} [°C][a]	172(3)	180(3)	>230 [b]	95(4), 272(2)	215, 308
ΔH_{dec} [kJ mol^{-1}]	–369(26)	–416(17)	–372 [c]	–234(5), –401(14)	-
ΔH_{dec} [kJ g^{-1}]	–1.0(1)	–1.07(4)	–1.84 [c]	–0.77(2), –1.32(5)	-

[a] Extrapolated onset temperature; [b] lowest of two measurements, may depend on local hotspot formation and grain size; [c] lower bound due to exotherm truncation by the instrument; G = guanidinium.

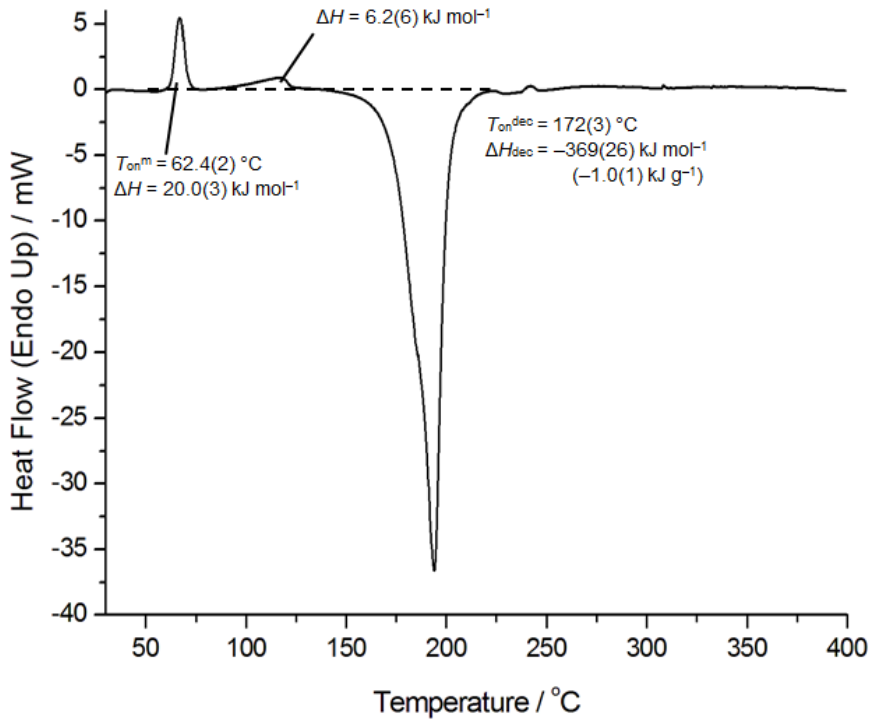

Figure 4.28. DSC trace of $Sn(N_3)_2(py)_2$ (**14**), heating rate 10 °C min^{-1}.

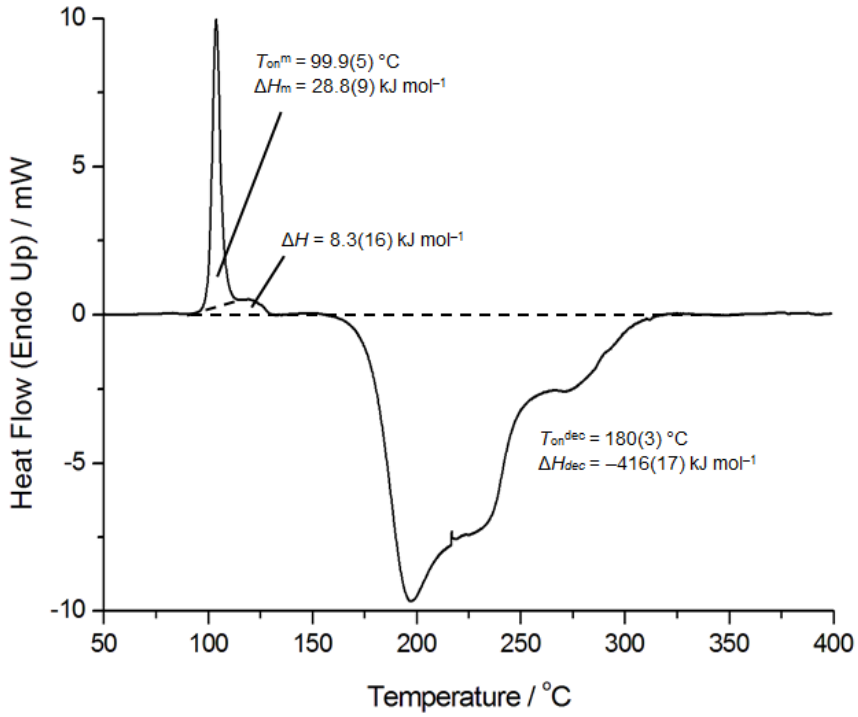

Figure 4.29. DSC trace of $Sn(N_3)_2(pic)_2$ (**15**), heating rate 10 °C min^{-1}.

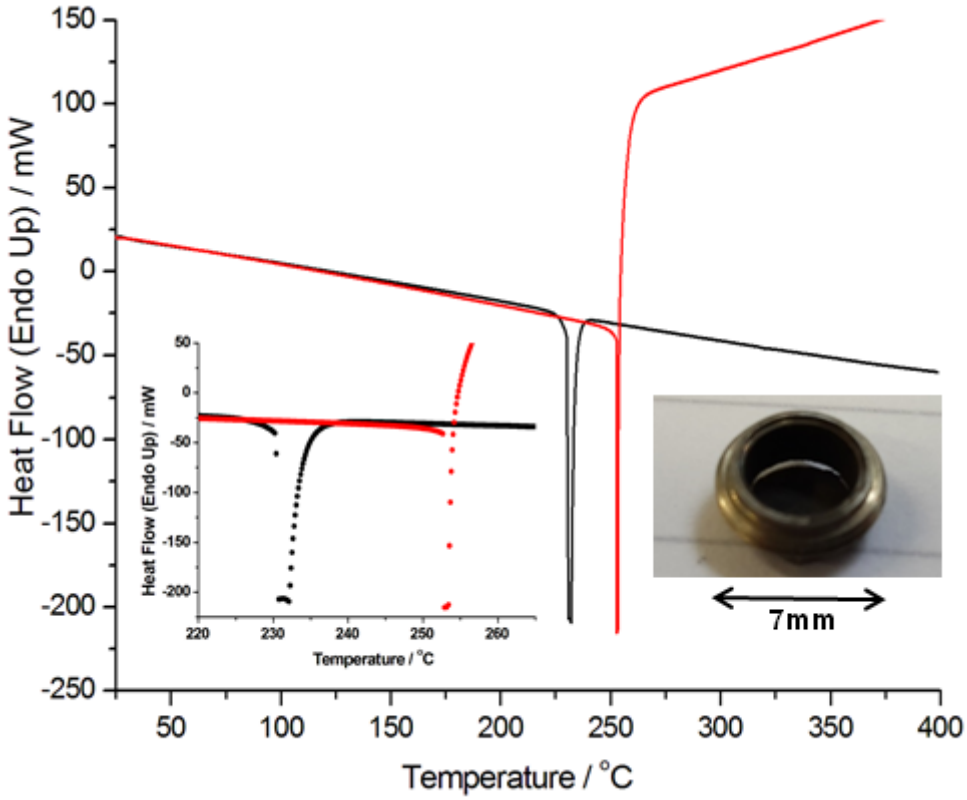

Figure 4.30. DSC traces of $Sn(N_3)_2$ (**16**) with heating rate 10 °C min^{-1}, masses: 1.80 mg (black), and 1.44 mg (red). Inset left: An expanded view showing the individual data points around the time of detonation. Inset right: The DSC capsule ruptured by detonation of $Sn(N_3)_2$ (red curve).

Guanidinium triazidostannate (**17**) has a melting point in between those of tin(II) azides **14** and **15**, and around 37 °C lower than $(PPh_4)[Sn(N_3)_3]$ (see Table 4.8 below). Baseline location in the DSC traces of **17** was not trivial due to the two broad exotherms spanning almost the whole temperature range. The decomposition of **17** seems to occur gradually in two stages with onset temperatures of around 95 °C and 272 °C (Figure 4.31), meaning it has even lower thermal stability than the recently reported $(PPh_4)[Sn(N_3)_3]$.[92] The endotherm corresponding to melting of **17** is immediately followed by the first stage of decomposition, which occurs coincidentally around the melting point of guanidinium azide (**1**, 99.9(3) °C, see chapter 2). If the compound decomposes *via* dissociation of an azide ligand, the release (and subsequent melting) of **1** could instigate the decomposition process. The respective enthalpies of the two decomposition steps are 234 (± 5) kJ mol^{-1} and 401 (± 14) kJ mol^{-1}, which would be approximately consistent with around 200 kJ mol^{-1} per azido ligand previously derived for similar main group polyazido complexes. The tin(IV) analogue bis(guanidinium) hexaazidostannate (**3**) has a higher melting point of 116 (± 1) °C and decomposes around 250 (± 3) °C with a greater overall molar (–1270 (± 30) kJ mol^{-1} *vs.* –635 (± 14) kJ mol^{-1}) and specific (–2.60 (± 5) kJ g^{-1} *vs.* –2.07 (± 9) kJ g^{-1}) enthalpies of decomposition. The enthalpies of decomposition are consistent with approximately 200 kJ mol^{-1} per azide group, as derived from similar thermal measurements on other main group polyazides including hexaazidostannate salts **3** and **9** and tin(IV) azide adducts **10**–**12**[85] (see chapter 3). The specific enthalpies of decomposition for bis(guanidinium) hexaazidostannate and guanidinium triazidostannate are in line with the observed positive correlation between nitrogen content and specific enthalpy of decomposition of main group polyazides (see Summary, Figure S1).

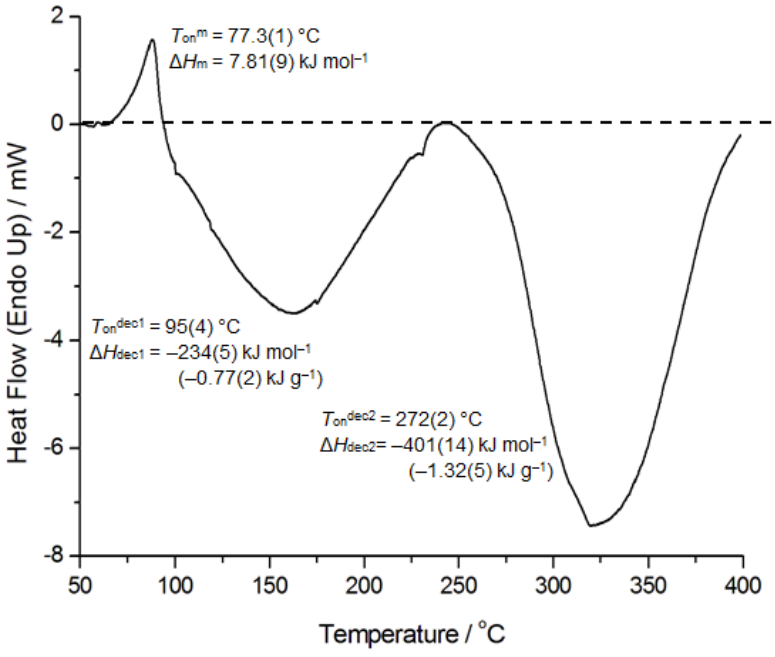

Figure 4.31. DSC trace of **17** showing endothermic melting immediately followed by two step exothermic decomposition.

4.2.6 Powder X-Ray diffraction (PXRD) experiments: *in-situ* heating study on $Sn(N_3)_2(py)_2$, and determination of the structure of $Sn(N_3)_2$

Outline of PXRD Experiments

Due to the highly sensitive nature of $Sn(N_3)_2$ (**16**) an *in-situ* heating study on $Sn(N_3)_2(py)_2$ (**14**) was carried out to see if $Sn(N_3)_2$ could be prepared by removal of the coordinated pyridine under a stream of hot nitrogen provided by a cryostream. DSC analysis of **14** suggests the onset of decomposition is around 170 °C, though the blu-tack holding the capillary in position on the adjustable goniometer limited the temperature to < 140 °C. A capillary was carefully loaded with $Sn(N_3)_2$ and subjected to a 16 hour PXRD experiment to attempt structure determination by Rietveld refinement. Additional 1 hour diffractograms were recorded before and after the main diffraction experiment period to check for sample deterioration during measurement. After data collection the sample appeared discoloured (yellow) selectively in the region of the sample where the X-ray beam was centred. Any degradation caused by oxygen ingress into the capillary would most likely have started from the end sealed by wax rather than the flame-sealed end, and though independent experiments have shown $Sn(N_3)_2$ to be light sensitive, the experiment was carried out overnight so daylight exposure would have been minimal. These combined observations suggest the observed change in appearance and in the diffractogram are due to the effects of X-ray exposure (see Figures 4.35 and 4.36 below).

Powder XRD study on the removal of pyridine from $Sn(N_3)_2(py)_2$ (14) by heating *in-situ* using a thermostat controlled nitrogen cryostream

A 0.7 mm capillary was loaded to 27 mm depth of finely ground white $Sn(N_3)_2(py)_2$ (**14**) crystals in the glovebox, and sealed with melted beeswax in the 'funnel' end. The powder was carefully shaken to the bottom by running the tweezers against the capillary. After the sample was removed from the glovebox it was quickly flame-sealed (with a lighter) at a total length of *ca*. 45mm. The sample was mounted in blu-tack on a fully adjustable goniometer and aligned on the diffractometer such that the most densely packed region (bottom of capillary) was in the beam. A diffractogram was recorded at 100 K over 6 hours for comparability with the single crystal data (T = 100 K), but build-up of ice on the external surface of the capillary precluded unit cell determination by Pawley refinement. The sample temperature was ramped to 298 K (heating rate 6 °C min^{-1}), and a second diffractogram was recorded at 298 K for 6 hours. The diffractograms at both temperatures were significantly different from the powder pattern calculated from the single crystal XRD data, suggesting a different unit cell (possibly of different symmetry). This could be a mixture of several phases of **14** or a poorly defined phase $Sn(N_3)_2(py)_{2-x}$ (x = 0–2) which is intermediate between **14** and **16**. The capillary was

'snipped' open using tweezers (and re-aligned) whilst in the N_2 stream at 298 K. A 5 minute data collection showed no change after opening the capillary. Starting at 298 K the temperature was ramped up, and a 5 minute diffractogram recorded at each 25 K interval, showing very subtle changes around 2θ = 33 °. Otherwise only incremental changes in peak positions due to thermal expansion were observed until at 398 K (125 °C) the diffractogram was fundamentally different, indicating the presence of a new phase. To minimise the chances of decomposition (explosive or thermal) the sample was only maintained at 125 °C for the duration of the 5 minute diffraction measurement and immediately cooled to 25 °C at the maximum rate of 6 °C min^{-1}. The diffraction intensity from the new phase was greatly reduced because the packing of the material had been disturbed by loss of pyridine, so a longer data collection was necessary to get an acceptable signal-to-noise ratio. The sample was allowed to cool to 298 K in the nitrogen stream, and a 1 h diffractogram was recorded and the data were indexed to the approximate unit cell dimensions: a = 6.4 Å, b = 11.7 Å, c = 6.0 Å, α = 90°, β ≈ 94°, γ = 90°.

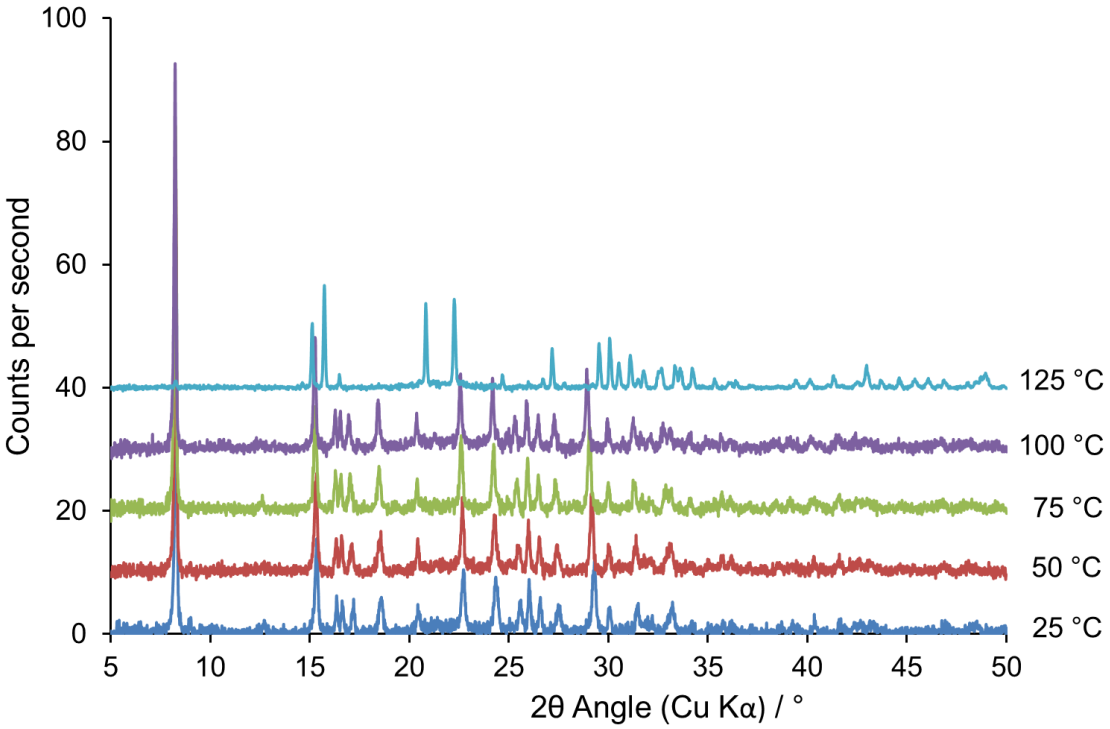

Figure 4.32. Overlay of powder diffractograms of $Sn(N_3)_2(py)_2$ (**14**) under nitrogen flow with increasing temperature. The y-axis applies to the data collected at 25 °C, and the subsequent data collections are offset by increments of 10 for clarity. The data collection time was 5 minutes at all temperatures except for 125 °C, which required a longer 1 hour data collection (after cooling to RT).

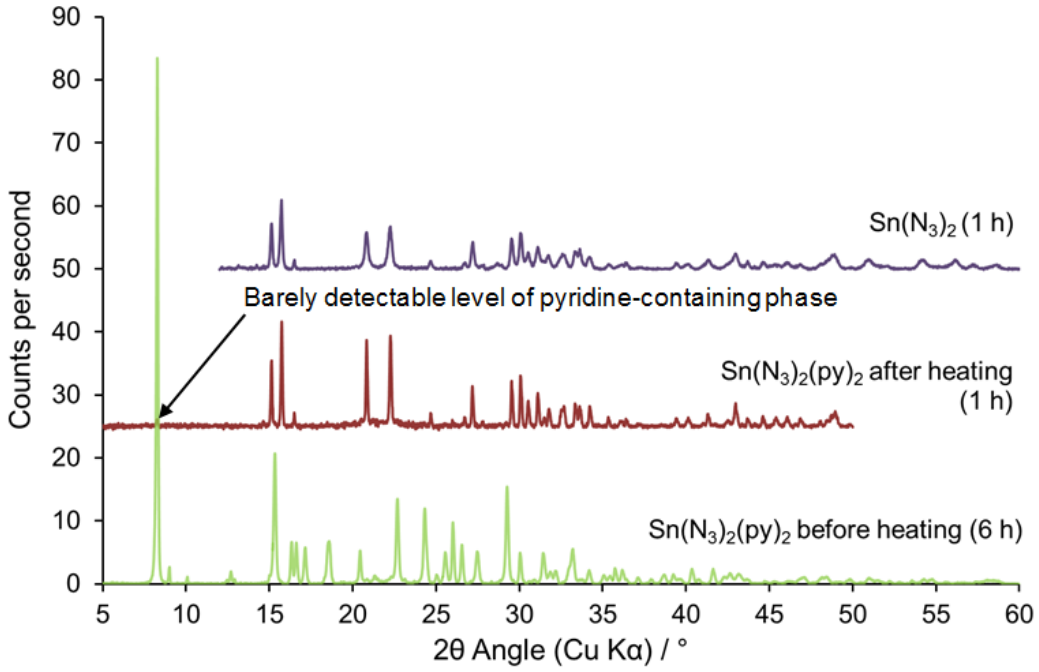

Figure 4.33. Comparison of the 6 h diffractogram of $Sn(N_3)_2(py)_2$ before heating (green), and initial 1 h diffractogram after heating to 125 °C in the cryostream (red), with a genuine sample of $Sn(N_3)_2$ (purple, see section 4.2.7 below. The pyridine-containing phase appeared to be depleted judging by the virtual absence of its principal peak at 8.3°, so a longer data collection (18 hours) was carried out (see Figure 4.34 below).

A longer measurement was carried out overnight for 18 hours to try to determine the structure of the new phase (see Figure 4.34 below), which was still hampered by the displacement of the material away from the beam path (up to 44 wt% mass loss would be expected for removal of 2 equivalents of pyridine). This resulted in fairly low average intensity sufficient only for unit cell determination, and the sample was discoloured (yellow/brown) after the measurements. Reappearance of the peaks corresponding to the initial pyridine-containing phase suggested that pyridine may not have been driven off completely in the constricted capillary geometry during the short time of heating at 125 °C. The yellow-brown discolouration of the sample seems to be localised to the region of the X-ray beam. To get around the problem of low intensity data, a capillary was loaded carefully with $Sn(N_3)_2$ (see section 4.2.7).

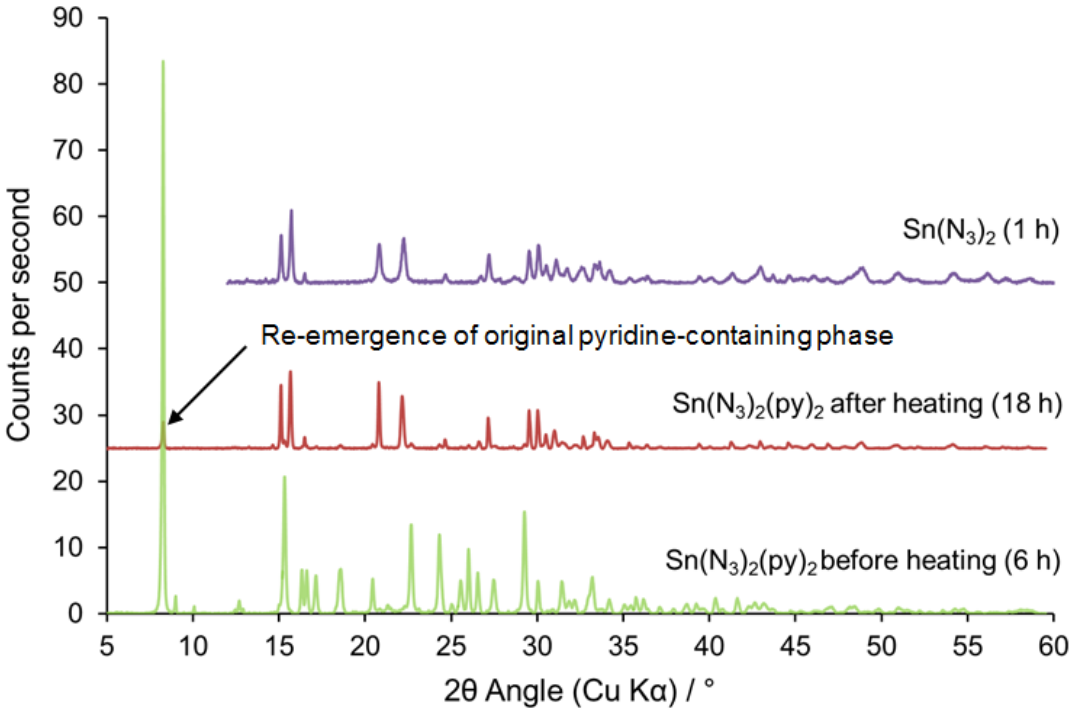

Figure 4.34. Comparison of the initial 6 h diffractogram of $Sn(N_3)_2(py)_2$ before heating (green), and 18 h diffractogram after heating to 125 °C in the cryostream (red), with a genuine sample of $Sn(N_3)_2$ (purple, see section 4.2.7 below. The re-emergence of the peak corresponding to the initial pyridine-containing phase, $Sn(N_3)_2(py)_2$, at 8.3° shows the material obtained is not pure $Sn(N_3)_2$.

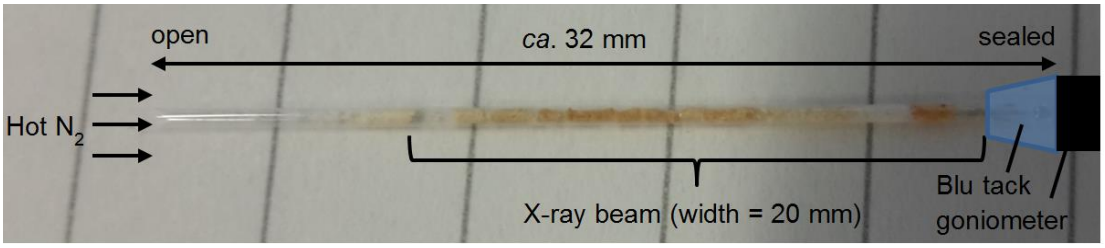

Figure 4.35. The sample of **14** after the *in-situ* heating study, showing dispersal of the material along the capillary which reduced the packing density, and some discolouration in the area exposed to X-rays. *[Photo: Rory Campbell]*

4.2.7 Powder X-Ray Diffraction Study on $Sn(N_3)_2$ (16)

Sample preparation and capillary loading

$Sn(N_3)_2$ (42 mg, 0.207 mmol) was prepared from $Sn(N_3)_2(py)_2$ (**14**) as described in the experimental details section 6.4.3. A sample was transferred carefully to a shortened capillary (0.7 mm internal diameter, 50 mm total length) to a depth of 25 mm to make use of the full width of the X-ray beam. Below is a detailed description of the experimental handling procedures. An extremely thin glass fibre was drawn out from a Pasteur pipette, which acted as an indicator to observe local static build-up in the glovebox before (and between) manipulations. The Schlenk tube seemed to accumulate the least static when kept in contact with the metal floor of the glovebox during manipulations. A Teflon-coated spatula (220 mm) was used to carefully move small (*ca.* 5 mg) portions from the Schlenk tube onto a mortar,

from which a smaller Teflon-coated (scoop) spatula was used to transfer the sample into the capillary *via* a 'funnel' cut from the mid-section of a Pasteur pipette. Once loaded the open end of the capillary was carefully sealed with melted beeswax and mounted in blu-tack on a fully adjustable goniometer.

Powder X-ray diffraction data collection

An initial 5 min data collection was carried out to test diffraction intensity and sample quality, and for comparison with the new phase observed in the previous experiment after heating $Sn(N_3)_2(py)_2$. A diffractogram was recorded overnight (15 hour) at 298 K, with a separate 1 hour diffractogram measured before and afterwards to check sample consistency. Visual inspection of the sample showed it had discoloured (turned yellow from off-white, Figure 4.36), and the differences between the initial and final 1 h data collections (see Figure 4.37) suggest the 15 hour overnight dataset is not valid. It was not possible to extract unit cell information from either the 15 hour data collection or the 1 hour diffractogram recorded afterwards, which suggests the material underwent partial decomposition during measurement. Indexing the initial 1 hour diffractogram gave a good fit to the following unit cell: Monoclinic ($P2_1/c$); a = 6.44051 Å; b = 11.69991 Å; c = 6.06118 Å; α = 90°, β = 94.26848°, γ = 90°, $V \approx 456$ Å^3. This was in very good agreement with the unit cell obtained from the *in-situ* heating study of $Sn(N_3)_2(py)_2$.

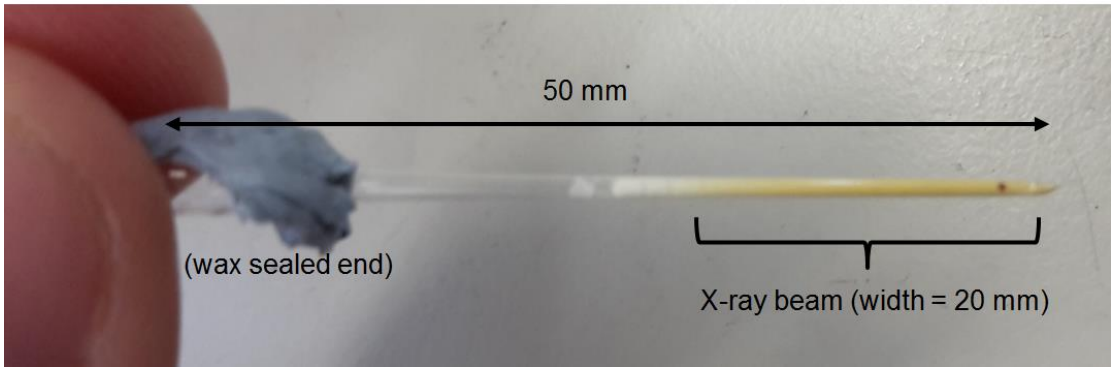

Figure 4.36. A photo of the sample after an overnight 15 hour powder diffraction experiment showing selective discolouration of the region of the sample in the X-ray beam. The white appearance of the material nearest the wax-sealed end (left) suggests it is not simply oxidation from air ingress, but an effect of X-ray radiation. *[Photo: Rory Campbell]*

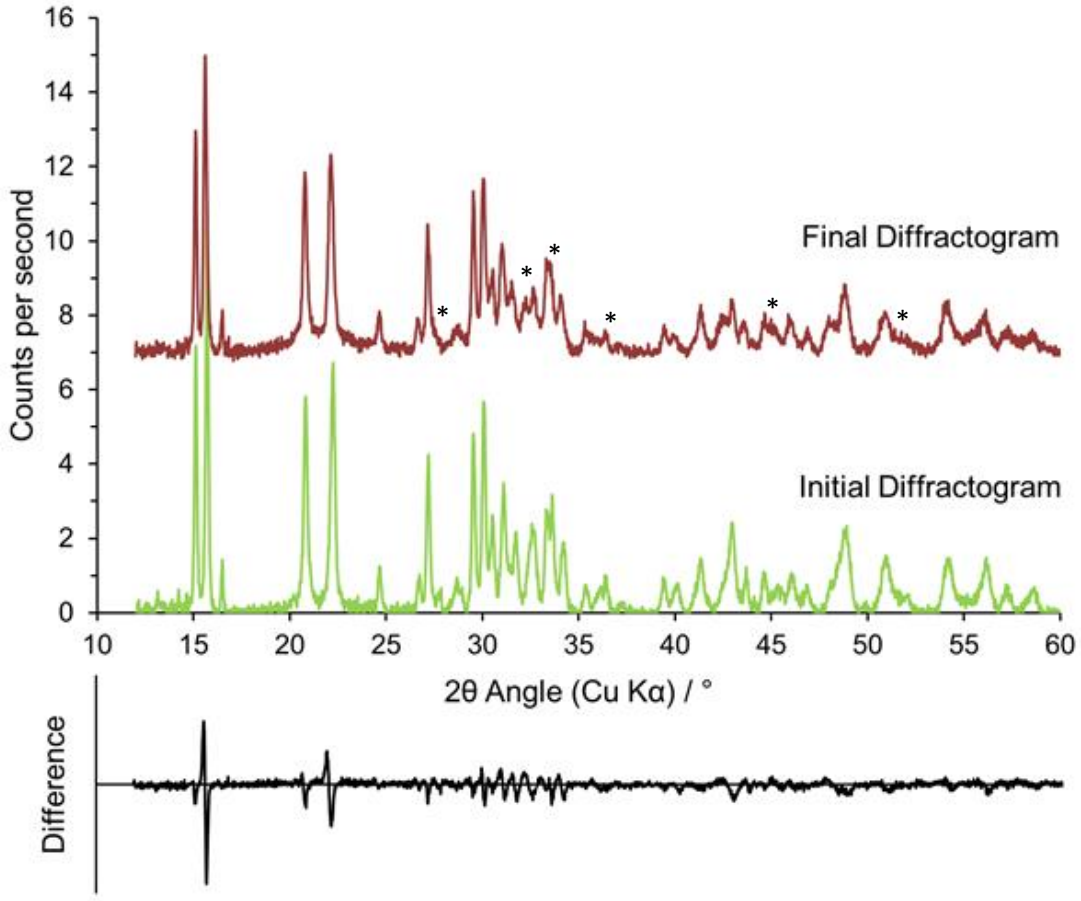

Figure 4.37. Comparison of the diffractograms of $Sn(N_3)_2$ obtained before (green) and after (red) X-ray irradiation (during a 16 hour XRD experiment) with the difference plot (black) to illustrate the changes.

The diffraction experiments have shown that $Sn(N_3)_2$ (at least partially crystalline) can be prepared *in-situ* in a capillary from $Sn(N_3)_2(py)_2$ by heating in a stream of hot nitrogen, but the resultant scattering of material by the evaporation of pyridine causes not only 44 wt% mass loss but displacement of some material from the beam path and dramatic drop off in diffraction intensity. A follow up experiment on $Sn(N_3)_2$ was carried out, which enabled determination of the unit cell of $Sn(N_3)_2$ from a 1 hour-long diffraction pattern. A longer data collection seemed to cause partial decomposition of the sample as the material became visibly discoloured, and no suitable unit cell could be determined from the obtained data.

Combined DFT and PXRD Investigation into the structure of $Sn(N_3)_2$

The structure has been determined experimentally by Rietveld refinement based on powder diffraction data collected in Sheffield. Employing a chemically reasonable set of restraints based on the single crystal diffraction data obtained for **14** and **15**. Using the preliminary unit cell determined by PXRD measurements as a starting point, the structure of $Sn(N_3)_2$ has been calculated using density functional theory. The two methods are qualitatively in very good agreement, showing the 1,1-bridges formed by azido ligands between the tin centres in the *c*-axis direction. Table 4.9 (below) shows a comparison of geometric parameters obtained by

the two methods, which are reasonably close together. The tin atom is penta-coordinate, with two formally bound azide ligands, two 1,1-bridging azides, and a 1,3-bridging azide group. The lone pair presumably occupies the remaining position. The unit cell calculated from DFT is decidedly shorter along the *b*-axis (11.06 *vs.* 11.77 Å), and slightly longer in the *a*-axis (6.78 *vs.* 6.44 Å) and *c*-axis (6.23 *vs.* 6.06 Å). The DFT calculations predict a shorter bridging interaction (2.33 *vs.* 2.51 Å) which would account for the shortening in the *b*-axis direction.

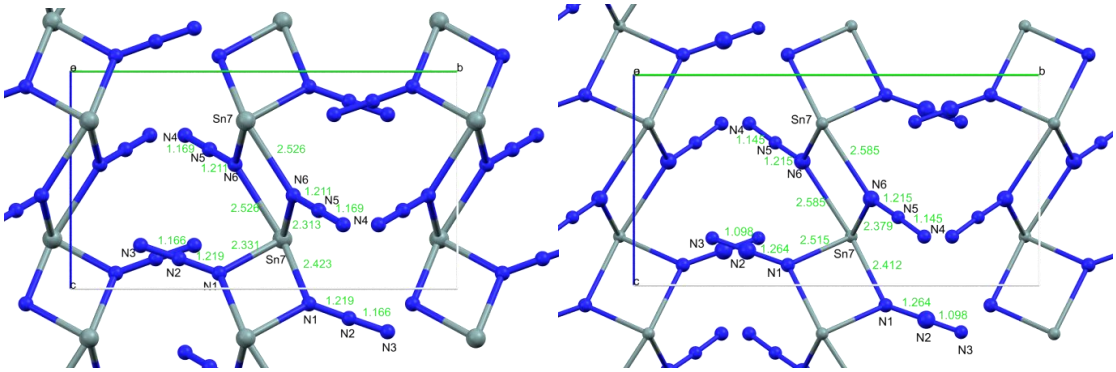

Figure 4.38. Left: Structure of $Sn(N_3)_2$ calculated by DFT methods (Dr. Stephen Hunter, University of Edinburgh). Right: The result of Rietveld refinement (Sumit Konar, University of Edinburgh) of the $Sn(N_3)_2$ PXRD data. Both structures are viewed along the *a*-axis.

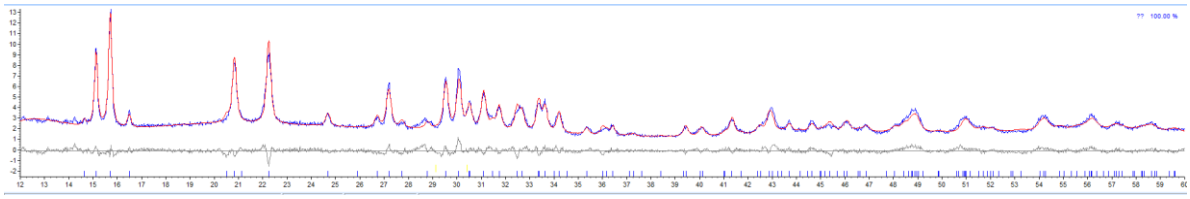

Figure 4.39. Overlay of the PXRD pattern with the final Rietveld refinement result (top), with the difference plot (bottom). R_{wp} = 6.751, R_{exp} = 3.708, R_p = 5.342, GOF = 1.820

Table 4.9. Comparison of molecular geometries obtained from DFT calculations and from refinement of PXRD data.

Distances [Å]			Angles [°]			Unit cell parameters		
	DFT	PXRD		DFT	PXRD		DFT	PXRD
N1–N2	1.219	1.26	N1–Sn–N6	86.5	79	*a* [Å]	6.776	6.446
N2–N3	1.166	1.10	N1–Sn–N6^{i}	144.3	156	*b* [Å]	11.059	11.702
N4–N5	1.169	1.14	N1–Sn–N1^{i}	69.9	78	*c* [Å]	6.233	6.060
N5–N6	1.211	1.21	N6–Sn–N6^{i}	67.3	76	*α* [°]	90	90
Sn–N1	2.331	2.42	N1–N2–N3	179.1	176	*β* [°]	94.67	94.24
Sn–N6	2.312	2.38	N4–N5–N6	179.5	176	*γ* [°]	90	90
Sn···N1	2.42	2.52	Sn–N1–N2	124.5	118	*V* [Å^3]	465.5	455.9
Sn···N6	2.53	2.59	Sn–N6–N5	119.3	119			
Sn···N4	2.79	2.92						

4.3 Conclusions

A variety of tin(II) azides are accessible *via* reaction of tin(II) halides, SnX_2 (X = F, Cl), with azide transfer reagents NaN_3 or TMS–N_3 in an appropriate polar coordinating solvent. Reaction of $SnCl_2$ with a twenty-fold excess of NaN_3 in THF produces $Na[Sn(N_3)Cl_2]$ but the exchange of the remaining chlorides seems to be slower than for $(PPh_4)[Sn(N_3)Cl_2]$.[92] Alternatively the $Sn(N_3)_2(L)_2$ complexes are produced when using the appropriate coordinating base L = pyridine (**14**), 4-picoline (**15**) as solvent. Ligand exchange of transition metal and main group fluorides, including tin(IV) fluoride, with trimethylsilyl azide has been shown to be an efficient route to many of the corresponding azides by elimination of trimethylsilyl fluoride. This methodology has been extended to SnF_2 by preparation of Diazidobis(pyridine)tin(II) (**14**) and diazidobis(4-picoline)tin(II) (**15**), which are the first two examples of neutral tin(II) azides without sterically demanding ligands. Except for $Sn(N_3)_2$ itself, the complex azides do not seem to be sensitive to friction or impact, though it must be noted that adduct **14** gradually loses pyridine to give $Sn(N_3)_2$ (even at 25 °C) except when stored in a sealed vessel. Conversely the 4-picoline adduct **15** is reasonably stable in air, with the FTIR spectrum after 24 hours air exposure showing only subtle changes. According to thermogravimetry measurements both adducts are converted to tin(II) azide when heated in a stream of nitrogen with extrapolated onset temperatures of 50 °C (**14**) and 75 °C (**15**), which is approximately the difference in boiling point between pyridine (115 °C) and 4-picoline (145 °C) and may be related to their volatility rather than strength of the coordinative bond. The absence of a 'dimeric' type $Sn\cdots N_\alpha$ non-bonded contact between adjacent tin atoms in the structure of **14**, which is observed in many tin azides including **15** and both known triazidostannate salts, could be partially responsible for the lability of the pyridine ligands compared to 4-picoline. During the characterisation of **14** a new preparative route for tin diazide, $Sn(N_3)_2$, has been developed which is faster, more convenient, and safer than the published procedure as it can be carried out at ambient temperature, and avoids the use of highly sensitive silver azide and the need for anhydrous ammonia as solvent. Tin(II) azide is a colourless solid and classified as a primary explosive due to its high sensitivity (particularly to electrostatic discharge) and may be even more sensitive than $Pb(N_3)_2$. The binary azide degrades slowly in air by oxidation, which can be observed by FTIR spectroscopy, and its moderate light sensitivity is apparent from gradual discolouration even under an argon atmosphere. This combination of properties posed significant risks and challenges in its handling and characterisation. The solid state structure of **16** has been determined by Rietveld refinement of powder XRD data obtained in Sheffield. An *in-situ* heating of **14** showed that the pyridine can be removed in a stream of hot nitrogen leads to formation of $Sn(N_3)_2$, though the volume of material lost during this process hampered the quality of the diffraction data. Using the unit cell dimensions obtained for tin diazide, the structure was calculated by DFT

methods which showed good agreement with the structural features observed experimentally. A further difficulty was partial sample decomposition during longer PXRD measurements, which could be a result of X-ray exposure as the tin content is 58 % by weight. The more convenient route to $Sn(N_3)_2$ means that with appropriate caution it is a viable intermediate in the preparation of other tin(II) azides including guanidinium triazidostannate(II) (**17**), which joins the rare class of homoleptic low valent group 14 azides. Nitrogen-rich salt **17** seems to be insensitive to friction and impact despite containing a binary azide species and around 55 wt% nitrogen overall, though high air and moisture sensitivity, and low thermal stability (T_{on}^{dec} = 95(4) °C) limit its utility at present. The crystal structure of **17** has an extensive 3D network of interionic hydrogen bonds and the complex $[Sn(N_3)_3]^-$ anion shows the shortest 'dimeric' $Sn\cdots N_\alpha$ contacts amongst the known tin(II) azides with this feature. The synthesis of aminoguanidinium triazidostannate was attempted using the same method as for **17** but the small amount of microcrystalline solid obtained was unsuitable for single crystal XRD. The tin(II) azides described in this work are readily oxidised to their tin(IV) analogues in solution by ethereal HN_3 as observed previously for $(PPh_4)[Sn(N_3)_3]$.[92] As in the case of bis(guanidinium) hexaazidostannate (**3**), the extensive hydrogen bond network in guanidinium triazidostannate may contribute towards the stabilisation of the nitrogen-rich (55 % N) compound, and its apparent insensitivity to friction and impact.

5. Exploring synthetic routes towards 2,4,6-tris(tetrazol-1-yl)-1,3,5-triazine (TTT)

Aims

I. Extend the 1,3,5-triazine unit to form nitrogen-rich polyheterocyclic compounds
II. Investigate the reliability of published procedures for synthesis of the title compound 2,4,6-tris(tetrazol-1-yl)-1,3,5-triazine (TTT)
III. Develop improved synthetic protocols for the synthesis of TTT, and investigate its capacity to act as a ligand in energetic coordination compounds
IV. Study the high-pressure behaviour of TTT to investigate the possible transformation to a novel 'polymeric' energetic material

5.1 Introduction

Molecular nitrogen can be transformed into solid polymeric nitrogen under extreme conditions,[209] though the hysteresis is not sufficient to recover the material to ambient conditions. By the choice of a suitable nitrogen-rich precursor compound it may be possible to produce a similar transformation to an energetic polymeric solid which is recoverable to ambient conditions. Studies on guanidinium nitrate[210] and perchlorate[211] have shown the effect of extremely high pressures on their solid state structures, and the modification of the hydrogen bond networks to accommodate the pressure increase. The physicochemical transformation of (energetic) materials is another avenue under investigation, including a high-pressure study of cyanuric triazide[212] that suggests compression of a material can not only influence intermolecular interactions, but form new covalent bonds. In the case of cyanuric triazide the transformation to the (unidentified) high pressure phase seems to be reversible according to *in-situ* IR spectroscopy as cyanuric triazide is recovered upon decompression to ambient conditions. The 1*H*-tetrazole analogue, 2,4,6-tris(tetrazol-1-yl)-1,3,5-triazine (**20**), may be able to undergo a similar transformation, and to this end the synthesis was investigated. Triazines are versatile building blocks which have found applications in diverse fields of research including materials for non-linear optics (NLO),[213] dendrimer syntheses,[214] potential antiviral[215] or antimalarial agents,[216] precursors to novel C–N materials,[217] and energetic materials. Cyanuric chloride, $(NCCl)_3$, the trimer of chlorocyanogen, has proved to be an convenient route to a multitude of mono- ($T \approx 0$ °C), di- ($T \approx 25$ °C), and trisubstituted derivatives ($T > 50$ °C) by tuning of the stoichiometry and reaction conditions. In this way many 'mixed' triazines are accessible, which further enhances

their synthetic versatility. Also it can act as a chlorine source in organic syntheses,[218–220] finding application as a milder alternative to reagents such as thionyl chloride. It gradually hydrolyses in aqueous solution,[221] reacts with DMF to form a Vilsmeier-Haack type compound (Me_2N^+=CHCl)($C_3N_3Cl_2O^-$),[220] and dissolving in DMSO leads to ring opening of the triazine and formation of Gold's reagent (Me_2N–CH=N–CH=N^+Me_2)Cl with liberation of dimethylsulfide.

5.2 Results and Discussion

5.2.1 Syntheses

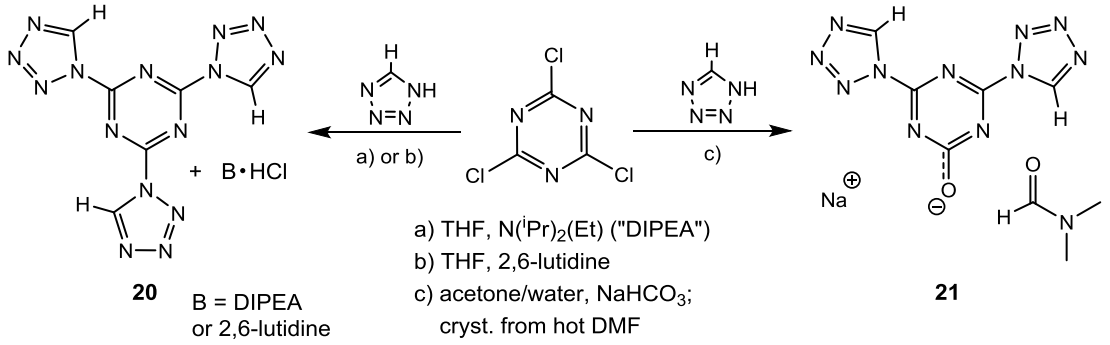

Scheme 5.1. Attempted syntheses of 2,4,6-tris(tetrazol-1-yl)-1,3,5-triazine (**20**) adapted from preparative methods for other triazines, and subsequent isolation of side product sodium 2,4-bis(tetrazol-1-yl)-1,3,5-triazinon-6-ate (**21**), which was crystallised as a DMF solvate from crude material obtained from a published procedure.[133]

Cyanuric chloride (2,4,6-trichloro-1,3,5-triazine) is an inexpensive and versatile synthon for a diverse range of mono-, di-, and trisubstituted 1,3,5-triazines. The original literature report of the synthesis of 2,4,6-tris(tetrazol-1-yl)-1,3,5-triazine (**20**) involves the addition of a slight excess of $NaHCO_3$ to a mixture of cyanuric chloride and 1*H*-tetrazole in a 10 : 1 mixture of acetone/water ("Method 1").[133]. When this procedure was followed, the crude material obtained was recrystallised by cooling of a hot, saturated solution to RT which yielded small block crystals. Investigation of the crystals by single crystal XRD showed the composition of the material to be sodium 2,4-bis(tetrazol-1-yl)-1,3,5-triazinon-6-ate DMF solvate (**21**) rather than compound **20**. The composition of the crystals was supported by elemental analysis, except the nitrogen content was 0.95 % low: Expected C: 29.28, H: 2.76, N: 51.2; Found: C: 29.15, H: 2.48, N: 50.25. The reported yield is 18 %, whereas during this work the (raw) yields of **21** were variable (*ca*. 4–30 %) and zero for **20**. Another similar procedure was reported by Ganta *et al.* as part of a patent for gas generant compositions and included protocols for preparing the intermediates between cyanuric chloride and **20**.[134] In these procedures the cyanuric chloride was added to a solution of 1*H*-tetrazole and $NaHCO_3$, and acetonitrile was used as reaction solvent instead of acetone ("Method 2"). However the reported yield exceeds 100 %, and attempts to replicate the synthesis have so far been unsuccessful. Following these attempts based on literature procedures, alternative routes have

been explored based on those applied for other triazines, including the use of sterically hindered organic bases 2,6-lutidine (2,6-dimethylpyridine) and diisopropylethylamine (DIPEA) instead of $NaHCO_3$.[214,215] After the isolation of side product **21**, reactions were carried out with exclusion of water as a precaution in hydrolysis of cyanuric chloride or intermediates was hampering the reaction. Addition of a three-fold excess of 2,6-lutidine to a solution of cyanuric chloride and 1*H*-tetrazole in THF resulted in almost immediate precipitation accompanied by colour change to yellow-orange ("Method 3"). Initially it was thought that this was due to reaction of 2,6-lutidine with the triazine core, leading to an extensively delocalised cation as for less sterically hindered pyridines.[222] However, examination of the precipitate *via* ^{1}H and ^{13}C NMR (dmso-d_6) revealed a mixture of compounds with several triazine and tetrazole environments and only one set of peaks for the 2,6-lutidinium cation. An FTIR spectrum of the solid as a nujol suspension confirmed the presence of an intense N–H stretch in the same position as observed in 2,6-lutidinium chloride.[223] In combination, these observations suggest that the only lutidine-based species present in the residue is the expected by-product 2,6-lutidinium chloride. By comparison with the NMR spectra of **21**, the tetrazolyltriazine species are assigned to the tris(tetrazolyl)triazine **20** and the chlorobis(tetrazolyl)triazine. When instead DIPEA was employed as the base, and the reaction mixture stirred overnight, the precipitation from the solution (and associated colour change) was markedly slower, initially giving a pale yellow solution which turned orange upon stirring overnight ("Method 4"). The reaction of sodium tetrazolate with cyanuric chloride in water and acetone/water mixtures appeared to lead to the formation of a product similar to **21**, albeit in a very low yield, and the fine suspensions obtained proved almost impossible to filter ("Method 5"). When the same reaction was carried out in anhydrous THF and stirred for an extended time at RT, a similarly fine suspension of off-white solid was obtained, filtration of which was impractically slow. Evaporation of the remaining solution resulted in isolation of a compound which matched the FTIR spectrum of **21**, and perhaps a trace of **20** ("Method 6"). Several potential avenues remain to be explored including the metathesis of silver tetrazolate with cyanuric chloride with elimination of AgCl. A potential problem would be the predicted insolubility of the product (**20**), which may prove difficult to separate from the similarly insoluble AgCl by-product.

5.2.2 Method 1: Using $NaHCO_3$ as base in acetone[133]

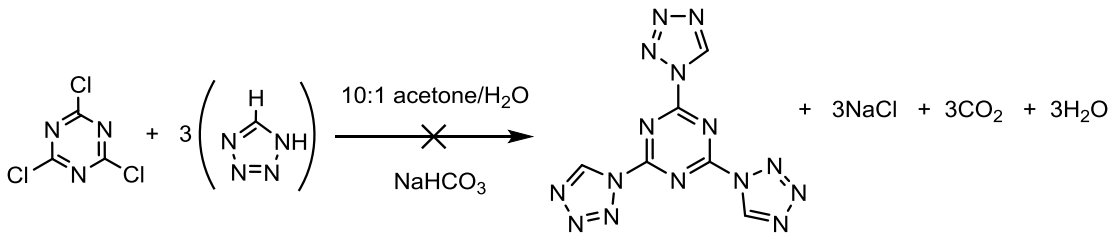

Scheme 5.2. Proposed scheme for the synthesis of **20** according to the literature procedure.[133]

FTIR Spectra of crude material obtained from method 1

The products of the various synthetic procedures were investigated by FTIR and NMR spectroscopies. The original literature procedure involving reaction of cyanuric chloride with 1*H*-tetrazole in 10 : 1 acetone/water mixture with $NaHCO_3$ as base gave an insoluble off-white solid, which was insoluble in most solvents except for dimethylsulfoxide and hot *N*,*N*-dimethylformamide. The peaks around 3100 cm^{-1} are most likely to be tetrazole-based CH stretches (*cf.* 1*H*-tetrazole 3157 cm^{-1}).[152] The broad features at 3487, 3401, and 3275 cm^{-1} could be due to the presence of water of crystallisation in the solid.

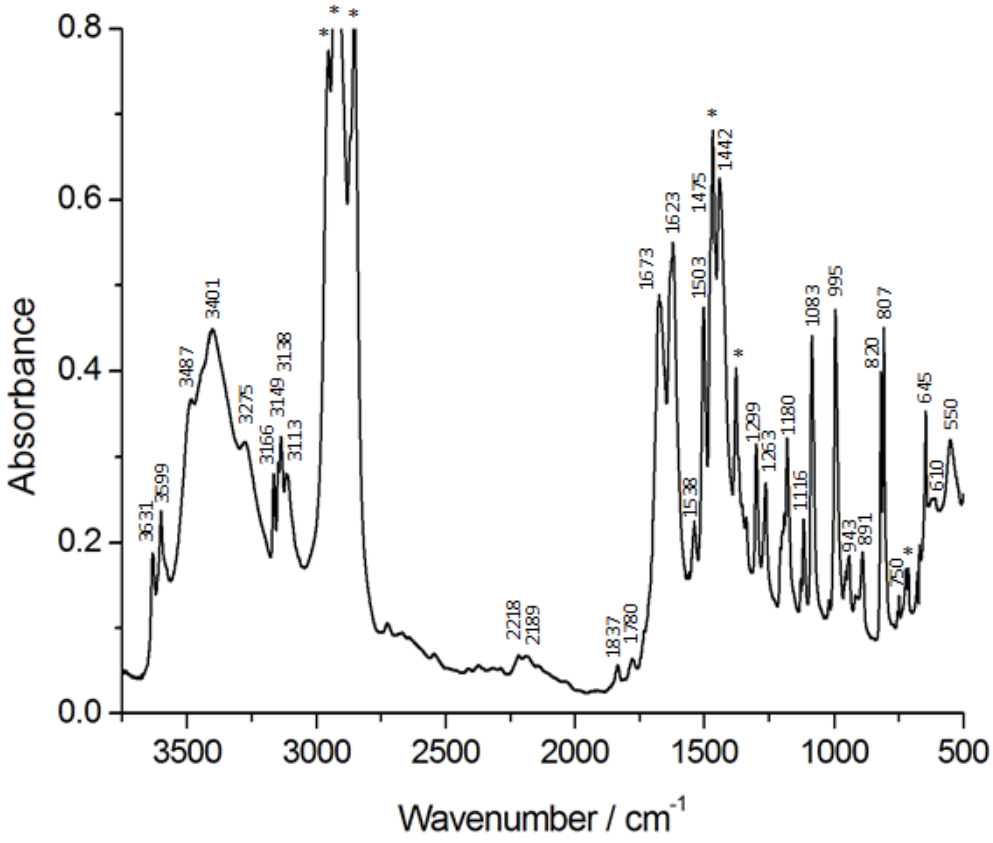

Figure 5.1. FTIR spectrum of the residue obtained by the original literature procedure (method 1).[133]

Recrystallisation of the crude material from DMF resulted in the disappearance of the broad bands around 3300–3500 cm^{-1}, which could be exchange of water for DMF. The reactivity of the Cl substituents decreases after each successive substitution. It is possible that the crude material prior to recrystallisation consisted of 2-chloro-4,6-bis(tetrazol-1-yl)-1,3,5-triazine with residual $NaHCO_3$, and when the mixture was heated to 80 °C during crystallisation attempt the Cl substituent reacted with the DMF solvent in the same way as cyanuric chloride,[220] eliminating HCl by reaction with residual $NaHCO_3$ and leaving behind **21**. When the material was recrystallised from hot DMF, the broad features around 3400 cm^{-1} disappeared, and the C=O of DMF is visible at 1690 cm^{-1}, and there is only a single tetrazole C–H stretch visible in the FTIR spectrum.

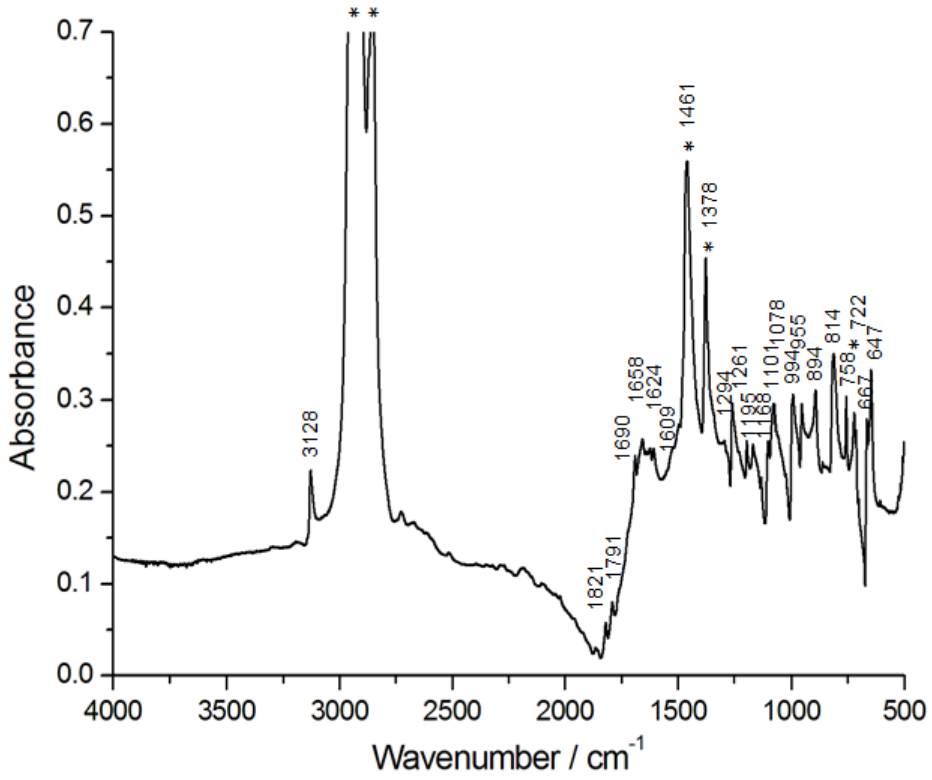

Figure 5.2. FTIR spectrum of the material after recrystallisation of the crude material (obtained *via* method 1) from hot DMF ($T \approx 80$ °C).

^{1}H and ^{13}C NMR spectra of crude material obtained from method 1

The crude material obtained by following the original literature procedure (method 1) was investigated by ^{1}H and ^{13}C NMR in dmso-d_6. There is a single tetrazole C–H environment at δ = 10.18 ppm, and a prominent water peak at 3.35 ppm, which combined with the FTIR spectrum of the material suggests it contains water. In the ^{13}C NMR spectrum there is a total of 3 carbon environments at 165.6, 160.3, and 143.1 ppm. The latter peak is consistent with the tetrazole-based environment and the two former peaks are in the region expected for 1,3,5-triazine carbon resonances. The presence of one tetrazole resonance in the NMR spectrum, and a single isolated peak for the tetrazole C–H in the FTIR spectrum suggest a single tetrazole environment, but the appearance of a second triazine environment at slightly higher frequency (165.6 ppm) suggests it is not a symmetrically substituted triazine. Upon crystallisation of the obtained crude material, additional DMF peaks are visible at 7.95, 2.89, and 2.73 ppm in the ^{1}H NMR, and 162, 35.8 and 30.8 ppm in the ^{13}C NMR which dominated the spectra. Finally, the subsequent crystallisation of sodium 2,4-bis(tetrazol-1-yl)-1,3,5-triazinon-6-ate (**21**) DMF solvate from the reaction mixture confirmed the unsymmetrical substitution.

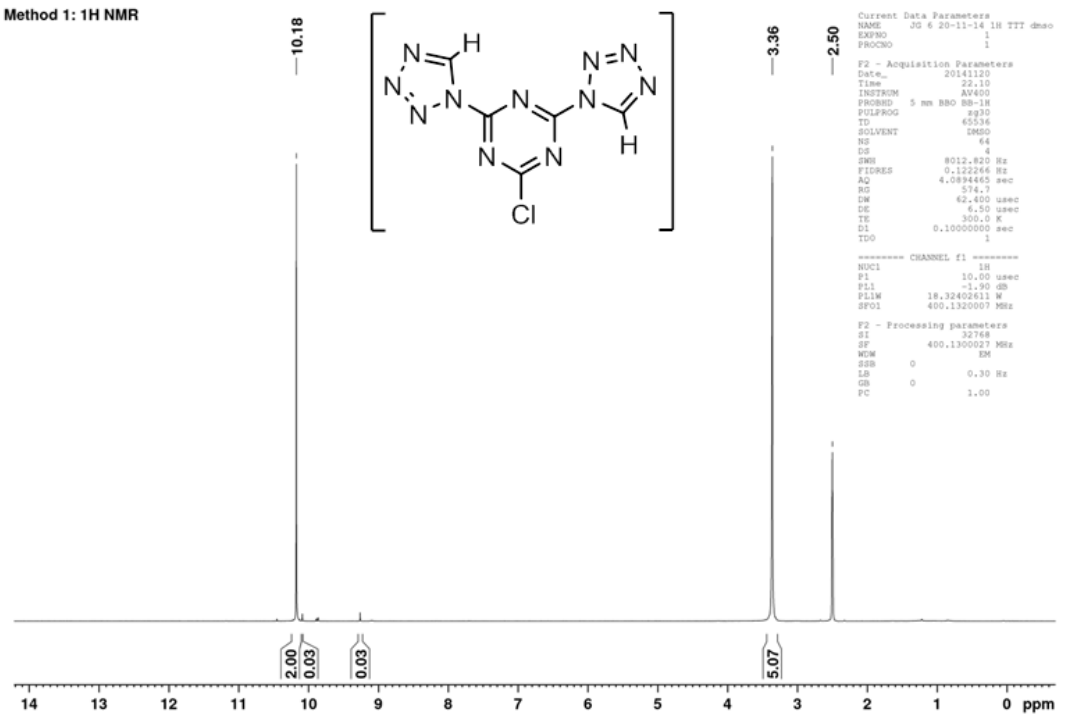

Figure 5.3. ^{1}H NMR spectrum (dmso-d_6) of the crude material obtained by method 1.

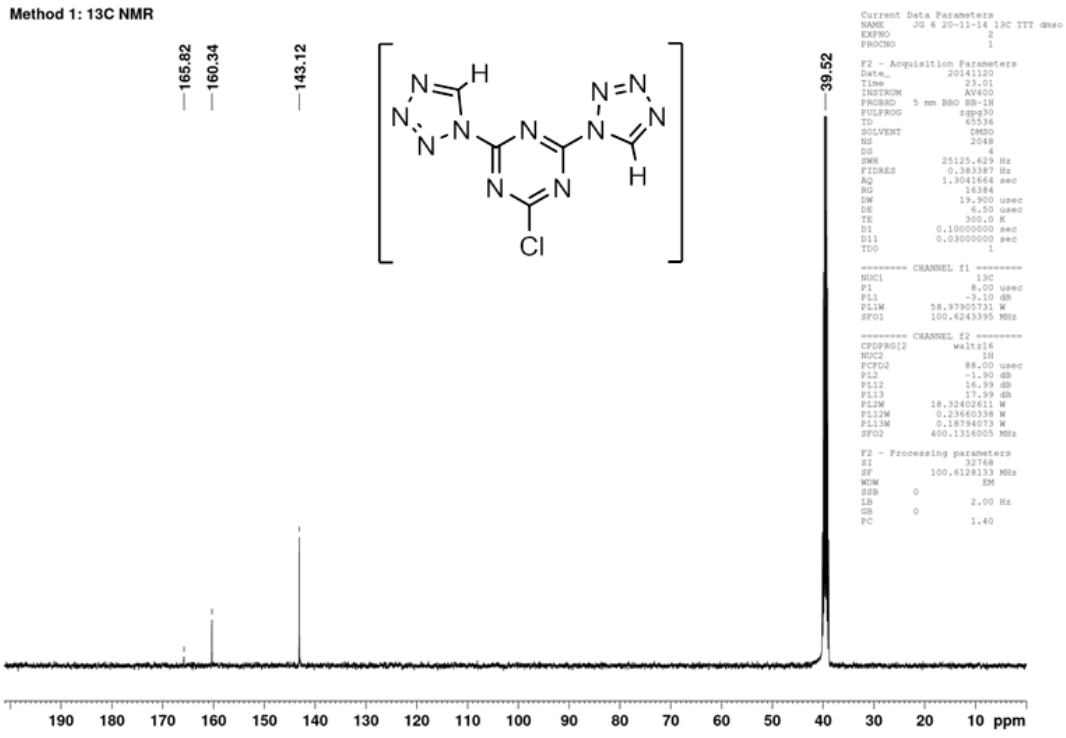

Figure 5.4. ^{13}C NMR spectrum of the crude material obtained by method 1.

^{1}H and ^{13}C NMR spectra of sodium 2,4-bis(tetrazol-1-yl)-1,3,5-triazinon-6-ate) DMF solvate (21)

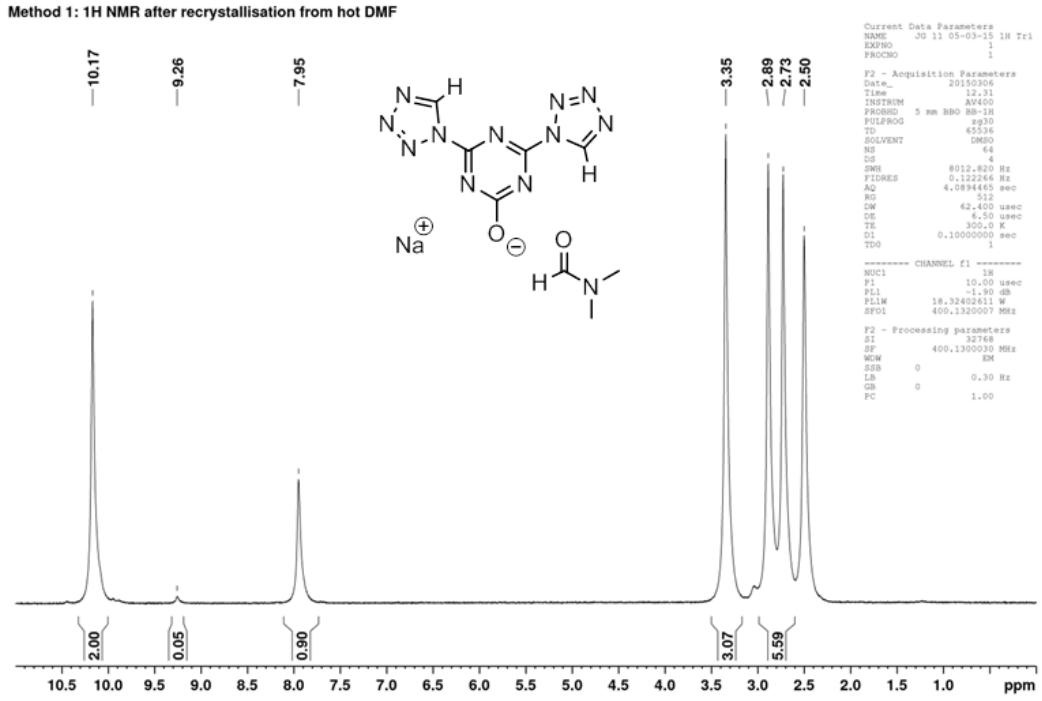

Figure 5.5. ^{1}H NMR spectrum of compound **21** obtained by recrystallisation of the crude material (Figure 5.3 above) from DMF. The peak integrals are consistent with the displayed structure (inset), which contains 1 equivalent of DMF.

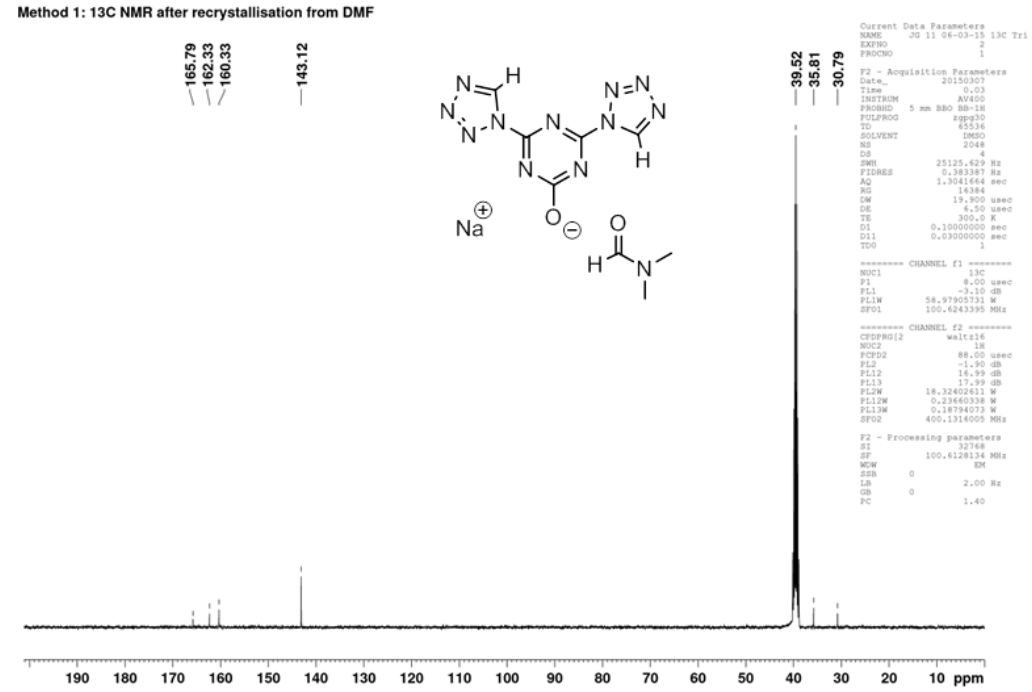

Figure 5.6. ^{13}C NMR of compound **21** in dmso-d_6 of the crude material (Figure 5.4) obtained by method 1 after recrystallisation from DMF.

Crystal structure of sodium 2,4-bis(tetrazol-1-yl)-1,3,5-triazinon-6-ate DMF solvate (21)

The crystals of sodium 2,4-bis(tetrazol-1-yl)-1,3,5-triazinon-6-ate (**21**) DMF solvate were obtained by cooling of a hot *N*,*N*-dimethylformamide solution to room temperature. The rate of cooling was not controlled, which may have led to the growth of more twinned crystals, and contributed to the poor diffraction data quality. A trial solution of the structure in space group $P2_1/c$ had a slightly lower R_1 value of 14.21 % (*ca*. 29 % before twin refinement) but some atoms had more severely distorted ellipsoids and 5 atoms were non-positive definite. Analysis of this initial solution with the ADDSYM tool in the *PLATON* software detected additional symmetry and suggested the space group $P2_1/m$. The reflection data showed signs of twinning, which was noticeable from the systematically distorted displacement ellipsoids (elongated along the *b*-axis, see Figure 5.7). The effect of twinning has been mitigated somewhat by twin refinement within *WinGX*, which improved the R_1 value from 22.9 to 15.7 %, but any structural insight beyond a chemically reasonable structure would require growth of superior quality crystals. The protons of the methyl groups in the DMF molecule were generated in fixed idealised geometry, and it was not possible to add the amide C–H either by location from residual electron density or in a calculated position. The only crystallographic restraint applied is a relaxed ISOR restraint to the disordered carbon C6 in the DMF residue.

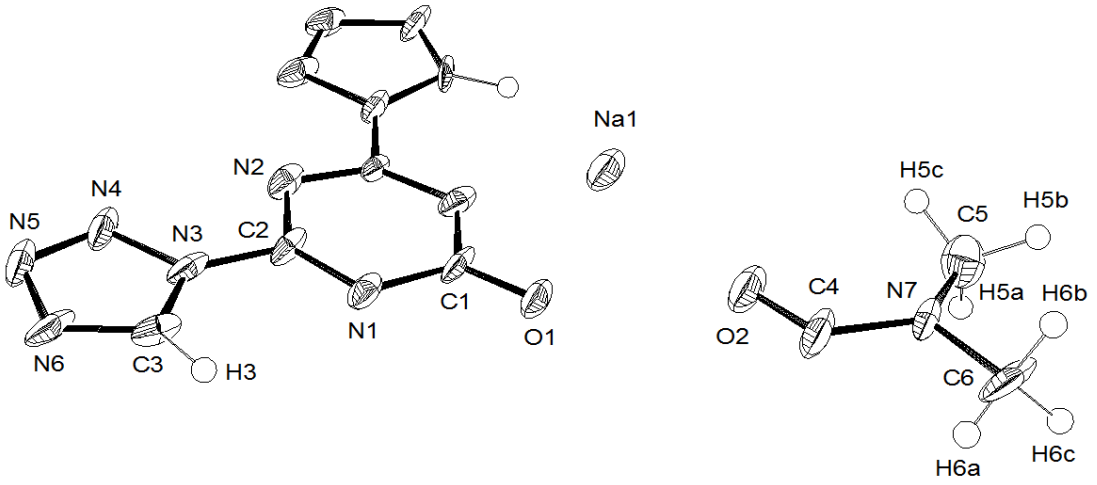

Figure 5.7. Molecular structure of **21** in the crystal at 100 K with labels omitted for the symmetry generated atoms, and one component of the disordered solvent (DMF) molecule is omitted for clarity. Thermal ellipsoids at the 50 % probability level, and hydrogen atoms represented by spheres of radius 0.15 Å. The quality of the structure solution is relatively poor, with R_1 = 15.7 % (22.9 % before twin refinement). It was not possible to locate the amide C–H of the DMF molecule due to its disordered orientation. Monoclinic ($P2_1/m$, Z = 2), a = 3.5885(3) Å, b = 13.5761(12) Å, c = 13.4946(8) Å, β = 93.706(3)°, V = 656.05(9) Å^3, R_1 = 0.1574. Selected bond lengths [Å] and angles [°]: Na1–O1 2.327(7), Na1–O2 2.448(8), C1–O1 1.216(11), C1–N1 1.406(7), N1–C2 1.287(9), C2–N2 1.346(8), C2–N3 1.430(10), N3–C3 1.364(10), C3–N6 1.301(11), N6–N5 1.364(9), N5–N4 1.309(10), N4–N3 1.348(8); O1–C1–N1 120.6(4), N1–C1–N1^{i} 118.8(9), C1–N1–C2 115.6(7), N1–C2–N2 130.1(7), C2–N2–C2^{i} 109.6(8), C1–O1–Na1 105.7(6), C1–O1–Na1^{i} 159.6(6), O1–Na1–O2 177.5(3).

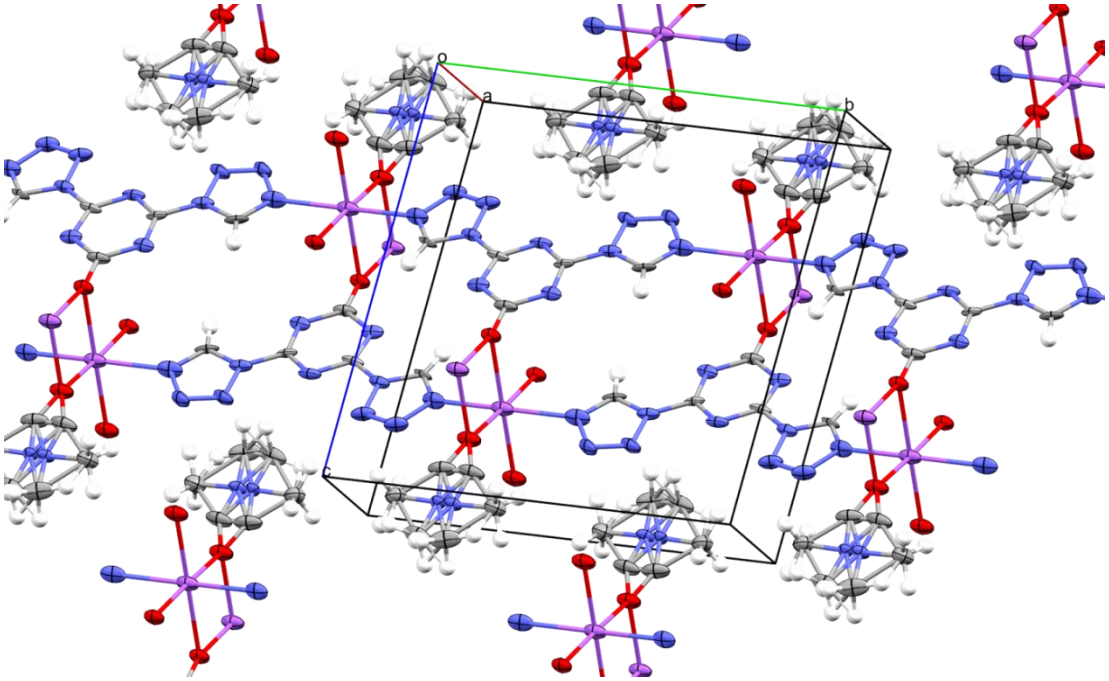

Figure 5.8. Packing in the crystal structure of **21** at 100 K. C: grey; H: white; N: blue; O: red; Na: purple.

The tetrazole and triazine rings are almost coplanar with an angle of around 4° between the average planes containing the heavy atoms. The sodium ion has distorted octahedral coordination by four triazinonate anions – two *via* the ring oxygen, two *via* tetrazole nitrogens – and two DMF solvent molecules. The triazinonate anions are bridged by sodium ions forming an infinite chain in the *b*-axis direction, and this framework may be responsible for both tetrazole protons pointing away from the DMF molecule rather than alternating orientation. The dimethylformamide solvent molecules form bridges between sodium ions in the *a*-axis direction, simultaneously occupying the voids between the two tetrazole rings. The symmetrical environment of the dimethylformamide molecule probably means there is no 'preferred' orientation and the size of the cavities allows conformational flexibility.

5.2.3 Method 2: Using acetonitrile as solvent instead of acetone/water

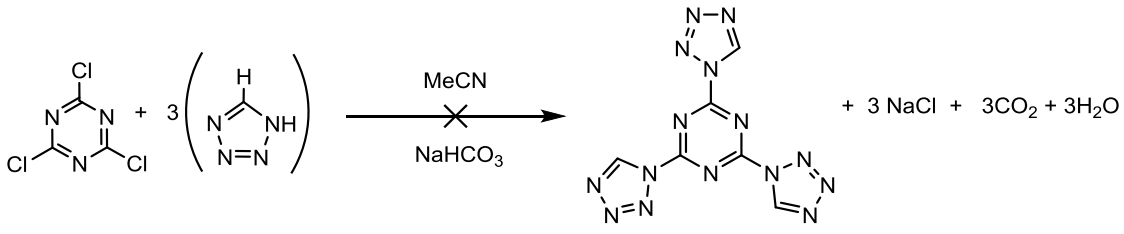

Scheme 5.3. Proposed reaction scheme for the preparation of **20** based on a patent for gas generant compositions,[134] in which acetonitrile is used as reaction solvent instead of acetone.

The method described by Ganta *et al.* (method 2)[134] in a patent on gas generant compositions described a very similar procedure which was carried out in acetonitrile instead of 10 : 1

acetone/water. The material obtained *via* this route was a bright yellow powder, from which there was a slight fizzing response to a flame test but the majority of the material did not melt or burn. The material contained a distinctive peak at 2195 cm^{-1}, and showed traces of residual water.

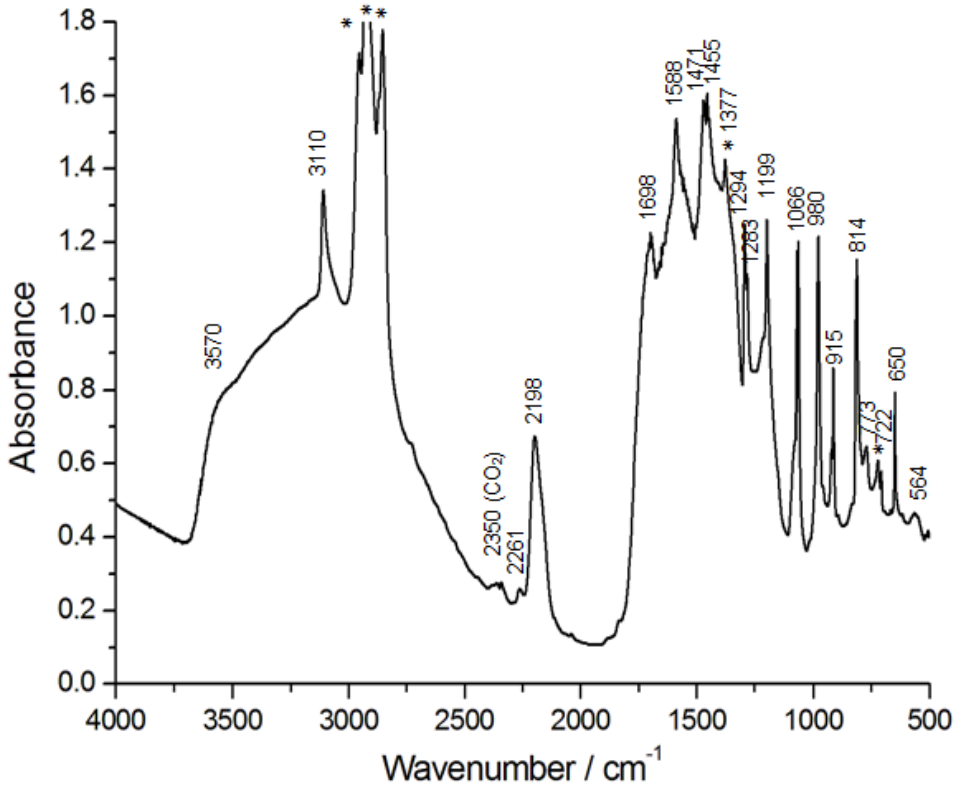

Figure 5.9. FTIR spectrum of the bright yellow powder residue obtained by the literature method of Ganta *et al.*[134] (method 2).

5.2.4 Method 3: Using the sterically hindered base 2,6-lutidine

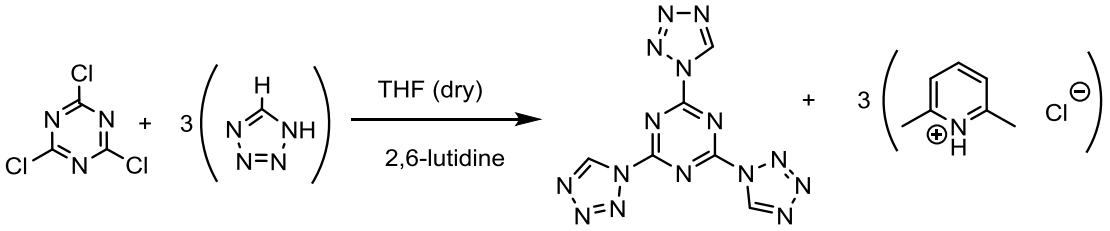

Scheme 5.4. Proposed alternative reaction for the synthesis of **20**.

After trying both published procedures (methods 1 & 2), an alternative route was investigated using 2,6-lutidine as base in THF with exclusion of moisture to minimise hydrolysis of cyanuric chloride (method 3). A rapid colour change to bright yellow-orange solution is observed almost instantaneously upon addition of the 2,6-lutidine to the reaction mixture, which was light orange after around 5 minutes. The solution was filtered off, and the residue washed with acetone leaving a peach/brown solid which was characterised by FTIR and NMR spectroscopies.

FTIR Spectrum of the material obtained from method 3

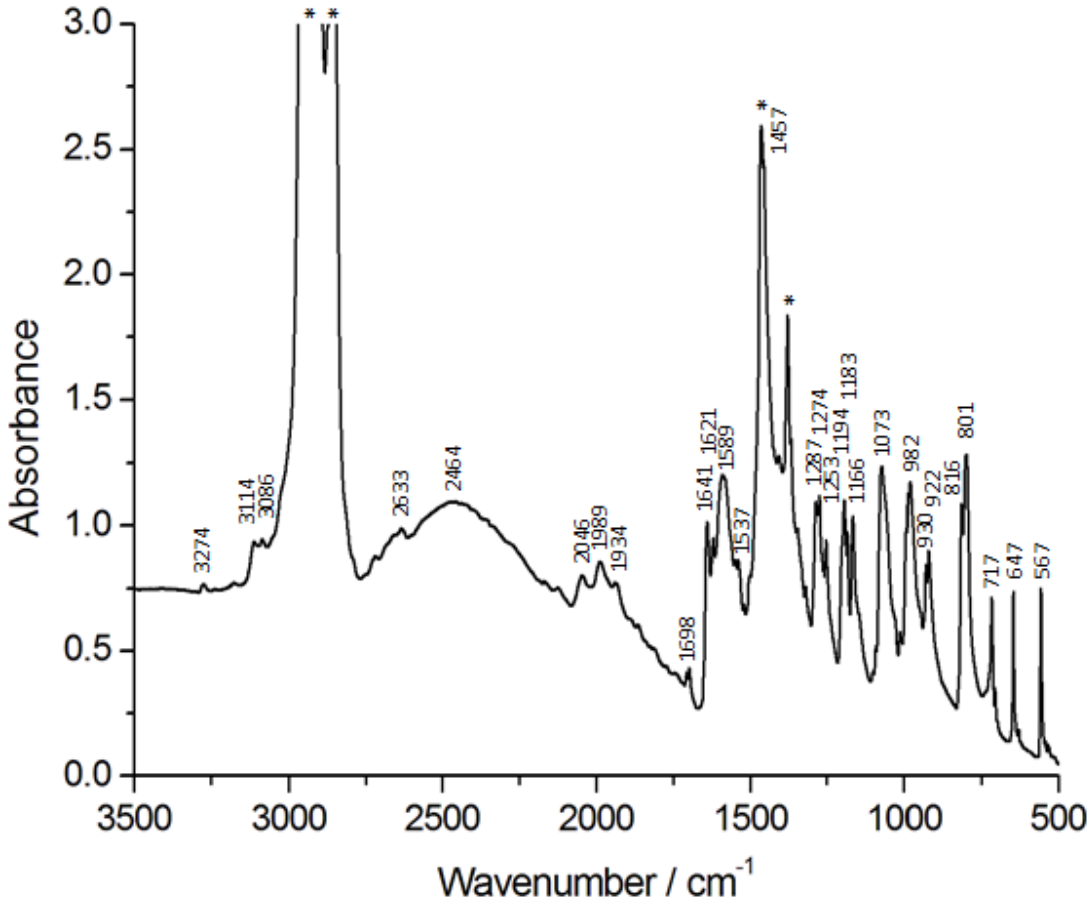

Figure 5.10. FTIR spectrum of the residue obtained from the reaction of cyanuric chloride with 1*H*-tetrazole in the presence of 2,6-lutidine in THF (method 3).

The broad peak at 2464 cm^{-1} is consistent with the N–H stretch of 2,6-lutidinium chloride,[223] which is the expected by-product of the reaction. The presence of several absorption bands between 3114–3086 cm^{-1} suggests the peach/brown powder is a mixture of at least two tetrazole derivatives as well as 2,6-lutidinium chloride. The presence of the latter by-product in significant concentration makes the unambiguous assignment of the infrared spectrum difficult.

^{1}H and ^{13}C NMR spectra of the material obtained from method 3

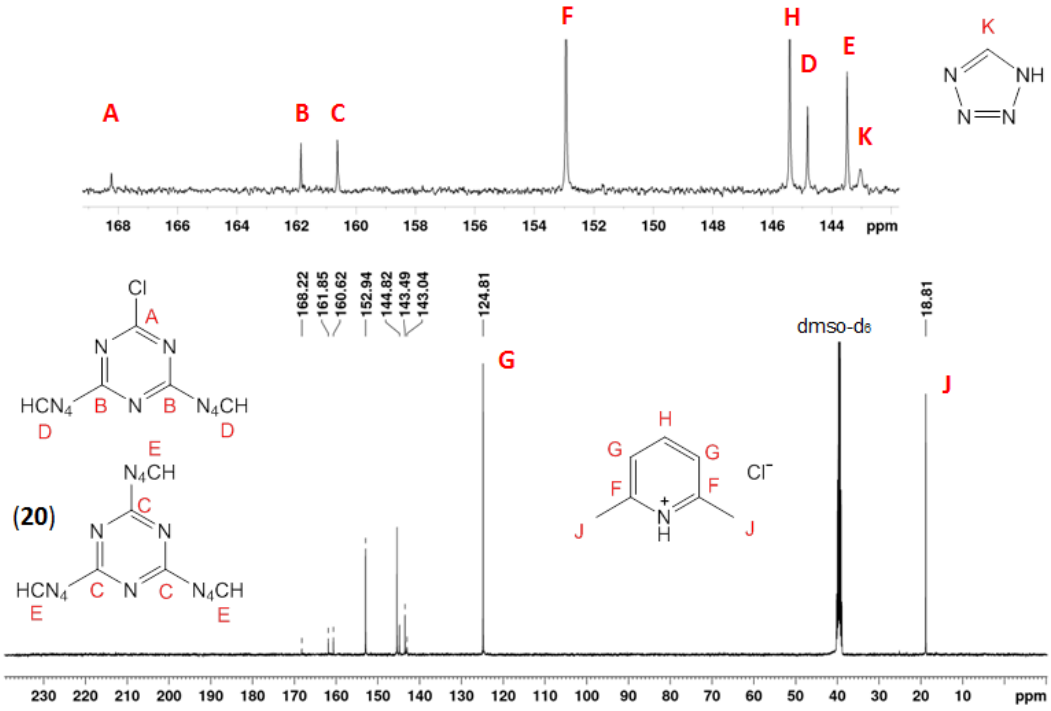

Figure 5.11. ^{13}C NMR in dmso-d_6 of the off-white powder obtained after reaction of cyanuric chloride with 1*H*-tetrazole in THF, with 2,6-lutidine acting as base (method 3). The peaks at 168.22 (**A**), 161.85 (**B**), and 144.82 ppm (**D**) are tentatively assigned to the 2-chloro-4,6-bis(tetrazol-1-yl)-1,3,5-triazine, with 160.62 (**C**) and 143.49 ppm (**E**) assigned to **20**, and 143.04 ppm (**K**) residual 1*H*-tetrazole. The peaks at 18.81 (**J**), 124.81 (**G**), 145.4 (**H**), and 152.94 ppm (**F**) are assigned to 2,6-lutidinium chloride. Lutidinium triflate (CD_2Cl_2): ^{13}C NMR δ [ppm] = 19.9, 125.5, 146.6, 154.4.[224]

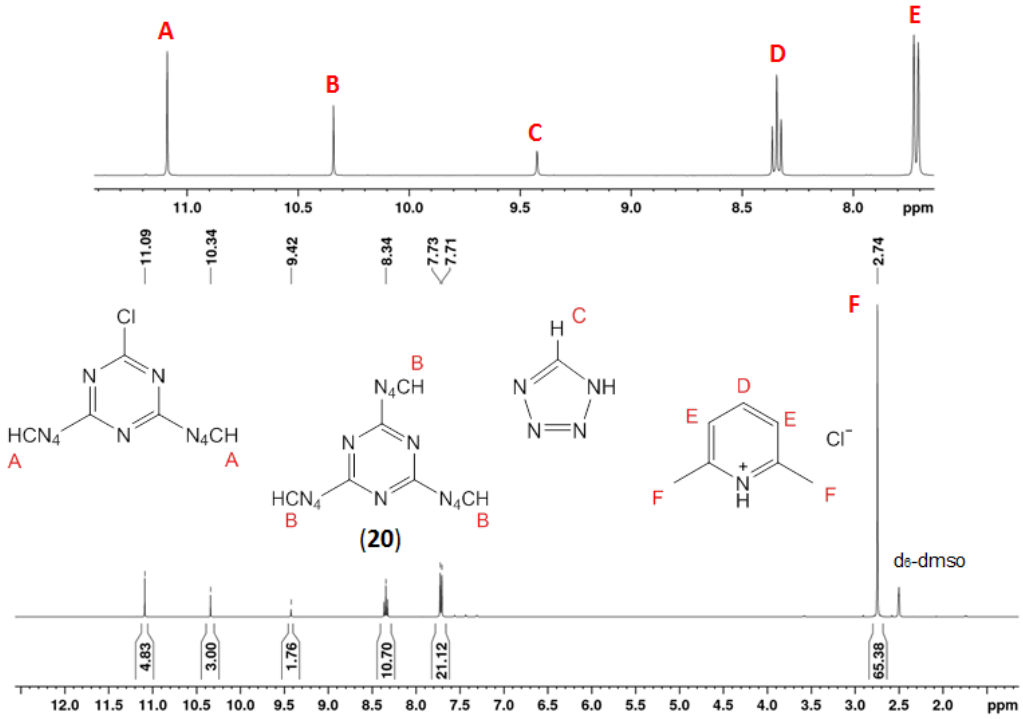

Figure 5.12. ^{1}H NMR in dmso-d_6 of the off-white powder obtained after reaction of cyanuric chloride with 1*H*-tetrazole in THF, with 2,6-lutidine acting as base (method 3). The spectrum has been tentatively assigned as follows: 2-chloro-4,6-bis(tetrazol-1-yl)-1,3,5-triazine, δ = 11.09 (**A**); **20,** δ = 10.34 (**B**); 1*H*-tetrazole δ = 9.42;[152]

2,6-lutidinium chloride, δ = 2.74 (s, 6*H*, **F**), 7.72 (**E**, d, 2*H*, $^{3}J_{HH}$ = 7.9 Hz, J_{CH} = 38, 172 Hz), and 8.34 (**D**, t, 1*H*, J_{HH} = 7.9 Hz, J_{CH} = 30, 45, 168 Hz). Available reference data for comparison: 2,6-lutidine ($CDCl_3$), ^{1}H NMR δ [ppm] = 2.44, 7.04, 7.58 ($^{3}J_{HH}$ = 8.2 Hz).[225] Lutidinium triflate (CD_2Cl_2), ^{1}H NMR δ [ppm] = 7.57, 8.24, 14.45 (chemical shift for Me protons not reported).[224]

The ^{1}H and ^{13}C NMR data seem to support the interpretation that compound **20** has formed, though constitutes a minor fraction of the material. It is expected with a longer reaction time the intermediate 2-chloro-4,6-bis(tetrazol-1-yl-1,3,5-triazine could be converted to **20**. The remaining impurities could be extracted by acetone to remove 1*H*-tetrazole, and CH_2Cl_2 to remove the 2,6-lutidinium chloride by-product (from which it can be crystallised),[226] or alternatively by washing with water.

5.2.5 Method 4: Using the sterically hindered base ethyldiisopropylamine (DIPEA)

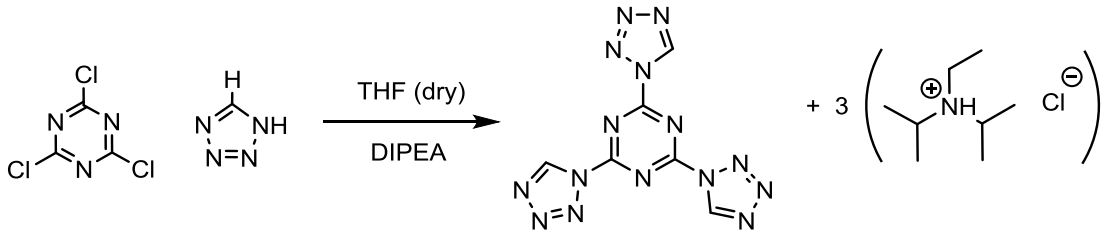

Scheme 5.5. Proposed reaction scheme for the preparation of 2,4,6-tris(tetrazol-1-yl)-1,3,5-triazine (**20**).

The sterically hindered amine diisopropylethylamine, “DIPEA”, has been used as a base in the preparation of other 1,3,5-triazine derivatives,[215,214] (method 4) and was tried as an alternative to 2,6-lutidine (method 3, above).

FTIR spectrum of material obtained by method 4

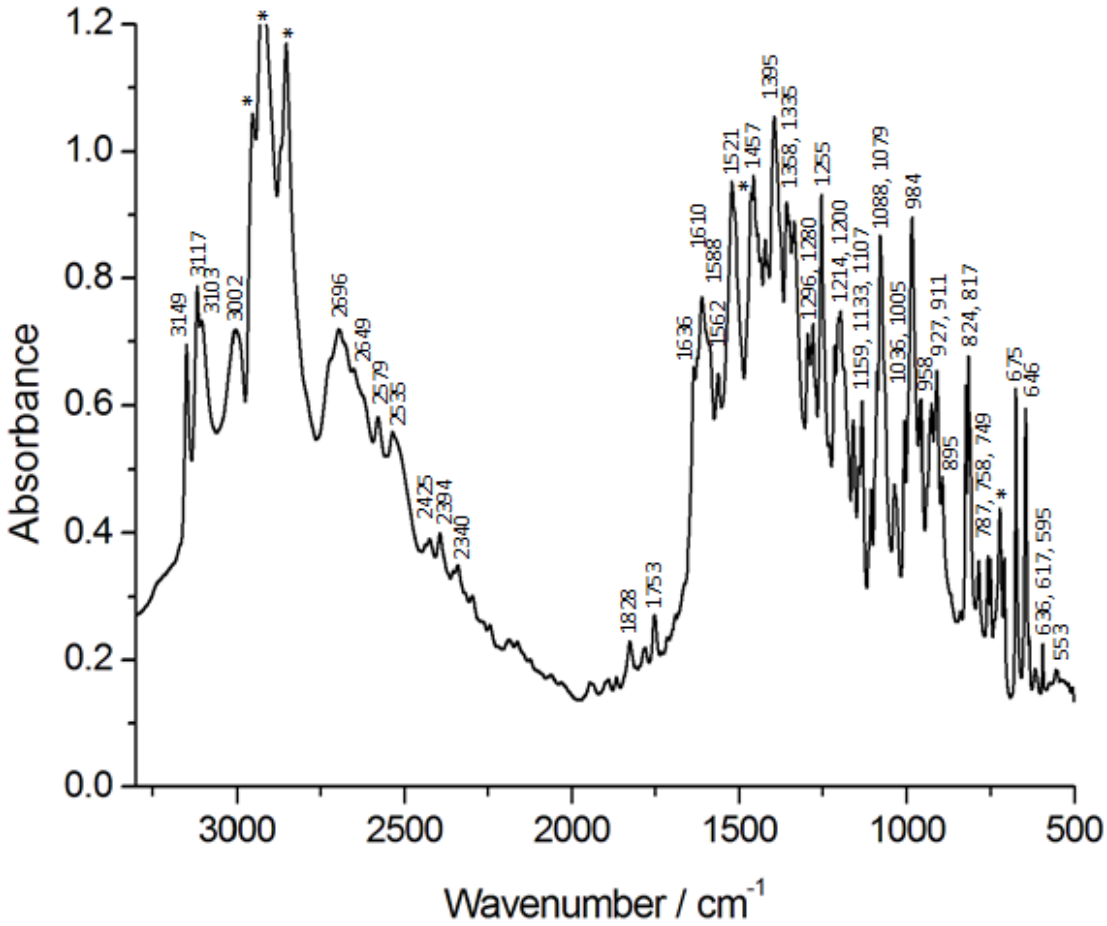

Figure 5.13. FTIR spectrum of the residue obtained from the reaction of cyanuric chloride with 1*H*-tetrazole in the presence of DIPEA in THF (method 4), filtering the solution off and washing the off-white residue with water.

The FTIR spectrum of the residue obtained by method 4 shows a broad peak similar to that observed in method 3 using 2,6-lutidine as base, indicative of the N–H···Cl of diisopropylethylammonium chloride by-product. The presence of multiple absorption bands in the region 3149–3103 cm^{-1} suggests the presence of several tetrazolyl CH proton environments.

NMR Spectroscopy

The ^{13}C NMR spectrum shows clearly the presence of more than one triazine-based species and the 2,6-lutidinium cation at 18.81, 124.81, 145.4, and 152.94 ppm, presumably as 2,6-lutidinium chloride. The corresponding ^{1}H NMR corroborates the presence of at least two tetrazole environments at δ = 10.3 and 11.1 ppm, and the 2,6-lutidinium cation at δ = 2.74 (s, 6*H*), 7.72 (d, 2*H*, $^{3}J_{HH}$ = 7.9 Hz, J_{CH} = 38, 172 Hz), and 8.34 ppm (t, 1*H*, J_{HH} = 7.9 Hz, J_{CH} = 30, 45, 168 Hz). The highest frequency carbon resonance at 168.2 ppm is assigned to the chlorobis(tetrazole) substituted species based on the higher frequency observed for the C–O

resonance compared to that of C–N_4CH in the triazinonate **21**. Similarly the ^{1}H signals at 11.1 and 10.3 ppm are assigned to the protons of the chlorobis(tetrazole) and tris(tetrazole) **20**, respectively.

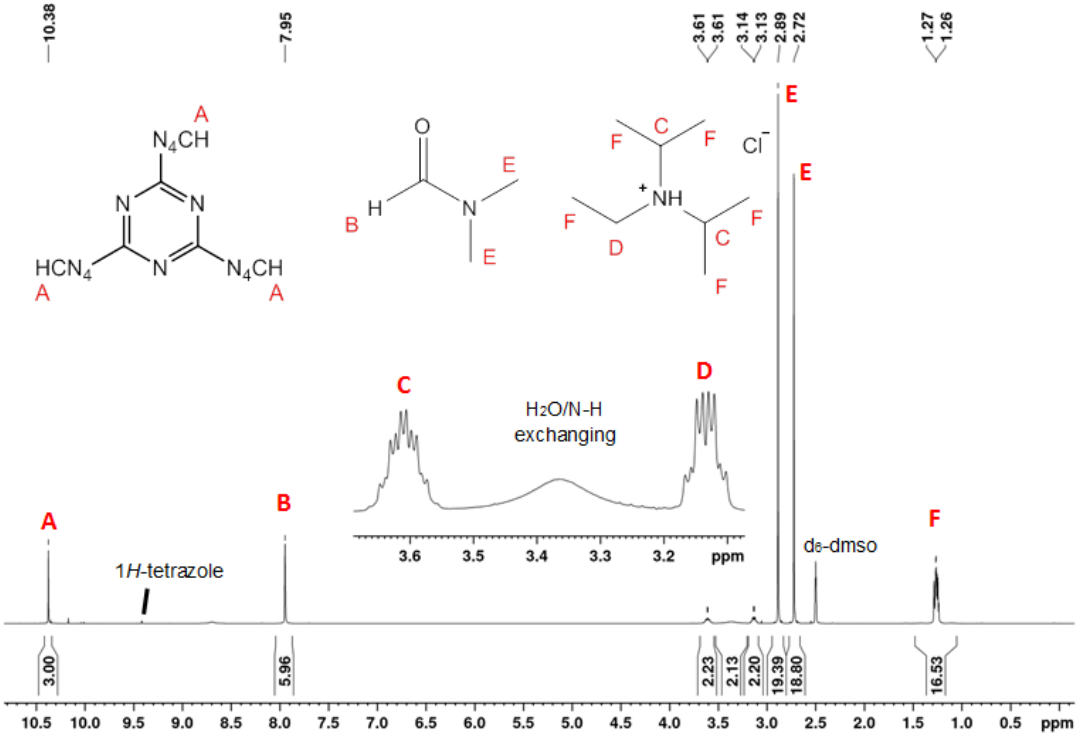

Figure 5.14. ^{1}H NMR in dmso-d_6 of the product mixture obtained from reaction of cyanuric chloride with 1*H*-tetrazole in THF, with diisopropylethylamine (DIPEA) acting as base (method 4). Residual DMF is present following an unsuccessful crystallisation attempt. The NMR spectrum has been tentatively assigned as follows: **20**, δ [ppm] = 10.38 (**A**); DIPEA·HCl, δ [ppm] = 3.61 (**C**, m, 2*H*), 3.13 (**D**, m, 2*H*), and (**F**, m, 15*H*); *N*,*N*-dimethylformamide, δ [ppm] = 7.95 (**B**, s, 1H), 2.69 (**E**, s, 3H), and 2.72 (**E**, s, 3H). An unknown (tetrazolyl)triazine-based trace impurity is also visible at 10.18 ppm.

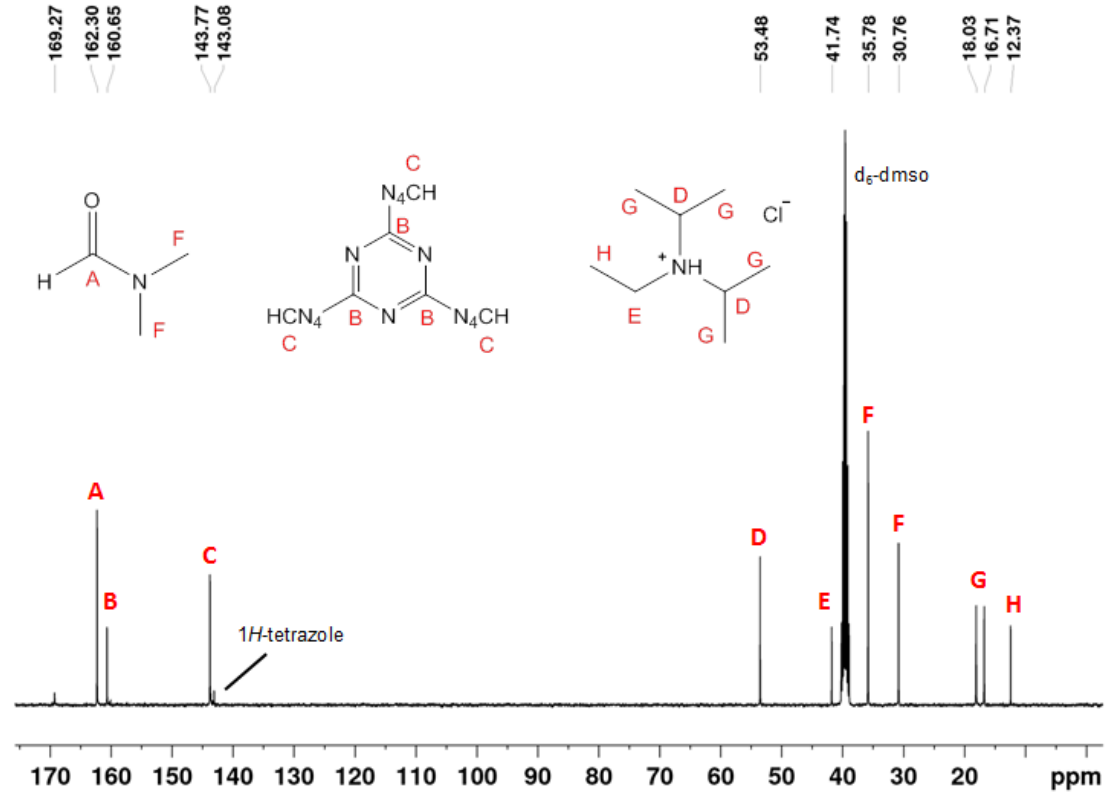

Figure 5.15. ^{13}C NMR in dmso-d_6 of the product mixture obtained from reaction of cyanuric chloride with 1*H*-tetrazole in THF, with diisopropylethylamine (DIPEA) acting as base (method 4). Residual DMF is present after an unsuccessful crystallisation attempt as the material was not rigorously dried. The NMR spectrum has been tentatively assigned as follows: **20**, δ [ppm] = 160.65 (**B**), 143.77 (**C**); *N*,*N*-dimethylformamide, δ [ppm] = 162.30 (**A**), 35.78 (**F**), and 30.76 (**F**); diisopropylethylamine hydrochloride, δ [ppm] = 53.48 (**D**), 41.74 (**E**), 18.03 (**G**), 16.71 (**G**), and 12.37 (**H**). DIPEA assignment consistent with the tris(2,6-difluorophenyl)hydridoborate salt in the supporting information of ref. [227]. A trace of 1*H*-tetrazole is visible at 143.08 ppm, and an unknown (presumably triazine-based) impurity is present at 169.27 ppm.

5.2.6 Methods 5 & 6

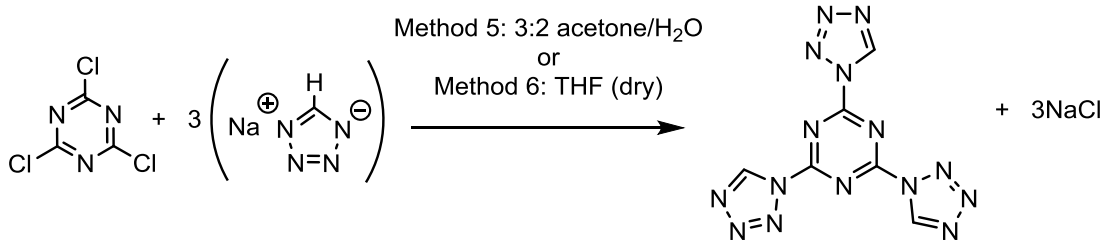

Scheme 5.6. Proposed reaction scheme for the preparation of **20** using sodium tetrazolate and cyanuric chloride. In method 5 the solvent was a 3 : 2 mixture of acetone and water, whereas in method 6 anhydrous THF was used.

Another alternative route involved the direct reaction of cyanuric chloride with sodium tetrazolate. The cyanuric chloride was dissolved in acetone and added to an aqueous solution of sodium tetrazolate resulting in a fine suspension, from which the solution was decanted (method 5). The FTIR spectrum matched very closely the spectrum obtained from method 1.

A very similar product mixture was obtained when instead anhydrous THF was used as reaction solvent (method 6).

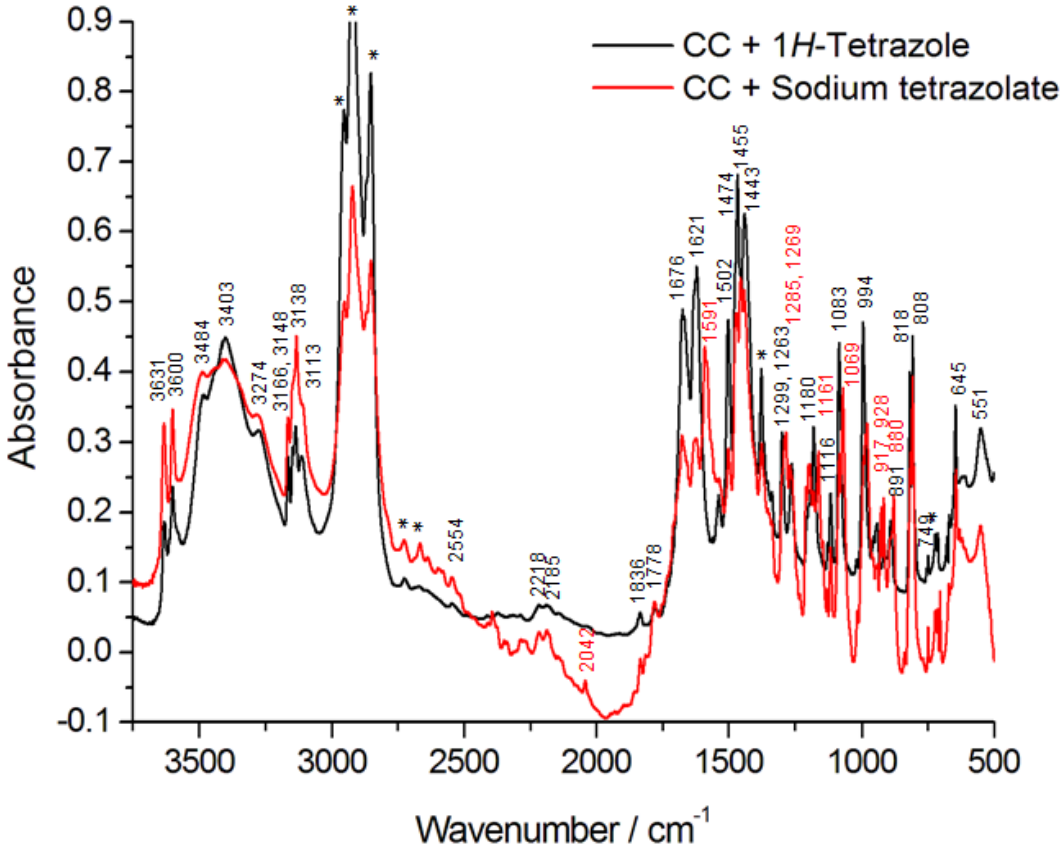

Figure 5.16. FTIR spectrum of the material obtained *via* reaction of cyanuric chloride with 1*H*-tetrazole in the presence of $NaHCO_3$ (black) compared to the residue obtained after reaction of cyanuric chloride with sodium tetrazolate (red, methods 5 & 6).

5.3 Conclusions

Despite previous publications on the synthesis of 2,4,6-tris(tetrazol-1-yl)-1,3,5-triazine (**20**), the compound was not isolated from either method 1 or 2, which suggests neither procedure is satisfactory. The original method eventually resulted in isolation of sodium 2,4-bis(tetrazol-1-yl)-1,3,5-triazinon-6-ate (**21**) DMF solvate after recrystallisation from DMF, which has been investigated by single crystal XRD. The isolation of this material in combination with literature on the reactivity of cyanuric chloride suggests the initial reaction before crystallisation formed the 6-chloro-2,4-bis(tetrazol-1-yl)-1,3,5-triazine, which subsequently reacted with DMF during crystallisation attempts.

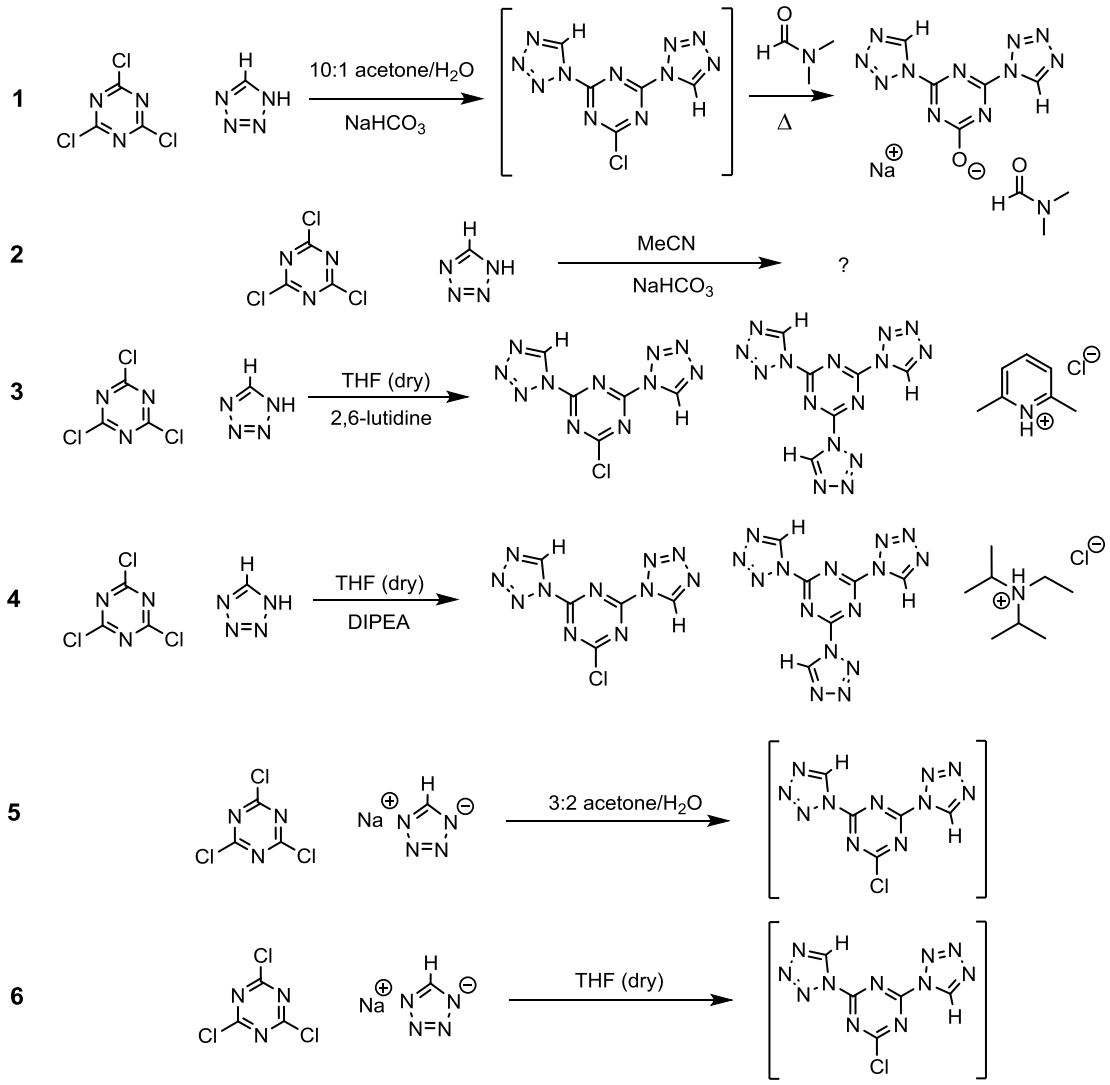

Scheme 5.7. A summary of the outcomes of each attempted synthesis of TTT (**20**) based on the available data. Square brackets indicate where there is insufficient evidence to unambiguously determine the outcome. The nature of the product formed by method 2 remains to be determined.

The preparation of **20** may be possible *via* this route with an extended reaction time at elevated temperature with a greater excess of 1*H*-tetrazole and $NaHCO_3$ to counteract the decreasing reactivity of the triazine chloride substituents. Alternatively employing the sterically hindered

bases 2,6-lutidine or diisopropylethylamine (DIPEA) seems to result in at least partial chloride/tetrazolate exchange as the NMR and FTIR spectroscopic data support the presence of the respective protonated bases. The direct reaction of sodium tetrazolate with cyanuric chloride in a mixture of acetone and water (method 5) or dry THF (method 6) resulted in the formation of a very similar product mixture obtained by the original literature procedure (method 1). The most promising of these methods for synthesis of **20** may be methods 3 and 4, except replacing THF with additional 2,6-lutidine or diisopropylethylamine respectively as reaction solvent. This would enable the reactions to be carried out at higher temperatures and could facilitate the substitution of the third position on the triazine.

Thesis Summary

New synthetic routes have been developed for the preparation of nitrogen-rich coordination compounds of tin, silicon and phosphorus. The synthesis of nitrogen-rich guanidinium azides **1** and **2** have been optimised (see Scheme S1), enabling the preparation of guanidinium salts with anionic polyazido complexes. The hydrogen bond networks exhibited by the crystal structures of nitrogen-rich tin polyazides bis(guanidinium) hexaazidostannate (**3**) and guanidinium triazidostannate (**17**) have been characterised by graph set analysis.

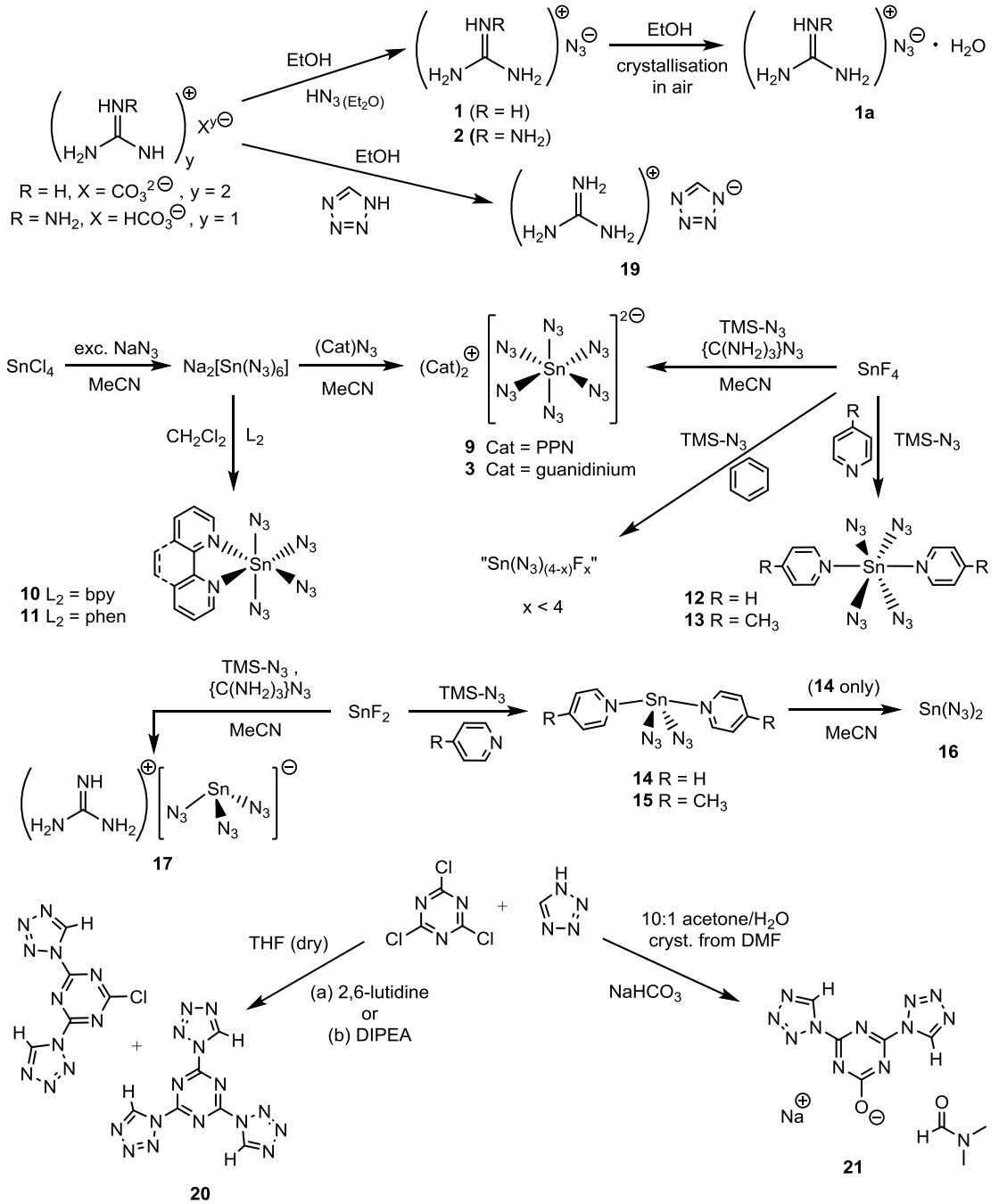

Scheme S1. Summary of reaction schemes for key synthetic procedures carried out during this project, with by-products of the reactions omitted for clarity.

During the reaction of disodium hexaazidosilicate with guanidinium azide, the double salt guanidinium sodium azide (**5b**) was crystallised as a side product, which has a 3D network composed of sodium ions linked by azide anions with guanidinium cations in the channels. In the attempted preparation of guanidinium hexaazidophosphate, the presence of $P(=O)(N_3)_3$ impurity in the $Na[P(N_3)_6]$ solution reacted with guanidinium azide to give an unusual phosphorus azide, $[P(=O)(N_3)_2\{NC(NH_2)_2\}]$ (**8**), according to a single crystal X-ray diffraction study. Guanidinium tetrazolate (**19**) was prepared for the first time, as it is a potential precursor to guanidinium salts of polytetrazolato complexes, which could be an interesting class of nitrogen-rich coordination compounds. The structure of guanidinium tetrazolate was determined by single crystal XRD, and exhibits extensive hydrogen bonding.

The reactivity of Sn(II) and Sn(IV) halides with ionic and covalent transfer reagents has been investigated, which has opened up new avenues for the synthesis of salts of homoleptic hexaazidostannate(IV) and triazidostannate(II) complexes, as well as the first charge-neutral Lewis base adducts of tin diazide and tin tetraazide. Bis(guanidinium) hexaazidostannate (**3**) and guanidinium triazidostannate (**17**) are the first examples of homoleptic azido complexes with nitrogen-rich counter ions, which have extensive hydrogen bonding in their crystal structures. However, these nitrogen-rich salts hydrolyse more rapidly in the presence of atmospheric moisture than those with traditional weakly coordinating cations. FTIR spectroscopic investigations into syntheses of other guanidinium salts of polyazido complexes of tin, silicon, and phosphorus were carried out. The *in-situ* solution FTIR spectra suggest that bis(aminoguanidinium) hexaazidostannate (**4**), bis(guanidinium) hexaazidosilicate (**5**), bis(aminoguanidinium) hexaazidosilicate (**6**), guanidinium hexaazidophosphate (**7**), aminoguanidinium triazidostannate (**18**), and perhaps more compounds of this class are accessible, though unfortunately repeated crystallisation attempts were fruitless.

Many binary azides of main group elements have been investigated previously, but at the outset of this project little information was available on tin diazide (**16**), and tin tetraazide, $Sn(N_3)_4$, remains elusive. A recent publication in 2014 described the first synthesis of $Sn(N_3)_2$ by oxidation of Sn metal with AgN_3, but little further characterisation was possible.

The newly developed synthesis of tin(II) azide (**16**) from tin(II) fluoride and trimethylsilyl azide has enabled a tenfold reduction in reaction timescale, and avoids the risks associated with silver azide and anhydrous ammonia. Furthermore, an investigation into the physical properties of tin diazide lacks some of the favourable properties of lead(II) azide, as it degrades upon exposure to sunlight or atmospheric moisture and oxygen. The structure of tin diazide has been determined by a combination of powder XRD and DFT calculations, and is only the second example (after $Pb(N_3)_2$) of a structurally characterised group 14 binary azide. The structure consists of infinite zig-zag chains in the *c*-axis direction, with pentacoordinate

$Sn(N_3)_2$ units rather than octahedral coordination sphere by virtue of the stereochemically active lone pair. The sharp, intense nature of the exotherms observed in DSC thermograms of $Sn(N_3)_2$ at T_{dec} > 230 °C were consistent with detonation, which in one case ruptured a stainless steel DSC sample capsule and caused minor damage to the DSC instrument. The enthalpy of decomposition was calculated to be around –370 kJ mol^{-1}, which is consistent with approximately 200 kJ mol^{-1} per azide group.

Neutral Lewis base adducts of tin tetraazide have been prepared for the first time, starting from either $SnCl_4$ or SnF_4. Existing syntheses for $E(N_3)_4(L_2)$, E = Si, Ge; L_2 = bpy, phen, have been adapted for the preparation of tin analogues $Sn(N_3)_4$(bpy) (**10**) and $Sn(N_3)_4$(phen) (**11**). Using polar coordinating solvents MeCN and THF, no reaction was observed between the versatile $Na_2[Sn(N_3)_6]$ intermediate and the chelating ligands, but exchange of the solvent for polar, non-coordinating solvent CH_2Cl_2 facilitated the ligand exchange reactions. Alternatively, the reaction of SnF_4 and TMS–N_3 in pyridine-based solvent enabled the preparation of the *trans*-$Sn(N_3)_4(L)_2$ adducts, L = pyridine (**12**), L = 4-picoline (**13**). NMR spectroscopic evidence has been obtained for the formation of the elusive tin tetraazide, $Sn(N_3)_4$, by reaction of SnF_4 with TMS–N_3, and subsequent reaction with 2,2'-bipyridine to form adduct **10**. These observations imply the formation of $Sn(N_3)_4$ from the reaction of SnF_4 with TMS–N_3, although further evidence is needed to determine the exact nature of the insoluble tin azide species.

The spectral positions of the asymmetric azide stretching vibrations ($\nu_{as}(N_3)$) in the FTIR spectra of azides can give insight into the balance of covalent and ionic contributions to the bonding of coordinated azide ligands. In general, the higher the frequency of the peak maxima or the $\nu_{as}(N_3)$ vibrations, the more covalent the coordinative E–N_α bonds. Descending group 14 from silicon to tin, the bonding of the azido ligands seems to become more ionic with increasing size of the coordination centre (see Figure S1 below). The low-valent Sn(II) azides, on average, seem to have a larger ionic contribution to the E–N_α bonds than the related tin(IV) azides. Tin diazide has an IR absorption band at higher frequency (2107 cm^{-1}, orange circles, Figure S1) than any other known tin(II) azide, which implies the Sn–N bonds have significant covalent character, which is consistent with its highly sensitive nature.

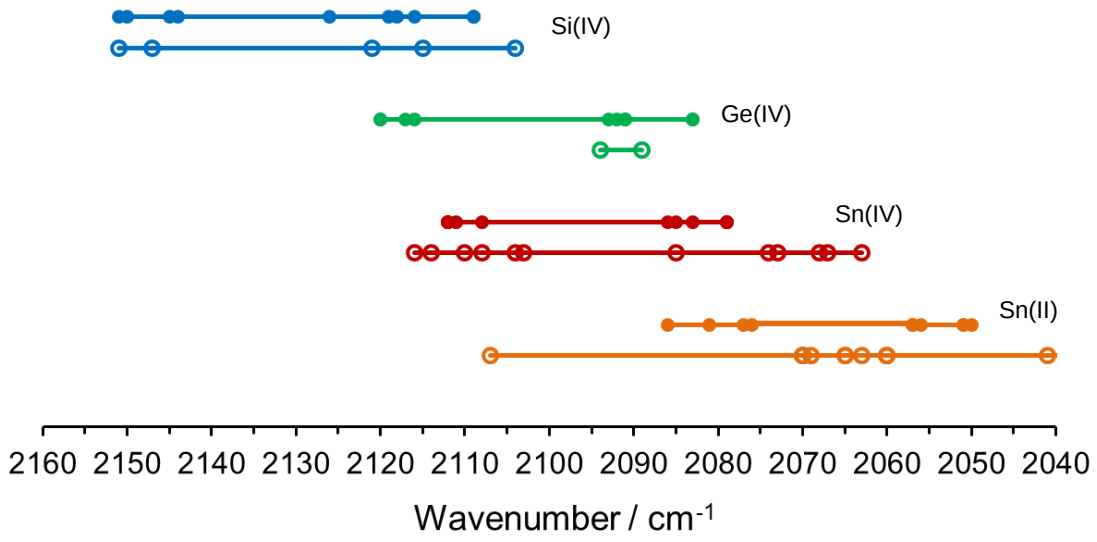

Figure S1. Plot showing the minimum and maximum frequency absorption bands in the FTIR spectra of a range of Si,[34,83] Ge,[33] Sn(IV),[85] and Sn(II)[92] azides from this work and from published data.[194,195,197] Solid circles represent data recorded from solution FTIR spectra, whereas hollow circles are from solid state FTIR spectra. For silicon, germanium, and tin(IV) azides, the solid state data are from nujol suspensions, and solution spectra were recorded in MeCN. For tin(II) azides solution spectra were recorded in various solvents, and some published solid state FTIR data were recorded in KBr rather than nujol.

DSC measurements performed for a range of tin azides have shown that Sn(IV) azides seem to have higher thermal stability than their tin(II) counterparts. Thermogravimetry of the tin(II) azide adducts $Sn(N_3)_2(py)_2$ (**14**) and $Sn(N_3)_2(pic)_2$ (**15**) shows that the pyridine ligands dissociate readily upon heating, leaving behind $Sn(N_3)_2$. The pyridine adduct $Sn(N_3)_2(py)_2$ loses pyridine at room temperature but the 4-picoline adduct, $Sn(N_3)_2(pic)_2$ only loses solvent upon heating. In contrast, FTIR spectroscopic data suggest that $Sn(N_3)_4(py)_2$ is quite stable in air, and in combination these observations suggests $Sn(N_3)_4$ is a stronger Lewis acid than $Sn(N_3)_2$, and that Lewis bases of equivalent strength of 4-picoline can stabilise Sn(II) azides, whereas pyridine and weaker Lewis bases may not be suitable for such stabilisation.

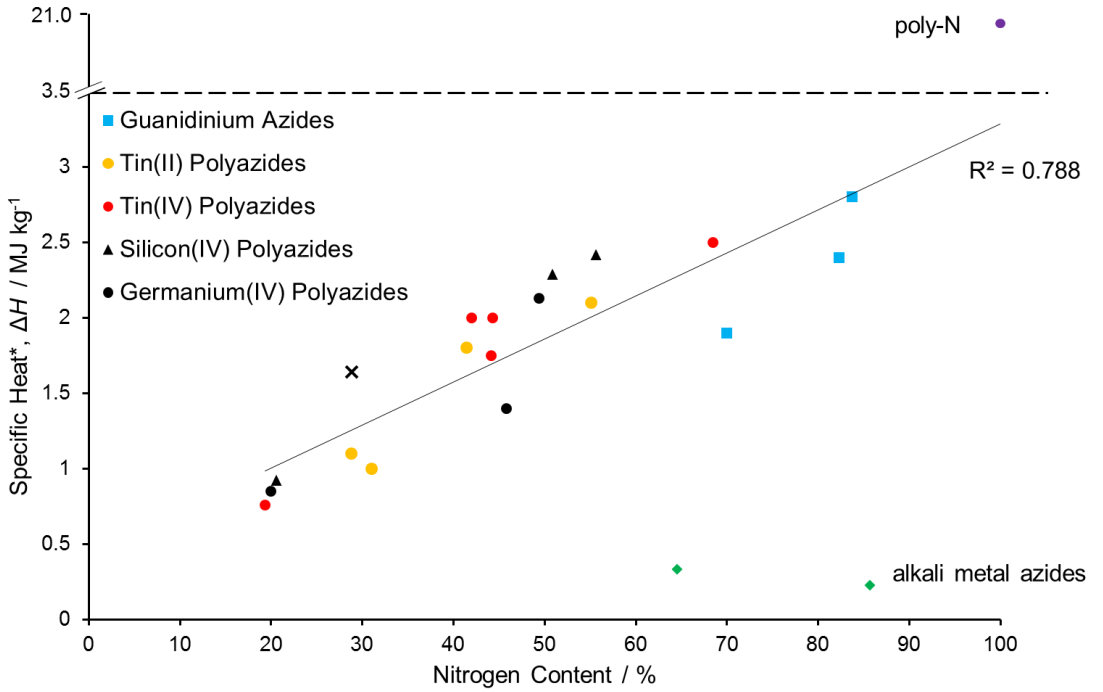

Figure S2. A collation of specific enthalpies of decomposition derived from DSC measurements for group 14 polyazides of the forms $E(N_3)_4(L_2)$ and $(PPN)_2[E(N_3)_6]$ (E = Si, Ge, and Sn; L_2 = bpy, phen), $Sn(N_3)_2$ and its adducts $Sn(N_3)_2(L)_2$ (L = pyridine or 4-picoline), and guanidinium azides. Lead azide, $Pb(N_3)_2$, (black cross),[228,8] and NaN_3 and LiN_3 (green diamonds),[229] and a predicted value for polymeric nitrogen ("poly-N") are shown for comparison. *Specific heat of decomposition for all Si, Ge, and Sn azides, specific heat of explosion for $Pb(N_3)_2$, and specific enthalpies of formation are quoted for the alkali metal azides and polymeric nitrogen.

The syntheses and thermal characterisation of the group 14 element polyazides has enabled assessment of various structural features which affect the specific enthalpy of decomposition. Although there are many other variables which affect the thermal behaviour of a compound, there is a significant positive correlation between the nitrogen content of a compound and its specific enthalpy of decomposition (see Figure S2). One such variable is the coordination centre, which is influential in determining the bond enthalpies, and in turn the magnitude of ΔH_{dec}, although the accuracy of the measurements is insufficient to draw any conclusions here. Another effect is the size (and atomic mass) of the coordination centre, which increases the molar mass and therefore decreases the specific heat for the equivalent ligand sphere. For the $(PPN)_2[E(N_3)_6]$ salts, E = Si, Ge, Sn, exchanging the central element has little effect on the overall mass, and therefore their specific enthalpies of decomposition are similar. The inclusion of crystal water in guanidinium azide monohydrate (**1a**) also decreases the specific enthalpy of decomposition compared to anhydrous **1**. Aminoguanidinium azide (**2**) has a higher specific enthalpy of decomposition than guanidinium azide or bis(guanidinium) hexaazidostannate. The as yet unknown guanidinium hexaazidosilicates or hexaazidogermanates are likely to have higher specific enthalpies of decomposition which are proportional to their overall molar mass difference, but in turn may have increased moisture sensitivity. Assuming a linear relationship between the nitrogen content and energy content,

and extrapolating to 100 % nitrogen content implies an upper limit of –3.28 kJ g^{-1} of the enthalpy of decomposition.

Related to the work on nitrogen-rich coordination compounds of tin, silicon, and phosphorus, the synthesis of novel nitrogen-rich ligands was investigated with an emphasis on tetrazolyl-substituted N-heterocycles. The intention was to determine whether an alternative nitrogen-rich ligand could be incorporated into a coordination compound with comparable energy density, but lower sensitivity than existing covalent azides. Progress was made in particular with 2,4,6-tris(tetrazol-1-yl)-1,3,5-triazine ("TTT"), the synthesis of which was investigated following one previous report containing scant information. The products obtained by following these procedures were characterised by their solid state FTIR spectra, and ^{1}H and ^{13}C NMR spectra in dmso-d_6. After recrystallisation of the crude material obtained by method 1, sodium 2,4-bis(tetrazol-1-yl)-1,3,5-triazinon-6-ate DMF solvate (**21**) was obtained according to elemental analysis and single crystal XRD. New methods for the synthesis of **20** were investigated, which employed sterically hindered organic bases 2,6-lutidine or ethyldiisopropylamine instead of $NaHCO_3$. Tentative assignment of the ^{1}H and ^{13}C NMR spectra by comparison with spectral data of **21** seems to show the presence of **20** in the product mixtures obtained by the new methods, as well as the corresponding 2,6-lutidinium chloride or ethyldiisopropylammonium chloride by-products. These signs are encouraging, and with a little more optimisation of the syntheses it seems as though the highly interesting novel energetic material **20** is accessible.

Outlook

The extension of these synthetic principles to a range of nitrogen-rich coordination compounds may give further insight into the effects which hydrogen bonding has on the coordination of the ligands and the properties of the compounds. A natural progression following on from this research would be investigation into the synthesis of guanidinium salts of anionic polytetrazolato complexes, which may exhibit hydrogen bonded structures similar to the azido complexes. In particular, preparation of complexes of light *p*-block elements (e.g. aluminium) would enable a systematic increase in specific energy content compared to the tin compounds described in this work. The 1,3-dipolar cycloaddition ('click') reactions of organic azides with nitriles are well-known,[31] and a recent review of analogous reactions with inorganic azides highlights the potential of this route for preparation of new tetrazolato complexes.[230]

The graph set analysis of hydrogen bonds has provided a qualitative means of characterising the hydrogen bond networks,[117] whereas quantitative information may be derived from DFT calculations, for example in the crystal structure of guanidine.[71] Evaluation of the strength of individual hydrogen bonds and their overall stabilising effect could help to identify which types of hydrogen bond donors are most effective. Such calculations on a range of energetic salts with nitrogen-rich cations would enable the evaluation of subtle differences in the effectiveness of hydrogen bonding in their structures.

Although tin tetraazide is likely to be even more sensitive than tin diazide, tin(IV) azides seem to be generally more resistant to hydrolysis than the equivalent tin(II) compound. Replacement of the pyridine ligands for those of higher nitrogen content may be able to replicate their stabilising effect whilst increasing the nitrogen content of the compound, and in turn its specific enthalpy of decomposition. Development of new nitrogen-rich ligands, for example those based on N-rich heterocycles such as 2,4,6-tris(tetrazol-1-yl)-1,3,5-triazine, could enable preparation of energetic compounds which are less sensitive than polyazides.

6. Experimental Section

6.1 General Procedures, Source of Reagents and Solvents, and Instrumentation and Software

6.1.1 General Procedures

Manipulations involving compounds known (or suspected) to be sensitive to air and/or moisture were performed using standard Schlenk, vacuum line, and glovebox techniques under an atmosphere of dry argon. The typical ultimate vacuum was around 4×10^{-2} mbar. Samples prepared for examination by spectroscopic and analytical methods were prepared in the glovebox whenever possible. During the preparation of samples of air or moisture sensitive solutions for Fourier transform infrared (FTIR) spectroscopy, a continuous low flow of argon was admitted via the sidearm of the Schlenk tube. A 1 ml glass piston pipette was purged in the argon stream five times then a sample was extracted, followed by a protective bubble of argon. The Specac cell was purged with argon for at least 30 s, before the sample was transferred (immediately) to the cell and the spectrum recorded promptly. Filtration of air and/or moisture sensitive compounds was achieved by the use of stainless steel filter canulas equipped with glass fibre filters secured by PTFE tape.

6.1.2 Source of Reagents and Solvents

Acetonitrile (Fisher, 99.9 %), acetonitrile-d_3 (Aldrich, 99.8 %), benzene (Merck, 99.5 %), benzene-d_6 (Sigma Aldrich, 99 %), dichloromethane (Sigma Aldrich, >99.8 %), diethyl ether (Sigma Aldrich, 98 %), *n*-hexane (Fisher, 99 %), and tetrahydrofuran (VWR, 99.99 % HPLC) were dried over calcium hydride (Acros, 93 %) for 18 h, before trap-to-trap condensation. Diisopropylethylamine (Sigma Aldrich, 99 %), 2,6-lutidine (Acros, 99 %), 4-picoline (Aldrich, 98 %), pyridine (Fisher Scientific, 99.8 %), and pyridine-d_5 (Sigma Aldrich, 99.5 %) were dried over calcium hydride for 18 h, and vacuum distilled. Ethanol (VWR, absolute, 99.9 %) was dried over 1.5 % w/v of Na metal (Sigma Aldrich, 99 % (lump, in kerosene)) for 4 h, distilled under argon flow at ambient pressure, degassed, and stored over molecular sieve (3 Å) under an argon atmosphere. Molecular sieve (Acros, 3 Å, 8–12 mesh) was activated by oven drying at 200 °C overnight immediately prior to use. All solvents were stored in suitably sized glass ampoules with a side inlet, which were sealed by J. Young's high vacuum greaseless stopcocks under an argon atmosphere. Acetone (VWR, 100 %), diglyme (Sigma Aldrich, 99 %), *N*,*N*-dimethylformamide (Fisher Scientific, 99 %), dimethylsulfoxide-d_6 (Sigma Aldrich, 99.9 %), *n*-heptane (BDH, 99 %), and hydrazine monohydrate (Sigma Aldrich, 98 %) were used as received.

Tin tetrachloride (Aldrich, 99 %), silicon tetrachloride (Aldrich, 99.9 %), and trimethylsilyl chloride (Alfa Aesar, 98 %) were stirred over anhydrous sodium carbonate (Fisher Scientific, >99.5 %) for 16 h, and vacuum transferred into ampoules and stored under an argon atmosphere. Phosphorus pentachloride (Fluka), 2,2'-bipyridine (Acros, 99 %), and 1,10-phenanthroline (Acros, 99.9 %) were sublimed prior to use. Guanidinium chloride (Alfa Aesar, 98 %) was dried under dynamic vacuum at 110 °C for 5 h. Guanidinium carbonate (Aldrich, 99 %), sodium azide (Aldrich, >99.9 % or Acros, 99 %), tin(II) chloride dihydrate (Sigma Aldrich, 98 %), tin(II) fluoride (Sigma Aldrich, 99 %), and tin(IV) fluoride (Alfa Aesar, 99.9 %) were dried under dynamic vacuum at 110 °C overnight. Aminoguanidinium bicarbonate (Aldrich, 97 %), cyanuric chloride (Alfa Aesar, 98 %), cyanuric acid (Sigma Aldrich, 98 %), D_2O (Aldrich, 99.9 %), phosphorus pentoxide (Sigma Aldrich, >98 %), sodium bicarbonate (Aldrich, 99 %), sodium hydroxide (VWR, 99 %, pellet), and sulphuric acid (Fisher Scientific, 95 % or Merck, 100 %) were used as received.

Bis(triphenylphosphine)iminium azide ($(PPN)N_3$),[159] sodium hexaazidophosphate (MeCN stock solution),[84] disodium hexaazidosilicate (MeCN stock solution),[34] 1*H*-tetrazole,[152] sodium tetrazolate,[152] and trimethylsilyl azide[231] were prepared according to literature procedures. $Sn(N_3)_4(phen)$ was prepared, and characterised by Matt Fazakerley. All dried solid reagents were stored in sealed vessels in a glovebox under an argon atmosphere.

6.1.3 Instrumentation, Software, and Calibrants

Infrared absorption spectra were recorded in the range 500–4000 cm^{-1} on a Bruker Tensor 27 Fourier Transform Infrared (FTIR) spectrometer running the Bruker *OPUS* software package, or Bruker Alpha FTIR spectrometer running Bruker *OPUS 7.0*, at a spectral resolution of 2 cm^{-1}, either as a nujol mull between NaCl windows or in solution using a Specac CaF_2 solution cell. When Fourier transform infrared (FTIR) spectra are discussed, the following abbreviations will be used to indicate the relative absorbance of bands: vs = very strong, s = strong, m = medium, w = weak, vw = very weak, sh = shoulder, br = broad. Elemental analyses were carried out by the University of Sheffield elemental analysis service on a PerkinElmer 2400 CHNS/O series II elemental analyser in an atmosphere of pure oxygen. ^{1}H and ^{13}C Nuclear magnetic resonance (NMR) spectra were recorded using a 400 MHz Bruker Avance 400 spectrometer; ^{31}P spectra were recorded on a 250 MHz Bruker Avance 250 spectrometer; ^{14}N and ^{119}Sn spectra were kindly recorded by Sue Bradshaw on a 500 MHz Bruker Avance 500 spectrometer. ^{1}H and ^{13}C NMR spectra were calibrated against the residual solvent peak according to ref. [190]. NMR spectra were processed using Bruker *TOPSPIN v3.2*. DSC measurements were performed on a PerkinElmer Pyris 1 Differential Scanning Calorimeter operated under nitrogen flow (20 ml min^{-1}) with a heating rate of 10 °C min^{-1}. The instrument was calibrated against a pure indium reference (99.999 %) with a sharp

transition at 156.60 °C, with a well-known enthalpy change of 28.45 J g^{-1}. The samples were sealed in PerkinElmer stainless steel high-pressure capsules (30 μL internal volume) with Au-plated Cu seals, which can operate up to 400 °C and 150 bar. The uncertainties associated with calculation of enthalpies of fusion and enthalpies of decomposition are at least ±10 %. Onset temperatures for melting and decomposition were calculated by the intersection of the tangent of maximum gradient with the projected position of the baseline, and quoted values are based on an average of a minimum of 3 measurements unless otherwise stated. Thermogravimetric analysis (TGA) was carried out using a Pyris 1 Thermogravimetric Analyser with a ceramic crucible using a heating rate of 10 °C min^{-1} under nitrogen flow (20 ml min^{-1}). Onset temperatures (T_{on}), mass losses, enthalpies of fusion (ΔH_{fus}), and decomposition (ΔH_{dec}) were calculated using the data analysis tools within the *Pyris 1* software. Single crystal X-ray diffraction (XRD) data collections (except for **13**) were performed using graphite-monochromated Mo $K_{\alpha 1,2}$ radiation (λ = 0.71073 Å) at 100 K (unless otherwise specified) on a Bruker Small Molecule Analytical Research Tool (SMART) 4000 diffractometer equipped with a CCD area detector and an Oxford Cryosystems Cobra cryocooler, or on a Bruker Kappa diffractometer equipped with a CCD area detector and an Oxford Cryosystems NHelix cryocooler. were collected. Single crystal XRD data collection for compound **13** was collected on a Bruker D8 Venture diffractometer using Cu-$K_{\alpha 1}$ radiation (λ = 1.54178 Å) equipped with a Bruker PHOTON CMOS detector. Data were collected using Bruker *APEX2*[232] software and integrated using Bruker *SAINT*,[233] absorption correction was applied using Siemens' Area Detector Absorption correction (*SADABS*)[234] within *APEX2*. All structures were solved using direct methods for the location of heavy atoms using *SHELXS-97* within *SHELXTL-2013*,[235,236] except $Sn(N_3)_4(py)_2$ which was solved by intrinsic phasing using *SHELXT*[237] within *APEX2*. Hydrogen atoms bound to heteroatoms were located *via* a Fourier difference map, and their position and isotropic thermal displacement parameters freely refined. Hydrogen atoms bound to carbon were calculated in idealised positions based on the hybridisation of the parent atom and data collection temperature, with isotropic displacement parameters of $1.2U_{eq}$ (see list of abbreviations) of the parent atom, using appropriate HFIX commands within *SHELXL-2014*. Additional twin refinement was carried out for the structures of guanidinium azide (**1**), and 2,4-bis(tetrazol-1-yl)-1,3,5-triazinon-6-ate DMF solvate (**21**), and to a lesser extent for diazidobis(pyridine)tin (**14**), using the twinning tools in *WinGX*,[238,239] and displacement ellipsoid plots of the crystal structures have been produced using *ORTEP-3 for Windows*.[240] Powder X-ray diffraction data were collected for a sample of $Sn(N_3)_2$ carefully loaded into a 0.7 mm borosilicate glass capillary prior to being mounted and aligned on a Bruker-AXS D8 Advance powder diffractometer operating with Ge-monochromated Cu-$K_{\alpha 1}$ radiation (λ = 1.54056 Å). Powder patterns were collected and baselined using the Bruker *DIFFRAC.EVA* software suite v3.1.[241] A Pawley refinement[242] was implemented to index the powder pattern using the program *TOPAS*.[243]

6.2 Guanidinium Azides and Polyazides of Silicon, Tin and Phosphorus

6.2.1 Preparation of guanidine,[70] $HN=C(NH_2)_2$

Guanidinium chloride (1.781 g, 18.6 mmol) was fully dissolved in 27 ml dry ethanol. Portions of sodium metal (total 450 mg, 19.6 mmol) were cut from larger blocks under kerosene, washed with 20 ml *n*-heptane and added immediately to 20 ml dry ethanol. The solution was stirred vigorously until the sodium had fully dissolved giving a solution of NaOEt. The NaOEt solution was transferred onto the vigorously stirred guanidinium chloride solution via filter canula causing immediate precipitation of a fine, white solid. The mixture was stirred for 15 minutes and then allowed to settle before the fine, white residue (0.978 g, 16.7 mmol based on NaCl) was filtered off yielding a perfectly clear solution, which was evaporated to dryness at RT under dynamic vacuum for a total of 13 h, yielding 1.002 g of a slightly pink-brown solid (16.7 mmol, 90 % yield based on guanidinium chloride). FTIR (nujol) $\tilde{\nu}$ [cm^{-1}] = 3600w,sh, 3437s, 3353s, 3216s, 1651s, 1623s, 1596s, 1341vw, 1315vw, 1260w, 1204m, 1155w, 1092vw, 1017w, 800m; FTIR (CH_3CN) $\tilde{\nu}$ [cm^{-1}] = 3482m, 3390s, 3329w, 1661vs, 1616s, 1260w,br, 1176m,br, 1041m, 1038m. This crude guanidine can be purified by sublimation.[75]

6.2.2 Ethereal Hydrazoic acid, HN_3

6.2.2a Preparation of ethereal hydrazoic acid, HN_3[50]

Sodium azide (15.056 g, 0.232 mol) was fully dissolved in 40 ml deionised water in a 2-neck (>100 ml) round-bottomed flask. Diethyl ether (55 ml) was added to the solution, forming the upper layer which prevents the formation of highly explosive neat HN_3. Effective cooling of the flask by immersion in an ice-water bath is essential to remove heat efficiently from the exothermic reaction. A dropping funnel was charged with 95 % sulphuric acid (15 ml, ρ = 1.83 g cm^{-3}, 0.279 mol), then inserted into the second neck of the reaction vessel and secured. The colourless solution was stirred vigorously whilst the sulphuric acid was added dropwise over a period of 30 minutes. Once all H_2SO_4 had been added the flask was allowed to warm to RT, and the solution stirred for 30 minutes. The (pre-weighed) receiver flask was charged with 33 ml diethyl ether as a further precaution against isolation of neat HN_3, and both flasks were attached to the distillation apparatus. A small paraffin bubbler was fitted just above the receiver flask to equilibrate distillation pressure with the ambient pressure. The distillation flask was immersed half way in an oil bath set at 55 °C, and distillation of the upper layer began at a head temperature of 40 °C with an approximate rate of one drop per second. The upper layer in the distillation flask was depleted after 90 minutes, yielding 69.2 g (ca. 98 ml) ethereal hydrazoic acid. The concentration was determined to be 1.95 (± 0.05) mol

dm^{-3} from an average of 3 titrations (details below). The typical concentration of stock solutions obtained via this procedure is around 1.5–2.0 mol dm^{-3}, with an average yield of 65–70 % based on NaN_3. FTIR (Et_2O) $\tilde{\nu}$ [cm^{-1}] = 3086s,br, 2481w,br, 2375w,br, 2131vs,br, 1303m,br, 1284w,sh, 1192s,br; a trace of water was usually visible at $\tilde{\nu}$ [cm^{-1}] = 3508br, 3448br, 1641br.

6.2.2b Determination of ethereal HN_3 concentration by titration

Aliquots of ethereal HN_3 solution (2.0 ml) were titrated against a dilute solution of NaOH in deionised water (typically c_{NaOH} = 0.1–0.2 mol dm^{-3}), using 2 drops of an ethanolic solution of phenolphthalein as the indicator. During titration, the ethereal HN_3 solution was cooled in an ice-water bath to lower the vapour pressure of Et_2O/HN_3, and stirred vigorously to prevent phase separation during titration in the sealed apparatus. This method of determination of the product only confirms the total acidic concentration, and doesn't prove unequivocally that the hydrazoic acid is free of inadvertently distilled traces of H_2SO_4. Alternatively the concentration can be estimated by considering the molar ratio of the solution components HN_3, Et_2O, and water by recording a ^1H NMR in $CDCl_3$, and measuring experimentally the density of the solution.

6.2.2c Drying of ethereal HN_3 using P_4O_{10} (Sicapent)

Sicapent (P_4O_{10} with indicator) was added to ethereal HN_3 (30 ml, 1.7 mol dm^{-3}) in portions (*ca*. 0.5 g) until there was no further blue discolouration of the desiccant upon addition. The mixture was stirred for 3 h, before the anhydrous ethereal HN_3 was trap-to-trap condensed. The concentration was estimated based on ratio of the absorbance at several points of the $\nu_{as}(N_3)$ band before and after drying.

6.2.3 Guanidinium Azide, $(C(NH_2)_3)N_3$ (1)

6.2.3a Preparation of guanidinium azide (1) via guanidine

Ethereal HN_3 (17 ml, 26 mmol) was added *via* 10 ml volumetric glass pipette to suspension of guanidine (0.970 g, 17.0 mmol) in 15ml dry CH_3CN. The pale brown colour of the suspended solid immediately became whiter but did not dissolve after stirring for 1 h at RT. The suspension was then filtered, yielding a clear, amber-coloured solution, and a pink-brown residue. An FTIR spectrum of the solution was recorded against a background of 2 : 1 Et_2O/CH_3CN, showing only HN_3 ($\tilde{\nu}$ [cm^{-1}] = 2136s, 1193m,br) with traces of water ($\tilde{\nu}$ [cm^{-1}] = 3613m,br, 3544m,br, 1638m,br) and **1** ($\tilde{\nu}$ [cm^{-1}] = 2029w, 1667s. An FTIR spectrum of the filter residue was recorded as a mull after drying under dynamic vacuum: FTIR (nujol) $\tilde{\nu}$ [cm^{-1}] = 3361vs,br, 3152s,br, 2132w,br {NaN_3}, 2058vs, 2037vs, 2026s,sh, 1649s,br, 1261vw, 1017vw, 1006vw, 738vw, 637w {NaN_3}, 534vw. This filter residue appears to be

partially hydrated guanidinium azide with a trace of sodium azide impurity, which is either due to residual NaOEt in guanidine, or reaction of **1**/**1a** with the NaCl windows. A sample of this powder attracted moisture after exposure to air overnight to become a translucent solid. The asymmetric azide stretch region of the FTIR spectrum confirmed hydration of hygroscopic **1** to **1a** by the coalescence of the $\nu_{as}(N_3)$ stretches to 2045 cm^{-1}: FTIR (nujol) $\tilde{\nu}$ [cm^{-1}] = 3650–3500w,sh, 3361vs,br, 3172s,br, 2132m,br, 2107w,sh, 2045vs,br, 1662s,br, 1570sh,br, 1541sh,br, 1133w,br, 1007vw, 738vw, 534vw, and a trace of NaN_3: $\tilde{\nu}$ [cm^{-1}] = 3389w,sharp, 3299vw,sharp, 2132m,br, 639m,sharp.

6.2.3b Preparation of guanidinium azide (1) via guanidinium carbonate (adapted from ref. [144])

An excess of ethereal hydrazoic acid (32.5 ml, 39 mmol, 1.9 mol dm^{-3}) was added to a stirred suspension of guanidinium carbonate (2.71 g, 30.0 mmol) in 15 ml dry EtOH at 20 °C. The tube was fitted with a small paraffin bubbler to inhibit the evaporation of HN_3 and to monitor CO_2 evolution. After stirring for 2 h the small amount of insoluble material was filtered off, and the clear filtrate was evaporated to dryness in a dynamic vacuum, giving the raw product **1** as a hygroscopic white powder (3.04 g, 99 %). Analytically pure material was obtained by dissolving the raw product in an anhydrous 3 : 1 EtOH / Et_2O mixture (15 ml) and subsequent crystallisation by cooling to –19 °C in the freezer overnight. DSC melting point: 99 °C (T_{on}), ΔH_{fus} = 13.8 kJ mol^{-1}; decomposition: *ca.* 254 °C (T_{on}), ΔH_{dec} = –243 kJ mol^{-1}. Elem. anal. (%) for CH_6N_6, 102.1 g mol^{-1}, calcd: C 11.76, H 5.92, N 82.31; found: C 12.00, H 5.76, N 81.93. FTIR (nujol) $\tilde{\nu}$ [cm^{-1}] = 3402s,br, 3334s,br, 3141s,br, 2180w,sh, 2078s, 2062s, 2020vs, 1656vs,br, 1262w, 1096w,br, 1024w,br, 802w, 738vw,sh, 638w, 515w; FTIR (CaF_2, CH_3CN) $\tilde{\nu}$ [cm^{-1}] = 3451m,br, 3372m,br, 3290m,br, 3202m,br, 2046vw,sh, 2029s, 2006w, 1669s. NMR δ [ppm] (dmso-d_6): ^1H = 2.50 (m, solvent residual), 6.94 (s); $^{13}C\{^1H\}$ = 39.52 (m, solvent residual), 157.97 (s); ^{14}N = –131.69 (N_β), –276.19 (N_α, N_γ). δ [ppm] (D_2O): ^1H = 4.70 (s). δ [ppm] (CD_3CN): ^1H = 6.42 (s).

6.2.4 Guanidinium azide monohydrate, $\{C(NH_2)_3\}N_3 \cdot H_2O$ (1a)

6.2.4a Preparation of guanidinium azide monohydrate

Ethereal HN_3 (60 mL, 99 mmol) was added to a suspension of guanidinium carbonate (6.306 g, 70.0 mmol) in 40 ml dry EtOH, a paraffin bubbler was attached and the mixture stirred for 16 h at RT. The slightly turbid solution was canula filtered into a 600 mL beaker, and **1a** was obtained as colourless needle crystals by slow evaporation of this EtOH–Et_2O solution in air. Yield: 8.126 g (97 %). DSC melting point: 41 °C (T_{on}), ΔH_{fus} = 23.0 kJ mol^{-1}; decomposition: *ca.* 253 °C (T_{on}), ΔH_{dec} = –226 kJ mol^{-1}. Elem. anal. (%) for CH_8N_6O, 120.12 g mol^{-1}, calcd: C 10.00, H 6.71, N 69.97; found: C 10.67, H 6.53, N 69.20. FTIR (nujol)

$\tilde{\nu}$ [cm^{-1}]: 3410s,br,sh, 3356s,br, 3169s,br, 2151w,sh, 2107vw, 2045vs,br, 1664s,br, 1575w,br, 1170vw,sh, 1150w,br, 1007vw, 971vw, 893vw; usually NaN_3 is visible from reaction with NaCl windows at $\tilde{\nu}$ [cm^{-1}] = 3389w, 3300vw, 2130m,br, 639m,sharp. NMR δ [ppm] (dmso-d_6): ^{1}H = 3.40 (s, 2*H*), 6.95 (s, 6*H*).

6.2.5 Aminoguanidinium Azide (2), $\{(H_2N)_2C{=}NHNH_2\}N_3$

6.2.5a Preparation of Aminoguanidinium azide (2)

An excess of ethereal HN_3 (22.7 ml, 1.9 mol dm^{-3}, *ca.* 43 mmol) was added to a vigorously stirred suspension of aminoguanidinium bicarbonate (4.658 g, 34.2 mmol) in 40 ml EtOH at 25 °C. The mixture was warmed to 40 °C, and stirred for 16 h. The suspension was allowed to cool to 25°C before addition of further ethereal hydrazoic acid (5 ml, 1.9 mol dm^{-3}, *ca.* 9.5 mmol) to the white suspension. After a further 16 h at 40 °C, filtration of the turbid solution afforded a clear, pale yellow filtrate solution, from which crystallisation of **2** started immediately at RT. The off-white filter residue was discarded. The filtrate solution was evaporated to dryness under dynamic vacuum giving aminoguanidinium azide as a semi-crystalline pale pink-orange solid. Raw yield 3.535 g (88 %). Analytically pure aminoguanidinium azide, and colourless crystals suitable for single crystal X-ray diffraction studies were obtained by recrystallisation from dry EtOH. DSC melting point: 125 °C (T_{on}), ΔH_{fus} = 28.6 kJ mol^{-1}; decomposition: 201 °C (T_{on}), ΔH_{dec} = –328 kJ mol^{-1}. Elem. anal. (%) for CH_7N_7, 117.12 g mol^{-1}, calcd = C 10.25, H 6.03, N 83.72; found: C 10.76, H 5.75, N 83.95. FTIR (nujol) $\tilde{\nu}$ [cm^{-1}] = 3386s, 3354s, 3282vs, 3243sh, 3186s, 3132s, 2055vs, 2023vs, 1679sh, 1663vs, 1577s, 1415w, 1341vw, 1262vw, 1210w, 1081vw,br, 1015m, 800vw,br, 727vw, 635w, 612w, 504w; NMR δ [ppm] (dmso-d_6): ^{1}H = 4.68 (s, 2*H*), 7.21 (s, 2*H*), 6.83 (s, 2*H*) 8.61 (s, 1*H*); ^{13}C{^{1}H} = 158.99; ^{14}N = –131.88 (N_β), –276.66 (N_α,N_γ).

6.2.5b Preparation of aminoguanidinium azide (2) at RT

Ethereal HN_3 (15.4 ml, 1.95 mol dm^{-3}, 30 mmol) was added to a suspension of aminoguanidinium bicarbonate (3.251, 23.9 mmol) in 20 ml dry EtOH and the pale pink-orange suspension was stirred for 16 h at RT. The rate of CO_2 evolution through the paraffin bubbler was too slow to be observed, suggesting a greatly reduced reaction rate. The suspension was filtered, and the residue extracted with 10 ml dry EtOH. The combined filtrate solution was evaporated to dryness giving **2** as a pale pink-orange semi-crystalline solid (339 mg, 12 % based on aminoguanidinium bicarbonate). The decrease in CO_2 evolution rate and reduced yield suggest that the rate enhancement when heating to 40 °C outweighs the evaporative losses of ethereal HN_3.

6.2.6 Preparation of triaminoguanidinium azide (adapted from (TAG)Cl synthesis in the SI of ref. [151])

Hydrazine monohydrate (1.0 ml, 1.032 g cm^{-3}, 20.6 mmol) was added to a stirred suspension of aminoguanidinium azide (237 mg, 2.02 mmol) in 10 ml dry EtOH, which quickly dissolved to give a clear solution. The mixture was heated to reflux in an oil bath set to 85 °C for 2 h. After cooling to RT all solvent was removed under vacuum leaving a translucent oil. Addition of 20 ml dry Et_2O caused precipitation of a white solid, from which the colourless solution was decanted. The white solid was dried under vacuum for 20 minutes at 40 °C. The solid was extracted with 40 ml warm (45 °C) EtOH, leaving behind 60 mg white filter residue. Evaporation of the EtOH filtrate solution under vacuum yielded triaminoguanidinium azide as fine needle crystals. Elem. anal. (%) for CH_9N_9, 147.11 g mol^{-1}, calcd: C 8.16, H 6.17, N 85.67; found: C 8.87, H 6.11, N 85.85. FTIR (nujol) $\tilde{\nu}$ [cm^{-1}] = 3341m,sh, 3301s,br, 3249s,br, 3204s,br, 2023vs,br, 1681vs,br, 1618m,br, 1340s,br, 1201vw, 1172vw, 1132m, 961s,br, 932vw,sh, 645m, 629m, 594m,br. Elemental analysis showed the filter residue to have nitrogen content of 88.43 %, which is most likely due to hydrazinium azide (or hydrazinium azide hydrazinate) impurity. The presence of water from the hydrazine hydrate could have (slowly) hydrolysed some of the triaminoguanidinium azide as observed previously,[146] and the liberated HN_3 would have reacted with the excess hydrazine to produce the hydrazinium azide hydrazinate impurity. (N.B. in the literature procedure for hydrazinium azide hydrazinate, the hydrazine of crystallisation is retained upon recrystallisation from methanol).[128]

6.2.7 Bis(guanidinium) hexa(azido)stannate, $\{C(NH_2)_3\}_2[Sn(N_3)_6]$ (3)

6.2.7a Direct reaction of $SnCl_4$ and guanidinium azide

$SnCl_4$ (0.14 ml, ρ = 2.2 g cm^{-3}, 1.18 mmol) was added using a 1 ml glass pipette to a stirred ice-water cooled suspension of guanidinium azide (**1**, 503 mg, 4.93 mmol) in 20 ml dry CH_3CN. The resulting mixture was allowed to warm to RT and gradually became more opaque over the first hour, and was left to stir for 24 h. The progress of the reaction was followed by *in-situ* FTIR spectroscopy. After 24 h a FTIR spectrum of the solution was recorded: FTIR (CH_3CN) $\tilde{\nu}$ [cm^{-1}] = 3454m,br 3368m,br, 3283w,br, 3214w,br, 2139vw {HN_3}, 2098m,sh, 2077vs, 1668vs, 1574w,br, 1341w,br, 1287m,br. The characteristic weak secondary band for $[Sn(N_3)_6]^{2-}$ at 2112 cm^{-1} was not visible, though the absorption bands at 1341 and 1287 cm^{-1} are very close to the symmetric azide stretches of $[Sn(N_3)_6]^{2-}$,[170] $\nu_s(N_3)$ = 1339 and 1287 cm^{-1}, which may be explained by incomplete Cl/N_3 exchange. This white suspension was filtered directly onto a second batch of **1** (501 mg, 4.91 mmol) suspended in dry CH_3CN, and stirred for 24 h at RT. Filtration of this white suspension yielded a perfectly clear, very pale orange solution: FTIR (CH_3CN) $\tilde{\nu}$ [cm^{-1}] = 3454m,br, 3369m,br, 3282m,br,

3214m,br, 2138vw {HN_3}, 2112m, 2079vs, 2046vw,sh, 2029w {**1**}, 1669s,br, 1575vw,br, 1339w, 1287m. A FTIR spectrum of the fine off-white powder filter residue was recorded: FTIR (nujol) $\tilde{\nu}$ [cm^{-1}] = 3384s,br, 3358s,br, 3275w,sh, 3162s,br, 2077s,br, 2061s, 2030vs, 1667s,br, 1644w,sh, 1630w,sh, 1580w. Examination of this spectrum indicates a mixture of guanidinium azide, bis(guanidinium) hexaazidostannate, and presumably guanidinium chloride by-product. The pale orange solution was concentrated under dynamic vacuum in a cold bath at –30 °C for 2 h, by which time a few crystals had formed on the side of the tube. The pale orange solution was filtered from the small white crystals (33 mg), which were washed with CH_3CN at –35 °C. FTIR (nujol) $\tilde{\nu}$ [cm^{-1}] = 3384s, 3358s, 3270w,sh, 3165s,br, 2077s,br, 2061m, 2031vs,br, 1667s, 1645m, 1630m,sh. The FTIR spectrum of the crystals did not change significantly upon exposure to atmosphere so it is unlikely to be **1** or **3**, but could be a mixture of **1** and guanidinium chloride by comparison with a reference spectrum of the latter. The crystals were low quality, and unsuitable for XRD. All CH_3CN was removed from the pale orange solution yielding a slightly oily orange solid, which exhibited a broad feature centred at 2075 cm^{-1} with multiple shoulder peaks, and 6 bands in the N–H stretch region: FTIR (nujol) $\tilde{\nu}$ [cm^{-1}]: 2122, 2114, 2102, 2084, 2073, 2059, 2037, 2026. This could be a mixture of guanidinium azido-chlorostannates and excess **1**. The solid was dissolved in 50 ml dry THF, and the slightly turbid solution was filtered and dried under dynamic vacuum. Recrystallisation from Et_2O, and from CH_2Cl_2 both proved unsuccessful as the solid was only sparingly soluble. NMR δ [ppm] (CD_3CN): ^1H = 1.94 (m, solvent residual), 6.18 (s). Difficulties in crystallisation from this direct synthesis lead to the development of alternative methods described below.

6.2.7b Reaction of $Na_2[Sn(N_3)_6]$ with guanidinium azide (1)

An aliquot of a stock solution of $Na_2[Sn(N_3)_6]$ (1.3 mmol) in CH_3CN was canula transferred onto guanidinium azide (**1**, 271 mg, 2.65 mmol), and the resultant white suspension was stirred for 24 h at RT. The suspension was filtered yielding a clear colourless solution, and the white filter residue was discarded. The solution was concentrated until onset of crystallisation, and cooled to –19 °C overnight, after which a small amount of white solid precipitated from solution. This process was repeated 3 times until colourless needle crystals formed in the 2–3 ml of CH_3CN solution. The solution was decanted from the colourless needle crystals, which were dried under dynamic vacuum, and examined by single crystal XRD. Yield: 280 mg (44 %).

6.2.7c Reaction of SnF_4 with TMS–N_3 and guanidinium azide (1)

Trimethylsilyl azide (500 mg, 4.34 mmol) was added dropwise to a stirred suspension of SnF_4 (196 mg, 1.01 mmol) and **1** (227 mg, 2.22 mmol) in 12 ml CH_3CN. After stirring for 1½ h, all volatiles were removed under vacuum and the white residue washed with 20 ml dry CH_2Cl_2.

Colourless needle crystals of bis(guanidinium) hexaazidostannate were obtained after slow cooling of a saturated MeCN solution to –19 °C overnight. Yield: 235 mg (47 %). Elem. anal. (%) for $C_2H_{12}N_{24}Sn$, 490.88 g mol^{-1}, calcd = C 4.89, H 2.46, N 68.46; found: C 5.54, H 2.62, N 69.11. DSC melting point: 116(1) °C (T_{on}), ΔH_{fus} = 34(3) kJ mol^{-1}; decomposition: 252(6) °C (T_{on}), ΔH_{dec} = –1270(30) kJ mol^{-1} (–2.59(7) kJ g^{-1}). FTIR (nujol) $\tilde{\nu}$ [cm^{-1}] = 3455s, 3434s, 3376w,sh, 3339m,br, 3258m,br, 3195s, 2116sh, 2099vs, 2079vs, 2067vs, 2031sh, 1662m,br, 1558w, 1342m,br, 1289w, 1272m, 1186w, 665m; (CaF_2, CH_3CN): 3454m,br, 3369m,br, 3282m,br, 3214m,br, 2112m, 2079vs, 1669s,br, 1575vw,br, 1339w, 1287m. NMR δ [ppm] (CD_3CN): ^{1}H = 6.14 (s); ^{13}C{^{1}H} = 159.04; ^{14}N = –135.22 (CD_3CN), –215.94 (N_γ), –301.64 (N_α); ^{119}Sn = –600.9.

6.2.8 Bis(aminoguanidinium) hexa(azido)stannate, $\{H_2NNHC(NH_2)_2\}_2[Sn(N_3)_6]$ (4)

6.2.8a Preparation via $Na_2[Sn(N_3)_6]$

Aminoguanidinium azide (**2**, 445 mg, 3.8 mmol) was suspended in an aliquot (9.4 ml, 1.5 mmol) of the MeCN stock solution of $Na_2[Sn(N_3)_6]$ and the mixture stirred for 24 h at RT. A FTIR spectrum of the solution was recorded: $\tilde{\nu}$ [cm^{-1}] = 3451m,br, 3361m,br, 3332w,sh, 3282w,br, 2113m, 2079vs,br, 1683w,sh, 1670vs, 1598w,br, 1339m,br, 1288m,br, 1201w,br. The increased absorbance of the N–H stretches compared to a reference spectrum of **2** in MeCN suggested the metathesis had occurred at least partially. The suspension was filtered to give a clear solution, leaving behind a white filter residue consisting largely of NaN_3 (and residual **2**) giving further evidence that the sodium had been displaced. Attempts to crystallise bis(aminoguanidinium) hexaazidostannate (**4**) resulted in a translucent oil, from which crude **4** was precipitated by storing under Et_2O overnight at –19 °C. After decantation of the Et_2O solution the slightly sticky solid residue (147 mg) was dried under vacuum, and an FTIR spectrum was recorded: $\tilde{\nu}$ [cm^{-1}] = 3446m,br, 3430m,br, 3361m,br, 3342w,br, 3282m,br, 3245m,br, 3200w,br, 3169w,br, 2727w, 2633vw,sh, 2608w, 2545w, 2535vw,sh, 2119w,sh, 2083vs, 2030w,sh, 1671s, 1659s, 1583w,br, 1342m,br, 1279m,br, 1272w,sh, 1261w,sh, 1200w,br, 1120vw,br, 1083vw,br, 1018w,br, 967vw,br, 930w,br, 904vw,br, 802w, 665w,br, 593w. The crude produce also contains a trace of NaN_3. If the reaction was incomplete, the residual $Na_2[Sn(N_3)_6]$ could have hindered crystallisation of **4**, and could be the origin of the trace NaN_3 after precipitation with Et_2O.

6.2.8b Preparation via SnF_4

TMS–N_3 was added dropwise to a stirred suspension of SnF_4 (100 mg, 0.51 mmol) and aminoguanidinium azide (130 mg, 1.11 mmol) in 12 ml dry MeCN. The suspension was warmed in an oil bath at 40 °C for 16 h with a Hg stop valve to allow pressure relief. The

virtually clear solution was filtered, leaving a negligible amount of off-white filter residue. A diluted sample (approximately 1:8) of the filtrate solution was investigated by FTIR: $\tilde{\nu}$ [cm^{-1}] = 3452m,br, 3366m,br, 3331w,sh, 3286w,br, 2111w,br, 2079vs,br, 1683w,sh, 1670s,br, 1340w,br, 1289w,br. The solution was placed in the freezer overnight after concentrating to 1 ml volume. The viscous pale yellow solution was decanted from the crystalline residue, which was dried in vacuo for ½ h giving 63 mg. The crystals were not suitable for XRD, but a FTIR spectrum prepared in the glovebox seemed to be consistent with bis(aminoguanidinium) hexaazidostannate with a trace of aminoguanidinium azide: $\tilde{\nu}$ [cm^{-1}] = 3439s,br, 3349s,br, 3281s,br, 3242w,sh, 3160s,br, 2735w,br, 2631w,br, 2549vw,br, 2118m,br, 2081vs,br, 2026w,sh, 1663vs,br, 1582m,br, 1534vw,br, 1417w, 1340m,br, 1282m,br, 1203w,br, 1088w,br, 1016w, 930w,br, 798vw,br, 662vw, 633vw, 597vw, 504w. Weak (sharp) absorption at 504 cm^{-1} may be ν(Sn–F) indicating a small amount of residual fluoride content, or may be noise. Cooling of the above viscous filtrate solution to –19 °C overnight after concentration to 0.5 ml left a pale yellow oil, to which 15 ml THF was added and a FTIR spectrum recorded: $\tilde{\nu}$ [cm^{-1}] = 3421w,br, 3363w,br, 3163w,br, 2109w,br, 2079vs,br, 1683vw,sh, 1670m,br, 1334w,br, 1283w,br, 1157vw,sh. A 2.5 ml aliquot of the THF solution was allowed to evaporate in the glovebox over 2 days, but left an oil which did not yield crystals . The remaining THF solution was evaporated to dryness for 3 h giving a colourless oil (163 mg) which was shaken with 20 ml Et_2O resulting in partial solidification of the oil to a translucent sticky solid.

6.2.9 Attempted Preparation of bis(guanidinium) hexa(azido)silicate, $(C(NH_2)_3)_2[Si(N_3)_6]$ (5)

6.2.9a Direct reaction of $SiCl_4$ with guanidinium azide

$SiCl_4$ (0.1 ml, 1,486 g cm^{-3}, 0.94 mmol) was added to a vigorously stirred suspension of guanidinium azide (1.339 g, 13.1 mmol) in 20 ml dry MeCN and stirred overnight at RT. An FTIR spectrum of the resulting solution confirmed the presence of $[Si(N_3)_6]^{2-}$ in solution according to literature:[83] FTIR (MeCN) $\tilde{\nu}$ [cm^{-1}] = 2110vs, 1317s. The absorption bands at 3454, 3371, 3283, 3213, 1669, 1050, and 1018 cm^{-1} are attributed to the guanidinium cation. An FTIR spectrum of the insoluble white residue after filtration could not confirm or exclude the presence or absence of guanidinium chloride owing to the large excess of guanidinium azide used. The filtrate solution was concentrated until the onset of crystallisation, and cooled to –19 °C overnight resulting in the formation of small block crystals. Single crystal XRD revealed a co-crystal of guanidinium azide and chloride, though the low crystal quality precluded an accurate structure determination. The chloride content in the crystals can only originate from $SiCl_4$, showing azide-chloride exchange has occurred at least partially, and that a mixture of guanidinium chloride and guanidinium azide has higher solubility in MeCN than

either of the pure compounds. Further attempts at purification by crystallisation were unsuccessful, resulting only in successive small crops of guanidinium azide, and eventually a viscous colourless oil.

6.2.9b Reaction of guanidinium azide with $Na_2[Si(N_3)_6]$, and subsequent isolation of guanidinium sodium azide 2 : 1 co–crystal (5b)

An aliquot of an MeCN stock solution of $Na_2[Si(N_3)_6]$ (5.6 ml, 0.11 mol dm^{-3}, 0.62 mmol) was added to a stirred suspension of guanidinium azide (153 mg, 1.5 mmol) in 20 ml MeCN. The suspension was noticeably finer after 1 h, and was stirred overnight at RT. A FTIR spectrum of the clear colourless solution obtained after filtration showed absorption bands for $[Si(N_3)_6]^{2-}$ (2110, 1316 cm^{-1}), the guanidinium cation (3452, 3371, 3281, 3213, 1668, 1037, 1018 cm^{-1}), GN_3 (2045, 2027 cm^{-1}). A weak band is also visible at 2141 cm^{-1}, which could be a secondary band due to $[Si(N_3)_6]^{2-}$ or another silicon azide species. Inspection of the filter residue by FTIR spectroscopy showed primarily NaN_3 which can only originate from $Na_2[Si(N_3)_6]$, and a trace of GN_3 from the slight excess used. Concentration of the filtrate solution, and cooling to –19 °C overnight afforded short rod-like crystals, which were investigated by single crystal XRD. The crystals proved to be a 2:1 co-crystal of GN_3 and NaN_3, suggesting residual sodium in solution – as either $Na_2[Si(N_3)_6]$, $Na\{MeCN\}_x(N_3)$ or $Na_{0.33}G_{0.67}(N_3)$ – after removal of NaN_3 by filtration. The solution filtered from the above co-crystal was left to evaporate slowly in the glovebox for several days, resulting in a waxy solid. Crystallisation by slow diffusion of Et_2O into the saturated MeCN solution was also unsuccessful.

6.2.9c Reaction of $Si(N_3)_4$(bpy) with guanidinium azide (1)

Crystalline $Si(N_3)_4$(bpy) (110 mg, 0.312 mmol) was dissolved in 17 ml dry MeCN, and a FTIR spectrum was recorded. Guanidinium azide (64 mg, 0.627 mmol) was added, forming a white suspension which gradually dissolved to a clear solution after stirring for 4 h. An FTIR spectrum of the solution showed dramatic reduction in the absorption bands of $Si(N_3)_4$(bpy) at 2152, 2124, 2117, and 1623 cm^{-1} the emergence of new bands at 3452, 3369, 3282, 3216, 2110, 1669, 1317 corresponding to bis(guanidinium) hexaazidosilicate, and free 2,2-bipyridine is also observed at 1584 cm^{-1}. Further portions of guanidinium azide (15 & 25 mg, total 0.4 mmol) were added resulting in almost complete disappearance of $Si(N_3)_4$(bpy), and a corresponding increase in $[Si(N_3)_6]^{2-}$ (and guanidinium azide) concentration. After storage of the solution at –19 °C for two weeks, colourless crystals had formed in the solution, which were shown to be guanidinium azide by FTIR spectroscopy. An FTIR spectrum of the filtrate solution showed the partial reformation of $Si(N_3)_4$(bpy), with HN_3 and guanidinium azide, which was corroborated by an FTIR spectrum of the residue after evaporation of all volatiles under vacuum. These observations suggest that guanidinium azide displaces 2,2'-bipyridine

from the complex to form bis(guanidinium) hexaazidosilicate in solution, however during concentration under vacuum the 2,2'-bipyridine concentration is increased and at lower temperature the reaction is reversed as the less soluble guanidinium azide precipitates. Isolation of bis(guanidinium) hexaazidosilicate would require removal of 2,2'-bipyridine from the equilibrium, possibly by sublimation.

6.2.10 Attempted Preparation of bis(aminoguanidinium) hexa(azido)silicate, $\{H_2NNHC(NH_2)_2\}_2[Si(N_3)_6]$ (6)

6.2.10a Direct reaction of $SiCl_4$ with aminoguanidinium azide

$SiCl_4$ (0.1 ml, 1.486 g cm^{-3}, 0.94 mmol) was added to a vigorously stirred suspension of aminoguanidinium azide (**2**, 1.536 g, 13.1 mmol) in 20 ml dry MeCN, and the solution monitored by in-situ FTIR spectroscopy: $\tilde{\nu}$ [cm^{-1}] = 3444w, 3363w, 3285w, 3228w, 2147w, 2139s {HN_3}, 2113vs, 1669s, 1316m, 1018w. Subsequent FTIR spectra recorded over 24 h were almost identical. Filtration was attempted using a Schlenk tube filter (no. 2 porosity) in the glovebox but resulted in a turbid solution. Subsequent attempts at canula filtration of the solution gave initially a clear solution, from which a fine white solid quickly precipitated. Addition of further MeCN (30 ml) did not dissolve the white precipitate, which was investigated by FTIR spectroscopy after filtration and drying under vacuum: $\tilde{\nu}$ [cm^{-1}] = 3427w, 3355w, 3159w, 2137m,br, 2115m,br, 2037m,br, 1665w, 1576s,br, 1308w, 1273m,br, 1037w, 693m. These observations could be explained if the reaction was incomplete and co-precipitated a mixture of aminoguanidinium chloride/azide and **6.** The white precipitate was too insoluble in MeCN, THF and CH_2Cl_2 to attempt crystallisation. Evaporation of the turbid solution to dryness produced more of the insoluble compound as a glassy solid.

6.2.10b Reaction of aminoguanidinium azide with $Na_2[Si(N_3)_6]$

An aliquot of a stock solution of $Na_2[Si(N_3)_6]$ (5.2 ml, 0.11 mol dm^{-3}, 0.57 mmol) was added to a stirred suspension of aminoguanidinium azide (162 mg, 1.38 mmol) in 20 ml MeCN, which quickly became more turbid and was stirred at RT for 16 h. The suspension was filtered to give an initially clear solution, from which a white solid precipitated gradually upon standing. An FTIR spectrum of the initial filter residue confirmed it was a mixture of aminoguanidinium azide and NaN_3. The precipitate from the filtrate solution Several successive filtrations of the turbid solution gave the same result, with gradual precipitation of a white solid upon standing. All solvent was removed under dynamic vacuum giving a white amorphous solid, which was characterised by FTIR spectroscopy: $\tilde{\nu}$ [cm^{-1}] = 3444w, 3363w, 3285w, 3228w, 2147w,sh, 2134s, 2118vs, 1669w, 1316w, 1038m.

6.2.11 Attempted preparation of guanidinium hexa(azido)phosphate, $\{C(NH_2)_3\}[P(N_3)_6]$ (7), and subsequent isolation of $[P(=O)(N_3)_2\{NC(NH_2)_2\}]$ (8)

A pale orange stock solution of $NaP(N_3)_6$ (0.64 mmol, 15 ml) in MeCN was added via canula to guanidinium azide (80 mg, 0.78 mmol) at –35 °C over a period of 20 minutes. The suspension was stirred for 16 h in the cold bath, which had warmed to –16 °C. The suspension appeared finer, the cold bath was removed and the suspension stirred for 24 h at RT. The solution was allowed to settle, and a FTIR spectrum was recorded of the pale orange solution: $\tilde{\nu}$ [cm^{-1}] = 3460m,br, 3370m,br, 3280w,br, 3211m,br, 2165w,sh, 2139s, 2116s, 2028w, 1669m, 1566w, 1287m, 1261m,sh, 1176w, 1040m. The solution was filtered, yielding a pale orange solution and filter residue, which was determined to be NaN_3 by FTIR spectroscopy. The filtrate solution was concentrated under dynamic vacuum to ca. 3 ml by which time the solution was dark orange, and cooled to –19 °C. After 48 h, a few pale yellow shard crystals had formed, from which the orange solution was carefully decanted via canula. Concentration of the filtrate solution gave an orange-brown viscous oil. The crystals were investigated by single crystal XRD, and proved to have the formula $P(=O)(N_3)_2(NC(NH_2)_2)$ (**8**), suggesting reaction of $P(=O)(N_3)_3$ impurity in $NaP(N_3)_6$ with guanidinium azide.

6.2.12 Attempted Preparation of Guanidinium Hexachlorophosphate, $(C(NH_2)_3)PCl_6$

Guanidinium chloride (108 mg, 1.13 mmol), and PCl_5 (192 mg, 0.92 mmol) were added to a Schlenk tube. Dry CH_3CN (*ca.* 15 ml) was added via canula, and the pale green-yellow suspension stirred overnight. The suspension was filtered to give a clear, pale green solution, leaving 84 mg of white filter residue. A FTIR spectrum of the solution was recorded: FTIR (MeCN) $\tilde{\nu}$ [cm^{-1}] = 3418m, 3375m, 3283m,sh, 3216m, 1692s, 1669s, 1545w, 1295w, 1281w,sh, 1069m. The filtrate solution was concentrated, and placed in the freezer overnight, which gave small colourless block crystals (*ca.* 19 mg). The solution was decanted from the crystals, and a FTIR spectrum of the crystals showed only guanidinium chloride. Combined with the mass of filter residue, (84 + 19 mg = 103 mg) this could mean that there was no reaction at RT overnight.

6.2.13 Guanidinium Tetrazolate, $(C(NH_2)_3)N_4CH$ (19)

A solution of anhydrous 1*H*–tetrazole (1.346 g, 19.2 mmol) in 35 ml dry ethanol was added to a suspension of guanidinium carbonate (2.066 g, 11.5 mmol) in 20 ml dry ethanol with noticeable gas evolution through the attached paraffin bubbler from the white suspension, which gradually became clear after around 10 minutes. The slightly turbid solution was concentrated by ¼ volume and the precipitate filtered off. The filtrate was concentrated to ½ volume until precipitation started, and placed in the freezer overnight at –19 °C, giving a white

solid (356 mg) which was confirmed to be excess guanidinium carbonate by a FTIR spectrum. Cooling the concentrated filtrate solution to –19 °C overnight gave a mixed precipitate of **19** and guanidinium carbonate (28 mg). The filtrate solution was concentrated by ¼ when crystallisation began at the solution surface. The solid redissolved upon warming, and slow cooling of this solution gave **19** as colourless shard-like crystals. Elem. anal. (%) for $C_2H_7N_7$, 129.10 g mol^{-1}, calcd: C 18.61, H 5.46, N 75.93; found: C 18.71, H 5.35, N 73.11. DSC melting point: 121(3) °C (T_{on}), ΔH_{fus} = 14.3(5) kJ mol^{-1}; decomposition: 280(8) °C (T_{on}), ΔH_{dec} = –194(3) kJ mol^{-1} (–1.50(3) kJ g^{-1}). FTIR (nujol) $\tilde{\nu}$ [cm^{-1}] = 3424s, 3353s,sh, 3165s, 3110vw, 2238w, 2187vw, 2135vw, 2051vw, 1713w,sh, 1682s, 1649s, 1647m,sh, 1288vw, 1281vw, 1183w, 1170vw, 1149w, 1133vw, 1068vw, 1017vw, 1007w, 993vw, 881w, 870w, 771vw, 697w. NMR (400 MHz, D_2O) δ [ppm]: ^{1}H = 4.79 (exchange with solvent), 8.47 (s); ^{13}C{^{1}H} = 150.68 (s), 158.59 (s), N.B. ^{13}C NMR in D_2O was calibrated against a trace of residual ethanol at 17.45, 58.05; ^{14}N = –4.55 (N2, N3), –73.32 (N1, N4); (dmso-d_6) δ [ppm]: ^{1}H = 6.94 (s), 8.24 (s); ^{13}C{^{1}H} = 149.7 (s), 158.7 (s). The ^{14}N chemical shifts of the tetrazolate anion are similar to those of the related compounds hydrazinium tetrazolate (δ (D_2O) ^{14}N = –7.6, –75.9 ppm), and ammonium tetrazolate monohydrate (δ (D_2O) ^{14}N = –7, –74 ppm).[152]

6.3 Tin(IV) Azides

6.3.1 Disodium hexa(azido)stannate(IV), $Na_2[Sn(N_3)_6]$

6.3.1a $Na_2[Sn(N_3)_6]$:[85] (adapted from ref. [169]) stock solution in MeCN

$SnCl_4$ (0.15 ml, ρ = 2.2 g cm^{-3}, 1.3 mmol) was added to a vigorously stirred suspension of NaN_3 (0.787 g, 12.1 mmol) in MeCN (20 ml) at 0 °C. The suspension was allowed to warm to RT, and was left to stir for 24 h before filtration onto a second batch of NaN_3 (522 mg, 8.03 mmol). The resultant white suspension was left to stir for a further 24 h before filtration, and the white filter residue was extracted with MeCN (2 × 15 ml) yielding a perfectly clear, colorless solution of $Na_2[Sn(N_3)_6]$. An approximate concentration was calculated based on complete conversion of $SnCl_4$ and the mass of the solution (ρ(MeCN) = 0.786 g cm^{-3}). The stock solution concentration typically ranged from 0.05–0.3 mol dm^{-3} depending on the amount of $SnCl_4$ (1.3 to 2.6 mmol) and MeCN used. FTIR (nujol) $\tilde{\nu}$ [cm^{-1}] = 3374vw,br, 3340vw, 2118vs, 2090sh, 2077vs, 1660w, 1349m, 1298m, 1293sh, 1247vw; MeCN: $\tilde{\nu}$ [cm^{-1}] = 2112w, 2078vs, 1339w, 1289w. Alternatively, the stock solution can be made up in THF as in the original report,[169] which has a subtly different FTIR spectrum: $\tilde{\nu}$ [cm^{-1}] = 2119w, 2083vs, 1340w, 1282w.

6.3.1b $Na_2[Sn(N_3)_6]$: Attempted crystallisation from THF/Et_2O

A 2 ml aliquot of a THF stock solution of $Na_2[Sn(N_3)_6]$ (0.13 mol dm^{-3}, 0.26 mmol, <108 mg) was concentrated under vacuum to around 1 ml, by which time the solution had become a

slightly turbid viscous oil. The solution was filtered through glass wool in the glovebox into a small vial equipped with a perforated cap. The vial of colourless solution was sealed within a HPLC bottle containing *ca*. 5 ml dry Et_2O, to allow slow diffusion into the THF solution. After several days a white powder was deposited under the solution, from which the solvent was allowed to evaporate. FTIR (nujol) $\tilde{\nu}$ [cm^{-1}] = 3374vw,br, 3340vw, 2118vs, 2090sh, 2077vs, 1660w, 1349m, 1298m, 1293sh, 1247vw. Sodium azide was present as a trace impurity (NaN_3: $\tilde{\nu}$ [cm^{-1}] = 3390w,br, 3300vw, 2130s,br, 639m.

6.3.2 Bis{bis(triphenylphosphine)iminium} hexa(azido)stannate(IV), $(PPN)_2[Sn(N_3)_6]$ (9),[85] {PPN = $(Ph_3P{=}N{=}PPh_3)^+$}

$(PPN)N_3$ (1.100 g, 1.89 mmol) was dissolved in an aliquot (15 ml, 0.95 mmol) of the MeCN stock solution of $Na_2[Sn(N_3)_6]$ and the resultant mixture stirred for 0.5 h yielding a fine, white suspension. In order to dissolve all soluble material, further MeCN (35 ml) was added to the stirred suspension until no further dissolution was noticeable. The suspension was then filtered yielding an absolutely clear, colourless solution and an off-white residue which was discarded. The volume of the solution was reduced until crystallisation commenced. Crystallization was completed by storing in the freezer overnight. The white, crystalline precipitate was isolated by decantation of the solvent, washing with MeCN at –35 °C and then drying in *vacuo* at RT for 3 h, giving 967 mg (0.668 mmol) of $(PPN)_2[Sn(N_3)_6]$ in 70 % yield with respect to $Na_2[Sn(N_3)_6]$. Elem. anal. (%) for $C_{72}H_{60}N_{20}P_4Sn$, 1447.99 g mol^{-1}, calcd: C 59.72, H 4.18, N 19.35; found: C 59.71, H 4.03, N 19.41. DSC melting T_{on} = 218 °C, decomposition T_{on} = 365 °C, ΔH_{dec} = –0.76 kJ g^{-1}. FTIR (nujol) $\tilde{\nu}$ [cm^{-1}] = 2104vw,br, 2074vs, 2060m,sh, 1438w, 1337w, 1316w, 1303w, 1288w, 1269w, 1118w, 693w, 551w, 532w; MeCN: 2111 w, 2078vs; CH_2Cl_2: 2111w, 2078vs; THF (sparingly soluble): 2108w,br, 2075vs. NMR (250 MHz, CD_3CN) δ [ppm] ^1H = 1.94 (solvent residual), 7.44–7.70 (m); δ (^{13}C) [ppm] = 1.32 (m, solvent residual), 118.3 (s, solvent residual), 129.2 (s, *ipso*), 130.4 (m, *ortho*), 133.3 (m, *meta*), 134.7 (s, *para*); δ(^{14}N) [ppm] = 135.7 (MeCN-d_3), 218.7 (N_γ), 299.1 (N_α); δ(^{31}P) [ppm] = 20.8.

6.3.3 Tetra(azido)(2,2'-bipyridine)tin(IV), $Sn(N_3)_4(bpy)$ (10)[85]

Dry, sublimed bipyridine (378 mg, 2.42 mmol) was added to an aliquot of a stock solution of $Na_2[Sn(N_3)_6]$ (11.0 ml, 1.6 mmol) in MeCN. The MeCN was removed in vacuo behind a blast shield, then CH_2Cl_2 (60 ml) was added. The stirred reaction mixture was heated to 40 °C for 2 h yielding a white suspension. The suspension was filtered and the residue extracted with a further 80 ml of boiling CH_2Cl_2. The combined filtrate and extract solutions were concentrated to a volume of 4 ml and then cooled to –28 °C for 1 h upon which crystallisation occurred. The supernatant solution was decanted, the residue extracted with MeCN (80 ml) at 60 °C and the solution then concentrated to 2 ml and cooled to –28 °C overnight which caused recrystallization. The cold mother liquid was decanted, the residue washed with MeCN (1 ml)

and dried in vacuo at 60 °C for 2 h, giving **10** (477 mg, 1.08 mmol) as a white powder in 67 % yield based on $Na_2[Sn(N_3)_6]$. Elem. anal. (%) for $C_{10}H_8N_{14}Sn$, 442.93 g mol^{-1}, calcd: C 27.12, H 1.82, N 44.26; found: C 27.72, H 1.86, N 42.91. FTIR (nujol) $\tilde{\nu}$ [cm^{-1}] = 3441vw, 3356m, 3334m, 3122vw, 3116vw, 3082w, 3065vw, 3040vw, 3033vw, 2110vs, 2092vs,br, 2075vs,br, 2067vs,br, 1612w, 1600w, 1573w, 1565w, 1497w, 1477w, 1445m, 1332m, 1318w, 1277w, 1273w, 1228vw, 1252w, 1176w, 1160w, 1108vw, 1073vw, 1061 vw, 1046vw, 1033m, 1023w, 776 m, 767w, 663vw, 651vw, 589vw; MeCN: 2112m, 2085vs, 1615w, 1604 w, 1331vw, 1321sh, 1282w; CH_2Cl_2: 2112m, 2084vs, 1614w, 1602w, 1332vw, 1321w. NMR (MeCN-d_3) δ(^{1}H) [ppm] = 8.08 (ddd, 2*H*, H5,5'), 8.55 (ddd, 2*H*, H4,4'), 8.72 (ddd, 2*H*, H3,3'), 9.12 (ddd, 2*H*, H6,6'); coupling constants [Hz]: ^3J(H3,H4) = 8.0, ^4J(H3, H5) = 1.1, ^5J(H3,H6) = 1.0, ^3J(H4,H5) = 7.7, ^4J(H4,H6) = 1.6, ^3J(H5,H6) = 5.5; δ(^{13}C) [ppm] = 125.5, 130.1, 144.6, 145.9, 147.5. DSC: melting T_{on} = 180 °C; decomposition 265 °C, ΔH_{dec} = –880 kJ mol^{-1} (–2.00 kJ g^{-1}).

6.3.4 Tetra(azido)(1,10-phenanthroline)tin(IV), $Sn(N_3)_4$(phen) (11)[85]

Dry, sublimed phenanthroline (242 mg, 1.34 mmol) was added to an aliquot of a stock solution of $Na_2[Sn(N_3)_6]$ (25.9 ml, *ca*. 1.3 mmol) in MeCN. The procedure for isolating the compound was carried out as for $Sn(N_3)_4$(bpy) (*vide supra*), except the crude product was extracted with 15 ml of MeCN at 40 °C. White crystals of $Sn(N_3)_4$(phen) (270 mg, 0.578 mmol) were obtained after recrystallization from MeCN in 44 % yield based on $Na_2[Sn(N_3)_6]$. Elem. anal. (%) for $C_{12}H_8N_{14}Sn$, 466.95 g mol^{-1}, calcd: C 30.87, H 1.73, N 41.98; found: C 31.07, H 1.45, N 41.92. DSC: melting T_{on} = 200 °C; decomposition T_{on}^{dec} = 301 °C, ΔH_{dec} = –934 kJ mol^{-1} (–2.00 kJ g^{-1}). FTIR (nujol) $\tilde{\nu}$ [cm^{-1}] = 2114s, 2096s, 2082s, 2068s, 1628vw, 1621w, 1610w, 1587 w, 1581w, 1573w, 1548w, 1519w, 1332m, 1275m, 1225w, 1147w, 1108w, 976w, 849w, 779 w, 717s, 653s, 594m; MeCN = 2112w, 2086vs, 1630w, 1612w, 1589vw, 1526sh; CH_2Cl_2: 2112m, 2085vs, 1630w, 1611w, 1588 vw, 1525sh. NMR (MeCN-d_3) δ(^{1}H) [ppm] = 8.34 (dd, 2*H*, H3,H8), 8.39 (s, 2*H*, H5,H6), 9.09 (dd, 2*H*, H4,H7), 9.42 (dd, 2*H*, H2,H9); coupling constants [Hz]: ^3J(H2,H3) = ^3J(H8,H9) = 5.1, ^4J(H2,H4) = ^4J(H7,H9) = 1.4, ^3J(H3,H4) = ^3J(H7,H8) = 8.3; δ (^{13}C) [ppm] = 127.7, 129.2, 131.2, 135.0, 144.7, 148.3.

6.3.5 Tetra(azido)bis(pyridine)tin(IV), $Sn(N_3)_4(py)_2$ (12)[85]

6.3.5a Preparation of $Sn(N_3)_4(py)_2$ (12) via SnF_4

SnF_4 (292 mg, 1.50 mmol) was suspended in pyridine (20 ml), and TMS–N_3 (710 mg, 6.16 mmol) was added dropwise to the suspension over approximately 1 minute under vigorous stirring. The Schlenk tube containing the off-white reaction mixture was fitted with a mercury bubbler to allow overpressure relief, immersed in an oil bath set to 45 °C, and the mixture stirred for 16 h during which time TMS–F (b.p. 15 °C) was driven off. The tube was then allowed to cool to RT. The supernatant liquid was decanted leaving 303 mg of white powder.

This residue was suspended in MeCN (25 ml) and warmed to 55 °C before as much pyridine was added dropwise until all material had dissolved. Slow cooling of this hot saturated solution to RT afforded colourless block crystals of $Sn(N_3)_4(py)_2$, from which the solvent was decanted, and the crystals dried in vacuo for 2 h. Yield 270 mg (40 % based on SnF_4). Elem. anal. (%) for $C_{10}H_8N_{14}Sn$, 444.99 g mol^{-1}, calcd: C 26.99, H 2.27, N 44.06; found: C 27.15, H 2.04, N 43.70. DSC: melting T_{on} = 265 °C; decomposition T_{on} = 305 °C, ΔH_{dec} = –775 ± 10 kJ mol^{-1} (–1.74 ± 0.02 MJ kg^{-1}). FTIR (nujol) $\tilde{\nu}$ [cm^{-1}] = 3405vw, 3347 w, 3114vw, 3104vw, 3076vw, 3054vw, 3034vw, 2600w, 2545vw, 2500vw, 2494vw, 2103sh, 2085vs, 1662vw, 1609m, 1571w, 1540vw, 1483s, 1450 vs, 1393vw, 1356vw, 1332s, 1280s, 1250 vw, 1209m, 1188vw, 1182vw, 1162m, 1144vw, 1094vw, 1063s, 1044s, 1015s, 1009vw, 877m, 782vw, 772vw, 760s, 705vw, 692s, 657m, 644s, 592m; pyridine: 2109m, 2081vs, 1610vw, 1560vw, 1540vw, 1488w, 1451 m, 1334m, 1283m, 1084 vw, 1046vw; MeCN: 2111m, 2083vs, 1612vw, 1335w, 1285m; CH_2Cl_2: 2107w, 2089s, 1613vw, 1327w. No reliable solution NMR data could be obtained due to the poor solubility of $Sn(N_3)_4(py)_2$. See section 6.3.5c for FTIR/NMR investigation of reaction of **12** with dimethylsulfoxide.

6.3.5b Attempted preparation of $Sn(N_3)_4(py)_2$ (12) via $Na_2[Sn(N_3)_6]$

A 5 ml aliquot of a stock solution of $Na_2[Sn(N_3)_6]$ (0.15 mol dm^{-3}, 0.75 mmol) was added to pyridine (1.006 g, 12.7 mmol, 17 eq.) under argon flow, resulting in some precipitation, and the turbid mixture was stirred overnight at RT before filtration, and extraction of the filter residue with 10 ml MeCN to prevent inadvertent isolation of $Na_2[Sn(N_3)_6]$. An FTIR spectrum of the insoluble residue showed primarily sodium azide, and the absence of any pyridine-containing species. The filtrate solution was concentrated to ca. 1 ml behind a blast shield, giving a turbid oil, from which around 20 mg of $Sn(N_3)_4(py)_2$ was isolated after extraction with 70 ml CH_2Cl_2. Extraction of the same residue with pyridine gave $Sn(N_3)_4(py)_2$ with a NaN_3 impurity, from which it was not possible to separate owing to their similarly low solubility in polar aprotic solvents. Preparation of $Sn(N_3)_4(py)_2$ by this method is therefore possible but impractical.

6.3.5c Reaction of $Sn(N_3)_4(py)_2$ (12) with dimethylsulfoxide: FTIR and multinuclear NMR spectra (^{1}H, ^{13}C, ^{14}N, and ^{119}Sn)

$Sn(N_3)_4(py)_2$ (20 mg, 0.045 mmol) was dissolved in 1.5 ml dimethylsulfoxide (in air) and a FTIR spectrum was recorded: $\tilde{\nu}$ [cm^{-1}] = 3342vw,br, 3077vw, 3055vw*, 2125w,br {HN_3}, 2107m, 2084m,sh, 2077s, 1598vw, 1582w, 1574vw,sh, 1484vw, 1343vw*, 1284w*, 1218vw, 1149vw. The weak absorption bands at 3077, 3055, 1598, 1582, 1574, 1484, 1218, and 1149 cm^{-1} correspond exactly to free pyridine in dimethylsulfoxide by comparison with a genuine sample. *These bands may be slightly distorted due to adjacent intense solvent absorptions. NMR (dmso-d_6) δ [ppm]: ^{1}H = 7.42 ppm (m,2H), J(^{1}H–^{13}C) = 164 Hz; 7.82 ppm (m,1H), J(^{1}H–^{13}C)= 166 Hz; 8.59 ppm (m, 2H), J(^{1}H–^{13}C) = 178 Hz; ^{13}C = 124.10, 136.68, 149.25; ^{14}N

= –67 (FWHM = 434 Hz, pyridine), –137.05 (FWHM = 98 Hz, –211.91, –214.20, –302.6 (FWHM = 885 Hz); ^{119}Sn = –603.34 (FWHM = 229 Hz), –607.44 (FWHM = 255 Hz). Peak at –607.44 ppm is around 5 times more intense than the –603.34 ppm.

6.3.6 Tetra(azido)bis(4-picoline)tin(IV), $Sn(N_3)_4(pic)_2$ (13)

TMS–N_3 (312 mg, 2.7 mmol) was added dropwise over 1 minute to a stirred suspension of SnF_4 (122 mg, 0.63 mmol) in 4 ml of dry 4-picoline at RT, and the mixture stirred overnight at RT in the glovebox. The resulting solution was evacuated almost to dryness, giving a pale orange paste, to which 15 ml of dry acetonitrile was added forming an off-white suspension. The suspension was warmed in a water bath until all virtually all material had dissolved at around 52 °C. Slow cooling of this solution to RT afforded a mixture of colourless block crystals and fine powder. A single crystal XRD study of these crystals showed the structure to be *trans*-$Sn(N_3)_4(pic)_2$ (**13**). The remaining crystals were re-dissolved by warming to 55 °C, and the solution filtered whilst warm to remove the insoluble material. Concentration of the filtrate solution and cooling to –19 °C overnight yielded a semi-crystalline pale orange solid. Yield 148 mg (50 % based on SnF_4). Elem. anal. (%) for $C_{12}H_{14}N_{14}Sn$, 472.99 g mol^{-1}, calcd: C 30.47, H 2.98, N 41.45; found: C 29.48, H 2.97, N 38.89. FTIR (nujol) $\tilde{\nu}$ [cm^{-1}] = 3420vw, 3397vw, 3367vw, 3351vw, 3333w, 3098vw, 3056vw, 2614w, 2588w, 2137sh, 2107s, 2088vs, 2073vs, 1952vw, 1914vw, 1687w, 1624m, 1614m, 1558vw, 1503m, 1456m, 1446sh, 1330m, 1276m, 1234w, 1213w,sh, 1206m, 1186vw, 1123m, 1103w, 1061m, 1032m, 989w, 969w, 874w, 816s, 717m, 667vw, 655s, 592s, 556s. The elemental analysis results suggest incomplete N_3/F exchange, showing that the reaction procedure must be carried out as for $Sn(N_3)_4(py)_2$, with heating to 45 °C (allowing overpressure relief), and using a slightly larger excess of TMS–N_3. Despite the incomplete N_3/F exchange in the bulk material, there is no obvious N_3/F disorder in the crystal selected for XRD analysis.

6.3.7 Reactions of Tin(IV) Halides with TMS–N_3 and NaN_3

6.3.7a Reaction of $SnCl_4$ with TMS–N_3 in benzene

TMS–N_3 (643 mg, 5.6 mmol, 5.8 eq.) was added dropwise to a solution of $SnCl_4$ (253 mg, 0.97 mmol) in 10 ml benzene with constant stirring, and gradually a white precipitate formed in the initially clear solution over the course of ½ h. The mixture was stirred for 16 h at RT. An FTIR spectrum of the solution showed only TMS–N_3, suggesting the precipitate must contain any tin azides formed during the reaction. This is consistent with the report of $SnCl_2(N_3)_2$ which was prepared similarly in CH_2Cl_2.[178]

6.3.7b Reaction of SnF_4 with TMS–N_3 in benzene

TMS–N_3 (970 mg, 8.43 mmol, 8.4 eq.) was added to a stirred suspension of SnF_4 (195 mg, 1.00 mmol) in 5 ml of dry benzene, and the pale grey mixture stirred at RT. After stirring for 4

h a FTIR spectrum of the solution showed only TMS–N_3 (3433vw,br, 3255vw,br, 2963m, 2901vw, 2139vs, 1329m,br, 1311m,br, 1267w,sh, 1257m) so the solution was stirred at 30 °C for 4 days, and increased to 40 °C for a further 3 days when still there were no visible changes in the appearance of the suspended solid. The solution was filtered off, and the solid dried under vacuum in a water bath at 30 °C for 1 h. Contact of a metal spatula on the white solid resulted in violent spontaneous decomposition with a loud, sharp report, also shattering the glass ampoule. This decomposition is consistent with a binary covalent azide such as $Sn(N_3)_4$ or $Sn(N_3)_xF_{(4-x)}$. This could mean that $Sn(N_3)_4$ is a solid, unlike its lighter homologues $C(N_3)_4$, $Si(N_3)_4$, and $Ge(N_3)_4$ which are highly sensitive colourless mobile liquids.[60,34,81] A FTIR spectrum was recorded of the white residue left on the canula head (unavoidably exposed to air for *ca.* 10 minutes): $\tilde{\nu}$ [cm^{-1}] = 3605vw,br, 3556vw,br, 3349w,br, 3170w,br, 2131m, 2120vw,sh, 2100s,br, 2030w,sh, 1342w, 1271vw, 1251vw, 1169m, 1150m, 966w, 938w, 919vw, 891w, 845w, 775w. The dominant features in the IR spectrum are the asymmetric azide stretches at 2131 (sharp) and 2100 cm^{-1} (broad). The broad feature could be $Sn(N_3)_4$ or $Sn(N_3)_xF_{(4-x)}$, possibly as an adduct with TMS–N_3 in a similar fashion as the TMS–Cl adduct of $SnCl_2(N_3)_2$ reported in the literature[178] during the reaction of $SnCl_4$ with TMS–N_3. The sharp feature could correspond to residual TMS–N_3, which may or may not be coordinated to tin.

6.3.7c Combined ^{1}H and ^{19}F Investigation into the Reactivity of SnF_4 with TMS–N_3 in C_6D_6

TMS–N_3 (27 mg, 0.23 mmol) was dissolved 1 ml C_6D_6 in an NMR tube equipped with a Young's greaseless stopcock. A ^{1}H NMR was recorded as a reference spectrum. SnF_4 (9 mg, 0.05 mmol) was added to the tube in the glovebox and a ^{1}H NMR recorded after 10 minutes showed no change. After 2½ h at RT without stirring, the ratio of TMS–N_3/TMS–F was 318 : 1, and when heated to 45 °C for 2 h the ratio was 60 : 1 corresponding to <2 % conversion assuming no loss of the volatile TMS–F (b.p. 15 °C). The tube was immersed in an oil bath to just above the level of solvent and held at 40 °C for 7 days, after which the conversion of TMS–N_3 (–0.08 ppm) to TMS–F (doublet, J = 7.4 Hz, 0.03 ppm) was around 95 % according to the ^{1}H NMR spectrum. There were traces of the hydrolysis product (hexamethyldisiloxane) at 0.12 ppm,[190] and diglyme throughout the experiment originating from the TMS–N_3. In the ^{19}F NMR spectrum TMS–F was visible at –157.1 ppm (vs. $CFCl_3$) with ^{29}Si satellites separated by 275 Hz as observed previously (N.B. TMS–F is 6.3 ppm vs. SiF_4, which is –163.3 vs. $CFCl_3$).[182] The C_6D_6 solution was carefully decanted from the tube, leaving an off white solid in a minimal amount of approximately 0.05–0.1 ml C_6D_6, to which 1 ml CD_3CN and 5–10mg of 2,2'-bipyridine were added, dissolving some of the solid. After warming to 40 °C briefly, ^{1}H and ^{19}F spectra were recorded, and the coordinated 2,2'-bipyridine protons acted as a sensitive probe to determine the nature of the (soluble) material. The ^{1}H NMR chemical

shifts of the 2,2'-bipyridyl protons suggested the presence of only $Sn(N_3)_4(bpy)$ (**10**) in appreciable concentration in solution at 8.08, 8.55, 8.72, and 9.12 ppm, but the ^{19}F spectrum suggested at least one fluorine-containing contaminant or side product in low concentration. The ^{19}F NMR in CD_3CN after addition of 2,2'-bipyridine shows peaks at –143.7, –151.8, –157.5 (multiplet, TMS–F), –167.9 with relative integrals 1.00 : 0.15 : 0.63 : 0.68. The peaks are in the region for tin(IV) fluoride adducts, for example the chemical shifts for $SnF_4(bpy)$ are –149.8 and –179.8 (triplets) due to the axial and equatorial environments.[183,184] If monofluorides were present the equatorial and axial fluoro isomers would have different chemical shifts. The multiplicity of the signals observed at –149.4 and –156.5 ppm suggests the corresponding species are monofluorides. The predominant formation of **10** in solution implies the presence of tin tetraazide in solution, but it cannot be proven beyond doubt as the benzene-d_6 solution was not completely decanted to avoid risks associated with its isolation.

6.3.7c Reaction of $SnCl_4(py)_2$ with TMS–N_3 in CH_2Cl_2

$SnCl_4(py)_2$ was prepared by slow addition of anhydrous pyridine to a solution of $SnCl_4$ in benzene, decantation of the solvent and drying the fine white precipitate in vacuo. $SnCl_4(py)_2$ (309 mg, 0.716 mmol) was added in portions to a solution of TMS–N_3 (371 mg, 3.22 mmol) in 20 ml of CH_2Cl_2. There was no change in the appearance of the solution after 48h stirring, or after heating to 50 °C for a further 5 days. The *in situ* FTIR spectra showed only TMS–N_3 in CH_2Cl_2 at 2142 cm^{-1}. An aliquot of the suspension was evaporated to dryness to give a white powder with an FTIR spectrum identical to $SnCl_4(py)_2$: FTIR (nujol) $\tilde{\nu}$ [cm^{-1}] = 3114vw, 3104vw, 3090vw, 3079vw, 2019vw, 1981vw, 1909vw, 1824vw, 1666vw, 1609m, 1600w,sh, 1572w, 1484m, 1450s, 1354vw, 1261vw, 1251vw,sh, 1207m, 1061s, 1042m, 1018m, 1011vw,sh, 801w,br, 756m, 684m, 649w,sh, 645m.

6.3.7d Reaction of $SnCl_4(py)_2$ with TMS–N_3 in pyridine

$SnCl_4(py)_2$ was prepared as above. TMS–N_3 (116 mg, 1.01 mmol) was added to a stirred suspension of $SnCl_4(py)_2$ (95 mg, 0.225 mmol) in 12 ml pyridine. The mixture was heated to 80 °C for 24 h, after which an FTIR spectrum of the solution showed an additional relatively weak absorption band at 2076 cm^{-1} which could be intermediate $SnCl_x(N_3)_{4-x}(py)_2$ complexes. The mixture was heated to 85 °C for a further 24 h, which showed no increase in the absorbance of the new azide species, so the mixture was discarded. Subsequent preparation of $Sn(N_3)_4(py)_2$ (**12**) showed it has low solubility in common solvents like the chloro-analogue, so it is possible the intermediate species are slightly more soluble and the solution was saturated and is not necessarily representative of the precipitate.

6.4 Tin(II) Azides

6.4.1 Diazidobis(pyridine)tin(II), $Sn(N_3)_2(py)_2$ (14)

6.4.1a Preparation of $Sn(N_3)_2(py)_2$ (14) via SnF_2

TMS–N_3 (442 mg, 3.84 mmol, 2.5 eq.) was added dropwise to a stirred suspension of SnF_2 (241 mg, 1.54 mmol) in 8 ml pyridine. The mixture became gradually clearer over ½ h, and was stirred at RT for 16h, before filtration of the slightly turbid solution. The clear filtrate solution was concentrated to 2 ml, crystalline precipitate was re-dissolved by warming to 35 °C in a water bath, and crystallisation from the pale yellow solution was achieved by cooling to –19 °C overnight. The solution was decanted, and the crystals of $Sn(N_3)_2(py)_2$ were dried in a stream of argon until the mass was constant (*ca.* 5 mins). Yield 363 mg (65 % based on SnF_2). Satisfactory elemental analyses could not be obtained due to rapid pyridine loss even at RT and sensitivity to moisture. FTIR (nujol) $\tilde{\nu}$ [cm^{-1}] = 3361w, 3315w, 3106vw, 3095w, 3072vw, 3058vw, 3035w, 3022w, 3000w, 2596w, 2066vs, 1945vw, 1869vw, 1640w, 1602s, 1573w, 1486m, 1448s, 1396w,br, 1360vw, 1324s, 1276s, 1247vw, 1216vw, 1194vw, 1157vw, 1064m, 1035, 1009, 755m, 700m, 652w, 645vw, 628m, 599w; pyridine: 2077s, 2057vs, 1325w,br, 1272vw,br. NMR (pyridine-d_5) δ [ppm] ^{1}H = solvent only: 7.22 (m, 2H), 7.59 (m, 1H), 8.74 (m, 2H); δ (^{13}C) [ppm] = 124.09 (t, C_5D_5N), 124.63 (s), 136.15 (t, C_5D_5N), 136.64 (s), 150.35 (t, C_5D_5N), 150.76 (s); δ(^{14}N) [ppm] = –62.92 (pyridine-d_5) FWHM = 363Hz, –258.71 (N_α) FWHM = 335 Hz, –135.1 (N_β) FWHM = 52 Hz; δ(^{119}Sn) [ppm] = –459.2 FWHM = 120 Hz. DSC melting T_{on} = 62.4(2) °C, decomposition T_{on} = 172(3) °C, ΔH_{dec} = –369(29) kJ mol^{-1}, –1.0(1) kJ g^{-1}.

N.B. drying under dynamic vacuum for > 1 h causes crepitation accompanied by disintegration of the crystals, giving $Sn(N_3)_2(py)_{(2-x)}$. Storing the solid in a sealed vial in the glovebox inhibits pyridine loss.

6.4.1b Preparation of $Sn(N_3)_2(py)_2$ (14) via reaction of $SnCl_2$ with NaN_3 in pyridine

$SnCl_2$ (365 mg, 1.92 mmol) was suspended in 15 ml of pyridine, and NaN_3 (2.601 g, 40 mmol, *ca.* 20 eq.), was added and the mixture stirred for 16 h at RT. A FTIR spectrum of the solution was recorded: $\tilde{\nu}$ [cm^{-1}] = 2076vw,sh, 2069vs, 2057w,sh, 1324m, 1272w. The suspension was filtered onto a second batch of NaN_3 (3.98 g, 61 mmol, *ca.* 30 eq.) and stirred for a further 16 h. A FTIR spectrum of a 30-fold diluted sample appears very similar to a genuine sample prepared via SnF_2 and TMS–N_3, except for a slight shoulder at 2068 cm^{-1} which could be due to a trace of $SnCl(N_3)(py)_2$ from incomplete N_3/Cl exchange. FTIR (pyridine) $\tilde{\nu}$ [cm^{-1}] = 2076s, 2069vw,sh, 2057vs, 1324m, 1273w. The isolation of **14** was carried out as for the above preparation in comparable yield.

6.4.2 Diazidobis(4-picoline)tin(II), $Sn(N_3)_2(pic)_2$ (15)

TMS–N_3 (294 mg, 2.55 mmol, *ca.* 2.5 eq.) was added dropwise over 1 minute to a stirred suspension of SnF_2 (162 mg, 1.03 mmol) in 5 ml of 4-picoline. The mixture was stirred for 16 h at RT, before a small amount of insoluble material was removed by filtration. The clear pale yellow filtrate solution was concentrated under vacuum until the onset of crystallisation, and cooled to –19 °C overnight giving $Sn(N_3)_2(pic)_2$ as colourless rod crystals. The pale yellow solution was decanted, and the crystals dried under dynamic vacuum until the mass remained constant (*ca.* ½ h). Yield 308 mg (77 % based on SnF_2). Elem. anal. (%) for $C_{12}H_{14}N_8Sn$, 389.01 g mol^{-1}, calcd: C 37.05, H 3.63, N 28.80; found: C 36.00, H 3.21, N 28.72. FTIR (nujol) $\tilde{\nu}$ [cm^{-1}] = 3400vw, 3380vw, 3349s, 3308m, 3291vw,sh, 3233vw, 3223vw, 3121w, 3078vw, 3060vw, 3047vw, 3027vw, 2743vw, 2678vw, 2662vw, 2646w, 2636vw,sh, 2597m, 2534w, 2493w, 2487w, 2433vw, 2419vw, 2400w, 2371vw, 2352vw, 2326vw, 2317vw, 2310vw, 2233w, 2226vw, 2183vw,sh, 2172vw,sh, 2063vs,br, 2041s, 1979w,sh, 1959w,sh, 1937w,sh, 1853w, 1770vw, 1687m, 1620vw, 1612s, 1560m, 1456w, 1321m, 1271m, 1243w, 1227m, 1216w, 1204m, 1118m, 1100m, 1067s, 1045m, 1014s ,1007s, 979m, 970w, 959w, 878m, 807vs,br, 667w, 649m, 641m, 604m, 537m, 526m, 518w; $Sn(N_3)_2(pic)_2$ in 4-picoline: 2076s, 2057vs, 1324w,br, 1273vw,br. NMR (pyridine-d_5) δ [ppm] ^{1}H = 2.12 (s, 6H) 7.04 (d, 4H) 8.62 (dd, 4H); δ (^{13}C) [ppm] = 21.13 (s), 125.51 (s), 147.69 (s), 150.47 (s); δ(^{14}N) [ppm] = –62.62 (pyridine-d_5) FWHM = 292 Hz, 135.2 (N_β) FWHM = 49 Hz, –260.4 (N_α) FWHM = 280 Hz; δ(^{119}Sn) [ppm] = –458.74. DSC melting T_{on} = 99.9(5) °C, decomposition T_{on} = 180(3) °C, ΔH_{dec} = –416(17) kJ mol^{-1}, –1.07(4) kJ g^{-1}.

6.4.3 Tin(II) Azide, $Sn(N_3)_2$ (16)

6.4.3a Safety Precautions for Handling of $Sn(N_3)_2$ (16)

Tin(II) azide is highly explosive, very sensitive to impact and friction, and extremely sensitive to electrostatic discharge. Appropriate additional personal protective equipment (PPE) must be worn during manipulations, including full face-shield, Kevlar gloves, and anti-static wristband. The use of Teflon coated spatulas is recommended for transferal of material between vessels.

6.4.3b Preparation of $Sn(N_3)_2$ (16) from $Sn(N_3)_2(py)_2$ (14)

Dry MeCN (10 ml) was added to $Sn(N_3)_2(py)_2$ (118 mg, 0.33 mmol) forming a fine white suspension, which was stirred vigorously for 2 h. The solution was decanted, and the off-white solid dried under vacuum for 1 h at RT. FTIR (nujol) $\tilde{\nu}$ [cm^{-1}] = 3380vw, 3325vw, 2613vw, 2593vw, 2554vw, 2536vw, 2107sh, 2090sh, 2070vs, 1339m, 1333m, 1286m, 1276m, 1184vw, 1177vw, 659m, 594w, 591w.

6.4.4 Reaction of $SnCl_2$ with NaN_3 in THF

NaN_3 (2.617 g, 40.3 mmol) was added to a clear solution of $SnCl_2$ (381 mg, 2.01 mmol) in 20 ml THF, and the suspension stirred for 16 h at RT. Filtration of the solution afforded a clear colourless solution, of which a FTIR spectrum was recorded: $\tilde{\nu}$ [cm^{-1}] = 3356vw, 2083s, 2061vs,br, 2053sh, 1323m, 1278w. The absorption band position at 2061 cm^{-1} is consistent with $[Sn(N_3)Cl_2]^-$ [92] suggesting that the reaction of $SnCl_2$ with NaN_3 is initially fast, but the rate of subsequent Cl/N_3 exchange processes are slower and require reaction with a second batch of NaN_3. It may mean that preparation of sodium triazidostannate directly via $SnCl_2$ is inefficient, and may form more readily from NaN_3 and $Sn(N_3)_2$. N.B. assignment of the asymmetric azide stretches to $(Na)Sn(N_3)_x$ rather than $Sn(N_3)_2$ is partly based on the insolubility of the latter in THF, though $SnCl_2$ is soluble so the intermediate $SnCl(N_3)$ may or may not be soluble.

6.4.5 Reaction of $SnCl_2$ with TMS–N_3 – formation of $SnCl(N_3)(py)_2$?

TMS–N_3 (770 mg, 6.7 mmol) was added dropwise to a stirred suspension of $SnCl_2$ (550 mg, 2.9 mmol) in 5 ml dry pyridine, and a FTIR spectrum was recorded after stirring at RT for 2 h. The high concentration of TMS–N_3 (A >>3) suggests the Cl/N_3 exchange is far from completion. A new absorption band is visible at 2068 cm^{-1}, which is halfway between the two absorption bands for $Sn(N_3)_2(py)_2$ in pyridine (2076 and 2056 cm^{-1}, see section 6.4.1), which could indicate the presence of $SnCl(N_3)(py)_2$. After heating the reaction to 80 °C for 24 h, the absorbance of the band at 2068 cm^{-1} was reduced from 1.95 to 1.09 but otherwise the spectrum was unchanged. The relatively high concentration of TMS–N_3 could be explained if only one azide is exchanged. The higher boiling point of TMS–Cl compared to TMS–F (59 °C vs 15 °C) coupled with the higher bond dissociation enthalpy of Si–F compared to Si–Cl means the reaction rate is likely to be significantly slower.

6.4.6 Guanidinium tri(azido)stannate(II), $(C(NH_2)_3)[Sn(N_3)_3]$ (17)

6.4.6a Direct preparation of 17 via SnF_2 with TMS–N_3 and guanidinium azide

TMS–N_3 (315 mg, 2.74 mmol) was added dropwise over 1 minute to a stirred suspension of SnF_2 (328 mg, 2.09 mmol), and guanidinium azide (236 mg, 2.31 mmol) in 15 ml CH_3CN. The mixture was stirred for 1½ h giving a white suspension, which was filtered and the residue extracted with 20 ml CH_3CN. The combined filtrate solution was concentrated to *ca*. 5 mL, and cooled to –19 °C overnight. The solution was decanted from the white microcrystalline whilst cold, and the solid dried under vacuum in a water bath at *ca*. 45 °C for 10 minutes. Yield: 368 mg (58 %). FTIR (nujol) $\tilde{\nu}$ [cm^{-1}] = 3460wsh, 3434sbr, 3405vsbr, 3337wsh, 3237sbr, 3168vsbr, 2071wsh, 2060vsbr, 2034sbr, 1659vsbr, 1332m, 1283m, 1262wsh, 1009vw, 654m, 600w; CH_3CN: 3457mbr, 3367mbr, 3282mbr, 3215mbr, 2086s, 2056vs, 1670m, 1323wbr, 1275vwbr; THF: 3350m,br, 3172m,br, 2081s, 2055vs, 1668m, 1582vw,

1321w, 1279w. NMR (400 MHz, CD_3CN) δ [ppm]: ^{1}H = 6.11; ^{13}C = 159.0; ^{14}N = –217.1, –260.1 ppm; ^{119}Sn = –284.8 ppm.

6.4.6b Preparation of 17 via $Sn(N_3)_2$ (16)

$Sn(N_3)_2$ (60 mg, 0.3 mmol) was prepared by stirring $Sn(N_3)_2(py)_2$ (101 mg, 0.36 mmol) in 15 ml dry MeCN for 30 minutes and decantation of the solvent. Guanidinium azide (38 mg, 0.37 mmol) was added followed by 20 ml of MeCN to give a suspension which gradually became clear over 20 minutes. The solution was stirred for a total of 2 h at RT before a FTIR spectrum of the solution was recorded, which confirmed the presence of guanidinium triazidostannate (see section 6.4.6a above), which was crystallised by cooling the solution to –19 °C overnight after concentration to *ca.* 1 ml.

6.4.7 Attempted preparation of aminoguanidinium triazidostannate (18)

$TMS–N_3$ (147 mg, 1.28 mmol) was added dropwise to a suspension of SnF_2 (85 mg, 0.54 mmol) and aminoguanidinium azide (**2**, 75 mg, 0.64 mmol) in 5 ml MeCN, and the mixture stirred for 3 h at RT. An FTIR spectrum of the solution showed the presence of $[Sn(N_3)_3]^-$ by the symmetric azide stretching vibrations: $\tilde{\nu}$ [cm^{-1}] = 3453m,br, 3362s,br, 3332w,sh, 3286m,br, 2085s,br*, 2049vs,br*, 1670s, 1595vw, 1323m,br, 1275vw,br, 1202vw,br; *high concentration of solution meant the band shape (and peak maxima) of these bands was not reliable (A_{max} > 2.5). A trace of HN_3 was visible at 2139 cm^{-1}, along with a trace of the tin(IV) oxidation product $(AG)_2[Sn(N_3)_6]$ (**4**) at 2112, 1287 cm^{-1} and TMS–X (F/N_3) = 1268 and 1258 cm^{-1}. The small amount of excess **2** was filtered off, and the filtrate concentrated until the onset of crystallisation, and cooled to –19 °C overnight. A white microcrystalline solid precipitated from solution, from which the solution was decanted and the solid dried in vacuo for ½ h. An FTIR spectrum of the solid was recorded: $\tilde{\nu}$ [cm^{-1}] = 3438m, 3382br,sh, 3360m, 3333w,sh, 3295m,br, 3242m,br, 3198m, 3164m, 3078vw,sh, 2670vw, 2615w, 2546vw, 2104w,sharp, 2074vw,sh, 2055br,sh, 2045vs,br, 1998vw,sh, 1666s,br, 1634m, 1585w, 1550w, 1426w, 1331s, 1282s, 1262vw,sh, 1210w, 1194vw, 1065vw,br, 1017vw, 888m, 650m, 629w, 609w, 534w,br. The broad nature of the asymmetric azide stretch absorption bands and a comparison with a genuine spectrum of **17** suggested the microcrystalline solid was **18** with a trace of **2**, which could have been due to slight decomposition or excess starting material.

6.4.8 Attempted preparation of SnF_2 urea adduct

SnF_2 (70 mg, 0.45 mmol) and sublimed urea (60 mg, 1.0 mmol) were suspended in 10 ml dry MeCN and stirred for 16 h at RT. A FTIR spectrum showed no indication of coordinated urea by comparison with a genuine sample of free urea. All solvent was removed and the solid residue dried under vacuum for 3 h, which showed only urea in the FTIR spectrum (nujol suspension).

6.5 Tris-2,4,6-tetrazol-1-yl-1,3,5-triazine (TTT) (20)

6.5.1 Reaction of cyanuric chloride with 1*H*-tetrazole and $NaHCO_3$ in acetone/water[133] – preparation of sodium bis(2,4-tetrazol-1-yl)-1,3,5-triazinon-6-ate DMF solvate (21)

Initial small scale reaction

1*H*-tetrazole (103 mg, 1.47 mmol) and cyanuric chloride (78 mg, 0.42 mmol) were dissolved in a mixture of 5 ml acetone and 1 ml water, and $NaHCO_3$ (120 mg, 1.43 mmol) was added and the mixture refluxed for ½ h. The mixture was clear initially, and during heating a white precipitate formed. The mixture was poured into a large excess of cold water (*ca*. 200 ml), and filtered through a no 4 sinter. The filter residue was washed with ethanol and dried under vacuum, leaving 39 mg of off-white solid (assuming composition is sodium 2,4-bis(tetrazol-1-yl)-1,3,5-triazinon-6-ate, $C_5H_2N_{11}ONa$: 0.153 mmol, 36 %). FTIR (nujol) $\tilde{\nu}$ [cm^{-1}] = 3631w, 3598w, 3484m,br, 3402m,br, 3274m,br, 3167m, 3148m, 3134m, 3114m, 1672m, 1620m, 1535w, 1504m, 1467vs, 1442m, 1354vw, 1336vw, 1298w, 1263m, 1207vw, 1198vw, 1190vw, 1180m, 1127vw, 1116w, 1083m, 1019vw, 996m, 942w, 891w, 820m, 808m, 750vw, 713vw, 671vw, 645w, 551m,br. NMR (dmso-d_6) δ [ppm]: ^{1}H = 3.37 (s, water), 9.26 (s, unknown impurity, <1.7 % area of main peak), 10.18 (s, $J_{C–H}$ = 39.9 Hz); ^{13}C{^{1}H}: δ = 143.12 (C–N_4<u>C</u>H), 160.34 (<u>C</u>–N_4CH), 165.82 (<u>C</u>–O).

Scaled-up attempted preparation of 20, and subsequent crystallisation of 21

1*H*-Tetrazole (872 mg, 12.4 mmol) and cyanuric chloride (717 mg, 3.89 mmol) were dissolved in a mixture of 10 ml acetone and 1 ml water, and $NaHCO_3$ (1.107 g, 13.2 mmol) was added in portions resulting in a thick suspension, to which 5 ml acetone was added and the mixture refluxed for ½ h. After filtration through a no 4 sinter, the residue was washed with boiling ethanol and dried under vacuum leaving 72 mg (*ca*. 6 % assuming composition is **21**) of off-white powder, which was insoluble in THF, CH_2Cl_2, MeCN, toluene, pyridine, hexane, and isopropanol. The powder eventually dissolved after warming in dimethylsulfoxide, and in hot *N*,*N*-dimethylformamide (80 °C). When a small sample was subjected to a flame the result was a 'pop', which also happened around 150 °C during melting point determination. The powder was dissolved in a minimum amount of hot *N*,*N*-dimethylformamide, and the clear solution cooled from 80 °C to RT, affording colourless block crystals of **21**, which were investigated by single crystal XRD. The quality of the diffraction data was sufficient to show the structure consisted of sodium 2,4-bis(tetrazol-1-yl)-1,3,5-triazinon-6-ate with one equivalent of *N*,*N*-dimethylformamide. The crystals were washed with dry Et_2O at –15 °C and left to dry in air. Elem. anal. (%) for $C_8H_9N_{12}NaO_2$, 328.23 g mol^{-1}, calcd: C 29.28; H, 2.76; N, 51.20; found: C 29.15; H, 2.48; N 50.25. NMR (dmso-d_6) δ [ppm]: ^{1}H = 2.73 (s, 3*H* (DMF)), 2.89 (s, 3*H* (DMF)), 3.37 (s, water), 7.95 (s, 1*H* (DMF)), 9.26 (s, unknown impurity, <1.7 % area of main peak), 10.17 (s, 2*H*); ^{13}C (dmso-d_6,

RT, ppm): δ = 30.79 (DMF), 35.81 (DMF), 143.12 (C–N_4<u>C</u>H), 160.33 (<u>C</u>–N_4CH), 162.33 (DMF), 165.82 (<u>C</u>–O).

6.5.2 Reaction of cyanuric chloride with 1*H*-tetrazole and $NaHCO_3$ in MeCN[134]

1*H*-tetrazole (104 mg, 1.48 mmol) and $NaHCO_3$ (120 mg, 1.43 mmol) were suspended in 15 ml acetonitrile and stirred at RT for 30 minutes. Cyanuric chloride (90 mg, 0.49 mmol) was added, and the suspension stirred for 90 minutes, before heating to 70 °C for 16 h forming a yellow precipitate. Water (25 ml) was added to the mixture, before filtration through a no. 4 sinter and the residue washed with 10 ml ethanol, leaving a clumped yellow powder (71 mg). An FTIR spectrum was recorded of the pale yellow solid: $\tilde{\nu}$ [cm^{-1}] = 3109m, 2195m, 1697m, 1586s, 1472s, 1453s, 1294m, 1198m, 1084w,sh, 1066m, 980m, 923w, 915m, 836vw, 813m, 708vw, 649m, 565w,br. Only one tetrazolyl C–H peak was discernible at 3109 cm^{-1} suggesting the presence of only one type of tetrazole compound.

6.5.3 Reaction of cyanuric chloride with 1*H*-tetrazole in THF using $NaHCO_3$ as base

1*H*-tetrazole (907 mg, 12.94 mmol) and cyanuric chloride (718 mg, 3.89 mmol) were dissolved in 25 ml THF giving a slightly turbid solution. To this solution $NaHCO_3$ (1.112 g, 13.2 mmol) was added in portions over several minutes and stirred at RT for 10 minutes. The mixture was warmed to 50 °C in a water bath, causing precipitation of a bright yellow solid. The suspension was allowed to cool, then the solution was filtered off, and a FTIR spectrum of the residue seemed to show $NaHCO_3$. The filtrate solution was evaporated to dryness to give an inhomogeneous yellow solid. An FTIR spectrum of the evaporation residue was recorded: $\tilde{\nu}$ [cm^{-1}] = 3153 ($\nu_{tetrazole}$(CH)), 1503, 1296vw, 1262vw. The filter residue was recombined with the evaporation residue in 15 ml wet THF, and warmed to 45°C for 20 minutes. Water (3 ml) was added to the solution and after 20 minutes stirring the solution was orange and most of the solid dissolved. The solution was filtered off, and the residue washed with 10 ml THF, and then dried under vacuum. IR (nujol) $\tilde{\nu}$ [cm^{-1}] = 1637br, 1503w, 1300vw, 1288vw, 1259w. The filtrate solution was evaporated to dryness on rotary evaporator, leaving a yellow solid. An FTIR spectrum of this solid was recorded: $\tilde{\nu}$ [cm^{-1}] = 3151vw, 3114vw, 2331w, 2186m, 1615m, br, 1501w, 1208w, 1178w, 1160w, 1083m, 1067vw, 1021w, 996m, 904vw, 890vw, 819w, 810w, 787vw, 704vw, 647vw, 553w,br.

6.5.4 Reaction of cyanuric chloride with 1*H*-tetrazole in THF using 2,6-lutidine (2,6-dimethylpyridine) as base

2,6-lutidine (1.2 ml, ρ = 0.92 g cm^{-3}, 10 mmol) was added dropwise to a suspension of 1*H*-tetrazole (238 mg, 3.40 mmol) and cyanuric chloride (172 mg, 0.93 mmol) in 10 ml dry THF. This produced a dark yellow precipitate, which turned light orange within 5 minutes. The solution was decanted via filter canula, and the filter residue was washed with acetone (2 × 5 ml) to produce a peach/brown coloured solid (363 mg). FTIR spectrum of the solid was

recorded: $\tilde{\nu}$ [cm^{-1}] = 3273w, 3179vw,br, 3113m, 3086m, 2718w, 2687vw,sh, 2662w,br, 2635w,br, 2457s,br, 2168w, 2126w, 2047m, 1990m, 1937w, 1866vw, 1812vw, 1706w, 1698w, 1640s, 1621m, 1587s,br, 1580vw,sh, 1549w, 1539w, 1521vw, 1501vw, 1407w, 1347vw, 1320vw, 1287m, 1280vw,sh, 1275m, 1262vw, 1253m, 1202vw,sh, 1194m, 1183w, 1166m, 1146vw, 1092vw, 1073m, 1057w,sh, 1027vw, 1012vw, 994vw,sh, 987vw,sh, 982m, 930w, 922w, 816m, 800m, 707vw, 648m, 631vw, 557m, 544vw, 534vw. The rapid change to a brightly coloured solution was initially assumed to be reaction of 2,6-lutidine with cyanuric chloride to give highly electronically delocalised (R-pyridyl)triazinium chlorides as observed for less sterically hindered pyridines,[222] but careful inspection of the spectroscopic data showed no evidence of this reactivity and confirmed suitably of 2,6-lutidine for this role. The broad feature at 2450 cm^{-1} was assigned to the hydrogen bonded ν(N–H···Cl) in 2,6-lutidinium chloride as observed previously.[244] ^{1}H and ^{13}C NMR spectra of the solid were recorded in dmso-d_6, and seemed to show a 1 : 2.4 : 10 : 1.8 mixture of 2-chloro-4,6-bis(tetrazol-1-yl)-1,3,5-triazine, 2,4,6-tris(tetrazol-1-yl)-1,3,5-triazine (**20**), 2,6-lutidinium chloride, and 1*H*–tetrazole. The most intense peaks in the ^{13}C NMR at δ [ppm] = 18.81, 124.81, 145.41, 152.94 are a close match for the 2,6-lutidinium triflate in the same solvent: δ(^{13}C) [ppm] = 19.04, 124.57, 145.56, 152.91.[224] By comparison with the NMR spectrum of **21**, which shows the triazine carbon resonances between 160–166 ppm, it is reasonable to suggest there are two (tetrazolyl)triazine species giving a total of 3 environments with peaks at 160.62, 161.85, and 168.22 (N.B. reference spectrum of cyanuric chloride in dmso-d_6 is not available as a reaction occurs, giving a dimethylsulfide as a by-product (strong, pungent smell). The absence of a peak in the region 149–151 ppm seems to suggest the absence of any ionic tetrazolate salts (such as 2,6-lutidinium tetrazolate) by comparison with a range of tetrazolate salts in ref. [152].

6.5.5 Reaction of cyanuric chloride with 1*H*-tetrazole in anhydrous THF using diisopropylethylamine (DIPEA) as base (adapted from refs. [214,215])

Diisopropylethylamine ("DIPEA", 0.9 ml, ρ = 0.742 g cm^{-3}, 5.17 mmol) was added dropwise to a mixture of 1*H*-tetrazole (96 mg, 1.37 mmol) and cyanuric chloride (88 mg, 0.48 mmol) in 15 ml dry THF. An off white solid precipitated rapidly during addition, and after two hours the solution was pale yellow with an off white precipitate. After 16 hours the solution was pale orange with a white solid which settled quickly upon standing. The solution was filtered off and a FTIR spectrum recorded of the filter residue: FTIR (nujol) $\tilde{\nu}$ [cm^{-1}]= 3148m, 3117m, 3104m, 2600–2400m,br, 1636w, 1626vw, 1611m, 1587w, 1562w, 1521s, 1456m, 1444w, 1435w, 1422w, 1394s, 1359m, 1349vw, 1341vw, 1334vw, 1295m, 1280m, 1255s, 1215m, 1203w, 1197vw, 1185w, 1160m, 1132m, 1102w, 1087w, 1078s, 1025m, 1005m, 984s, 957m, 933vw, 927sh, 912w, 896vw, 881vw, 848vw, 824m, 817s, 786sh, 780m, 760vw, 751vw, 709vw, 675s, 646s, 636vw, 582s. The residue was washed with 10 ml water and dried under

vacuum leaving a yellow solid (20 mg) with a very similar FTIR spectrum except with a greatly reduced intensity broad NH stretch between 2400–2600 cm^{-1}, and absence of bands at 1184, 1026, 848, 780, and 582 cm^{-1}, which may be partial removal of DIPEA·HCl by-product. Solubility of small samples of the solid was tested in MeCN, CH_2Cl_2, THF, toluene, Et_2O, DMF, and pyridine. Only *N*,*N*-dimethylformamide and dimethylsulfoxide showed any dissolution (apart from hot pyridine, which seemed to react, as it gave a colour change). Crystallisation was attempted from warm DMF but was unsuccessful. After removal of DMF under vacuum, ^{1}H and ^{13}C NMR spectra were recorded: ^{1}H (dmso-d_6) δ [ppm] = 1.27, 9.42 s (tetrazole C<u>H</u>), 10.18, 10.38; ^{13}C (dmso-d_6) δ [ppm] = 12.37, 16.71, 18.03, 53.48, 143.08, 143.77, 160.65, 162.32, 169.29. The spectra suggest a 1 : 1 : 6 ratio of **20**, diisopropylethylammonium chloride (DIPEA·HCl),[227] and residual DMF.[190]

6.5.6 Reaction of cyanuric chloride with sodium tetrazolate in H_2O(/acetone)

A solution of cyanuric chloride (164mg, 0.89 mmol) in 4 ml acetone was added dropwise over approximately 15 minutes to a stirred solution of sodium tetrazolate (282mg, 3.06 mmol) in 6 ml de-ionised water. The initially very fine suspension slowly thickened until the consistency became a thick paste. The solvent was decanted (filtration was very slow) and the residue washed with 3 ml water. FTIR (nujol) $\tilde{\nu}$ [cm^{-1}] = 3633m, 3600m, 3500–3200m,br, 3165m, 3134s, 1675m, 1625m, 1590s, 1501m, 1441s, 1283s, 1267m, 1115w. This material decomposed with loud report when subjected to a small scale flame test (<5 mg). The residue was insoluble in most solvents, with the exceptions of *N*,*N*-dimethylformamide, and (hot) pyridine which seemed to react. Unfortunately, even after several attempts the yield was unacceptably poor so no NMR data were recorded. The FTIR spectrum of the residue contained all peaks belonging to sodium 2,4-bis(tetrazol-1-yl)-1,3,5-triazinon-6-ate (**21**): FTIR (nujol) $\tilde{\nu}$ [cm^{-1}] = 3631w, 3598w, 3484m,br, 3402m,br, 3274m,br, 3167m, 3148m, 3134m, **3113m**, 1672m, 1620m, 1535w, 1504m, **1467vs**, **1442m**, 1354vw, 1336vw, 1298w, 1263m, 1207vw, 1198vw, 1190vw, 1180m, 1127vw, 1116w, 1083m, 1019vw, 996m, 942w, 891w, 820m, 808m, 750vw, 713vw, 671vw, 645w, 551m,br.

An additional set of peaks were also visible: FTIR (nujol) $\tilde{\nu}$ [cm^{-1}] = **1637m**, **1590s**, 1456s, 1194w, 1161m, 1145vw, 1069s, 986m, 980m, 930w, 918w, 840vw, 816w, 630w.

These additional absorption bands are present in each of the product mixtures obtained by various synthetic efforts described in this section, and thus could form part of the IR fingerprint of **20**. The peaks highlighted in bold are consistent with the limited IR spectroscopic data available in the literature. Vereschagin *et al*. reported a single frequency at 1636 cm^{-1},[133] and in their patent Ganta *et al*. report IR absorption bands at 1444 and 1473 cm^{-1} for the triazine ring vibrations, and 3110 cm^{-1} (tetrazolyl C–H stretch) and 1588 cm^{-1} for the tetrazolyl moiety.[134]

6.5.7 Reaction of cyanuric chloride with sodium tetrazolate in anhydrous THF

Sodium tetrazolate (550 mg, 5.98 mmol) and cyanuric chloride (363 mg, 1.97 mmol) were suspended in 20 ml THF, and the mixture was stirred for 72 h. Approximately ¾ of the solution was decanted from the extremely fine off-white suspension (very slow filtration, eventually stopped altogether) before the remaining 5 ml was removed under vacuum at RT, and an FTIR spectrum of the pale yellow residue (377 mg) was recorded. The spectrum appeared almost identical to **21** (see 6.5.1 above), with additional peaks at $\tilde{\nu}$ [cm^{-1}] = 2200m,br, 1770w,br, 1711m, 1590w, 1066vw, 539w. This suggests the main IR-active species in the THF-insoluble material is sodium 2,4-bis(tetrazol-1-yl)-1,3,5-triazinon-6-ate (**21**) with perhaps a trace of **20** and almost certainly residual NaCl. After washing the pale yellow solid with 20 ml MeOH, decantation, and drying of the residue under vacuum (6×10^{-2} mbar) left <20 mg of insoluble solid which was analysed by FTIR: (nujol) $\tilde{\nu}$ [cm^{-1}] = 3109m,sharp, 2385vw, 2339vw, 2265vw, 2202vw, 2108vw, 1698w, 1669vw, 1624w,sh, 1588vs, 1544vw, 1531vw, 1473vs, 1455s, 1339vw, 1294s, 1281m, 1261m, 1197s, 1148vw, 1095w,br, 1065s, 1020w,br, 978vs, 958w,sh, 922w, 914m, 813vs, 796w,br, 708w,sharp, 650m,sharp.

6.5.8 Reaction of cyanuric acid with 1*H*-tetrazole in ethanol

1*H*-Tetrazole (114 mg, 1.63 mmol) was added in portions over a period of 5 minutes to a suspension of cyanuric acid (69 mg, 0.53 mmol) in 10 ml EtOH. No changes were visible after 1 h at RT, so the mixture was refluxed for 72 h. The solution was filtered off and the solid dried under vacuum, which was exclusively cyanuric acid according to the FTIR spectrum.

7. Appendix

7.1 NMR Spectra

7.1.1a Guanidinium Azide (1) in D_2O

^{1}H NMR spectrum

7.1.1b Guanidinium Azide (1) in dmso-d_6

^{1}H NMR spectrum

^{13}C NMR spectrum

^{14}N NMR spectrum

7.1.2 Guanidinium Azide Monohydrate (1a) in dmso-d_6

^{1}H NMR spectrum

^{14}N NMR spectrum

7.1.3 Aminoguanidinium Azide (2) in dmso-d_6

^{1}H NMR spectrum

^{13}C NMR spectrum

^{14}N NMR spectrum

7.1.4 Bis(guanidinium) Hexaazidostannate (3) in CD_3CN

^{1}H NMR spectrum

^{13}C NMR spectrum

^{14}N NMR spectrum

^{119}Sn NMR spectrum

7.1.5 $(PPN)_2Sn(N_3)_6$ (9) in CD_3CN

^{1}H NMR spectrum

^{13}C NMR spectrum

^{14}N NMR spectrum

^{31}P NMR spectrum

7.1.6a Tetraazido(2,2'-bipyridine)tin, $Sn(N_3)_4(bpy)$ (10) in CD_3CN

^{1}H NMR spectrum

^{13}C NMR spectrum

7.1.6b Tetraazido(2,2'-bipyridine)tin, $Sn(N_3)_4(bpy)$ (10) in CD_2Cl_2

^{1}H NMR spectrum

7.1.7 Tetraazido(1,10-phenanthroline)tin, $Sn(N_3)_4(phen)$ (11) in CD_3CN

^{1}H NMR spectrum

7.1.8 Tetraazidobis(pyridine)tin, $Sn(N_3)_4(py)_2$ (12) in dmso-d_6

^{1}H NMR spectrum

^{13}C NMR spectrum

^{14}N NMR spectrum

^{119}Sn NMR spectrum

7.1.9 Reaction of SnF_4 with TMS-N_3 (in C_6D_6), and assessment of F/N_3 exchange progress *via* chelation of $Sn(N_3)_xF_{(4-x)}$ with 2,2'-bipyridine in CD_3CN

^{19}F NMR spectrum

^{1}H NMR spectrum

7.1.10 Diazidobis(pyridine)tin, $Sn(N_3)_2(py)_2$ (14) in pyridine-d_5

^{1}H NMR spectrum

^{1}H NMR spectrum (expanded view)

^{13}C NMR spectrum

^{14}N NMR spectrum

^{119}Sn NMR spectrum

7.1.11 Diazidobis(4-picoline)tin, $Sn(N_3)_2(pic)_2$ (15) in pyridine-d_5

^{1}H NMR spectrum

^{13}C NMR spectrum

^{14}N NMR spectrum

^{119}Sn NMR spectrum

7.1.12 Guanidinium Triazidostannate (17) in CD_3CN

^{1}H NMR spectrum

^{13}C NMR spectrum

^{14}N NMR spectrum

^{119}Sn NMR spectrum

7.2 FTIR Spectra

7.2.1 Guanidinium Azide (1)

IR spectrum (nujol suspension)

IR spectrum in MeCN solution

7.2.2 Guanidinium azide monohydrate (1a)

IR spectrum (nujol suspension)

7.2.3 Aminoguanidinium azide (2)

IR spectrum (nujol suspension)

7.2.4 Bis(guanidinium) hexaazidostannate (3)

IR spectrum (nujol suspension)

IR spectrum in MeCN solution

7.2.5 Tetraazidobis(4-picoline)tin(IV) (13)

IR spectrum (nujol suspension)

IR spectrum in 4-picoline solution

7.2.6 Diazidobis(pyridine)tin(II) (14)

IR spectrum in pyridine solution

IR spectrum (nujol suspension)

7.2.7 Diazidobis(4-picoline)tin(II) (15)

IR spectrum in 4-picoline solution

IR spectrum (nujol suspension)

7.2.8 Guanidinium triazidostannate (17)

IR spectra in MeCN solution and THF solution

IR spectrum (nujol suspension)

7.2.9 Guanidinium tetrazolate (19)

IR spectrum (nujol suspension)

7.3 DSC thermograms and TGA traces

7.3.1 Guanidinium Tetrazolate (**19**) DSC

7.3.2 Tetraazido(2,2'-bipyridine)tin (**10**) DSC

7.3.3 Tetraazido(1,10-phenanthroline)tin (**11**) DSC

7.4 X-Ray Crystallography

7.4.1 Guanidinium Azide (**1**) – ch1ppx192

7.4.2 Guanidinium Azide Monohydrate (**1a**) – ch1ppx175

7.4.3a Aminoguanidinium Azide (**2**) at T = 100 K – ch1ppx183

7.4.3b Aminoguanidinium Azide (**2**) at T = 150 K – ch1ppx190

7.4.4 Bis(guanidinium) hexaazidostannate (**3**) – ch1ppx182

7.4.5 Sodium guanidinium azide (**5b**) – ch1ppx210

7.4.6 $P(=O)(N_3)_2(NC(NH_2)_2)$ (**8**) – ch1ppx197

7.4.7 Guanidinium Tetrazolate (**19**) – ch1ppx205

7.5 Graph Set Matrices for Hydrogen Bond Networks

7.1 NMR Spectra

7.1.1 Guanidinium Azide in D_2O

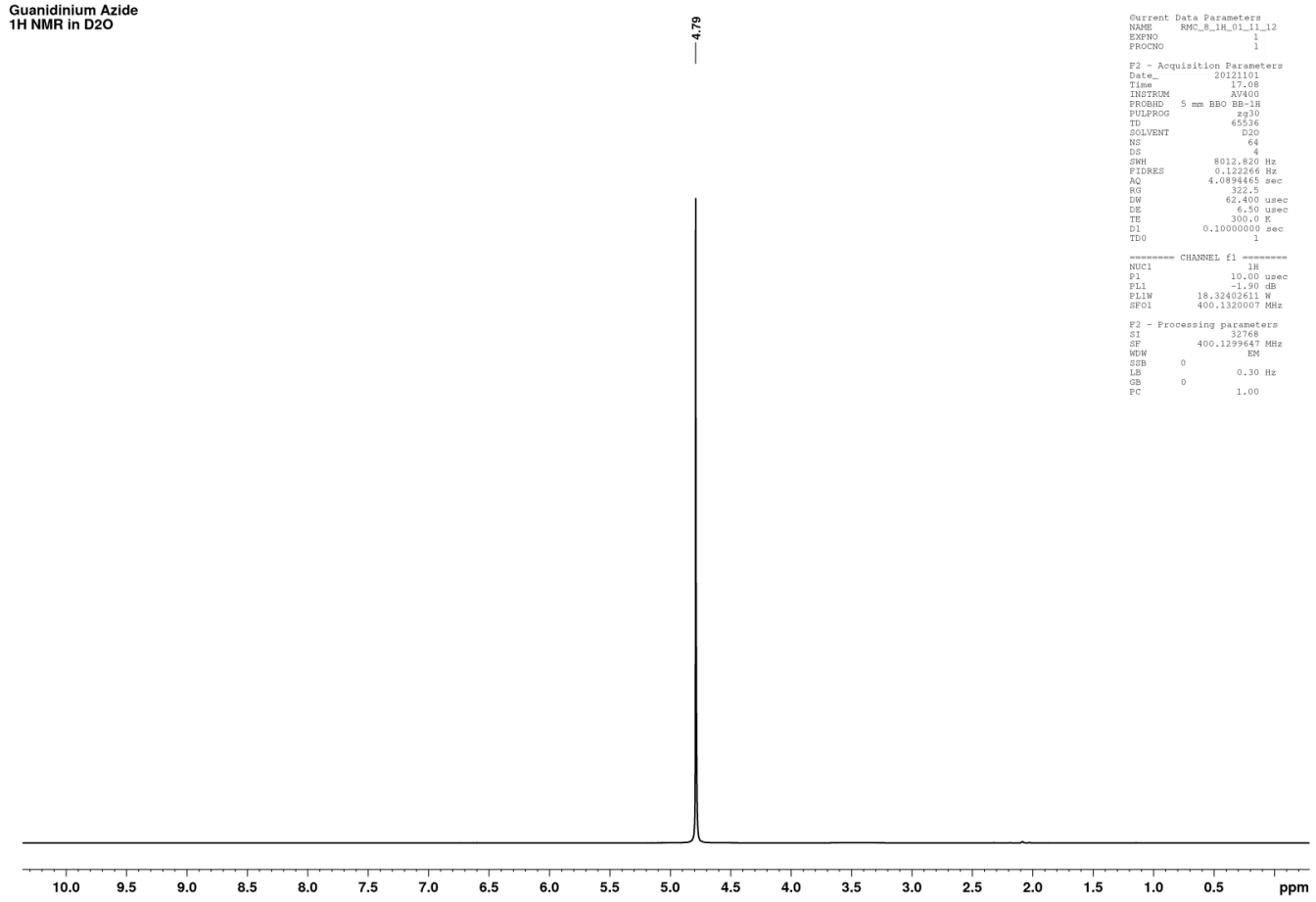


```
Current Data Parameters
NAME      RMC_8_1H_01_11_12
EXPNO                    11
PROCNO                    1

F2 - Acquisition Parameters
Date_              20121101
Time                  17.08
INSTRUM               AV400
PROBHD     5 mm BBO BB-1H
PULPROG               zg30
TD                   65536
SOLVENT                D2O
NS                        64
DS                         4
SWH                8012.820 Hz
FIDRES            0.122266 Hz
AQ                4.0894465 sec
RG                     322.5
DW                  62.400 usec
DE                   6.50 usec
TE                   300.0 K
D1                0.10000000 sec
TD0                       1

======== CHANNEL f1 ========
NUC1                      1H
P1                    10.00 usec
PL1                   -1.90 dB
PL1W          18.32402611 W
SFO1          400.1320007 MHz

F2 - Processing parameters
SI                        32768
SF            400.1299647 MHz
WDW                        EM
SSB       0
LB                     0.30 Hz
GB        0
PC                     1.00
```

Figure 7.1. ^{1}H NMR spectrum of guanidinium azide (**1**) in D_2O, showing only the solvent residual peak, implying fast exchange with the protons of the guanidinium cation.

7.1.1 Guanidinium Azide in dmso-d_6

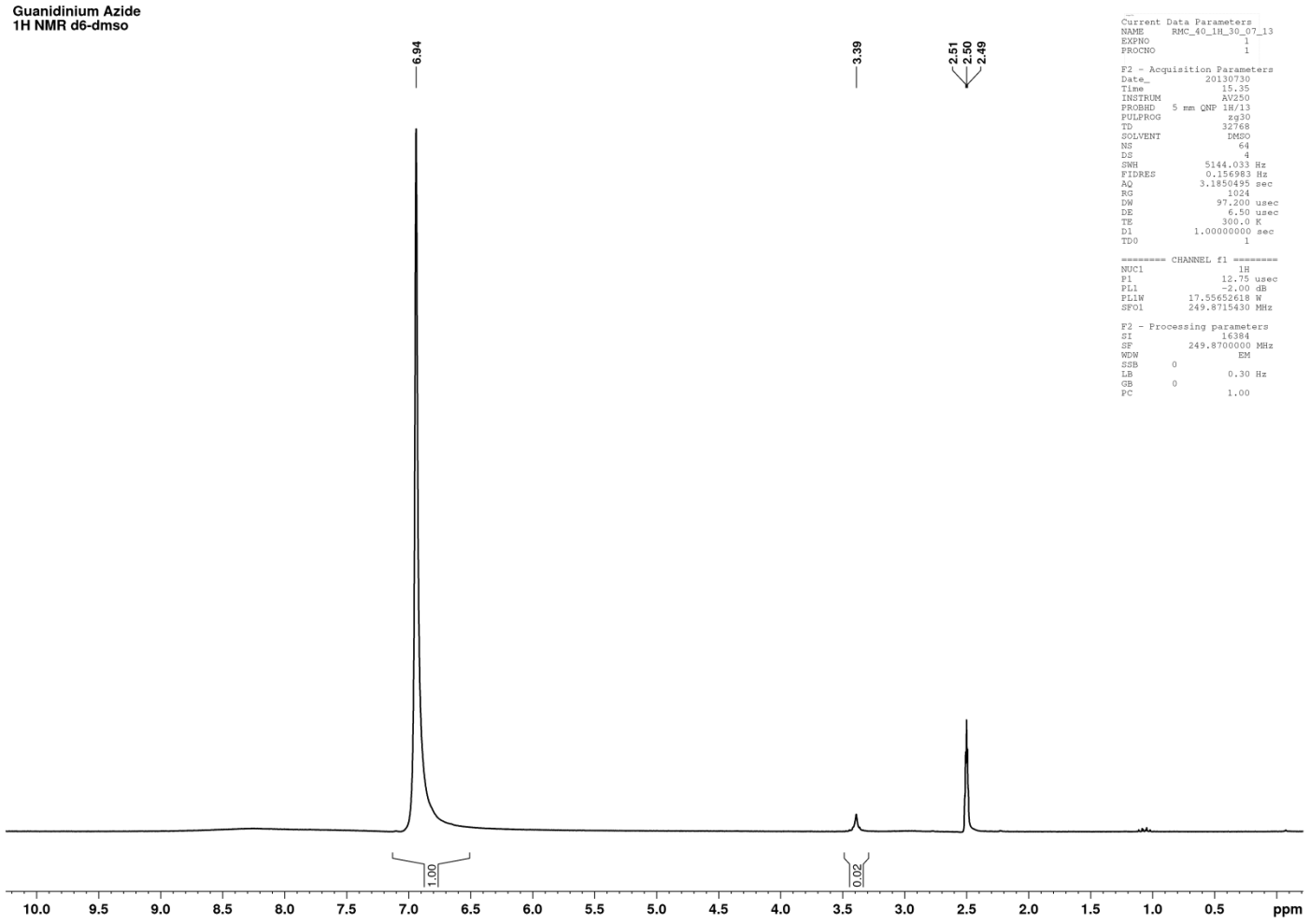

Figure 7.2. ^{1}H NMR spectrum of guanidinium azide (**1**) in dimethylsulfoxide-d_6.

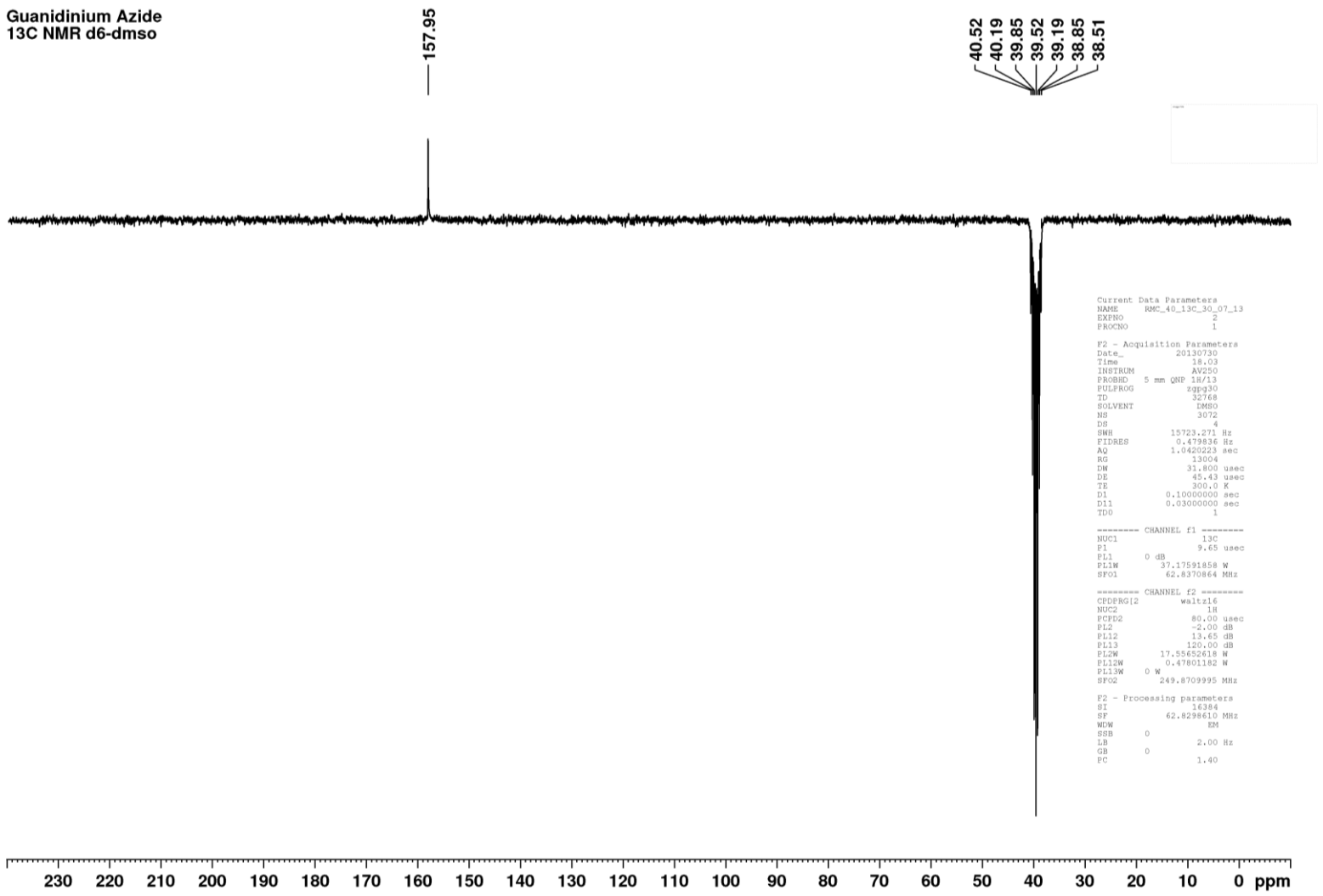

Figure 7.3. ^{13}C NMR spectrum of guanidinium azide (**1**) in dimethylsulfoxide-d_6.

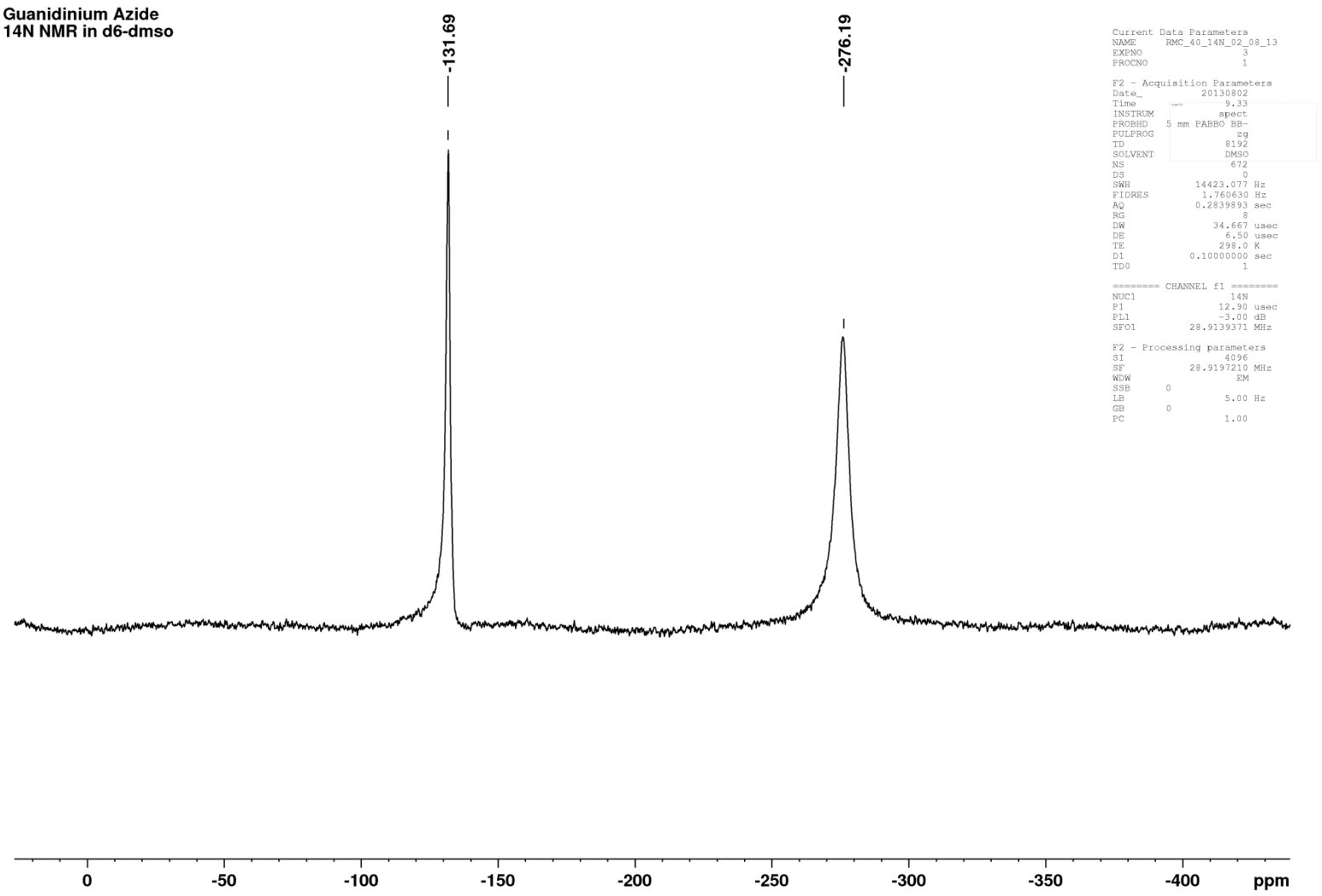

Figure 7.4. ^{14}N NMR spectrum of guanidinium azide (**1**) in dimethylsulfoxide-d_6.

7.1.2 Guanidinium Azide Monohydrate in dmso-d_6

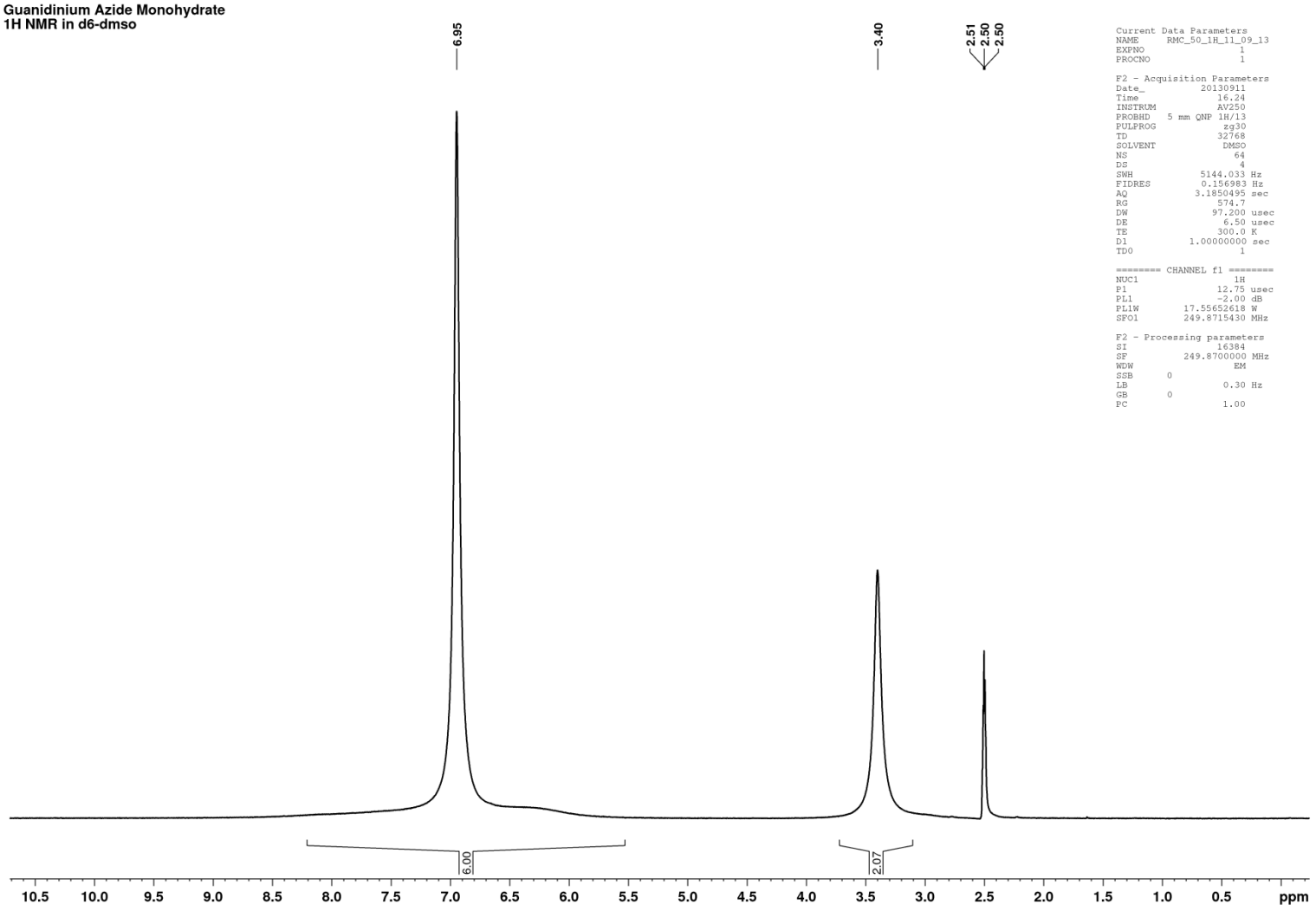

Figure 7.5. ^{1}H NMR spectrum of guanidinium azide monohydrate (**1a**) in dimethylsulfoxide-d_6.

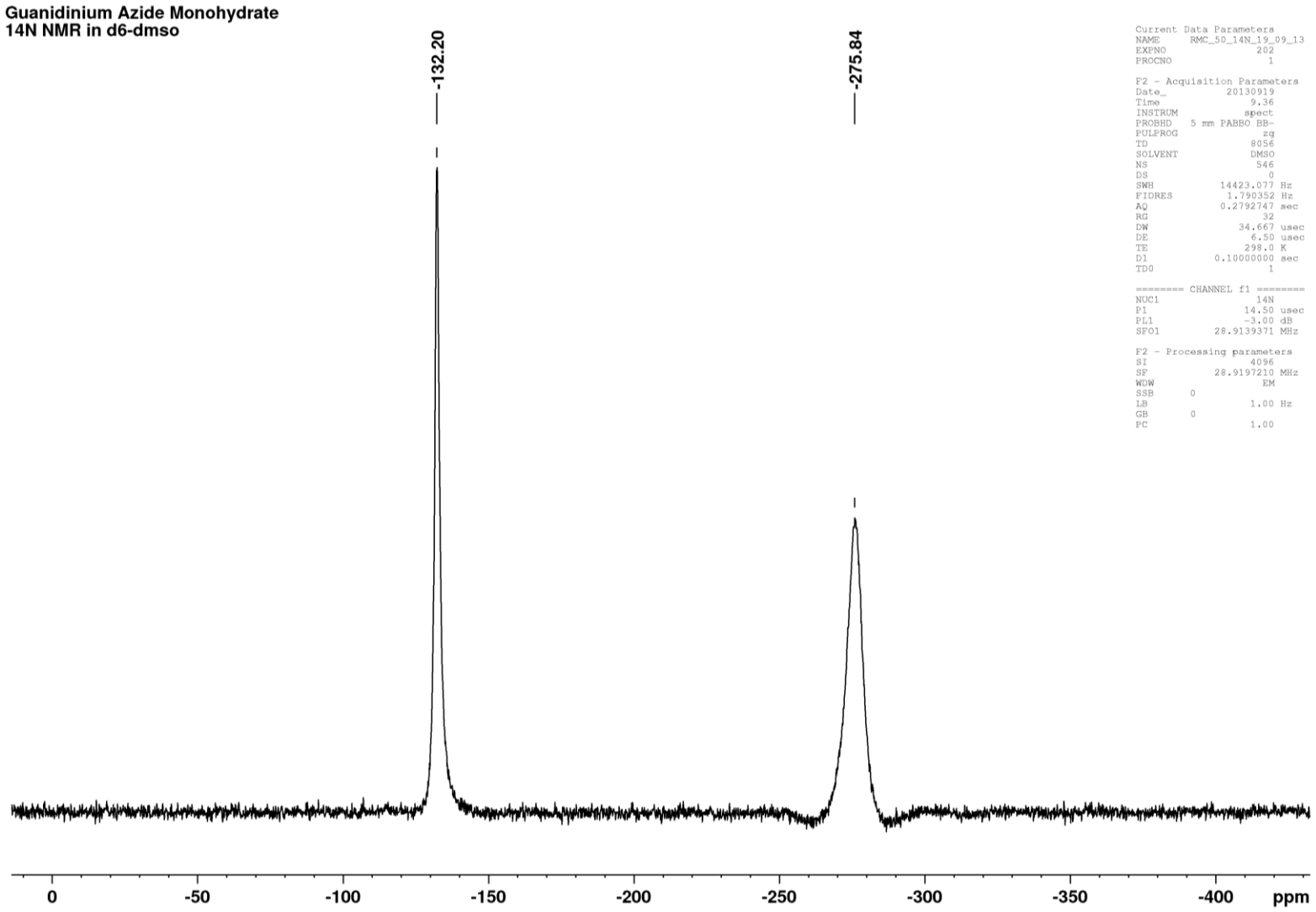

Figure 7.6. ^{14}N NMR spectrum of guanidinium azide monohydrate (**1a**) in dimethylsulfoxide-d_6.

7.1.3 Aminoguanidinium Azide in dmso-d_6

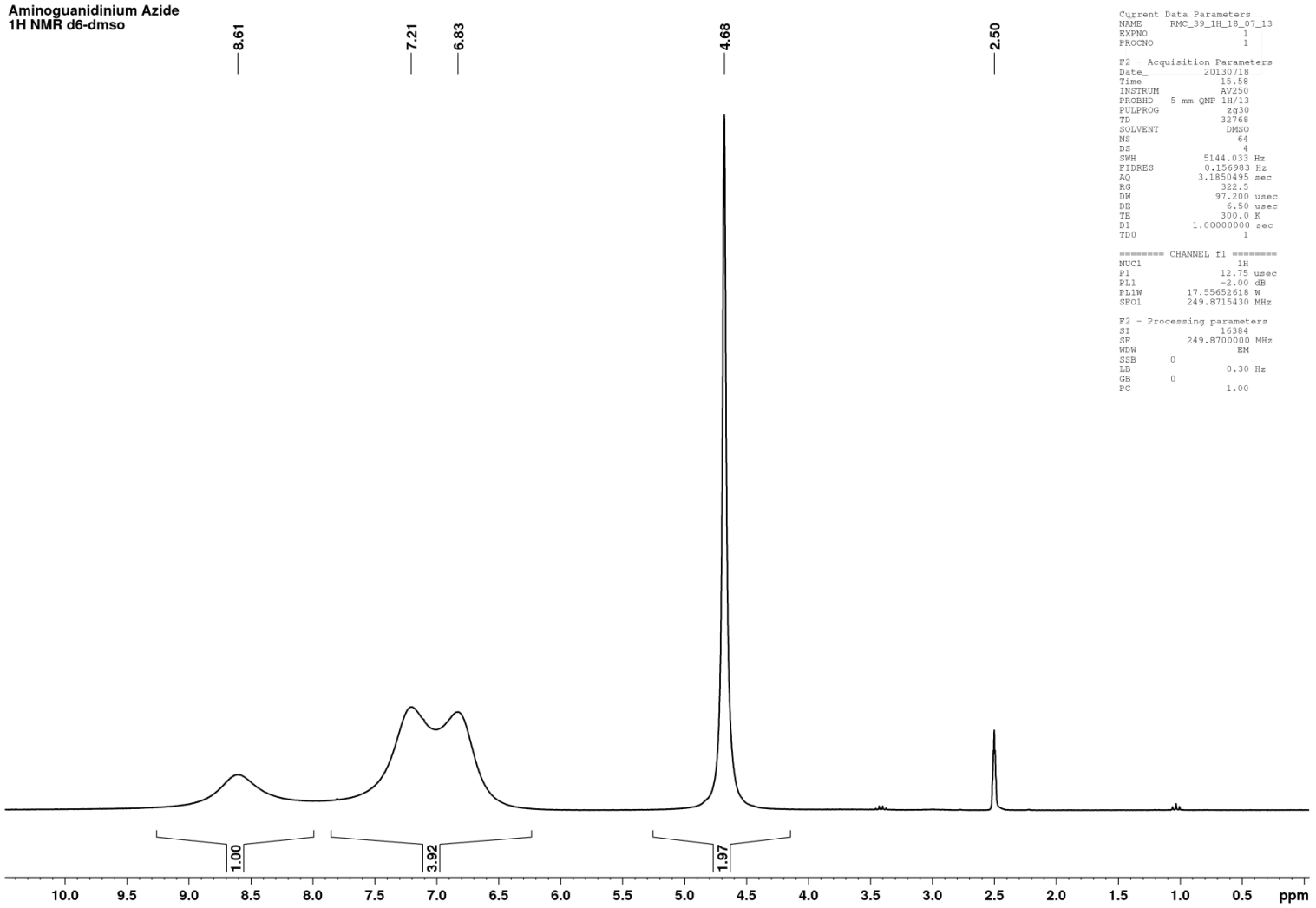

Figure 7.7. ^{1}H NMR spectrum of aminoguanidinium azide (**2**) in dimethylsulfoxide-d_6.

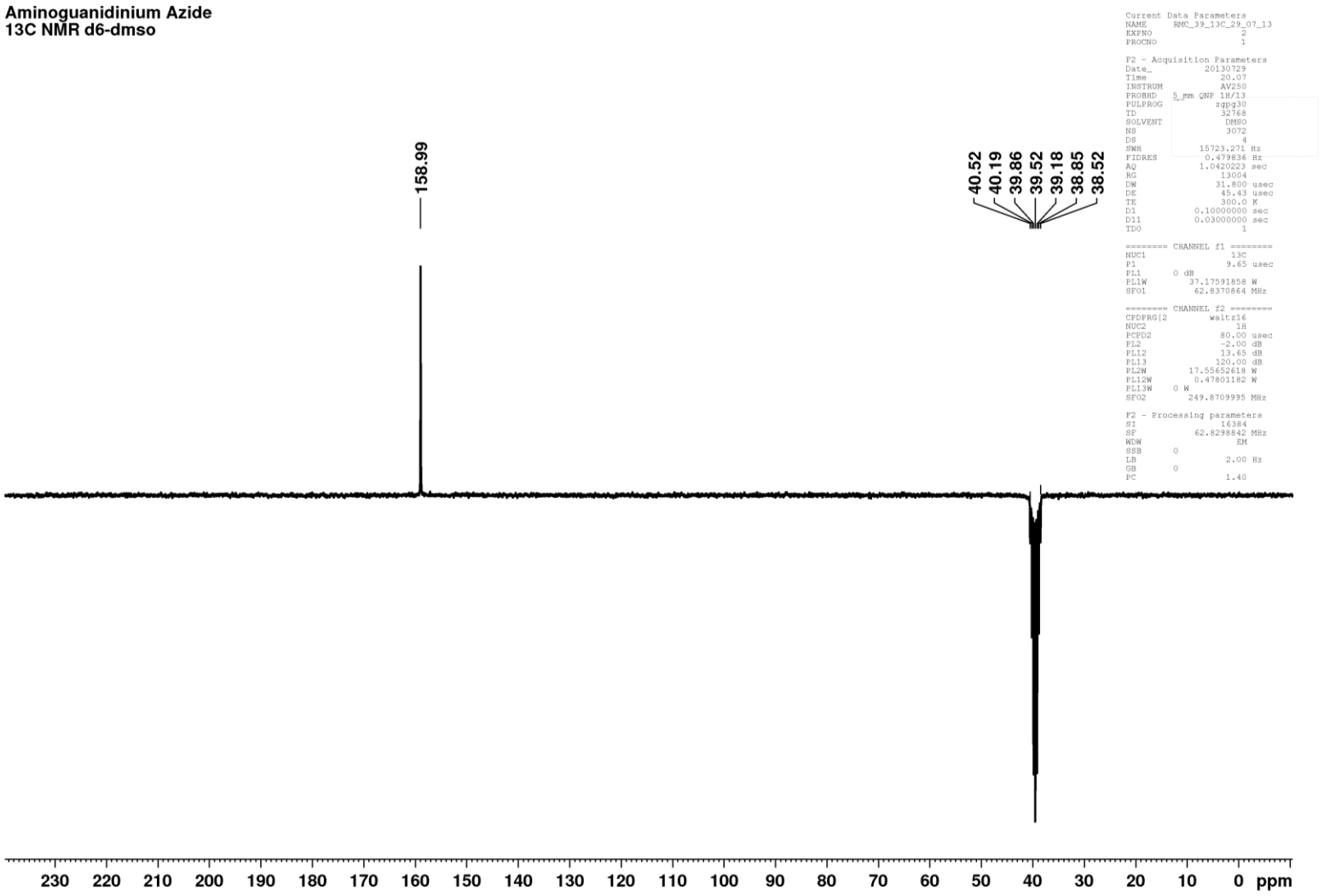

Figure 7.8. ^{13}C NMR spectrum of aminoguanidinium azide (**2**) in dimethylsulfoxide-d_6.

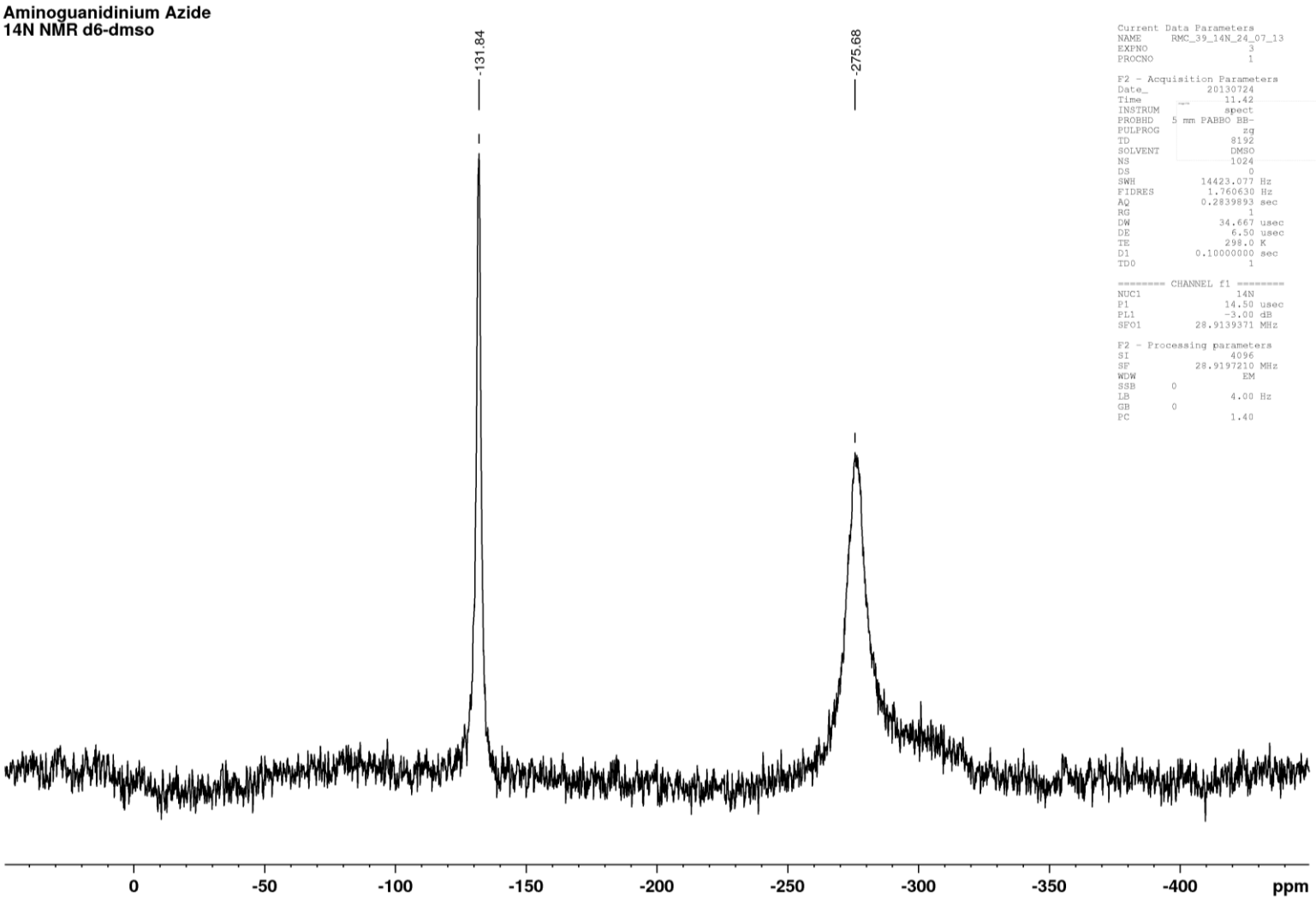

Figure 7.9. ^{14}N NMR spectrum of aminoguanidinium azide (**2**) in dimethylsulfoxide-d_6.

7.1.4 Bis(guanidinium) hexa(azido)stannate(IV), $(C(NH_2)_3)_2Sn(N_3)_6$ (3) in CD_3CN

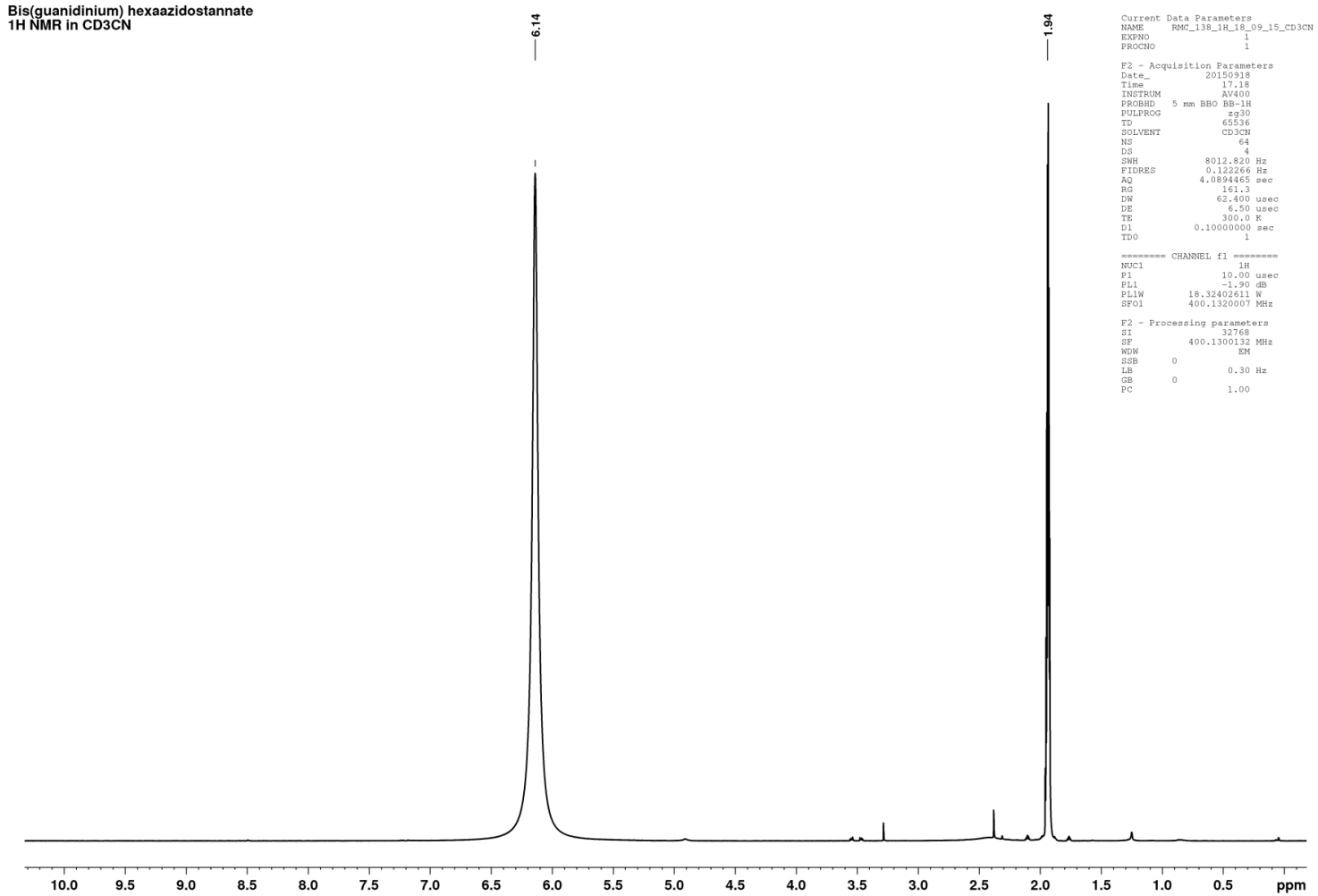

Figure 7.10. ^{1}H NMR spectrum of bis(guanidinium) hexaazidostannate (**3**) in CD_3CN, with trace impurities of TMS–N_3, diglyme (trace impurity in TMS–N_3), and an unknown trace impurity at 2.4 ppm.

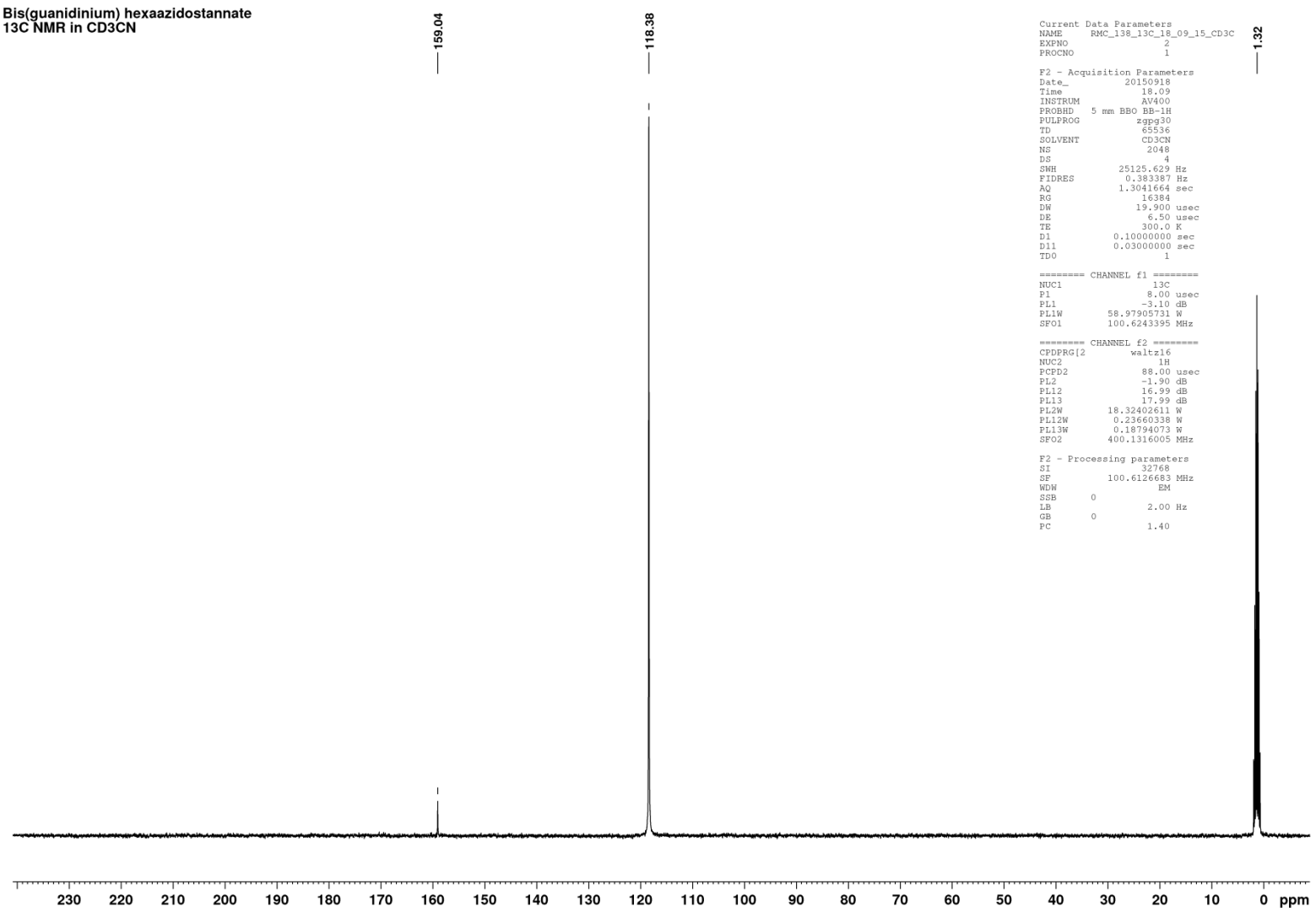

Figure 7.11. ^{13}C NMR spectrum of bis(guanidinium) hexaazidostannate (**3**) in CD_3CN.

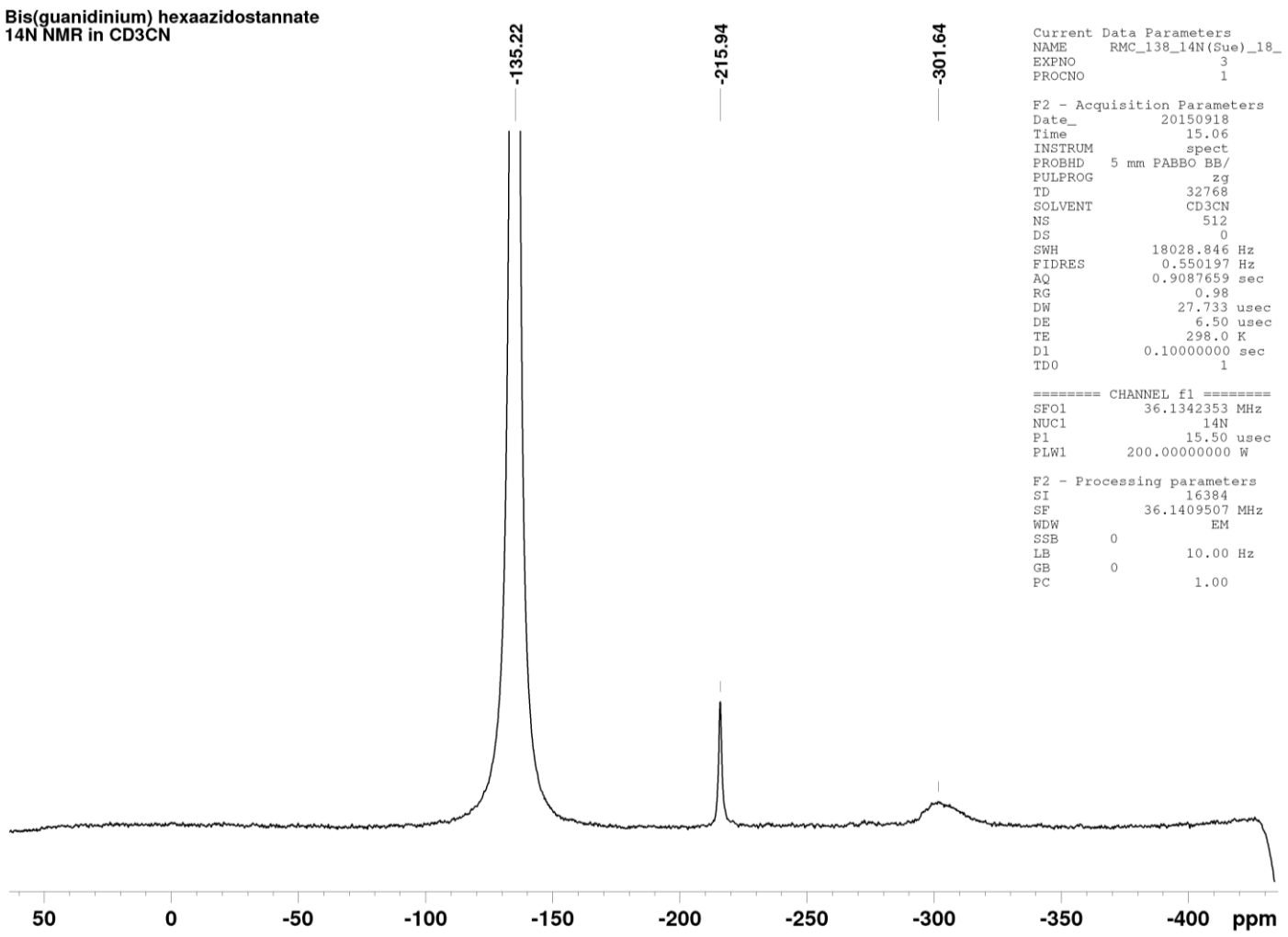

Figure 7.12. ^{14}N NMR spectrum of bis(guanidinium) hexaazidostannate (**3**) in CD_3CN.

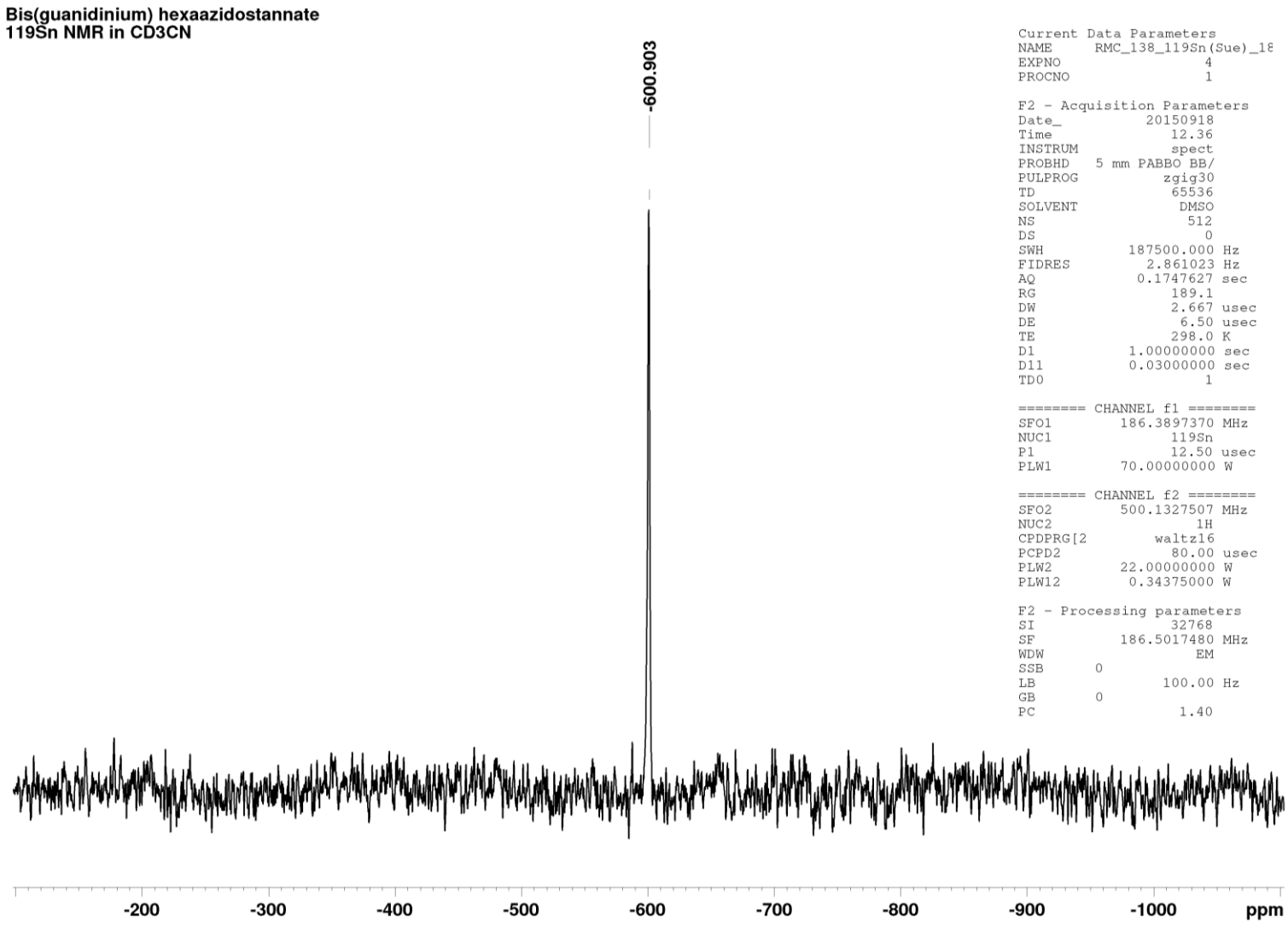

Figure 7.13. ^{119}Sn NMR of bis(guanidinium) hexaazidostannate (**3**) in CD_3CN.

7.1.5 bis(bis(triphenylphosphine)iminium) hexa(azido)stannate(IV), $(PPN)_2Sn(N_3)_6$[85] (9) in CD_3CN

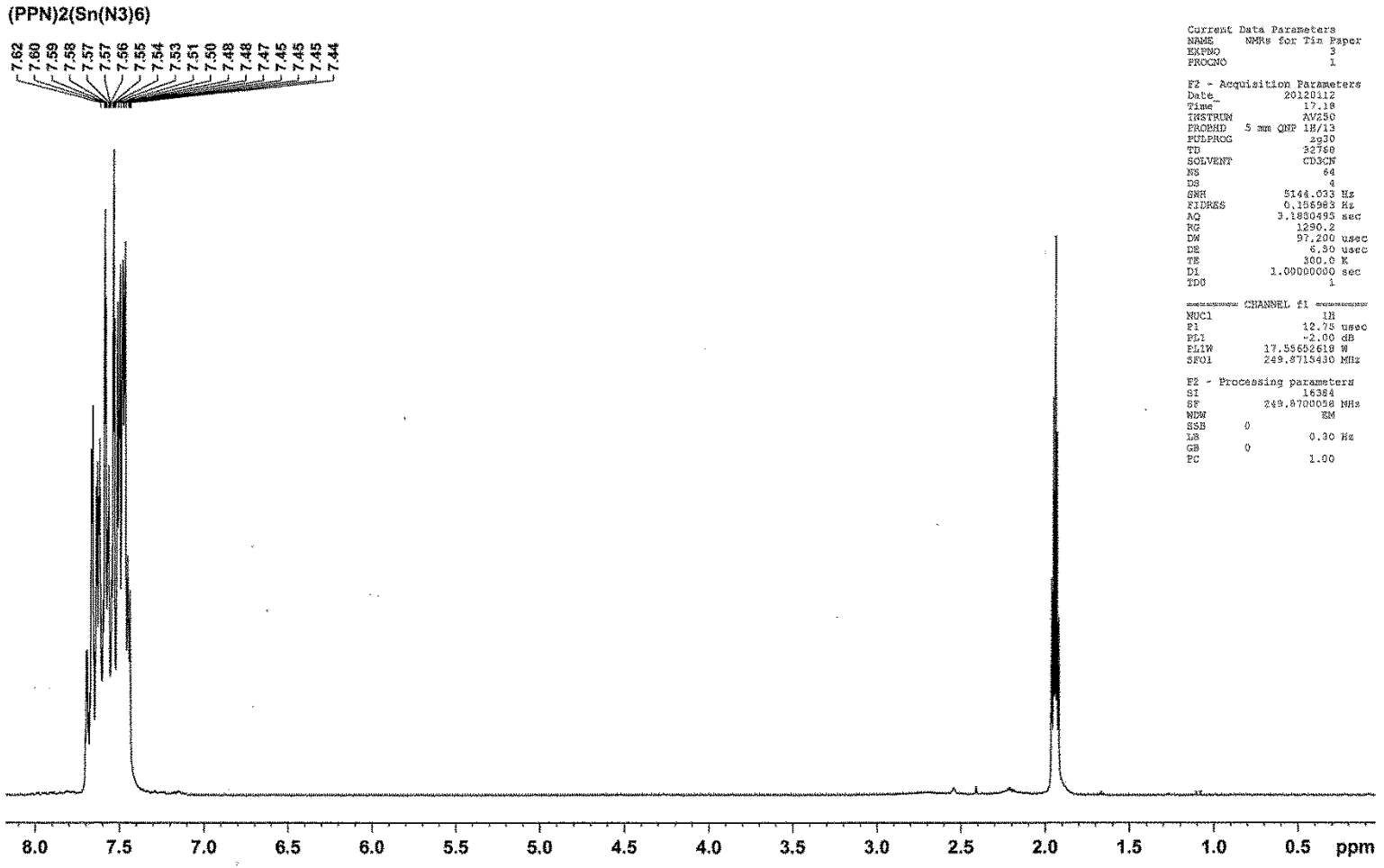

Figure 7.14. ^1H NMR spectrum of $(PPN)_2Sn(N_3)_6$ (**9**) in CD_3CN.

Figure 7.15. ^{13}C NMR spectrum of $(PPN)_2Sn(N_3)_6$ (**9**) in CD_3CN.

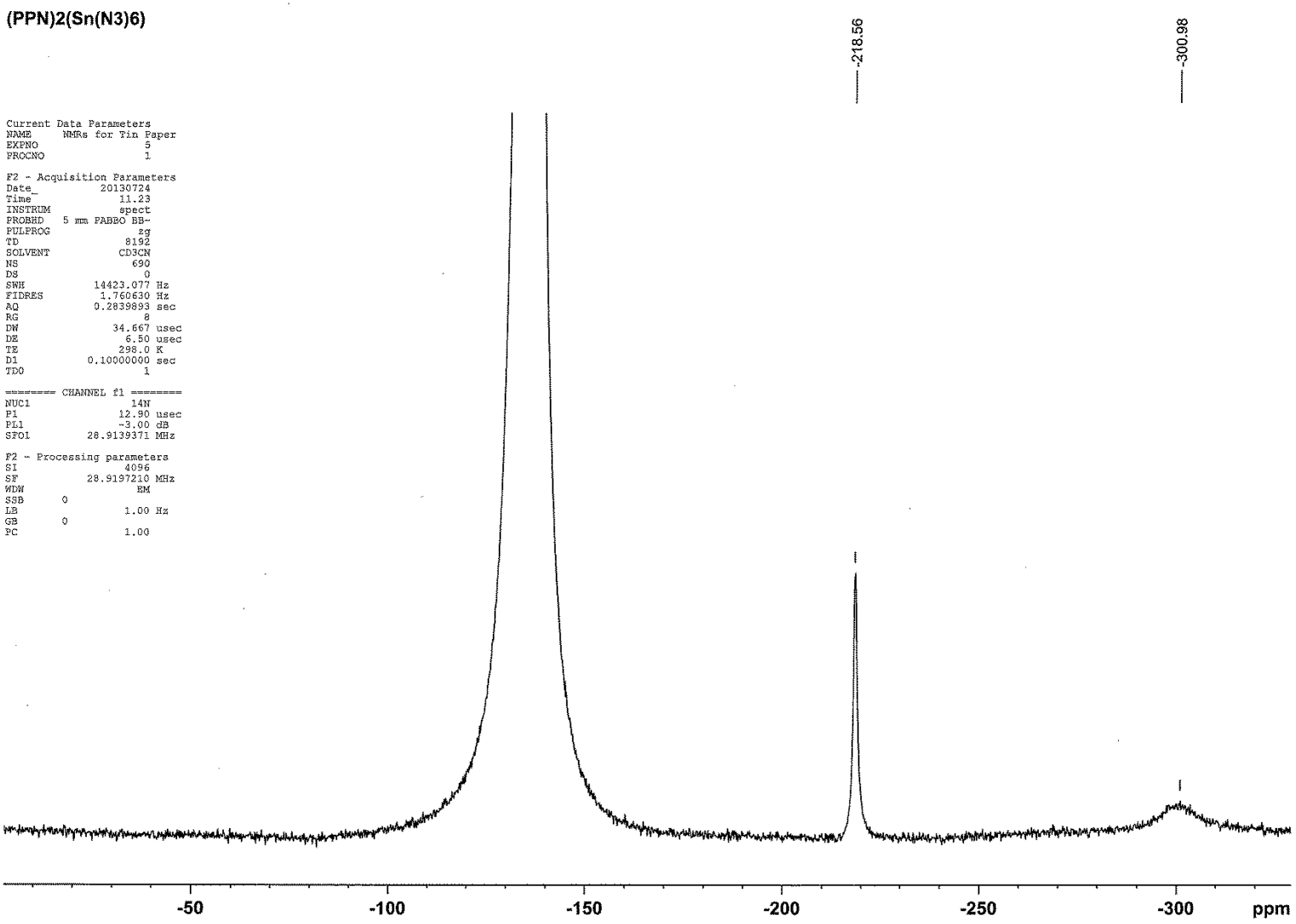

Figure 7.16. ^{14}N NMR spectrum of $(PPN)_2Sn(N_3)_6$ (**9**) in CD_3CN.

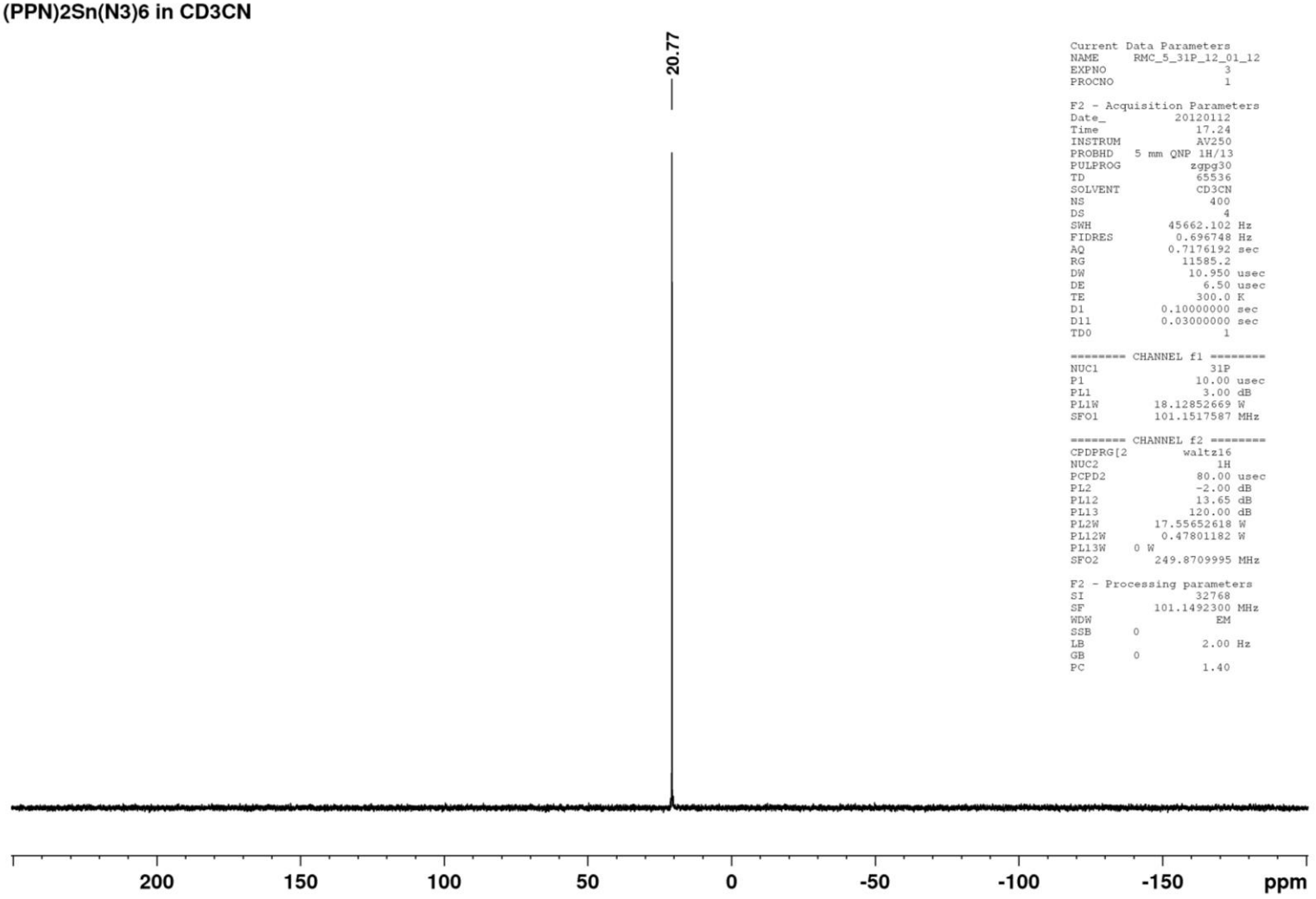

Figure 7.17. ^{31}P NMR of $(PPN)_2Sn(N_3)_6$ (**9**) in CD_3CN.

7.1.6 Tetra(azido)(2,2'-bipyridyl)tin(IV), $Sn(N_3)_4(bpy)$[85] (10) in CD_3CN

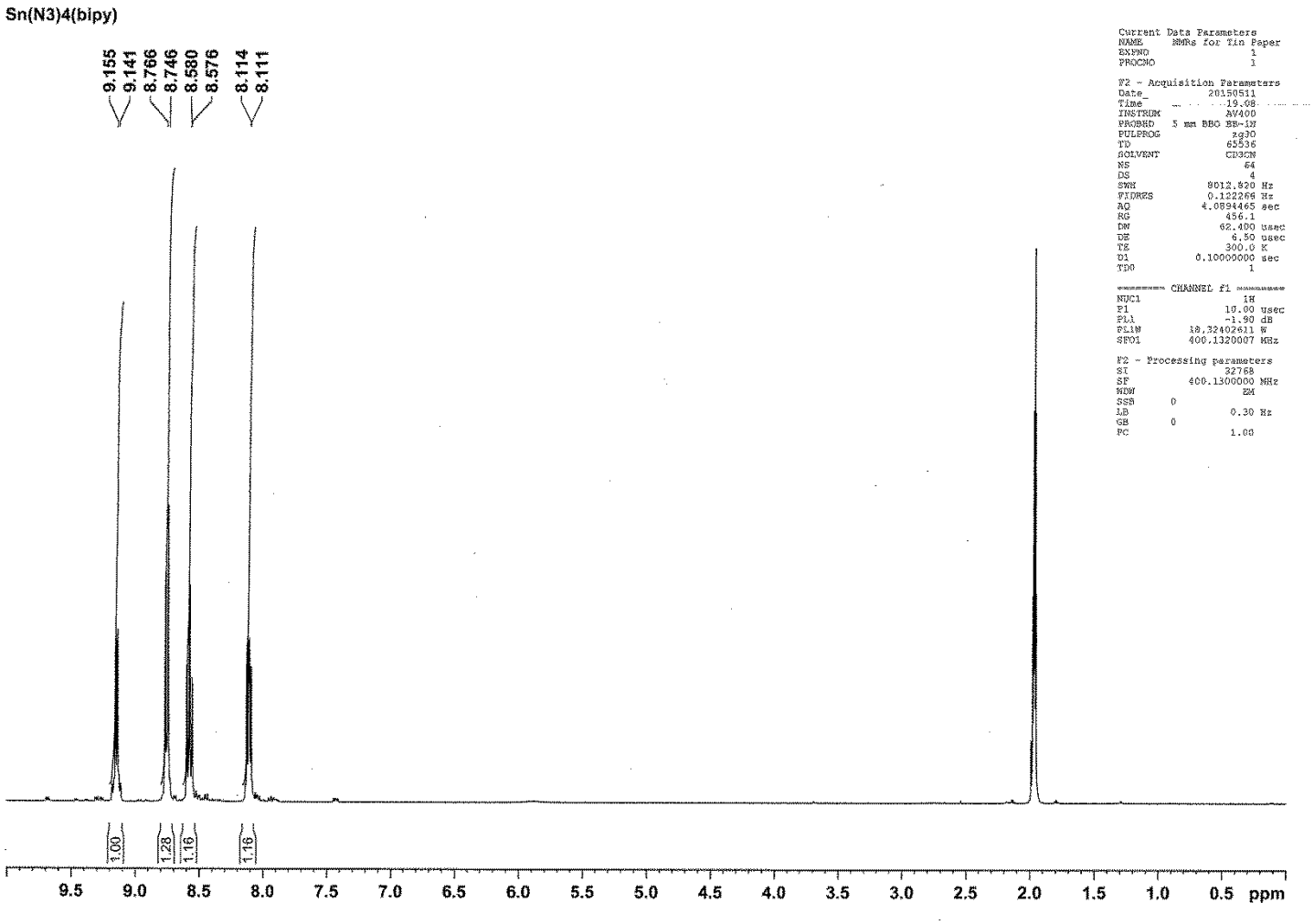

Figure 7.18. ^1H NMR spectrum of $Sn(N_3)_4(bpy)$ (**10**) in CD_3CN.

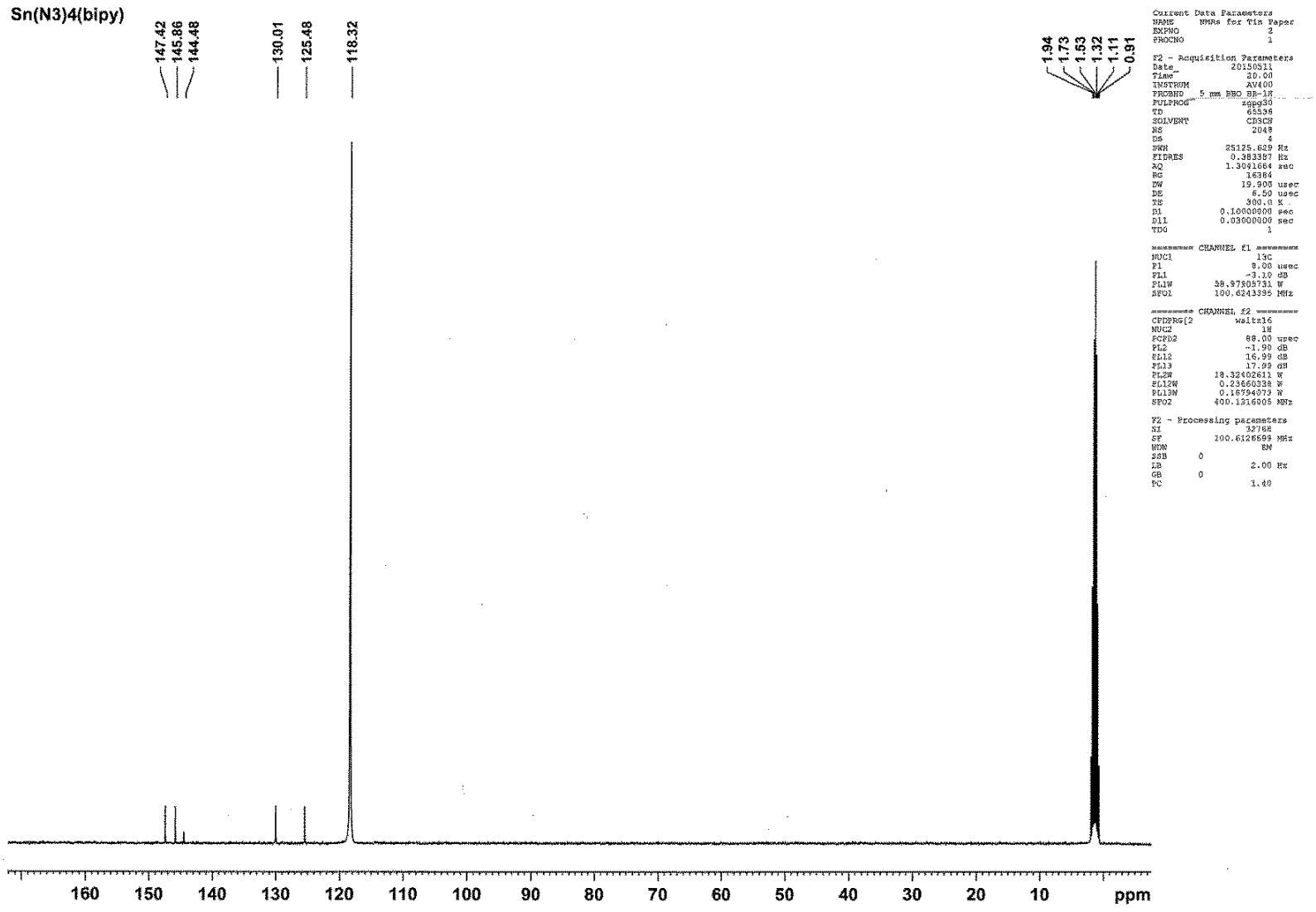

Figure 7.19. ^{13}C NMR spectrum of $Sn(N_3)_4(bpy)$ (**10**) in CD_3CN.

7.1.6 Tetra(azido)(2,2'-bipyridyl)tin(IV), $Sn(N_3)_4(bpy)$[85] (10) in CD_2Cl_2

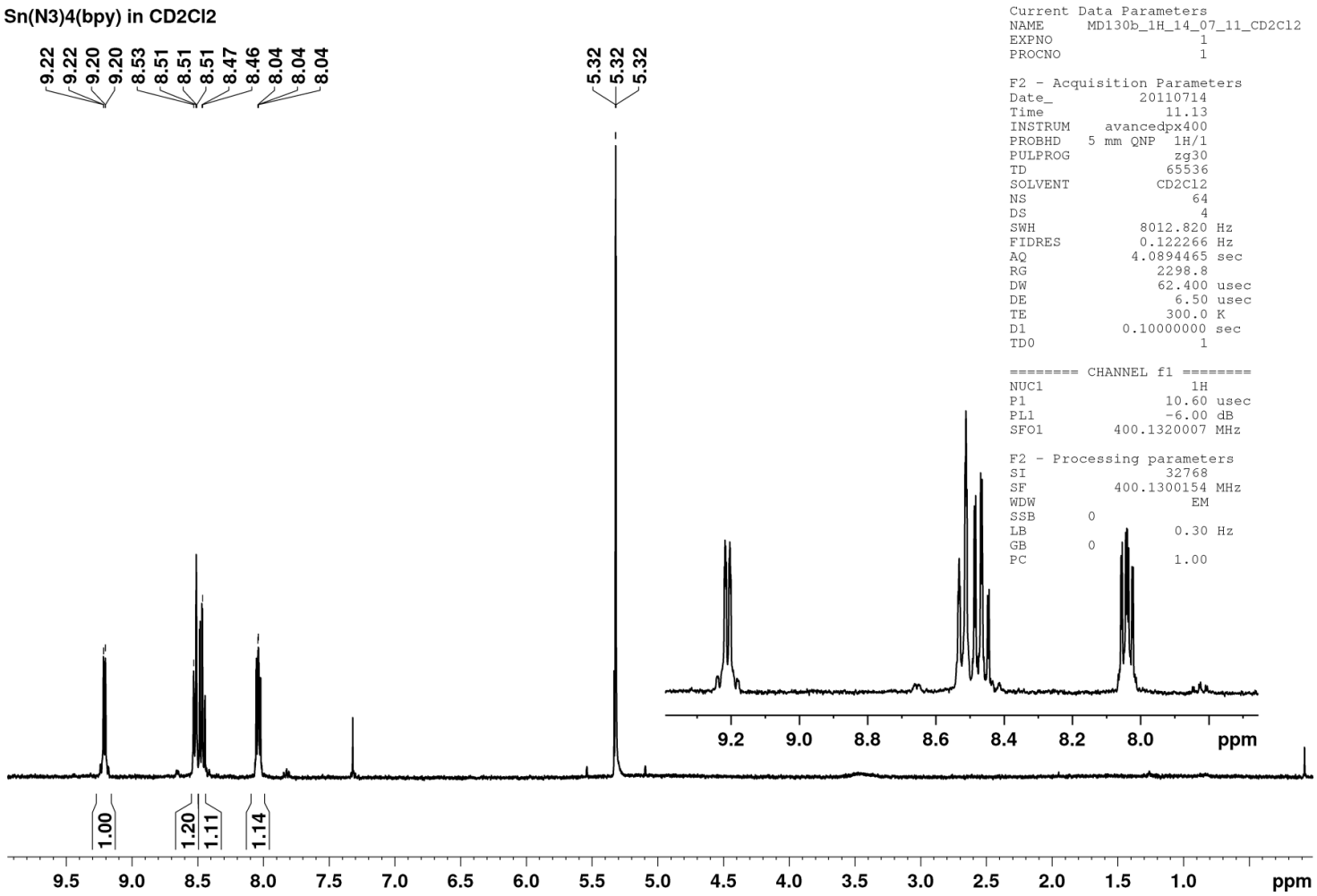

Figure 7.20. ^{1}H NMR of $Sn(N_3)_4(bpy)$ (**10**) in CD_2Cl_2, with 2,2'-bipyridine (*ca*. 6%) as an impurity.

7.1.7 Tetra(azido)(1,10-phenanthroline)tin(IV), Sn(N3)4(phen)[85] (11) in CD_3CN

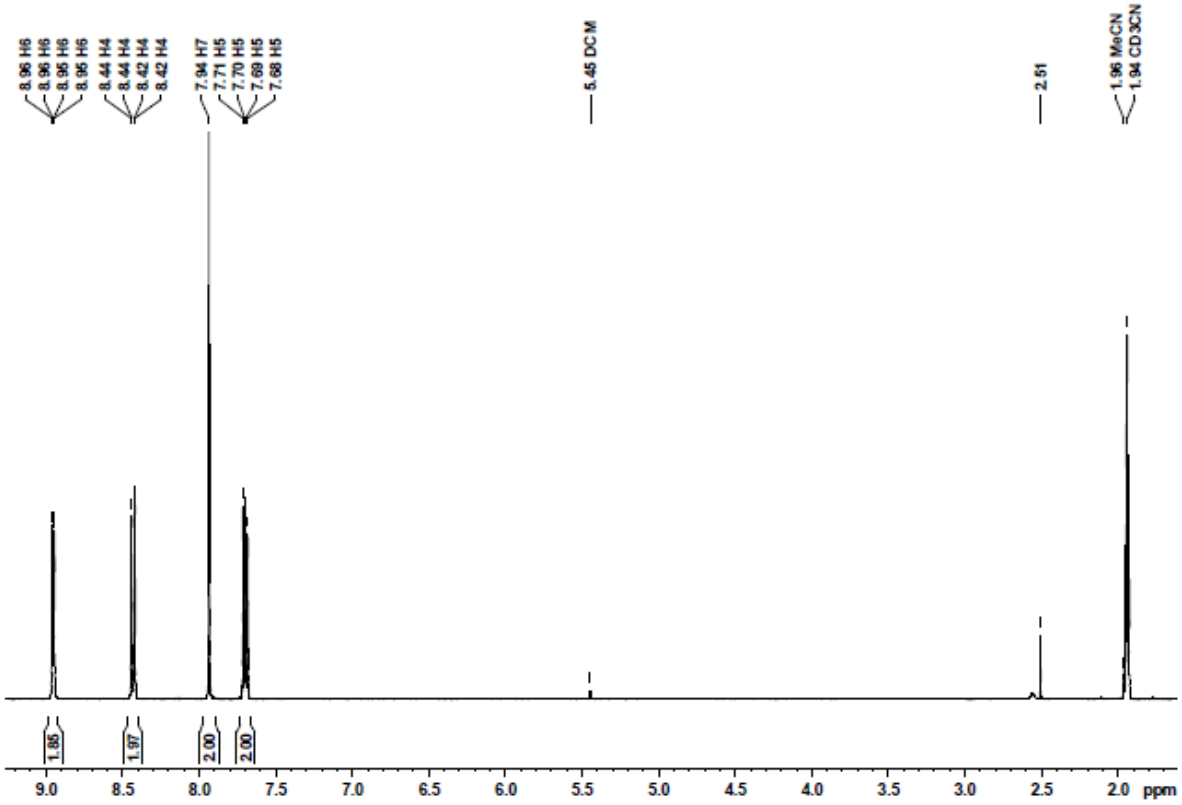

Figure 7.21. ^{1}H NMR of $Sn(N_3)_4(phen)$ (**11**) in CD_3CN.

7.1.8 Tetra(azido)bis(pyridine)tin(IV), $Sn(N_3)_4(py)_2$[85] (12) in dmso-d_6

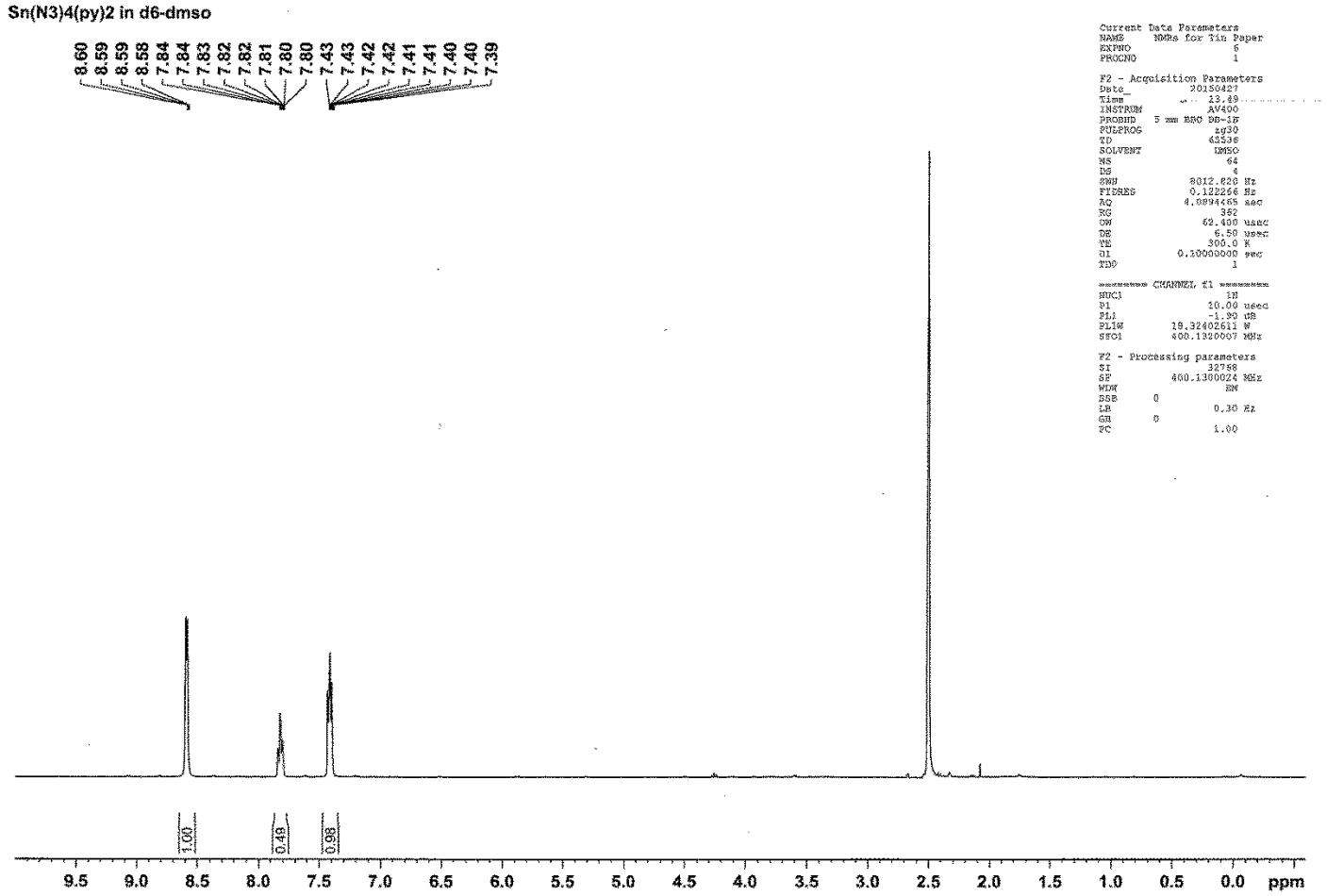

Figure 7.22. ^{1}H NMR of $Sn(N_3)_4(py)_2$ (**12**) in dimethylsulfoxide-d_6 with a trace impurity of acetonitrile at 2.07 ppm calibrated to the solvent residual peak at 2.50 ppm.[190] Appears to show free pyridine, suggesting that DMSO displaced the coordinated pyridine from the complex. No tin satellites are observed around the dimethylsulfoxide solvent residual peak, suggesting exchange with the solvent is fast. δ = 7.42 ppm (m,2H), $J(^1H\text{-}^{13}C)$ = 164 Hz; 7.82 ppm (m,1H), $J(^1H\text{-}^{13}C)$= 166 Hz; 8.59 ppm (m, 2H), $J(^1H\text{-}^{13}C)$ = 178 Hz; solvent residual 2.50 ppm (septet) $J(^1H\text{-}^{13}C)$= 137 Hz.

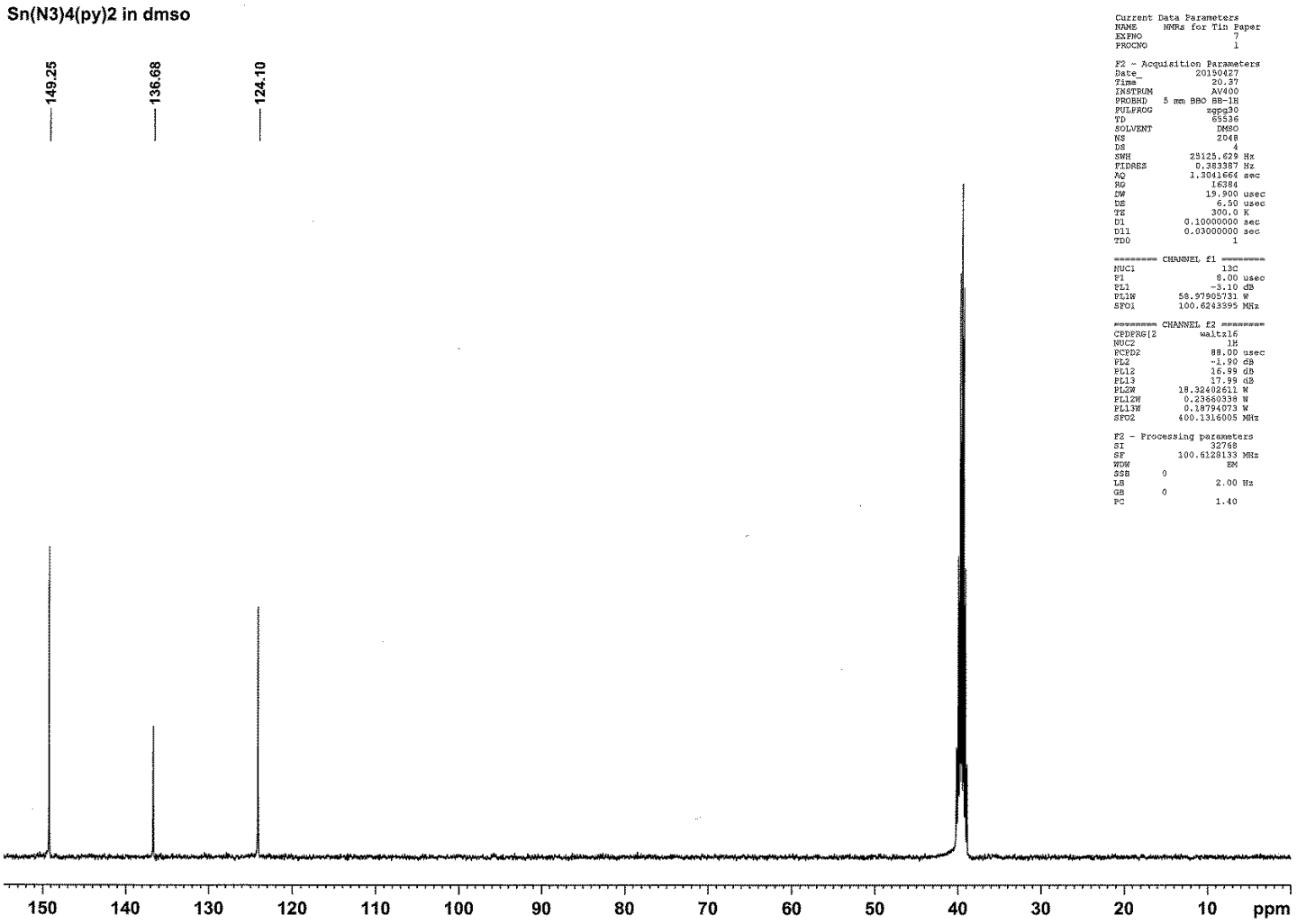

Figure 7.23. ^{13}C NMR spectrum of $Sn(N_3)_4(py)_2$ (**12**) in dimethylsulfoxide-d_6. Appears to show only free pyridine, suggesting that DMSO at least partially displaces pyridine from the complex. δ [ppm] = 124.10, 136.68, 149.25.

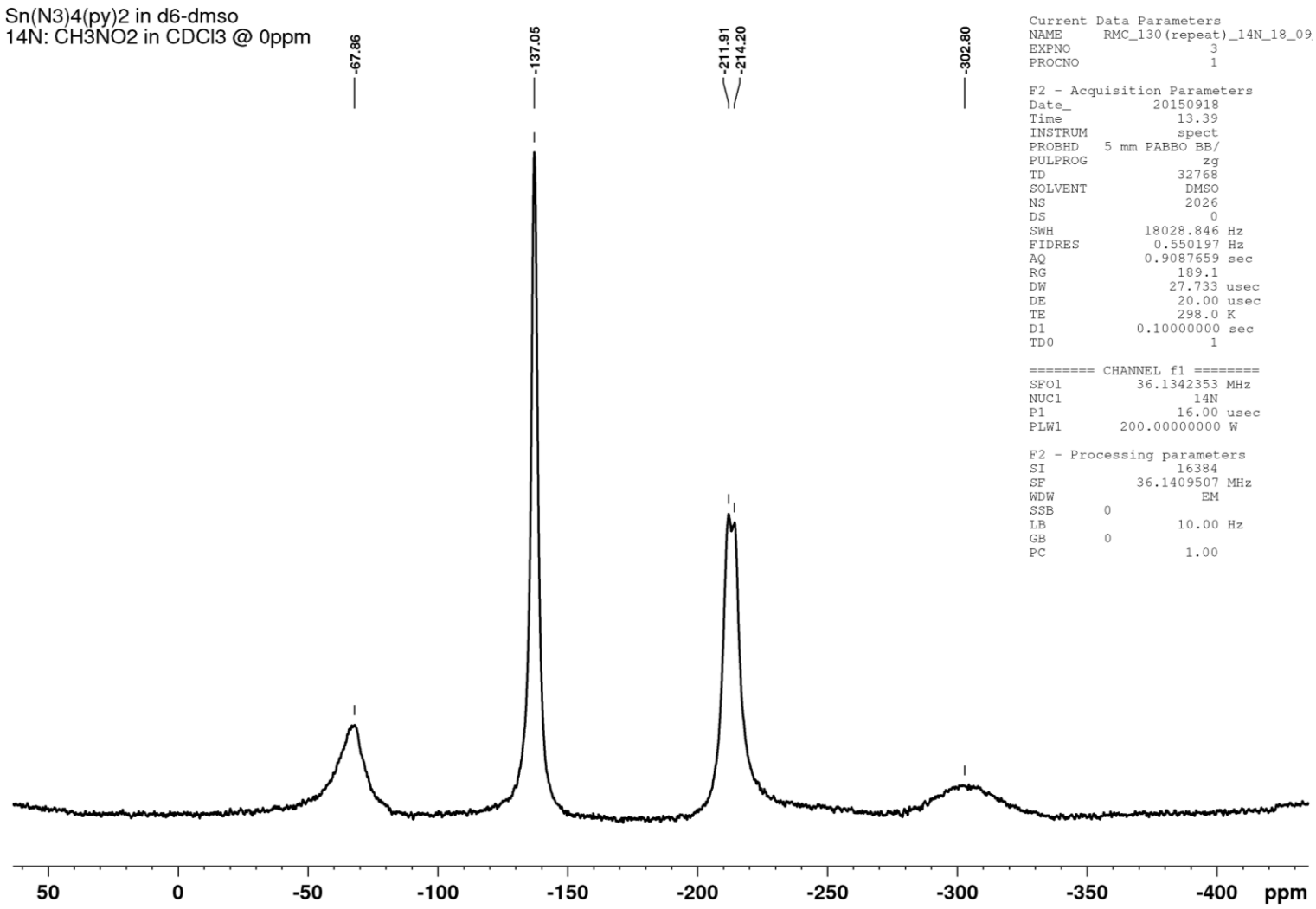

Figure 7.24. ^{14}N NMR spectrum of $Sn(N_3)_4(py)_2$ (**12**) in dimethylsulfoxide-d_6. δ [ppm] = –67 (pyridine); –303 (N_α), –137 (N_β), and –212/–214 (N_γ).

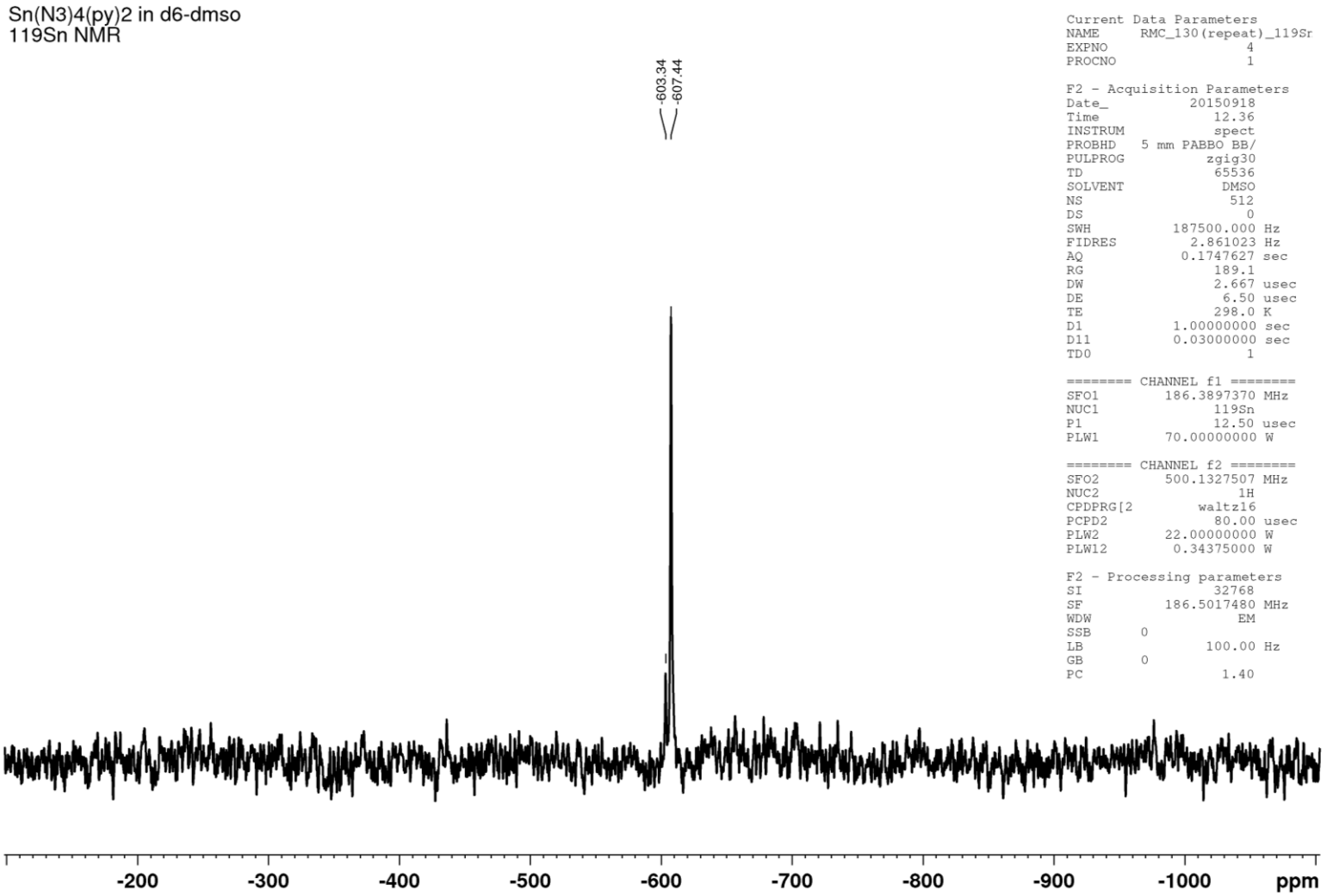

Figure 7.25. ^{119}Sn NMR spectrum of $Sn(N_3)_4(py)_2$ (**12**) in dimethylsulfoxide-d_6. δ [ppm] = –603, –607.

7.1.9 Reaction of SnF_4 with TMS-N_3 in C_6D_6, and assessment of F/N_3 exchange progress via chelation of $Sn(N_3)_xF_{(4-x)}$ with 2,2'-bipyridine

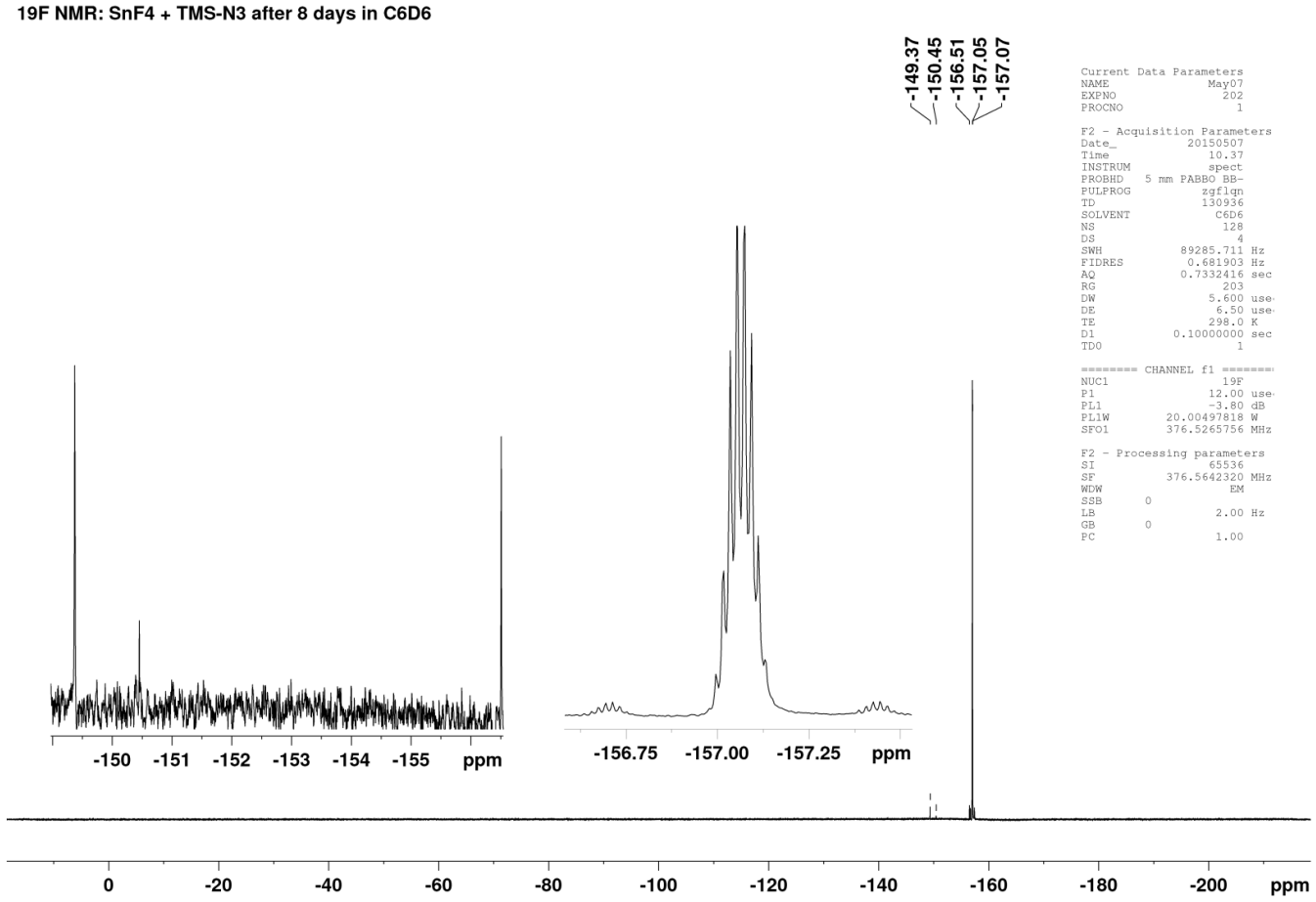

Figure 7.26. ^{19}F NMR spectrum after reaction of SnF_4 with TMS–N_3 in C_6D_6 for 8 days. An expanded view of the multiplet arising from TMS–F at –157.1 ppm is shown. $J(^{29}Si\text{-}^{19}F)$ = 275 Hz. Chemical shift from the literature ^{19}F spectrum of TMS–F is 6.3 ppm downfield from SiF_4,[182] which is –163.3 relative to the $CFCl_3$ calibrant used in this work, and therefore TMS–F appears at –157.0 ppm relative to $CFCl_3$.

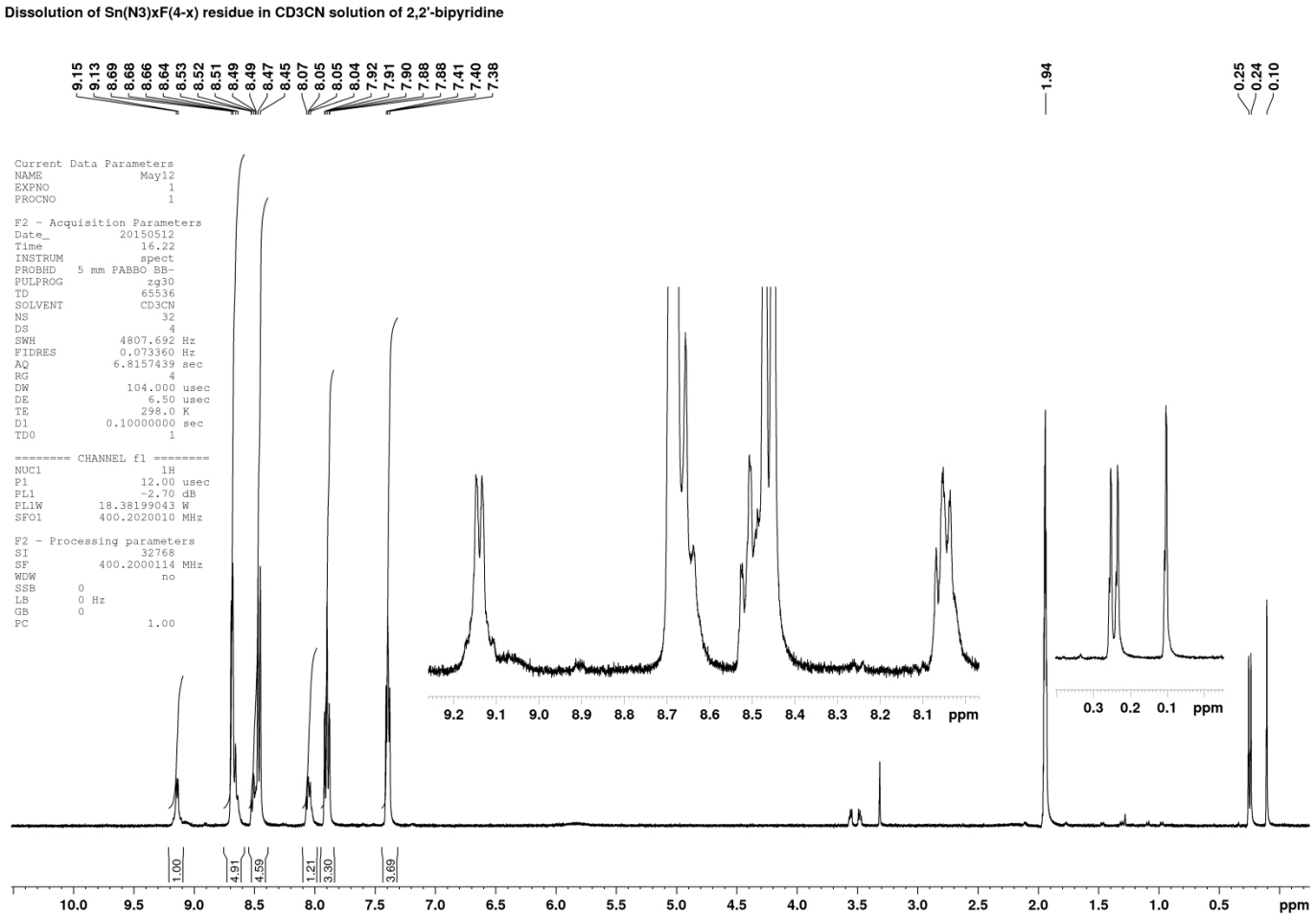

Figure 7.27. ^{1}H NMR spectrum in CD_3CN of the residue obtained by reaction of SnF_4 and TMS–N_3 for 8 days in benzene-d_6, after addition of an excess of 2,2'-bipyridine. The spectrum shows predominantly 2,2'-bipyridine at 7.40, 7.90, 8.46, and 8.69 ppm, with $Sn(N_3)_4$(bpy) (**10**) at 8.05, 8.52, 8.65, and 9.14 ppm. Residual diglyme (3.2–3.5 ppm) and hydrolysis product hexamethyldisiloxane (0.1 ppm) originating from the TMS–N_3 are also visible as impurities.[190]

7.1.10 Diazidobis(pyridine)tin, $Sn(N_3)_2(py)_2$ (14) in pyridine-d_5

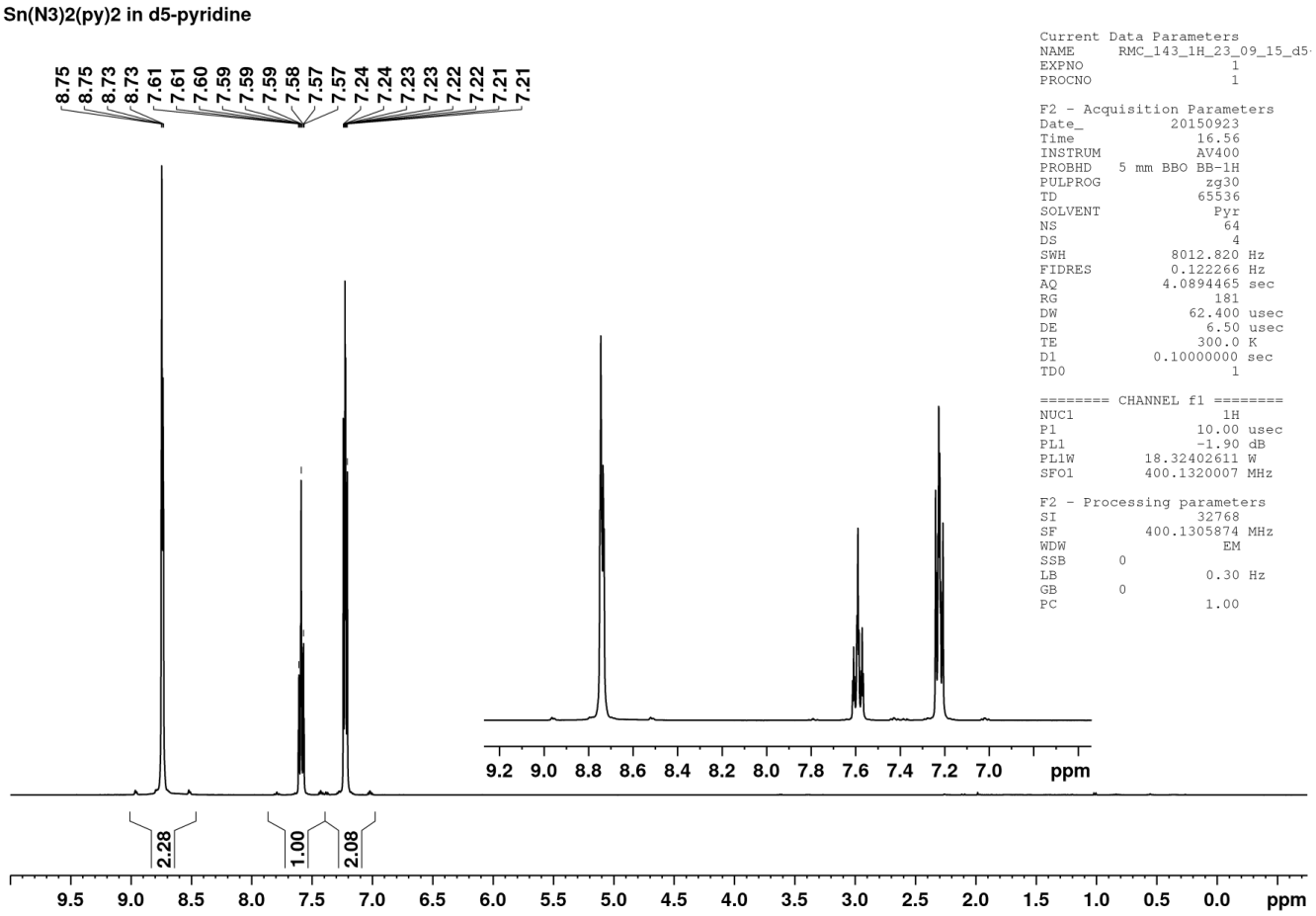

Figure 7.28. ^{1}H NMR of $Sn(N_3)_2(py)_2$ (**14**) in pyridine-d_5. The spectrum has been calibrated against the solvent residual according to Cambridge Isotope Laboratories: http://www2.chem.umd.edu/nmr/reference/isotope_solvent.pdf. The absence of an external calibrant limits any conclusions which can be drawn about exchange. Analysis of the splitting patterns observed in the multiplets seem to be similar to those of pyridine-h_5.[245] See Figure 7.29 below for an expanded view showing the coupling with ^{13}C.

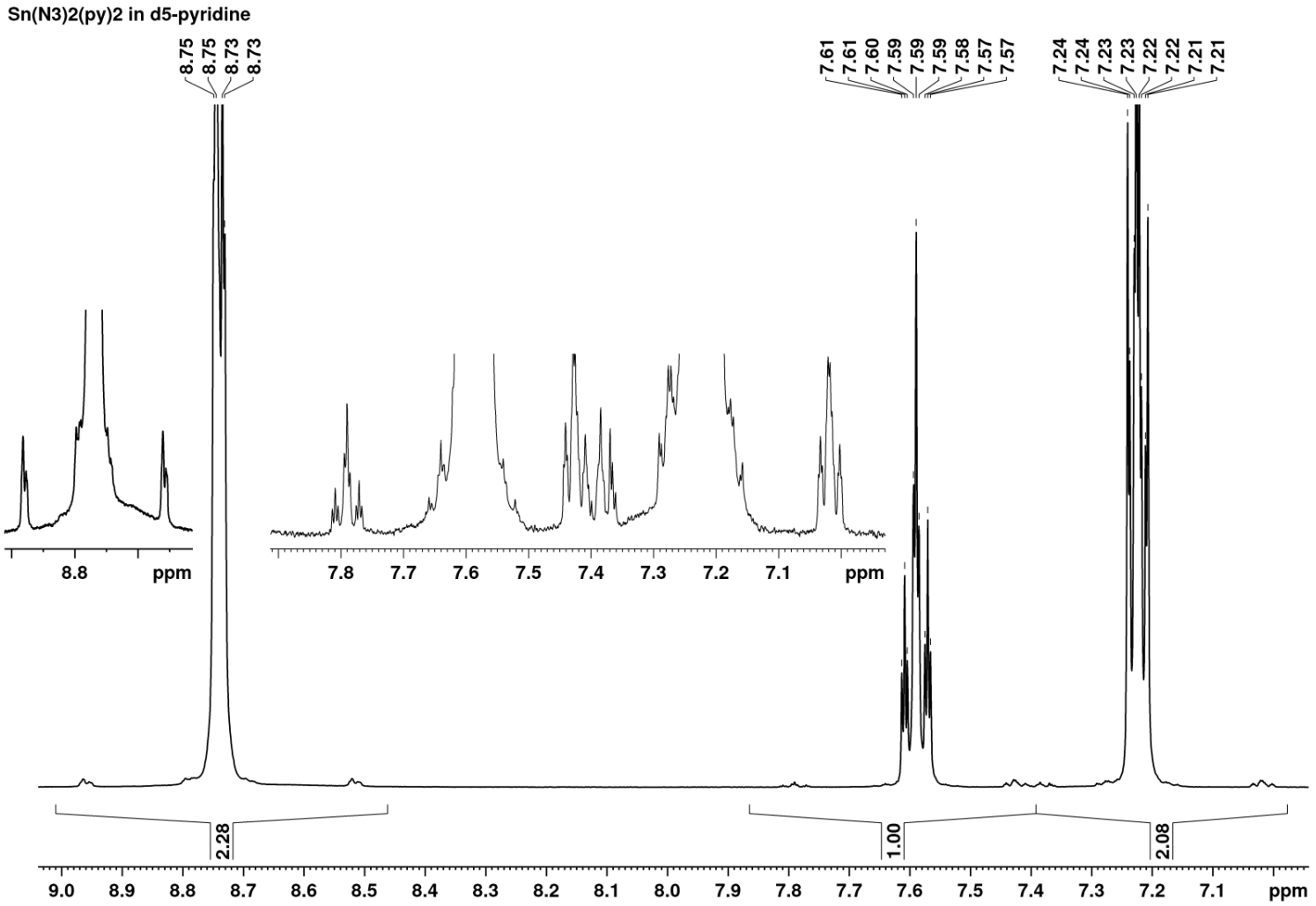

Figure 7.29. Expanded view of the ^{1}H NMR spectrum of $Sn(N_3)_2(py)_2$ (**14**) in pyridine-d_5 showing the fine structure of satellite peaks due to ^{1}H-^{13}C coupling. Coupling constants: $J(^{1}H_{ortho}\text{-}^{13}C)$ = 40 Hz, $J(^{1}H_{ortho}\text{-}^{13}C)$ = 178 Hz; $J(^{1}H_{meta}\text{-}^{13}C)$ = 40 Hz, $J(^{1}H_{meta}\text{-}^{13}C)$ = 162 Hz; $J(^{1}H_{para}\text{-}^{13}C)$ = 40 Hz, $J(^{1}H_{para}\text{-}^{13}C)$ = 163 Hz.

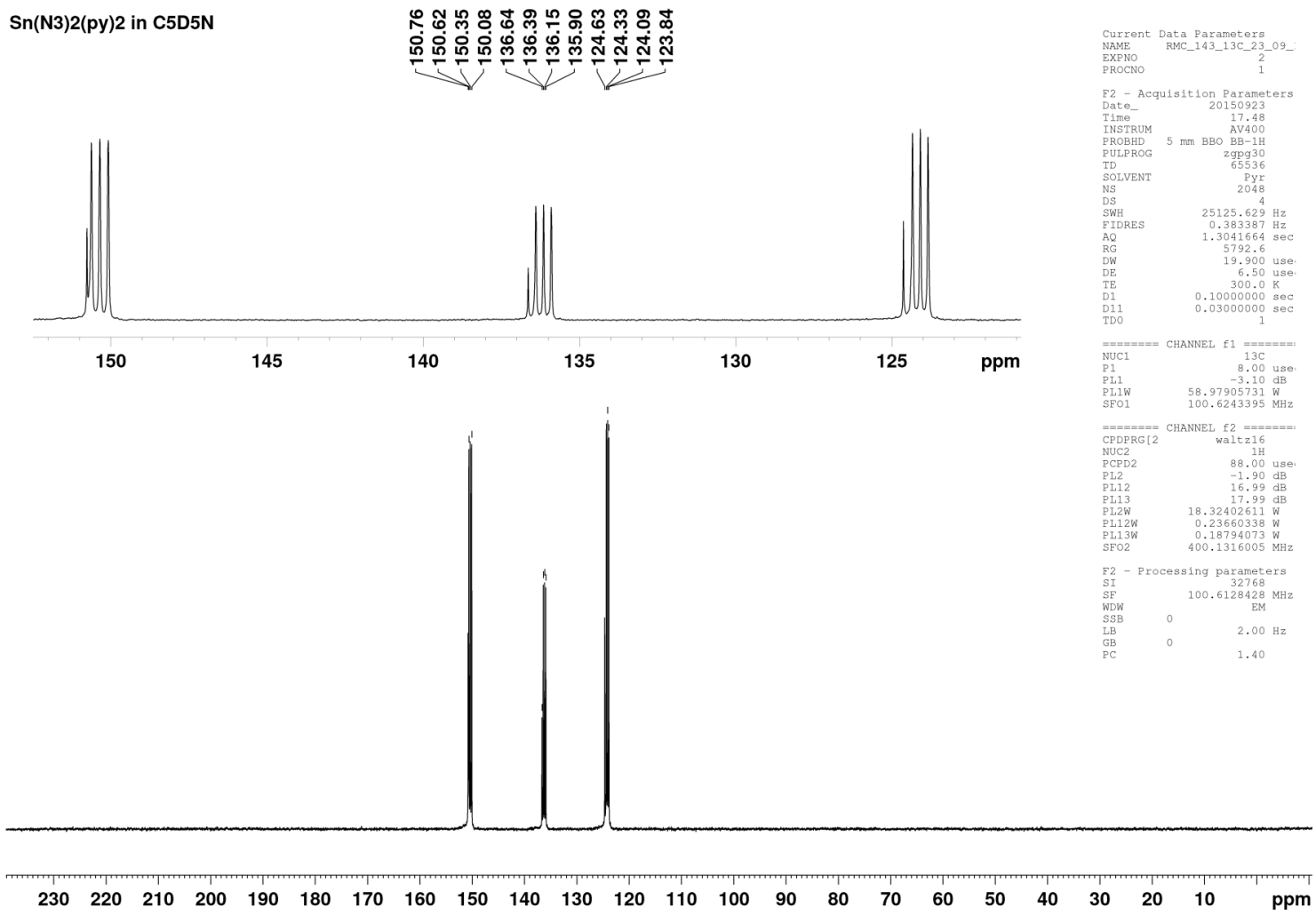

Figure 7.30. ^{13}C NMR spectrum of $Sn(N_3)_2(py)_2$ (**14**) in pyridine-d_5 calibrated against the solvent residual peak at 150.35 ppm (1 : 1 : 1 triplet) according to Cambridge Isotope Laboratories: http://www2.chem.umd.edu/nmr/reference/isotope_solvent.pdf. Less intense singlet peaks are visible very close to the solvent residual peaks, which are likely to be free pyridine.

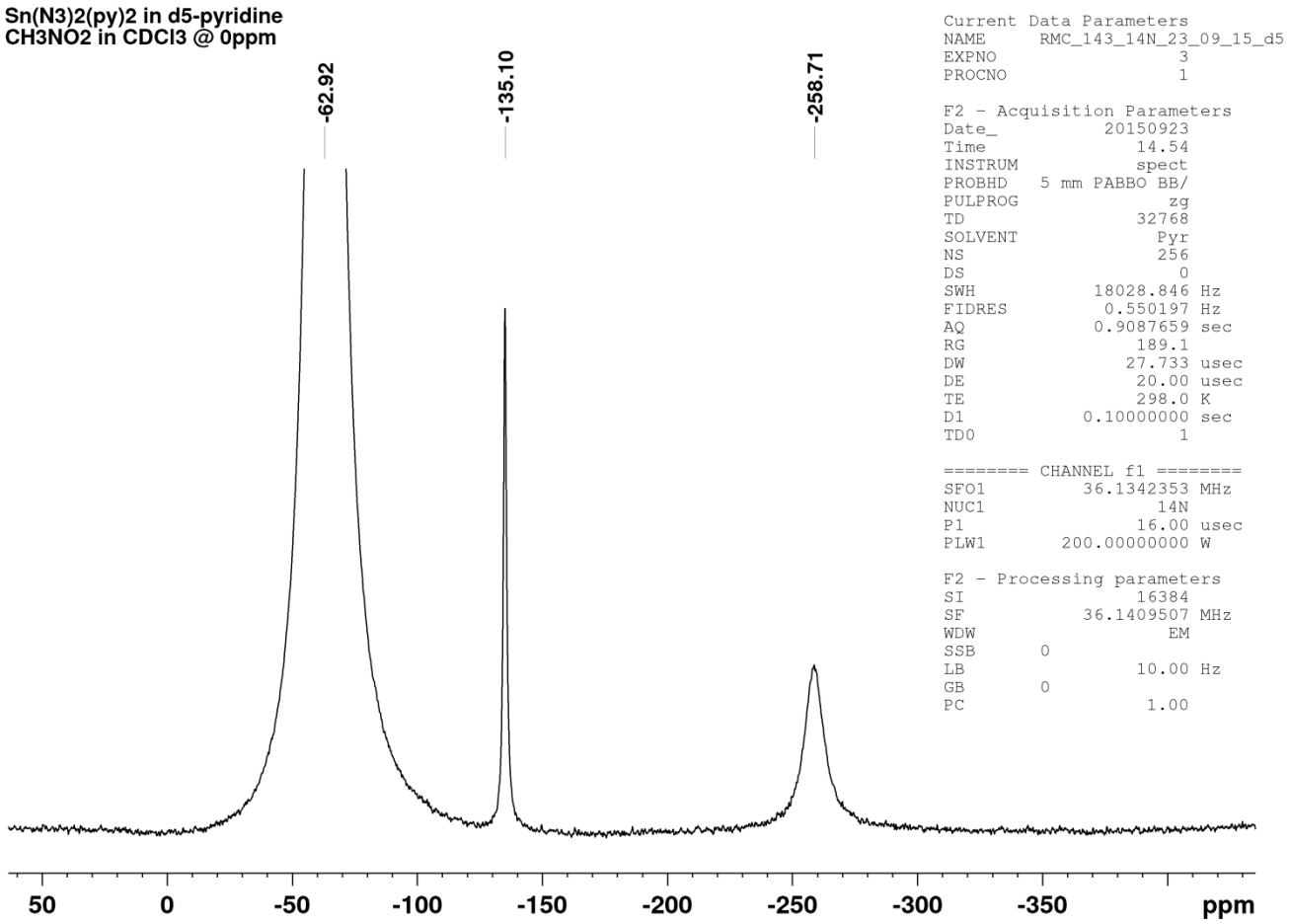


```
Current Data Parameters
NAME     RMC_143_14N_23_09_15_d5
EXPNO                 3
PROCNO                1

F2 - Acquisition Parameters
Date_          20150923
Time              14.54
INSTRUM           spect
PROBHD   5 mm PABBO BB/
PULPROG             zg
TD                32768
SOLVENT             Pyr
NS                  256
DS                    0
SWH           18028.846 Hz
FIDRES         0.550197 Hz
AQ            0.9087659 sec
RG                189.1
DW               27.733 usec
DE                20.00 usec
TE                298.0 K
D1           0.10000000 sec
TD0                   1

======== CHANNEL f1 ========
SFO1         36.1342353 MHz
NUC1                14N
P1                16.00 usec
PLW1       200.00000000 W

F2 - Processing parameters
SI                16384
SF           36.1409507 MHz
WDW                  EM
SSB       0
LB                10.00 Hz
GB        0
PC                 1.00
```

Figure 7.31. ^{14}N NMR of $Sn(N_3)_2(py)_2$ (**14**) in pyridine-d_5 referenced to CH_3NO_2 in $CDCl_3$ at 0 ppm.

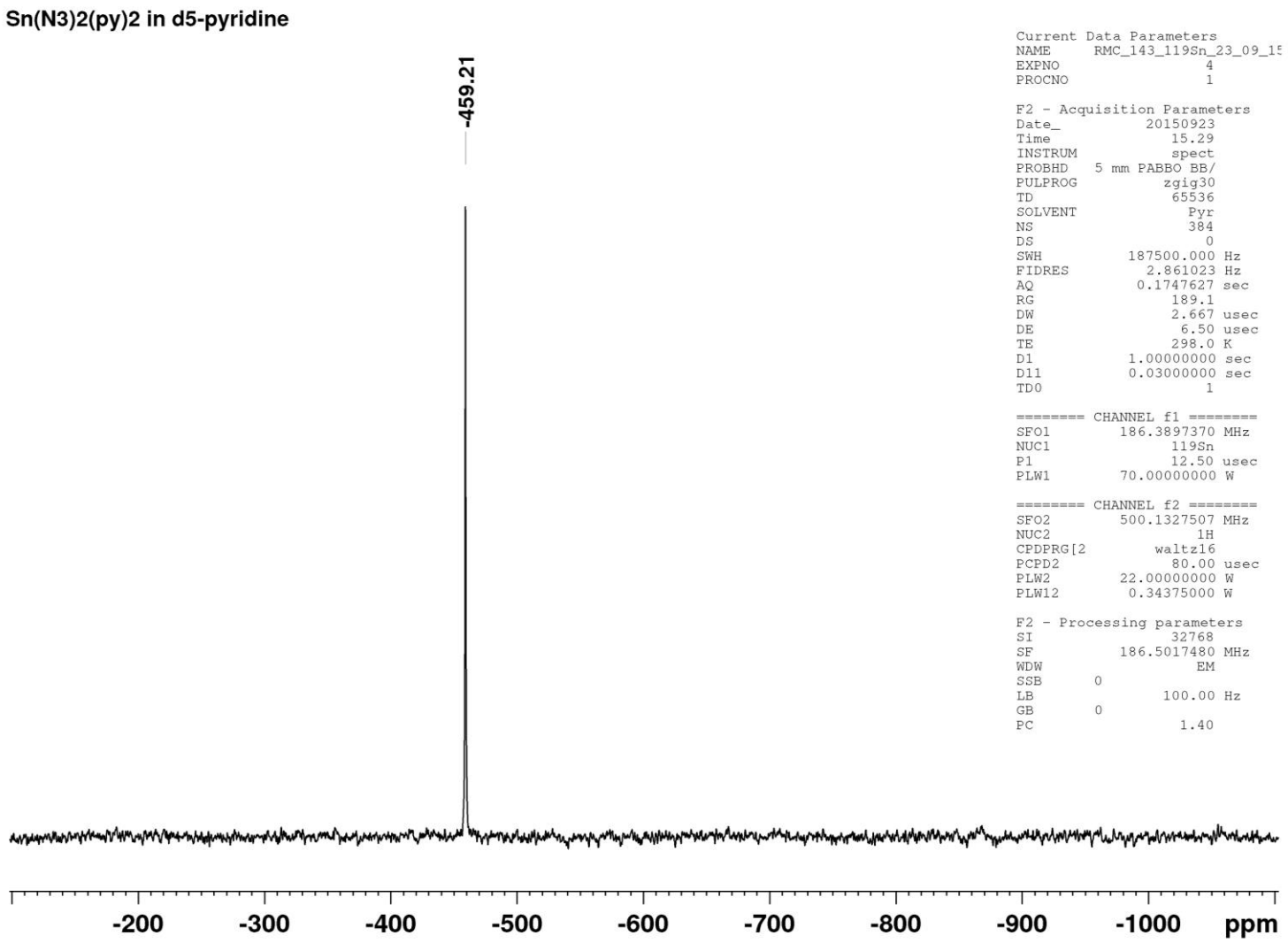

Figure 7.32. ^{119}Sn NMR of $Sn(N_3)_2(py)_2$ (**14**) in pyridine-d_5.

7.1.11 Diazidobis(4-picoline)tin, $Sn(N_3)_2(pic)_2$ (15) in d_5-pyridine

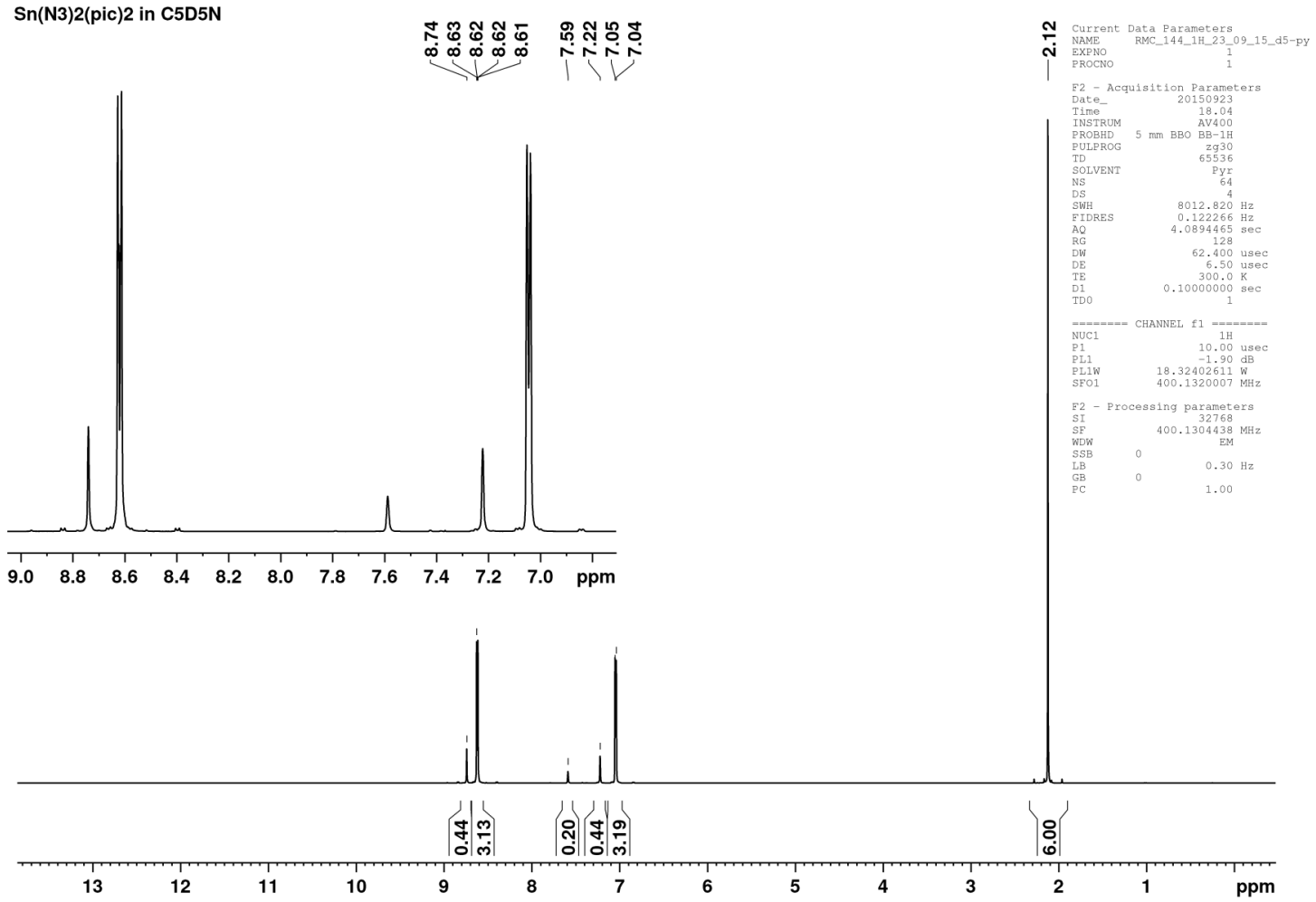

Figure 7.33. ^{1}H NMR spectrum of $Sn(N_3)_2(pic)_2$ (**15**) in pyridine-d_5, calibrated against solvent residual at 8.74 ppm according to Cambridge Isotope Laboratories: http://www2.chem.umd.edu/nmr/reference/isotope_solvent.pdf.

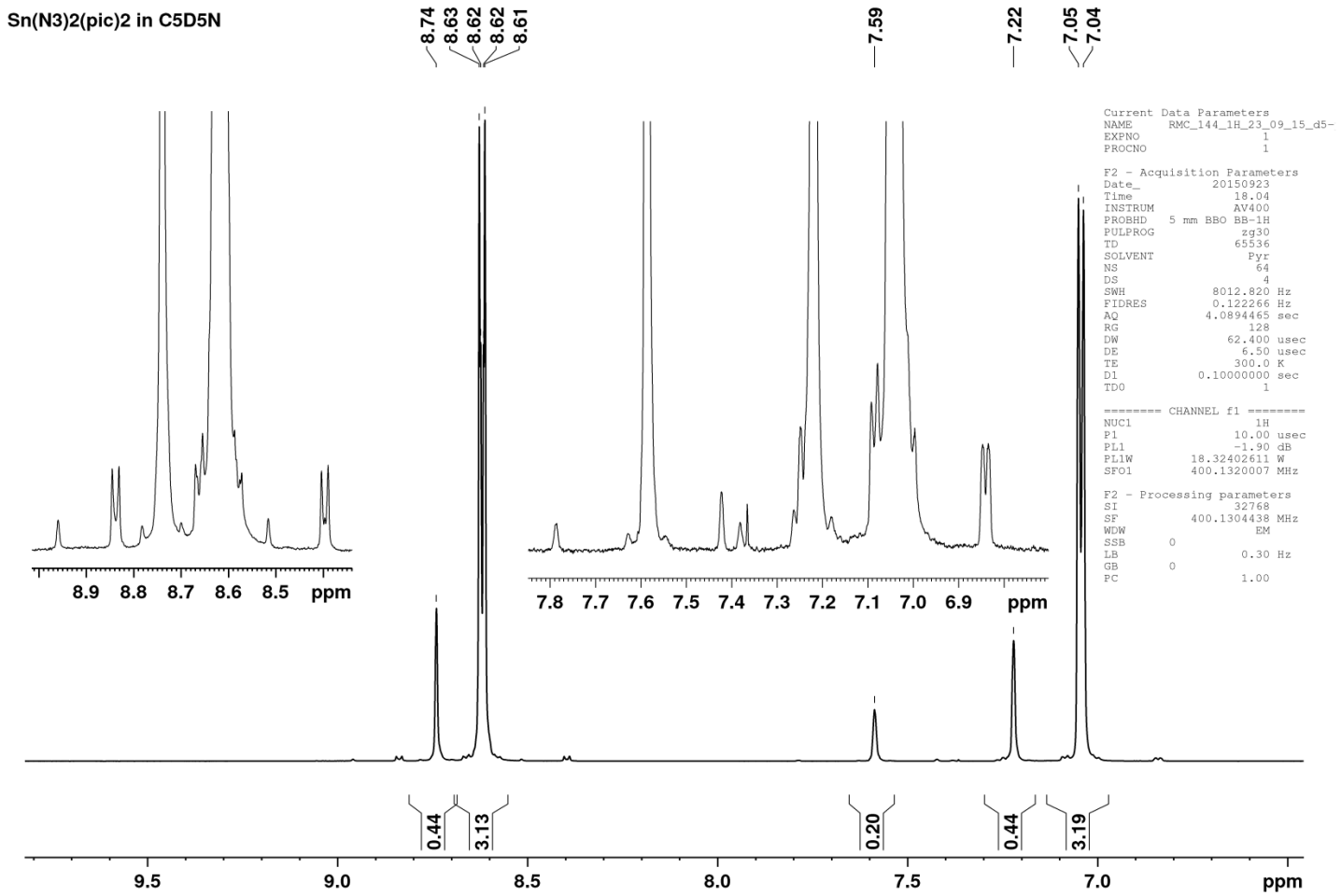

Figure 7.34. Expanded view of the ^{1}H NMR spectrum of $Sn(N_3)_2(pic)_2$ (**15**) in d_5-pyridine showing the satellite peaks due to coupling to ^{13}C and ^{119}Sn. Coupling constants for 4-picoline: $J(^{1}H_{methyl}\text{-}^{13}C)$ = 33 Hz, $J(^{1}H_{methyl}\text{-}^{13}C)$ = 127 Hz; $J(^{1}H_{ortho}\text{-}^{13}C)$ = 33 Hz, $J(^{1}H_{ortho}\text{-}^{13}C)$ = 177 Hz; $J(^{1}H_{meta}\text{-}^{13}C)$ = 33 Hz, $J(^{1}H_{meta}\text{-}^{13}C)$ = 160 Hz. Coupling constants for pyridine solvent residual: $J(^{1}H_{ortho}\text{-}^{13}C)$ = 33 Hz, $J(^{1}H_{ortho}\text{-}^{13}C)$ = 178 Hz; $J(^{1}H_{para}\text{-}^{13}C)$ = 33 Hz, $J(^{1}H_{para}\text{-}^{13}C)$ = 163 Hz; $J(^{1}H_{meta}\text{-}^{13}C)$ = 33 Hz, $J(^{1}H_{meta}\text{-}^{13}C)$ = 163 Hz.

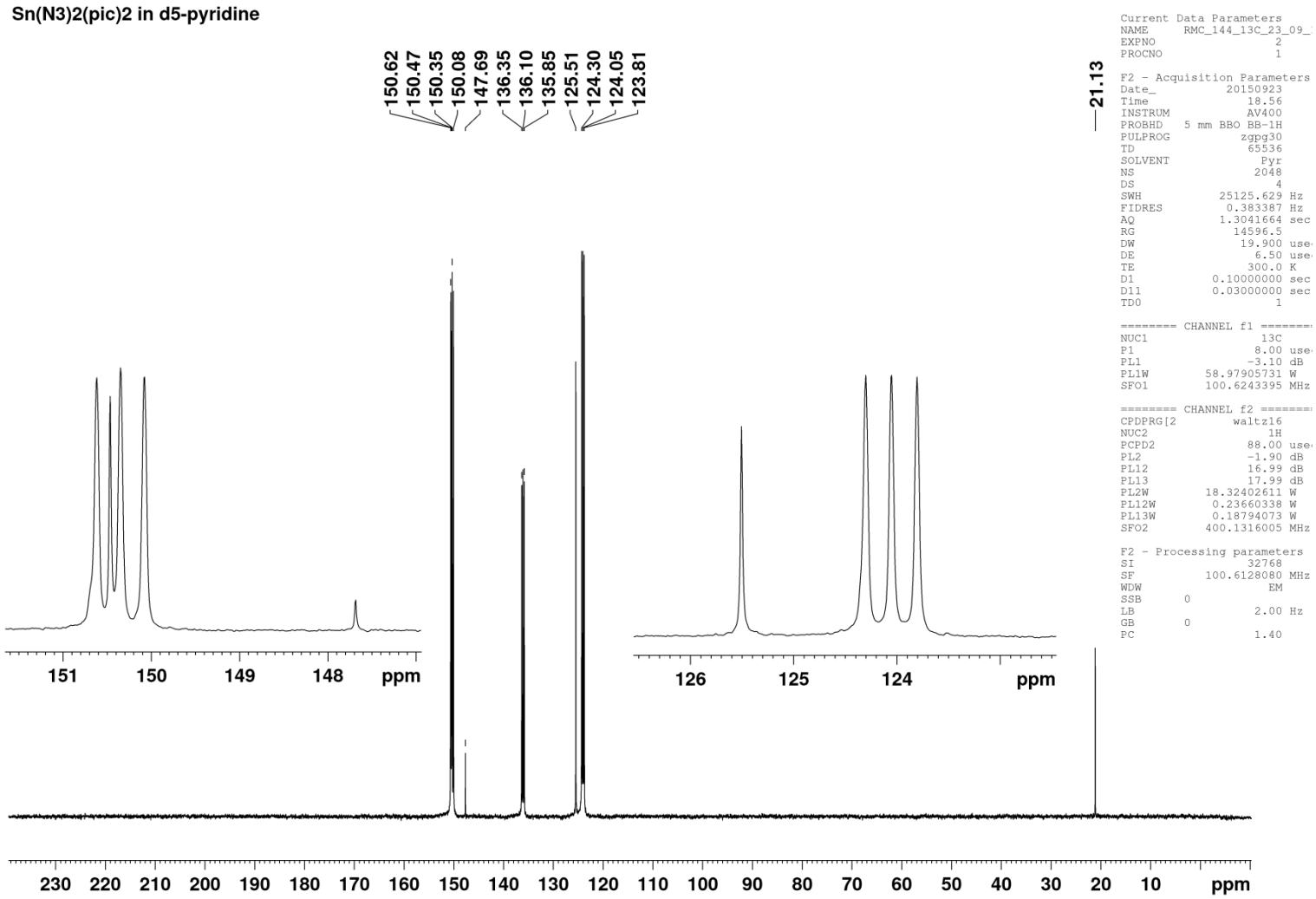

Figure 7.35. ^{13}C NMR spectrum of $Sn(N_3)_2(pic)_2$ (**15**) in pyridine-d_5.

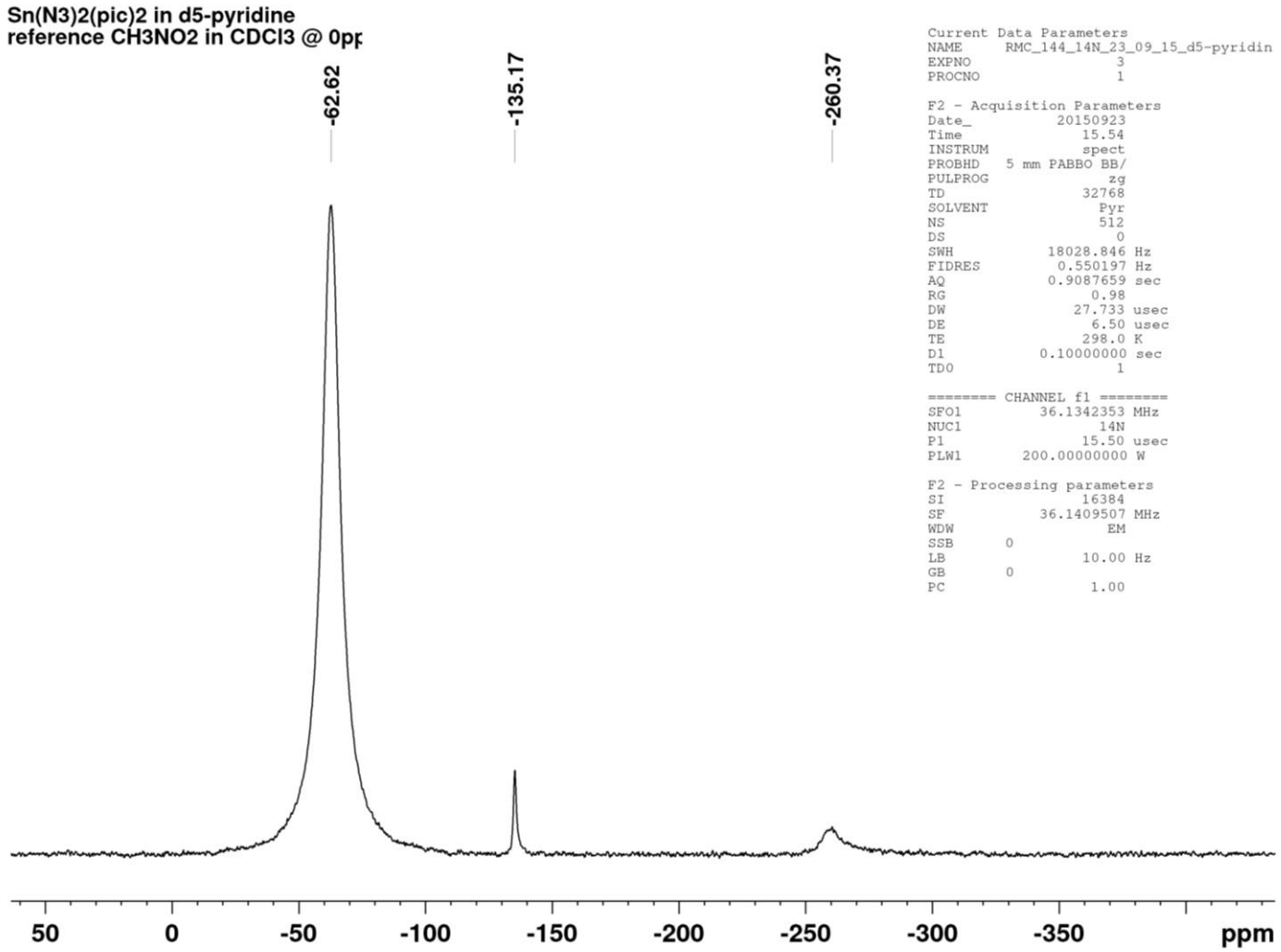

Figure 7.36. ^{14}N NMR of $Sn(N_3)_2(pic)_2$ (**15**) in pyridine-d_5 referenced against CH_3NO_2 in $CDCl_3$ at 0 ppm. Solvent/4-picoline: –62.6 ppm, $\Delta\nu_{1/2}$ = 292 Hz; N_β = –135.1 ppm, $\Delta\nu_{1/2}$ = 51 Hz; N_α = –260.4 ppm, $\Delta\nu_{1/2}$ = 305 Hz.

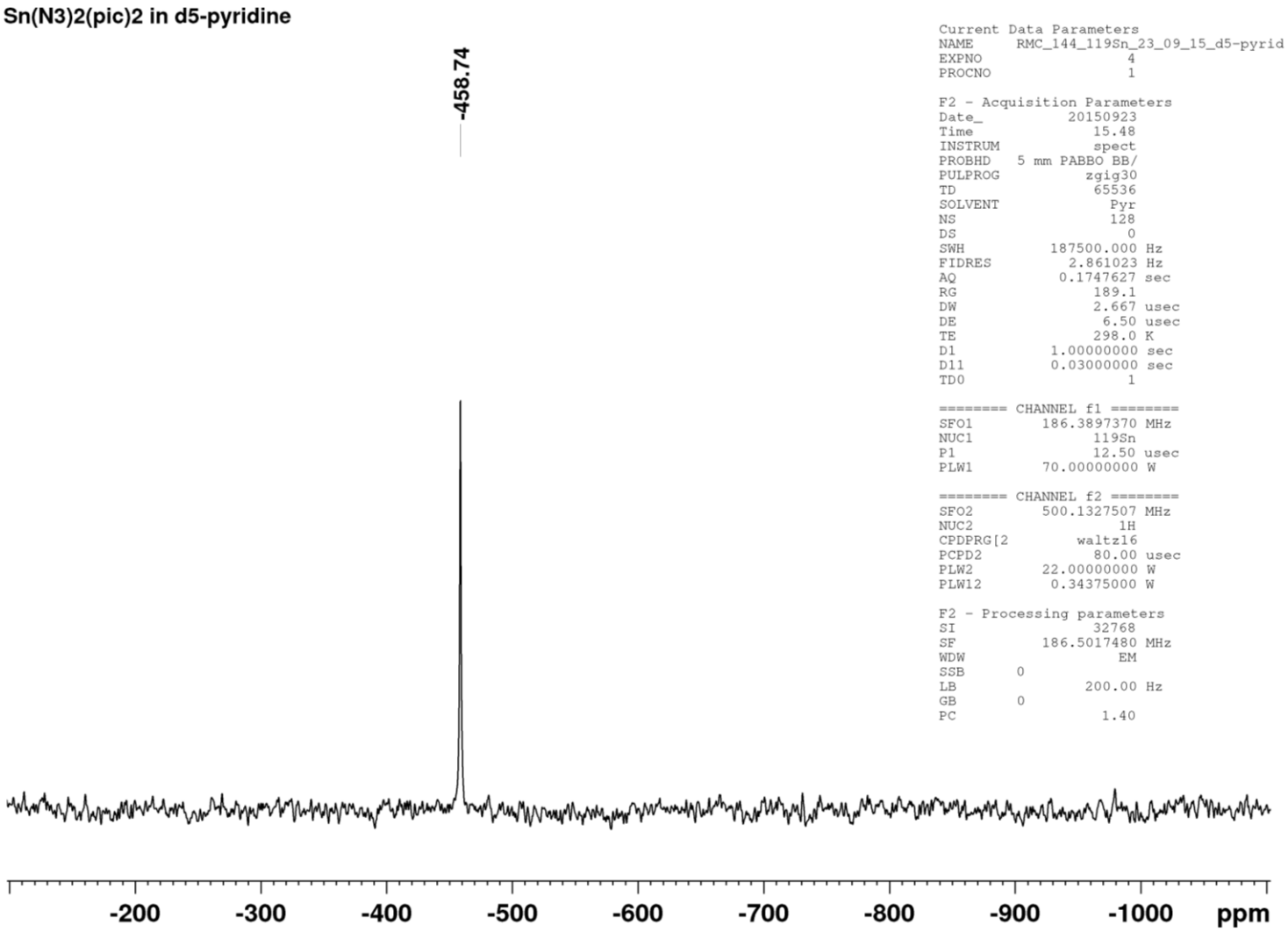

Figure 7.37. ^{119}Sn NMR of $Sn(N_3)_2(pic)_2$ (**15**) in pyridine-d_5.

7.1.12 Guanidinium Triazidostannate, $GSn(N_3)_3$ (17) in CD_3CN

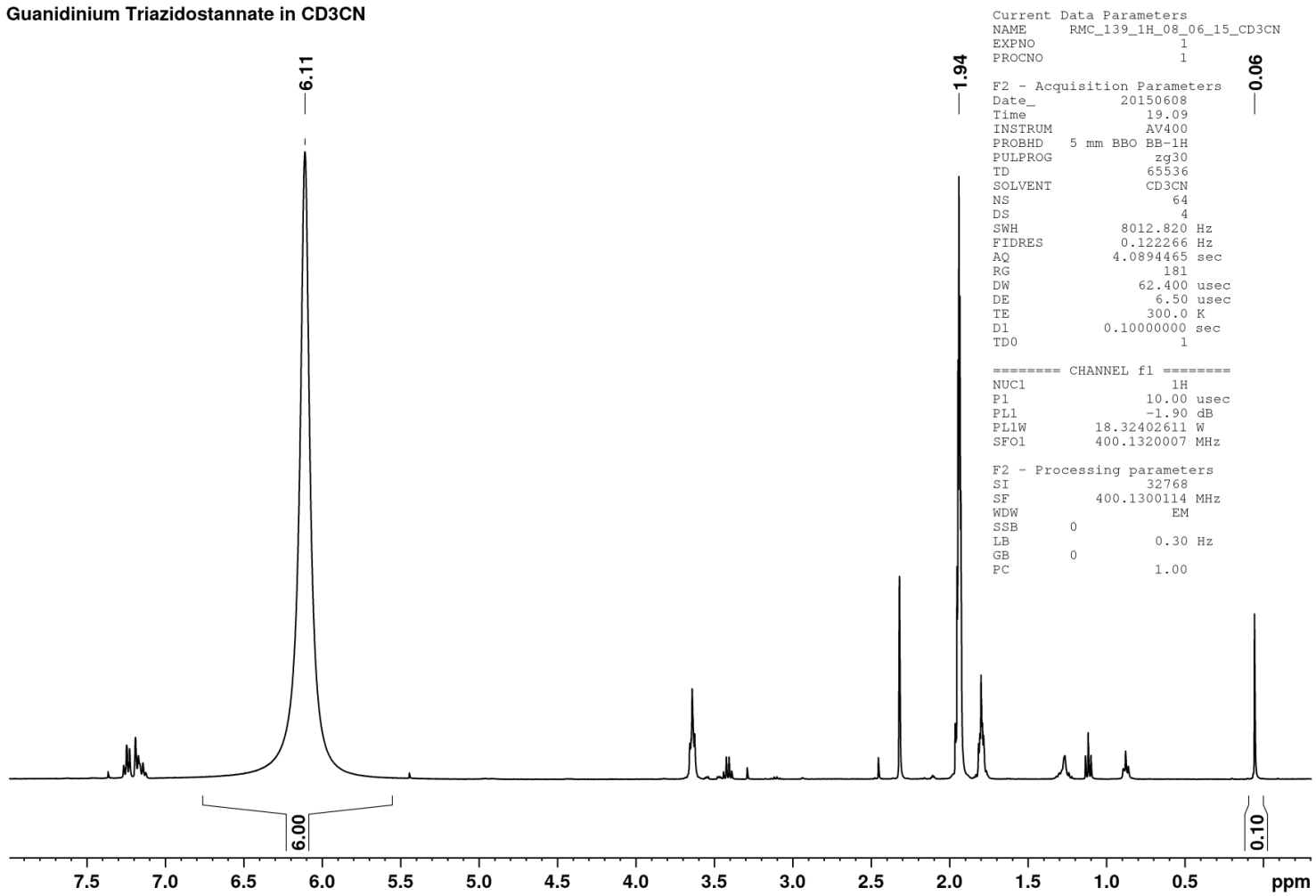

Figure 7.38. ^{1}H NMR of guanidinium triazidostannate (**17**) in CD_3CN, with a trace (*ca.* 1 %) of residual TMS–N_3 at 0.05 ppm. Additional peaks are contamination of the NMR solvent by Et_2O, THF, *n*-hexane and toluene.

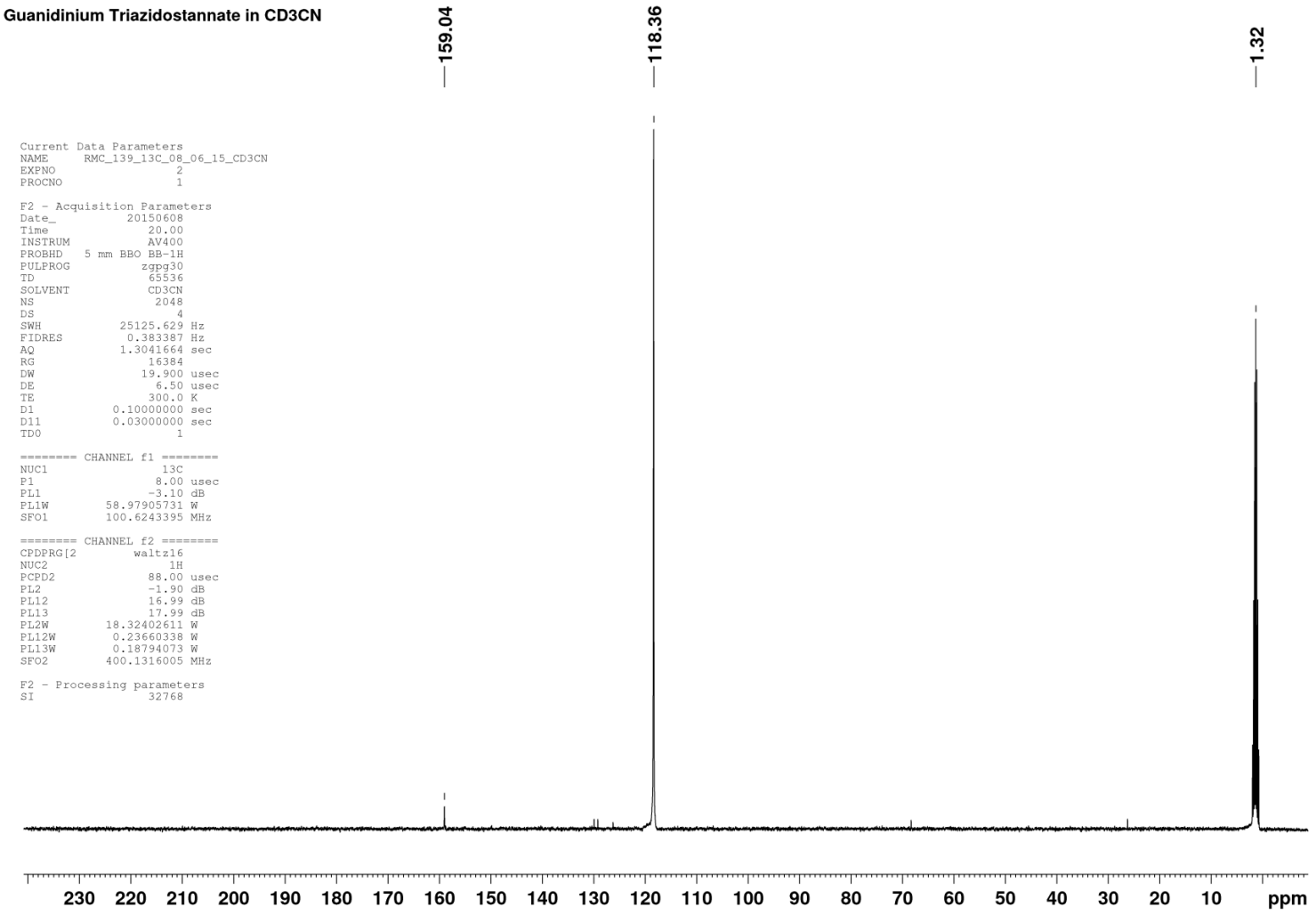

Figure 7.39. ^{13}C NMR (cpd) of guanidinium triazidostannate (**17**) in CD_3CN. Additional peaks are due to contamination of the NMR solvent with toluene and THF.

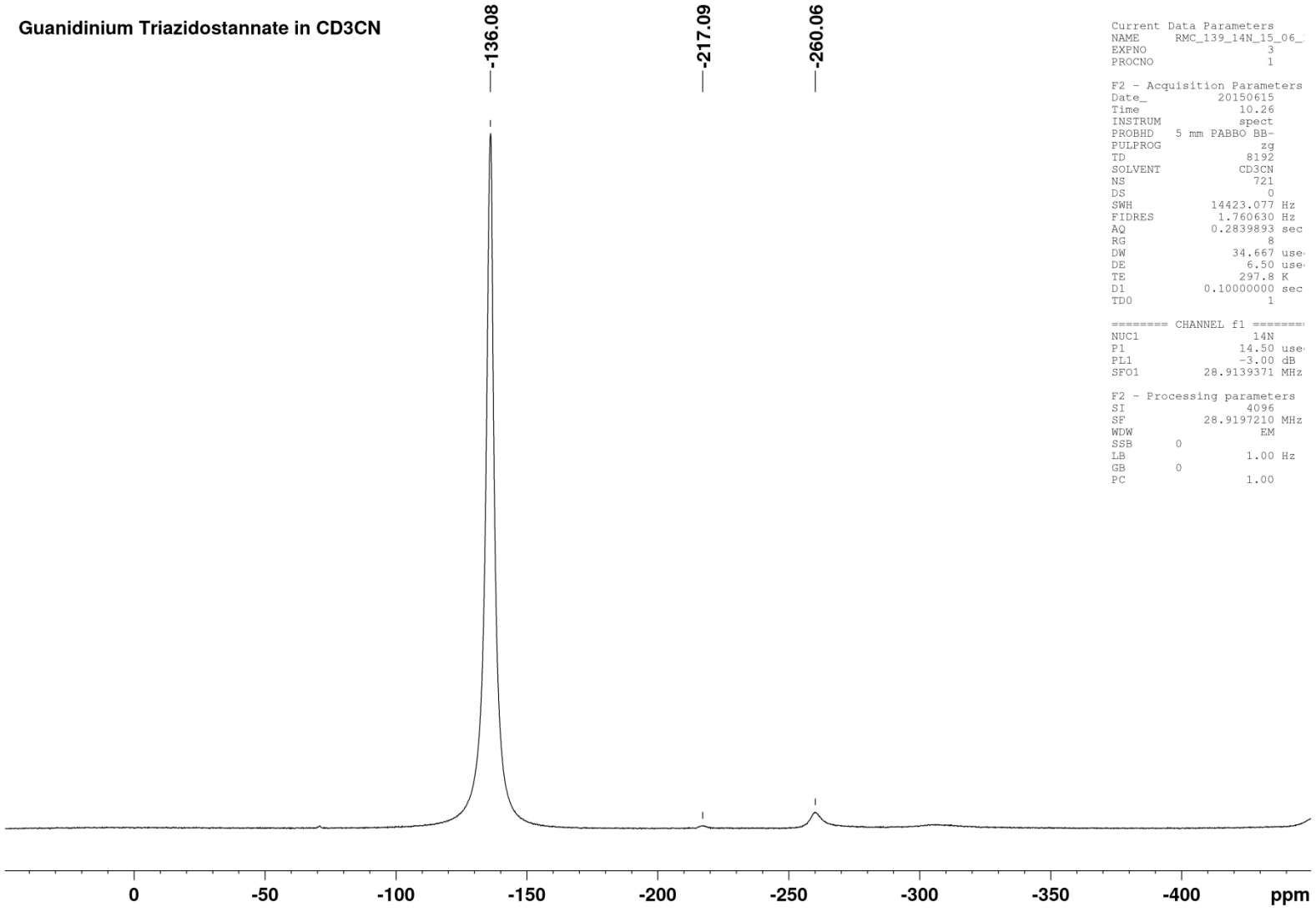

Figure 7.40. ^{14}N NMR of guanidinium triazidostannate (**17**) in CD_3CN. δ [ppm]= –217.09, $\Delta\nu_{1/2}$ = 108 Hz, –260.06 $\Delta\nu_{1/2}$ = 162 Hz.

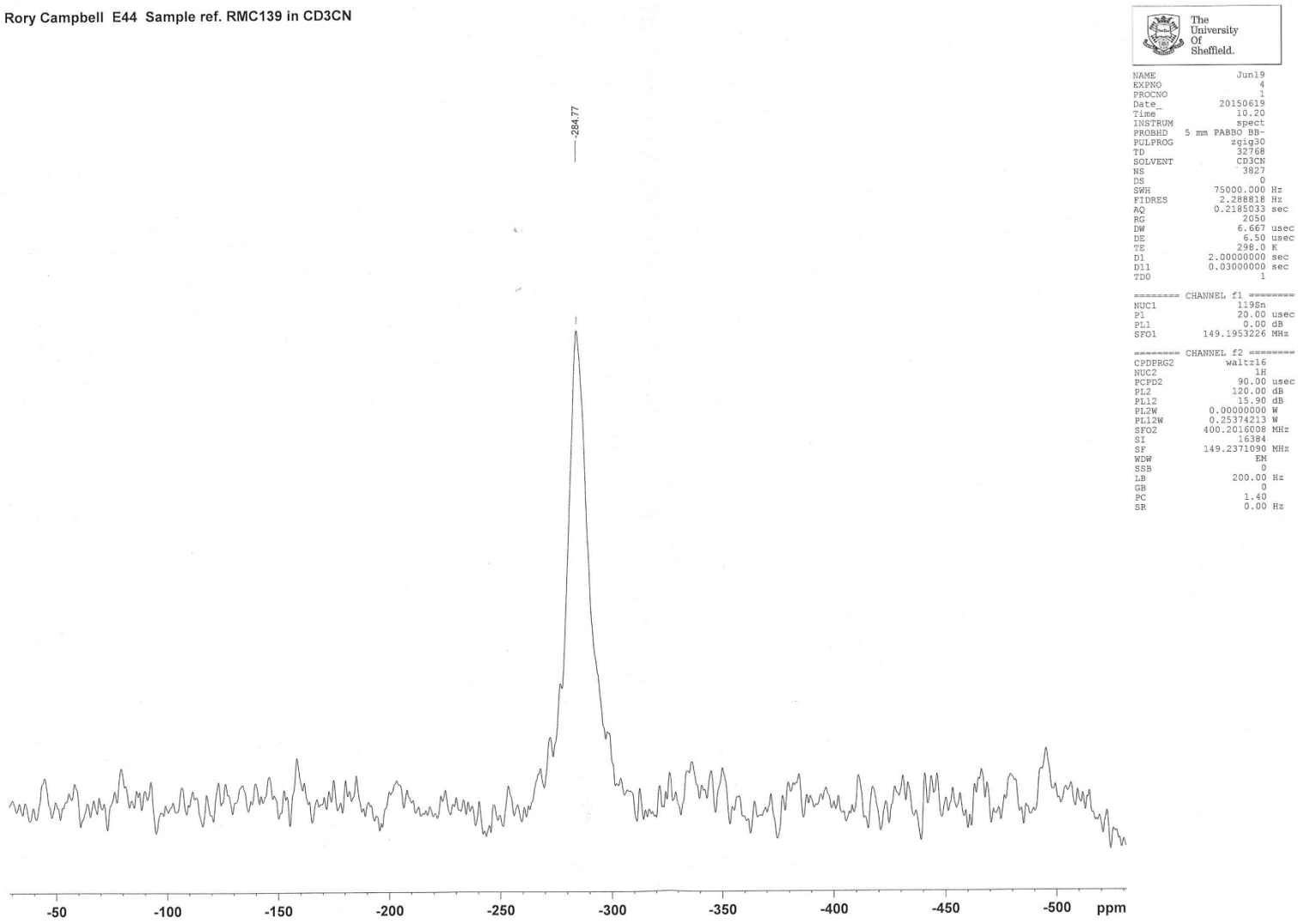

The University Of Sheffield.

NAME	Jun19
EXPNO	4
PROCNO	1
Date_	20150619
Time	10.20
INSTRUM	spect
PROBHD	5 mm PABBO BB-
PULPROG	zgig30
TD	32768
SOLVENT	CD3CN
NS	3827
DS	0
SWH	75000.000 Hz
FIDRES	2.288818 Hz
AQ	0.2185033 sec
RG	2050
DW	6.667 usec
DE	6.50 usec
TE	298.0 K
D1	2.00000000 sec
D11	0.03000000 sec
TD0	1
======== CHANNEL f1 ========	
NUC1	119Sn
P1	20.00 usec
PL1	0.00 dB
SFO1	149.1953226 MHz
======== CHANNEL f2 ========	
CPDPRG2	waltz16
NUC2	1H
PCPD2	90.00 usec
PL2	120.00 dB
PL12	15.90 dB
PL2W	0.00000000 W
PL12W	0.25374213 W
SFO2	400.2016008 MHz
SI	16384
SF	149.2371090 MHz
WDW	EM
SSB	0
LB	200.00 Hz
GB	0
PC	1.40
SR	0.00 Hz

Figure 7.41. ^{119}Sn NMR of guanidinium triazidostannate (**17**) in CD_3CN. Spectrum shows a single relatively low intensity peak (limited by solubility) at δ = –284.77 ppm.

7.2 FTIR Spectra

FTIR Spectra of compounds **9-12** are included in the supporting information of ref. [85].

7.2.1 Guanidinium Azide (1)

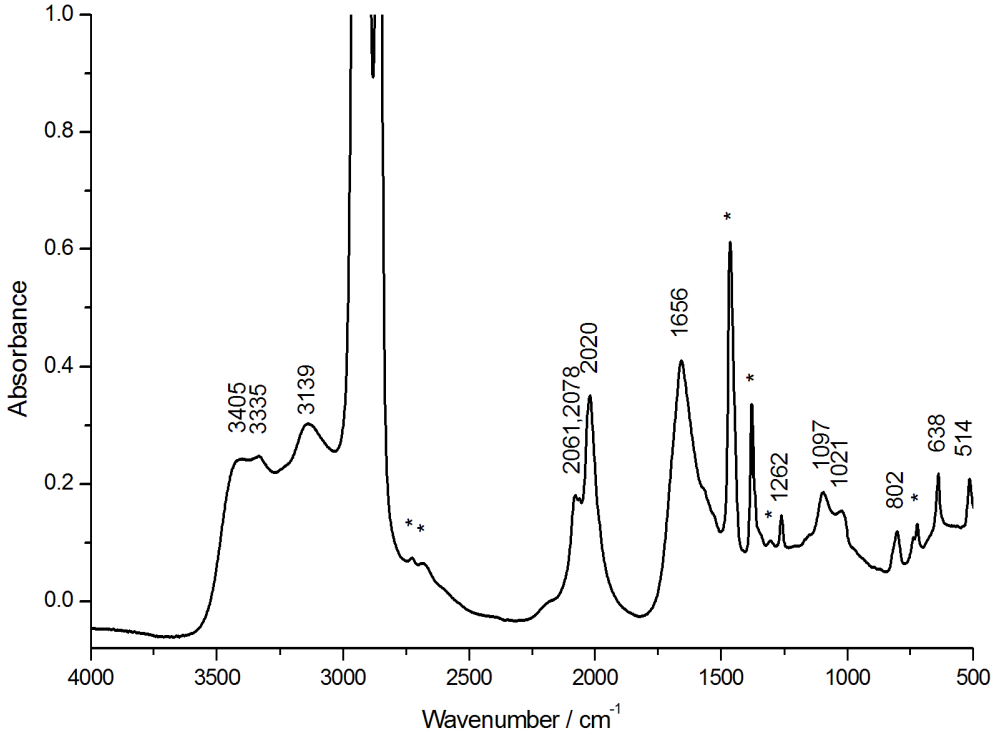

Figure 7.42. FTIR spectrum of guanidinium azide (**1**) in a nujol suspension. Peaks marked with an asterisk are those of the nujol mulling agent.

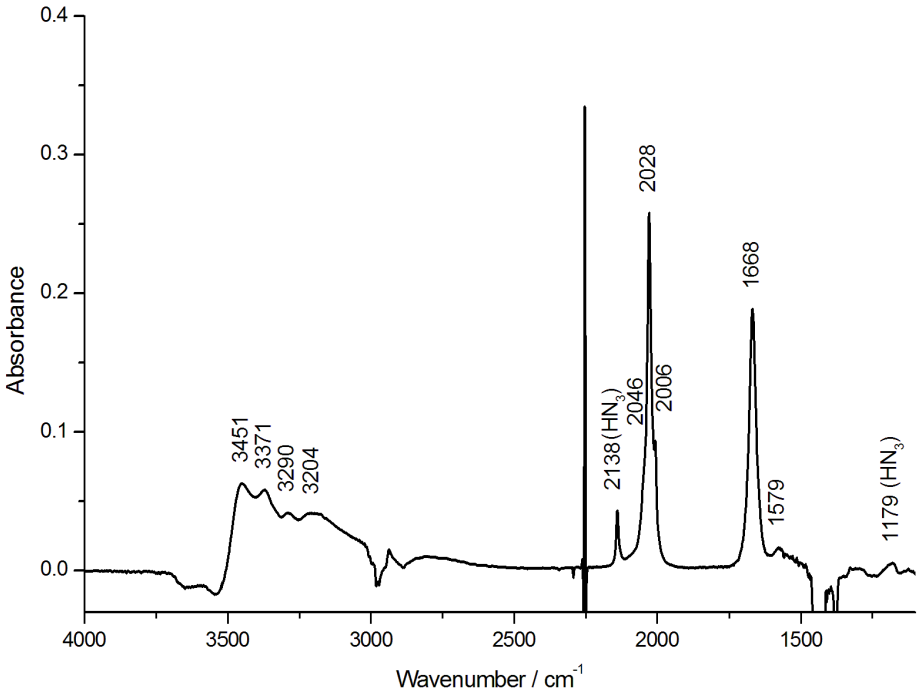

Figure 7.43. FTIR spectrum of a saturated solution of guanidinium azide (**1**) in MeCN.

7.2.2 Guanidinium azide monohydrate (1a)

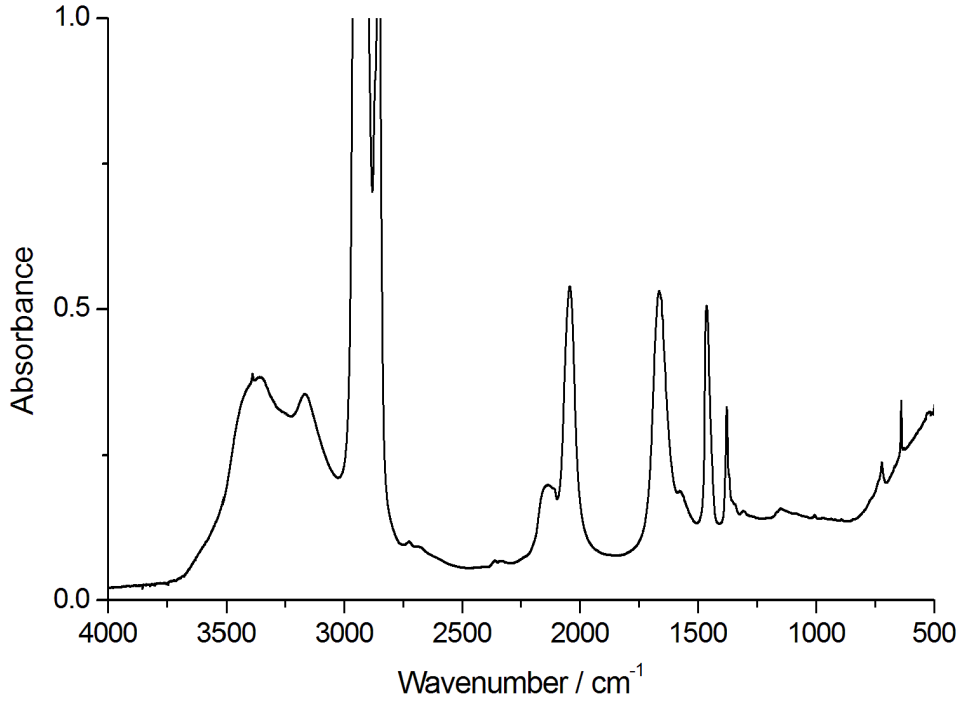

Figure 7.44. FTIR spectrum of guanidinium azide monohydrate (**1a**) as a nujol suspension. The spectrum always showed traces of NaN_3 at $\tilde{\nu}$ = 3389, 3300, 2130, and 639 cm^{-1} due to grinding between the NaCl windows.

7.2.3 Aminoguanidinium azide (2)

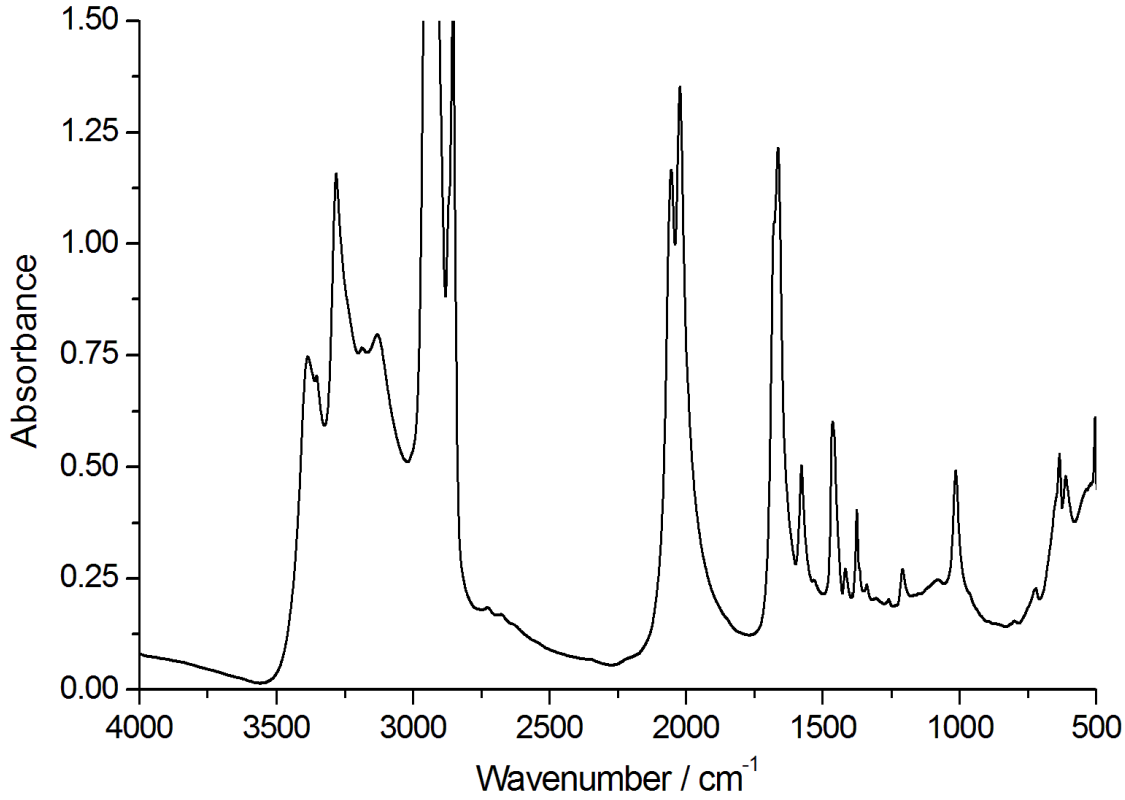

Figure 7.45. FTIR spectrum of aminoguanidinium azide (**2**) as a nujol suspension.

7.2.4 Bis(guanidinium) hexaazidostannate (3)

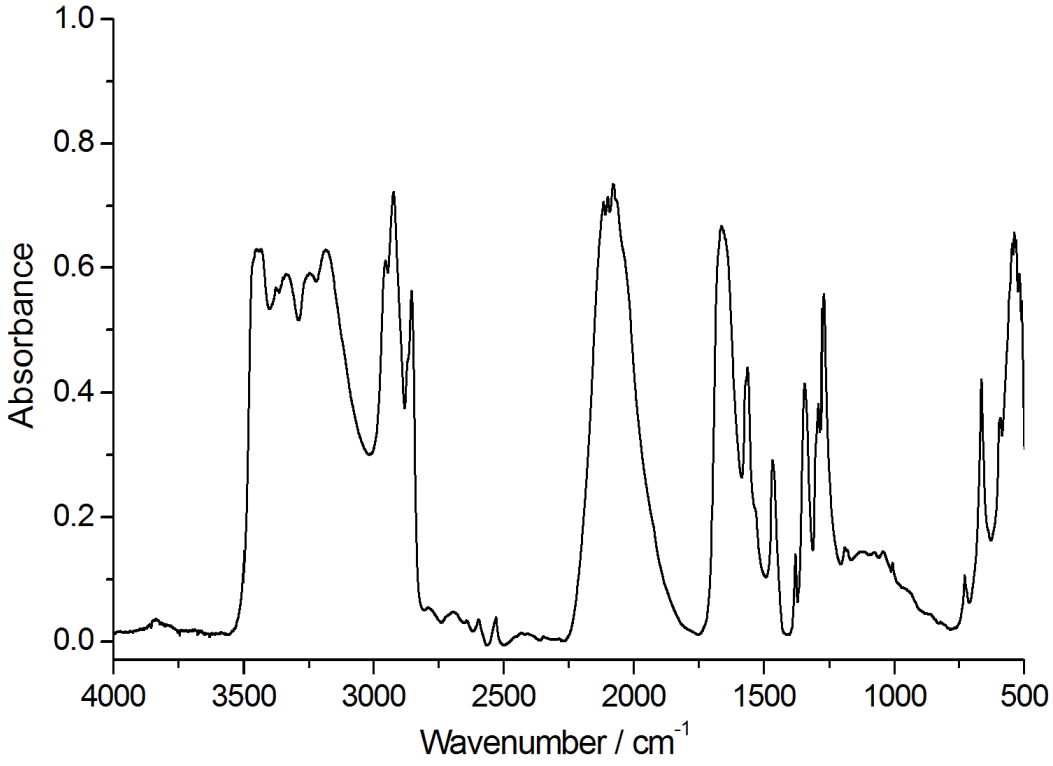

Figure 7.46. FTIR spectrum of bis(guanidinium) hexaazidostannate (**3**) as a nujol suspension.

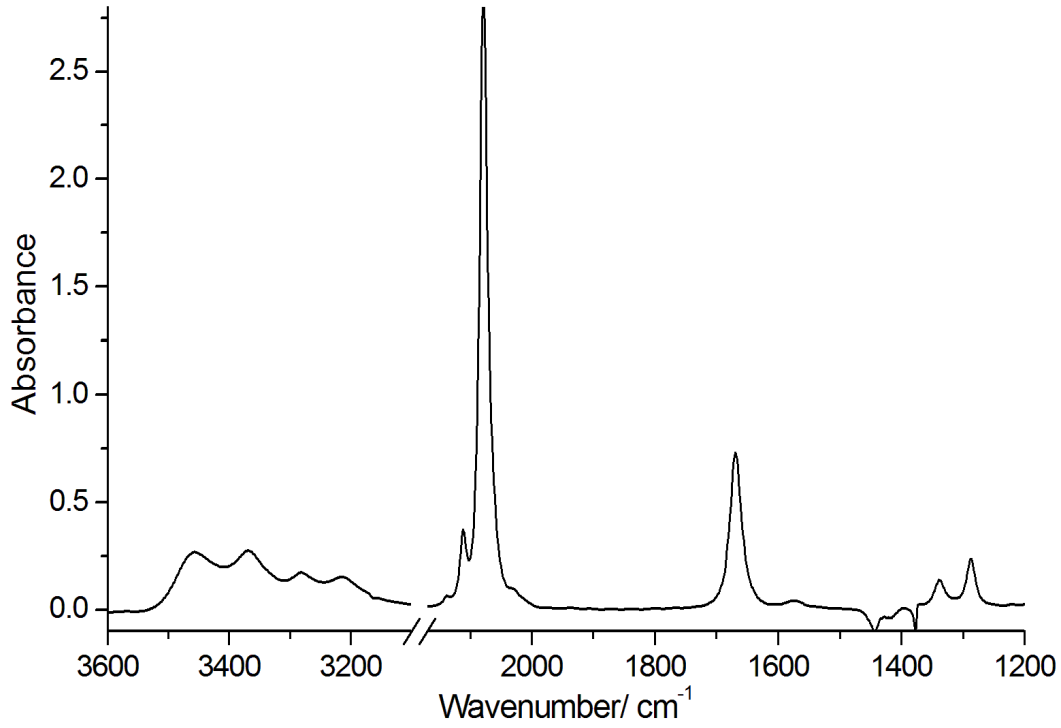

Figure 7.47. FTIR spectrum of bis(guanidinium) hexaazidostannate (**3**) in acetonitrile solution. N.B. spectral window 3100 – 2170 cm^{-1} omitted to allow expanded view.

7.2.5 Tetraazidobis(4-picoline)tin(IV) (13)

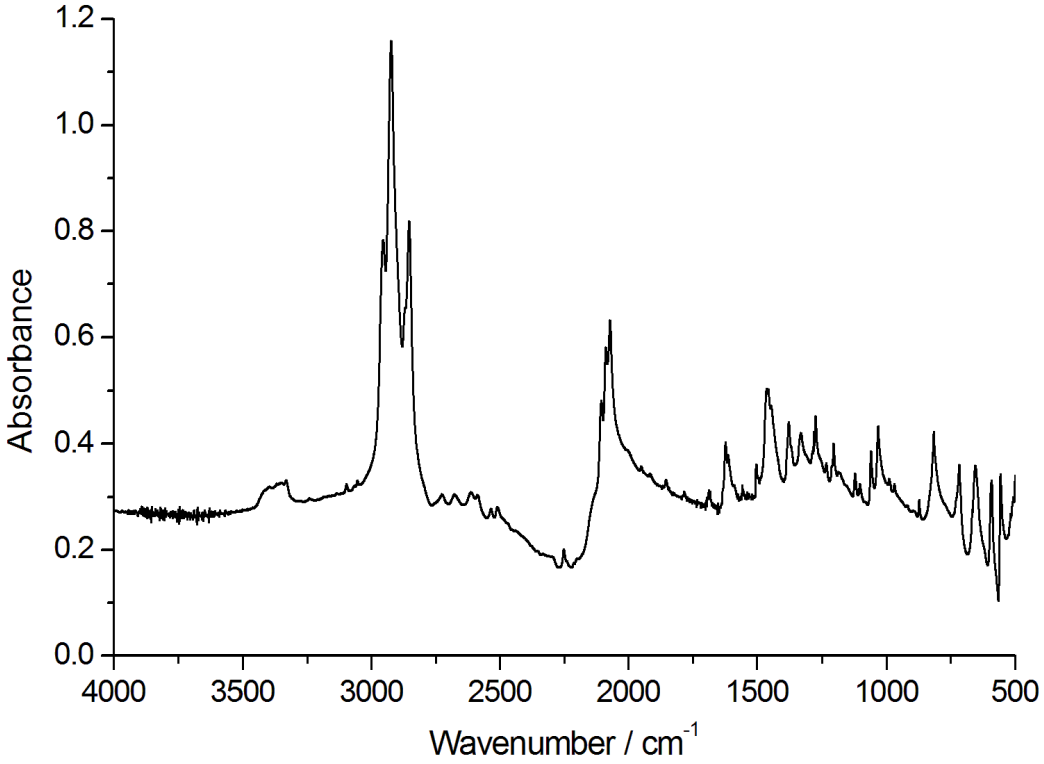

Figure 7.48. FTIR spectrum of tetraazidobis(4-picoline)tin (**13**) as a nujol suspension. N.B. the solid was crystallised from a warm mixture of acetonitrile and 4-picoline, and still contains a trace of acetonitrile (ν(CN) = 2254 cm^{-1}).

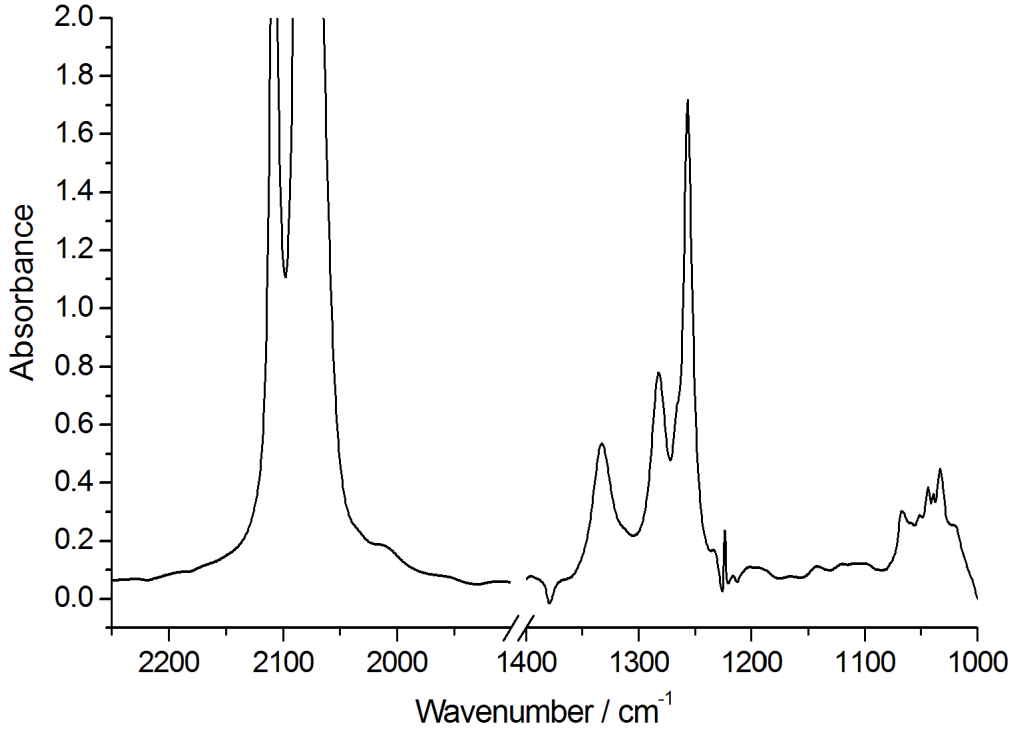

Figure 7.49. FTIR spectrum of tetraazidobis(4-picoline)tin (**13**) in 4-picoline solution. N.B. the spectrum is of a reaction solution, and still contains TMS–N_3/TMS–F at 1258 cm^{-1}.

7.2.6 Diazidobis(pyridine)tin(II) (14)

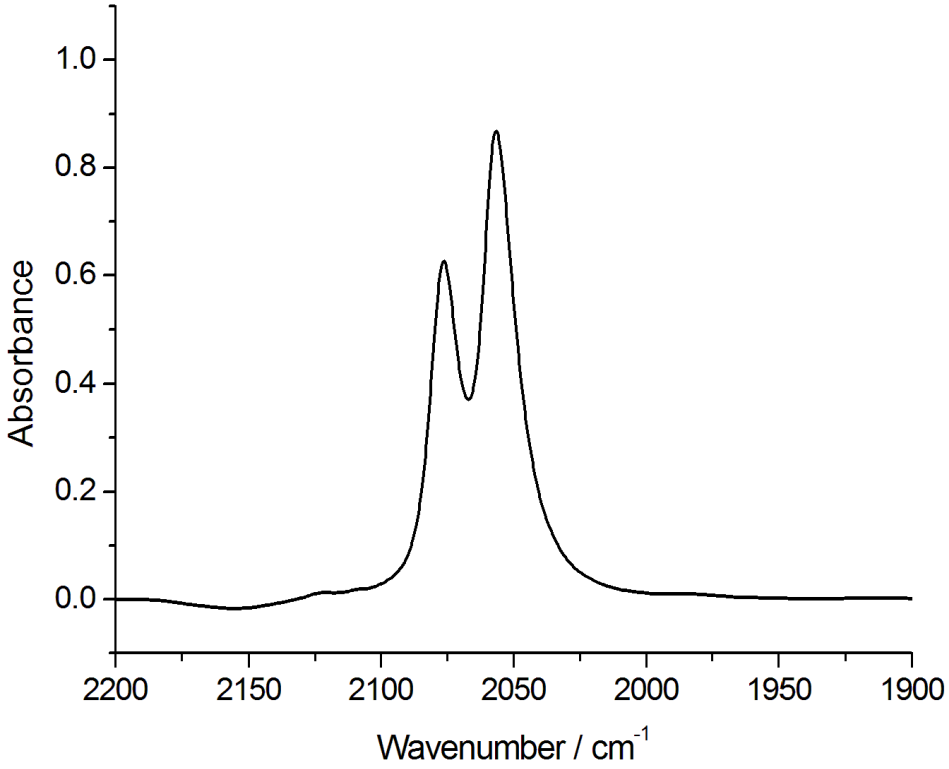

Figure 7.50. FTIR spectrum of $Sn(N_3)_2(py)_2$ (**14**) in pyridine solution showing the asymmetric azide stretch region.

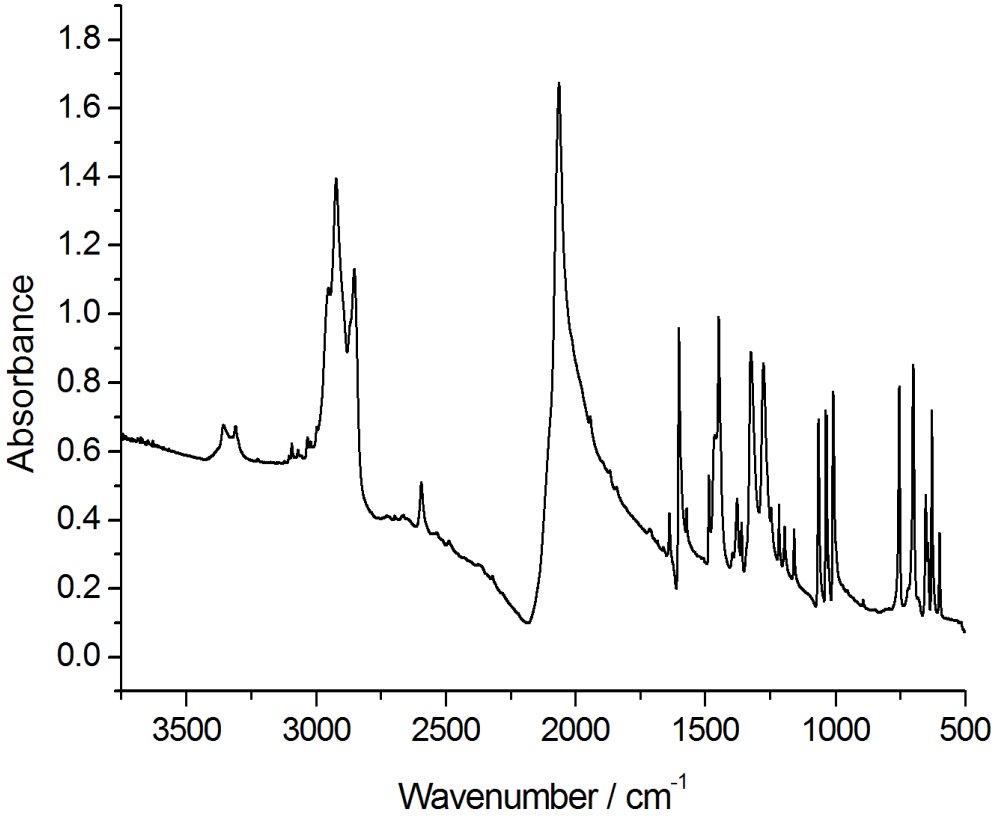

Figure 7.51. FTIR spectrum of $Sn(N_3)_2(py)_2$ (**14**) as a nujol suspension.

7.2.7 Diazidobis(4-picoline)tin(II) (15)

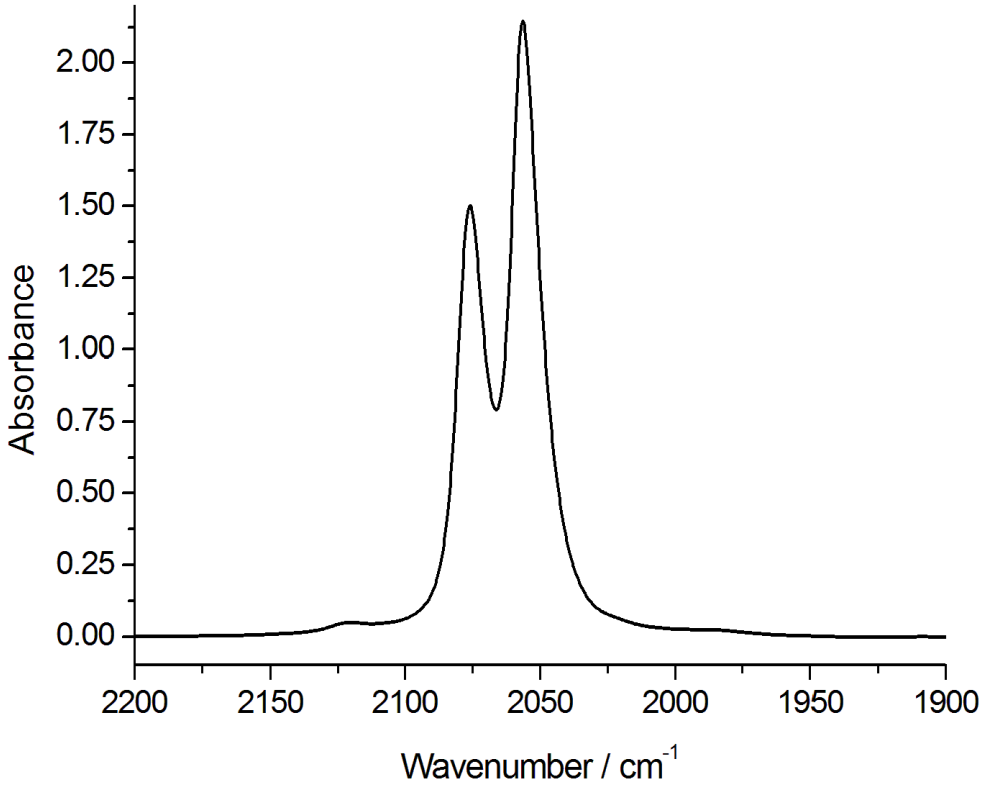

Figure 7.52. FTIR spectrum of $Sn(N_3)_2(pic)_2$ (**15**) in 4-picoline solution.

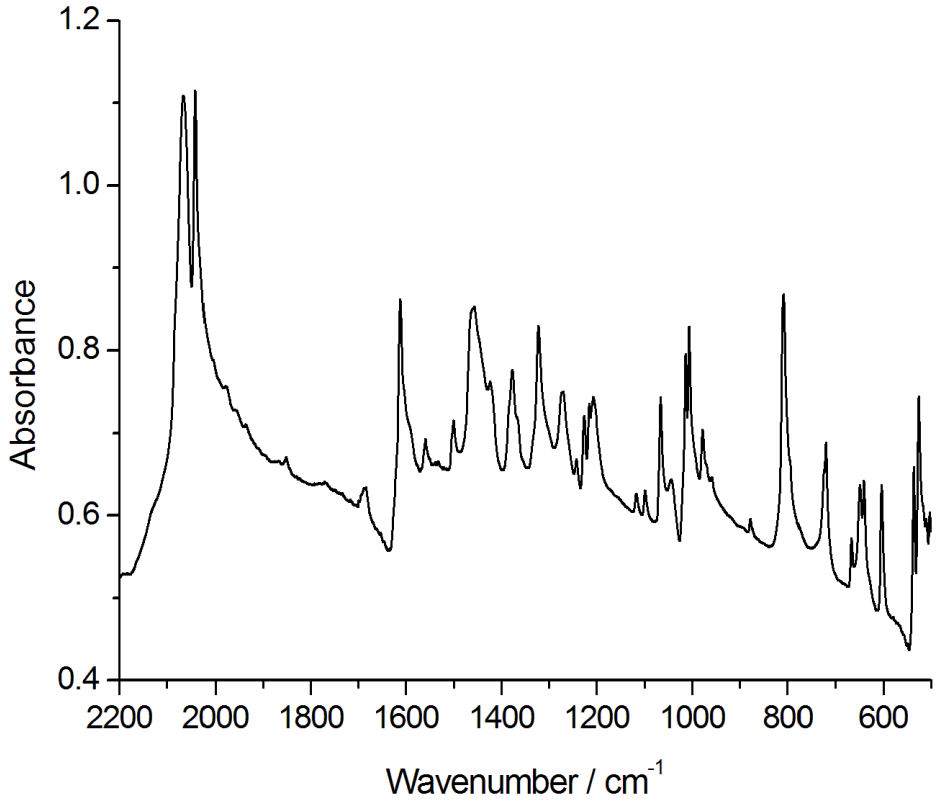

Figure 7.53. FTIR spectrum of $Sn(N_3)_2(pic)_2$ (**15**) as a nujol suspension.

7.2.8 Guanidinium triazidostannate(II) (17)

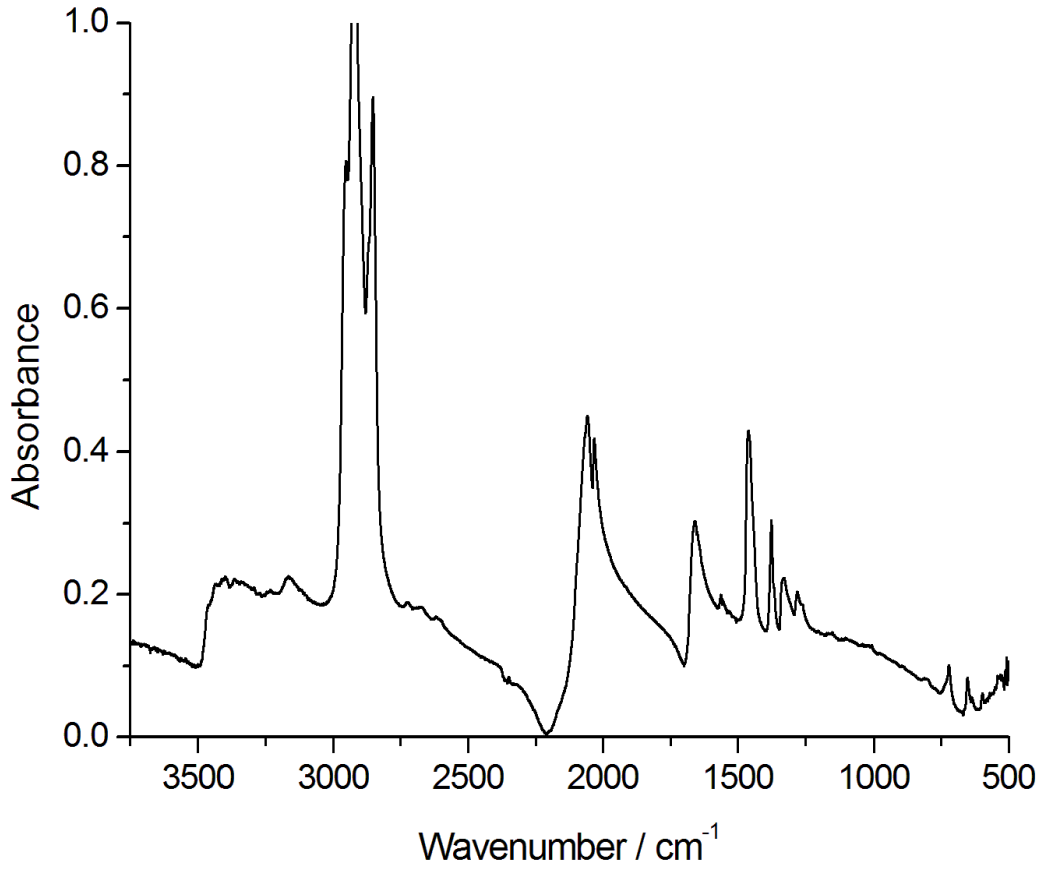

Figure 7.54. FTIR spectrum of guanidinium triazidostannate (**17**) as a nujol suspension.

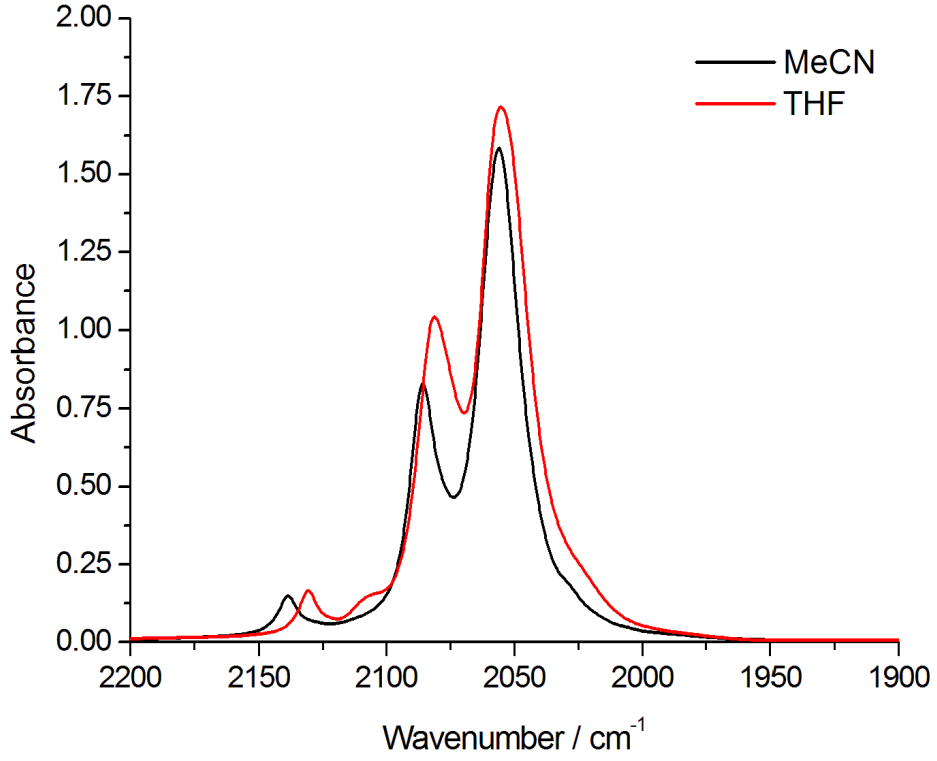

Figure 7.55. FTIR spectra of guanidinium triazidostannate (**17**) in acetonitrile (black) and THF (red) solutions.

7.2.9 Guanidinium tetrazolate (19)

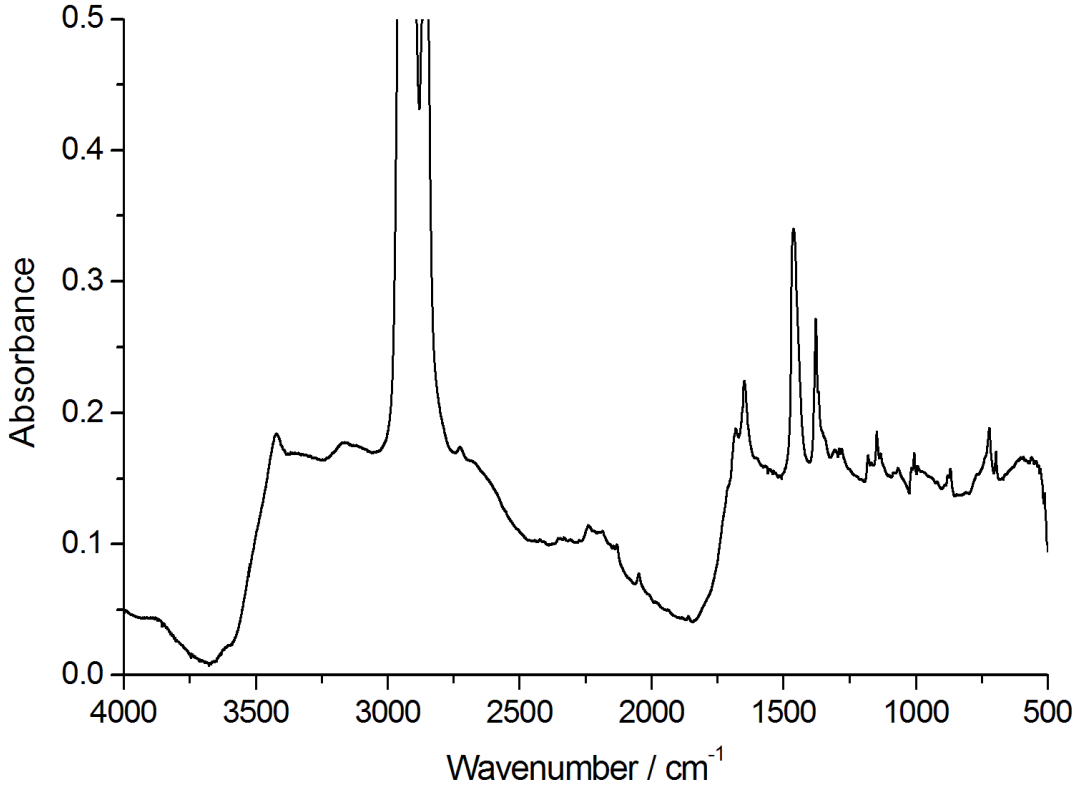

Figure 7.56. FTIR spectrum of guanidinium tetrazolate (**19**) as a nujol suspension.

7.3 DSC Thermograms

For full details on the methods, instruments, software, and calibrants used during thermal measurements see Experimental section 6.1.

7.3.1 Guanidinium tetrazolate DSC

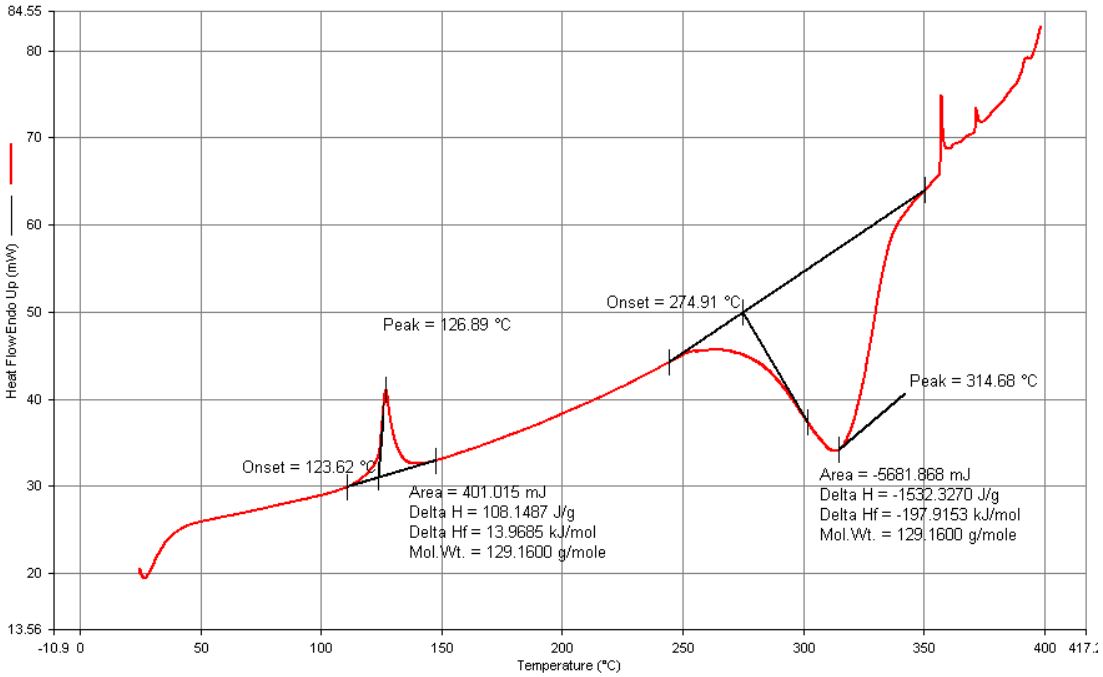

Figure 7.57. Differential scanning calorimetry trace of guanidinium tetrazolate (**19**). Heating rate 10 °C min^{-1}, nitrogen flow rate 20 ml min^{-1}.

7.3.2 Tetraazido(2,2'-bipyridine)tin (10) DSC

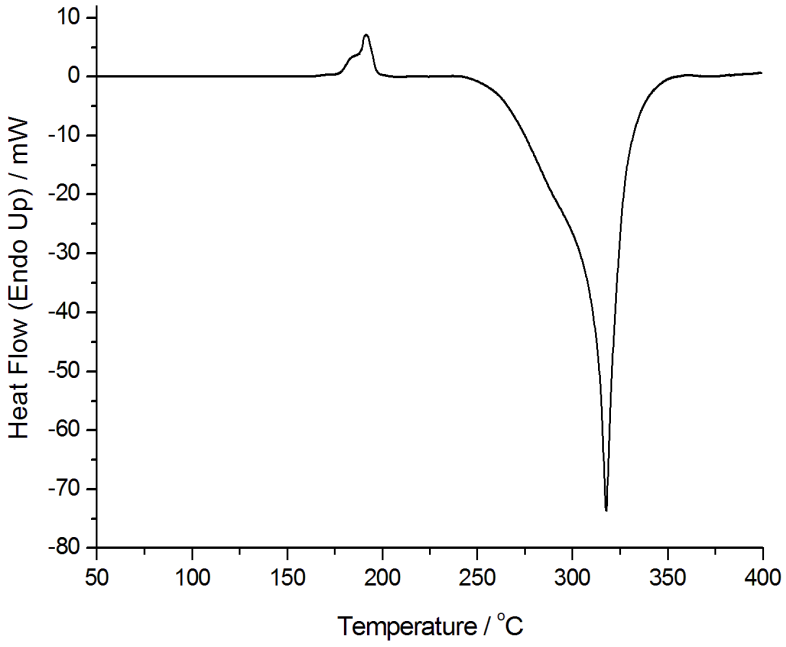

Figure 7.58. Differential scanning calorimetry trace of tetraazido(2,2'-bipyridine)tin (**10**). Heating rate 10 °C min^{-1}, nitrogen flow rate 20 ml min^{-1}.

7.3.3 Tetraazido(1,10-phenanthroline)tin (11) DSC

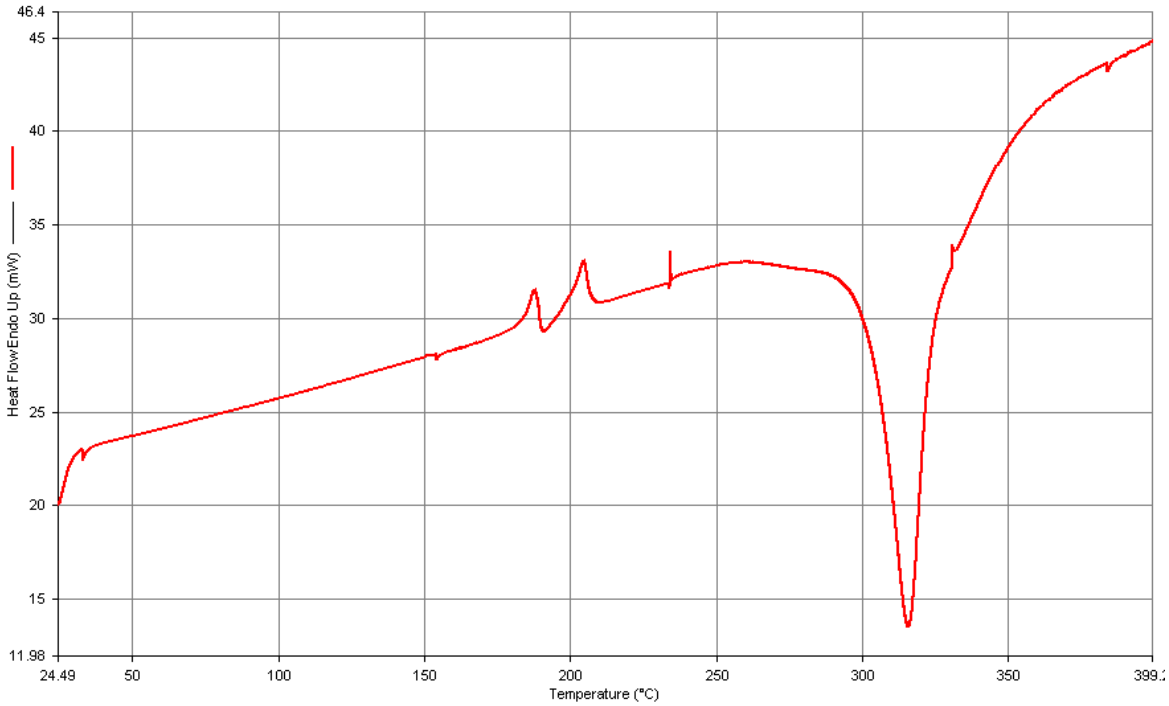

Figure 7.59. Differential scanning calorimetry trace of tetraazido(1,10-phenanthroline)tin (**11**). Heating rate 10 °C min^{-1}, nitrogen flow rate 20 ml min^{-1}.

7.4 X-Ray Crystallography Data

7.4.1 Guanidinium azide (1)

Dataset code	ch1ppx192_0m	
Empirical formula	C H6 N6	
Formula weight	102.12	
Temperature	100(2) K	
Wavelength	0.71073 Å	
Crystal system	Monoclinic	
Space group	*C*2/*c*	
Unit cell dimensions	a = 20.410(3) Å	α = 90 °
	b = 11.6649(15) Å	β = 90.101(6) °
	c = 12.2223(16) Å	γ = 90 °
Volume	2909.9(6) Å^3	
Z	24	
Density (calculated)	1.399 g cm^{-3}	
Absorption coefficient	0.110 mm^{-1}	
F(000)	1296	
Crystal size	0.500 × 0.480 × 0.150 mm^3	
Theta range for data collection	1.996–27.592 °	
Index ranges	$-24 \le h \le 26$, $-15 \le k \le 15$, $-15 \le l \le 15$	
Reflections collected	17272	
Independent reflections	17272 [R(int) = ?]	
Completeness to theta = 25.000°	100.0 %	
Absorption correction	Semi-empirical from equivalents	
Max. and min. transmission	1 and 0.782	
Refinement method	Full-matrix least-squares on F^2	
Data / restraints / parameters	17272 / 12 / 192	
Goodness-of-fit on F^2	1.083	
Final R indices [I > 2sigma(I)]	R1 = 0.0756, wR2 = 0.2016	
R indices (all data)	R1 = 0.1333, wR2 = 0.2326	
Extinction coefficient	n/a	
Largest diff. peak and hole	0.353 and –0.472 e Å^{-3}	

7.4.2 Guanidinium azide monohydrate (1a)

Dataset code	ch1ppx175_0m	
Empirical formula	C H8 N6 O	
Formula weight	120.13	
Temperature	100(2) K	
Wavelength	0.71073 Å	
Crystal system	Monoclinic	
Space group	$P2_1/c$	
Unit cell dimensions	a = 8.3174(6) Å	α = 90 °
	b = 10.9115(8) Å	β = 103.776(3) °
	c = 6.4713(4) Å	γ = 90 °
Volume	570.41(7) Å^3	
Z	4	
Density (calculated)	1.399 g cm^{-3}	
Absorption coefficient	0.117 mm^{-1}	
F(000)	256	
Crystal size	0.460 × 0.320 × 0.180 mm^3	
Theta range for data collection	2.521–27.521°.	
Index ranges	$-10 \le h \le 10$, $-14 \le k \le 14$, $-8 \le l \le 8$	
Reflections collected	5293	
Independent reflections	1307 [R(int) = 0.0243]	
Completeness to theta = 25.242 °	99.9 %	
Absorption correction	Semi-empirical from equivalents	
Max. and min. transmission	1.00 and 0.933	
Refinement method	Full-matrix least-squares on F^2	
Data / restraints / parameters	1307 / 0 / 105	
Goodness-of-fit on F^2	1.084	
Final R indices [I > 2sigma(I)]	R1 = 0.0265, wR2 = 0.0788	
R indices (all data)	R1 = 0.0277, wR2 = 0.0798	
Extinction coefficient	n/a	
Largest diff. peak and hole	0.188 and –0.302 e Å^{-3}	

7.4.3a Aminoguanidinium azide (2) (*T* = 100 K)

Dataset code	ch1ppx183_0m	
Empirical formula	C H7 N7	
Formula weight	117.14	
Temperature	100(2) K	
Wavelength	0.71073 Å	
Crystal system	Monoclinic	
Space group	$P2_1/c$	
Unit cell dimensions	a = 7.3030(4) Å	α = 90 °
	b = 12.3379(7) Å	β = 107.583(2) °
	c = 6.1442(3) Å	γ = 90 °
Volume	527.75(5) Å^3	
Z	4	
Density (calculated)	1.474 g cm^{-3}	
Absorption coefficient	0.116 mm^{-1}	
F(000)	248	
Crystal size	0.450 × 0.400 × 0.400 mm^3	
Theta range for data collection	3.302–27.658 °	
Index ranges	$-9 \le h \le 9, -16 \le k \le 13, -8 \le l \le 7$	
Reflections collected	4955	
Independent reflections	1221 [R(int) = 0.0156]	
Completeness to theta = 25.000 °	99.8 %	
Absorption correction	Semi-empirical from equivalents	
Max. and min. transmission	1.000 and 0.885	
Refinement method	Full-matrix least-squares on F^2	
Data / restraints / parameters	1221 / 0 / 101	
Goodness-of-fit on F^2	1.026	
Final R indices [I > 2sigma(I)]	R1 = 0.0270, wR2 = 0.0720	
R indices (all data)	R1 = 0.0311, wR2 = 0.0751	
Extinction coefficient	n/a	
Largest diff. peak and hole	0.209 and –0.210 e Å^{-3}	

7.4.3b Aminoguanidinium azide (2) (*T* = 150 K)

Dataset code	ch1ppx190	
Empirical formula	C H7 N7	
Formula weight	117.14	
Temperature	150(2) K	
Wavelength	0.71073 Å	
Crystal system	Monoclinic	
Space group	$P2_1/c$	
Unit cell dimensions	a = 7.328(11) Å	α = 90 °
	b = 12.45(2) Å	β = 107.32(3) °
	c = 6.208(11) Å	γ = 90 °
Volume	540.6(16) Å^3	
Z	4	
Density (calculated)	1.439 g cm^{-3}	
Absorption coefficient	0.113 mm^{-1}	
F(000)	248	
Crystal size	0.450 × 0.250 × 0.200 mm^3	
Theta range for data collection	2.912–27.272 °	
Index ranges	$-9 \le h \le 8, -15 \le k \le 16, -7 \le l \le 7$	
Reflections collected	7658	
Independent reflections	1205 [R(int) = 0.0299]	
Completeness to theta = 25.242 °	100.0 %	
Absorption correction	Semi-empirical from equivalents	
Refinement method	Full-matrix least-squares on F^2	
Data / restraints / parameters	1205 / 0 / 101	
Goodness-of-fit on F^2	1.016	
Final R indices [I > 2sigma(I)]	R1 = 0.0297, wR2 = 0.0792	
R indices (all data)	R1 = 0.0348, wR2 = 0.0835	
Extinction coefficient	n/a	
Largest diff. peak and hole	0.169 and –0.205 e Å^{-3}	

7.4.4 Bis(guanidinium) hexaazidostannate (3)

Dataset code	ch1ppx182_0m	
Empirical formula	C2 H12 N24 Sn	
Formula weight	491.05	
Temperature	100(2) K	
Wavelength	0.71073 Å	
Crystal system	Monoclinic	
Space group	$P2_1/c$	
Unit cell dimensions	a = 8.2382(5) Å	α = 90 °
	b = 28.1101(16) Å	β = 117.525(2) °
	c = 8.7003(5) Å	γ = 90 °
Volume	1786.73(18) Å^3	
Z	4	
Density (calculated)	1.825 g cm^{-3}	
Absorption coefficient	1.480 mm^{-1}	
F(000)	968	
Crystal size	0.500 × 0.350 × 0.300 mm^3	
Theta range for data collection	2.738–27.554 °	
Index ranges	$-10 \leq h \leq 10$, $-36 \leq k \leq 36$, $-11 \leq l \leq 11$	
Reflections collected	36901	
Independent reflections	4097 [R(int) = 0.0304]	
Completeness to theta = 25.242 °	100.0 %	
Absorption correction	Semi-empirical from equivalents	
Refinement method	Full-matrix least-squares on F^2	
Data / restraints / parameters	4097 / 0 / 292	
Goodness-of-fit on F^2	1.080	
Final R indices [I > 2sigma(I)]	R1 = 0.0180, wR2 = 0.0348	
R indices (all data)	R1 = 0.0218, wR2 = 0.0359	
Extinction coefficient	n/a	
Largest diff. peak and hole	0.338 and –0.298 e Å^{-3}	

7.4.5 Sodium guanidinium azide (5b)

Dataset code	ch1ppx210_0m	
Empirical formula	C2 H12 N15 Na	
Formula weight	269.26	
Temperature	100(2) K	
Wavelength	0.71073 Å	
Crystal system	Orthorhombic	
Space group	*Ibam*	
Unit cell dimensions	a = 12.7824(5) Å	α = 90 °
	b = 13.3056(9) Å	β = 90 °
	c = 13.9637(5) Å	γ = 90 °
Volume	2374.9(2) Å^3	
Z	8	
Density (calculated)	1.506 g cm^{-3}	
Absorption coefficient	0.148 mm^{-1}	
F(000)	1120	
Crystal size	0.450 × 0.250 × 0.200 mm^3	
Theta range for data collection	2.209–27.565 °	
Index ranges	$-16 \le h \le 16$, $-17 \le k \le 16$, $-18 \le l \le 18$	
Reflections collected	13521	
Independent reflections	1428 [R(int) = 0.0522]	
Completeness to theta = 25.242 °	99.9 %	
Absorption correction	Semi-empirical from equivalents	
Refinement method	Full-matrix least-squares on F^2	
Data / restraints / parameters	1428 / 0 / 116	
Goodness-of-fit on F^2	1.030	
Final R indices [I > 2sigma(I)]	R1 = 0.0377, wR2 = 0.0983	
R indices (all data)	R1 = 0.0621, wR2 = 0.1128	
Extinction coefficient	n/a	
Largest diff. peak and hole	0.255 and –0.179 e Å^{-3}	

7.4.6 $P(=O)(N_3)_2(NC(NH_2)_2)$ (8)

Dataset code	ch1ppx197_0m	
Empirical formula	C H4 N9 O P	
Formula weight	189.10	
Temperature	100(2) K	
Wavelength	0.71073 Å	
Crystal system	Monoclinic	
Space group	*I*2/*a*	
Unit cell dimensions	*a* = 10.5081(13) Å	*α* = 90 °
	b = 11.7968(8) Å	*β* = 92.677(2) °
	c = 12.2631(8) Å	*γ* = 90 °
Volume	1518.5(2) $Å^3$	
Z	8	
Density (calculated)	1.654 g cm^{-3}	
Absorption coefficient	0.333 mm^{-1}	
F(000)	768	
Crystal size	0.480 × 0.450 × 0.400 mm^3	
Theta range for data collection	2.397–27.546°.	
Index ranges	$-13 \le h \le 13, -11 \le k \le 15, -15 \le l \le 15$	
Reflections collected	10716	
Independent reflections	1746 [*R*(int) = 0.0273]	
Completeness to theta = 25.242°	100.0 %	
Absorption correction	Semi-empirical from equivalents	
Refinement method	Full-matrix least-squares on F^2	
Data / restraints / parameters	1746 / 0 / 125	
Goodness-of-fit on F^2	1.014	
Final *R* indices [*I* > 2sigma(*I*)]	*R*1 = 0.0272, *wR*2 = 0.0747	
R indices (all data)	*R*1 = 0.0309, *wR*2 = 0.0775	
Extinction coefficient	n/a	
Largest diff. peak and hole	0.429 and –0.283 e $Å^{-3}$	

7.4.6 Guanidinium tetrazolate (19)

Dataset code	ch1ppx209_0m	
Empirical formula	C2 H7 N7	
Formula weight	129.15	
Temperature	100(2) K	
Wavelength	0.71073 Å	
Crystal system	Monoclinic	
Space group	$P2_1/c$	
Unit cell dimensions	a = 4.7296(16) Å	α = 90 °
	b = 13.894(5) Å	β = 92.96(2) °
	c = 8.754(3) Å	γ = 90 °
Volume	574.5(3) Å^3	
Z	4	
Density (calculated)	1.493 g cm^{-3}	
Absorption coefficient	0.115 mm^{-1}	
F(000)	272	
Crystal size	0.600 × 0.200 × 0.200 mm^3	
Theta range for data collection	2.753–27.483 °	
Index ranges	$-4 \leq h \leq 6, -17 \leq k \leq 15, -11 \leq l \leq 9$	
Reflections collected	6101	
Independent reflections	1304 [R(int) = 0.0839]	
Completeness to theta = 25.000 °	100.0 %	
Absorption correction	Semi-empirical from equivalents	
Max. and min. transmission	0.7456 and 0.6422	
Refinement method	Full-matrix least-squares on F^2	
Data / restraints / parameters	1304 / 0 / 110	
Goodness-of-fit on F^2	1.065	
Final R indices [I > 2sigma(I)]	R1 = 0.0523, wR2 = 0.1171	
R indices (all data)	R1 = 0.0816, wR2 = 0.1341	
Extinction coefficient	n/a	
Largest diff. peak and hole	0.270 and –0.314 e Å^{-3}	

7.4.7 Bis{bis(triphenylphosphine)iminium} hexaazidostannate, $(PPN)_2Sn(N_3)_6$ (9)

Dataset code	ch1ppx154_0m	
Empirical formula	C72 H60 N20 P4 Sn	
Formula weight	1447.97	
Temperature	100(2) K	
Wavelength	0.71073 Å	
Crystal system	Triclinic	
Space group	$P\bar{1}$	
Unit cell dimensions	a = 11.7012(8) Å	α = 94.143(4) °
	b = 12.5721(9) Å	β = 101.080(4) °
	c = 24.4651(17) Å	γ = 103.058(4) °
Volume	3415.3(4) $Å^3$	
Z	2	
Density (calculated)	1.408 g cm^{-3}	
Absorption coefficient	0.527 mm^{-1}	
F(000)	1484	
Crystal size	0.500 × 0.380 × 0.300 mm^3	
Theta range for data collection	1.675–25.000 °	
Index ranges	$-13 \leq h \leq 13$, $-14 \leq k \leq 14$, $-29 \leq l \leq 29$	
Reflections collected	58063	
Independent reflections	11980 [R(int) = 0.0513]	
Completeness to theta = 25.000°	99.8 %	
Absorption correction	Semi-empirical from equivalents	
Max. and min. transmission	1 and 0.909	
Refinement method	Full-matrix least-squares on F^2	
Data / restraints / parameters	11980 / 66 / 956	
Goodness-of-fit on F^2	1.079	
Final R indices [I > 2sigma(I)]	$R1$ = 0.0283, $wR2$ = 0.0706	
R indices (all data)	$R1$ = 0.0361, $wR2$ = 0.0771	
Extinction coefficient	n/a	
Largest diff. peak and hole	0.509 and –0.729 e $Å^{-3}$	

7.4.8 Tetraazido(2,2'-bipyridine)tin (10)

Dataset code	ch1ppx137_0m	
Empirical formula	C10 H8 N14 Sn	
Formula weight	442.99	
Temperature	120(2) K	
Wavelength	0.71073 Å	
Crystal system	Monoclinic	
Space group	*Cc*	
Unit cell dimensions	a = 11.6427(19) Å	α = 90 °
	b = 8.3153(13) Å	β = 96.783(6) °
	c = 15.866(2) Å	γ = 90 °
Volume	1525.2(4) Å^3	
Z	4	
Density (calculated)	1.929 g cm^{-3}	
Absorption coefficient	1.706 mm^{-1}	
F(000)	864	
Crystal size	0.270 × 0.180 × 0.100 mm^3	
Theta range for data collection	3.525–27.538 °	
Index ranges	$-14 \le h \le 15$, $-10 \le k \le 10$, $-20 \le l \le 20$	
Reflections collected	7830	
Independent reflections	3423 [R(int) = 0.0409]	
Completeness to theta = 25.000 °	99.7 %	
Absorption correction	Semi-empirical from equivalents	
Max. and min. transmission	1 and 0.849	
Refinement method	Full-matrix least-squares on F^2	
Data / restraints / parameters	3423 / 2 / 226	
Goodness-of-fit on F^2	1.019	
Final R indices [I > 2sigma(I)]	R1 = 0.0325, wR2 = 0.0730	
R indices (all data)	R1 = 0.0362, wR2 = 0.0755	
Absolute structure parameter	0.02(2)	
Extinction coefficient	n/a	
Largest diff. peak and hole	1.178 and –0.850 e Å^{-3}	

7.4.9 Tetraazido(1,10-phenanthroline)tin (11)

Dataset code	ch1ppx151_0m	
Empirical formula	C12 H8 N14 Sn	
Formula weight	467.01	
Temperature	100(2) K	
Wavelength	0.71073 Å	
Crystal system	Trigonal	
Space group	$P3_1$	
Unit cell dimensions	a = 9.985(5) Å	α = 90.000(5) °
	b = 9.985(5) Å	β = 90.000(5) °
	c = 14.325(5) Å	γ = 120.000(5) °
Volume	1236.9(13) Å^3	
Z	3	
Density (calculated)	1.881 g cm^{-3}	
Absorption coefficient	1.583 mm^{-1}	
F(000)	684	
Crystal size	0.370 × 0.270 × 0.200 mm^3	
Theta range for data collection	2.355–27.454 °	
Index ranges	$-12 \le h \le 12$, $-12 \le k \le 12$, $-18 \le l \le 18$	
Reflections collected	14479	
Independent reflections	3516 [R(int) = 0.0206]	
Completeness to theta = 25.000 °	100.0 %	
Absorption correction	Semi-empirical from equivalents	
Max. and min. transmission	1 and 0.885	
Refinement method	Full-matrix least-squares on F^2	
Data / restraints / parameters	3516 / 1 / 244	
Goodness-of-fit on F^2	1.042	
Final R indices [I > 2sigma(I)]	R1 = 0.0123, wR2 = 0.0300	
R indices (all data)	R1 = 0.0124, wR2 = 0.0300	
Absolute structure parameter	0.004(6)	
Extinction coefficient	n/a	
Largest diff. peak and hole	0.329 and –0.267 e Å^{-3}	

7.4.10 Tetraazidobis(pyridine)tin (12)

Dataset code	ch1ppx266_0m	
Empirical formula	C10 H10 N14 Sn	
Formula weight	445.01	
Temperature	100(2) K	
Wavelength	0.71073 Å	
Crystal system	Triclinic	
Space group	$P\bar{1}$	
Unit cell dimensions	a = 7.2058(7) Å	α = 116.634(6) °
	b = 8.1954(8) Å	β = 94.618(7) °
	c = 8.4689(7) Å	γ = 109.252(6) °
Volume	406.31(7) Å^3	
Z	1	
Density (calculated)	1.819 g cm^{-3}	
Absorption coefficient	1.601 mm^{-1}	
F(000)	218	
Crystal size	0.170 × 0.060 × 0.060 mm^3	
Theta range for data collection	2.795–27.189 °	
Index ranges	$-9 \leq h \leq 9, -10 \leq k \leq 10, -10 \leq l \leq 10$	
Reflections collected	5861	
Independent reflections	1767 [R(int) = 0.0283]	
Completeness to theta = 25.242 °	99.0 %	
Absorption correction	Semi-empirical from equivalents	
Max. and min. transmission	1 and 0.8803	
Refinement method	Full-matrix least-squares on F^2	
Data / restraints / parameters	1767 / 38 / 133	
Goodness-of-fit on F^2	1.065	
Final R indices [I > 2sigma(I)]	R1 = 0.0190, wR2 = 0.0379	
R indices (all data)	R1 = 0.0195, wR2 = 0.0380	
Extinction coefficient	n/a	
Largest diff. peak and hole	0.499 and –0.501 e Å^{-3}	

7.4.11 Tetraazidobis(4-picoline)tin (13)

Dataset code	ch1ppx267_0m	
Empirical formula	C12 H14 N14 Sn	
Formula weight	473.06	
Temperature	100(2) K	
Wavelength	1.54178 Å	
Crystal system	Monoclinic	
Space group	$P2_1/c$	
Unit cell dimensions	a = 8.3796(3) Å	α = 90 °
	b = 14.5515(6) Å	β = 113.9102(14) °
	c = 7.9765(3) Å	γ = 90 °
Volume	889.15(6) Å^3	
Z	2	
Density (calculated)	1.767 g cm^{-3}	
Absorption coefficient	11.721 mm^{-1}	
F(000)	468	
Crystal size	0.220 × 0.150 × 0.150 mm^3	
Theta range for data collection	5.776–66.540 °	
Index ranges	$-9 \leq h \leq 9, -14 \leq k \leq 17, -9 \leq l \leq 8$	
Reflections collected	4031	
Independent reflections	1528 [R(int) = 0.0242]	
Completeness to theta = 67.000 °	96.4 %	
Absorption correction	Semi-empirical from equivalents	
Max. and min. transmission	0.6208 and 0.2949	
Refinement method	Full-matrix least-squares on F^2	
Data / restraints / parameters	1528 / 0 / 125	
Goodness-of-fit on F^2	1.119	
Final R indices [I > 2sigma(I)]	R1 = 0.0254, wR2 = 0.0648	
R indices (all data)	R1 = 0.0273, wR2 = 0.0662	
Extinction coefficient	n/a	
Largest diff. peak and hole	0.462 and –1.255 e Å^{-3}	

7.4.12 Diazidobis(pyridine)tin (14)

Dataset code	ch1ppx246_0m	
Empirical formula	C10 H10 N8 Sn	
Formula weight	360.95	
Temperature	100(2) K	
Wavelength	0.71073 Å	
Crystal system	Monoclinic	
Space group	$P2_1/c$	
Unit cell dimensions	a = 9.9291(4) Å	α = 90 °
	b = 7.8096(3) Å	β = 97.7471(19) °
	c = 17.4056(7) Å	γ = 90 °
Volume	1337.35(9) Å^3	
Z	4	
Density (calculated)	1.793 g cm^{-3}	
Absorption coefficient	1.911 mm^{-1}	
F(000)	704	
Crystal size	0.270 × 0.130 × 0.100 mm^3	
Theta range for data collection	2.070–26.394 °	
Index ranges	$-12 \leq h \leq 12$, $-9 \leq k \leq 9$, $-21 \leq l \leq 21$	
Reflections collected	13446	
Independent reflections	13446 [R(int) = ?]	
Completeness to theta = 25.000 °	98.6 %	
Absorption correction	Semi-empirical from equivalents	
Max. and min. transmission	1.00 and 0.761	
Refinement method	Full-matrix least-squares on F^2	
Data / restraints / parameters	13446 / 0 / 173	
Goodness-of-fit on F^2	1.005	
Final R indices [I > 2sigma(I)]	R1 = 0.0454, wR2 = 0.1512	
R indices (all data)	R1 = 0.0498, wR2 = 0.1592	
Extinction coefficient	n/a	
Largest diff. peak and hole	1.658 and –2.054 e Å^{-3}	

7.4.13 Diazidobis(4-picoline)tin (15)

Dataset code	ch1ppx257_0m	
Empirical formula	C12 H14 N8 Sn	
Formula weight	389.00	
Temperature	100(2) K	
Wavelength	0.71073 Å	
Crystal system	Triclinic	
Space group	$P\bar{1}$	
Unit cell dimensions	a = 9.1912(2) Å	α = 115.8848(13) °
	b = 9.3972(2) Å	β = 99.0170(13) °
	c = 10.0132(2) Å	γ = 90.6836(13) °
Volume	765.32(3) Å^3	
Z	2	
Density (calculated)	1.688 g cm^{-3}	
Absorption coefficient	1.676 mm^{-1}	
F(000)	384	
Crystal size	0.170 × 0.160 × 0.100 mm^3	
Theta range for data collection	3.154–27.554 °	
Index ranges	$-11 \le h \le 11$, $-12 \le k \le 12$, $-12 \le l \le 13$	
Reflections collected	16634	
Independent reflections	3503 [R(int) = 0.0349]	
Completeness to theta = 25.242 °	99.8 %	
Absorption correction	Semi-empirical from equivalents	
Max. and min. transmission	1 and 0.854	
Refinement method	Full-matrix least-squares on F^2	
Data / restraints / parameters	3503 / 0 / 192	
Goodness-of-fit on F^2	1.030	
Final R indices [I > 2sigma(I)]	R1 = 0.0202, wR2 = 0.0402	
R indices (all data)	R1 = 0.0238, wR2 = 0.0418	
Extinction coefficient	n/a	
Largest diff. peak and hole	0.610 and –0.344 e Å^{-3}	

7.4.14 Guanidinium triazidostannate (17)

Dataset code	ch1ppx280_0m	
Empirical formula	C H6 N12 Sn	
Formula weight	304.87	
Temperature	100(2) K	
Wavelength	0.71073 Å	
Crystal system	Monoclinic	
Space group	*C*2/*c*	
Unit cell dimensions	a = 18.8171(6) Å	α = 90 °
	b = 7.1260(2) Å	β = 95.1374(18) °
	c = 13.9984(4) Å	γ = 90 °
Volume	1869.51(10) Å^3	
Z	8	
Density (calculated)	2.166 g cm^{-3}	
Absorption coefficient	2.722 mm^{-1}	
F(000)	1168	
Crystal size	0.140 × 0.050 × 0.050 mm^3	
Theta range for data collection	2.173–27.508 °	
Index ranges	$-24 \leq h \leq 24$, $-8 \leq k \leq 9$, $-18 \leq l \leq 17$	
Reflections collected	15303	
Independent reflections	2154 [R(int) = 0.0343]	
Completeness to theta = 25.242 °	100.0 %	
Absorption correction	Semi-empirical from equivalents	
Refinement method	Full-matrix least-squares on F^2	
Data / restraints / parameters	2154 / 0 / 151	
Goodness-of-fit on F^2	0.985	
Final R indices [I > 2sigma(I)]	R1 = 0.0180, wR2 = 0.0393	
R indices (all data)	R1 = 0.0235, wR2 = 0.0418	
Extinction coefficient	n/a	
Largest diff. peak and hole	0.395 and –0.309 e Å^{-3}	

7.4.15 Sodium 2,4-bis(tetrazol-1-yl)-1,3,5-triazinon-6-ate DMF solvate (21)

Dataset code	ch1ppx239_0m	
Empirical formula	C8 H8 N12 Na O2	
Formula weight	327.25	
Temperature	100(2) K	
Wavelength	0.71073 Å	
Crystal system	Monoclinic	
Space group	$P2_1/m$	
Unit cell dimensions	a = 3.5885(3) Å	α = 90°
	b = 13.5761(12) Å	β = 93.706(3)°
	c = 13.4946(8) Å	γ = 90°
Volume	656.05(9) Å^3	
Z	2	
Density (calculated)	1.657 g cm^{-3}	
Absorption coefficient	0.156 mm^{-1}	
F(000)	334	
Crystal size	0.22 × 0.05 × 0.03 mm^3	
Theta range for data collection	1.512–27.485°	
Index ranges	$-4 \le h \le 4, -17 \le k \le 17, -17 \le l \le 17$	
Reflections collected	4147	
Independent reflections	4147 [R(int) = ?]	
Completeness to theta = 25.000 °	96.8 %	
Refinement method	Full-matrix least-squares on F^2	
Data / restraints / parameters	4147 / 6 / 132	
Goodness-of-fit on F^2	1.530	
Final R indices [I > 2sigma(I)]	R1 = 0.1574, wR2 = 0.3934	
R indices (all data)	R1 = 0.1909, wR2 = 0.4507	
Extinction coefficient	0.03(2)	
Largest diff. peak and hole	1.869 and –1.763 e Å^{-3}	

7.5 Graph Set Matrices

Table 7.1. Second level graph set matrix showing graph sets assigned to pairs of hydrogen bonds in the structure of guanidinium azide (**1**).

	1A	1B	2A	2B	3A	3B	4A	4A'	4B	4B'	5A	5A'	5B	5B'	6A	6A'	6B	6B'	7A	7A'	7B	7B'	8A	8A'	8B	8B'	9A	9A'	9B	9B'
1A	D2,2(5)																													
1B	D4,4(11)	D																												
2A	R4,4(16)	D4,4(15)	D2,2(5)																											
2B	D4,4(15)	D2,2(7)	D4,4(11)	D																										
3A	D4,4(15)	R4,4(16)	D4,4(15)	D2,2(7)	D																									
3B	D4,4(15)	D2,2(7)	D4,4(15)	R4,4(16)	D2,2(5)	D																								
4A	D[D2,2(5)]	D^2	D[D2,2(5)]	D2,2(5)	D^2	D1,2(3)	D																							
4A'	$[D2,2(5)]^2$	D[D2,2(5)]	D2,4(7)	D[D2,2(5)]	D[D2,2(5)]	D[D2,2(5)]	D4,2(7)	D2,2(5)																						
4B	D2,4(7)	D[D2,2(5)]	$[D2,2(5)]^2$	D[D2,2(5)]	D[D2,2(5)]	D[D2,2(5)]	D4,4(11)	R4,4(12)	D2,2(5)																					
4B'	$[D2,2(5)]^2$	D[D2,2(5)]	D2,4(7)	D[D2,2(5)]	D[D2,2(5)]	D[D2,2(5)]	D4,4(11)	D2,4(7)	R4,2(8)	D2,2(5)																				
5A	D2,4(7)	D[D2,2(5)]	$[D2,2(5)]^2$	D[D2,2(5)]	D[D2,2(5)]	D[D2,2(5)]	D4,4(15)	R4,4(16)	D2,4(7)	R4,4(16)	D2,2(5)																			
5A'	D[D2,2(5)]	D2,2(5)	D[D2,2(5)]	D^2	D1,2(3)	D^2	D2,2(7)	D4,4(15)	D4,4(15)	D4,4(15)	D4,2(7)	D																		
5B	D[D2,2(5)]	D^2	D[D2,2(5)]	D1,2(3)	D^2	D2,2(5)	C2,2(8)	D4,4(15)	D4,4(15)	D4,4(15)	D4,4(11)	D2,2(5)	D																	
5B'	D[D2,2(5)]	D2,2(5)	D[D2,2(5)]	D^2	D1,2(3)	D^2	D2,2(7)	D4,4(15)	D4,4(15)	D4,4(15)	D4,4(11)	R1,2(4)	D2,1(3)	D																
6A	D[D2,2(5)]	D^2	D[D2,2(5)]	D2,2(5)	D^2	D1,2(3)	R1,2(6)	D4,4(15)	D4,4(15)	D4,4(15)	D4,4(15)	D2,2(7)	D2,2(5)	D2,2(7)	D															
6A'	D[D2,2(5)]	D1,2(3)	D[D2,2(5)]	D^2	D2,2(5)	D^2	D2,2(7)	D4,4(15)	D4,4(15)	D4,4(15)	D4,4(15)	C2,2(8)	D2,2(7)	C2,2(8)	D2,1(3)	D														
6B	D[D2,2(5)]	D^2	D[D2,2(5)]	D1,2(3)	D^2	D2,2(5)	C2,2(8)	D4,4(15)	D4,4(15)	D4,4(15)	D4,4(15)	D2,2(7)	R1,2(6)	D2,2(7)	C2,2(6)	D2,2(5)	D													
6B'	D[D2,2(5)]	D1,2(3)	D[D2,2(5)]	D^2	D2,2(5)	D^2	D2,2(7)	D4,4(15)	D4,4(15)	D4,4(15)	D4,4(15)	C2,2(8)	D2,2(7)	C2,2(8)	D2,2(5)	R1,2(4)	D2,1(3)	D												
7A	D[D2,2(5)]	D2,2(5)	D[D2,2(5)]	D^2	D1,2(3)	D^2	D^2	D[D2,2(5)]	D[D2,2(5)]	D[D2,2(5)]	D[D2,2(5)]	D1,2(3)	D^2	D1,2(3)	D^2	D2,2(5)	D^2	D2,2(5)	D											
7A'	D[D2,2(5)]	D^2	D[D2,2(5)]	D1,2(3)	D^2	D2,2(5)	D2,2(5)	D[D2,2(5)]	D[D2,2(5)]	D[D2,2(5)]	D[D2,2(5)]	D^2	D1,2(3)	D^2	D2,2(5)	D^2	D1,2(3)	D^2	D2,1(3)	D										
7B	$[D2,2(5)]^2$	D[D2,2(5)]	D2,4(7)	D[D2,2(5)]	D[D2,2(5)]	D[D2,2(5)]	D[D2,2(5)]	D2,4(7)	$[D2,2(5)]^2$	D2,4(7)	$[D2,2(5)]^2$	D[D2,2(5)]	D[D2,2(5)]	D[D2,2(5)]	D[D2,2(5)]	D[D2,2(5)]	D[D2,2(5)]	D[D2,2(5)]	D4,4(11)	D4,4(11)	D2,2(5)								
7B'	D[D2,2(5)]	D^2	D[D2,2(5)]	D1,2(3)	D^2	D2,2(5)	D2,2(5)	D[D2,2(5)]	D[D2,2(5)]	D[D2,2(5)]	D[D2,2(5)]	D[D2,2(5)]	D1,2(3)	D^2	D2,2(5)	D^2	D1,2(3)	D^2	D2,2(5)	R1,2(4)	D4,2(7)	D								
8A	D[D2,2(5)]	D1,2(3)	D[D2,2(5)]	D^2	D2,2(5)	D^2	D^2	D[D2,2(5)]	D[D2,2(5)]	D[D2,2(5)]	D[D2,2(5)]	D2,2(5)	D^2	D2,2(5)	D^2	D1,2(3)	D^2	D1,2(3)	C2,2(8)	D2,2(7)	D4,4(15)	D2,2(7)	D							
8A'	D2,4(7)	D[D2,2(5)]	$[D2,2(5)]^2$	D[D2,2(5)]	D[D2,2(5)]	D[D2,2(5)]	D[D2,2(5)]	$[D2,2(5)]^2$	D2,4(7)	$[D2,2(5)]^2$	D2,4(7)	D[D2,2(5)]	D[D2,2(5)]	D[D2,2(5)]	D[D2,2(5)]	D[D2,2(5)]	D[D2,2(5)]	D[D2,2(5)]	D4,4(15)	D4,4(15)	R4,4(16)	D4,4(15)	D4,2(7)	D2,2(5)						
8B	$[D2,2(5)]^2$	D[D2,2(5)]	D2,4(7)	D[D2,2(5)]	D[D2,2(5)]	D[D2,2(5)]	D[D2,2(5)]	D2,4(7)	$[D2,2(5)]^2$	D2,4(7)	$[D2,2(5)]^2$	D[D2,2(5)]	D[D2,2(5)]	D[D2,2(5)]	D[D2,2(5)]	D[D2,2(5)]	D[D2,2(5)]	D[D2,2(5)]	D4,4(15)	D4,4(15)	D2,4(7)	D4,4(15)	D4,4(11)	R4,4(12)	D2,2(5)					
8B'	D2,4(7)	D[D2,2(5)]	$[D2,2(5)]^2$	D[D2,2(5)]	D[D2,2(5)]	D[D2,2(5)]	D[D2,2(5)]	$[D2,2(5)]^2$	D2,4(7)	$[D2,2(5)]^2$	D2,4(7)	D[D2,2(5)]	D[D2,2(5)]	D[D2,2(5)]	D[D2,2(5)]	D[D2,2(5)]	D[D2,2(5)]	D[D2,2(5)]	D4,4(15)	D4,4(15)	R4,4(16)	D4,4(15)	D4,4(11)	D2,4(7)	R4,2(8)	D2,2(5)				
9A	D[D2,2(5)]	D2,2(5)	D[D2,2(5)]	D^2	D1,2(3)	D^2	D^2	D[D2,2(5)]	D[D2,2(5)]	D[D2,2(5)]	D[D2,2(5)]	D1,2(3)	D[D2,2(5)]	D1,2(3)	D^2	D2,2(5)	D^2	D2,2(5)	R1,2(6)	D2,2(7)	D4,4(15)	D2,2(7)	C2,2(8)	D4,4(15)	D4,4(15)	D4,4(15)	D			
9A'	D[D2,2(5)]	D^2	D[D2,2(5)]	D2,2(5)	D^2	D1,2(3)	D1,2(3)	D[D2,2(5)]	D[D2,2(5)]	D[D2,2(5)]	D[D2,2(5)]	D^2	D2,2(5)	D^2	D1,2(3)	D^2	D2,2(5)	D^2	D2,2(7)	C2,2(8)	D4,4(15)	C2,2(8)	D2,2(7)	D4,4(15)	D4,4(15)	D4,4(15)	D2,1(3)	D		
9B	D[D2,2(5)]	D1,2(3)	D[D2,2(5)]	D^2	D2,2(5)	D^2	D^2	D[D2,2(5)]	D[D2,2(5)]	D[D2,2(5)]	D[D2,2(5)]	D2,2(5)	D^2	D2,2(5)	D^2	D1,2(3)	D^2	D1,2(3)	C2,2(8)	D2,2(7)	D4,4(15)	D2,2(7)	R1,2(6)	D4,4(15)	D4,4(15)	D4,4(15)	C2,2(6)	D2,2(5)	D	
9B'	D[D2,2(5)]	D^2	D[D2,2(5)]	D2,2(5)	D^2	D1,2(3)	D1,2(3)	D[D2,2(5)]	D[D2,2(5)]	D[D2,2(5)]	D[D2,2(5)]	D^2	D2,2(5)	D^2	D1,2(3)	D^2	D2,2(5)	D^2	D2,2(7)	C2,2(8)	D4,4(15)	C2,2(8)	D2,2(7)	D4,4(15)	D4,4(15)	D4,4(15)	D2,2(5)	R1,2(4)	D2,1(3)	D

Table 7.2. Second level graph set matrix guanidinium azide monohydrate (**1a**).

	1A	**1A'**	**1B**	**1B'**	**2A**	**2A'**	**2B**	**3A**	**3B**	**3B'**	**1W**	**2W**
1A	D											
1A'	R4,2(8)	D										
1B	D2,2(5)	D2,2(5)	D									
1B'	R4,4(12)	R1,2(4)	D2,1(3)	D								
2A	D2,2(7)	D2,2(7)	R1,2(6)	D2,2(7)	D							
2A'	C2,2(8)	C1,2(6)	D2,2(7)	C1,2(6)	D2,1(3)	D						
2B	D2,2(7)	D2,2(7)	C1,2(6)	D2,2(7)	C2,2(4)	D2,2(5)	D					
3A	C2,4(6)	C2,2(8)	D2,2(7)	C2,2(8)	D2,2(7)	R4,4(16)	D2,2(7)	D				
3B	R1,2(6)	R4,4(16)	D2,2(7)	R4,4(16)	D2,2(7)	C2,2(8)	D2,2(7)	C2,2(4)	D			
3B'	C2,2(8)	C1,2(6)	D2,2(7)	C2,2(6)	D2,2(7)	C1,2(6)	D2,2(7)	R4,4(12)	D2,1(3)	D		
1W	D2,2(5)	D1,2(3)	D2,2(4)	D1,2(3)	D2,2(4)	D1,2(3)	D2,2(4)	D2,2(5)	D2,2(5)	D1,2(3)	D	
2W	D1,2(3)	D2,2(5)	D2,2(4)	D2,2(5)	D2,2(4)	D2,2(5)	D2,2(4)	D2,2(5)	D1,2(3)	D2,2(5)	C2,2(6)	D

Table 7.3. Second level graph set matrix showing graph sets assigned to pairs of hydrogen bonds in the structure of aminoguanidinium azide (**2**).

	1A	**1A'**	**1B**	**2**	**2'**	**3A**	**3B**	**4A**	**4B**
1A	D								
1A'	C2,1(5)	D							
1B	C2,2(6)	R2,4(8)	D						
2	C2,2(7)	R2,4(10)	C1,2(7)	D					
2'	D2,2(6)	C2,2(7)	C2,2(7)	C2,1(5)	D				

	1A	1A'	1B	2	2'	3A	3B	4A	4B
3A	R2,4(14)	C2,2(9)	C2,2(9)	C1,2(6)	C2,2(8)	D			
3B	D3,3(10)	D3,3(10)	D3,3(10)	D3,3(10)	D3,3(10)	D3,3(10)	R2,2(10)		
4A	C2,2(9)	R2,4(14)	C1,2(7)	C2,2(8)	R1,2(6)	C2,2(8)	D3,3(10)	D	
4B	R2,4(14)	C2,2(9)	C2,2(9)	C1,2(6)	C2,2(8)	R1,2(6)	D3,3(10)	C2,2(6)	D

Table 7.4. Second level graph set matrix showing graph sets assigned to pairs of hydrogen bonds in the structure of bis(guanidinium) hexaazidostannate (**3**).

	19A	19A'	19B	20A	20B	21A	21B	22A	22A'	22B	23A	23B	24A	24B
19A	D													
19A'	D2,1(3)	D												
19B	R4,4(16)	C2,2(8)	D											
20A	R4,4(20)	C2,2(8)	R2,2(8)	D										
20B	C2,2(8)	R4,4(20)	R4,4(16)	R4,4(12)	D									
21A	C2,2(10)	R4,4(20)	R4,4(16)	R4,4(16)	R2,2(8)	D								
21B	R1,2(6)	R4,4(24)	R4,4(20)	R4,4(20)	C2,2(8)	C2,2(8)	D							
22A	D2,2(9)	D2,2(9)	D2,2(7)	D2,2(7)	D2,2(7)	D2,2(7)	D2,2(9)	D						
22A'	D1,2(3)	D1,2(3)	D2,2(7)	D2,2(5)	D2,2(7)	D2,2(7)	D2,2(9)	D2,1(3)	D					
22B	D2,2(7)	D2,2(7)	D2,2(5)	D2,2(5)	D2,2(5)	D2,2(5)	D2,2(7)	C2,2(8)	C2,2(8)	D				
23A	D2,2(7)	D2,2(7)	D2,2(5)	D2,2(5)	D2,2(5)	D2,2(5)	D2,2(7)	C2,2(8)	C2,2(10)	R2,2(8)	D			
23B	D2,2(9)	D2,2(9)	D2,2(7)	D2,2(7)	D2,2(7)	D2,2(5)	D2,2(9)	C2,2(12)	C2,2(12)	C2,2(10)	C2,2(8)	D		
24A	D2,2(9)	D2,2(9)	D2,2(7)	D2,2(7)	D2,2(7)	D2,2(5)	D2,2(9)	C2,2(12)	C2,2(12)	C2,2(10)	C2,2(10)	R1,2(6)	D	
24B	D2,2(9)	D2,2(9)	D2,2(7)	D2,2(7)	D2,2(7)	D2,2(7)	D2,2(9)	R1,2(6)	R2,2(12)	C2,2(10)	C2,2(8)	C2,2(12)	C2,2(10)	D

Table 7.5. Second level graph set matrix showing graph sets assigned to pairs of hydrogen bonds in the structure of sodium guanidinium azide (**5b**).

	7	**8A**	**8B**	**9**	**10A**	**10B**
7	C2,2(6)					
8A	D4,4(15)	R2,2(8)				
8B	C2,2(6)C2,2(8) $\{R1,2(6)\}^2$	C4,4(12) {R2,2(8)}	C2,2(8)			
9	$[C2,2(6)]^2$	C2,2(6)R2,2(8)	C2,2(8)C2,2(6)	C2,2(6)		
10A	R2,2(8)C2,2(6)	$[R2,2(8)]^2$	C2,2(8)R2,2(8)	C2,2(6)R2,2(8)	R2,2(8)	
10B	C2,2(8)R2,2(8)	C2,2(8)R2,2(8)	C2,2(8)C2,2(6)	C2,2(6)C2,2(8) $\{R1,2(6)\}^2$	C4,4(12) {R2,2(8)}	C2,2(6)

Table 7.6. Second level graph set matrix showing graph sets assigned to pairs of hydrogen bonds in the structure of $P(=O)(N_3)_2(NC(NH_2)_2)$ (**8**).

	8A	8B	9A	9B
8A	C1,1(6)			
8B	C2,2(8)[R2,2(8)]	R2,2(8)		
9A	C2,2(6)[S(6)]	R2,2(8)S(6)	S(6)	
9B	C1,1(6)[R1,2(6)]	C2,2(6)[R2,2(8)]	C2,2(4)S(6)	C1,1(6)

Table 7.7. Second level graph set matrix showing graph sets assigned to pairs of hydrogen bonds in the structure of guanidinium triazidostannate (**17**).

	10A	10B	3	4	5	6	7
10A	D						
10B	C2,2(8)	D					
11A	R4,4(20)	C2,2(12)	D				
11B	R2,2(8)	C2,2(8)	R4,4(16)	D			
12A	C2,2(10)	R1,2(6)	C2,2(12)	C2,2(8)	D		
12B	R4,4(20)	C2,2(12)	R1,2(6)	R4,4(20)	C2,2(10)	D	
12B’	C2,2(8)	C2,2(12)	R4,4(24)	C2,2(10)	C2,2(10)	D2,1(3)	D

Table 7.8. Second level graph set matrix showing graph sets assigned to pairs of hydrogen bonds in the structure of guanidinium tetrazolate (**19**).

	5A	5A'	5B	6A	6B	7A	7B
5A	D						
5A'	D2,1(3)	D					
5B	C2,2(6)	C2,2(5)	D				
6A	C2,2(7)	C2,2(6)	R2,2(7)	D			
6B	C2,2(8)	C2,2(8)	C2,2(7)	C2,2(6)	D		
7A	R2,2(12)	C2,2(7)	C2,2(8)	C2,2(7)	R4,4(16)	D	
7B	R1,2(6)	C2,2(7)	C2,2(8)	C2,2(7)	C2,2(8)	R2,4(8)	D

References

1. T. Curtius, *Berichte der Dtsch. Chem. Gesellschaft*, 1890, **23**, 3023–3033.
2. E. F. Scriven and K. Turnbull, *Chem. Rev.*, 1988, **88**, 297–368.
3. B. L. Evans, A. D. Yoffe, and P. Gray, *Chem. Rev.*, 1959, **59**, 515–568.
4. B. Reitzner and R. P. Manno, *Nature*, 1963, **198**, 991.
5. U. Müller, *Struct. Bond.*, 1973, **14**, 141–172.
6. M. Zhang, P. E. Eaton, and R. Gilardi, *Angew. Chem. Int. Ed.*, 2000, **39**, 401–404.
7. *UN Recommendations on the Transport of Dangerous Goods - Manual of Tests and Criteria*, United Nations, New York and Geneva, Sixth Revi., 2016.
8. T. M. Klapötke, *Chemistry of High-Energy Materials*, De Gruyter, Berlin, Boston, 2012.
9. *www.reichel-partner.com*, 2015.
10. *www.ozm.cz/en/sensitivity-tests/small-scale-electrostatic-spark-x-spark-10/*, 2016.
11. M. H. V Huynh, M. D. Coburn, T. J. Meyer, and M. Wetzler, *Proc. Natl. Acad. Sci.*, 2006, **103**, 10322–7.
12. D. Fischer, T. M. Klapötke, and J. Stierstorfer, *Angew. Chemie - Int. Ed.*, 2014, **53**, 8172–8175.
13. D. D. Ford, S. Lenahan, M. Jörgensen, P. Dubé, M. Delude, P. E. Concannon, S. R. Anderson, K. D. Oyler, G. Cheng, N. Mehta, and J. S. Salan, *Org. Process Res. Dev.*, 2015, **19**, 673–680.
14. M. Huynh, M. Hiskey, T. Meyer, and M. Wetzler, *Proc. Natl. Acad. Sci.*, 2006, **103**, 5409–5412.
15. J. J. Sabatini, J. M. Raab, R. K. Hann, R. Damavarapu, and T. M. Klapötke, *Chem. Asian J.*, 2012, **7**, 1657–63.
16. J. J. Sabatini and J. D. Moretti, *Chem. Eur. J.*, 2013, **19**, 12839–45.
17. J. J. Sabatini, A. V Nagori, G. Chen, P. Chu, R. Damavarapu, and T. M. Klapötke, *Chem. Eur. J.*, 2012, **18**, 628–31.
18. J. J. Sabatini, A. V. Nagori, E. A. Latalladi, J. C. Poret, G. Chen, R. Damavarapu, and T. M. Klapötke, *Propellants Explos. Pyrotech.*, 2011, **36**, 373–378.
19. P. Portius and M. Davis, *Coord. Chem. Rev.*, 2013, **257**, 1011–1025.
20. K. O. Christe, *Propellants Explos. Pyrotech.*, 2007, **32**, 194–204.
21. M. I. Eremets, R. J. Hemley, H.-k. Mao, and E. Gregoryanz, *Nature*, 2001, **411**, 170–4.
22. M. I. Eremets, A. G. Gavriliuk, I. A. Trojan, D. A. Dzivenko, and R. Boehler, *Nat. Mater.*, 2004, **3**, 558–63.
23. M. I. Eremets, A. G. Gavriliuk, and I. A. Trojan, *Appl. Phys. Lett.*, 2007, **90**, 171904.
24. B. A. Thrush, *Proc. R. Soc. A Math. Phys. Eng. Sci.*, 1956, **235**, 143–147.
25. K. O. Christe, W. W. Wilson, J. A. Sheehy, and J. A. Boatz, *Angew. Chem. Int. Ed.*, 1999, **38**, 2004–2009.

26. W. W. Wilson, A. Vij, V. Vij, E. Bernhardt, and K. O. Christe, *Chem. Eur. J.*, 2003, **9**, 2840–2844.
27. R. Haiges, S. Schneider, T. Schroer, and K. O. Christe, *Angew. Chem. Int. Ed.*, 2004, **43**, 4919–24.
28. F. Cacace, G. de Petris, and A. Troiani, *Science (80-.).*, 2002, **295**, 480–1.
29. E. C. E. Franklin, *J. Am. Chem. Soc.*, 1934, **56**, 568–571.
30. H. Östmark, S. Wallin, T. Brinck, P. Carlqvist, R. Claridge, E. Hedlund, and L. Yudina, *Chem. Phys. Lett.*, 2003, **379**, 539–546.
31. H. C. Kolb, M. G. Finn, and K. B. Sharpless, *Angew. Chem. Int. Ed.*, 2001, **40**, 2004–2021.
32. W. P. Fehlhammer and W. Beck, *Z. Anorg. Allg. Chem.*, 2013, **639**, 1053–1082.
33. A. C. Filippou, P. Portius, D. U. Neumann, and K.-D. Wehrstedt, *Angew. Chem. Int. Ed.*, 2000, **39**, 4333–4336.
34. P. Portius, A. C. Filippou, G. Schnakenburg, M. Davis, and K.-D. Wehrstedt, *Angew. Chem. Int. Ed.*, 2010, **49**, 8013–6.
35. M. N. Glukhovtsev, H. Jiao, and P. V. R. Schleyer, *Inorg. Chem.*, 1996, **35**, 7124–7133.
36. A. Vij, W. W. Wilson, V. Vij, F. S. Tham, J. A. Sheehy, and K. O. Christe, *J. Am. Chem. Soc.*, 2001, **123**, 6308–13.
37. P. Portius, M. Davis, R. Campbell, F. Hartl, Q. Zeng, A. J. H. M. Meijer, and M. Towrie, *J. Phys. Chem. A*, 2013, **117**, 12759–12769.
38. U. Geiger, Y. Haas, and D. Grinstein, *J. Photochem. Photobiol. A Chem.*, 2014, **277**, 53–61.
39. A. Vij, J. Pavlovich, and W. Wilson, *Angew. Chem. Int. Ed.*, 2002, **41**, 3051–3054.
40. R. N. Butler, J. M. Hanniffy, J. C. Stephens, and L. A. Burke, *J. Org. Chem.*, 2008, **73**, 1354–64.
41. R. N. Butler, J. C. Stephens, and L. A. Burke, *Chem. Commun.*, 2003, **2**, 1016–7.
42. L. A. Burke, R. N. Butler, and J. C. Stephens, *J. Chem. Soc. Perkin Trans. 2*, 2001, 1679–1684.
43. T. Schroer, R. Haiges, S. Schneider, and K. O. Christe, *Chem. Commun.*, 2005, 1607–9.
44. Y.-H. Joo, H. Gao, Y. Zhang, and J. M. Shreeve, *Inorg. Chem.*, 2010, **49**, 3282–8.
45. S. Schneider, T. Hawkins, and M. Rosander, *Inorg. Chem.*, 2008, **47**, 3617–3624.
46. S. Schneider, T. Hawkins, M. Rosander, J. Mills, G. Vaghjiani, and S. Chambreau, *Inorg. Chem.*, 2008, **47**, 6082–9.
47. S. Schneider, T. Hawkins, Y. Ahmed, S. Deplazes, and J. Mills, in *In Ionic Liquids: Science and Applications; ACS Symposium Series*, American Chemical Society, Washington, DC, 2012, pp. 1–25.
48. A. G. Davies and P. J. Smith, *Advances in Inorganic Chemistry and Radiochemistry*, Academic Press, New York, 1980.
49. H. S. Booth, in *Inorganic Syntheses, Volume I*, eds. H. S. Booth, L. Audrieth, J. Bailar Jr., W.

Conard Fernelius, W. Johnson, and R. Kirk, McGraw-Hill Book Company, Inc., New York and London, 1939, vol. I, pp. 77–79.

50. W. Frost, J. Cothran, and A. Browne, *J. Am. Chem. Soc.*, 1933, **55**, 3516–3518.
51. J. Evers, M. Göbel, B. Krumm, F. Martin, S. Medvedyev, G. Oehlinger, F. X. Steemann, I. Troyan, T. M. Klapötke, and M. I. Eremets, *J. Am. Chem. Soc.*, 2011, **133**, 12100–5.
52. T. Klapötke, *Chem. Ber.*, 1997, **130**, 443–452.
53. C. M. Carmalt, A. H. Cowley, R. D. Culp, R. A. Jones, Y. M. Sun, B. Fitts, S. Whaley, and H. W. Roesky, *Inorg. Chem.*, 1997, **36**, 3108–3112.
54. T. G. Müller, F. Karau, W. Schnick, and F. Kraus, *Angew. Chem. Int. Ed.*, 2014, **53**, 13695–13697.
55. R. Haiges, J. A. Boatz, S. Schneider, T. Schroer, M. Yousufuddin, and K. O. Christe, *Angew. Chem. Int. Ed.*, 2004, **43**, 3148–3152.
56. R. Haiges, J. A. Boatz, and K. O. Christe, *Angew. Chem. Int. Ed.*, 2010, **49**, 8008–12.
57. R. Haiges, J. A. Boatz, R. Bau, S. Schneider, T. Schroer, M. Yousufuddin, and K. O. Christe, *Angew. Chem. Int. Ed.*, 2005, **44**, 1860–5.
58. H. Lund, O. Oeckler, T. Schröder, A. Schulz, and A. Villinger, *Angew. Chem. Int. Ed.*, 2013, **52**, 10900–10904.
59. C. L. Schmidt, R. Dinnebier, U. Wedig, and M. Jansen, *Inorg. Chem.*, 2007, **46**, 907–916.
60. K. Banert, Y.-H. Joo, T. Rüffer, B. Walfort, and H. Lang, *Angew. Chem. Int. Ed.*, 2007, **46**, 1168–71.
61. E. Wiberg and H. Michaud, *Z. Naturforsch. B*, 1954, **9**, 500.
62. J. E. Drake and R. T. Hemmings, *Can. J. Chem.*, 1973, **51**, 302–311.
63. T. M. Klapötke, B. Krumm, M. Scherr, R. Haiges, and K. O. Christe, *Angew. Chem. Int. Ed.*, 2007, **46**, 8686–8690.
64. T. M. Klapötke, B. Krumm, P. Mayer, and I. Schwab, *Angew. Chem. Int. Ed.*, 2003, **42**, 5843–5846.
65. C. Knapp and J. Passmore, *Angew. Chem. Int. Ed.*, 2004, **43**, 4834–6.
66. I. C. Tornieporth-Oetting and T. M. Klapötke, *Angew. Chem. Int. Ed.*, 1995, **34**, 511–20.
67. M. Göbel, K. Karaghiosoff, and T. M. Klapötke, *Angew. Chem. Int. Ed.*, 2006, **45**, 6037–40.
68. K. Karaghiosoff, T. M. Klapötke, B. Krumm, H. Nöth, T. Schütt, and M. Suter, *Inorg. Chem.*, 2002, **41**, 170–9.
69. A. Strecker, *Liebigs Ann. Chem.*, 1861, **118**, 151–177.
70. T. Yamada, X. Liu, U. Englert, H. Yamane, and R. Dronskowski, *Chem. Eur. J.*, 2009, **15**, 5651–5.
71. V. Hoepfner, V. L. Deringer, and R. Dronskowski, *J. Phys. Chem. A*, 2012, **116**, 4551–4559.
72. S. Angyal and W. Warburton, *J. Chem. Soc.*, 1951, 2492–2494.
73. V. Hoepfner and R. Dronskowski, *Inorg. Chem.*, 2011, **50**, 3799–803.

74. P. K. Sawinski and R. Dronskowski, *Inorg. Chem.*, 2012, **51**, 7425–30.
75. P. K. Sawinski, V. L. Deringer, and R. Dronskowski, *Dalt. Trans.*, 2013, 15080–7.
76. P. J. Bailey and S. Pace, *Coord. Chem. Rev.*, 2001, **214**, 91–141.
77. R. Caminiti, A. Pieretti, L. Bencivenni, F. Ramondo, N. Sanna, *J. Phys. Chem.*, 1996, **100**, 10928–10935.
78. A. Skancke, *J. Phys. Chem.*, 1994, **98**, 5234–5239.
79. A. Gobbi and G. Frenking, *J. Am. Chem. Soc.*, 1993, **115**, 2362–2372.
80. K. Wiberg, *J. Am. Chem. Soc.*, 1990, **112**, 4177–4182.
81. L. James, PhD Thesis, *"Synthesis and Reactivity of Main Group Coordination Complexes Bearing N-containing Ligands"*, University of Sheffield, 2013.
82. B. F. Crozier, PhD Thesis, *"Nitrogen-Rich Heterocycles - A Study of the Use of Tetrazole and Pentazole as Ligands"*, University of Sheffield, 2016.
83. A. C. Filippou, P. Portius, and G. Schnakenburg, *J. Am. Chem. Soc.*, 2002, **124**, 12396–7.
84. P. Portius, P. Fowler, H. Adams, and T. Todorova, *Inorg. Chem.*, 2008, **47**, 12004–12009.
85. R. Campbell, M. F. Davis, M. Fazakerley, and P. Portius, *Chem. Eur. J.*, 2015, **21**, 18690–8.
86. D. Fenske, H. Dörner, and K. Dehnicke, *Z. Naturforsch. B*, 1983, **38**, 1301–3.
87. R. Haiges, J. A. Boatz, A. Vij, M. Gerken, S. Schneider, T. Schroer, and K. O. Christe, *Angew. Chem. Int. Ed.*, 2003, **42**, 5847–5851.
88. R. Haiges, J. A. Boatz, J. M. Williams, and K. O. Christe, *Angew. Chem. Int. Ed.*, 2011, **50**, 8828–8833.
89. W. Beck, E. Schuierer, P. Pöllmann, and W. P. Fehlhammer, *Z. Naturforsch. B*, 1966, **21**, 811–12.
90. K. Polborn, E. Leidl, and W. Beck, *Z. Naturforsch., B J. Chem. Sci.*, 1988, **43**, 1206–1208.
91. W. Fraenk, T. Habereder, A. Hammerl, T. M. Klapötke, B. Krumm, P. Mayer, H. Nöth, and M. Warchhold, *Inorg. Chem.*, 2001, **40**, 1334–40.
92. B. Peerless, T. Keane, A. J. H. M. Meijer, and P. Portius, *Chem. Commun.*, 2015, **51**, 7435–7438.
93. C. Domene, P. Portius, P. W. Fowler, and L. Bernasconi, *Inorg. Chem.*, 2013, **52**, 1747–54.
94. A. Schulz and A. Villinger, *Chem. Eur. J.*, 2012, **18**, 2902–11.
95. H. Sussek, F. Stowasser, H. Pritzkow, and R. A. Fischer, *Eur. J. Inorg. Chem.*, **2000**, 455–461.
96. T. M. Klapötke, D. G. Piercey, and J. Stierstorfer, *Eur. J. Inorg. Chem.*, **2012**, 5694–5700.
97. A. Hammerl, M. A. Hiskey, G. Holl, T. M. Klapötke, K. Polborn, and J. J. Weigand, *Chem. Mater.*, 2005, **17**, 3784–3793.
98. M. A. Petrie, J. A. Sheehy, J. A. Boatz, G. Rasul, G. K. S. Prakash, G. A. Olah, and K. O. Christe, *J. Am. Chem. Soc.*, 1997, **119**, 8802–8808.
99. M. Drozd, *Mater. Sci. Eng. B*, 2007, **136**, 20–28.
100. Y. Marcus, *J. Chem. Thermodyn.*, 2012, **48**, 70–74.

101. D. Li, M. Wang, J. Wu, Q. Zhang, Y. Luo, Z. Yu, Q. Meng, and Z. Wu, *Langmuir*, 2009, **25**, 4808–14.
102. W. Ogihara, M. Yoshizawa, and H. Ohno, *Chem. Lett.*, 2004, **33**, 1022–23.
103. P. S. Kulkarni, L. C. Branco, J. G. Crespo, M. C. Nunes, A. Raymundo, and C. A. M. Afonso, *Chem. Eur. J.*, 2007, **13**, 8478–88.
104. M.-J. Crawford, K. Karaghiosoff, T. M. Klapötke, and F. A. Martin, *Inorg. Chem.*, 2009, **48**, 1731–1743.
105. T. Klapötke and J. Stierstorfer, *Cent. Eur. J. Energ. Mater.*, 2008, **5**, 13–30.
106. M. Göbel and T. M. Klapötke, *Zeitschrift für Anorg. und Allg. Chemie*, 2007, **633**, 1006–1017.
107. T. Steiner, *Angew. Chem. Int. Ed.*, 2002, **41**, 48–76.
108. P. Needham, *Stud. Hist. Philos. Sci.*, 2013, **44**, 51–65.
109. E. Arunan, G. R. Desiraju, R. A. Klein, J. Sadlej, S. Scheiner, I. Alkorta, D. C. Clary, R. H. Crabtree, J. J. Dannenberg, P. Hobza, H. G. Kjaergaard, A. C. Legon, B. Mennucci, and D. J. Nesbitt, *Pure Appl. Chem.*, 2011, **83**, 1637–1641.
110. E. Arunan, G. R. Desiraju, R. A. Klein, J. Sadlej, S. Scheiner, I. Alkorta, D. C. Clary, R. H. Crabtree, J. J. Dannenberg, P. Hobza, H. G. Kjaergaard, A. C. Legon, B. Mennucci, and D. J. Nesbitt, *Pure Appl. Chem.*, 2011, **83**, 1619–1636.
111. G. R. Desiraju, *Angew. Chem. Int. Ed.*, 2011, **50**, 52–9.
112. T. Steiner and G. R. Desiraju, *Chem. Commun.*, 1998, 891–892.
113. G. A. Jeffrey, *An Introduction to Hydrogen Bonding*, Oxford University Press, Oxford, 1997.
114. R. S. Rowland and R. Taylor, *J. Phys. Chem.*, 1996, **100**, 7384–7391.
115. F. H. Allen, O. Kennard, D. G. Watson, L. Brammer, A. G. Orpen, and R. Taylor, *J. Chem. Soc. Perkin Trans. 2*, 1987, S1.
116. M. C. Etter, J. C. MacDonald, and J. Bernstein, *Acta Cryst. B*, 1990, **46**, 256–262.
117. J. Bernstein, R. E. Davis, L. Shimoni, and N.-L. Chang, *Angew. Chem. Int. Ed.*, 1995, **34**, 1555–1573.
118. N. Fischer, T. M. Klapötke, M. Reymann, and J. Stierstorfer, *Eur. J. Inorg. Chem.*, 2013, 2167–2180.
119. T. M. Klapötke, P. Mayer, C. Miró Sabaté, J. M. Welch, and N. Wiegand, *Inorg. Chem.*, 2008, **47**, 6014–27.
120. T. M. Klapötke and J. Stierstorfer, *J. Am. Chem. Soc.*, 2009, **131**, 1122–34.
121. G.-H. Tao, Y. Guo, Y.-H. Joo, B. Twamley, and J. M. Shreeve, *J. Mater. Chem.*, 2008, **18**, 5524.
122. T. M. Klapötke and C. Miró Sabaté, *Zeitschrift für Anorg. und Allg. Chemie*, 2009, **635**, 1812–1822.
123. T. M. Klapötke, F. A. Martin, and J. Stierstorfer, *Chem. Eur. J.*, 2012, **18**, 1487–1501.
124. M.-J. Crawford, T. M. Klapötke, F. A. Martin, C. M. Sabaté, and M. Rusan, *Chem. Eur. J.*,

2011, **17**, 1683–1695.

125. T. M. Klapötke and C. M. Sabaté, *Chem. Mater.*, 2008, **20**, 3629–3637.
126. J. Wu, J. Zhang, T. Zhang, and L. Yang, *Cent. Eur. J. Energ. Mater.*, 2015, **12**, 417–437.
127. H. Gao and J. M. Shreeve, *Chem. Rev.*, 2011, **111**, 7377–436.
128. A. Hammerl, T. Klapötke, and H. Piotrowski, *Propellants Explos. Pyrotech.*, 2001, **26**, 161–164.
129. T. Fendt, N. Fischer, T. M. Klapötke, and J. Stierstorfer, *Inorg. Chem.*, 2011, **50**, 1447–58.
130. A. Hammerl, T. M. Klapötke, H. Nöth, M. Warchhold, G. Holl, M. Kaiser, and U. Ticmanis, *Inorg. Chem.*, 2001, **40**, 3570–5.
131. N. Fischer, D. Izsák, T. M. Klapötke, S. Rappenglück, and J. Stierstorfer, *Chem. Eur. J.*, 2012, **18**, 4051–62.
132. T. M. Klapötke, P. Mayer, J. Stierstorfer, and J. J. Weigand, *J. Mater. Chem.*, 2008, **18**, 5248.
133. L. I. Vereshchagin, O. N. Verkhozina, F. A. Pokatilov, A. G. Proidakov, and V. N. Kizhnyaev, *Chem. Heterocycl. Compd.*, 2010, **46**, 206–211.
134. S. R. Ganta, C. G. Miller, and G. K. Williams, 2011, 2.
135. B. Lyhs, D. Bläser, and C. Wölper, *Inorg. Chem.*, 2012, **51**, 5897–5902.
136. S. Schulz, B. Lyhs, G. Jansen, D. Bläser, and C. Wölper, *Chem. Commun.*, 2011, **47**, 3401–3.
137. G. Da Silva and E. D. C. Mattos, *J. Aerosp. Technol. Manag.*, 2011, **3**, 65–72.
138. U. Bemm and H. Östmark, *Acta Cryst. C.*, 1998, **54**, 1997–1999.
139. J. Evers, T. M. Klapötke, P. Mayer, G. Oehlinger, and J. Welch, *Inorg. Chem.*, 2006, **45**, 4996–5007.
140. A. J. Papa, 1969, US3429879.
141. E. T. Niles and B. H. Seaman, 1966, US3288660.
142. K. Banert, S. Richter, D. Schaarschmidt, and H. Lang, *Angew. Chem. Int. Ed.*, 2013, **52**, 3499–502.
143. A. Papa, *J. Org. Chem.*, 1966, **31**, 1426–1430.
144. J. Craik, H. Berger, and A. W. Browne, *J. Am. Chem. Soc.*, 1934, **56**, 2380–2381.
145. E. T. Niles, 1967.
146. A. J. Bracuti and C. Y. Manning, *ADA199160 The Synthesis of Triaminoguanidinium Azide (TAZ)*, Picatinny Arsenal, NJ, 1988.
147. A. J. Bracuti and M. W. Extine, *J. Cryst. Spectrosc. Res.*, 1990, **20**, 31–35.
148. V. P. Sinditskii, A. E. Fogelzang, V. Y. Egorshev, V. V. Serushkin, and V. I. Kolesov, in *Progress in Astronautics and Aeronautics: Volume 185, Solid Propellant Chemistry, Combustion and Motor Interior Ballistics*, eds. V. Yang, T. Brill, and W. Ren, AIAA, Reston, VA, 2000, pp. 99–128.
149. C. W. Fong, *AFATL-TR-81-101 The Formation of Colored Impurities in Triaminoguanidine Nitrate and Related Incompatibility Problems in Gun Propellants*, Elgin AFB Florida, 1981.

150. D. A. Dows, E. Whittle, and G. C. Pimentel, *J. Chem. Phys.*, 1955, **23**, 1475–79.
151. Y. K. Gun'ko and H. Hayden, in *Proc. SPIE 5826, Opto-Ireland 2005: Optical Sensing and Spectroscopy*, eds. H. J. Byrne, E. Lewis, B. D. MacCraith, E. McGlynn, J. A. McLaughlin, G. D. O'Sullivan, A. G. Ryder, and J. E. Walsh, SPIE, Dublin, 2005, vol. 5826, pp. 628–635.
152. T. M. Klapötke, M. Stein, and J. Stierstorfer, *Z. Anorg. Allg. Chem.*, 2008, **634**, 1711–1723.
153. X. Zeng, E. Bernhardt, H. Beckers, and H. Willner, *Inorg. Chem.*, 2011, **50**, 11235–41.
154. J. Bryden, *Acta Cryst.*, 1957, **10**, 677.
155. R. Haiges, M. Rahm, D. A. Dixon, E. B. Garner, and K. O. Christe, *Inorg. Chem.*, 2012, **51**, 1127–1141.
156. J. Adams and R. Small, *Acta Cryst. B*, 1974, **30**, 2191–2193.
157. O. Kennard, J. Coppola, D. Wampler, and K. A. Kerr, *Acta Cryst. B*, 1979, **35**, 3000–3003.
158. R. S. Damse, *J. Hazard. Mater.*, 2009, **172**, 1383–7.
159. J. Songstad and A. Martinsen, *Acta Chim. Scand.*, 1977, **31**, 645–650.
160. G. A. Webb, M. Witanowski, E. W. Randall, J. M. Lehn, J. P. Kintzinger, L. Stefaniak, H. Januszewski, T. Axenrod, and N. Logan, *Nitrogen NMR*, Plenum Publishing Company Ltd., London, 1973.
161. M. Witanowski, *Pure Appl. Chem.*, 1974, **37**, 225–233.
162. W. Beck, W. Becker, K. F. Chew, W. Derbyshire, N. Logan, D. M. Revitt, and D. B. Sowerby, *J. Chem. Soc., Dalt. Trans.*, 1972, 245–247.
163. A. Marshall, Durham University, 1982.
164. C. S. Choi and H. P. Boutin, *Acta Cryst. B*, 1969, **25**, 982–987.
165. T. Gora, *J. Chem. Phys. Solids*, 1971, **32**, 529–534.
166. D. A. Johnson and K. Warr, *The Molecular World: Metals and Chemical Change, Volume 1*, The Open University, Milton Keynes, 2002.
167. J. Thayer and R. West, *Inorg. Chem.*, 1964, **3**, 406–409.
168. J. Thayer and R. West, *Inorg. Chem.*, 1964, **3**, 889–893.
169. E. Wiberg and H. Michaud, *Z. Naturforsch. B*, 1954, **9**, 500–501.
170. D. Forster and W. Horrocks Jr., *Inorg. Chem.*, 1966, **5**, 1510–14.
171. W. Beck, W. P. Fehlhammer, P. Pöllmann, E. Schuirer, and K. Feldl, *Chem. Ber.*, 1967, **100**, 2335–2361.
172. F. Petillon, M.-T. Youinou, and J.-E. Guerchais, *Bull. Soc. Chim. Fr.*, 1969, **12**, 4293.
173. A. Vogler, C. Quett, A. Paukner, and H. Kunkely, *J. Am. Chem. Soc.*, 1986, **108**, 8263–8265.
174. M. Hampden-Smith, D. Lei, and E. Duesler, *J. Chem. Soc., Dalt. Trans.*, 1990, 2953–2957.
175. P. B. Hitchcock, M. F. Lappert, A. V Protchenko, and P. G. H. Uiterweerd, *Dalt. Trans.*, 2009, 353–61.
176. J. Halfpenny, *Acta Cryst. C.*, 1995, **51**, 2044–2046.
177. P. A. W. Dean and D. F. Evans, *J. Chem. Soc. A*, 1968, 1154.

178. N. Wiberg and K. Schmid, *Chem. Ber.*, 1967, **100**, 748–754.
179. V. B. Busch, J. Pebler, and K. Dehnicke, *Z. Anorg. Allg. Chem.*, 1975, **416**, 203–210.
180. R. H. Herber and H.-S. Cheng, *Inorg. Chem.*, 1969, **8**, 2145–2148.
181. H.-S. Cheng and R. H. Herber, *Inorg. Chem.*, 1970, **9**, 1686–1690.
182. R. B. Johannesen, F. E. Brinckman, and T. D. Coyle, *J. Phys. Chem.*, 1968, **72**, 660–667.
183. M. F. Davis, M. Clarke, W. Levason, G. Reid, and M. Webster, *Eur. J. Inorg. Chem.*, 2006, **2006**, 2773–2782.
184. M. F. Davis, W. Levason, G. Reid, and M. Webster, *Polyhedron*, 2006, **25**, 930–936.
185. V. N. N. Zakharov, A. V. V. Yatsenko, A. L. L. Kamyshnyi, and L. A. A. Aslanov, *Koord. Khim.*, 1991, **17**, 789–794.
186. Z.-H. Su, B.-B. Zhou, Z.-F. Zhao, and S. W. Ng, *Acta Cryst. E*, 2007, **63**, m394–m395.
187. M. Webster, P. J. Jones, R. C. G. Killean, and J. L. Lawrence, *J. Chem. Soc. A*, 1969, 482–485.
188. S. Alvarez, *Dalt. Trans.*, 2013, **42**, 8617–36.
189. G. Matsubayashi and J. Iyoda, *Bull. Chem. Soc. Jpn.*, 1977, **50**, 3055–3056.
190. G. R. Fulmer, A. J. M. Miller, N. H. Sherden, H. E. Gottlieb, A. Nudelman, B. M. Stoltz, J. E. Bercaw, and K. I. Goldberg, *Organometallics*, 2010, **29**, 2176–2179.
191. D. Tudela and F. Rey, *Z. Anorg. Allg. Chem.*, 1989, **575**, 202–208.
192. R. Haiges, A. Vij, J. A. Boatz, S. Schneider, T. Schroer, M. Gerken, and K. O. Christe, *Chem. Eur. J.*, 2004, **10**, 508–517.
193. A. Schulz and A. Villinger, *Chem. Eur. J.*, 2016, **22**, 2032–2038.
194. A. E. Ayers, D. S. Marynick, and H. V Dias, *Inorg. Chem.*, 2000, **39**, 4147–51.
195. H. V. R. Dias and A. E. Ayers, *Polyhedron*, 2002, **21**, 611–618.
196. A. Akkari, J. J. Byrne, I. Saur, G. Rima, H. Gornitzka, and J. Barrau, *J. Organomet. Chem.*, 2001, **622**, 190–198.
197. A. E. Ayers, T. M. Klapötke, and H. V. R. Dias, *Inorg. Chem.*, 2001, **40**, 1000–1005.
198. Y. Ding, H. W. Roesky, M. Noltemeyer, and P. P. Power, *Organometallics*, 2001, **20**, 1190–1194.
199. V. N. Khrustalev, I. A. Portnyagin, N. N. Zemlyansky, I. V. Borisova, Y. A. Ustynyuk, and M. Y. Antipin, *J. Organomet. Chem.*, 2005, **690**, 1056–1062.
200. W. P. Leung, K. W. Kan, Y. C. Chan, and T. C. W. Mak, *Eur. J. Inorg. Chem.*, 2014, 3191–3199.
201. T. Ochiai, D. Franz, E. Irran, and S. Inoue, *Chem. - A Eur. J.*, 2015, **21**, 6704–6707.
202. T. Ochiai and S. Inoue, *Phosphorus. Sulfur. Silicon Relat. Elem.*, 2016, **191**, 624–627.
203. D. Amalric-Popescu and F. Bozon-Verduraz, *Catal. Today*, 2001, **70**, 139–154.
204. I. Agrell, *Acta Chem. Scand.*, 1969, **23**, 1667–1678.
205. I. Agrell, *Acta Chem. Scand.*, 1970, **24**, 1247–61.
206. A. Pacher, C. Schrenk, and A. Schnepf, *J. Organomet. Chem.*, 2010, **695**, 941–944.

207. R. Cortés, M. Drillon, L. Lezama, X. Solans, and T. Rojo, *Inorg. Chem.*, 1997, **36**, 677–683.
208. B. Peerless and P. Portius, 2014, unpublished results.
209. I. A. Trojan, M. I. Eremets, S. A. Medvedev, A. G. Gavriliuk, and V. B. Prakapenka, *Appl. Phys. Lett.*, 2008, **93**, 91907.
210. A. Katrusiak, M. Szafrański, and M. Podsiadło, *Chem. Commun.*, 2011, **47**, 2107–9.
211. S. Li, Q. Li, K. Wang, X. Tan, M. Zhou, B. Li, B. Liu, G. Zou, and B. Zou, *J. Phys. Chem. B*, 2011, **115**, 11816–22.
212. D. Laniel, L. E. Downie, J. S. Smith, D. Savard, M. Murugesu, and S. Desgreniers, *J. Chem. Phys.*, 2014, **141**, 234506.
213. K. Srinivas, S. Sitha, V. J. Rao, K. Bhanuprakash, and K. Ravikumar, *J. Mater. Chem.*, 2006, **16**, 496.
214. A. Chouai and E. E. Simanek, *J. Org. Chem.*, 2008, **73**, 2357–2366.
215. N. Mibu, K. Yokomizo, A. Koga, M. Honda, K. Mizokami, H. Fujii, N. Ota, A. Yuzuriha, K. Ishimaru, J. Zhou, T. Miyata, and K. Sumoto, *Chem. Pharm. Bull.*, 2014, **62**, 1032–1040.
216. D. Kumar, S. I. Khan, P. Ponnan, and D. S. Rawat, *New J. Chem.*, 2014, **38**, 5087–5095.
217. B. V. Lotsch and W. Schnick, *Chem. Mater.*, 2006, **18**, 1891–1900.
218. L. De Luca, G. Giacomelli, and A. Porcheddu, *Org. Lett.*, 2002, **4**, 553–555.
219. S. Khan, S. Roy, R. Roy, A. Ghatak, A. Pramanik, and S. Bhar, *Tetrahedron Lett.*, 2014, **55**, 5019–5024.
220. M. Shariat, M. W. Samsudin, and Z. Zakaria, *Molecules*, 2012, **17**, 11607–11615.
221. Z. Yan, W. L. Xue, Z. X. Zeng, and M. R. Gu, *Ind. Eng. Chem. Res.*, 2008, **47**, 5318–5322.
222. F. Cherioux, P. Audebert, and P. Hapiot, *Chem. Mater.*, 1998, **10**, 1984–1989.
223. R. F. Evans and W. Kynaston, *J. Chem. Soc.*, 1962, 1005–1008.
224. J. J. Curley, R. G. Bergman, and T. D. Tilley, *Dalt. Trans.*, 2012, **41**, 192–200.
225. W. Z. Bruegel, *Elektrochem. (Ber. Bunsenes. Phys. Chem.)*, 1962, **66**, 159.
226. H. Nuss, J. Nuss, and M. Jansen, *Z. Krist. New Cryst. Struct.*, 2005, **220**, 95–96.
227. V. Morozova, P. Mayer, and G. Berionni, *Angew. Chem. Int. Ed.*, 2015, **2**, 14508–14512.
228. R. Meyer, J. Köhler, and A. Homburg, *Explosives*, Wiley-VCH & Co. KGaA, Weinheim, Sixth Ed., 2007.
229. P. Gray, *Q. Rev. Chem. Soc.*, 1963, **17**, 441–473.
230. W. P. Fehlhammer and W. Beck, *Z. Anorg. Allg. Chem.*, 2015, **641**, 1599–1678.
231. L. Birkofer and P. Wegner, *Org. Synth.*, 1970, **50**, 107.
232. Bruker *APEX2*, Bruker AXS Inc., Madison, Wisconsin, 2012.
233. Bruker *SAINT*, Bruker AXS Inc., Madison, Wisconsin, 2007.
234. Siemens Area Detector Absorption Correction *(SADABS)*, G. M. Sheldrick, 2007.
235. *SHELXS-97*, G. M. Sheldrick, *Acta Cryst. A*, 2008, **64**, 112–22
236. *Shelxtl*, G. M. Sheldrick, *Acta Cryst. A*, 2008, **64**, 112–22.

237. *SHELXT*, G. M. Sheldrick, *Acta Cryst. A*, 2015, **71**, 3–8.
238. L. J. Farrugia, *J. Appl. Crystallogr.*, 1999, **32**, 837–838.
239. L. J. Farrugia, *J. Appl. Crystallogr.*, 2012, **45**, 849–854.
240. L. J. Farrugia, *J. Appl. Crystallogr.*, 1997, **30**, 565–565.
241. *DIFFRAC.EVA* v3.1, Bruker AXS Inc., 2010.
242. G. S. Pawley, *J. Appl. Crystallogr.*, 1981, **14**, 357–361.
243. *TOPAS Academic*, A. A. Coelho, 2007.
244. E. M. Arnett and B. Chawla, *J. Am. Chem. Soc.*, 1978, **100**, 214–216.
245. R. L. Lichter and J. D. Roberts, *J. Am. Chem. Soc.*, 1971, **93**, 5218–5224.